RECENT TRENDS IN COMPUTATIONAL FLUID DYNAMICS,
2nd Edition

EDITED BY: Muhammad Mubashir Bhatti, Marin I. Marin, Ahmed Zeeshan and Sara I. Abdelsalam
PUBLISHED IN: Frontiers in Physics

frontiers Research Topics

Frontiers eBook Copyright Statement

The copyright in the text of individual articles in this eBook is the property of their respective authors or their respective institutions or funders. The copyright in graphics and images within each article may be subject to copyright of other parties. In both cases this is subject to a license granted to Frontiers.

The compilation of articles constituting this eBook is the property of Frontiers.

Each article within this eBook, and the eBook itself, are published under the most recent version of the Creative Commons CC-BY licence. The version current at the date of publication of this eBook is CC-BY 4.0. If the CC-BY licence is updated, the licence granted by Frontiers is automatically updated to the new version.

When exercising any right under the CC-BY licence, Frontiers must be attributed as the original publisher of the article or eBook, as applicable.

Authors have the responsibility of ensuring that any graphics or other materials which are the property of others may be included in the CC-BY licence, but this should be checked before relying on the CC-BY licence to reproduce those materials. Any copyright notices relating to those materials must be complied with.

Copyright and source acknowledgement notices may not be removed and must be displayed in any copy, derivative work or partial copy which includes the elements in question.

All copyright, and all rights therein, are protected by national and international copyright laws. The above represents a summary only. For further information please read Frontiers' Conditions for Website Use and Copyright Statement, and the applicable CC-BY licence.

ISSN 1664-8714
ISBN 978-2-88966-900-4
DOI 10.3389/978-2-88966-900-4

About Frontiers

Frontiers is more than just an open-access publisher of scholarly articles: it is a pioneering approach to the world of academia, radically improving the way scholarly research is managed. The grand vision of Frontiers is a world where all people have an equal opportunity to seek, share and generate knowledge. Frontiers provides immediate and permanent online open access to all its publications, but this alone is not enough to realize our grand goals.

Frontiers Journal Series

The Frontiers Journal Series is a multi-tier and interdisciplinary set of open-access, online journals, promising a paradigm shift from the current review, selection and dissemination processes in academic publishing. All Frontiers journals are driven by researchers for researchers; therefore, they constitute a service to the scholarly community. At the same time, the Frontiers Journal Series operates on a revolutionary invention, the tiered publishing system, initially addressing specific communities of scholars, and gradually climbing up to broader public understanding, thus serving the interests of the lay society, too.

Dedication to Quality

Each Frontiers article is a landmark of the highest quality, thanks to genuinely collaborative interactions between authors and review editors, who include some of the world's best academicians. Research must be certified by peers before entering a stream of knowledge that may eventually reach the public - and shape society; therefore, Frontiers only applies the most rigorous and unbiased reviews.
Frontiers revolutionizes research publishing by freely delivering the most outstanding research, evaluated with no bias from both the academic and social point of view.
By applying the most advanced information technologies, Frontiers is catapulting scholarly publishing into a new generation.

What are Frontiers Research Topics?

Frontiers Research Topics are very popular trademarks of the Frontiers Journals Series: they are collections of at least ten articles, all centered on a particular subject. With their unique mix of varied contributions from Original Research to Review Articles, Frontiers Research Topics unify the most influential researchers, the latest key findings and historical advances in a hot research area! Find out more on how to host your own Frontiers Research Topic or contribute to one as an author by contacting the Frontiers Editorial Office: frontiersin.org/about/contact

RECENT TRENDS IN COMPUTATIONAL FLUID DYNAMICS,
2nd Edition

Topic Editors:
Muhammad Mubashir Bhatti, Shanghai University, China
Marin I. Marin, Transilvania University of Brașov, Romania
Ahmed Zeeshan, International Islamic University, Islamabad, Pakistan
Sara I. Abdelsalam, National Autonomous University of Mexico, Mexico

Publisher's note: This is a 2nd edition due to an article retraction.

Citation: Bhatti, M. M., Marin, M. I., Zeeshan, A., Abdelsalam, S. I., eds. (2021). Recent Trends in Computational Fluid Dynamics, 2nd Edition. Lausanne: Frontiers Media SA. doi: 10.3389/978-2-88966-900-4

Table of Contents

frontiers in Physics

EDITORIAL
published: 01 October 2020
doi: 10.3389/fphy.2020.593111

Editorial: Recent Trends in Computational Fluid Dynamics

M. M. Bhatti[1]*, M. Marin[2], A. Zeeshan[3] and Sara I. Abdelsalam[4]

[1] College of Mathematics and Systems Science, Shandong University of Science and Technology, Qingdao, China, [2] Department of Mathematics and Computer Science, Transilvania University of Brasov, Brasov, Romania, [3] Department of Mathematics and Statistics, FBAS, IIU, Islamabad, Pakistan, [4] Basic Science, Faculty of Engineering, The British University in Egypt, Al-Shorouk City, Egypt

Keywords: computational fluid dynamics, non-Newtonian/Newtonian fluids, heat and mass transfer, multiphase flow simulations, thermodynamics, nanofluids

Editorial on the Research Topic

Recent Trends in Computational Fluid Dynamics

Computational fluid dynamics (CFD) [1] can be described as the set of techniques that assist the computer to provide the numerical simulation of the fluid flows. The three basic principles that can determine the physical aspects of any fluid are the i) energy conservation, ii) Newton's second law, and the iii) mass conservation. These flow problem can be described in terms of these basic laws. Mathematical equations, which are usually in the form of partial differential equations, portrayed the fluid behavior in the flow domain.

The solutions and interactive behavior of solid boundaries with fluid or interaction between the layers of the fluid while flowing are visualized using some CFD techniques. CFD helps replace these differential equations of fluid flow into numbers, and these numbers are beneficial in time and/or space which enable a numerical picture of the complete fluid flow. CFD is powerful in examining a system's behavior, beneficial, and more innovative in designing a system [2]. Also, It is efficient in exploring the system's performance metrics, whether it is for the yielding higher profit margins or in enhancing operational safety, and in various advantageous features [3].

Nowadays, CFD techniques are usually applied in various fields [4–8] i.e. car design, turbomachinery, ship design, and aircraft manufacturing. Moreover, it is beneficial in astrophysics, biology, oceanography, oil recovery, architecture, and meteorology. Numerous numerical Algorithm and software have been developed to perform CFD analysis. Due to the recent advancement in computer technology, numerical simulation for physically and geometrically complex systems can also be evaluated using PC clusters. Large scale simulations in different fluid flow on grids containing millions and trillions of elements can be achieved within a few hours via supercomputers. However, it is completely incorrect to think that CFD describes a mature technology, there are numerous open questions related to heat transfer, combustion modeling, turbulence, and efficient solution methods or discretization methods, etc. The coupling between CFD and other disciplines required further research, therefore, the main goal of this issue is to fill an essential gap that is greatly missed in this field. We sincerely hope that this issue will be beneficial to the readers to present the recent findings in the field and shed some light on the industrial sector.

Rafique et al. [9] used Buongiorno model to discuss the Casson nanofluid boundary layer flow through an inclined surface under the impact of Dufour and Soret. This nonlinear model is beneficial to understand the mechanism of heat and mass transfer by contemplating various essential features of the proposed boundary layer. Further, the Keller-box technique has been used to simulate the results. The results show that the Dufour effect has a strong impact on the temperature profile and

OPEN ACCESS

Edited and reviewed by:
José S. Andrade Jr,
Federal University of Ceara, Brazil

***Correspondence:**
M. M. Bhatti
mmbhatti@sdust.edu.cn;
mubashirme@yahoo.com

Specialty section:
This article was submitted to Mathematical and Statistical Physics, a section of the journal Frontiers in Physics

Received: *09 August 2020*
Accepted: *11 September 2020*
Published: *01 October 2020*

Citation:
Bhatti M.M, Marin M, Zeeshan A and Abdelsalam SI (2020) Editorial: Recent Trends in Computational Fluid Dynamics. Front. Phys. 8:593111. doi: 10.3389/fphy.2020.593111

that the thermophoresis produces an inverse impact on the concentration profile as compared with the temperature profile.

Shah et al. [10] investigated the CVFEM simulation to determine the nanoparticle's migration toward a permeable domain. The considered fluid model contains aluminum oxide nanoparticles. Darcy law, thermal radiation, Lorentz force, and shape factor. The proposed approach is beneficial for the two common schemes of CFD. In the proposed study, it was found that higher convection occurs due to the great influence of shape factor. According to the authors' simulation, it was shown that the magnetic field and temperature gradient have an inverse relationship. Later, Shah et al. [11] studied the behavior of couple stress fluid and non-isothermal convection with magnetic effects over a nonlinear sheet. Analytical simulation with the help of homotopy analysis method has been proposed for the solutions. According to their study, they found that the primary velocity faces significant resistance during the flow. In their proposed simulation, they noticed that magnetic effects produce resistance in the angular velocity, but enhances the temperature profile. Also, the Grashof number and Hall effects show a positive response to the temperature profile.

Shah et al. [12] contemplated the Mohand decomposition scheme to examine the Kortewege–De Vries equations. The fractional derivatives are expressed by Caputo fractional derivative operator. The validation and effectiveness of this scheme have been determined using numerical examples for integer order and fractional problems. According to their results, they concluded that the proposed scheme is easily adaptable, straightforward, and beneficial to solve nonlinear problems.

Irfan et al. [13] investigated the magnetized nanofluid motion with variable features propagating through a radiatively stretching sheet. Their proposed scheme was a numerical shooting method and the bvp4c built-in command in MATLAB. It was noticed that the thermophoresis, thermal conductivity, radiation parameter, and Brownian motion boost the thermal boundary layer. Further, in the proposed simulation, it was found that the Prandtl number suppresses the thermal profile. On the other hand, Brownian motion and Lewis numbers were seen to cause a strong influence on concentration profile, whereas the thermophoretic force was seen to produce and opposite effects. Later, Irfan et al. [14] used computational formulation, i.e., simplified finite difference scheme to establish and discuss the effects of porosity, thermal radiation, a magnetic and electric field with heat generation and absorption. A comparative study is also given using the simplified finite difference scheme and bvp4c where it was noticed that the model has a higher convergence rate.

Shafiq et al. [15] examined and discussed the motion of carbon nanotubes (CNTs) (single- and multi-walled) over a Riga plate. The Riga plate is filled with water as a base fluid. They used the Marangoni model for the fully developed electro-magnetohydrodynamics flow. They proposed homotopy analysis method for the graphical and numerical outcomes. They noticed that multi-walled CNTs have higher velocity as compared with single-walled CNTs. They found similar outcomes of the magnetic field on temperature as already done by Shah et al. [11].

Bilal et al. [16] used a similar scheme used by Rafique et al. [9] to examine flow behavior betwixt a pair of rotating disks. They used the theory of the Cattaneo–Christov and Darcy model to formulate the proposed formulation. Further, Karman transformations have been used to model the mathematical modeling and numerical outcomes presented using the finite difference approach. They found that a higher Reynolds number produces resistance in the radial and axial velocities at the lower disk as compared with the upper disk. Further, the thermal profile was reduced due to the strong impact of the Prandtl number. At the lower disk, the shear drag coefficient diminishes while at the upper disk, the wall shear coefficient increases. Later, Ullah et al. [17] considered a similar geometry [16] with a three-dimensional Darcy–Forchheimer model and nanofluid flow. A computational shooting scheme was used to operate the proposed formulation. They found that the Darcy–Forchheimer model effects are negligible on the concentration and temperature profile.

Ahmed et al. [18] analyzed the concealed behavior of thermally radiative and magnetically influenced γAl_2O_3–H_2O and Al_2O_3–H_2O nanofluid flow through a wedge. Combined simulation of shooting and RK scheme was used to evaluate the numerical outcomes. Their simulation shows that the Hartree pressure gradient significantly enhances the nanofluids velocity. The proposed composition of γAl_2O_3–H_2O and Al_2O_3–H_2O becomes denser due to the strong impact of volume fraction and accordingly opposes the velocity field. The thermal profile γAl_2O_3–H_2O and Al_2O_3–H_2O rises for higher volume fraction.

Ahmed and Khan [19] examined the mechanism of sodium-alginate ($C_6H_9NaO_7$) through a vertical heated plate with acceleration. Further, they contemplated the effects of convection and discussed the entropy generation. Laplace transforms with a combination of integral transforms that were used to generate the exact results. It was concluded that the maximal entropy can be achieved by taking higher values of Brinkmann number, fluid parameter, and Grashof number. It was also noticed that the Bejan number can also be maximal if the Prandtl number is high. The proposed fluid model reveals a dual impact.

Bhatti et al. [20] performed a theoretical analysis of the blood flow under the suspension of nanoparticles and microorganisms through an anisotropic artery in a sinusoidal form. The authors investigated a nonlinear Sutterby fluid model as blood to examine the rheological effects. A perturbation approach was used to elaborate on the series solutions. In their analysis, it was found that the non-Newtonian effects are in favor to resist the flow. Further, they noticed that the wall shear stress diminishes due to the stenosis, nanoparticle, and thermal Grashof number. Moreover, The Peclet number was found to create resistance in the microorganism profile. The results of this study play a significant role in biomedical engineering. Riaz et al. [21] presented a study that is beneficial for the urinary tract infections when the flow is sinusoidal. This analysis is essential to examine white particles occurring in the urine. They investigated the flow in a curved configuration with flexible walls and filled with particles in a fluid. A lubrication theory and perturbation approach was used to formulate the governing equations. Further, they also carried out the numerical results for the pressure along the whole channel.

Alzahrani et al. [22] investigated the magnetohydrodynamics of a 3D flow through a rotating permeable conduit under the effect of Dufour and Soret and viscous dissipation. A viscous electrically-conducting fluid is considered upon which applied a magnetic field. Suitable transformations are used to transform from a nonlinear partial differential system of equations to an ordinary system of equations after which results were computed numerically using the shooting method. Then the pertinent parameters affecting the physical variables of the flow field have been thoroughly investigated.

Sanni et al. [23] studied the MHD flow of an incompressible Maxwell fluid flow induced by a quadratic stretching sheet through a 2D boundary layer. A variable magnetic field was applied to the flow with heat transfer, thermal radiation, and viscous dissipation. The system of partial differential equations has been transformed into ordinary differential equations (ODEs) by using some similarity variables. Numerical results have been achieved to find solutions to the energy and momentum equations in a closed-form.

Ahmed et al. [24] studied the peristaltic micropolar fluid flow influenced upon by heat and mass transfer with the magnetic field. The system of governing equations has been presented using a curvilinear coordinate system where they were further reduced using a lubrication approximation. Solutions were then derived by implementing the finite difference method.

Khan et al. [25] explored the thermal Eyring–Powell nano-liquid with triple diffusion via a periodic-moving system. A combination of some important parameters, such as the porosity parameter and magnetic effect, was also discussed. The Buongiorno's nanofluid theory was investigated through the thermophoretic and Brownian motion effects. Further, the homotopy algorithm was used in order to analyze the fluid flow in a non-dimensional form.

Karuppusamy et al. [26] examined an entropy generation of a nanofluid of third-order with slip effect. The flow investigated was caused by a stretchable sheet through a porous plate under the influence of thermal radiation. Several other influential effects were taken into accounts such as the non-Fourier heat flux, convective surface boundary, and nanoparticle concentration on zero mass flux conditions. Similarity variables have been used in order to solve the governing physical system of equations and modify it into a nonlinear system of ODEs. Results were obtained using the usual homotopy algorithm to discuss the outcomes of the analysis.

AUTHOR CONTRIBUTIONS

MMB and MM drafted the first version of the editorial. AZ and SIA revised the first draft and made contributions about papers they edited.

FUNDING

MMB was supported by the Cultivation Project of Young and Innovative Talents in Universities of Shandong Province (Nonlinear Sciences Research Team).

REFERENCES

1. Anderson JD, Wendt J. *Computational fluid dynamics.* New York, NY: McGraw-Hill (1995).
2. Andersson B, Andersson R, Håkansson L, Mortensen M, Sudiyo R, Van Wachem B. *Computational fluid dynamics for engineers.* Cambridge, England:Cambridge University Press (2011).
3. Ferziger JH, Perić M, Street RL. *Computational methods for fluid dynamics.* Berlin: Springer (2002).
4. Chen Q. *Computational fluid dynamics of HVAC: successes and failures.* Atlanta, GA: American Society of Heating, Refrigerating and Air-Conditioning Engineers, Inc. (1997).
5. Kamyar A., Saidur R., Hasanuzzaman M. Application of computational fluid dynamics (CFD) for nanofluids. *Int J Heat Mass Transf* (2012) **55**(15–16): 4104–4115. doi:10.1016/j.ijheatmasstransfer.2012.03.052
6. Zakaria MS, Ismail F, Tamagawa M, Azi AF, Wiriadidjaya S, Basri AA, et al. Computational fluid dynamics study of blood flow in aorta using OpenFOAM. *J Adv Res Fluid Mech Thermal Sci* (2018) **43**:81–9.
7. Kozelkov AS, Kurulin VV, Lashkin SV, Shagaliev RM, Yalozo AV. Investigation of supercomputer capabilities for the scalable numerical simulation of computational fluid dynamics problems in industrial applications. *Comput Math Math Phys* (2016) **56**(8):1506–1516. doi:10.1134/s0965542516080091
8. Mader CA, Kenway GK, Yildirim A, Martins JR. ADflow: an open-source computational fluid dynamics solver for aerodynamic and multidisciplinary optimization. *J Aero Inf Syst* (2020) **17**:1–20. doi:10.2514/1.i010796
9. Rafique K, Anwar MI, Misiran M, Khan I, Alharbi SO, Thounthong P, et al. Numerical solution of Casson nanofluid flow over a non-linear inclined surface with Soret and Dufour effects by Keller–Box method. *Front Phys* (2020) **7**:1–21.
10. Shah Z, Babazadeh H, Kumam P, Shafee A, Thounthong P. Numerical simulation of magnetohydrodynamic nanofluids under the influence of shape factor and thermal transport in a porous media using CVFEM. *Front Phys* (2019) **7**:2396. doi:10.3389/fphy.2019.00164
11. Shah Z, Kumam P, Dawar A, Alzahrani EO, Thounthong P. Study of the couple stress convective micropolar fluid flow in a hall MHD generator system. *Front Phys* (2020) **7**:171. doi:10.3389/fphy. 2019 Nov 5.
12. Shah R, Farooq U, Khan H, Baleanu D, Kumam P, Arif M. Fractional view analysis of third order Kortewege–De Vries equations, using a new analytical technique. *Front Phys* (2020) **7**:244. doi:10.3389/fphy.2019.00244
13. Irfan M, Farooq MA, Iqra T. Magnetohydrodynamic free stream and heat transfer of nanofluid flow over an exponentially radiating stretching sheet with variable fluid properties. *Front Phys* (2019) **7**:186. doi:10.3389/fphy.2019.00186
14. Irfan M, Farooq MA, Iqra T. A new computational technique design for EMHD nanofluid flow over a variable thickness surface with variable liquid characteristics. *Front Phys* (2020) **8**:66. doi:10.3389/fphy.2020.00066
15. Shafiq A, Zari I, Khan I, Khan TS. Marangoni driven boundary layer flow of carbon nanotubes towards a Riga plate. *Front Phys* (2019) **7**:215. doi:10.3390/math7111087
16. Bilal S, Tassaddiq A, Majeed AH, Ali F, Malik MY. Computational and physical examination about the aspects of fluid flow between two coaxially rotated disks by capitalizing non-Fourier heat flux theory: finite difference approach. *Front Phys* (2020) **7**:209. doi:10.3389/fphy.2019.00209
17. Ullah MZ, Serra-Capizzano S, Baleanu D. A numerical simulation for Darcy–Forchheimer flow of nanofluid by a rotating disk with partial slip effects. *Front Phys* (2020) **7**:741–52. doi:10.3389/fphy.2019.00219
18. Naveed Ahmed A, Khan U, Mohyud-Din S-T, Khan I, Murtaza R, Hussain I, et al. Novel investigation and hidden effects of MHD and thermal radiations in viscous dissipative nanofluid flow models. *Front Phys* (2020) **8**:75. doi:10.3389/fphy.2020.00075
19. Ahmed TN, Khan I. Entropy generation in $C_{(6)}H_{(9)}NAO_{(7)}$ fluid over an accelerated heated plate. *Front Phys.* (2020) **7**:250. doi:10.3389/fphy.2019.00250

20. Bhatti MM, Marin M, Zeeshan A, Ellahi R, Abdelsalam SI. Swimming of motile gyrotactic microorganisms and nanoparticles in blood flow through anisotropically tapered arteries. *Front Phys* (2020) **8**:95. doi:10.3389/fphy.2020.00095
21. Riaz A, Sadiq MA. Particle–fluid suspension of a non-Newtonian fluid through a curved passage: an application of urinary tract infections. *Front Phys* (2020) **8**:109. doi:10.3389/fphy.2020.00109
22. Alzahrani AK, Ullah MZ, Muhammad T. Numerical treatment for 3D squeezed flow in a rotating channel with Soret and Dufour effects. *Front Phys* (2020) **8**:201. doi:10.3389/fphy.2020.00201
23. Sanni KM, Hussain Q, Asghar S. Heat transfer analysis for non-linear boundary driven flow over a curved stretching sheet with a variable magnetic field. *Front Phys* (2020) **8**:113. doi:10.3389/fphy.2020.00113
24. Ahmed R, Ali N, Khan SU, Rashad AM, Nabwey HA, Tlili I. Novel microstructural features on heat and mass transfer in peristaltic flow through a curved channel. *Front Phys* (2020) **8**:178. doi:10.3389/fphy.2020.00178
25. Khan SU, Vaidya H, Tlili I, Prasad KV. Triple diffusive unsteady flow of Eyring–Powell nanofluid over a periodically accelerated surface with variable thermal features. *Front Phys* (2020) **8**:246. doi:10.3389/fphy.2020.00246
26. Karuppusamy L, Muhiuddin G, Alanazi AM, Alkhaldi AH, Rajan S. Entropy optimization of 3rd-grade nanofluid slip flow embedded in a porous sheet with zero mass flux and non-Fourier heat flux model. *Front Phys* (2020) **8**:250.

Conflict of Interest: The authors declare that the research was conducted in the absence of any commercial or financial relationships that could be construed as a potential conflict of interest.

Copyright © 2020 Bhatti, Marin, Zeeshan and Abdelsalam. This is an open-access article distributed under the terms of the Creative Commons Attribution License (CC BY). The use, distribution or reproduction in other forums is permitted, provided the original author(s) and the copyright owner(s) are credited and that the original publication in this journal is cited, in accordance with accepted academic practice. No use, distribution or reproduction is permitted which does not comply with these terms.

frontiers in Physics

ORIGINAL RESEARCH
published: 11 October 2019
doi: 10.3389/fphy.2019.00139

Check for updates

Numerical Solution of Casson Nanofluid Flow Over a Non-linear Inclined Surface With Soret and Dufour Effects by Keller-Box Method

Khuram Rafique [1], Muhammad Imran Anwar [1,2,3], Masnita Misiran [1], Ilyas Khan [4], S. O. Alharbi [5], Phatiphat Thounthong [6] and K. S. Nisar [7]*

[1] School of Quantitative Sciences, Universiti Utara Malaysia, Sintok, Malaysia, [2] Department of Mathematics, Faculty of Science, University of Sargodha, Sargodha, Pakistan, [3] Higher Education Department (HED) Punjab, Lahore, Pakistan, [4] Faculty of Mathematics and Statistics, Ton Duc Thang University, Ho Chi Minh City, Vietnam, [5] Department of Mathematics, College of Science Al-Zulfi, Majmaah University, Al Majmaah, Saudi Arabia, [6] Department of Teacher Training in Electrical Engineering, Faculty of Technical Education, Renewable Energy Research Centre, King Mongkut's University of Technology North Bangkok, Bang Sue, Thailand, [7] Department of Mathematics, College of Arts and Sciences, Prince Sattam bin Abdulaziz University, Wadi Al Dawasir, Saudi Arabia

In this article, the effects of a Casson Nanofluid boundary layer flow, over an inclined extending surface with Soret and Dufour, is scrutinized. The model used in this study is based on the Buongiorno model of the thermal efficiencies of the fluid flows in the presence of Brownian motion and thermophoresis properties. The non-linear problem for Casson Nanofluid flow over an inclined channel is modeled to gain knowledge on the heat and mass exchange phenomenon, by considering important flow parameters of the intensified boundary layer. The governing non-linear partial differential equations are changed to non-linear ordinary differential equations and are afterward illustrated numerically by the Keller-Box scheme. A comparison of the established results, if the incorporated effects are lacking, is performed with the available outcomes of Khan and Pop [1] and recognized in a nice settlement. Numerical and graphical results are also presented in tables and graphs.

Keywords: casson nanofluid, MHD, power law fluid, soret effect, dufour effect, inclined surface

OPEN ACCESS

Edited by:
Muhammad Mubashir Bhatti, Shanghai University, China

Reviewed by:
Devendra Kumar, University of Rajasthan, India
Mohammad Rahimi Gorji, Ghent University, Belgium
Mohammad Mehdi Rashidi, Tongji University, China

****Correspondence:***
Ilyas Khan
ilyaskhan@tdtu.edu.vn

Specialty section:
This article was submitted to Mathematical Physics, a section of the journal Frontiers in Physics

Received: *08 July 2019*
Accepted: *06 September 2019*
Published: *11 October 2019*

Citation:
Rafique K, Anwar MI, Misiran M, Khan I, Alharbi SO, Thounthong P and Nisar KS (2019) Numerical Solution of Casson Nanofluid Flow Over a Non-linear Inclined Surface With Soret and Dufour Effects by Keller-Box Method. Front. Phys. 7:139. doi: 10.3389/fphy.2019.00139

INTRODUCTION

In recent times, nanofluid has accomplished an incredible position among scientists because of its dynamic thermal performance and notable potential in the number of heat transfers without any pressure drops. Nanofluid is a formula of various nanoparticles, containing Al_2O_3, Cu, CuO, in a base liquid, for example, oil, water, ethylene glycol, and so forth. It is investigated through examination that the thermal conductivity of base fluid is usually not exactly the same as the nanofluid Choi and Eastman [2]. Nanofluid is used as a working fluid (base fluid) due to its high thermal conductivity. Buongiorno [3] examined the causes that perform a key job in the advancement of nanofluid's thermal conductivity. He perceived that the Brownian movement and thermophoresis effects in conventional fluid play an important role to enhance the thermal conductivity of the fluid. Nield and Kuznetsov [4] considered the result of thermophoresis and Brownian movement on the boundary layer stream. The steady flow of nanofluid on an extending sheet was examined by Khan and Pop [1]. Anwar et al. [5] presented the Brownian movement and thermophoresis impact on the heat and mass exchange of nanofluids over a non-linear extending sheet. Suriyakumar and Devi [6] examined the nanofluid flow over a slanted sheet. Ziaei-Rad et al. [7] investigated a similar solution of nanofluid stream on a slanted surface. Thumma et al. [8]

discussed the nanofluid flow on a slanted plate by incorporating the heat source. Govindarajan [9] discussed the flow of nanofluid over a slanted sheet by incorporating a non-uniform temperature. Khan et al. [10] illustrated the heat and mass transfer of MHD Jeffery nanofluid flow over an inclined sheet. Nanofluid flow with radiation effects on a slanted surface was examined by Chakraborty [11]. Recently, different scholars investigated the nanofluid flow on different models, as some of them are given in references [12–18].

The investigation of boundary layer flow and heat exchange on a stretching surface has been considered by various experts due to its immense mechanical and designing applications in the field of industry, and engineering, for example, strengthening and tinning of copper wires, assembling plastic and elastic sheets, non-stop cooling and fiber turning, expulsion of polymer, wire drawing, food processing, and paper, and so forth. Boundary layer flow on a steady surface was first investigated by Sakiadis [19]. Additionally, Crane [20] considered the closed structure solution of boundary layer flow on an extending sheet. Ali et al. [21] investigated the conjugate effects of heat and mass exchange on MHD free convection flow over an inclined plate. Ramesh et al. [22] investigated the boundary layer flow over the slanted sheet with convective boundaries. MHD free convection dissipative fluid stream past over an inclined sheet was investigated by Malik [23]. The boundary layer flow on a slanted sheet through convective boundaries was discussed by Ramesh et al. [24]. Griffiths [25] investigated the non-Newtonian boundary layer flow over a slanted sheet. Soret and Dufour effect over a slanted plate was discussed by Pal and Mondal [26]. Pandya and Shukla [27] investigated the unsteady MHD flow over a slanted surface by taking viscous dissipations. Thermal radiation impacts are important in solar plants [28].

In 1959, Casson offered the Casson fluid model for the flow of viscoelastic liquids. Casson fluid is a shear thinning fluid which should have zero viscosity at an infinite rate of shear and infinite viscosity at zero rates of shear, yielding stress under which no flow takes place. Some examples of Casson fluid are, honey, jelly, sauce, soup etc. [29] Ali et al. [30] examined the Casson fluid flow on a slanted sheet by incorporating the Soret-Dufour effects. Manideep et al. [31] studied the Casson fluid flow on vertically inclined sheets. Shamshuddin et al. [32] numerically investigated the effect of chemical reaction on Casson fluid flow on a slanted plate. Casson fluid flow over a slanted plate calculated by Vijayaragavan and Kavitha [33]. Prasad et al. [34] investigated the Casson fluid flow over an inclined sheet by considering the hall current. Jain and Parmar [35] studied the inclined Casson fluid flow on a permeable sheet. Sailaja et al. [36] studied the Casson fluid flow on a vertical sheet by incorporating the angle effect. Rawi et al. [37] discussed the Casson fluid flow over a slanted sheet by considering nanoparticles. Rauju et al. [38] discussed the Casson fluid flow on a vertically slanted sheet. The Casson fluid model is more compatible with blood flow simulation [39, 40].

Persuaded by the above referred literature review, and due to the growing needs of non-Newtonian nanofluid flows in industry and engineering areas, the present work focuses on the Casson nanofluid flow over a non-linear inclined stretching surface with Soret and Dufour effects. Casson nanofluid is more helpful for cooling and friction reducing agents compared to Newtonian based nanofluid flow [15]. To the best of the author's knowledge, the solution of the Casson nanofluid flow over a non-linear inclined stretching surface with radiation, as well as Soret and Dufour effects with the Keller-Box method, has not yet been reported. The model under consideration is newly developed from Khan and Pop [1] and results obtained from the current study are new. In this work, we found that the Dufour effect reduces the Nusselt and Sherwood number due to Soret impact. A non-linear form of radiative heat exchange also enhances the fluid temperature. This study is very useful in nuclear reactors, MHD generators, and in geothermal energy. In the future, it can be extended on an exponentially inclined stretching surface.

PROBLEM FORMULATION

A steady, two-dimensional boundary layer flow of Casson Nano fluid over a non-linear slanted extending surface on angle γ is considered. The extending and free stream velocities are taken as, $u_w(x) = ax^m$ and $u_\infty(x) = 0$. Where, "x" is the coordinate dignified in the direction of the extending surface with "a" supposed constant. An external transverse magnetic field is assumed normal to the flow path. The Brownian motion and thermophoresis effects are considered. The temperature T and Nano particle fraction C at the wall take the constant values T_w and C_w, while the ambient forms for the nanofluid mass and temperature fractions C_∞ and T_∞ are accomplished as y approaches to immensity, as shown in **Figure 1**.

The flow equations for this study [1] are given by:

$$\frac{\partial u}{\partial x} + \frac{\partial v}{\partial y} = 0 \tag{1}$$

$$u\frac{\partial u}{\partial x} + v\frac{\partial u}{\partial y} = \nu(1+\frac{1}{\beta})\frac{\partial^2 u}{\partial y^2} + g\left[\beta_t\left(T - T_\infty\right) + \beta_c\left(C - C_\infty\right)\right]cos\gamma - \frac{\sigma B_0{}^2(x)u}{\rho} \tag{2}$$

$$u\frac{\partial T}{\partial x} + v\frac{\partial T}{\partial y} = \alpha\frac{\partial^2 T}{\partial y^2} - \frac{1}{(\delta c)_f}\frac{\partial q_r}{\partial y} + \tau\left[D_B\frac{\partial C}{\partial y}\frac{\partial T}{\partial y} + \frac{D_T}{T_\infty}\left(\frac{\partial T}{\partial y}\right)^2\right] + \frac{D_T K_T}{C_s C_p}\frac{\partial^2 C}{\partial y^2}, \tag{3}$$

$$u\frac{\partial C}{\partial x} + v\frac{\partial C}{\partial y} = D_B\frac{\partial^2 C}{\partial y^2} + \frac{D_T K_T}{T_\infty}\frac{\partial^2 T}{\partial y^2}, \tag{4}$$

Here, the Rosseland approximation (for radiation flux) is defined as:

$$qr = -\frac{4\sigma^*}{3k^*}\frac{\partial T^4}{\partial y}, \tag{5}$$

Where, σ^* is the Stefan-Boltzmann constant and k^* is the mean absorption coefficient. It is assumed that the temperature difference between the free steam T_∞ and local temperature T is small enough, expanding T^4 in Taylor series about T_∞ and neglecting higher order terms for:

$$T^4 \cong 4T_\infty^3 T - 3T_\infty^4, \tag{6}$$

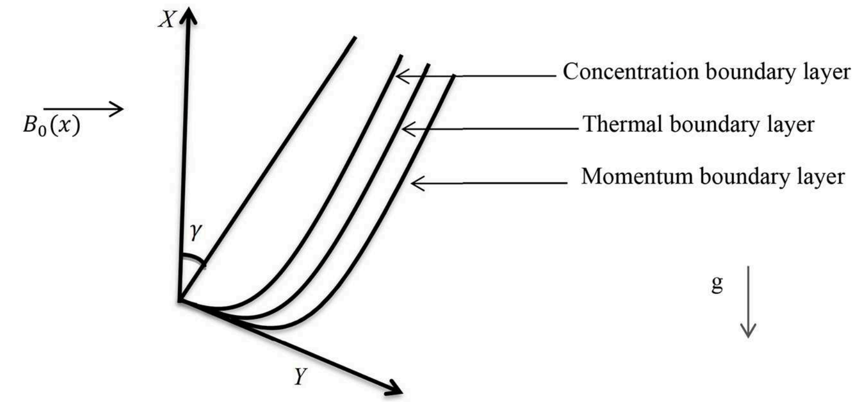

FIGURE 1 | Physical geometry and coordinate system.

Using Equations (5) and (6) the Equation (3) converts into:

$$u\frac{\partial T}{\partial x}+v\frac{\partial T}{\partial y}=(\alpha+\frac{16\sigma^{*}}{3k^{*}\,(\delta c)_f})\frac{\partial^2 T}{\partial y^2}+\tau\left[D_B\frac{\partial C}{\partial y}\frac{\partial T}{\partial y}+\frac{D_T}{T_\infty}\left(\frac{\partial T}{\partial y}\right)^2\right]+\frac{D_T K_T}{C_s C_p}\frac{\partial^2 C}{\partial y^2}, \tag{7}$$

Where u and v are the velocity components in the x and y directions, respectively, g is the acceleration due to gravity, B_0 is the uniform magnetic field strength, σ is the electrical conductivity, u is the viscosity, δ_f is the density of the base fluid, δ_p is the density of the nanoparticle, β is the Casson parameter, β_t is the coefficient of thermal expansion, β_c is the coefficient of concentration expansion, D_B is the Brownian diffusion coefficient and D_T is the thermophoresis diffusion coefficient, k is the thermal conductivity, $(\delta c)_p$ is the heat capacitance of the nanoparticles, $(\delta c)_f$ is the heat capacitance of the base fluid, $\alpha = \frac{k}{(\delta c)_f}$ is the thermal diffusivity parameter, $\tau = \frac{(\delta c)_p}{(\delta c)_f}$ is the ratio between the effective heat capacity of the nanoparticle and heat capacity of the fluid.

The subjected boundary conditions are:

$$\begin{aligned} &u=u_w(x)=ax^m,\ v=0,\ T=T_w,\ C=C_w\ \ at\ \ y=0,\\ &u\to u_\infty(x)=0,\ v\to 0,\ T\to T_\infty,\ C\to C_\infty\ \ at\ \ y\to\infty, \end{aligned} \tag{8}$$

The non-linear partial differential equations are reduced into non-linear ordinary differential equations. For that purpose, the stream function $\psi=\psi(x,y)$ is defined as:

$$u=\frac{\partial\psi}{\partial y}, v=-\frac{\partial\psi}{\partial x}, \tag{9}$$

continuity (Equation 1) is satisfied identically.

The similarity transformations are defined as:

$$\psi=\sqrt{\frac{2vax^{m+1}}{m+1}}f(\eta),\ \theta(\eta)=\frac{T-T_\infty}{T_w-T_\infty},$$

$$\phi(\eta)=\frac{C-C_\infty}{C_w-C_\infty}, \eta=y\sqrt{\frac{(m+1)ax^{m-1}}{2v}}. \tag{10}$$

On substituting (Equation 7), system of Equations (2), (3), and (7) reduce to the following non-linear ordinary differential equations:

$$(1+\frac{1}{\beta})f'''+ff''-\left(\frac{2m}{m+1}\right)f'^2+\frac{2}{m+1}(\lambda\theta-\delta\phi)\cos\gamma-\left(\frac{2M}{m+1}\right)f'=0 \tag{11}$$

$$Pr_N\theta''+f\theta'+N_b\phi'\theta'+N_t\theta'^2+D_f\phi''=0 \tag{12}$$

$$\phi''+Lef\phi'+SrLe\theta''=0 \tag{13}$$

Where,

$$\begin{aligned} &\lambda=\frac{Gr_x}{Re}, \delta=\frac{Gc}{Re}, M=\frac{\sigma B_0{}^2(x)}{a\rho}, Le=\frac{\nu}{D_B}\ Pr=\frac{\nu}{\alpha},\\ &N_b=\frac{\tau D_B(C_w-C_\infty)}{\nu}, N_t=\frac{\tau D_t(T_w-T_\infty)}{\nu\,T_\infty},\\ &Gr_x=\frac{g\beta_t(T_w-T_\infty)x}{a\nu}, Re=\frac{u_w x}{\nu}, Gc_x=\frac{g\beta_c(C_w-C_\infty)x}{a\nu},\\ &Pr_N=\frac{1}{Pr}(1+\frac{4}{3}N), N=\frac{4\sigma^{*}T_\infty^3}{\alpha k^{*}},\\ &D_f=\frac{D_T K_T(C_w-C_\infty)}{\nu C_s C_p(T_w-T_\infty)}, Sr=\frac{D_T K_T(T_w-T_\infty)}{\nu T_\infty(C_w-C_\infty)}, \end{aligned} \tag{14}$$

Here, primes denote the differentiation with respect to η, λ Buoyancy parameter, δ Solutal buoyancy parameter, M is the magnetic parameter called Hartmann number, ν is the kinematic viscosity of the liquid, Pr denotes the Prandtl number, Le denotes the Lewis number, N_b denotes the Brownian motion parameter, N_t indicates thermophoresis parameter, and N is the radiation parameter.

The corresponding boundary conditions are transformed to:

$$\begin{aligned} &f(\eta)=0,\ \ f'(\eta)=1,\ \theta(\eta)=1,\ \phi(\eta)=1\ \ at\ \eta=0,\\ &f'(\eta)\to 0,\ \ \theta(\eta)\to 0,\ \phi(\eta)\to 0\ as\ \ \eta\to\infty, \end{aligned} \tag{15}$$

The skin friction, Sherwood number and Nusselt number for the present problem are defined as:

$$Nu_x = \frac{xq_w}{k\left(T_w - T_\infty\right)}, Sh_x = \frac{xq_m}{D_B\left(C_w - C_\infty\right)}, C_f = \frac{t_w}{{u_w}^2 \rho_f} \quad (16)$$

Where,

$$q_w = -k\frac{\partial T}{\partial y}, q_m = -D_B\frac{\partial C}{\partial y}, \tau_w = \mu(1+\frac{1}{\beta})\frac{\partial u}{\partial y}\ at\ y = 0 \quad (17)$$

The associated expressions of dimensionless reduced Nusselt number $-\theta'(0)$, reduced Sherwood number $-\phi'(0)$, and skin friction coefficient C_{fx} are defined as

$$-\theta'(0) = \frac{Nu_x}{(1+\frac{4}{3}N)\sqrt{\frac{m+1}{2}Re}}, -\phi'(0) = \frac{Sh_x}{\sqrt{\frac{m+1}{2}Re}}, C_{fx} = C_f\sqrt{\frac{2}{m+1}Re} \quad (18)$$

Where, $Re = \frac{u_w x}{\nu}$ is the local Reynolds number.

The converted non-linear differential (Equations 9–12) with the boundary conditions (14) are elucidated by the Keller box scheme consisting of the steps; finite-differences technique, Newton's scheme, and the block elimination process clearly explained by Anwar et al. [41]. This method has been extensively applied and it looks to be the most flexible compared to common techniques. It has been presented as much quicker, easier to program, more efficient and easier to practice. Currently, there are many alternative techniques to solve such types of problems [42].

TABLE 1 | Comparison of the reduced Nusselt number $-\theta'(0)$ and the reduced Sherwood number $-\theta'(0)$ when M, $N = 0$, $\beta \to \infty$, δ, Sr, Df, $\lambda = 0$, $m = 1$, $Pr = Le = 10$ and $\gamma = 90°$.

Nb	Nt	Khan and Pop [1]		Present Results	
		$-\theta'(0)$	$-\phi'(0)$	$-\theta'(0)$	$-\phi'(0)$
0.1	0.1	0.9524	2.1294	0.9524	2.1294
0.2	0.2	0.3654	2.5152	0.3654	2.5152
0.3	0.3	0.1355	2.6088	0.1355	2.6088
0.4	0.4	0.0495	2.6038	0.0495	2.6038
0.5	0.5	0.0179	2.5731	0.0179	2.5731

RESULTS AND DISCUSSION

This portion of study manages the calculated results of converted non-linear ordinary differential (Equations 8–10) with boundary conditions (12) elucidated via Killer-box method. Concerning numerical results of physical parameters, including Brownian motion parameter Nb, radiation parameter N, thermophoresis parameter Nt, magnetic factor M, buoyancy factor λ, solutal buoyancy factor δ, inclination factor γ, Prandtl number Pr, Lewis number Le, Dufour effect Df, Soret effect Sr, non-linear stretching parameter m, and Casson fluid parameter β, several figures and tables are prepared. In **Table 1**, in the deficiency of Dufour effect Df, Soret effect Sr, buoyancy parameter λ, solutal buoyancy constraint δ, magnetic factor M, radiation parameter N and non-linear stretching parameter 'm' K with $\gamma = 90^{\circ}$ when Casson parameter $\beta \to \infty$ produces a reduced Nusselt number $-\theta'(0)$, the reduced Sherwood number $-\phi'(0)$ equate with existing outcomes of Khan and Pop [1]. The consequences establishes a brilliant settlement. The effects of $-\theta'(0)$, $-\phi'(0)$, and $C_{fx}(0)$, against changed values of involved physical parameters Nb, Nt, M, β, λ, δ, γ, m, Le, Df, Sr, N, and Pr are shown in **Table 2**. From **Table 2** is can be clearly seen that $-\theta'(0)$ declines for growing values of Nb,Nt, M,Le, Df, m, γ, β, N, and increases with enhancing numerical values of λ, δ, Sr, and Pr. Moreover, it is perceived that $-\phi'(0)$ enhanced with the larger values of Nb, λ, δ, Nt, Le, N, Pr, Df, and drops for bigger values of M, m, β, Sr, and γ. Physically, the thermal boundary layer thickness enhances, as the Brownian

TABLE 2 | Values of the reduced Nusselt number $-\theta'(0)$, the Sherwood number $-\phi'(0)$ and the Skin-friction coefficient $C_{fx}(0)$.

Nb	Nt	Pr	Le	M	N	β	λ	δ	Sr	Df	m	γ	$-\theta'(0)$	$-\phi'(0)$	$C_{fx}(0)$
0.1	0.1	6.5	5.0	0.1	1.0	1.0	0.1	0.9	0.1	0.1	0.1	45^0	0.6916	1.6014	0.3363
0.5	0.1	6.5	5.0	0.1	1.0	1.0	0.1	0.9	0.1	0.1	0.1	45^0	0.2708	1.7585	0.3372
0.1	**0.5**	6.5	5.0	0.1	1.0	1.0	0.1	0.9	0.1	0.1	0.1	45^0	0.3705	1.7040	0.3361
0.1	0.1	**10.0**	5.0	0.1	1.0	1.0	0.1	0.9	0.1	0.1	0.1	45^0	0.7296	1.6079	0.3373
0.1	0.1	6.5	**10.0**	0.1	1.0	1.0	0.1	0.9	0.1	0.1	0.1	45^0	0.4719	2.4822	0.3832
0.1	0.1	6.5	5.0	**0.5**	1.0	1.0	0.1	0.9	0.1	0.1	0.1	45^0	0.6544	1.5441	0.5936
0.1	0.1	6.5	5.0	0.1	**5.0**	1.0	0.1	0.9	0.1	0.1	0.1	45^0	0.4602	1.6358	0.3283
0.1	0.1	6.5	5.0	0.1	1.0	**5.0**	0.1	0.9	0.1	0.1	0.1	45^0	0.6746	1.5789	0.3587
0.1	0.1	6.5	5.0	0.1	1.0	1.0	**0.5**	0.9	0.1	0.1	0.1	45^0	0.7039	1.6218	0.2119
0.1	0.1	6.5	5.0	0.1	1.0	1.0	0.1	**2.0**	0.1	0.1	0.1	45^0	0.7115	1.6356	0.0927
0.1	0.1	6.5	5.0	0.1	1.0	1.0	0.1	0.9	**0.2**	0.1	0.1	45^0	0.7168	1.5084	0.3096
0.1	0.1	6.5	5.0	0.1	1.0	1.0	0.1	0.9	0.1	**0.2**	0.1	45^0	0.4126	1.7004	0.3367
0.1	0.1	6.5	5.0	0.1	1.0	1.0	0.1	0.9	0.1	0.1	**1.0**	45^0	0.6629	1.5541	0.6146
0.1	0.1	6.5	5.0	0.1	1.0	1.0	0.1	0.9	0.1	0.1	0.1	$\mathbf{60^0}$	0.6854	1.5909	0.4058

Bold values show variation in that parameter.

parameter *Nb* increases impacting a large extent of the fluid. Moreover, for large values of thermophoresis effects, the Nusselt number decreases and the Sherwood number increases because, the thermal boundary layer becomes thicker due to deeper diffusion penetration into the fluid. On the other hand, $C_{fx}(0)$ rises with the growing values of Nb, Le, M, β, Pr, γ, m, Df, and drops with the higher values of, λ, δ, Nt, N, and Sr. The current results are novel and show the impact of the buoyancy parameter, solutal buoyancy parameter and inclination parameter impacts on the driven flow in the presence of Soret and Dufour effects on power-law fluid which is currently unavailable in the literature.

An image of the effect of factor M on velocity profile is portrayed in **Figure 2**. According to **Figure 2**, by improving the constraint M, the velocity outline reduces. Since the magnetic field produces Lorentz force, by slowing down the speed of the liquid. On the other hand, the velocity profile slows down for large values of the non-linear stretching parameter m, shown in **Figure 3**. Physically, the momentum boundary layer thickness reduces for higher values of m.

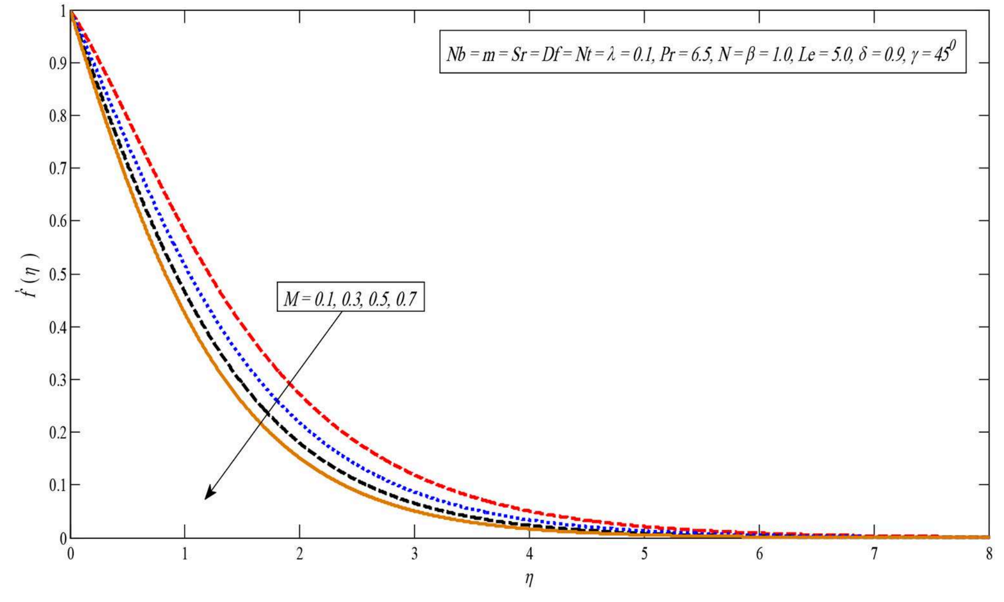

FIGURE 2 | Velocity profile for several values of M.

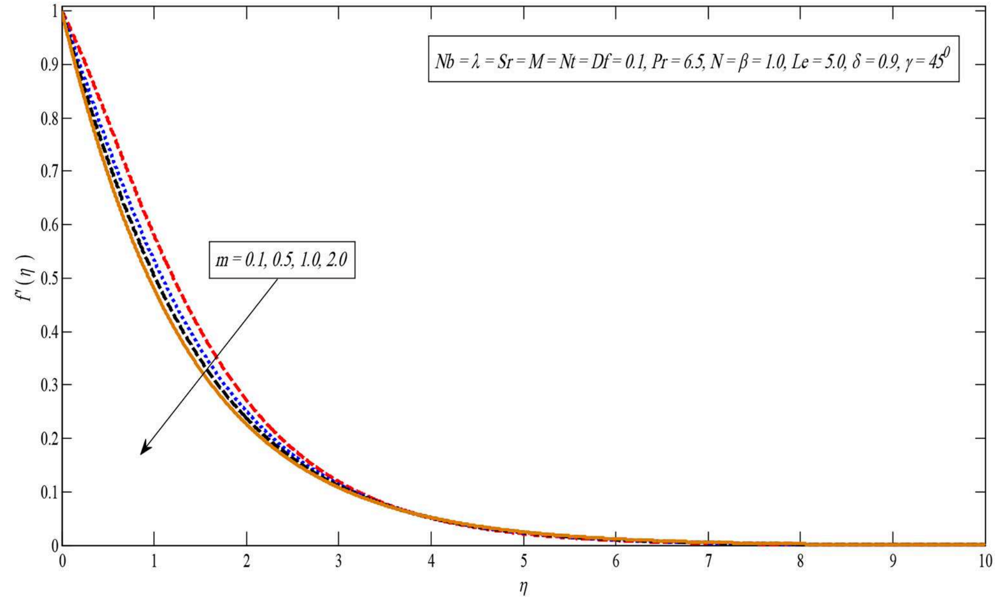

FIGURE 3 | Velocity profile for several values of m.

The impact of the buoyancy factor is shown in **Figure 4**. It is observed that the velocity profile rises by improving the buoyancy limit. It is due to the fact that buoyancy effect increases the strength of the fluid flow whereby the boundary layer thickness and velocity enhances. **Figure 5** indicates that the velocity outline increases by enhancing the solutal buoyancy factor. Physically, the buoyancy parameter reduces the viscous forces whereby the velocity upturns. In addition, the opposite impact can be seen in temperature and concentration profiles for large values of δ.

Figure 6 interprets the significance of inclination factor γ on the velocity outline. It is perceived in **Figure 6** that the velocity outline runs down by enhancing the values of γ. Moreover, the circumstances indicate that the maximum gravitational force acts on flow in the case of $\gamma = 0$, because in this state the sheet will be vertical. On the other hand, for $\gamma = 90^0$, the sheet will

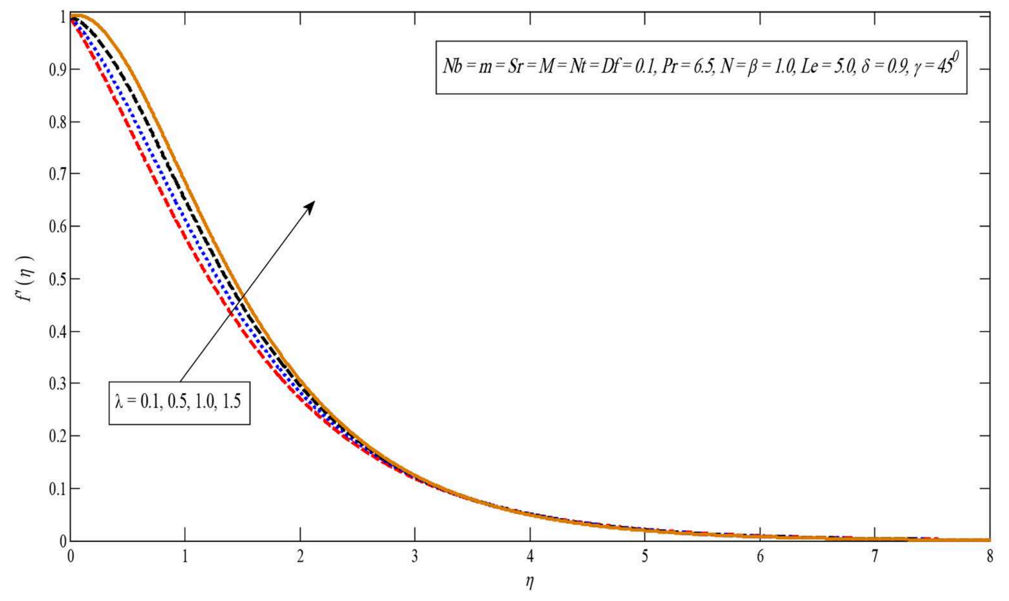

FIGURE 4 | Velocity profile for several values of λ.

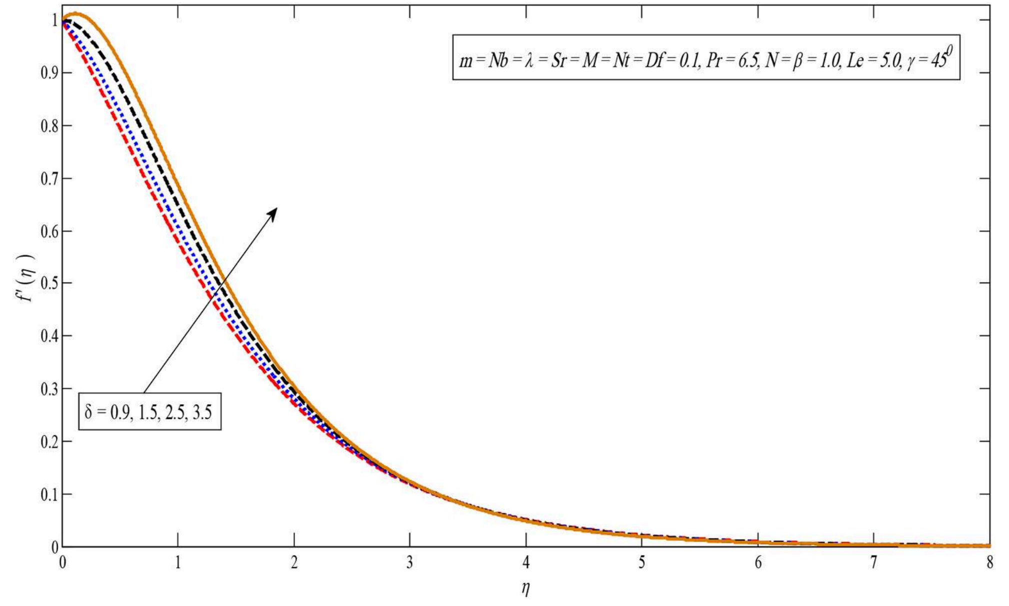

FIGURE 5 | Velocity profile for several values of δ.

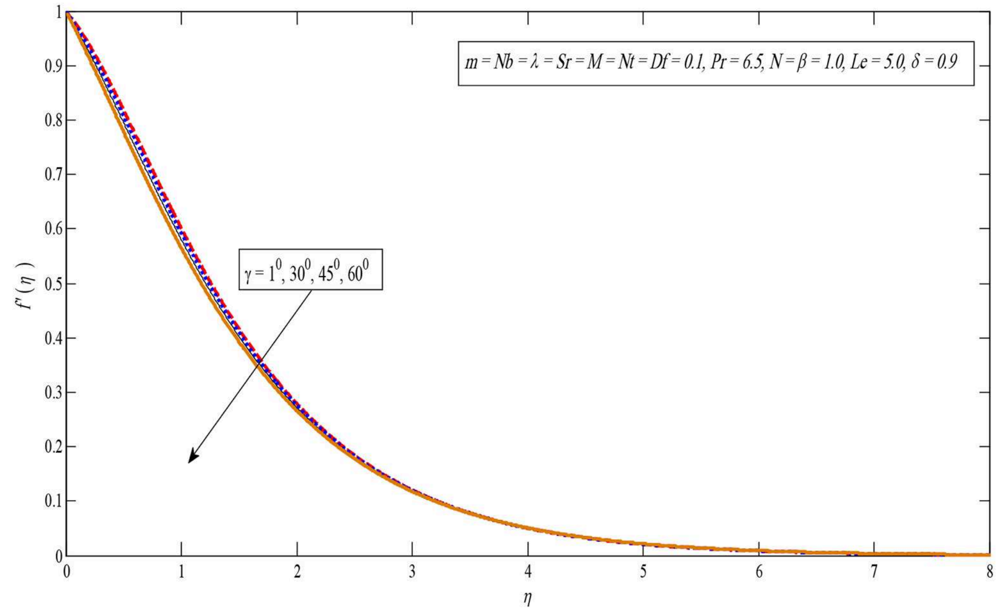

FIGURE 6 | Velocity profile for several values of γ.

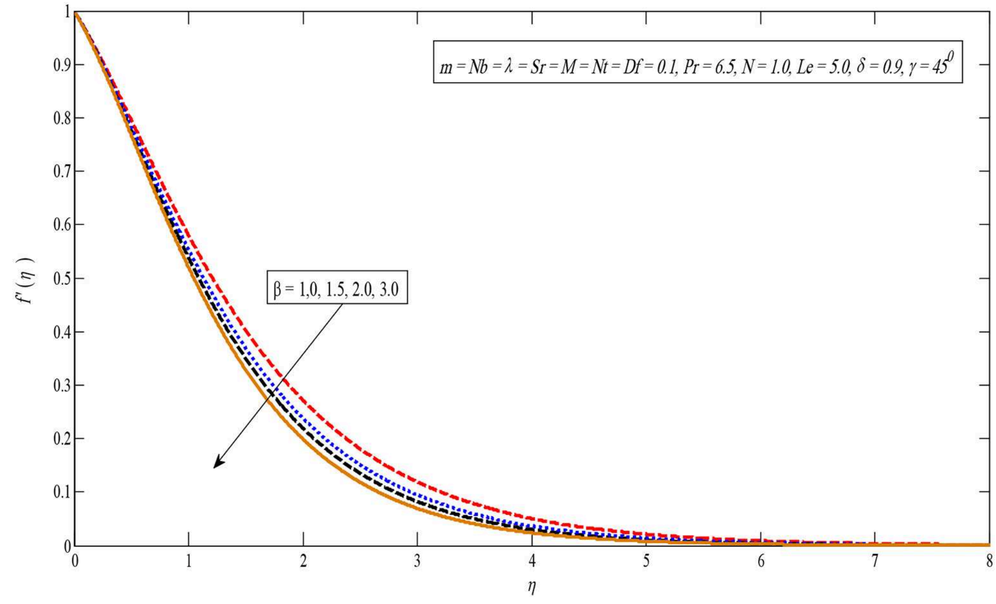

FIGURE 7 | Velocity profile for several values of β.

be horizontal which causes the decline in velocity profile as the power of the bouncy forces drop.

The effect of the Casson parameter on the velocity parameter is presented in **Figure 7**. It is observed that for large values of the Casson parameter, the velocity profile decreases. The reason behind this behavior is that by increasing the values of the Casson parameter, β increases the fluid viscosity i.e., reducing the yield stress. Therefore, the momentum boundary layer thickness reduces [43].

Figures 8, **9** show the effect of the Brownian motion on the temperature and concentration profiles, respectively. The temperature sketch enlarges on enlarging *Nb*; on the other hand, concentration distribution enlightens a dissimilar style. Physically, the boundary layer heats up due to the development in the Brownian motion which is inclined to transport nanoparticles from the extending sheet to the motionless liquid. Therefore, the absorption nanoparticle lessens. **Figures 10**, **11** present temperature and concentration profiles for altered values

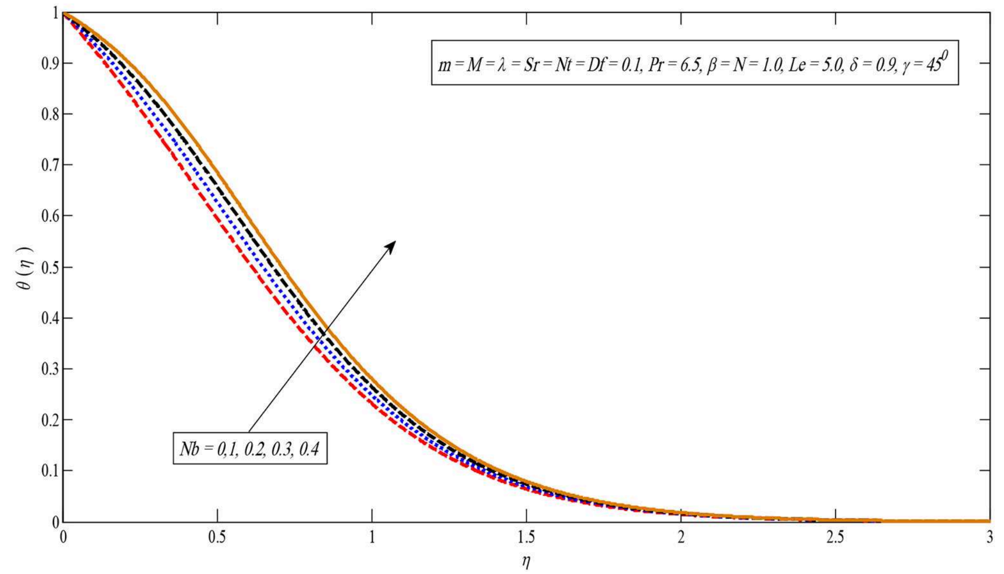

FIGURE 8 | Temperature profile for several values of *Nb*.

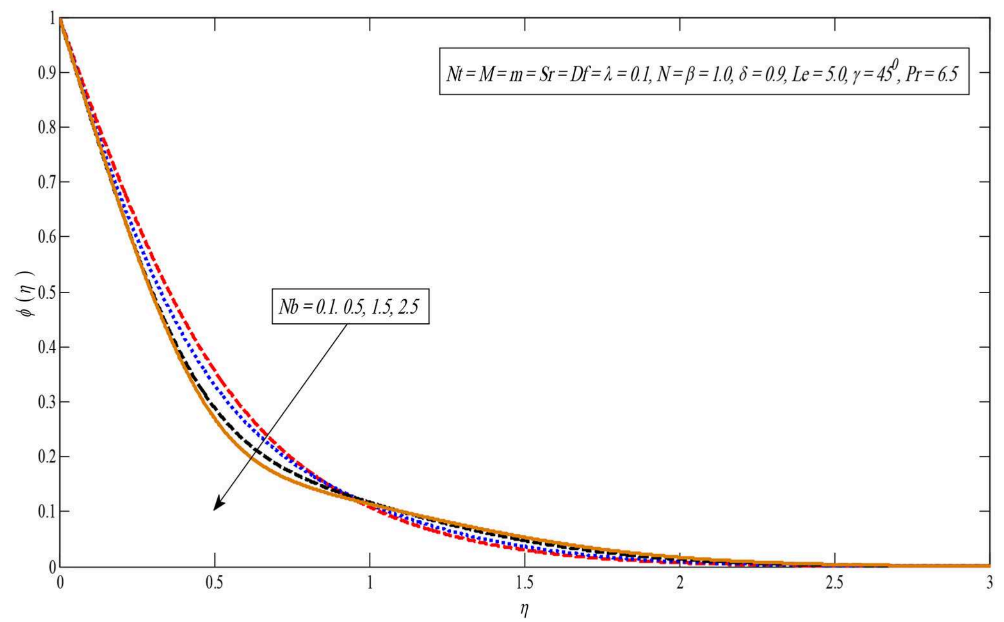

FIGURE 9 | Concentration profile for several values of *Nb*.

of thermophoresis parameters Nt. It is perceived that both temperature and concentration contours upsurge by growing the thermophoresis parameter because thermophoresis causes the small particles to compel away from a warm surface to the cold one.

Figure 12 reveals that by growing the values of the Prandtl number parameter Pr, the temperature profile drops because the thermal boundary layer viscosity declines when growing the Prandtl number Pr. In short an upturn in the Prandtl number Pr means a deliberate amount of thermal dispersion.

Figure 13 shows that the temperature profile becomes large for larger values in parameter D_f. This can be justified as an increase in the Dufour parameter, causing an increase in the concentration gradient, resulting in a mass diffusion taking place more rapidly. In this way, the rate of energy transfer related to the particles becomes higher. That is why the temperature

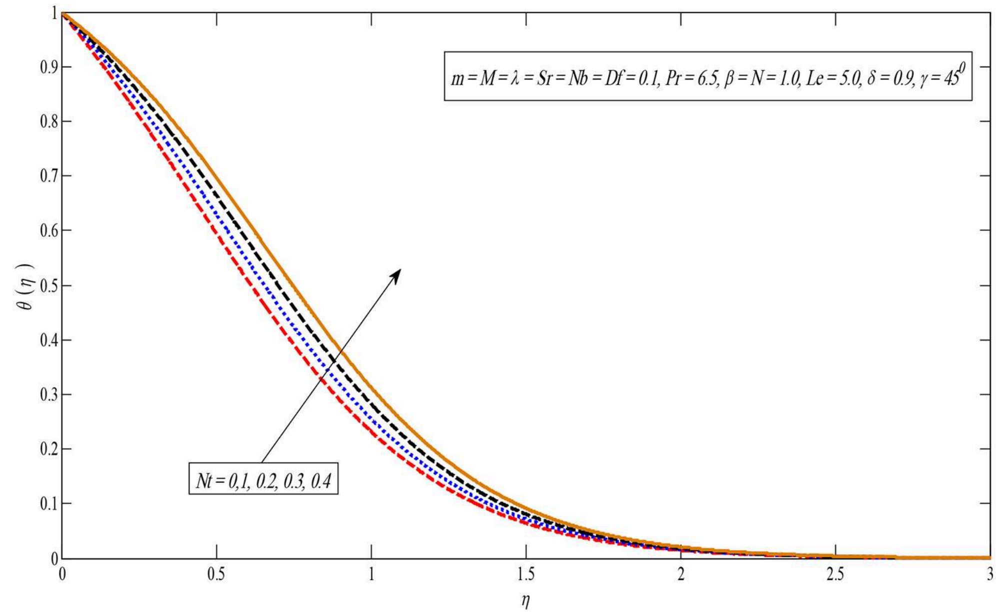

FIGURE 10 | Temperature profile for several values of *Nt*.

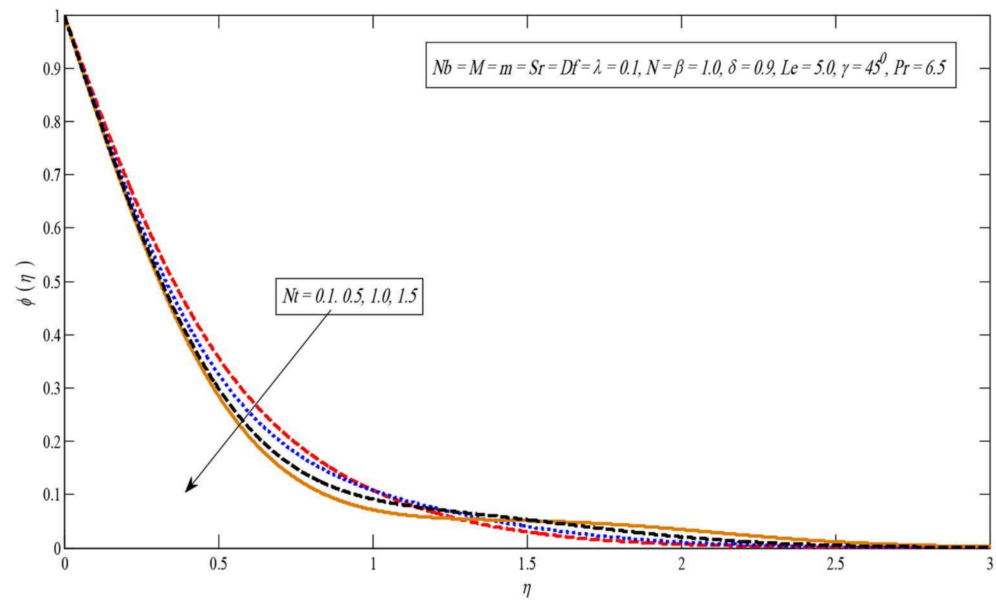

FIGURE 11 | Concentration profile for several values of *Nt*.

profiles enhance. The impact of the Soret number on the concentration profile is observed similar to the impact of the Dufour number on the temperature profile. As parameter S_r increases, the concentration profile increases as displayed in **Figure 14**. Additionally, **Figure 15** indicates a temperature profile enhanced for large values of N.

CONCLUSIONS

This study explored the heat and mass exchange of Casson nanofluid flow over a non-linear slanted extending sheet. The numerical results are successfully obtained *via* the Keller-Box method and are finally performed with the resulting outcomes

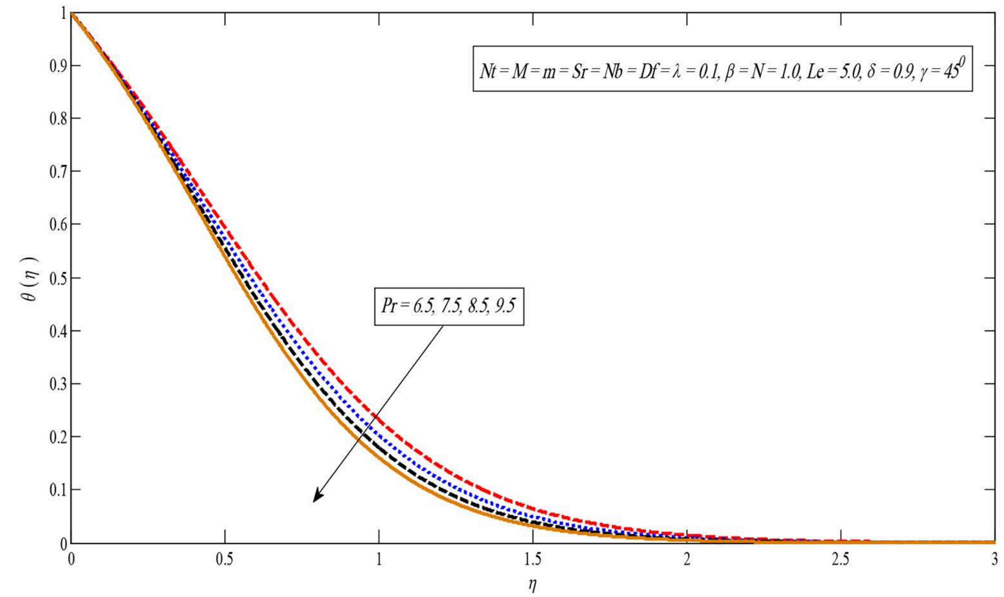

FIGURE 12 | Temperature profile for several values of *Pr*.

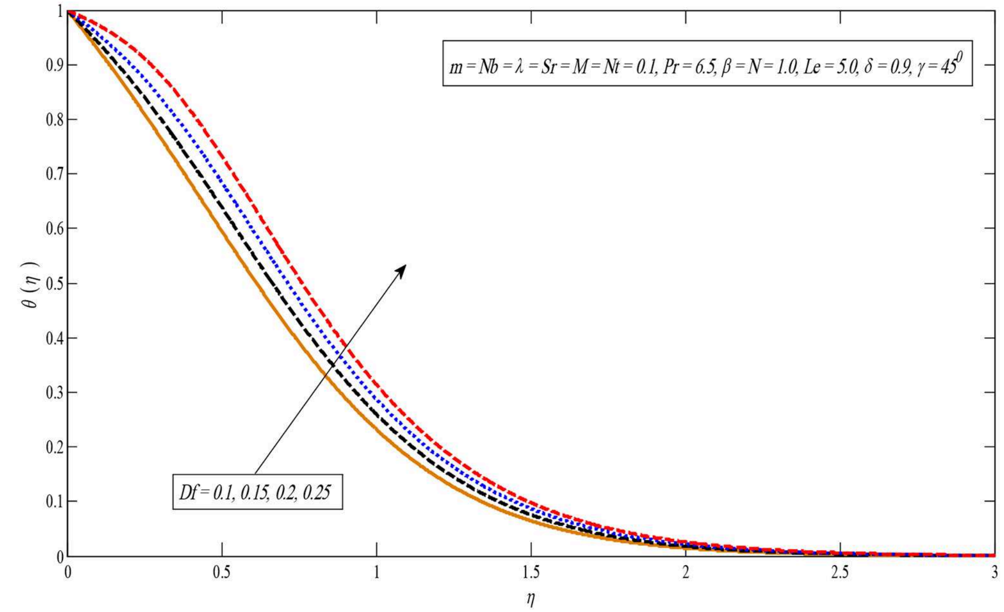

FIGURE 13 | Temperature profile for several values of *Df*.

of already published work [1]. The main findings of the current study are summarized as:

- The velocity outline decreases by enhancing the inclination parameter.
- An increment in Casson fluid factor declines the velocity profile.
- Improving the buoyancy and solutal buoyancy parameters cause an enhancement in the velocity profile.
- Temperature profile upturns when increasing the radiation factor.
- Dufour effect causes the enhancement in the temperature profile.
- Mass diffusion and energy of the fluid upturns by enhancing the Brownian motion factor.
- The thermophoresis factor increases the temperature profile and decreases the concentration profile.

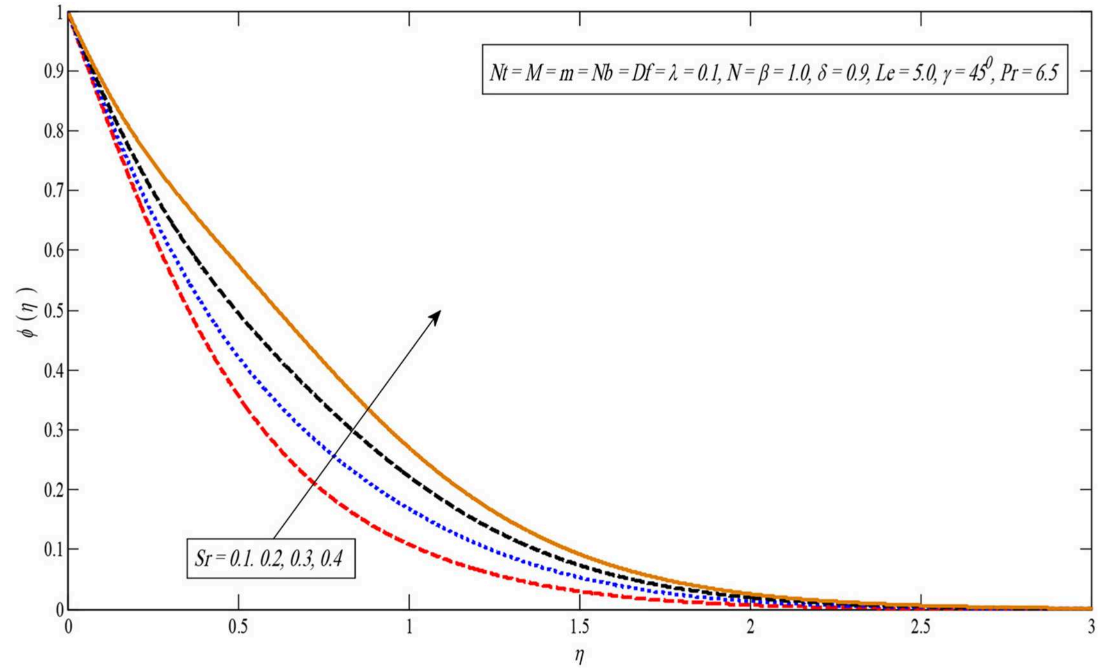

FIGURE 14 | Concentration profile for several values of *Sr*.

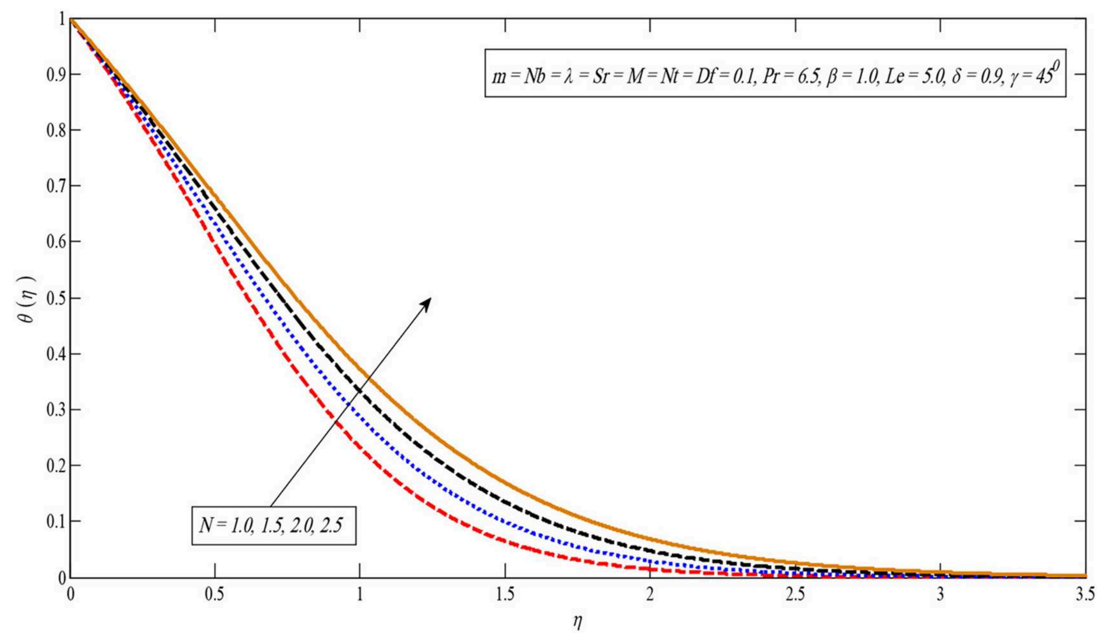

FIGURE 15 | Temperature profile for several values of *N*.

DATA AVAILABILITY STATEMENT

The datasets generated for this study are available on request to the corresponding author.

AUTHOR CONTRIBUTIONS

The formulation was done by KR and MA. Similarity transformation was done by MM. Problem solved by IK and SA. Results plotted and discussed by PT and KN. All authors equally contributed in writing this manuscript.

ACKNOWLEDGMENTS

The author (SA) would like to thank the Deanship of Scientific Research (DSR) Majmaah University for supporting this work.

REFERENCES

1. Khan WA, Pop I. Boundary-layer flow of a nanofluid past a stretching sheet. *Int J Heat Mass Trans*. (2010) **53**:2477–83. doi: 10.1016/j.ijheatmasstransfer.2010.01.032
2. Choi SUS, Eastman JA. Enhancing thermal conductivity of fluids with nanoparticle. *Mater Sci*. (1995) **231**:99–105
3. Buongiorno J. Convective transport in nanofluids. *J Heat Transf*. (2006) **128**:240–50. doi: 10.1115/1.2150834
4. Nield DA, Kuznetsov AV. The Cheng–Minkowycz problem for natural convective boundary-layer flow in a porous medium saturated by a nanofluid. *Int J Heat Mass Transf*. (2009) **52**:5792–5. doi: 10.1016/j.ijheatmasstransfer.2009.07.024
5. Anwar MI, Khan I, Sharidan S, Salleh MZ. Conjugate effects of heat and mass transfer of nanofluids over a nonlinear stretching sheet. *Int J Phys Sci*. (2012) **7**:4081–92. doi: 10.5897/IJPS12.358
6. Suriyakumar P, Devi SPA. Effects of suction and internal heat generation on hydromagnetic mixed convective nanofluid flow over an inclined stretching plate. *Eur J Adv Eng Technol*. (2015) **2**:51–8.
7. Ziaei-Rad M, Kasaeipoor A, Rashidi MM, Lorenzini G. A similarity solution for mixed-convection boundary layer nanofluid flow on an inclined permeable surface. *J Therm Sci Eng Appl*. (2017) **9:**021015 doi: 10.1115/1.4035733
8. Thumma T, Bég OA, Sheri SR. Finite element computation of magnetohydrodynamic nanofluid convection from an oscillating inclined plate with radiative flux, heat source and variable temperature effects. *Proc Inst Mech Eng Part N J Nanomater Nanoeng Nanosyst*. (2017) **231:**179–94. doi: 10.1177/2397791417731452
9. Govindarajan A. Radiative fluid flow of a nanofluid over an inclined plate with non-uniform surface temperature. *J Phys Conf*. (2018) **1000**:012173. doi: 10.1088/1742-6596/1000/1/012173
10. Khan M, Shahid A, Malik MY, Salahuddin T. Thermal and concentration diffusion in Jeffery nanofluid flow over an inclined stretching sheet: a generalized Fourier's and Fick's perspective. *J Mol Liquids*. (2018) **251**:7–14. doi: 10.1016/j.molliq.2017.12.001
11. Chakraborty T, Das K, Kundu PK. Ag-water nanofluid flow over an inclined porous plate embedded in a non-Darcy porous medium due to solar radiation. *J Mech Sci Technol*. (2017) **31**:2443–9. doi: 10.1007/s12206-017-0442-4
12. Bhatti MM, Abbas T, Rashidi MM. Effects of thermal radiation and electromagnetohydrodynamics on viscous nanofluid through a Riga plate. *Multidiscipline Model Mater Struct*. (2016) **12**:605–18. doi: 10.1108/MMMS-07-2016-0029
13. Bhatti MM, Mishra SR, Abbas T, Rashidi MM. A mathematical model of MHD nanofluid flow having gyrotactic microorganisms with thermal radiation and chemical reaction effects. *Neural Comput Appl*. (2018) **30**:1237–49. doi: 10.1007/s00521-016-2768-8
14. Hussanan A, Khan I, Gorji MR, Khan WA. CNT S-water–based nanofluid over a stretching sheet. *BioNanoScience*. (2019) **9**:21–9. doi: 10.1007/s12668-018-0592-6
15. Souayeh B, Reddy MG, Sreenivasulu P, Poornima T, Rahimi-Gorji M, Alarifi IM. Comparative analysis on non-linear radiative heat transfer on MHD Casson nanofluid past a thin needle. *J Mol Liquids*. (2019) **284**:163–74. doi: 10.1016/j.molliq.2019.03.151
16. Ma Y, Mohebbi R, Rashidi MM, Yang Z. Study of nanofluid forced convection heat transfer in a bent channel by means of lattice Boltzmann method. *Phys Fluids*. (2018) **30**:032001. doi: 10.1063/1.5022060
17. Makulati N, Kasaeipoor A, Rashidi MM. Numerical study of natural convection of a water–alumina nanofluid in inclined C-shaped enclosures under the effect of magnetic field. *Adv Powder Technol*. (2016) **27**:661–72. doi: 10.1016/j.apt.2016.02.020
18. Bhatti MM, Abbas T, Rashidi MM. Entropy generation as a practical tool of optimisation for non-Newtonian nanofluid flow through a permeable stretching surface using SLM. *J Comput Design Eng*. (2017) **4**:21–8. doi: 10.1016/j.jcde.2016.08.004
19. Sakiadis BC. Boundary-layer behavior on continuous solid surfaces: I. Boundary-layer equations for two-dimensional and axisymmetric flow. *AIChE J*. (1961) **7**:26–8. doi: 10.1002/aic.690070108
20. Crane LJ. Flow past a stretching plate. *Z Angew Mathematik Physik*. (1970) **21**:645–7. doi: 10.1007/BF01587695
21. Ali M, Alim MDA, Alam MS. Heat transfer boundary layer flow past an inclined stretching sheet in the presence of magnetic field. *Int J Adv Res Technol*. (2014) **3**:34–40.
22. Ramesh GK, Gireesha BJ, Bagewadi CS. Heat transfer in MHD dusty boundary layer flow over an inclined stretching sheet with non-uniform heat source/sink. *Adv Math Phys*. (2012) **2012**:657805. doi: 10.1155/2012/657805
23. Malik MY. effects of second order chemical reaction on MHD free convection dissipative fluid flow past an inclined porous surface by way of heat generation: a lie group analysis 1 introduction 2 flow analysis. (2016) **45**:35–45. doi: 10.18576/isl/050201
24. Ramesh GK, Chamkha AJ, Gireesha BJ. Boundary layer flow past an inclined stationary/moving flat plate with convective boundary condition. *Afrika Matematika*. (2016) **27**:87–95. doi: 10.1007/s13370-015-0323-x
25. Griffiths PT. Stability of the shear-thinning boundary-layer flow over a flat inclined plate. *Proc R Soc A Math Phys Eng Sci*. (2017) **473**:20170350. doi: 10.1098/rspa.2017.0350
26. Pal D, Mondal H. Influence of Soret-Dufour and thermophoresis on hydromagnetic mixed convection heat and mass transfer over an inclined flat plate with non-uniform heat source/sink and chemical reaction. *Int J Comput Methods Eng Sci Mech*. (2018) **19**:49–60. doi: 10.1080/15502287.2018.1430073
27. Pandya N, Shukla AK. Soret-Dufour and radiation effect on unsteady MHD flow over an inclined porous plate embedded in porous medium with viscous dissipation. *Int J Adv Appl Math Mech*. (2014) **2**:107–19.
28. Qing J, Bhatti M, Abbas M, Rashidi M, Ali M. Entropy generation on MHD Casson nanofluid flow over a porous stretching/shrinking surface. *Entropy*. (2016) **18**:123. doi: 10.3390/e18040123
29. Bhatti MM, Abbas MA, Rashidi MM. Entropy generation for peristaltic blood flow with casson model and consideration of magnetohydrodynamics effects. *Walail J Sci Techn*. (2016) **14**:451–61.
30. Ali M, Aruna G, Raju RS. MHD boundary layer casson fluid flow over a vertically inclined plate: grid study and convergence analysis of finite element technique. *J Nanofluids*. (2018) **7**:1195–207. doi: 10.1166/jon.2018.1541
31. Manideep P, Raju RS, Rao TS N, Reddy GJ. Unsteady MHD free convection flow of casson fluid over an inclined vertical plate embedded in a porous media. In: *AIP Conference Proceedings*. Bikaneer: AIP Publishing. (2018). p. 140038. doi: 10.1063/1.5033213

32. Shamshuddin MD, Mishra SR, Thumma T. Chemically reacting radiative casson fluid over an inclined porous plate: a numerical study. In: *Numerical Heat Transfer and Fluid Flow*. Singapore: Springer. (2019) p. 469–479. doi: 10.1007/978-981-13-1903-7_54
33. Vijayaragavan R, Kavitha MA. Heat and mass transfer in unsteady MHD casson fluid flow past an inclined plate with thermal radiation and heat source/sink. *Res J Eng Techn.* (2018) **9**:214–33. doi: 10.5958/2321-581X.2018.00030.2
34. Prasad DK, Chaitanya GK, Raju RS. Role of casson fluid on MHD natural convective flow towards vertically inclined plate with hall current. In: *AIP Conference Proceedings*. Bikaneer: AIP Publishing. (2018). p. 140073. doi: 10.1063/1.5033248
35. Jain S, Parmar A. Multiple slip effects on inclined MHD Casson fluid flow over a permeable stretching surface and a melting surface. *Int J Heat Techn.* (2018) **36**:585–94. doi: 10.18280/ijht.360222
36. Sailaja SV, Shanker B, Raju RS. Finite element analysis of magneto-hydrodynamic casson fluid flow past a vertical plate with the impact of angle of inclination. *J Nanofluids.* (2018) **7**:383–95. doi: 10.1166/jon.2018.1456
37. Rawi NA, Ilias MR, Lim YJ, Isa ZM, Shafie S. Unsteady mixed convection flow of Casson fluid past an inclined stretching sheet in the presence of nanoparticles. In: *Journal of Physics: Conference Series*. Kuantan: IOP Publishing. (2017) p. 012048. doi: 10.1088/1742-6596/890/1/012048
38. Raju RS, Reddy BM, Reddy GJ. Finite element solutions of free convective Casson fluid flow past a vertically inclined plate submitted in magnetic field in presence of heat and mass transfer. *Int J Comput Methods Eng Sci Mechan.* (2017) **18**:250–65. doi: 10.1080/15502287.2017.1339139
39. Rashidi MM, Yang Z, Bhatti MM, Abbas MA. Heat and mass transfer analysis on MHD blood flow of Casson fluid model due to peristaltic wave. *Therm Sci*. (2018) **22:**2439–48. doi: 10.2298/TSCI160102287R
40. Abbas MA, Bai YQ, Rashidi MM, Bhatti MM. Application of drug delivery in magnetohydrodynamics peristaltic blood flow of nanofluid in a non-uniform channel. *J Mechan Med Biol.* (2016) **16**:1650052. doi: 10.1142/S0219519416500524
41. Anwar MI, Shafie S, Hayat T, Shehzad SA, Salleh MZ. Numerical study for MHD stagnation-point flow of a micropolar nanofluid towards a stretching sheet. *J Braz Soc Mechan Sci Eng.* (2017) **39**:89–100. doi: 10.1007/s40430-016-0610-y
42. Kumar D, Singh J, Purohit SD, Swroop R. A hybrid analytical algorithm for nonlinear fractional wave-like equations. *Math Model Nat Phenom*. (2019) **14**:304. doi: 10.1051/mmnp/2018063
43. Ullah I, Khan I, Shafie S. MHD natural convection flow of Casson nanofluid over nonlinearly stretching sheet through porous medium with chemical reaction and thermal radiation. *Nanoscale Res Lett.* (2016) **11**:527. doi: 10.1186/s11671-016-1745-6

Conflict of Interest: The authors declare that the research was conducted in the absence of any commercial or financial relationships that could be construed as a potential conflict of interest.

Copyright © 2019 Rafique, Anwar, Misiran, Khan, Alharbi, Thounthong and Nisar. This is an open-access article distributed under the terms of the Creative Commons Attribution License (CC BY). The use, distribution or reproduction in other forums is permitted, provided the original author(s) and the copyright owner(s) are credited and that the original publication in this journal is cited, in accordance with accepted academic practice. No use, distribution or reproduction is permitted which does not comply with these terms.

frontiers in Physics

ORIGINAL RESEARCH
published: 05 November 2019
doi: 10.3389/fphy.2019.00171

Check for updates

Study of the Couple Stress Convective Micropolar Fluid Flow in a Hall MHD Generator System

Zahir Shah[1]*, *Poom Kumam*[2,3,4]*, *Abdullah Dawar*[5], *Ebraheem O. Alzahrani*[6] and *Phatiphat Thounthong*[7]

[1] Center of Excellence in Theoretical and Computational Science (TaCS-CoE), SCL 802 Fixed Point Laboratory, King Mongkut's University of Technology Thonburi (KMUTT), Bangkok, Thailand, [2] KMUTT Fixed Point Research Laboratory, SCL 802 Fixed Point Laboratory, Department of Mathematics, Faculty of Science, King Mongkut's University of Technology Thonburi (KMUTT), Bangkok, Thailand, [3] KMUTT-Fixed Point Theory and Applications Research Group, Theoretical and Computational Science Center (TaCS), Faculty of Science, King Mongkut's University of Technology Thonburi (KMUTT), Bangkok, Thailand, [4] Department of Medical Research, China Medical University Hospital, China Medical University, Taichung, Taiwan, [5] Department of Mathematics, Abdul Wali Khan University Mardan, Mardan, Pakistan, [6] Department of Mathematics, Faculty of Science, King Abdulaziz University, Jeddah, Saudi Arabia, [7] Renewable Energy Research Centre, Department of Teacher Training in Electrical Engineering, Faculty of Technical Education, King Mongkut's University of Technology North Bangkok, Bangkok, Thailand

OPEN ACCESS

Edited by:
Muhammad Mubashir Bhatti, Shanghai University, China

Reviewed by:
R. Ellahi, University of California, Riverside, United States
Arash Asadollahi, Southern Illinois University Carbondale, United States

***Correspondence:**
Zahir Shah
zahir.sha@kmutt.ac.th
Poom Kumam
poomkumam@kmutt.ac.th

Specialty section:
This article was submitted to Mathematical Physics, a section of the journal Frontiers in Physics

Received: 25 August 2019
Accepted: 16 October 2019
Published: 05 November 2019

Citation:
Shah Z, Kumam P, Dawar A, Alzahrani EO and Thounthong P (2019) Study of the Couple Stress Convective Micropolar Fluid Flow in a Hall MHD Generator System. Front. Phys. 7:171. doi: 10.3389/fphy.2019.00171

The steady non-isothermal convective heat transfer in magnetohydrodynamic micropolar fluid flow over a non-linear extending wall is examined. The fluid flow is treated with strong magnetic field. The influence of magnetic field, Hall current, and couple stress are mainly focused in this work. The fluid flow problem is solved analytically. The impact of developing dimensionless parameters on primary, secondary, and angular velocity components and temperature profile are determined through graphs. The primary velocity component has reduced throughout the flow study. The greater magnetic parameter, Hall parameter and couple stress parameter have increased the secondary velocity component while the local Grashof number has reduced the secondary velocity component. The greater magnetic parameter and Hall parameter have reduced the angular velocity component. The greater magnetic parameter has increased the temperature profile while the Hall parameter and local Grashof number have decreased the temperature profile. The impact of developing dimensionless parameters on skin friction coefficient and local Nusselt number are determined through Tables.

Keywords: hall MHD generator system, convective heat transfer, magnetohydrodynamic, micropolar fluid, couple stress, hall current, HAM

INTRODUCTION

The flow of non-Newtonian fluids has plentiful importance in industries and modern technology. Recently, the couple stress fluid among non-Newtonian fluid has acquired the exceptional position due to the spin field in the fluid. The elementary concept of couple stress was established by Stokes [1]. Khan et al. [2] deliberated the suggested model of couple stress fluid in a uniformly porous stretching channel. The axial velocity function heightens while the radial velocity function declines for escalating couple stress. The couple stress effect on heat transfer in four different nanofluids flows was determined by Farooq et al. [3]. Srinivasacharya et al. [4] explored the couple stress fluid flow. They originate that the couple stress parameter diminishes the fluid velocity and temperature while heightens the concentration. Ramzan et al. [5] deliberated the couple stress fluid flow over extending sheet. It is found that velocity profiles along both directions are declined with the escalation in couple stress parameter. Also the fluid temperature escalated with viscous dissipation effect. Hayat et al. [6] determined the heat transmission rate in the couple stress flow over extending surface and originate that the heat transfer intensifies with the rising estimations of the couple stress. Over an extending sheet, the couple stress fluid flow was determined by Turkyilmazoglu [7]. It is concluded that over a stretching sheet the couple stress gives double solution while over shrinking sheet it gives triple solution. The unsteady couple stress fluid flow was determined by Awad et al. [8]. Here, the fluid velocity and temperature decline with heightened couple stress. Sreenadh et al. [9] examined the fluid flow with couple stress impact. Hayat et al. [10] analyzed the mass transfer in couple stress fluid with chemical reaction. Khan et al. [11] scrutinized the incompressible and unsteady couple stress fluid flow considering three dimensional cylindrical polar coordinate systems. Hayat et al. [12] measured the flow of couple stress nanofluid with convective conditions. The fluid temperature and concentration are increased with escalating couple stress parameter. The dissipation influence on couple stress nanofluid flow was determined by Ramzan [13]. The magnetic field impact on couple stress nanofluid flow was determined by Hayat et al. [14]. In this article, the authors determined that temperature of fluid flow up surged with the large estimation of couple stress parameter. With Cattaneo-Chritov heat flux Hayat et al. [15] deliberated the flow of couple stress nanofluid flow. They found that the velocity components are increased while the temperature is decreased with the couple stress parameter. Umavathi et al. [16] deliberated the laminar flow of couple stress fluid and heat transmission considering horizontal plates. Umavathi et al. [17] scrutinized the fluid flow with couple stress impact in between two infinite porous walls. They concluded that the fluid velocity and temperature are reduced in the boundary layer regime. Srinivasacharyulu et al. [18] observed the couple stress fluids flow over stretching walls. Zueco et al. [19] inspected the couple stress nanofluid in a rigid channel. Zakaria [20] deliberated the couple stress fluid under magnetic field impact. Ellahi et al. [21] determined the couple stress blood flow under the impact of activation energy and chemical reaction.

In recent times, the researchers have got interest in megnetohydrodynamic (MHD) owing to plentiful applications in industrial, engineering, and medical devices. Rudolf et al. [22] briefly reviewed the properties of magnetic field in the universe. The MHD nanofluid flow with chemical reaction was deliberated by Hayat et al. [23]. The fluid flow velocity is reduced with higher estimation of magnetic field, and temperature escalated with chemical reactions and Dufour influences. The heat transmission in the flow of MHD nanofluid over unsteady extending sheet was observed by Lin et al. [24]. The fluid flow velocity is reduced with heightens in magnetic field while the temperature of the fluid escalated. The heat transfer in the flow of MHD incompressible second-grade nanofluid was deliberated by Ramesh et al. [25]. The MHD nanofluid flow in a symmetric channel was probed by Reddy et al. [26]. The elementary study of micropolar fluid was introduced by Eringen [27]. Bég et al. [28] presented the applications of micropolar fluid flow. Uddin et al. [29] probed the MHD micropolar fluid with Hall effect. Here, interesting results are concluded. The velocity of the fluid heightens with the escalation in magnetic field while the temperature of the fluid reduces with higher estimation of magnetic field (i.e. $M>2$). Khan et al. [30] determined the radiation and inertial coefficient influences on the flow of nanofluid. The higher inertial coefficient, porosity parameter, and coupling parameter reduce the fluid velocity and the temperature heightens with the escalation in thermal radiation. Dawar et al. [31] deliberated the unsteady MHD nanofluid with viscous dissipation effect. Here, the authors originate that the fluid flow velocity reduces with escalation in magnetic field and the fluid flow temperature reduces with viscous dissipation impacts. Kumam et al. [32] probed the MHD Casson nanofluid flow. Shah et al. [33] deliberated the flow of MHD thin film fluid with radiation impact. The MHD Casson nanofluid flow in a cylindrical tube was considered by Ali et al. [34]. The nanofluid flow with Hall effect was studied by Shah et al. [35]. The MHD nanofluid flow with magnetic and electric fields, and Hall impacts was determined by Shah et al. [36]. Kumar et al. [37] investigated the MHD nanofluid with magnetic and heat sink/source impacts. Temple et al. [38] scrutinized the nanoparticles of ferromagnetic for their size and magnetic properties. Ellahi et al. [39] examined the MHD nanofluid flow with thermal conductivity. Asadollahi et al. [40] deliberated the phase change of a fluid in a square microchannel. The most relevant and new studied studies can be reads in Ellahi et al. [41–43], Bhatti et al. [44], Ameen et al. [45], Vo et al. [46], Ahmad et al. [47], Sheikholeslami et al. [48], Ali et al. [49], and Ullah et al. [50].

In view of the above mentioned literature survey, the authors are in position to examine the three-dimensional MHD micropolar fluid flow over an extending wall with couple stress, Hall current and viscous dissipation influences. Section of Problem Formulation agrees with problem formulation. In the section of Solution by HAM, the recommended model is solved by HAM. Results section includes the results of the problem and the section of Discussion of the problem is presented independently. The final observations are obtainable in the section of Conclusion.

PROBLEM FORMULATION

We assume the incompressible, steady, and electrically conducting couple stressed flow of micropolar fluid and heat transfer in the near wall zone of MHD Hall generator. The wall is considered as non-linearly stretching and concerned with $x-$direction (as shown in **Figure 1**). The magnetic field B_0 is functional in $y-$axis. In the presence of magnetic field, the Hall current influences the electrically conducting fluid. The flow of fluid develops to 3D due to the Hall current, which increases the force in $z-$direction. All properties of fluid are considered constant and isotropic.

The principal equations for the fluid flow can be written as [27, 28]:

$$\frac{\partial v}{\partial y} + \frac{\partial u}{\partial x} = 0, \tag{1}$$

$$v\frac{\partial u}{\partial y}+u\frac{\partial u}{\partial x}=\nu\frac{\partial^2 u}{\partial y^2}-\nu'\frac{\partial^4 u}{\partial y^4}-\frac{B_0}{\rho}J_z+g\beta\left(T-T_\infty\right)+K_1\frac{\partial N}{\partial y},\qquad(2)$$

$$v\frac{\partial w}{\partial y}+u\frac{\partial w}{\partial x}=\nu\frac{\partial^2 w}{\partial y^2}-\nu'\frac{\partial^4 w}{\partial y^4}+\frac{B_0}{\rho}J_x,\qquad(3)$$

$$\frac{G_1}{K_2}\frac{\partial^2 N}{\partial y^2}=2N+\frac{\partial u}{\partial y},\qquad(4)$$

$$v\frac{\partial T}{\partial y}+u\frac{\partial T}{\partial x}=\frac{\kappa}{\rho c_p}\frac{\partial^2 T}{\partial y^2}+\frac{\sigma\mu_e B_0^2\lambda}{\rho c_p\left(m^2\lambda^2+1\right)}\left(w^2+u^2\right),\qquad(5)$$

with

$$u=U=\mathrm{P}x^n,\ v=0,\ w=0,\ N=0,\ T=T_w=T_\infty+Ax^\gamma\ \text{at}\ y=0,$$
$$u\to 0,\ w\to 0,\ N\to 0,\ T\to T_\infty\ \text{at}\ y\to\infty.\qquad(6)$$

Here, the positive n indicates the acceleration of the wall and negative n indicates the deceleration of wall form the origin whereas $n = 0$ is the case for stationary wall, u, v and w are the velocity components, N is the micro-rotation, T denotes the fluid temperature, $J_x = \frac{\sigma\mu_e B_0\lambda}{1+m^2\lambda^2}(\lambda m u - w)$ and $J_z = \frac{\sigma\mu_e B_0\lambda}{1+m^2\lambda^2}(u-\lambda m w)$ are the currents along $x-$ and $z-$directions correspondingly, also electrical conductivity-σ, fluid viscosity-μ_e, applied uniform magnetic field-B_0, Hall parameter-m, couple stress viscosity-ν', $\lambda = \cos\alpha$ where α indicates the angle between the magnetic field and the transverse plane to the plate, thermal expansion volumetric coefficient-β, kinematic viscosity-ν, fluid density-ρ, Eringen vortex viscosity-K_2, thermal conductivity-κ, Eringen spin gradient viscosity-G_1, specific heat-c_p, γ, and A-constants.

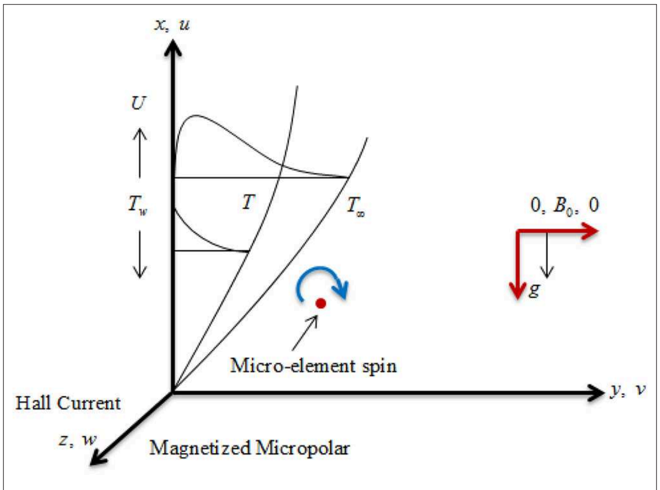

FIGURE 1 | Geometrical illustration of the micropolar fluid flow.

To transform the coordinate system to a non-dimensional one and this is achieved readily via non-similar transformations, simultaneously eliminating one of the independent variables and reducing the PDEs into ODEs, the following transformation variables are defined.

$$\xi=y\sqrt{\frac{\mathrm{P}\left(n+1\right)}{2\nu}}x^{\frac{n-1}{2}},\ u=\mathrm{P}x^n f'\left(\xi\right),$$
$$v=-\sqrt{\mathrm{P}\nu\left(\frac{n+1}{2}\right)}x^{\frac{n-1}{2}}\left(f+\frac{n-1}{n+1}\xi f'\left(\xi\right)\right),\qquad(7)$$
$$w=\mathrm{P}x^n g\left(\xi\right),\ N=\mathrm{P}\sqrt{\frac{\mathrm{P}\left(n+1\right)}{2\nu}}x^{\frac{3n-1}{2}}h\left(\xi\right),$$
$$\theta\left(\xi\right)=\frac{T-T_\infty}{T_w-T_\infty},$$

The transformed equations are defined as:

$$f'''+ff''-N1h'-\frac{2}{n+1}\left[nf'^2-Gr\theta+\frac{M\lambda}{1+m^2\lambda^2}\left(f'+m\lambda g\right)\right]-\frac{n+1}{2}Kf'''''=0,\qquad(8)$$

$$g''+fg'-\frac{2}{n+1}\left[nf'g-\frac{M\lambda}{1+m^2\lambda^2}\left(m\lambda f'-g\right)\right]-\frac{n+1}{2}Kg''''=0,\qquad(9)$$

$$G\left(\frac{n+1}{2}\right)h''-f''-2h=0,\qquad(10)$$

$$\frac{1}{\mathrm{Pr}}\theta''+f\theta'-\frac{2}{n+1}\left[\gamma f'\theta-\frac{M\lambda}{1+m^2\lambda^2}Ec\left(f'^2+g^2\right)\right]=0,\qquad(11)$$

with transformed boundary conditions:

$$f=0,\ f'=1,\ g=0,\ h=0,\ \theta=1\ \text{at}\ \xi=0,$$
$$f'\to 0,\ g\to 0,\ h\to 0,\ \theta\to 0\ \text{as}\ \xi\to\infty.\qquad(12)$$

Here, $G_r = \frac{g\beta(T_w-T_\infty)x}{U^2}$ symbolizes the Grashof number, $M = \frac{\sigma\mu_e B_0^2 x}{\rho U}$ characterizes the Hartmann number in which $B_0 = \frac{\mathrm{P}}{\sqrt{x}}$ is the scaled magnetic field strength, $G = \frac{G_1 \mathrm{P}x^{n-1}}{K_2\nu}$ represents the micro-rotation parameter, m Hall parameter, $K = \frac{\nu'}{\nu^2 \mathrm{P}x^{2(n-1)}}$ represents the dimensionless couple stress parameter, γ indicates the non-isothermal power-law index, $N1 = \frac{K_1}{\nu}$ characterizes the material parameter, $\mathrm{Pr} = \frac{\rho\nu c_p}{\kappa}$ embodies the Prandtl number, $Ec = \frac{U^2}{c_p(T_w-T_\infty)}$ epitomizes the Eckert number, and n represents the non-linear wall geometric parameter.

For primary and secondary velocity components, the skin frication are defined as:

$$\tau_{wx}=\mu\left.\frac{\partial u}{\partial y}\right|_{y=0}=\frac{\mu U}{\sqrt{x}}\sqrt{\left(\frac{U\left(n+1\right)}{2\nu}\right)}f''\left(0\right),\qquad(13)$$

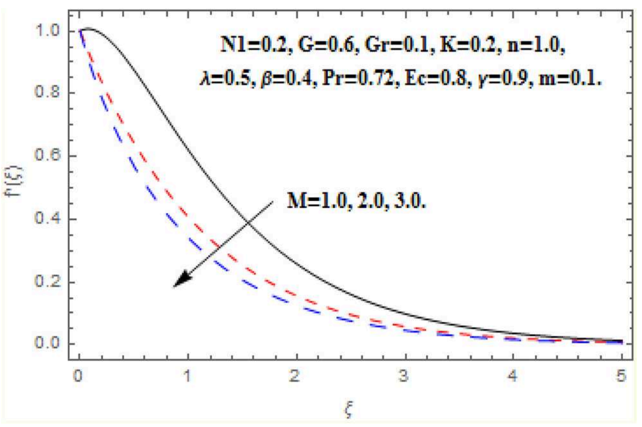

FIGURE 2 | Impact of M on $f'(\xi)$.

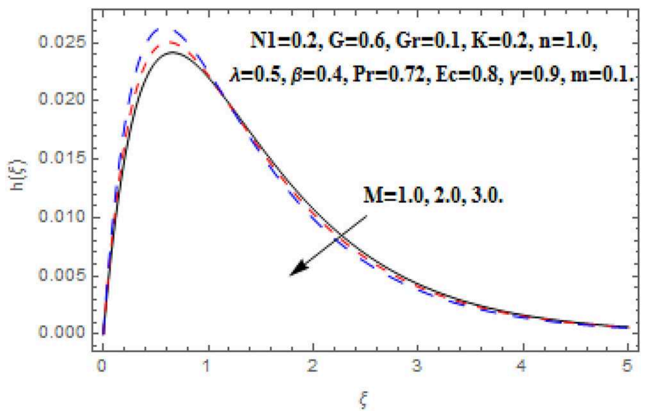

FIGURE 4 | Impact of M on $h(\xi)$.

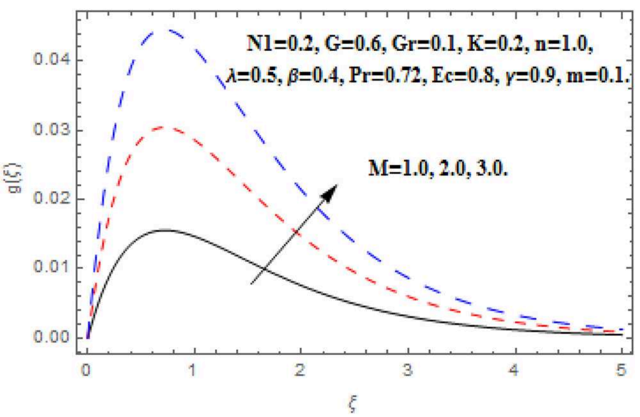

FIGURE 3 | Impact of M on $g(\xi)$.

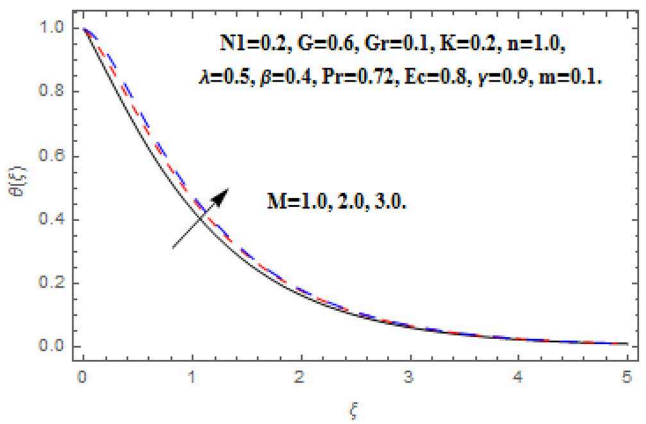

FIGURE 5 | Impact of M on $\theta(\xi)$.

$$\tau_{wz} = \mu \left.\frac{\partial w}{\partial y}\right|_{y=0} = \frac{\mu U}{\sqrt{x}}\sqrt{\left(\frac{U(n+1)}{2\nu}\right)} g'(0), \quad (14)$$

Using Equation (7), the skin fraction coefficients for primary and secondary velocities are reduced as:

$$C_{fx} = \frac{\tau_{wx}}{\frac{1}{2}\rho U^2} = \sqrt{\frac{2(n+1)}{\text{Re}}} f''(0), \quad (15)$$

$$C_{fz} = \frac{\tau_{wz}}{\frac{1}{2}\rho U^2} = \sqrt{\frac{2(n+1)}{\text{Re}}} g'(0). \quad (16)$$

The Nusselt number is specified by:

$$Nu_x = -\frac{x}{(T_w - T_\infty)} \left.\frac{\partial T}{\partial y}\right|_{y=0} = -\sqrt{\frac{\text{Re}(n+1)}{2}} \theta'(0), \quad (17)$$

SOLUTION BY HAM

To solve the Equations (8)–(11) using boundary conditions (12), we proceed HAM with the following manners.

Initial gausses

$$f_0(\xi) = 1 - e^{\xi},\ g_0(\xi) = 0,\ h_0(\xi) = 0,\ \theta_0(\xi) = e^{-\xi}. \quad (18)$$

Linear operators

$$L_f(f) = \frac{d^3 f}{d\xi^3} - \frac{df}{d\xi,} L_g(g) = \frac{d^2 g}{d\xi^2} - g, L_h(h) = \frac{d^2 h}{d\xi^2} - h,$$
$$L_\theta(\theta) = \frac{d^2\theta}{d\xi^2} - \theta, \quad (19)$$

with the following properties:

$$\begin{aligned} &L_f(s_1 + s_2 e^{-\xi} + s_3 e^{\xi}) = 0,\ L_g(s_4 e^{-\xi} + s_5 e^{\xi}) = 0, \\ &L_h(s_6 e^{-\xi} + s_7 e^{\xi}) = 0,\ L_\theta(s_8 e^{-\xi} + s_9 e^{\xi}) = 0, \end{aligned} \quad (20)$$

where $s_i (i = 1 - 9)$ are arbitrary constants.

The consequential non-linear operators N_f, N_g, N_h, and N_θ are specified as:

$$N_f\left[f(\xi;\Theta), g(\xi;\Theta), h(\xi;\Theta), \theta(\xi;\Theta)\right]$$

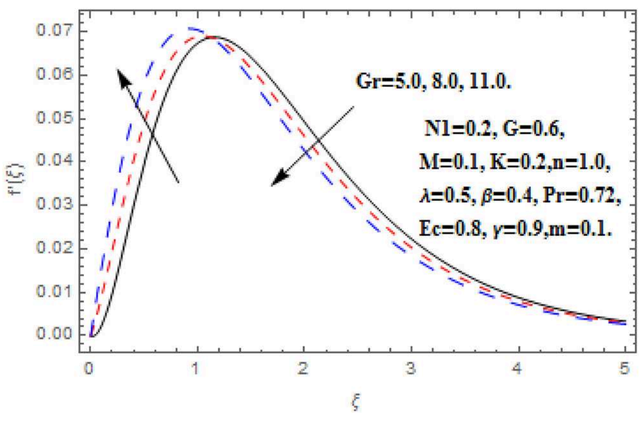

FIGURE 6 | Impact of *Gr* on $f'(\xi)$.

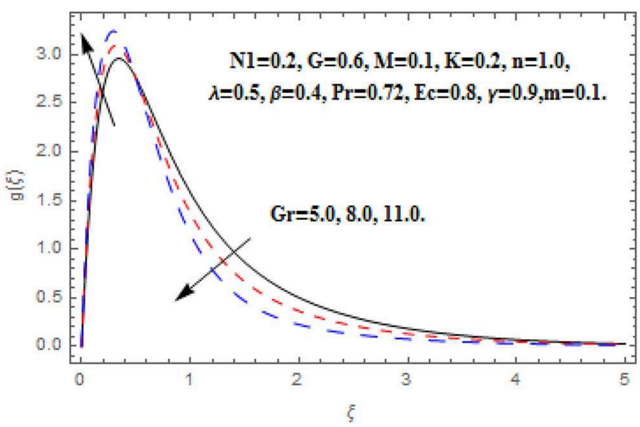

FIGURE 7 | Impact of *Gr* on $g(\xi)$.

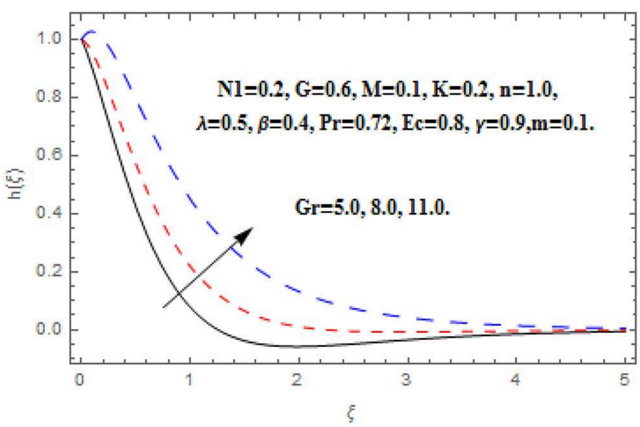

FIGURE 8 | Impact of *Gr* on $h(\xi)$.

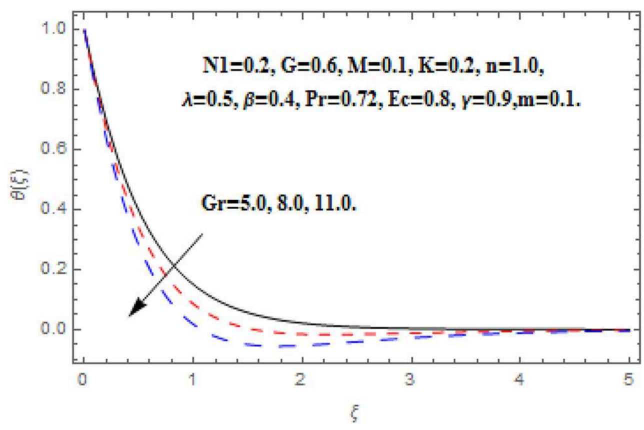

FIGURE 9 | Impact of *Gr* on $\theta(\xi)$.

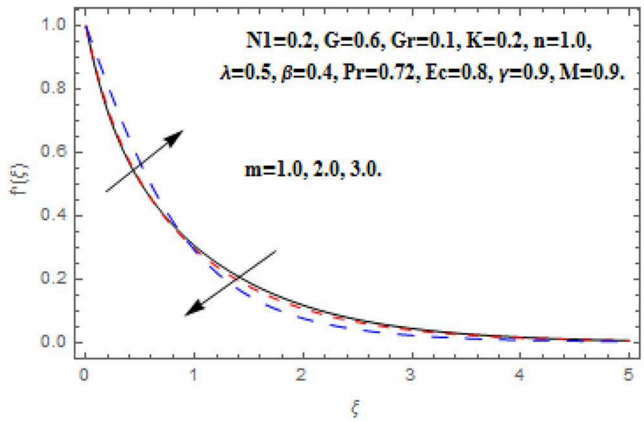

FIGURE 10 | Impact of *m* on $f'(\xi)$.

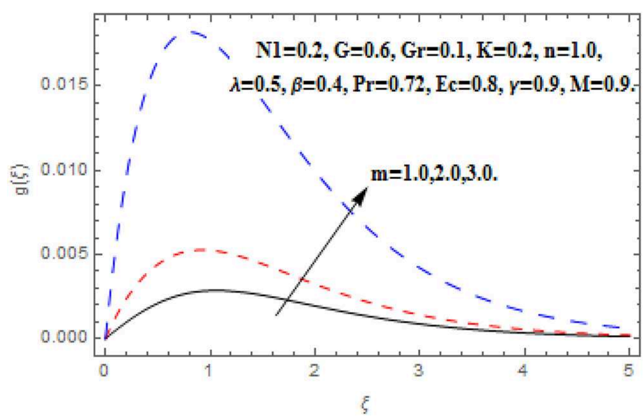

FIGURE 11 | Impact of *m* on $g(\xi)$.

$$= \frac{\partial^3 f(\xi;\Theta)}{\partial \xi^3} + f(\xi;\tau)\frac{\partial^2 f(\xi;\Theta)}{\partial \xi^2} - N1\frac{\partial h(\xi;\Theta)}{\partial \xi} - \frac{2}{n+1}\left[n\left(\frac{\partial f(\xi;\Theta)}{\partial \xi}\right)^2 - Gr\theta(\xi;\Theta) + \frac{M\lambda}{1+m^2\lambda^2}\left(\frac{\partial f(\xi;\Theta)}{\partial \xi} + m\lambda g(\xi;\Theta)\right)\right] - \frac{n+1}{2}K\frac{\partial^5 f(\xi;\Theta)}{\partial \xi^5}, \tag{21}$$

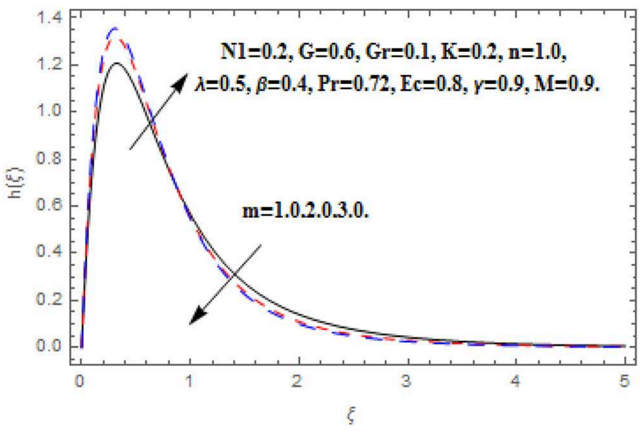

FIGURE 12 | Impact of m on $h(\xi)$.

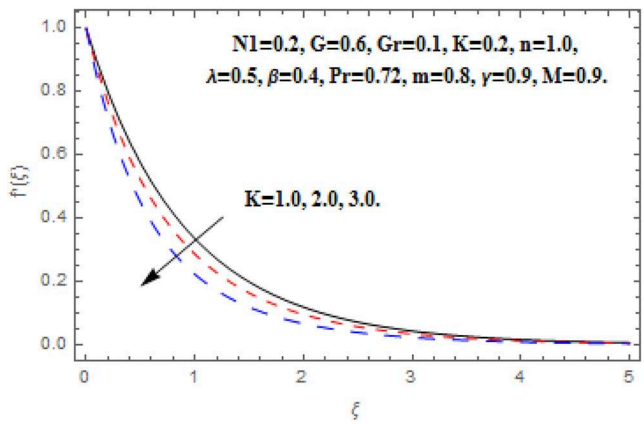

FIGURE 14 | Impact of K on $f'(\xi)$.

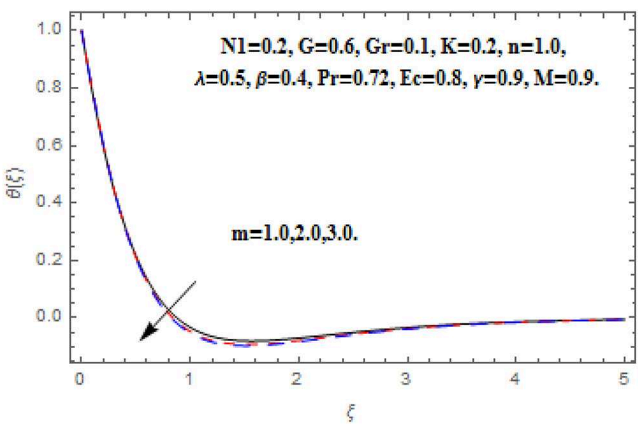

FIGURE 13 | Impact of m on $\theta(\xi)$.

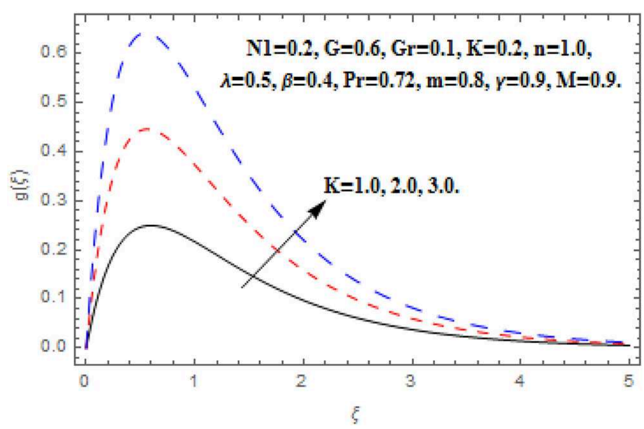

FIGURE 15 | Impact of K on $g(\xi)$.

$$N_g\left[g(\xi;\Theta),f(\xi;\Theta)\right]=\frac{\partial^2 g(\xi;\Theta)}{\partial\xi^2}-f(\xi;\Theta)\frac{\partial g(\xi;\Theta)}{\partial\xi}-\frac{2}{n+1}\left[ng(\xi;\Theta)\frac{\partial f(\xi;\Theta)}{\partial\xi}-\frac{M\lambda}{1+m^2\lambda^2}\left(m\lambda\frac{\partial f(\xi;\Theta)}{\partial\xi}-g(\xi;\Theta)\right)\right]-\frac{n+1}{2}K\frac{\partial^4 g(\xi;\Theta)}{\partial\xi^4}, \quad (22)$$

$$N_h\left[h(\xi;\Theta),f(\xi;\Theta)\right]=G\left(\frac{n+1}{2}\right)\frac{\partial^2 h(\xi;\Theta)}{\partial\xi^2}-\frac{\partial^2 f(\xi;\Theta)}{\partial\xi^2}-2h(\xi;\Theta), \quad (23)$$

$$N_\theta\left[\theta(\xi;\Theta),f(\xi;\Theta),g(\xi;\Theta)\right]=\frac{1}{\Pr}\frac{\partial^2\theta(\xi;\Theta)}{\partial\xi^2}+f(\xi;\Theta)\frac{\partial\theta(\xi;\Theta)}{\partial\xi}-\frac{2}{n+1}\left[\gamma\theta(\xi;\Theta)\frac{\partial f(\xi;\Theta)}{\partial\xi}-\frac{M\lambda}{1+m^2\lambda^2}Ec\left(\left(\frac{\partial f(\xi;\Theta)}{\partial\xi}\right)^2+\left(g(\xi;\Theta)\right)^2\right)\right], \quad (24)$$

The zeroth-order problems from Equations (8)–(11) are:

$$(1-\Theta)L_f\left[f(\xi;\Theta)-f_0(\xi)\right]=\Theta\hbar_f N_f\left[f(\xi;\Theta),g(\xi;\Theta),h(\xi;\Theta),\theta(\xi;\Theta)\right], \quad (25)$$

$$(1-\Theta)L_g\left[g(\xi;\Theta)-g_0(\xi)\right]=\Theta\hbar_g N_g\left[g(\xi;\Theta),f(\xi;\Theta)\right], \quad (26)$$
$$(1-\Theta)L_h\left[h(\xi;\Theta)-f_0(\xi)\right]=\Theta\hbar_h N_h\left[h(\xi;\Theta),f(\xi;\Theta)\right], \quad (27)$$
$$(1-\Theta)L_\theta\left[\theta(\xi;\Theta)-\theta_0(\xi)\right]=\Theta\hbar_\theta N_\theta\left[\theta(\xi;\Theta),f(\xi;\Theta),g(\xi;\Theta)\right]. \quad (28)$$

The equivalent boundary conditions are:

$$\left.\frac{\partial f(\xi;\Theta)}{\partial\xi}\right|_{\xi=0}=1,\ \left.f(\xi;\Theta)\right|_{\xi=0}=0,\ \left.g(\xi;\Theta)\right|_{\xi=0}=0,\ \left.h(\xi;\Theta)\right|_{\xi=0}=0,\ \left.\theta(\xi;\Theta)\right|_{\xi=0}=1,\ \left.\frac{\partial f(\xi;\tau)}{\partial\xi}\right|_{\xi\to\infty}=0,\ \left.g(\xi;\tau)\right|_{\xi\to\infty}=0,\ \left.h(\xi;\tau)\right|_{\xi\to\infty}=0,\ \left.\theta(\xi;\tau)\right|_{\xi\to\infty}=0. \quad (29)$$

TABLE 1 | Influence of M, Gr, G, $N1$, m, Ec, Pr, n, and K on C_{fx}.

M	*Gr*	*G*	*N1*	*m*	*Ec*	Pr	*n*	*K*	C_{fx}
0.2	0.2	0.3	0.2	1.1	0.1	0.72	1.1	0.1	−1.233236
0.3									−1.339327
0.4									−1.443959
	0.4								−1.391409
	0.6								−1.338869
	0.8								−1.286370
		0.4							−1.286278
		0.6							−1.286189
		0.8							−1.286101
			0.3						−1.288813
			0.4						−1.291526
			0.5						−1.294238
				1.3					−1.173870
				1.5					−1.097241
				1.7					−1.042032
					0.3				−1.045267
					0.6				−1.044867
					0.9				−1.044467
						1.0			−1.046198
						5.0			−1.050270
						10.0			−1.050834
							1.2		−1.081639
							1.3		-.1117715
							1.4		−1.152781
								0.3	−1.561382
								0.5	−2.936200
								0.7	−8.747216

When $\Theta = 0$ and $\Theta = 1$ we have:

$$f(\xi;1) = f(\xi),\ g(\xi;1) = g(\xi),\ h(\xi;1) = h(\xi),\ \theta(\xi;1) = \theta(\xi). \tag{30}$$

By Taylor's series expansion $f(\xi;\Theta)$, $g(\xi;\Theta)$, $h(\xi;\Theta)$, and $\theta(\xi;\Theta)$ can be written as:

$$\begin{aligned} f(\xi;\Theta) &= f_0(\xi) + \sum_{q=1}^{\infty} f_q(\xi)\Theta^q,\ g(\xi;\Theta) = g_0(\xi) + \sum_{q=1}^{\infty} g_q(\xi)\Theta^q, \\ h(\xi;\Theta) &= h_0(\xi) + \sum_{q=1}^{\infty} h_q(\xi)\Theta^q,\ \theta(\xi;\Theta) = \theta_0(\xi) + \sum_{q=1}^{\infty} \theta_q(\xi)\Theta^q, \end{aligned} \tag{31}$$

where

$$\begin{aligned} f_q(\xi) &= \frac{1}{q!}\frac{\partial f(\xi;\Theta)}{\partial \xi}\bigg|_{\Theta=0},\ g_q(\xi) = \frac{1}{q!}\frac{\partial g(\xi;\Theta)}{\partial \xi}\bigg|_{\Theta=0}, \\ h_q(\xi) &= \frac{1}{q!}\frac{\partial h(\xi;\Theta)}{\partial \xi}\bigg|_{\Theta=0},\ \theta_q(\xi) = \frac{1}{q!}\frac{\partial f(\xi;\Theta)}{\partial \xi}\bigg|_{\Theta=0}. \end{aligned} \tag{32}$$

The secondary constraints $\hbar_f, \hbar_g$, $\hbar_h$ and $\hbar_\theta$are nominated in such a way that the series (31) converges at $\Theta = 1$, changing $\Theta = 1$ in Equation (31), we get:

$$\begin{aligned} f(\xi) &= f_0(\xi) + \sum_{q=1}^{\infty} f_q(\xi),\ g(\xi) = g_0(\xi) + \sum_{q=1}^{\infty} g_q(\xi), \\ h(\xi) &= h_0(\xi) + \sum_{q=1}^{\infty} h_q(\xi),\ \theta(\xi) = \theta_0(\xi) + \sum_{q=1}^{\infty} \theta_q(\xi). \end{aligned} \tag{33}$$

The $q^{th}-$order problem satisfies the following:

$$\begin{aligned} L_f\left[f_q(\xi) - \chi_q f_{q-1}(\xi)\right] &= \hbar_f U_q^f(\xi), \\ L_g\left[d_q(\xi) - \chi_q d_{q-1}(\xi)\right] &= \hbar_g U_q^g(\xi), \\ L_h\left[F_q(\xi) - \chi_q F_{q-1}(\xi)\right] &= \hbar_h U_q^h(\xi), \\ L_\theta\left[D_q(\xi) - \chi_q D_{q-1}(\xi)\right] &= \hbar_\theta U_q^\theta(\xi). \end{aligned} \tag{34}$$

The equivalent boundary conditions are:

$$\begin{aligned} f_q(0) = f'_q(0) = f'_q(\infty) = 0,\ g_q(0) = g_q(\infty) = 0, \\ h_q(0) = h_q(\infty) = 0,\ \theta_q(0) = \theta'_q(\infty) = 0. \end{aligned} \tag{35}$$

Here,

$$U_q^f(\xi) = f'''_{q-1} + \sum_{k=0}^{q-1} f_{q-1-k} f''_k - N1 h'_{q-1}$$

TABLE 2 | Influence of M, Gr, G, $N1$, m, Ec, Pr, n, and K onC_{fz}.

M	*Gr*	*G*	*N1*	*m*	*Ec*	Pr	*n*	*K*	C_{fz}
0.2	0.2	0.3	0.2	1.1	0.1	0.72	1.1	0.1	0.210288
0.3									0.312368
0.4									0.410969
	0.4								0.412875
	0.6								0.414780
	0.8								0.416684
		0.4							0.416776
		0.6							0.416866
		0.8							0.416953
			0.3						0.414227
			0.4						0.411502
			0.5						0.408776
				1.3					0.295179
				1.5					0.221561
				1.7					0.171285
					0.3				0.171296
					0.6				0.171313
					0.9				0.171330
						1.0			0.171273
						5.0			0.171144
						10.0			0.171127
							1.2		0.166810
							1.3		0.162582
							1.4		0.158615
								0.3	0.191738
								0.5	0.184492
								0.7	0.184488

$$-\frac{2}{n+1}\left[n\left(f'_{q-1}\right)^2 - Gr\theta_{q-1} + \frac{M\lambda}{1+m^2\lambda^2}\left(f'_{q-1}+m\lambda g_{q-1}\right)\right] - \frac{n+1}{2}Kf''''_{q-1}, \quad (36)$$

$$U_q^g(\xi) = g''_{q-1} + \sum_{k=0}^{q-1} f_{q-1-k}g'_k - \frac{2}{n+1}\left[n\sum_{k=0}^{q-1} f'_{q-1-k}g_k - \frac{M\lambda}{1+m^2\lambda^2}\left(m\lambda f'_{q-1} - g_{q-1}\right)\right] - \frac{n+1}{2}Kg'''_{q-1}, \quad (37)$$

$$U_q^h(\xi) = G\left(\frac{n+1}{2}\right)h''_{q-1} - f''_{q-1} - 2h_{q-1}, \quad (38)$$

$$U_q^\theta(\xi) = \frac{1}{\Pr}\theta''_{q-1} + \sum_{k=0}^{q-1} f_{q-1-k}\theta'_k - \frac{2}{n+1}\left[\gamma\sum_{k=0}^{q-1} f'_{q-1-k}\theta_k - \frac{M\lambda}{1+m^2\lambda^2}Ec\left(\left(f'_{q-1}\right)^2 + \left(g_{q-1}\right)^2\right)\right], \quad (39)$$

where,

$$\chi_q = \begin{cases} 0, \text{ if } \Theta \le 1 \\ 1, \text{ if } \Theta > 1. \end{cases}$$

RESULTS

Electrically conducting steady non-isothermal convective heat transfer in magnetohydrodynamic micropolar fluid flow over a non-linear extending wall is examined. Modeled equations are solved analytically through HAM. The impact of obtained important parameters M, Gr, m, and K on the fluid flow behavior are displayed in **Figures 2–15**.

DISCUSSION

In this section we have discussed the effects of obtained parameter which are shown graphically and numerically through tables. The greater Hartmann number strongly reduced the primary and angular velocity profile owing to the Lorentz drag force components as appear in Equations (8) and (9). The components are negative and positive and thus inhibit the fluid flow. According to the secondary Lorentz drag force is truthfully positive and is assistive to secondary

TABLE 3 | Influence of M, Gr, G, $N1$, m, Ec, Pr, n, and K on Nu_x.

M	Gr	G	$N1$	m	Ec	Pr	n	K	Nu_x
0.2	0.2	0.3	0.2	1.1	0.1	0.72	1.1	0.1	1.567232
0.3									1.553232
0.4									1.539852
	0.4								1.540408
	0.6								1.540960
	0.8								1.541507
		0.4							1.541508
		0.6							1.541508
		0.8							1.541508
			0.3						1.541500
			0.4						1.541493
			0.5						1.541486
				1.3					1.557281
				1.5					1.567616
				1.7					1.574715
					0.3				1.530638
					0.6				1.464505
					0.9				1.398349
						1.0			1.524106
						5.0			1.893057
						10.0			1.952805
							1.2		1.437652
							1.3		1.475901
							1.4		1.513178
								0.3	1.515541
								0.5	1.518194
								0.7	1.523959

momentum development when the magnetic field is positive. These impacts are depicted in **Figures 2**, **4**. The opposite impacts of M on secondary velocity and temperature functions are depicted in **Figures 3**, **5**. It is perceived that the strong magnetic field has direct relationship with the secondary velocity and temperature functions. Against the magnetic field, the upsurge in temperature function is an attribute to the dissipation in kinetic energy consumed in dragging the micropolar. In addition, the temperature is always supreme at the wall.

Figures 6–9 display the consequence of Gr on $f'(\xi)$, $g(\xi)$, $h(\xi)$, and $\theta(\xi)$. The influence of Gr on $f'(\xi)$ is portrayed in **Figure 6**. Here, the velocity heightens with the acceleration in Grashof number near the wall. However, the free convention current deteriorates at a critical distance from the wall which conserved into the free stream. A similar impact of Grashof number secondary velocity can be seen in **Figure 7**. Near the wall the fluid flow escalates with greater Grashof number but thereafter a deceleration started after some critical distance. Furthermore, the greater proportion of the region is observed for secondary velocity in comparison of primary velocity. **Figure 8** reveals the consequence of Gr on $h(\xi)$. The angular velocity heightens via Grashof number. A very quick growing behavior in the whole boundary layer regime is observed in the angular velocity. **Figure 9** reveals the impact of Gr on $\theta(\xi)$. The intensifying Grashof number shrinks the boundary layer thickness, consequently the decline in temperature function is depicted.

Figures 10–13 reveal the impact m on $f'(\xi)$, $g(\xi)$, $h(\xi)$, and $\theta(\xi)$. **Figure 10** reveals the impact of m on $f'(\xi)$. Acceleration in m escalates the $f'(\xi)$ in the neighborhood of the wall. Further toward the free stream, after some critical points the primary velocity function reduces. The drag force moderates which produce acceleration in $f'(\xi)$ and in conclusion $f'(\xi)$ diminishes. **Figure 11** reveals the impact of m on $g(\xi)$. Acceleration in m escalates the $g(\xi)$ throughout the fluid flow. The Hall term in Equation (9) is effectively positive for positive magnetic field parameter. This assists to support the cross flow and demonstrates in significant cross flow spurt. **Figure 12** reveals the impact of m on $h(\xi)$. The Hall current parameter shows dual behavior in the flow of fluid. An enhancement in $h(\xi)$ is perceived nearer to the wall and then deceleration to the flow stream is observed at some critical points. Generally, nevertheless the Hall current emboldens the rotary motions of microelements. **Figure 13** reveals the impact of m on $\theta(\xi)$. The temperature function is regularly inhibited with Hall current parameter. Here, the decline in thickness of the boundary layer is perceived.

Figures 14, **15** reveal the impact of K on $f'(\xi)$, $g(\xi)$, $h(\xi)$, and $\theta(\xi)$. At the point when an extra force added to the fluid which contradicts the fluid stream, this resistance makes a couple forces thus a couple stresses are persuaded in the fluid. This sort of fluid is recognized as couple stress fluid. Generally, the couple stress parameter and couple stress viscosity parameter n' has direct relationship. The growing couple stress parameter leads the fluid to be more viscous which reduces the fluid flow. Therefore, the escalation approximations of couple stress parameter reduced the primary and secondary velocity as shown in **Figures 14**, **15**. Additionally, the couples stress parameter is associated with the fluid motion. Therefore, it has no impact on temperature function.

Tables 1–3 are displayed to observe the impact of embedded parameters on velocities and temperature profiles. The impact M, Gr, G, $N1$, m, Ec, Pr, n, and K on C_{fx} and C_{fz} are shown in **Tables 1**, **2**. The rising value of M, $N1$, n, and K augmented the skin friction along x-axis C_{fx} where Gr, G, and m have opposite impact on the skin friction along x-axis C_{fx}. The higher value of M, Gr, G, and Ec augmented skin friction along z-axis C_{fz} where, m, $N1$, n, and K reduces the skin friction along z-axis C_{fz}. The influence of M, Gr, $N1$, m, Ec, Pr, n, and K on heat flux Nu_x are presented in **Table 3**. The greater value of Gr, m, Pr, n, and K augmented the heat flux Nu_x while, remaining parameter reduces the heat flux Nu_x. It should be noted that G has no impact on Nu_x.

CONCLUSION

In the current paper, the MHD micropolar boundary layer flow and heat transfer over a non-linear extending sheet infused by a strong magnetic field with couple stress, viscous dissipation and Hall impact have been determined.

The final observations are:

- The primary velocity reduces with greater magnetic parameter, local Grashof number, Hall parameter and couples stress parameter.
- The secondary velocity increases with greater magnetic parameter, Hall parameter and couple stress parameter.
- The secondary velocity decreases with greater local Grashof number.
- The angular velocity reduces with greater magnetic parameter and Hall parameter.
- The angular velocity increases with greater local Grashof number.
- The temperature profile increases with greater magnetic parameter.
- The temperature profile increases with greater Hall parameter and local Grashof number.

DATA AVAILABILITY STATEMENT

The datasets generated for this study are available on request to the corresponding author.

AUTHOR CONTRIBUTIONS

ZS and PK developed the numerical method and led the manuscript preparation. AD contributed to the code development and to the article preparation. EA and PT contributed to the analysis and discussion of the results.

FUNDING

This research was funded by the Center of Excellence in Theoretical and Computational Science (TaCS-CoE), KMUTT under Grant KMUTNB-61-GOV-A-0.

ACKNOWLEDGMENTS

This work was supported by the research program International Research Common Laboratory in cooperation under Renewable Energy Research Centre (RERC)—King Mongkut's University of Technology North Bangkok (KMUTNB), Center of Excellence in Theoretical and Computational Science (TaCS-CoE)—King Mongkut's University of Technology Thonburi (KMUTT), and Groupe de Recherche en Energie Electrique de Nancy (GREEN)—Université de Lorraine (UL) under Grant KMUTNB-61-GOV-A-01.

REFERENCES

1. Stokes VK. Couple stresses in fluids. *Phys Fluids*. (1966) **9**:1710–5. doi: 10.1063/1.1761925
2. Khan NA, Mahmood A, Ara A. Approximate solution of couple stress fluid with expanding or contracting porous channel. *Eng Comput*. (2013) **30**:399–408. doi: 10.1108/02644401311314358
3. Farooq M, Islam S, Haroon T. Heat transfer analysis of the couple stress fluid between two parallel plates. *Heat Trans Res*. (2011) **42**:737–80. doi: 10.1615/HeatTransRes.2012000996
4. Srinivasacharya D, Kaladhar K. Mixed convection flow of couple stress fluid in a non-darcy porous medium with Soret and Dufour effects. *J Appl Sci Eng*. (2012) **15**:415–22.
5. Ramzan M, Farooq M, Alsaedi A, Hayat T. MHD three-dimensional flow of couple stress fluid with Newtonian heating. *Eur Phys J Plus*. (2013) **128**:49. doi: 10.1140/epjp/i2013-13049-5
6. Hayat T, Mustafa M, Iqbal Z, Alsaedi A. Stagnation-point flow of couple stress fluid with melting heat transfer. *Appl Math Mech*. (2013) **34**:167–76. doi: 10.1007/s10483-013-1661-9
7. Turkyilmazoglu M. Exact solutions for two-dimensional laminar flow over a continuously stretching or shrinking sheet in an electrically conducting quiescent couple stress fluid. *Int J Heat Mass Transfer*. (2014) **72**:1–8. doi: 10.1016/j.ijheatmasstransfer.2014.01.009
8. Awad F, Haroun NAH, Sibanda P, Khumalo M. On couple stress effects on unsteady nanofluid flow over stretching surfaces with vanishing nanoparticle flux at the wall. *J Appl Fluid Mech*. (2016) **9**:1937–44. doi: 10.18869/acadpub.jafm.68.235.24940

9. Sreenadh S, Kishore SN, Srinivas ANS, Reddy RH. MHD free convection flow of couple stress fluid in a vertical porous layer. *Adv Appl Sci Res.* (2011) **2**:215–22.
10. Hayat T, Awais M, Safdar A, Hendi AA. Unsteady three dimensional flow of couple stress fluid over a stretching surface with chemical reaction. *Nonlin Analy Mod. Cont.* (2012) **17**:47–59. doi: 10.15388/NA.17.1.14077
11. Khan NA, Aziz S, Khan NA. Numerical simulation for the unsteady MHD flow and heat transfer of couple stress fluid over a rotating disk. *PLoS ONE.* (2014) **9**:e95423. doi: 10.1371/journal.pone.0095423
12. Hayat T, Aziz A, Muhammad T, Ahmad B. Influence of magnetic field in three-dimensional flow of couple stress nanofluid over a nonlinearly stretching surface with convective condition. *PLoS ONE.* (2015) **10**:e0145332. doi: 10.1371/journal.pone.0145332
13. Ramzan M. Influence of Newtonian heating on three dimensional MHD flow of couple stress nanofluid with viscous dissipation and joule heating. *PLoS ONE.* (2015) **10**:e0124699. doi: 10.1371/journal.pone.0124699
14. Hayat T, Muhammad T, Shehzad SA, Alsaedi A. Simultaneous effects of magnetic field and convective condition in three dimensional flow of couple stress nanofluid with heat generation/absorption. *J Braz Soc Mech Sci Eng.* (2017) **39**:1165–76. doi: 10.1007/s40430-016-0632-5
15. Hayat T, Muhammad T, Alsaedi A. On three-dimensional flow of couple stress fluid with Cattaneo–Christov heat flux. *Chin J Phys.* (2017) **55**:930–8. doi: 10.1016/j.cjph.2017.03.003
16. Umavathi JC, Chamkha AJ, Manjula MH, Al-Mudhaf A. Flow and heat transfer of a couple-stress fluid sandwiched between viscous fluid layers. *Can J Phys.* (2005) **83**:705–20. doi: 10.1139/p05-032
17. Umavathi JC, Malashetty MS. Oberbeck convection flow of a couple stress fluid through a vertical porous stratum. *Int J Nonlin Mech.* (1999) **34**:1037–45. doi: 10.1016/S0020-7462(98)00074-2
18. Srinivasacharyulu N, Odelu O. Flow and heat transfer of couple stress fluid in a porous channel with expanding and contracting walls. *Int Commun Heat Mass Transfer.* (2009) **36**:180–5. doi: 10.1016/j.icheatmasstransfer.2008.10.005
19. Zueco J, Beg OA. Network numerical simulation applied to pulsatile non-Newtonian flow through a channel with couple stress and wall mass flux effects. *Int J Appl Math Mech.* (2009) **5**:1–16.
20. Zakaria M. Hydromagnetic fluctuating flow of a couple stress fluid through a porous medium. *Korean J Comput Appl Math.* (2002) **10**:175–91. doi: 10.1007/BF02936216
21. Ellahi R, Zeeshan A, Hussain F, Asadollahi A. Peristaltic blood flow of couple stress fluid suspended with nanoparticles under the influence of chemical reaction and activation energy, *Symmetry.* (2019) **11**:276. doi: 10.3390/sym11020276
22. Rudolf AT, Baumjohann W, Balogh. A. The strongest magnetic fields in the universe: how strong can they become? *Front Phys.* (2014) **2**:59. doi: 10.3389/fphy.2014.00059
23. Hayat T, Iqbal R, Tanveer A, Alsaed A. Soret and Dufour effects in MHD peristalsis of pseudoplastic nanofluid with chemical reaction. *J Mol Liq.* (2016) **220**:693–706. doi: 10.1016/j.molliq.2016.04.123
24. Lin Y, Zheng L, Zhang X, Chen G. MHD pseudo-plastic nanofluids unsteady flow and heat transfer in a finite thin film over stretching sheet with internal heat generation. *Int J Heat Mass Transf.* (2015) **84**:903–11. doi: 10.1016/j.ijheatmasstransfer.2015.01.099
25. Ramesh K, Devakar M. The influence of heat transfer on peristaltic transport of MHD second grade fluid through porous medium in a vertical asymmetric channel. *J Appl Fluid Mech.* (2015) **8**:351–65. doi: 10.18869/acadpub.jafm.67.222.23471
26. Reddy MG, Reddy KV. Influence of Joule heating on MHD peristaltic flow of a nanofluid with compliant walls. *Process Eng.* (2015) **127**:1002–9. doi: 10.1016/j.proeng.2015.11.449
27. Eringen AC. Theory of micropolar fluids. *J Math Mech.* (1966) **16**:1–18. doi: 10.1512/iumj.1967.16.16001
28. Bég AO, Bhargava R, Rashidi MM. *Numerical Simulation in Micropolar Fluid Dynamics*. Saarbrücken: Lap Lambert Academic Publishing GmbH KG (2011).
29. Uddin Z, Kumar M. Hall and ion-slip effect on MHD boundary layer flow of a micro polar fluid past a wedge. *Sci Iran*. (2013) **20**:467–76. doi: 10.1016/j.scient.2013.02.013
30. Khan A, Shah Z, Islam S, Dawar A, Bonyah E, Ullah H, Khan A. Darcy-Forchheimer flow of MHD CNTs nanofluid radiative thermal behaviour and convective non uniform heat source/sink in the rotating frame with microstructure and inertial characteristics, *AIP Adv.* (2018) **8**:125024. doi: 10.1063/1.5066223
31. Dawar A, Shah Z, Khan W, Idrees M, Islam S. Unsteady squeezing flow of magnetohydrodynamic carbon nanotube nanofluid in rotating channels with entropy generation and viscous dissipation. *Adv Mech Eng.* (2019) **11**:1–18. doi: 10.1177/1687814018823100
32. Kumam P, Shah Z, Dawar A, Rasheed HU, Islam S. Entropy Generation in MHD radiative flow of CNTs casson nanofluid in rotating channels with heat source/sink. *Math Problems Eng.* (2019) **2019**:9158093. doi: 10.1155/2019/9158093
33. Shah Z, Dawar A, Kumam P, Khan W, Islam S. Impact of nonlinear thermal radiation on MHD nanofluid thin film flow over a horizontally rotating disk. *Appl. Sci*. (2019) **9**:1533. doi: 10.3390/app9081533
34. Ali F, Sheikh NA, Khan I, Saqib M. Magnetic field effect on blood flow of Casson fluid in axisymmetric cylindrical tube: a fractional model. *J Magn Magn Mater*. (2017) **423**:327–36. doi: 10.1016/j.jmmm.2016.09.125
35. Shah Z, Dawar A, Alzahrani EO, Kumam P, Khan A, Islam S. Hall effect on couple stress 3D nanofluid flow over an exponentially stretched surface with Cattaneo Christov Heat Flux Mode. *IEEE Access*. (2019) **7**:64844–55. doi: 10.1109/ACCESS.2019.2916162
36. Shah Z, Islam S, Gul T, Bonyah E, Altaf Khan M. The electrical MHD and Hall current impact on micropolar nanofluid flow between rotating parallel plates. *Results Phys.* (2018) **9**:1201–14. doi: 10.1016/j.rinp.2018.01.064
37. Kumar KA, Reddy JV, Sugunamma V, Sandeep N. Simultaneous solutions for MHD flow of williamson fluid over a curved sheet with nonuniform heat source/sink. *Heat Transfer Res.* (2019) **50**:581–603. doi: 10.1615/HeatTransRes.2018025939
38. Temple RC, Mihai AP, Arena DA, Marrows CH. Ensemble magnetic behavior of interacting CoFe nanoparticles. *Front Phys*. (2015) **3**:52. doi: 10.3389/fphy.2015.00052
39. Ellahi R, Zeeshan A, Shehzad N, Alamri SZ. Structural impact of Kerosene-Al2O3 nanoliquid on MHD Poiseuille flow with variable thermal conductivity: application of cooling process. *J Mol Liquids.* (2018) **264**:607–15. doi: 10.1016/j.molliq.2018.05.103
40. Asadollahi A, Rashidi S, Esfahani JA, Ellahi R. Simulating phase change during the droplet deformation and impact on a wet surface in a square microchannel: An application of oil drops collision. *Eur Phys J Plus.* (2018) **133**:306. doi: 10.1140/epjp/i2018-12135-6
41. Ellahi R, Alamri SZ, Basit A, Majeed A. Effects of MHD and slip on heat transfer boundary layer flow over a moving plate based on specific entropy generation. *J Taibah Univ Sci.* (2018) **12**:476–82. doi: 10.1080/16583655.2018.1483795
42. Ellahi R, Bhatti M, Pop I. Effects of hall and ion slip on MHD peristaltic flow of Jeffrey fluid in a non-uniform rectangular duct. *Int J Num Methods Heat Fluid Flow.* (2016) **26**:1802–20. doi: 10.1108/HFF-02-2015-0045
43. Ellahi R, Sait SM, Shehzad N, Mobin N. Numerical simulation and mathematical modeling of electro-osmotic couette–poiseuille flow of MHD power-law nanofluid with entropy generation. *Symmetry*. (2019) **11**:1038. doi: 10.3390/sym11081038
44. Bhatti MM, Zeeshan A, Ellahi R, Shit GC. Mathematical modeling of heat and mass transfer effects on MHD peristaltic propulsion of two-phase flow through a Darcy-Brinkman-Forchheimer Porous medium. *Adv Powder Technol.* (2018) **29**:1189–97. doi: 10.1016/j.apt.2018.02.010
45. Ameen I, Shah Z, Islam S, Nasir S, Khan W, Kumam P, Thounthong P. Hall and Ion-Slip Effect on CNTS nanofluid over a porous extending surface through heat generation and absorption. *Entropy.* (2019) **21**:801. doi: 10.3390/e21080801

46. Vo DD, Shah Z, Sheikholeslami M, Shafee A, Nguyen TK. Numerical investigation of MHD nanomaterial convective migration and heat transfer within a sinusoidal porous cavity. *Phys. Scr*. (2019) **94**:115225. doi: 10.1088/1402-4896/ab2ced
47. Ahmad MW, Kumam P, Shah Z, Farooq AA, Nawaz R, Dawar A, et al. Darcy–Forchheimer MHD Couple Stress 3D nanofluid over an exponentially stretching sheet through cattaneo–christov convective heat flux with zero nanoparticles mass flux conditions. *Entropy*. (2019) **21**:867. doi: 10.3390/e21090867
48. Sheikholeslami M, Shah Z, Shafee A, Khan I, Tlili I. Uniform magnetic force impact on water based nanofluid thermal behavior in a porous enclosure with ellipse shaped obstacle. *Sci Rep*. (2019) **9**:1196. doi: 10.1038/s41598-018-37964-y
49. Ali AY, Ali Y, Kumam P, Babar K, Ahmed A, Shah Z. Flow of a nanofluid and heat transfer in channel with contractingexpanding walls. *IEEE Access*. (2019) **7**:102427–36. doi: 10.1109/ACCESS.2019.2928030
50. Ullah A, Alzahrani EO, Shah Z, Ayaz M, Islam S. Nanofluids thin film flow of reiner-philippoff fluid over an unstable stretching surface with brownian motion and thermophoresis effects. *Coatings*. (2019) **9**:21. doi: 10.3390/coatings9010021

Conflict of Interest: The authors declare that the research was conducted in the absence of any commercial or financial relationships that could be construed as a potential conflict of interest.

Copyright © 2019 Shah, Kumam, Dawar, Alzahrani and Thounthong. This is an open-access article distributed under the terms of the Creative Commons Attribution License (CC BY). The use, distribution or reproduction in other forums is permitted, provided the original author(s) and the copyright owner(s) are credited and that the original publication in this journal is cited, in accordance with accepted academic practice. No use, distribution or reproduction is permitted which does not comply with these terms.

frontiers in Physics

ORIGINAL RESEARCH
published: 06 November 2019
doi: 10.3389/fphy.2019.00164

Numerical Simulation of Magnetohydrodynamic Nanofluids Under the Influence of Shape Factor and Thermal Transport in a Porous Media Using CVFEM

Zahir Shah[1]*, *Houman Babazadeh*[2,3], *Poom Kumam*[4,5,6]*, *Ahmad Shafee*[7] and *Phatiphat Thounthong*[8]

[1] SCL 802 Fixed Point Laboratory, Science Laboratory Building, Center of Excellence in Theoretical and Computational Science (TaCS-CoE), King Mongkut's University of Technology Thonburi (KMUTT), Bangkok, Thailand, [2] Department for Management of Science and Technology Development, Ton Duc Thang University, Ho Chi Minh City, Vietnam, [3] Faculty of Environment and Labour Safety, Ton Duc Thang University, Ho Chi Minh City, Vietnam, [4] KMUTT-Fixed Point Research Laboratory, Room SCL 802 Fixed Point Laboratory, Science Laboratory Building, Department of Mathematics, Faculty of Science, King Mongkut's University of Technology Thonburi (KMUTT), Bangkok, Thailand, [5] KMUTT-Fixed Point Theory and Applications Research Group, Science Laboratory Building, Faculty of Science, Theoretical and Computational Science Center (TaCS), King Mongkut's University of Technology Thonburi (KMUTT), Bangkok, Thailand, [6] Department of Medical Research, China Medical University Hospital, China Medical University, Taichung, Taiwan, [7] Public Authority of Applied Education and Training, Applied Science Department, College of Technological Studies, Shuwaikh, Kuwait, [8] Department of Teacher Training in Electrical Engineering, Faculty of Technical Education, Renewable Energy Research Centre, King Mongkut's University of Technology North Bangkok, Bangkok, Thailand

OPEN ACCESS

Edited by:
Muhammad Mubashir Bhatti, Shanghai University, China

Reviewed by:
Tehseen Abbas, University of Education Lahore, Pakistan
Titan Chandra Paul, University of South Carolina Aiken, United States

***Correspondence:**
Zahir Shah
zahir.sha@kmutt.ac.th
Poom Kumam
poom.kum@kmutt.ac.th

Specialty section:
This article was submitted to Mathematical Physics, a section of the journal Frontiers in Physics

Received: *19 August 2019*
Accepted: *11 October 2019*
Published: *06 November 2019*

Citation:
Shah Z, Babazadeh H, Kumam P, Shafee A and Thounthong P (2019) Numerical Simulation of Magnetohydrodynamic Nanofluids Under the Influence of Shape Factor and Thermal Transport in a Porous Media Using CVFEM. Front. Phys. 7:164. doi: 10.3389/fphy.2019.00164

In this article, the migration of nanomaterials through a permeable domain was modeled numerically. Aluminum oxide was dispersed into testing fluid which was selected water in the current paper. Utilizing Darcy LAW for a porous medium helps us to find simpler form of equations. Influences of shape factor and radiation on the thermal conduct of nanoparticles within a porous region were scrutinized. Nanomaterial within such region is applied under the Lorentz force. CVFEM approach for simulation goals has been applied. This approach provides the advantages of two common CFD methods. Impacts of radiation, magnetic, buoyancy parameters on the treatment of nanomaterials were demonstrated. Outcomes showed that greater amounts of shape factor cause stronger convection. Reverse relationships exist between the Hartmann number and temperature gradient.

Keywords: nanoparticle's shape, porous space, magnetic force, darcy LAW, radiation, nanofluid, CVFEM

INTRODUCTION

Nanotechnology is one of the most interesting fields nowadays. It is interesting due to its vast applications in solar cells, food, fuel cells, batteries, and fuel, etc. In simple, nanotechnology has made its way to each and every branch. Investigators started interest in this field and developed a new sub-branch of nanotechnology, nanofluids. Nanofluids were utilized by Choi [1] for the first time. In real-world fluids exist in abundance, among all, nanopowders can be offered as the most applicable fluids both from its use and its unique nature. Nanofluids are two-phase nanometer-size fluids in which base fluid ranging up to 100 nm. Nanofluids are used in metal oxides, oxides ceramics, and allotropes of carbon and in other chemical stable elements. Nanoparticles nowadays play a key role in thermal analysis. Pak and Cho [2] used titanium dioxide and, and found an improvement in the heat flux. Nanofluids in which the nanoparticles size range less than are considered more ideal [3]. Radiation impact on nanomaterial flow was performed by Zeeshan et al. [4] and they added the impact of MHD on titanium dioxide transportation. Impose of nanomaterial into usual carrier fluid leads to greater conductivity [5–10]. Copper oxide migration within an absorptive medium with the use of Lorentz force in the actuality of magnetic force has been demonstrated by Sheikholeslami [11]. A numerical survey is performed by Sheikholeslami [12] for CuO-H_2O nanofluid in a penetrable medium with the help of a microscopic technique. Shah et al. [13] have worked on the 3-D nanofluid flow of third-grade fluid with physical properties inside a rotating frame. An analytical investigation is performed by Dawar et al. [14] for Casson fluid with MHD carbon nanotubes (CNT's) inside a rotating channel. A numerical survey is presented by Sheikholeslami and Shehzad [15] by analyzing Fe_3O_4–H_2O nanofluid flow with inside a permeable channel. To depict the changes in flow style in the appearance of Kelvin forces, Sheikholeslami and Vajravelu [16] examined the FHD impact on nanomaterial flow. CNT migration in a time-dependent problem has been analyzed by Ahmed et al. [17] and they supposed the plate is porous and Lorentz force was added in momentum equations. The transfer of heat due to convection of ferrofluid is described by Yimin et al. [18]. In recent years, Thermal irreversibility in nanofluid through a pipe with a turbulator by means of FVM was analyzed by Sheikholeslami et al. [19]. For a detailed survey, interested readers are referred to Sheikholeslami et al. [20], Dat et al. [21], Bhatti et al. [22], Sheikholeslami [23], Cattaneo [24], Sheikholeslami and Shehzad [25] for more detail and related study of nanofluids flow. Cattaneo [24] made a modification in the thermal relaxation time to improve the heat transfer effects. Cattaneo attempt made for a specific material and obtained some interesting results in the heat transmission investigation by presenting an innovative flux approach. A Maxwell fluid was realized to this model by Mustafa [26] for the study of upper convection. A numerical investigation is performed by Ai and Sandeep [27] by considering this model for MHD Casson-ferrofluid for heat transfer analysis. Previous articles on Nanomaterials for dissimilar phenomena and their usages can be found [28–33]. Sheikholeslami et al. [34] recently presented the application of electric and magnetic field of nanofluid and ferrofluid and with transfer in an enclosure walls. Jawad et al. [35, 36] studied nanofluid thin film and their applications. Nasir et al. [37, 38] have studied 3-D nanomaterial flow CNTs and thermal analysis along a stretching surface. Entropy generation in nanofluid flow can be studied in Alharbi et al. [39]. The studied of nanofluids are further extended to liquid film due to its abundant uses in various sciences [40–48]. Nanomaterial transportation over a wedge was scrutinized by Hassan et al. [49]. An experimental approach was performed by Sheikholeslami et al. [50] to study the boiling of refrigerant with the use of nanoparticles.

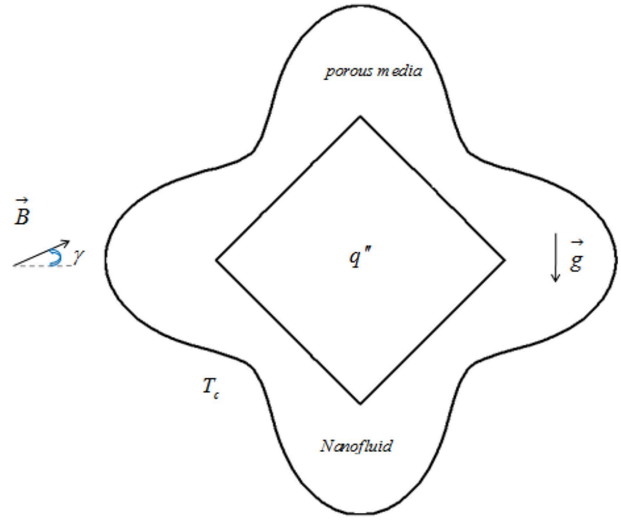

FIGURE 1 | Present tank and sample element.

TABLE 1 | Coefficient of carrier fluid.

Coefficient values	Al_2O_3-H_2O
α_1	52.813488759
α_2	6.115637295
α_3	0.6955745084
α_4	4.17455552786
α_5	0.176919300241
α_6	−298.19819084
α_7	−34.532716906
α_8	−3.9225289283
α_9	−0.2354329626
α_{10}	−0.999063481

Though there is intense research in the literature about nanofluid modeling and the MHD effect in different categories, there is still limited information about the complex geometries and Darcy model. Additionally, the radiative effect is an important source. The determination of this article is to study the migration of nanopowder within a porous space. The effects of shape factor and radiation on the thermal conduct of nanomaterials within a porous space were scrutinized.

PROBLEM EXPLANATION

In this modeling and simulation, water-based nanofluid exists through permeable geometry has considered. Impact of Lorentz force and thermal behavior are taken on nanofluid. Sketch of the porous tank is depicted in **Figure 1**. Nanofluid is thermally conducting and impact of Lorentz force was involved. Control Volume finite element technique with a triangular element has been used (see **Figure 1**). Needed boundary constraints were established in **Figure 1**. The Darcy LAW [15] is involved for porous terms.

TABLE 2 | Some physical thermal features.

	C_p $(jkg^{-1}K^{-1})$	C_p $(jkg^{-1}K^{-1})$	$\beta \times 10^5$ (K^{-1})	K $(Wm^{-1}.K^{-1})$	$\sigma\,(\Omega \cdot m)^{-1}$
H_2O	4,179	4,179	21	0.613	0.05
Al_2O_3	765	765	0.85×10^{-5}	25	1×10^{-10}

TABLE 3 | Structure of m at dissimilar values.

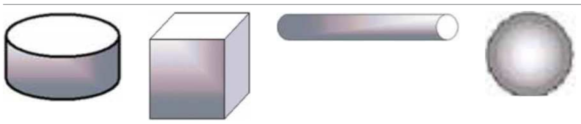

				Shape
5.7	3.7	4.8	3	m

TABLE 4 | Deviation of Nu_{ave} at different mesh size when $Ra = 600$, $Ha = 0, Rd = 0.8$ and $\phi = 0.04$.

Mesh size				
41 × 121	51 × 151	61 × 181	71 × 211	81 × 241
5.0591	5.0688	5.0715	5.0767	5.0793

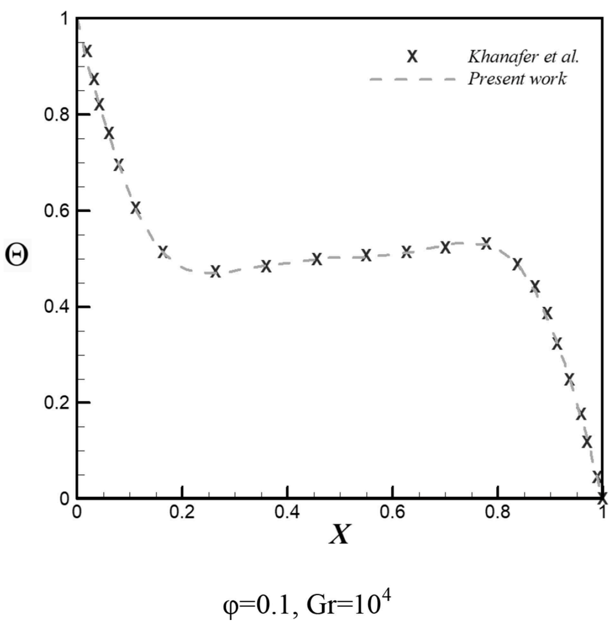

FIGURE 2 | Justification for nanofluid [5].

GOVERNING EQUATIONS, FORMULATION, AND CVFEM

Nanopowder migration through a permeable domain with the help of Darcy model was considered in the current article and involving single-phase model results in below equations:

$$\frac{\partial u}{\partial x} + \frac{\partial v}{\partial y} = 0 \tag{1}$$

$$\frac{\mu_{nf}}{K} u = -\frac{\partial P}{\partial x} + \sigma_{nf} B_0^2 \left[(\sin\gamma)\, v\,(\cos\gamma) - u(\sin\gamma)^2\right] \tag{2}$$

$$\frac{\mu_{nf}}{K} v = -\frac{\partial P}{\partial y} + (T - T_c)\, g\rho_{nf}\beta_{nf} + \sigma_{nf} B_0^2 (\cos\gamma)\left[(\sin\gamma)\, u - (\cos\gamma)\, v\right] \tag{3}$$

$$\frac{\partial q_r}{\partial y}\left(\rho C_p\right)_{nf}^{-1} + \left(\frac{\partial T}{\partial y} v + u\frac{\partial T}{\partial x}\right) = k_{nf}\left(\frac{\partial^2 T}{\partial y^2} + \frac{\partial^2 T}{\partial x^2}\right)\left(\rho C_p\right)_{nf}^{-1}, \quad , \left[T^4 \cong 4T_c^3 T - 3T_c^4, q_r = -\frac{4\sigma_e}{3\beta_R}\frac{\partial T^4}{\partial y}\right] \tag{4}$$

The fundamental characteristics of nanofluid are estimated as:

$$\Re_{nf} = \Re_f + \left(\Re_s - \Re_f\right)\phi, \quad \Re = C_p\rho \tag{5}$$

$$(\rho\beta)_{nf} + (\rho\beta)_f(\phi - 1) = \phi(\rho\beta)_s \tag{6}$$

$$\rho_{nf} = (1-\phi)\rho_f + \phi\rho_s \tag{7}$$

$$\frac{\sigma_{nf}}{\sigma_f} - 1 = \frac{\left(-1 + \frac{\sigma_s}{\sigma_f}\right)(3\phi)}{\left(2 + \frac{\sigma_s}{\sigma_f}\right) + \phi\left(1 - \frac{\sigma_s}{\sigma_f}\right)} \tag{8}$$

To apply the effects of shape factor and $k_{Brownian}$, the following correlations were examined:

$$\mu_{eff} = \mu_{static} + \frac{k_{Brownian}}{k_f} \times \frac{\mu_f}{\Pr_f}$$

$$k_{Brownian} = 5\times10^4 c_{p,f}\rho_f g'(d_p,\phi,T)\phi\sqrt{\frac{\kappa_b T}{\rho_p d_p}} \tag{9}$$

$$g'\left(d_p,\phi,T\right) = \Big(a_1 + a_5 Ln\big(d_p\big)^2 + Ln(\phi)\, a_4 Ln\left(d_p\right) + a_2 Ln\left(d_p\right) + a_3 Ln(\phi)\Big) Ln(T) + \Big(a_6 + a_{10} Ln\big(d_p\big)^2 + a_8 Ln(\phi) + a_7 Ln\left(d_p\right) + a_9 Ln\left(d_p\right) Ln(\phi)\Big)$$

$$\frac{k_{nf}}{k_f} = \frac{-\Im m\phi + k_p + \Im\phi + k_f + mk_f + k_f}{k_f m + k_p + \Im\phi + k_f}, \quad \Im = k_p - k_f \tag{10}$$

Equation (11) presents a dimensionless form:

$$\Psi = \psi/\alpha_{nf},\ \theta = \frac{T - T_c}{\Delta T},\ \Delta T = L\frac{q''}{k_f},\ (X, Y) = L^{-1}\left(x, y\right) \tag{11}$$

So, the last format of equations is:

$$\frac{\partial^2\Psi}{\partial Y^2} + \frac{\partial^2\Psi}{\partial X^2} = -Ha\frac{A_6}{A_5}\left[2(\sin\gamma)\frac{\partial^2\Psi}{\partial X\,\partial Y}(\cos\gamma) + \frac{\partial^2\Psi}{\partial Y^2}\left(\sin^2\gamma\right) + (\cos\gamma)\frac{\partial^2\Psi}{\partial X^2}(\cos\gamma)\right] - \frac{A_3}{A_4}\frac{A_2}{A_5}\frac{\partial\theta}{\partial X} Ra \tag{12}$$

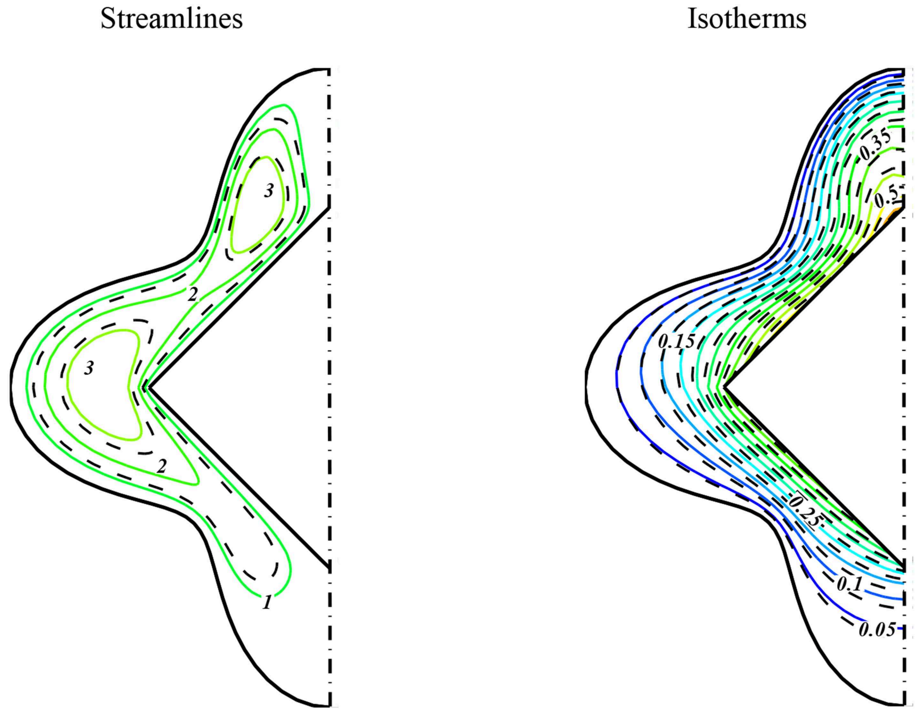

FIGURE 3 | Changing in behavior of nanofluid with rise of ϕ on nanofluid behavior. ($\phi = 0.04$ (—) and $\phi = 0$ (– – –)) when $m = 5.7, Rd = 0.8, Ra = 600, Ha = 0$.

$$\left(1 + \frac{4}{3} Rd\, A_4\right) \frac{\partial^2 \theta}{\partial Y^2} + \left(\frac{\partial^2 \theta}{\partial X^2}\right) = \frac{\partial \theta}{\partial X}\frac{\partial \Psi}{\partial Y} - \frac{\partial \Psi}{\partial X}\frac{\partial \theta}{\partial Y} \quad (13)$$

The mentioned variables in Equation (13) are:

$$\begin{array}{l} Ha = \frac{\sigma_f K B_0^2}{\mu_f},\ Ra = \frac{g\,K\,(\rho\beta)_f L\,\Delta T}{\mu_f\,\alpha_f},\ Rd = 4\sigma_e T_c^3 / \left(\beta_R k_f\right) \\ A_1 = \frac{\rho_{nf}}{\rho_f},\quad A_2 = \frac{(\rho C_P)_{nf}}{(\rho C_P)_f},\ A_5 = \frac{\mu_{nf}}{\mu_f}, \\ A_3 = \frac{(\rho\beta)_{nf}}{(\rho\beta)_f},\quad A_6 = \frac{\sigma_{nf}}{\sigma_f},\ A_4 = \frac{k_{nf}}{k_f} \end{array} \quad (14)$$

Besides, summarizations of boundaries are:

$$\begin{aligned} \theta &= 0.0 \text{ on outer surfaces} \\ \Psi &= 0.0 \text{ on all walls} \\ \frac{\partial \theta}{\partial n} &= 1.0 \text{ on inner wall} \end{aligned} \quad (15)$$

Nu_{loc} and Nu_{ave} are:

$$Nu_{loc} = \frac{1}{\theta}\left(1 + \frac{4}{3}\left(\frac{k_{nf}}{k_f}\right)^{-1} Rd\right)\left(\frac{k_{nf}}{k_f}\right) \quad (16)$$

$$Nu_{ave} = \frac{1}{S}\int_0^s Nu_{loc}\, ds \quad (17)$$

Simulation Technique, Grid and Verification

Sheikholeslami [29] has been discovered a new approach namely CVFEM for analyzing thermal problems. This technique utilizes a triangular element and the Gauss-Seidel approach uses for the final step of calculating scalars. **Tables 1–3** illustrate the properties of carrier fluid. Grid size must be independent of outcomes and we present special cases in **Table 4**. Validation for presents study for nanofluid [5] are presented in **Figure 2** and provide nice accuracy.

RESULTS AND DISCUSSION

In this article transportation of electrically and thermally conducting nanomaterial with different shapes were modeled numerically. Aluminum oxide was dispersed into testing fluid which was selected water in current paper. Utilizing Darcy low for porous medium helps us to find simpler form of equations. Impacts of shape factor and the radiation on thermal conduct of nanoparticles inside a permeable space were investigated. Impacts of Radiation parameter, shape factor, magnetic force, and fraction of alumina have been demonstrated. The Darcy Law is involved for a permeable term in geometry.

Impacts of imposing nanopowders into H_2O by selecting other parameters are shown in **Figure 3**. Actually this is the nanofluid scattering rule. It is observed that nanofluid motion augmented with the imposing of nanoparticles. The impacts of Hartmann for different cases were plotted in **Figures 4**, **5**. Impose of the Lorentz effect declines the motion of nanoparticles.

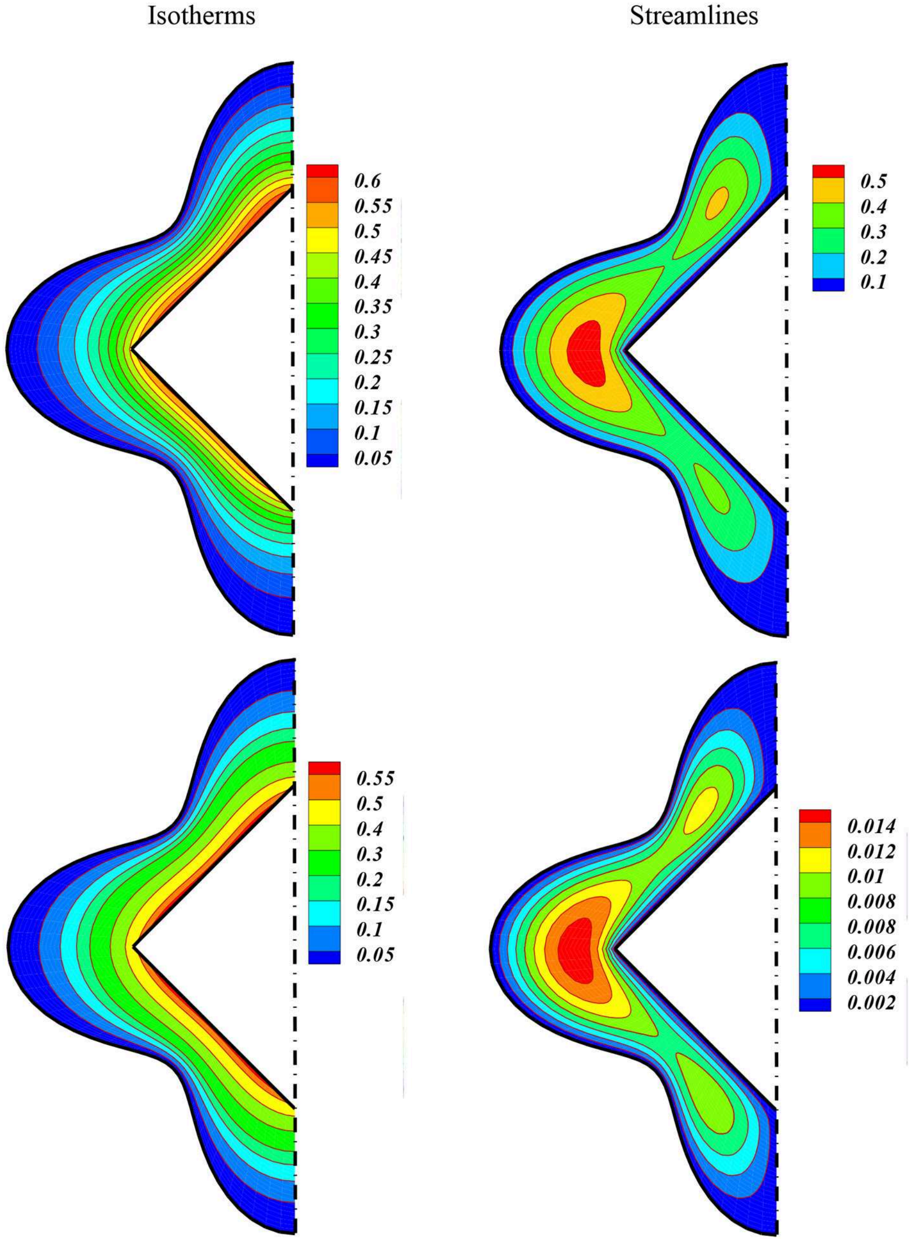

FIGURE 4 | Showing variation of Ha when $\phi = 0.04$, $m = 5.7$, $Rd = 0.8$, $Ra = 100$.

Actually, with the augmentation of the magnetic parameter, the top two eddies were amalgamate together and the thermal spiral disappear. It is observed that adding magnetic impact, stronger conduction occurs. Reverse relationships exist between the Hartmann number and temperature gradient. Impacts of scrutinized variables on Nusselt number were displayed in **Figure 6**. Variations for different cases are presented here.

Distortion of isotherms augments in consequence of augment in buoyancy and makes stronger vortex which indicates the growth of free convection. With the domination of convective mode, isotherms become more complex with generating plume. Therefore, increasing permeability and buoyancy term makes the Nusselt number to augment. Resistance against the nanomaterial migration reduces with augment of Lorentz forces and in turn, Nusselt number can reduce. Temperature distribution becomes less complex with involving magnetic field and higher Lorentz force can eliminate the plumes. Shear stress among nanoparticles declines with augment of permeability of the region. So, the power of the flow augments with rise of permeability which indicates greater convective flow. The influence of permeability on the style of nanofluid flow reduces with decreasing buoyancy forces. Greater nanofluid mixing occurs within the domain with

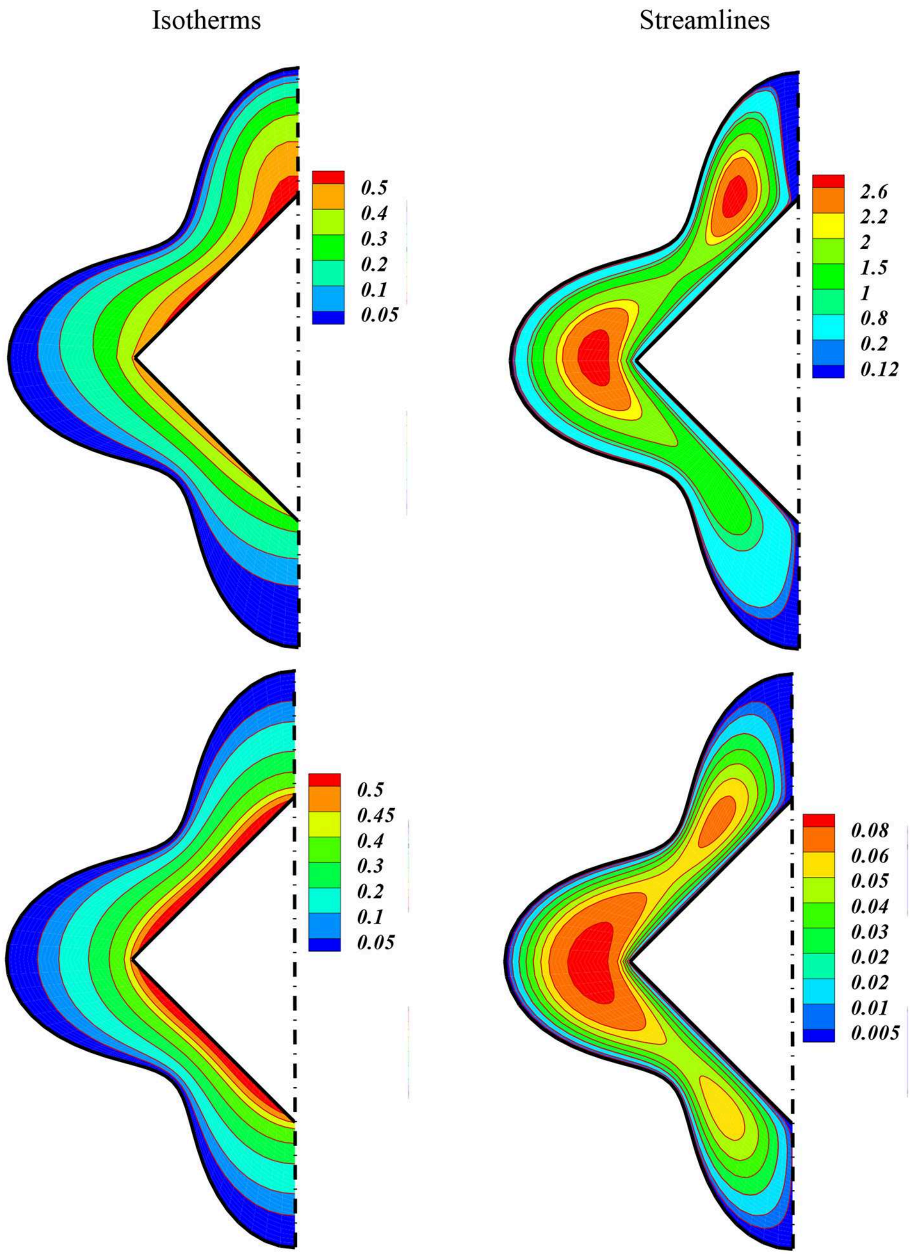

FIGURE 5 | Showing variation of Ha when $\phi = 0.04$, $m = 5.7$, $Rd = 0.8$, $Ra = 600$.

the rise of buoyancy forces and this influence reduces with imposing magnetic field. Resistance against the nanomaterial migration declines with augment of Darcy number but opposite phenomena appear with augment of the Hartmann number. Magnetic forces work against buoyancy forces, which can reduce the strength of streamline and imposing greater magnetic force, leads to conduction domination. The temperature gradient becomes independent on the Lorentz forces again, owing to the weakening of the buoyancy.

Changes of Nusselt number respect to variables are presented in **Figure 6**. The mathematical relationship has presented in Equation (18).

$$\begin{aligned} Nu_{ave} = {} & 3.34 + 0.087m + 1.04Rd + 0.19Ra - 0.14Ha \\ & + 1.1 \times 10^{-2} m\,Ha - 0.092Rd\,Ha - 0.19RaHa \\ & + 1.359 \times 10^{-4} m^2 \end{aligned} \tag{18}$$

It is concluded that the augment in distortion of temperature with buoyancy terms and permeability enhances the gradient of temperature. Moreover, transmission mode improves with a boost of the Lorentz force. Thus, convection diminishes with the

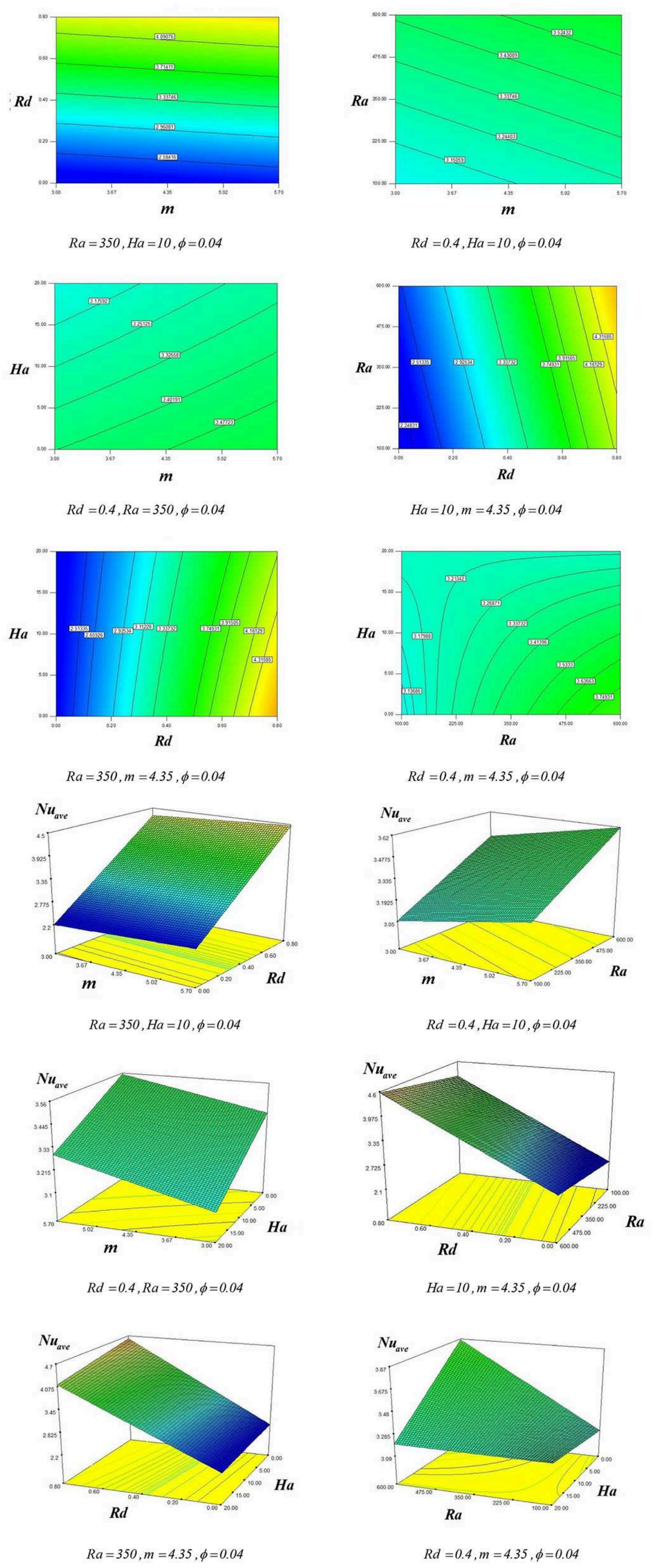

FIGURE 6 | How Rd, m, ϕ, Rd, Ha affect the Nu_{ave}.

escalation of the magnetic field. It is found from **Figure 6** that Nusselt number is augmenting function for radiation parameter.

CONCLUSIONS

In current CVFEM simulation, nanomaterial was offered as a feasible way to more augmentation of convection in permeable tank and various shapes of powder ware involved. To manage the migration of particles, magnetic forces was employed, and the influence of radiation has been imposed in the energy equation. Outcomes prove that augmenting Lorentz force declines the convection and make isotherms to lower dense near the wall. An indirect relationship was reported for temperature gradient and Lorentz forces. Furthered distortion was observed in isotherms with the rise of buoyancy force.

DATA AVAILABILITY STATEMENT

The datasets generated for this study are available on request to the corresponding author.

AUTHOR CONTRIBUTIONS

ZS developed the numerical method and led the manuscript preparation. HB and PK contributed to the code development and to the article preparation. AS and PT contributed to the analysis and discussion of the results.

FUNDING

This research was funded by the Center of Excellence in Theoretical and Computational Science (TaCS-CoE), KMUTT.

ACKNOWLEDGMENTS

This project was supported by the Theoretical and Computational Science (TaCS) Center under Computational and Applied Science for Smart Innovation Research Cluster (CLASSIC), Faculty of Science, KMUTT.

REFERENCES

1. Choi SUS. Enhancing thermal conductivity of fluids with nanoparticles. *ASME Int Mech Eng Congr Expos*. (1995) **231**:99–105.
2. Pak BC, Cho YI. Hydrodynamic and heat transfer study of dispersed fluids with submicron metallic oxide particles. *Exp Heat Transfer*. (1998) **11**:151–70. doi: 10.1080/08916159808946559
3. Sheikholeslami M, Rokni HB. Magnetic nanofluid flow and convective heat transfer in a porous cavity considering Brownian motion effects. *Phys Fluids*. (2018) **30**:1. doi: 10.1063/1.5012517
4. Zeeshan A, Shehzad N, Abbas T, Ellahi R. Effects of radiative electro-magnetohydrodynamics diminishing internal energy of pressure-driven flow of titanium dioxide-water nanofluid due to entropy generation. *Entropy*. (2019) **21**:236. doi: 10.3390/e21030236
5. Khanafer K, Vafai K, Lightstone M. Buoyancy-driven heat transfer enhancement in a two-dimensional enclosure utilizing nanofluids. *Int J Heat Mass Transf*. (2003) **46**:3639–53. doi: 10.1016/S0017-9310(03)00156-X
6. Sheikholeslami M, Shehzad SA. CVFEM for influence of external magnetic source on Fe_3O_4-H_2O nanofluid behavior in a permeable cavity considering shape effect. *Int J Heat Mass Transf*. (2017) **115**:180–91. doi: 10.1016/j.ijheatmasstransfer.2017.07.045
7. Sheikholeslami M, Jafaryar M, Hedayat M, Shafee A, Li Z, Nguyen TK, et al. Heat transfer and turbulent simulation of nanomaterial due to compound turbulator including irreversibility analysis. *Int J Heat Mass Transf*. (2019) **137**:1290–300. doi: 10.1016/j.ijheatmasstransfer.2019.04.030
8. Farshad SA, Sheikholeslami M. Nanofluid flow inside a solar collector utilizing twisted tape considering exergy and entropy analysis. *Renew Energy*. (2019) **141**:246–58. doi: 10.1016/j.renene.2019.04.007
9. Sheikholeslami M, Zareei A, Jafaryar M, Li Z, Smida A, Tlili I. Heat transfer simulation during charging of nanoparticle enhanced PCM within a channel. *Phys A*. (2019) **525**:557–65. doi: 10.1016/j.physa.2019.03.082
10. Sheikholeslami M, Jafaryar M, Shafee A, Li Z, Haq UH. Heat transfer of nanoparticles employing innovative turbulator considering entropy generation. *Int J Heat Mass Transf*. (2019) **136**:1233–40. doi: 10.1016/j.ijheatmasstransfer.2019.03.091
11. Sheikholeslami M. CuO-water nanofluid flow due to magnetic field inside a porous media considering Brownian motion. *J Mol Liquids*. (2018) **249**:921–9. doi: 10.1016/j.molliq.2017.11.118
12. Sheikholeslami M. Numerical investigation for CuO-H_2O nanofluid flow in a porous channel with magnetic field using mesoscopic method. *J Mol Liquids*. (2018) **249**:739–46. doi: 10.1016/j.molliq.2017.11.069
13. Shah Z, Islam S, Gul T, Bonyah E, Khan MA. Three dimensional third grade nanofluid flow in a rotating system between parallel plates with Brownian motion and thermophoresis effects. *Results Phys*. (2018) **10**:36–45. doi: 10.1016/j.rinp.2018.05.020
14. Dawar A, Shah Z, Khan W, Idrees M, Islam S. Unsteady squeezing flow of MHD CNTS nanofluid in rotating channels with entropy generation and viscous dissipation. *Adv Mech Eng*. (2019) **10**:1–18. doi: 10.1177/1687814018823100
15. Sheikholeslami M, Shehzad SA. Numerical analysis of Fe_3O_4-H_2O nanofluid flow in permeable media under the effect of external magnetic source. *Int J Heat Mass Transf*. (2018) **118**:182–92. doi: 10.1016/j.ijheatmasstransfer.2017.10.113
16. Sheikholeslami M, Vajravelu K. Nanofluid flow and heat transfer in a cavity with variable magnetic field. *Appl Math Comput*. (2017) **298**:272–82. doi: 10.1016/j.amc.2016.11.025
17. Ahmed Z, Nadeem S Saleem S, Ellahi R. Numerical study of unsteady flow and heat transfer CNT-based MHD nanofluid with variable viscosity over a permeable shrinking surface. *Int J Num Methods Heat Fluid Flow*. (2019). doi: 10.1108/HFF-04-2019-0346. [Epub ahead of print].
18. Yimin X, Li Q, Ye M. Investigations of convective heat transfer in ferrofluid microflows using lattice-Boltzmann approach. *Int J Thermal Sci*. (2007) **46**:105–11. doi: 10.1016/j.ijthermalsci.2006.04.002
19. Sheikholeslami M, Jafaryar M, Ali JA, Hamad SM, Divsalar A, Shafee A, et al. Simulation of turbulent flow of nanofluid due to existence of new effective turbulator involving entropy generation. *J Mol Liquids*. (2019) **291**:111283. doi: 10.1016/j.molliq.2019.111283
20. Sheikholeslami M, Haq RU, Shafee A, Li Z, Elaraki YG, Tlili I. Heat transfer simulation of heat storage unit with nanoparticles and fins through a heat exchanger. *Int J Heat Mass Transf*. (2019) **135**:470–8. doi: 10.1016/j.ijheatmasstransfer.2019.02.003
21. Dat DV, Shah Z, Sheikholeslami M, Shafee A, Nguyen TK. Numerical investigation of MHD nanomaterial convective migration and heat transfer within a sinusoidal porous cavity. *Phys Scr*. (2019) **94**:115225. doi: 10.1088/1402-4896/ab2ced
22. Bhatti MM, Abbas T, Rashidi MM. A new numerical simulation of MHD stagnation-point flow over a permeable stretching/shrinking sheet in porous media with heat transfer. *Iran J Sci Technol Trans A Sci*. (2017) **41**:779–85. doi: 10.1007/s40995-016-0027-6

23. Sheikholeslami M. Magnetic field influence on CuO-H_2O nanofluid convective flow in a permeable cavity considering various shapes for nanoparticles. *Int J Hydrogen Energy.* (2017) **42**:19611–21. doi: 10.1016/j.ijhydene.2017.06.121
24. Cattaneo C. Sulla conduzionedelcalore. *AttiSemin Mat Fis Univ Modena Reggio Emilia*. (1948) **3**:83–101.
25. Sheikholeslami M, Shehzad SA. CVFEM simulation for nanofluid migration in a porous medium using Darcy model. *Int J Heat Mass Transf.* (2018) **122**:1264–71. doi: 10.1016/j.ijheatmasstransfer.2018.02.080
26. Mustafa M. Cattaneo-Christov heat flux model for rotating flow and heat transfer of upper-convected Maxwell flud. *AIP Adv.* (2015) **5**:047109. doi: 10.1063/1.4917306
27. Ali ME, Sandeep N. Cattaneo-Christov model for radiative heat transfer of magnetohydrodynamic Casson-ferrofluid: a numerical study. *Results Phys.* (2017) **7**:21–30. doi: 10.1016/j.rinp.2016.11.055
28. Sheikholeslami M, Rokni HB. Influence of EFD viscosity on nanofluid forced convection in a cavity with sinusoidal wall. *J Mol Liquids.* (2017) **232**:390–5. doi: 10.1016/j.molliq.2017.02.042
29. Sheikholeslami M. *Application of Control Volume Based Finite Element Method (CVFEM) for Nanofluid Flow and Heat Transfer*. Elsevier (2019).
30. Sheikholeslami M. New computational approach for exergy and entropy analysis of nanofluid under the impact of Lorentz force through a porous media. *Comput Methods Appl Mech Eng.* (2019) **344**:319–33. doi: 10.1016/j.cma.2018.09.044
31. Sheikholeslami M. Numerical approach for MHD Al_2O_3-water nanofluid transportation inside a permeable medium using innovative computer method. *Comput Methods Appl Mech Eng.* (2019) **344**:306–18. doi: 10.1016/j.cma.2018.09.042
32. Sheikholeslami M, Zeeshan A. Analysis of flow and heat transfer in water based nanofluid due to magnetic field in a porous enclosure with constant heat flux using CVFEM. *Comput Methods Appl Mech Eng.* (2017) **320**:68–81. doi: 10.1016/j.cma.2017.03.024
33. Sheikholeslami M, Shah Z, Tassaddiq A, Shafee A, Khan I. Application of electric field transfer in an enclosure including double for augmentation of ferrofluid heat moving walls. *IEEE Access*. (2019) **7**:21048–56. doi: 10.1109/ACCESS.2019.2896206
34. Sheikholeslami M, Shah Z, Shafi A, Khan I, Itili I. Uniform magnetic force impact on water based nanofluid thermal behavior in a porous enclosure with ellipse shaped obstacle. *Sci Rep.* (2019) **9**:1196. doi: 10.1038/s41598-018-37964-y
35. Jawad M, Shah Z, Islam S, Bonyah E, Khan ZA. Darcy-Forchheimer flow of MHD nanofluid thin film flow with Joule dissipation and Navier's partial slip. *J Phys Commun.* (2018) **11**:115014. doi: 10.1088/2399-6528/aaeddf
36. Jawad M, Shah Z, Islam S, Majdoubi J, Tlili I, Khan W, et al. Impact of nonlinear thermal radiation and the viscous dissipation effect on the unsteady three-dimensional rotating flow of single-wall carbon nanotubes with aqueous suspensions. *Symmetry.* (2019) **11**:207. doi: 10.3390/sym11020207
37. Nasir S, Shah Z, Islam S, Khan W, Bonyah E, Ayaz M, et al. Three dimensional Darcy-Forchheimer radiated flow of single and multiwall carbon nanotubes over a rotating stretchable disk with convective heat generation and absorption. *AIP Adv.* (2019) **9**:035031. doi: 10.1063/1.5087468
38. Nasir S, Shah Z, Islam S, Khan W, Khan SN. Radiative flow of magneto hydrodynamics single-walled carbon nanotube over a convectively heated stretchable rotating disk with velocity slip effect. *Adv Mech Eng.* (2019) **11**:1–11. doi: 10.1177/1687814019827713
39. Alharbi SO, Dawar A, Shah Z, Khan W, Idrees M, Islam S, et al. Entropy generation in MHD eyring–powell fluid flow over an unsteady oscillatory porous stretching surface under the impact of thermal radiation and heat source/sink. *Appl Sci.* (2018) **8**:2588. doi: 10.3390/app8122588
40. Sheikholeslami M, Mahian O. Enhancement of PCM solidification using inorganic nanoparticles and an external magnetic field with application in energy storage systems. *J Clean Prod.* (2019) **215**:963–77. doi: 10.1016/j.jclepro.2019.01.122
41. Khan NS, Gul T, Kumam P, Shah Z, Islam S, Khan W, et al. Influence of inclined magnetic field on Carreau nanoliquid thin film flow and heat transfer with graphene nanoparticles. *Energies.* (2019) **12**:1459. doi: 10.3390/en12081459
42. Saeed A, Islam S, Dawar A, Shah Z, Kumam P, Khan W. Influence of Cattaneo–Christov heat flux on MHD Jeffrey, Maxwell, and Oldroyd-B nanofluids with homogeneous-heterogeneous reaction. *Symmetry*. (2019) **11**:439. doi: 10.3390/sym11030439
43. Sheikholeslami M, Ghasemi A. Solidification heat transfer of nanofluid in existence of thermal radiation by means of FEM. *Int J Heat Mass Transf.* (2018) **123**:418–31. doi: 10.1016/j.ijheatmasstransfer.2018.02.095
44. Gao W, Wang WF. The eccentric connectivity polynomial of two classes of nanotubes. *Chaos Solit Fract.* (2016) **89**:290–4. doi: 10.1016/j.chaos.2015.11.035
45. Qin Y, He Y, Hiller JE, Mei G. A new water-retaining paver block for reducing runoff and cooling pavement. *J Clean Prod.* (2018) **199**:948–56. doi: 10.1016/j.jclepro.2018.07.250
46. Sheikholeslami M. Finite element method for PCM solidification in existence of CuO nanoparticles. *J Mol Liquids.* (2018) **265**:347–55. doi: 10.1016/j.molliq.2018.05.132
47. Jalali E, Akbari OA, Sarafraz MM, Abbas T, Safaei MR. Heat transfer of Oil/MWCNT nanofluid jet injection inside a rectangular microchannel. *Symmetry.* (2019) **11**:757. doi: 10.3390/sym11060757
48. Qin Y, He H, Ou X, Bao T. Experimental study on darkening water-rich mud tailings for accelerating desiccation. *J Clean Prod.* (2019) **240**:118235. doi: 10.1016/j.jclepro.2019.118235
49. Hassan M, Ellahi R, Bhatti MM, Zeeshan A. A comparative study on magnetic and non-magnetic particles in nanofluid propagating over a wedge. *Can J Phys.* (2018) **97**:277–85. doi: 10.1139/cjp-2018-0159
50. Sheikholeslami M, Rezaeianjouybari B, Darzi M, Shafee A, Li Z, Nguyen TK. Application of nano-refrigerant for boiling heat transfer enhancement employing an experimental study. *Int J Heat Mass Transf.* (2019) **141**:974–80. doi: 10.1016/j.ijheatmasstransfer.2019.07.043

Conflict of Interest: The authors declare that the research was conducted in the absence of any commercial or financial relationships that could be construed as a potential conflict of interest.

Copyright © 2019 Shah, Babazadeh, Kumam, Shafee and Thounthong. This is an open-access article distributed under the terms of the Creative Commons Attribution License (CC BY). The use, distribution or reproduction in other forums is permitted, provided the original author(s) and the copyright owner(s) are credited and that the original publication in this journal is cited, in accordance with accepted academic practice. No use, distribution or reproduction is permitted which does not comply with these terms.

NOMENCLATURE

L_f	Latent heat of solidification
C_p	Heat capacity
d_p	Diameter of alumina
NEPCM	Alumina-enhanced PCM
$T^{\cdot}$	Temperature
k	Thermal conductivity
CVFEM	Control volume based finite Element method
E_{total}	Energy saving
Greek symbols	
ϕ	Concentration of alumina
κ_b	Boltzmann constant
α	Diffusivity
Subscripts	
nf	Nano enriched PCM
f	fluid
P	solid

frontiers in Physics

ORIGINAL RESEARCH
published: 15 November 2019
doi: 10.3389/fphy.2019.00186

Magnetohydrodynamic Free Stream and Heat Transfer of Nanofluid Flow Over an Exponentially Radiating Stretching Sheet With Variable Fluid Properties

Muhammad Irfan, Muhammad Asif Farooq and Tousif Iqra*

Department of Mathematics, School of Natural Sciences, National University of Sciences and Technology, Islamabad, Pakistan

This article deals with the nanofluid flow and heat transfer of the MHD free stream over an exponentially radiating stretching sheet accompanied by constant and variable fluid characteristics together. The underlying governing partial differential equations (PDEs) have been translated into nonlinear ordinary differential equations (ODEs) by incorporating adequate similarity transformations. By using the shooting method and the MATLAB built-in solver *bvp4c*, the corresponding ODEs are effectively solved. The impact on the skin friction coefficient (quantifying resistance), the local Nusselt number (heat transfer rate) and the local Sherwood number (mass transfer rate) on the surface due to the flow field variables has been computed against various parameters i.e., magnetic parameter M, Prandtl number Pr_o, Lewis number Le, thermophoresis parameter Nt, Brownian motion parameter Nb, velocity parameter λ, radiation parameter Rd and thermal conductivity parameter ϵ. Graphs are also plotted to study the impact of distinct parameters on velocity, temperature and concentration profiles. It has been noted by raising the values of ϵ, the heat transfer rate reduces for variable fluid properties. On the other hand, raising Pr_o increases the heat transfer rate.

Keywords: magnetohydrodynamics (MHD), exponentially stretching sheet, nanofluid, shooting method, constant and variable fluid properties

OPEN ACCESS

Edited by:
Muhammad Mubashir Bhatti, Shanghai University, China

Reviewed by:
Tehseen Abbas, University of Education Lahore, Pakistan
Anwar Shahid, International Islamic University, Islamabad, Pakistan

****Correspondence:***
Muhammad Irfan
irfan.akbar30@gmail.com

Specialty section:
This article was submitted to Mathematical Physics, a section of the journal Frontiers in Physics

Received: *11 September 2019*
Accepted: *29 October 2019*
Published: *15 November 2019*

Citation:
Irfan M, Farooq MA and Iqra T (2019) Magnetohydrodynamic Free Stream and Heat Transfer of Nanofluid Flow Over an Exponentially Radiating Stretching Sheet With Variable Fluid Properties. Front. Phys. 7:186. doi: 10.3389/fphy.2019.00186

1. INTRODUCTION

Because of a stretching surface, studying fluid dynamics is essential as it has many practical and industrial applications. In a number of industrial and manufacturing processes, material production occurs and involves sheets of metal, and polymer. For instance, cooling an infinite metal plate in a cooling bath, the boundary layer along material handling conveyors, plastic sheet aerodynamic extrusion, the boundary layer along a liquid film in condensation procedures, paper manufacturing, glass blowing, steel spinning and plastic film drawing.

Boundary layer for incompressible flow on a moving flat plate was studied by Sakiadis [1]. The study focused on the flow through a moving flat plate while considered static fluid contrary to the work by Blasius [2] who considered flow over a fixed plate. The study carried out by Crane [3] diverted to the study of boundary layer flow of a fluid with high viscosity and uniform density on a plate being stretched linearly. Magyari and Keller [4] conducted the research on an exponentially stretching steady surface to explore heat and mass transfer in the boundary layers but without variable fluid properties and MHD consideration. Elbashbeshy [5], who researched the features of flow and heat transfer over an exponentially stretching permeable sheet, adds a different dimension to this inquiry. The considered research is without the characteristics of MHD and varying fluid properties. Many researchers have extended the work for different flow model. But most of those studies have been focusing on constant fluid properties. The analysis of boundary layer flow with variable fluid properties on a moving flat plate in a parallel free stream was studied by Bachok et al. [6]. They computed solution numerically. Andersson and Aarseth [7] investigated the properties of fluid under the influence of temperature.

Magnetohydrodynamics (MHD) is the study of the flow of electrically conducting fluids in an electro-magnetic-fields. MHD flow research is of significant concern in contemporary processes of metallurgy and metalworking. Makinde et al. [8] examined the MHD flow of variable viscosity of nanofluid over a radially stretching sheet. They indicated that Brownian motion enhances the rate of mass transfer. Mukhopadhyay et al. [9] carried out the study of investigation of magnetic field effects on a fluid flow with variable viscosity on heated surface. They reported that the fluid velocity reduces as the viscosity declines. The influence of temperature on viscosity during heating surface was investigated by Elbashbeshay and Bazid [10] and evaluated solution with the help of a shooting method. The effect of variable fluid properties on the hydro-magnetic flow and heat transfer over a nonlinearly stretching sheet was discussed by Popley et al. [11]. They have numerically addressed their problem. Similarly, the influence of a study of temperature-dependent fluid properties on MHD free stream flow and heat transfer over a nonlinearly stretching sheet was studied by Prasad et al. [12].

Some important applications for radiative heat transfer are the MHD accelerator, high temperature plasmas, power generation devices and cooling of nuclear reactors. Many procedures occur in engineering areas at higher temperatures and understanding the transfer of radiative heat becomes very crucial for the design of appropriate equipment. Heat transfer assessment of boundary layer flow with radiation is also vital in electrical power generation, astrophysical flows, solar power technology, and other industrial areas. Raptis et al. [13] recorded the impact of thermal radiation over a semi-infinite stationary plate on the MHD flow of a viscous fluid. Devi and Reddy [14] presented analysis of the radiation and mass transfer effects on MHD boundary layer flow due to an exponentially stretching sheet with heat source. Mukhopadhyay [15] discussed the slip effects on MHD flow over an radiating exponentially stretching sheet with suction/blowing. The influence of radiation effect over an exponentially stretching sheet was studied by Ishak [16] and Mabood et al. [17]. Bidin and Nazar [18] carried out a numerical study to investigate the effect of thermal radiation on boundary layer flow over an exponentially stretching sheet. Poornima and Reddy [19] presented an analysis of the radiation effects on MHD free convective boundary layer flow of nanofluids over a nonlinear stretching sheet. Most of the above studies have not discussed variable fluid properties and radiation simultaneously.

Because of the unique physical and chemical properties of nanometer-sized products, nanofluids have many applications in the industrial sector. Nanofluids are composites of solid-liquid materials, typically 1–100 nm, consisting of powerful nanoparticles or liquid-suspended nanofibers. The term nanofluid was suggested by Choi [20]. He revealed that supplying a tiny quantity of nanoparticles to conventional fluids (<1 percent by volume fraction) improved the heat conductivity of the fluid by ∼2 times. Nield and Kuznestov [21] studied convected boundary layer flow of nanofluid in a porous medium. They considered natural convection past a vertical flat plate. Khan et al. [22] presented non-aligned MHD stagnation point flow of nanofluid with variable viscosity over a stretching sheet with radiation effect. They found that non-alignment of the reattachment point decreases with an increase in magnetic parameter M. Bachok et al. [23] discussed stagnation-point and heat transfer flow over an exponentially stretching/shrinking sheet in a nanofluid. They discovered that the solution obtained for shrinking sheet is not unique. Nada et al. [24] examined the effect of nanofluid while variable properties are taken into account. They considered enclosures for the studies. Malik et al. [25] studied Casson nanofluid's boundary layer flow over a cylinder that stretches exponentially and found solution numerically. Eid [26] addressed the impact of chemical reaction over an exponentially stretching sheet on the MHD boundary layer flow of two-phase nanofluid. They found that thermal boundary layer is dependent on the reaction and source parameter. Gangaiah et al. [27] examined the MHD flow of nanofluid in the presence of viscous dissipation and chemical reaction over an exponentially stretching sheet. They showed that thermal boundary layer depends on viscous dissipation parameter. The effect of different variables like variable viscosity, buoyancy and variable thermal conductivity on mixed convection heat transfer due to an exponentially stretching sheet was discussed

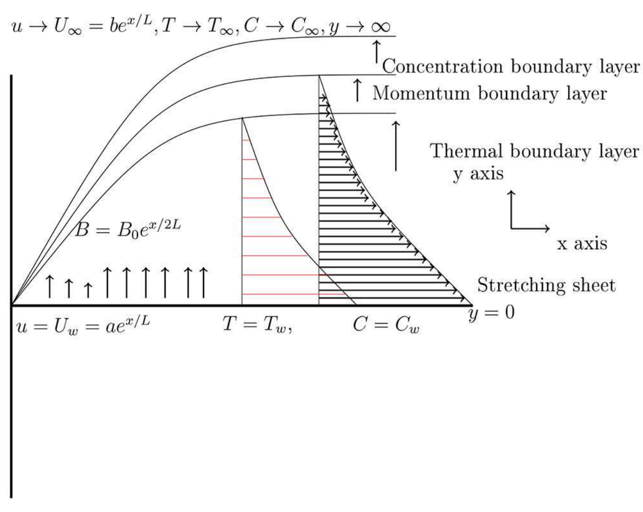

FIGURE 1 | Structure of the flow problem.

by Abel et al. [28]. They obtained solution numerically. In Yousif et al. [29] and Ellahi et al. [30], they have discussed MHD Carreau and non-Newtonian nanofluid flow over an exponentially and slippery walls, respectively. Unsteady flow with CNT-based MHD nanofluid, variable viscosity and a permeable shrinking surface have been discussed in Ahmed et al. [31]. See also Thoi et al. [32] for a different fluid flow aspect in a Y-shaped fin. Previous studies mostly concern with nanofluid with variable viscosity but these are devoid of variable thermal conductivity.

There exists a very extensive literature with and without nanofluid on the topic of a constant fluid properties. But not many studies were dedicated to explore the effects of variable fluid properties on nanofluid flow. To bridge that gap, the present research focuses on the effects of variable viscosity and variable thermal conductivity on the boundary layer nanofluid flow. The structure of the paper is as follows. In section 2, we formulate the fundamental physical problem's mathematical model. The constant and variable fluid characteristics are discussed in section 3. The numerical methods are outlined in section 4. Results and analysis are presented in section 5. Conclusion of the current work is drawn at the end in section 6.

2. PROBLEM FORMULATION

We consider a laminar, MHD nanofluid flow over an exponentially stretching sheet with thermal radiation. The sheet is situated at $y = 0$. A variable magnetic field $B(x) = B_o e^{\frac{x}{2L}}$ has been applied normal to the sheet. **Figure 1** is the geometry of the flow, in which x-axis is along and y-axis is taken as normal to the sheet.

Let $U_w = ae^{\frac{x}{L}}$ is the wall velocity, whereas $U_\infty = be^{\frac{x}{L}}$ is a free stream velocity, in which stretching parameters $a, b > 0$. The sheet has been kept at constant wall temperature T_w and T_∞ refers to the ambient temperature. Under the hypothesis of a low magnetic Reynolds number, the induced magnetic field is ignored. The boundary layer equations with Buongiorno model [33] which regulate the above flow are:

$$\frac{\partial u}{\partial x} + \frac{\partial v}{\partial y} = 0, \tag{1}$$

$$u\frac{\partial u}{\partial x} + v\frac{\partial v}{\partial y} = U_\infty \frac{dU_\infty}{dx} + \frac{1}{\rho}\frac{\partial}{\partial y}(\frac{\mu \partial u}{\partial y}) - \frac{\sigma B^2}{\rho}(u - U_\infty), \tag{2}$$

$$u\frac{\partial T}{\partial x} + v\frac{\partial T}{\partial y} = \frac{1}{\rho c_p}\frac{\partial}{\partial y}(\frac{k\partial T}{\partial y}) + \tau(D_B \frac{\partial T}{\partial y}\frac{\partial C}{\partial y} + \frac{D_T}{T_\infty}(\frac{\partial T}{\partial y})^2) - \frac{1}{\rho c_p}\frac{\partial q_r}{\partial y}, \tag{3}$$

$$u\frac{\partial C}{\partial x} + v\frac{\partial C}{\partial y} = D_B \frac{\partial^2 C}{\partial y^2} + \frac{D_T}{T_\infty}\frac{\partial^2 T}{\partial y^2}, \tag{4}$$

where the coordinates of velocities (u, v) are along $x-$ and $y-$ axes, respectively. μ is a fluid viscosity coefficient, $B(x)$ is a variable magnetic field along the $y-$ axis. Here T is the temperature, C is the nanoparticles concentration, c_p is the specific heat constant, D_B is the Brownian motion coefficient, D_T is the thermophoretic diffusion coefficient, $\tau = \frac{(\rho c)_p}{(\rho c)_f}$ is the ratio of the effective heat capacity of the nanoparticle material to the heat capacity of the fluid and q_r is the radiative heat flux. Appropriate boundary conditions complete the above system by:

$$u = U_w(x) = ae^{\frac{x}{L}}, v = 0, T = T_w, C = C_w \text{ at } y = 0$$
$$u \to U_\infty = be^{x/L}, T \to T_\infty, C \to C_\infty \text{ as } y \to \infty \tag{5}$$

Using the following similarity transformation on above equations which are defined as:

$$\eta = \sqrt{\frac{a}{2\nu L}} e^{\frac{x}{2L}} y, \quad \psi = \sqrt{2a\nu L} e^{\frac{x}{2L}} f(\eta), \quad \theta = \frac{T - T_\infty}{T_w - T_\infty},$$
$$u = ae^{\frac{x}{L}} f'(\eta), \quad v = -\sqrt{\frac{\nu a}{2L}} e^{\frac{x}{2L}} (f(\eta) + \eta f'(\eta)). \tag{6}$$

Equation (1) is identically satisfied. Moreover, when above similarity variables used in Equations (2), (3), and (4) which yields:

$$(\frac{\mu}{\mu_o} f'')' + 2(\lambda^2 - (f')^2) + ff'' - M(f' - \lambda) = 0, \tag{7}$$

$$(1 + \frac{4}{3}R_d)(\frac{k}{k_o}\theta')' + Pr_o(f\theta' - f'\theta + N_b\theta'\phi' + N_t(\theta')^2) = 0, \tag{8}$$

$$\phi'' + \frac{N_t}{N_b}\theta'' + L_e(f\phi' - f'\phi) = 0. \tag{9}$$

The boundary conditions transformed into:

$$f(0) = 0, f'(0) = 1, \theta(0) = 1, f'(\infty) = \lambda, \theta(\infty) = 0, \phi(0) = 1, \phi(\infty) = 0, \tag{10}$$

where $M = \frac{2\sigma B_0^2 L}{\rho a}$ is a magnetic parameter, $\lambda = \frac{b}{a}$ is a ratio of the free stream velocity to the velocity of the stretching sheet, $Pr_o = \frac{\mu_o c_{po}}{k_o}$ is the Prandtl number, $N_b = \frac{\tau D_B (C_w - C_\infty)}{\nu}$ is the Brownian motion parameter, $N_t = \frac{\tau D_T (T_w - T_\infty)}{T_\infty \nu}$ is the thermophoresis parameter, $R_d = \frac{4\sigma^* T_\infty^3}{k_0 k^*}$ denotes the radiation parameter and $L_e = \frac{\nu}{D_B}$ is the Lewis number.

3. ANALYSIS ON FLUID PROPERTIES

This section comprises of two subsections. Firstly, an overview of the constant fluid properties will be presented followed by the discussion on variable fluid properties.

3.1. Case A: Constant Fluid Properties

For this case, Equations (7), (8), and (9) can be adjusted as follows to incorporate constant fluid properties:

$$f''' + 2(\lambda^2 - (f')^2) + ff'' - M(f' - \lambda) = 0 \quad (11)$$

$$(1 + \frac{4}{3}R_d)\theta'' + Pr_o(f\theta' - f'\theta + N_b\theta'\phi' + N_t(\theta')^2) = 0 \quad (12)$$

$$\phi'' + \frac{N_t}{N_b}\theta'' + L_e(f\phi' - f'\phi) = 0 \quad (13)$$

3.2. Case B: Variable Fluid Properties

For this case, viscosity and thermal conductivity in Equations (7), (8), and (9) is considered variable and taken as a function of a temperature. For viscosity we write:

$$\mu(T) = \frac{\mu_{ref}}{1 + \gamma(T - T_{ref})}, \quad (14)$$

where we follow Andersson and Aarseth [7] and reference within to write above expression (14). In above γ is a fluid property. If

TABLE 1 | (**For Case A**) Comparison of $-\theta'(0)$ for different values of M, R_d and Pr_0, when $\lambda = N_b = N_t = L_e = 0$.

R_d	M	Pr_0	Magyari and Keller [4]	Ishak [16]	Mukhopadhay [15]	Mabood et al. [17]	Present study
0	0	1	0.9548	0.9548	0.9548	0.95478	0.9548
		2	–	–	1.4715	1.47151	1.4715
		3	1.8691	1.8691	1.8691	1.86909	1.8691
		5	2.5001	2.5001	2.5001	2.50012	2.5001
		10	3.6604	3.6604	3.6604	3.66039	3.6603
1	0	1	–	–	0.5312	0.53121	0.5312
0	1	1	–	–	0.8611	0.86113	0.8611
0.5	0	2	–	1.0735	1.0735	1.07352	1.0735
		3	–	1.3807	–	1.38075	1.3808
1			–	1.1214	–	1.12142	1.1214
	1	1	–	–	0.4505	0.45052	0.4505

TABLE 2 | (**For Case B**) Comparison of the values of $f''(0)$, $\theta'(0)$ and $\phi'(0)$ for different values of ϵ and λ when $M = \lambda = R_d = 0, Pr_0 = 1, \theta_r = -5, L_e = 1.3$.

λ	ϵ	$-f''(0)$ bvp4c	$f''(0)$ Shooting Method	$-\theta'(0)$ bvp4c	$-\theta'(0)$ Shooting Method	$-\phi'(0)$ bvp4c	$-\phi'(0)$ Shooting Method
0	0	1.4218	1.4218	0.6162	0.6162	0.8951	0.8951
0	0.2	1.4204	1.4204	0.5604	0.5604	0.9188	0.9188
0	0.4	1.4193	1.4192	0.5163	0.5163	0.9367	0.9367
0.5	0	0.9771	0.9771	0.6898	0.6898	1.1075	1.1075
0.5	0.2	0.9762	0.9762	0.6383	0.6383	1.1292	1.1292
0.5	0.4	0.9755	0.9755	0.5975	0.5975	1.1455	1.1455
2	0	–3.0187	–3.0188	0.9261	0.9261	1.6143	1.6143
2	0.2	–3.0163	–3.0165	0.8716	0.8716	1.6337	1.6337
2	0.4	–3.0143	–3.0145	0.8274	0.8274	1.6482	1.6483

TABLE 3 | (**For Case B**) Comparison of the values of $f''(0)$ and $\theta'(0)$ for different values of θ_r and λ when $M = 0, Pr_0 = 10, \epsilon = 0$.

λ	θ_r	$f''(0)$ bvp4c	$f''(0)$ Shooting method	$-\theta'(0)$ bvp4c	$-\theta'(0)$ Shooting method	$-\phi'(0)$ bvp4c	$-\phi'(0)$ Shooting method
0	–10	1.3539	1.3539	0.6223	0.6223	0.9082	0.9081
0	–1	1.8658	1.8657	0.5753	0.5753	0.8085	0.8085
0	–0.5	2.2863	2.2863	0.5360	0.5360	0.7281	0.7281
0.5	–10	0.9299	0.9299	0.6923	0.6923	1.1119	1.1119
0.5	–1	1.2869	1.2868	0.6744	0.6744	1.0814	1.0814
0.5	–0.5	1.5816	1.5810	0.6220	0.6620	1.0611	1.0611
2	–10	–2.8719	–2.8720	0.9227	0.9227	1.6088	1.6088
2	–1	–3.9846	–3.9848	0.9459	0.9459	1.6457	1.6457
2	–0.5	–4.9021	–4.9026	0.9611	0.9611	1.6692	1.6692

$T_o \approx T_{ref}$ then above formula (14) becomes:

$$\mu = \frac{\mu_o}{1 - \frac{T-T_o}{\theta_r(T_w-T_o)}} = \frac{\mu_o}{1 - \frac{\theta(\eta)}{\theta_r}}, \tag{15}$$

here $\theta_r = \frac{-1}{\gamma(T_w-T_o)}$. If the above viscosity relation is incorporated in the Equation (7), then it can be rewritten as:

$$\frac{\theta_r}{(\theta r - \theta)} f^{'''} + \frac{f^{''}\theta^{'}\theta_r}{(\theta_r - \theta)^2} + 2(\lambda^2 - (f^{'})^2) + ff^{''} - M(f^{'} - \lambda) = 0. \tag{16}$$

The variable thermal conductivity is expressed in terms of temperature by following Prasad et al. [12] as:

$$k(T) = k_o(1 + \epsilon\theta) \tag{17}$$

Under this above relation the mathematical form of Equation (8) can be described as:

$$\begin{aligned}&(1 + \frac{4}{3}R_d)((1 + \epsilon\theta)\theta^{''} + \epsilon(\theta^{'})^2)\\ &+P_{r_o}(f\theta^{'} - f^{'}\theta + N_b\theta^{'}\phi^{'} + N_t(\theta^{'})^2) = 0.\end{aligned} \tag{18}$$

To measure the roughness, heat transfer rate and mass transfer rate onto the surface, we calculate the skin friction coefficient C_f the local Nusselt number Nu_x and the local Sherwood number Sh_x, respectively, i.e.,

$$C_f = \frac{\tau_w}{\rho U_w^2} = \frac{f^{''}(0)}{\sqrt{2Re_x}}, \tag{19}$$

$$Nu_x = -\frac{xq_w}{T_w - T_\infty} = -\sqrt{\frac{xRe_x}{2L}}\theta^{'}(0), \tag{20}$$

$$Sh_x = -\frac{xj_w}{C_w - C_\infty} = -\sqrt{\frac{xRe_x}{2L}}\phi^{'}(0). \tag{21}$$

4. NUMERICAL PROCEDURE

4.1. Shooting Method

To apply the shooting technique to Cases A and B together with the boundary conditions, we transformed boundary value problem (BVP) into an initial value problem (IVP) and convert higher order ODEs into a system of first order ODEs. The Newton-Raphson technique was used to locate the root. After that, the order five Runge-Kutta method was implemented to determine the IVP solution. The shooting method is implemented in MATLAB. For Cases A and B, the system of first order ODEs are written as,

(a) Case A:

$$\begin{aligned}f = y_1, f^{'} = y_2, f^{''} = y_3, f^{'''} = y_3^{'} &= -2(\lambda^2 - y_2^2) - y_1y_3\\ &+M(y_2 - \lambda),\\ y_4 = \theta, y_5 = \theta^{'}, \theta^{''} = y_5^{'} &= -\frac{Pr_o}{(1 + \frac{4}{3})R_d}(y_1y_5 - y_2y_4 + N_by_5y_7\\ &+N_ty_5^2),\\ y_6 = \phi, y_7 = \phi^{'}, \phi^{''} = y_7^{'} &= -L_e(y_1y_7 - y_2y_6) - \frac{N_t}{N_b}y_5^{'}.\end{aligned}$$

(b) Case B:

$$\begin{aligned}f &= y_1, f^{'} = y_2, f^{''} = y_3, f^{'''} = y_3^{'} = \frac{(y_3y_5)}{(y_4 - \theta_r)}\\ &+ \frac{(y_4 - \theta_r)}{\theta_r}(2(\lambda^2 - y_2^2) + y_1y_3 - M(y_2 - \lambda)),\\ y_4 &= \theta, y_5 = \theta^{'}, \theta^{''} = y_5^{'} = \frac{-\epsilon y_5^2}{1 + \epsilon y_4}\\ &- \frac{P_{r_o}}{(1 + \epsilon y_4)(1 + \frac{4}{3}R_d)}(y_1y_5 - y_2y_4 + N_by_5y_7 + N_ty_5^2),\\ y_6 &= \phi, y_7 = \phi^{'}, \phi^{''} = y_7^{'} = -L_e(y_1y_7 - y_2y_6) - \frac{N_t}{N_b}y_5^{'}.\end{aligned}$$

TABLE 4 | (**For Case B**) Comparison of the values of $f^{''}(0)$ and $\theta^{'}(0)$ for different values of R_d and Pr_0 when $M = \lambda = \epsilon = 0, \theta_r = -5, N_b = 0.8, N_t = 0.5, L_e = 1.3$.

R_d	Pr_o	$-f^{''}(0)$ bvp4c	$-f^{''}(0)$ Shooting method	$-\theta^{'}(0)$ bvp4c	$-\theta^{'}(0)$ Shooting method	$-\phi^{'}(0)$ bvp4c	$-\phi^{'}(0)$ Shooting method
0	1	1.4218	1.4218	0.6162	0.6162	0.8951	0.8951
	2	1.4264	1.4263	0.7611	0.7610	0.8452	0.8452
	3	1.4285	1.4285	0.8193	0.8193	0.8274	0.8274
	5	1.4304	1.4304	0.8608	0.8608	0.8186	0.8186
	10	1.4319	1.4319	0.8805	0.8805	0.8196	0.8196
0.5	1	1.4181	1.4181	0.4910	0.4910	0.9396	0.9396
	2	1.4231	1.4231	0.6585	0.6585	0.8802	0.8802
	3	1.4257	1.4257	0.7423	0.7423	0.8514	0.8514
	5	1.4285	1.4285	0.8193	0.8193	0.8274	0.8274
	10	1.4309	1.4309	0.8687	0.8687	0.8182	0.8182
1	1	1.4158	1.4158	0.4162	0.4163	0.9689	0.9689
	2	1.4207	1.4207	0.5790	0.5790	0.9082	0.9082
	3	1.4235	1.4235	0.6738	0.6738	0.8749	0.8749
	5	1.4268	1.4268	0.7726	0.7726	0.8415	0.8415
	10	1.4299	1.4299	0.8517	0.8517	0.8199	0.8199

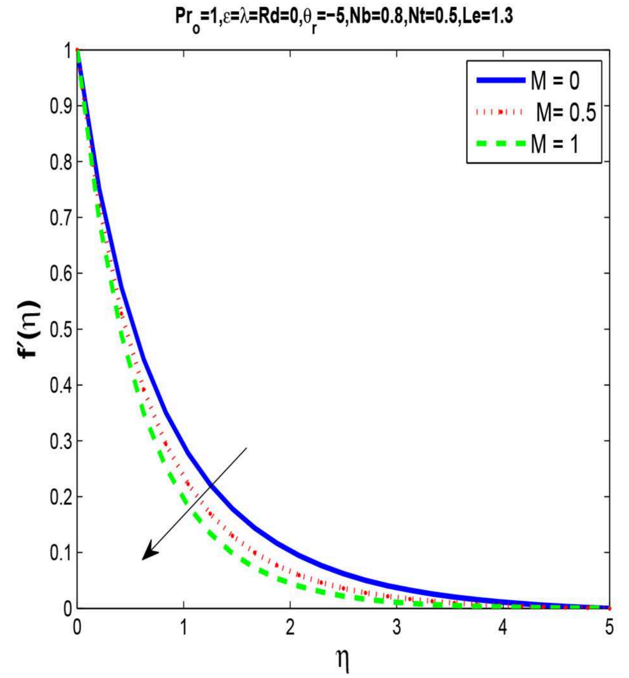

FIGURE 2 | Velocity profile $f'(\eta)$ for different M (**For Case B).**

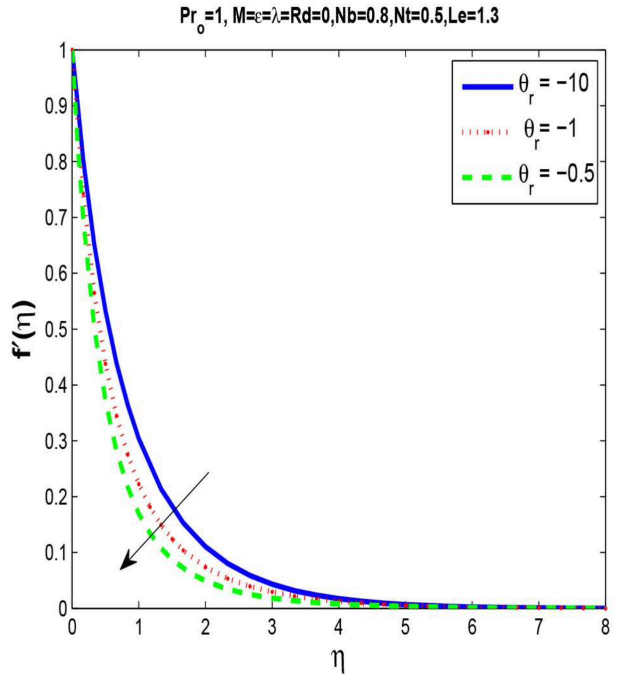

FIGURE 3 | Velocity profile $f'(\eta)$ for different θ_r (**For Case B).**

4.2. bvp4c

Using MATLAB *bvp4c* algorithm, BVP can even be solved. *bvp4c* solver employs the collocation technique in the background. It manages to find a solution after supplying initial guess, domain size and the number of points. Please see reference [34] for more detail and examples.

5. RESULTS AND DISCUSSION

In **Table 1**, we compute the local Nusselt number and compared its values with published results for distinct parameters Prandtl number Pr_0, radiation parameter Rd and magnetic parameter M.

Table 2 illustrates that the skin friction coefficient is not significantly changed whereas the local Nusselt number drops for ϵ and increases for the values of λ. The local Sherwood number grows with the rise of λ and ϵ. It is observed in **Table 3** that the local Nusselt and the Sherwood numbers rises with a rise of λ but the skin friction coefficient held opposite behavior. For fixed values of $\lambda = 0, 0.5$ and an increase in viscosity parameter θ_r brings the increasing change in the skin friction coefficient but the local Nusselt and Sherwood numbers has shown decreasing behavior. **Table 4** demonstrates that as Pr_o and R_d rises, there is a negligible change in the skin friction coefficient. But the local Nusselt numbers decreases and local Sherwood number increases by increasing the values of radiation parameter R_d. Moreover, the local Nusselt number increases by increasing Prandtl number but the local Sherwood number decreases.

Figure 2 shows that the momentum boundary layer thickness is reduced with the increase in M. It happens because of a transverse magnetic field as it opposes the phenomenon of transport. The Lorentz force generates resistance to the fluid flow with a rise of M and slows down the velocity.

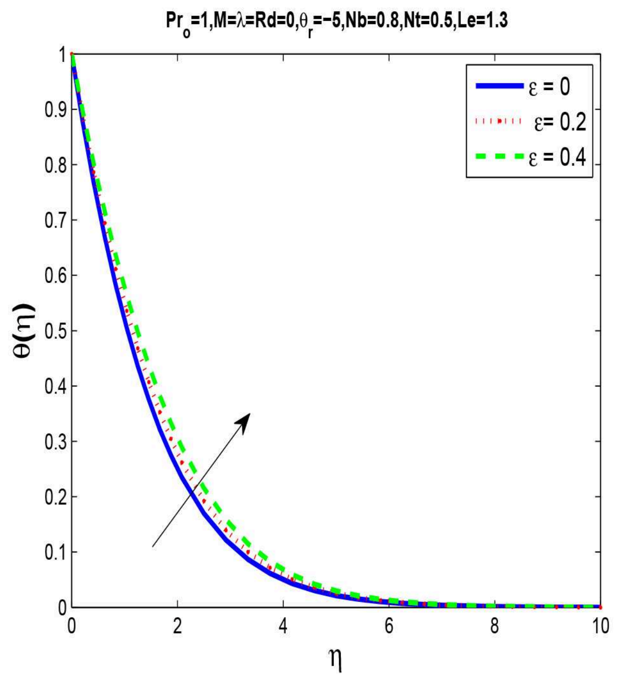

FIGURE 4 | Temperature profile $\theta(\eta)$ for different ϵ (**For Case B).**

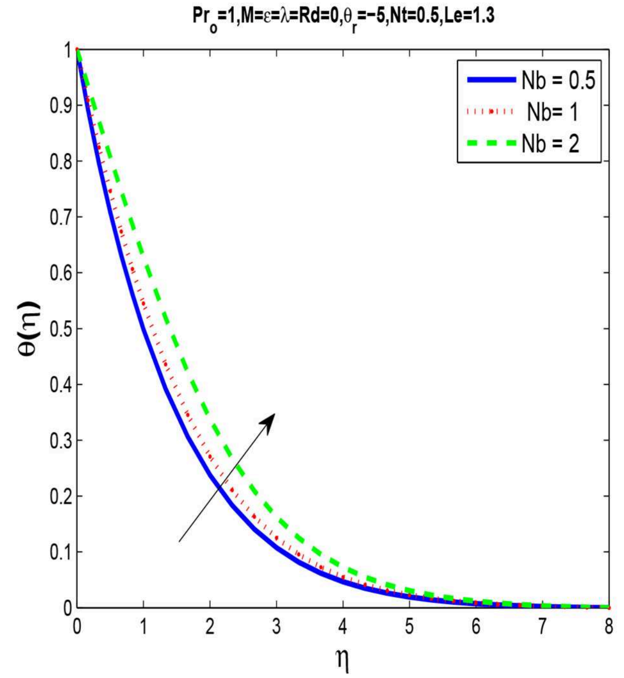

FIGURE 5 | Temperature profile $\theta(\eta)$ for different N_b (**For Case B).**

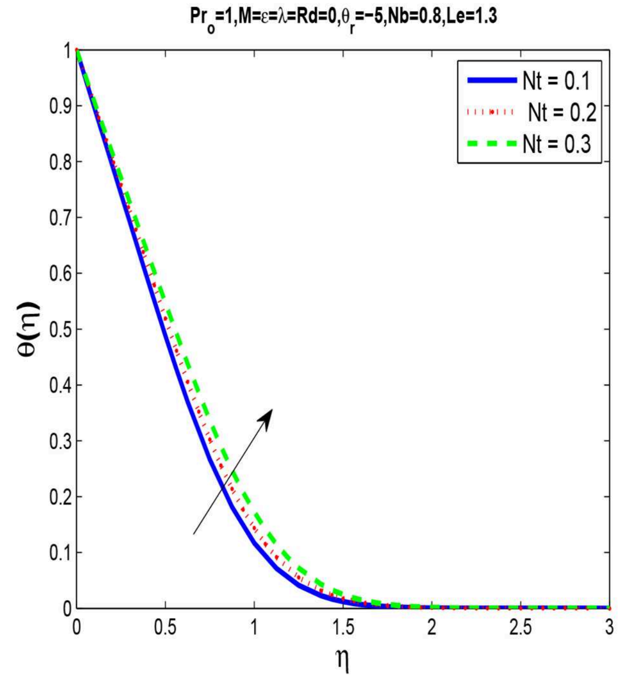

FIGURE 7 | Temperature profile $\theta(\eta)$ for different N_t (**For Case B).**

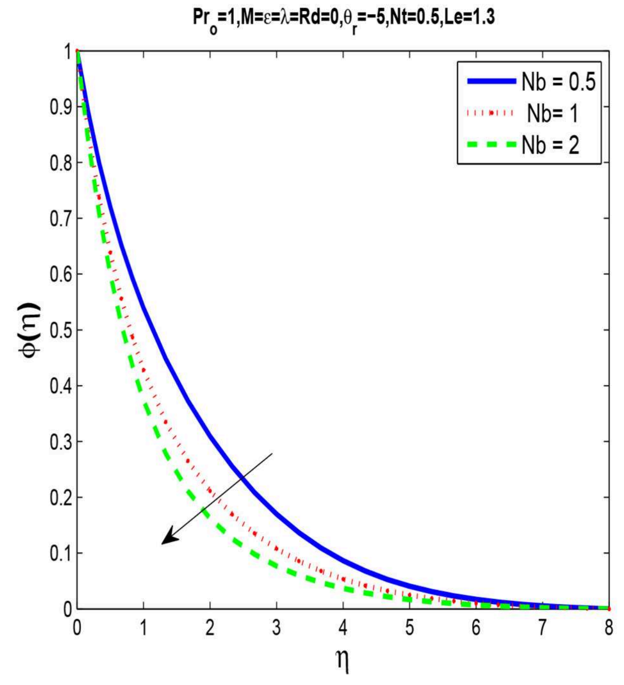

FIGURE 6 | The concentration profile $\phi(\eta)$ for different N_b (**For Case B).**

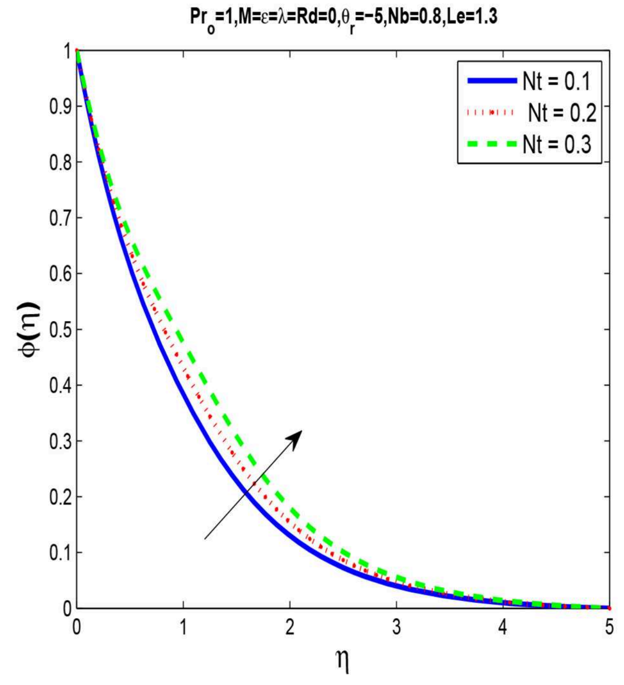

FIGURE 8 | Concentration profile $\phi(\eta)$ for different N_t (**For Case B).**

In **Figure 3**, we observe that by rising the viscosity parameter θ_r, a momentum boundary layer thins. **Figure 4** shows that there is a rise in temperature profile with an increase in thermal conductivity parameter ϵ.

Figures 5, **6** are plotted for different values of Brownian motion parameter N_b and we observe that by increasing N_b thermal boundary layer thickness increases while concentration boundary layer decrease by increasing N_b.

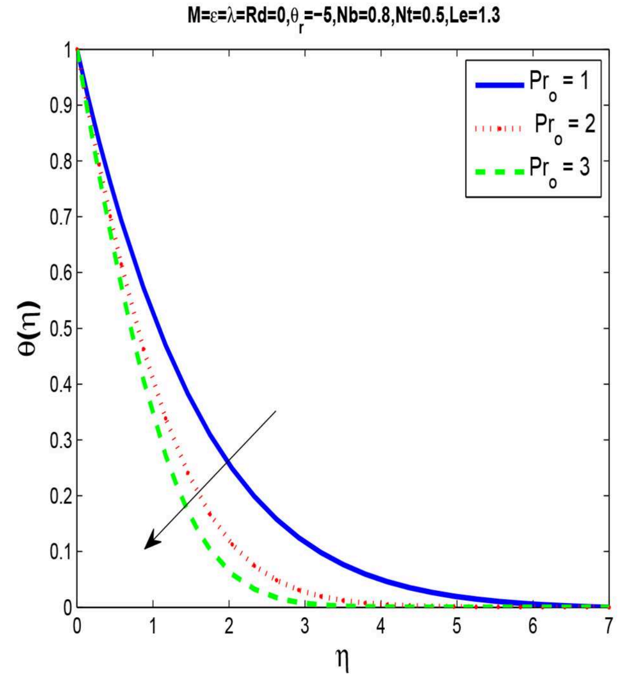

FIGURE 9 | Temperature profile $\theta(\eta)$ for different Pr_o (**For Case B).**

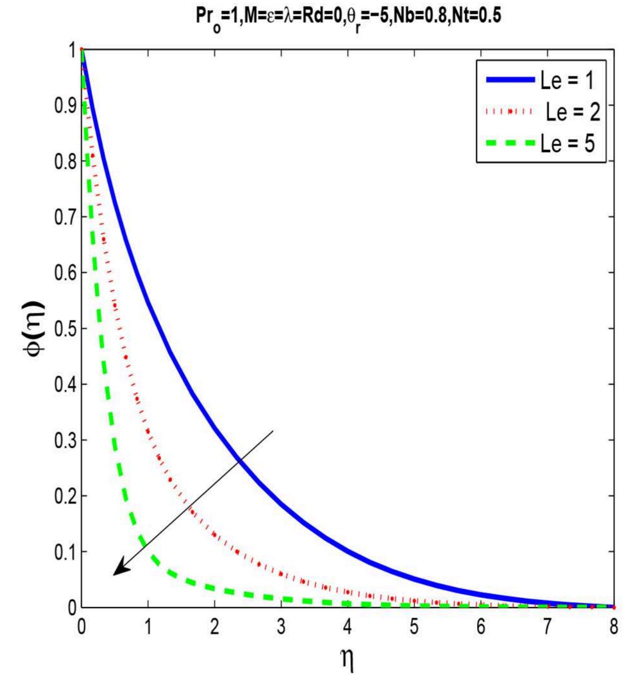

FIGURE 11 | Concentration profile $\phi(\eta)$ for different *Le* (**For Case B).**

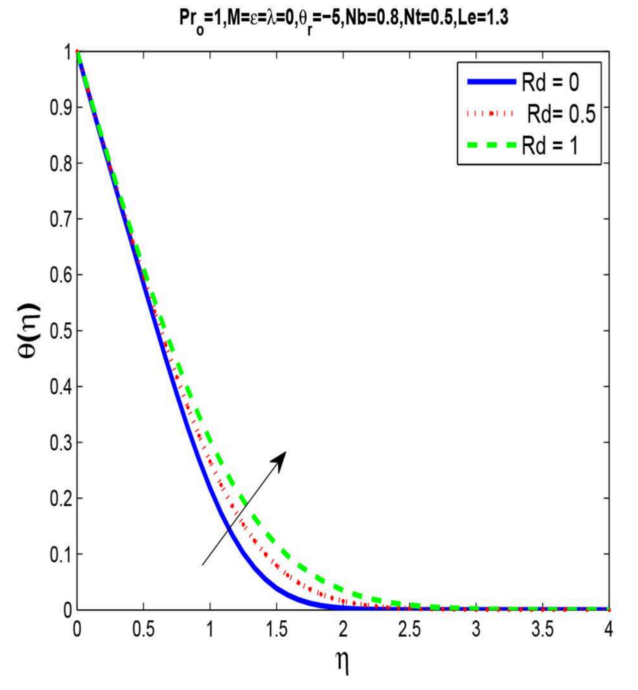

FIGURE 10 | Temperature profile $\theta(\eta)$ for different *Rd* (**For Case B).**

As seen in **Figures 7**, **8** that by increasing thermophoresis parameter N_t, temperature and concentration profiles increases.

Figure 9 indicates that by increasing Pr_o the thermal boundary layer thickness decreases. This is because, when Pr_o increases, the thermal diffusivity decreases and thus the heat is diffused away from the heated surface more slowly and in consequence increase the temperature gradient at surface.

Figure 10 shows that temperature and thermal boundary layer thickness increases when the radiation parameter intensifies. **Figure 11** describe the influence of the Lewis number *Le* on concentration profile. We observe that by increasing *Le* there is decrease in concentration profile. Lewis number is the ratio of Prandtl number and Schmidt number, so with the increase in Lewis number *Le*, molecular diffusivity decreases. As a result, increase in *Le* the nanoparticle fraction is lowered.

6. CONCLUSIONS

The current study offers the findings of a two-dimensional MHD flow of an incompressible fluid through an exponentially stretched sheet whereas treating viscosity and thermal conductivity constant in Case A and variable for Case B. The significance of various parameters on velocity, temperature and concentration is examined. The study's main results for Case B are as follows:

- Momentum boundary layer thickness decrease by increasing fluid viscosity parameter θ_r and magnetic parameter M.

- Thermal boundary layer thickness increases by increasing the thermal conductivity parameters ϵ, Brownian motion parameter N_b and thermophoretic parameter N_t.
- Thermal boundary layer thickness decreases by increasing the Prandtl number Pr_0 whereas increases for radiation parameter Rd.
- Concentration boundary layer thickness increases by increasing thermophoretic parameter N_t whereas decreases by increasing Brownian motion parameter N_b and Lewis number Le.

DATA AVAILABILITY STATEMENT

All datasets generated for this study are included in the article/supplementary material.

AUTHOR CONTRIBUTIONS

MI collected the data and wrote the paper. MF made the analysis of the paper. TI made the geometry of problem and arrange the setting of the paper.

REFERENCES

1. Sakiadis BC. Boundary layer behavior on continuous solid surfaces: I. Boundary layer equations for two-dimensional and axisymmetric flow. *AIChE J.* (1961) **7**:26–8. doi: 10.1002/aic.690070108
2. Blasius H. Grenzschichten in Flussigkeiten mit Kleiner Reibung. *Z Angew Math Phys*. (1908) **56**:1–37.
3. Crane LK. Flow past a stretching plate. *Z Angew Math Phys*. (1961) **7**:21–8.
4. Magyari E, Keller B. Heat and mass transfer in the boundary layers on an exponentially stretching continuous surface. *J Phys D Appl Phys.* (1999) **32**:577.
5. Elbashbeshy EMA. Heat transfer over an exponentially stretching continuous surface with suction. *Arch Mechan.* (2001) **53**:643–51.
6. Norfifah B, Ishak A, Pop I. Boundary layer flow and heat transfer with variable fluid properties on a moving flat plate in a parallel free stream. *J Appl Math.* (2012) 2012:372623. doi: 10.1155/2012/372623
7. Andersson HI, Jan B. Aarseth. Sakiadis flow with variable fluid properties revisited. *Int J Eng Sci.* (2007) **45**:554–61. doi: 10.1016/j.ijengsci.2007.04.012
8. Makinde OD, Mabood F, Khan WA, Tshehla MS. MHD flow of a variable viscosity nanofluid over a radially stretching convective surface with radiative heat. *J Mol Liquids.* (2016) **219**:624–30. doi: 10.1016/j.molliq.2016.03.078
9. Mukhopadhyay S, Layek GC, Samad SkA. Study of MHD boundary layer flow over a heated stretching sheet with variable viscosity. *Int J Heat Mass Transfer*. (2005) **48**:4460–6. doi: 10.1016/j.ijheatmasstransfer.2005.05.027
10. Elbashbeshy EMA, Bazid MAA. The effect of temperature-dependent viscosity on heat transfer over a continuous moving surface. *J Phys D Appl Phys.* (2000) **33**:2716. doi: 10.1088/0022-3727/33/21/309
11. Poply V, Singh P, Yadav AK. A study of Temperature-dependent fluid properties on MHD free stream flow and heat transfer over a non-linearly stretching sheet. *Proc Eng.* (2015) **127**:391–7. doi: 10.1016/j.proeng.2015.11.386
12. Prasad KV, Vajravelu K, Datti PS. The effects of variable fluid properties on the hydro-magnetic flow and heat transfer over a non-linearly stretching sheet. *Int J Thermal Sci.* (2010) **49**:603–10. doi: 10.1016/j.ijthermalsci.2009.08.005
13. Raptis A, Christos P, Takhar HS. Effect of thermal radiation on MHD flow. *Appl Math Comput.* (2004) **153**:645–9. doi: 10.1016/S0096-3003(03)00657-X
14. RLV Renuka D, Poornima T, Bhaskar Reddy N, Venkataramana S. Radiation and mass transfer effects on MHD boundary layer flow due to an exponentially stretching sheet with heat source. *Int J Eng Innovative Technol.* (2014) **3**:33–9.
15. Mukhopadhyay S. Slip effects on MHD boundary layer flow over an exponentially stretching sheet with suction/blowing and thermal radiation. *Ain Shams Eng J.* (2013) **4**:485–91. doi: 10.1016/j.asej.2012.10.007
16. Ishak A. MHD boundary layer flow due to an exponentially stretching sheet with radiation effect. *Sains Malaysiana.* (2011) **40**:391–5.
17. Mabood F, Khan WA, Md Ismail AI. MHD flow over exponential radiating stretching sheet using homotopy analysis method. *J King Saud Univ Eng Sci.* (2017) **29**:68–74. doi: 10.1016/j.jksues.2014.06.001
18. Bidin B, Nazar R. Numerical solution of the boundary layer flow over an exponentially stretching sheet with thermal radiation. *Eur J Sci Res.* (2009) **33**:710–7.
19. Poornima T, Bhaskar Reddy N. Radiation effects on MHD free convective boundary layer flow of nanofluids over a nonlinear stretching sheet. *Adv Appl Sci Res.* (2013) **4**:190–202.
20. Choi SUS, Eastman JA. *Enhancing Thermal Conductivity of Fluids With Nanoparticles.* Argonne National Lab. (1995).
21. Nield DA, Kuznetsov AV. The Cheng-Minkowycz problem for natural convective boundary-layer flow in a porous medium saturated by a nanofluid. *Int J Heat Mass Transf.* (2009) **52**:5792–5. doi: 10.1016/j.ijheatmasstransfer.2009.07.024
22. Khan WA, Makinde OD, Khan ZH. Non-aligned MHD stagnation point flow of variable viscosity nanofluids past a stretching sheet with radiative heat. *Int J Heat Mass Transf.* (2016) **96**:525–34. doi: 10.1016/j.ijheatmasstransfer.2016.01.052
23. Bachok N, Ishak A, Pop I. Boundary layer stagnation-point flow and heat transfer over an exponentially stretching/shrinking sheet in a nanofluid. *Int J Heat Mass Transf.* (2012) **55**:8122–8. doi: 10.1016/j.ijheatmasstransfer.2012.08.051
24. Abu-Nada E, Masoud Z, Oztop HF, Campo A. Effect of nanofluid variable properties on natural convection in enclosures. *Int J Therm Sci.* (2010) **49**:479–91. doi: 10.1016/j.ijthermalsci.2009.09.002
25. Malik MY, Naseer M, Nadeem S, Rehman A. The boundary layer flow of Casson nanofluid over a vertical exponentially stretching cylinder. *Appl Nanosci.* (2014) **4**:869–73. doi: 10.1007/s13204-013-0267-0
26. Eid MR. Chemical reaction effect on MHD boundary-layer flow of two-phase nanofluid model over an exponentially stretching sheet with a heat generation. *J Mol Liquids.* (2016) **220**:718–25. doi: 10.1016/j.molliq.2016.05.005
27. Gangaiah T, Saidulu N, Venkata Lakshmi A. Magnetohydrodynamic flow of nanofluid over an exponentially stretching sheet in presence of viscous dissipation and chemical reaction. *J Nanofluids.* (2018) **7**:439–48. doi: 10.1166/jon.2018.1465
28. Abel M. Mahantesh S, Nandeppanavar M, Basanagouda V. Effects of variable viscosity, buoyancy and variable thermal conductivity on mixed convection heat transfer due to an exponentially stretching surface with magnetic field. *Proc Natl Acad Sci India Sec A Phys Sci.* (2017) **87**:247–56. doi: 10.1007/s40010-016-0338-1
29. Yousif MA, Farhan Ismael H, Abbas T, Ellahi R. Numerical study of momentum and heat transfer of MHD Carreau nanofluid over an exponentially stretched plate with internal heat source/sink and radiation. *Heat Transf Res.* (2019) **50**: 649–58. doi: 10.1615/HeatTransRes.2018025568
30. Ellahi R, Zeeshan A, Hussain F, Abbas T. Thermally charged MHD Bi-phase flow coatings with non-Newtonian nanofluid and Hafnium particles along slippery walls. *Coatings.* (2019) **9**:300. doi: 10.3390/coatings9050300
31. Ahmed Z, Nadeem S, Saleem S, Ellahi R. Numerical study of unsteady flow and heat transfer CNT-based MHD nanofluid with variable viscosity over a permeable shrinking surface. *Int J Numer*

Methods Heat Fluid Flow. (2019). doi: 10.1108/HFF-04-2019-0346. [Epub ahead of print].

32. Nguyen-Thoi T, Bhatti MM, Ali JA, Mustafa Hamad S, Sheikholeslami M, Shafee A, Haq R. Analysis on the heat storage unit through a Y-shaped fin for solidification of NEPCM. *J Mol Liquids*. (2019) **292**:111378. doi: 10.1016/j.molliq.2019.111378
33. Buongiorno J. Convective transport in nanofluids. *J Heat Transf*. (2006) **128**:240–50.
34. Shampine LF, Kierzenka J, Reichelt MW. Solving boundary value problems for ordinary differential equations in MATLAB with bvp4c. *Tutor Notes*. (2000) **2000**:1–27.

Conflict of Interest: The authors declare that the research was conducted in the absence of any commercial or financial relationships that could be construed as a potential conflict of interest.

Copyright © 2019 Irfan, Farooq and Iqra. This is an open-access article distributed under the terms of the Creative Commons Attribution License (CC BY). The use, distribution or reproduction in other forums is permitted, provided the original author(s) and the copyright owner(s) are credited and that the original publication in this journal is cited, in accordance with accepted academic practice. No use, distribution or reproduction is permitted which does not comply with these terms.

NOMENCLATURE

a, b	positive constant (ms^{-1})
(u, v)	the velocity components ($m\ s^{-1}$)
μ	the coefficient of viscosity ($Pa\ s$)
ρ	the density of fluid ($kg\ m^{-3}$)
ϵ	the thermal conductivity parameter of the fluid
M	magnetic parameter
T	fluid temperature (K)
k	the thermal conductivity ($W\ m^{-1}\ K^{-1}$)
c_p	the specific heat capacity ($J\ kg^{-1}\ K^{-1}$)
q_r	the radiative heat flux ($W\ m^{-2}$)
τ	ratio of heat capacities of nanofluid and base fluid
D_B	Brownian coefficients ($m^2\ s^{-1}$)
D_T	thermophoresis diffusion coefficients ($m^2\ s^{-1}$)
T_∞	the ambient fluid temperature (K)
σ	the electrical conductivity ($S\ m^{-1}$) (S is siemens)
T_w	constant temperature at the wall (K)
B_0	applied magnetic field ($N\ m^{-1}\ A^{-1}$)
σ^*	Stefan-Boltzman constant ($W\ m^{-2}K^{-4}$)
k_*	mean absorption coefficient (m^{-1})
C_∞	the ambient fluid concentration
Pr_o	the ambient Prandtl number
θ_r	fluid viscosity parameter
T_{ref}	reference temperature (K)
L_e	Lewis number
N_t	thermophoresis parameter
N_b	Brownian motion parameter
λ	free stream velocity parameter
R_d	thermal radiation parameter
C_f	the skin friction coefficient
Nu_x	the local Nusselt parameter
Sh_x	the local Sherwood parameter

ORIGINAL RESEARCH
published: 09 January 2020
doi: 10.3389/fphy.2019.00209

Computational and Physical Examination About the Aspects of Fluid Flow Between Two Coaxially Rotated Disks by Capitalizing Non-fourier Heat Flux Theory: Finite Difference Approach

Sardar Bilal[1]*, *Asifa Tassaddiq*[2], *A. H. Majeed*[1], *Kottakkaran Sooppy Nisar*[3], *Farhad Ali*[4] and *M. Y. Malik*[5]

[1] Department of Mathematics, Air University, Islamabad, Pakistan, [2] College of Computer and Information Sciences, Majmaah University, Al Majma'ah, Saudi Arabia, [3] Department of Mathematics, College of Arts and Sciences, Prince Sattam Bin Abdulaziz University, Wadi Aldawaser, Saudi Arabia, [4] Department of Mathematics, City University of Science and Information Technology, Peshawar, Pakistan, [5] Department of Mathematics, College of Sciences, King Khalid University, Abha, Saudi Arabia

OPEN ACCESS

Edited by:
Muhammad Mubashir Bhatti, Shanghai University, China

Reviewed by:
Anwar Shahid, Nanjing University of Aeronautics and Astronautics, China
Ilyas Khan, Ton Duc Thang University, Vietnam
Kh S. Mekheimer, Al-Azhar University, Egypt

***Correspondence:**
Sardar Bilal
sardarbilal@mail.au.edu.pk

Specialty section:
This article was submitted to Mathematical Physics, a section of the journal Frontiers in Physics

Received: *21 September 2019*
Accepted: *21 November 2019*
Published: *09 January 2020*

Citation:
Bilal S, Tassaddiq A, Majeed AH, Nisar KS, Ali F and Malik MY (2020) Computational and Physical Examination About the Aspects of Fluid Flow Between Two Coaxially Rotated Disks by Capitalizing Non-fourier Heat Flux Theory: Finite Difference Approach. Front. Phys. 7:209. doi: 10.3389/fphy.2019.00209

This pagination is executed to exemplify flow features exhibited by viscous fluid between two coaxially rotated disks. Thermal analysis is performed by using Cattaneo-Christov heat flux theory. Porosity aspects are also taken into account. Mathematically structured non-linear PDEs are transmuted into non-linear ODEs by employing Karman transformations. Afterward, solution is heeded by applying implicit finite difference scheme renowned as Keller box method. Interpretation of flow controlling parameters on axial, tangential, and radial components of velocity, thermal distribution is exhibited. Assurance of computed data is done by managing comparison for skin friction coefficients at walls of disks. From the attained outcomes, it is addressed that the magnitude of axial and radial velocities diminishes at lower disk contrary to upper disk for intensifying magnitude of Reynolds number. Increment in tangential component of velocity is also demonstrated for uplifts values of Reynolds number. It is also concluded that thermal field decrements for increasing of *Pr* and thermal relaxation parameter. It is worthy to mention that shear drag coefficient at wall of lower disk decreases conversely to the wall shear coefficient magnitude at wall of upper disk.

Keywords: Cattaneo Christov heat flux model, permeable medium, fluid flow with coaxially rotated disks, implicit finite difference scheme, coaxially rotated disks, viscous fluid

INTRODUCTION

Rotational fluid flow generated by coaxial disks is one of the classical problems of fluid mechanics. In recent years, it has become a popular research area and has persuaded researchers due to magnificent theoretical and practical significance in engineering and applied sciences. Some important practical fields in which rotatory flow is capitalized are rotor–stator system, gas turbine engineering, air rotational cleaners, medical equipment, chemical engineering, and thermal power–generating systems. In view of its capitalization in various processes, researcher fraternity is examining such type of flows in current days. Inaugurated work on flow induced due to rotating disk is performed by Karman [1]. He introduced transformations and provided a mathematical framework for construction of ordinary differential systems of rotational flows from Navier Stokes theory. Cochran [2] also used these transformations to scrutinize rotating disk flow by using numerical integration scheme. Batchelor [3] validated that Karman transformation can be evenly used for fluid flow between two coaxial rotating disks. Rotating flow by two coaxial disks is primarily examined by Stewartson [4]. Chapple and Stokes [5] elucidated the flow features of fluid between two coaxially rotated disks. Mellor et al. [6] bestowed comprehensive treatment of fluid flow restricted between two coaxial infinite disks, one rotating, and other stationary. Thermal aspects of fluid between rotational disks were discussed by Arora and Stokes [7]. Interpretation of flow phenomenon between porous stationary disk and solid rotating disk was manipulated by Kumar et al. [8]. Xun et al. [9] considered rotating disk of variable thickness and adumbrated the flow features of Power law fluid. Hall effects on an unsteady MHD (magneto hydrodynamics) flow of viscous incompressible electrically conducting fluid between two rotating disks with non-coincident parallel axes embedded in a porous viscous medium were accorded by Das et al. [10]. Asgher et al. [11] conducted Lie group analysis on the thermal features of fluid manifested by rotating disks. Elmaboud et al. [12] discussed peristaltic flow induced by sinusoidal wave propagating with constant speed on the walls of two-dimensional infinite rotating channel by heeding semi-analytical solutions.

In the most recent couple of decades, researcher fraternity has shown fantastic energy in exploring the heat propagation by means of a wave mechanism rather than essentially by diffusion. Late studies affirm that this is not just a low-temperature phenomenon but heat transfer mechanism also occurs at high temperature through diffusion. Just about 200 years prior, thermal features in various circumstances and especially in flowing fluid environment were interpreted by Fourier law of heat conduction [13]. However, this law is inadequate in comprehending complete description about the heat exchange procedure among multiple connected surfaces in various conditions because of its disablement to fulfill the principle of causality. Later on, in 1948, Cattaneo [14] modified Fourier law by viewing the inadequateness generated by Fourier law of heat conduction and explored that this law explains the thermal attribute at low temperature because it generates parabolic heat equation in which initial disturbance are felt throughout the domain. After getting thorough analysis about Fourier law and viewing vector field aspect of heat flux, he included thermal relaxation time term to control generated thermal inertia, which is known as Maxwell-Cattaneo law. Afterward, Christov [15] proposed that objective time derivative instead of material time derivative is used for exact fulfillment of causality principle. He changed the time derivative in Maxwell-Cattaneo model by Oldryod upper convective derivative, which has successfully preserved the material invariant formulation and famously known as Cattaneo-Christov heat flux law. Cattaneo-Christov heat flux model has bounteous applications in engineering and modern industrial procedures like in skin burns and nanofluids, cooling of electronic devices, food technology, nuclear reactor cooling, power generation, heat exchangers, heat propagation in tissues, and so many. The uniqueness and stability of the solution for governing temperature equations by Cattaneo-Christov model in some initial and boundary value problems were proven by Straughan [16]. Additionally, steadiness of structure of Cattaneo-Christov heat flux model with uniqueness was revealed by Ciarletta and Straughan [17]. Tibullo and Zampoli [18] explicated the behavior of Cattaneo-Christov heat flux model in incompressible fluid flows. Aqsa [19] and Haddad [20] heeded numerical solution for thermal convection of an incompressible viscous fluid by obliging Cattaneo-Christov heat flux model. Mekheimer and Elmaboud [21] interpreted the aspects of temperature-dependent viscosity and thermal conductivity on peristaltic flow of a Newtonian fluid in a vertical asymmetric channel. Mekneimer [22] addressed heat transfer features of peristaltic couple stress fluid in asymmetric channel generated by wave with different phase and amplitudes. All of the abovementioned thought-provoking investigations have generated prodigious interest of researchers toward the analysis of flow in the presence of thermal aspects [23–26].

Transport procedures through porous space are commonly encountered in various chemical, mechanical, geophysical, electrochemical, and metallurgical routines. The theory about macroscopic movement of fluid in porous medium comprises differential equation that expresses linear relation between velocity and pressure gradient. Initially, Henry Darcy [27] (in 1856) presented a law to explicate the dynamic phenomenon in porous medium by working on the flow of sandy water through pebbles. Several technological processes depend on porous media theory, such as hydrology, oil exploration, solar collectors, porous insulations, packed beds, chromatography, heterogeneous catalysis, control of shear stresses at the seabed bottom, and oscillatory flow through seabed ripples. Darcy theory has promising applications in the field of biomedicine and the development of biological clogging and flow through tissues [28]. Granular material [29] where significant amount of pore structures exist has application in manufacturing, paper, ceramic products, and textiles. Taseer et al. [30] addressed the flow behavior of Maxwell nanofluid in porous medium by implementing zero mass flux condition. They capitalized on Darcy-Forchheimer law to depict the flow pattern. They found that porosity parameter mounts the magnitude of temperature and concentration of particles. Seddeek [31] probed convective heat transfer in fluid immersed in porous medium. Analytical results for Darcy flow was described by Jha and Kaurangini [32]. Aziz et al. [33] computed the traveling wave solution for the time-dependent viscoelastic fluid by way of a porous flat plate.

Magnetohydrodynamics is the study of the interaction between magnetic field and conductive fluid. The essence about magnetization is that the external magnetic field controls the turbulence in flow field. In addition, the magnetized flows differ from ordinary fluids because the generated current in the bulk fluid produces volumetric Lorentz force that extensively modifies the features. In recent years, magnetization and its impact on flow features have attained pervasive focus due to its extraordinary industrial applications, such as magnetized materials processes, manufacturing of glass, and MHD controlled electric generators. So the analysis of application of magnetic field has experienced great development and diversity. Andersson [34] performed exclusive study by manipulating electromagnet hydrodynamic waves mathematically. The stretched flow of two-dimensional Newtonian fluid under the effects of applied magnetic field was contemplated by Andersson [34]. Liu [35] extended the work of Andersson [34] and described the heat and mass transfer of MHD viscous fluid flow over stretching surface. He computed exact solution of the problem by following the procedure of Andersson [34]. The impact of normally impinging magnetic field on boundary layer flow of Newtonian fluid over permeable stretching sheet was analyzed by Kumaran et al. [36]. Yirga and Tesfay [37] developed the numerical simulations for MHD viscous fluid flow over non-linear stretching sheet. The fluid flow equations were solved *via* Keller-Box method, and variations in physical quantities were presented regarding different parametric conditions. Recently, Yasin et al. [38] simulated the problem of two-dimensional MHD viscous nanofluid flow over porous stretched sheet. The formulated equations were solved by implementing well-known shooting technique. Mabood et al. [39] developed the approximate analytic solution of MHD boundary layer fluid flow over exponentially stretching surface. Some of the literature regarding the mentioned aspects is accessed through the references [40–43].

Present disquisition is addressed to excogitate thermophysical features exhibited in viscous fluid flow between two coaxially rotating disks embedded in permeable medium by obliging Cattaneo-Christov heat flux law. According to author's knowledge and available literature survey, it is found that very concise work is done so far in this direction. Tremendous engineering and practical application generated by rotating disk flows make present analysis highly potential. The authors hope that this manuscript will serve as a reference study for future researches. The article is strategized in such a way that the literature assessment is presented in section Introduction, whereas the mathematical structuring is provided in section Mathematical Model. The explanation about the solution methodology is debated in section Numerical Procedure. Comprehensive analysis and interpretation of flow controlling parameters are disclosed in section Results and Discussion. Last, the outcome norms are listed in section Conclusions.

MATHEMATICAL MODEL

Consider a steady, incompressible flow of viscous fluid between two coaxially rotated disks. The lower disk is placed at $z = 0$, whereas the distance between the disks is h units. Lower and upper disks possess angular velocities Ω_1 and Ω_2, respectively, and a_1 and a_2 are corresponding stretching rates (**Figure 1**). Porous medium between disks is considered, and Cattaneo-Christov heat flux model is obliged to analyze thermal features of fluid flow model.

We have used cylindrical coordinates (r, θ, z) with velocity components $(\hat{u}, \hat{v}, \hat{w})$ to the velocity profile and temperature equations as follows:

$$\frac{\partial \hat{u}}{\partial r} + \frac{\hat{u}}{r} + \frac{\partial \hat{w}}{\partial z} = 0, \tag{1}$$

$$\hat{u}\frac{\partial \hat{u}}{\partial r} + \hat{w}\frac{\partial \hat{u}}{\partial z} - \frac{\hat{v}^2}{r} = -\frac{1}{\rho}\frac{\partial \hat{p}}{\partial r} + \upsilon\left(\frac{\partial^2 \hat{u}}{\partial r^2} + \frac{1}{r}\frac{\partial \hat{u}}{\partial r} + \frac{\partial^2 \hat{u}}{\partial z^2} - \frac{\hat{u}}{r^2}\right) - \frac{\sigma \beta_0^2}{\rho}\hat{u} - \frac{\mu}{k_0}\hat{u}, \tag{2}$$

$$\hat{u}\frac{\partial \hat{v}}{\partial r} + \hat{w}\frac{\partial \hat{v}}{\partial z} + \frac{\hat{u}\hat{v}}{r} = \upsilon\left(\frac{\partial^2 \hat{v}}{\partial r^2} + \frac{1}{r}\frac{\partial \hat{v}}{\partial r} + \frac{\partial^2 \hat{v}}{\partial z^2} - \frac{\hat{v}}{r^2}\right) - \frac{\sigma \beta_0^2}{\rho}\hat{v} - \frac{\mu}{k_0}\hat{v} \tag{3}$$

$$\hat{u}\frac{\partial \hat{w}}{\partial r} + \hat{w}\frac{\partial \hat{w}}{\partial z} = -\frac{1}{\rho}\frac{\partial \hat{p}}{\partial z} + \upsilon\left(\frac{\partial^2 \hat{w}}{\partial r^2} + \frac{1}{r}\frac{\partial \hat{w}}{\partial r} + \frac{\partial^2 \hat{w}}{\partial z^2}\right) - \frac{\mu}{k_0}\hat{w}, \tag{4}$$

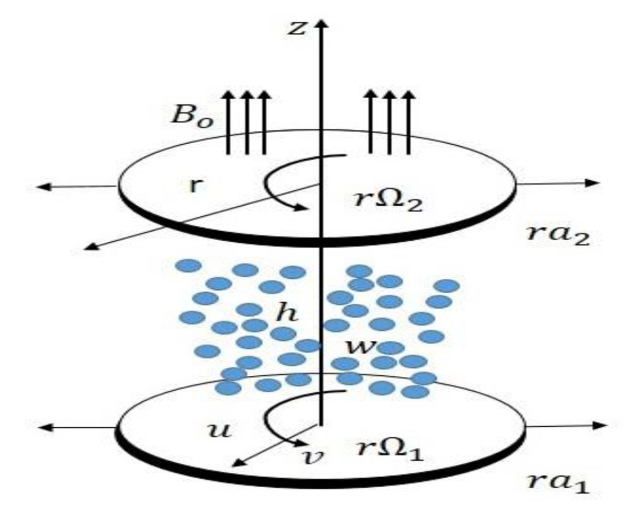

FIGURE 1 | Physical configuration of the problem.

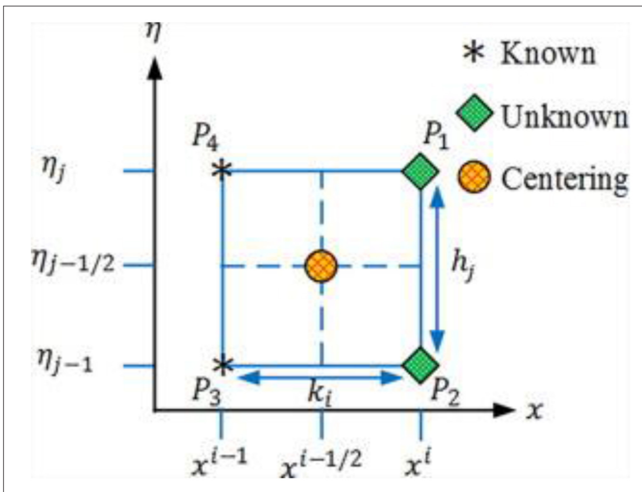

FIGURE 2 | Schematic representation of domain.

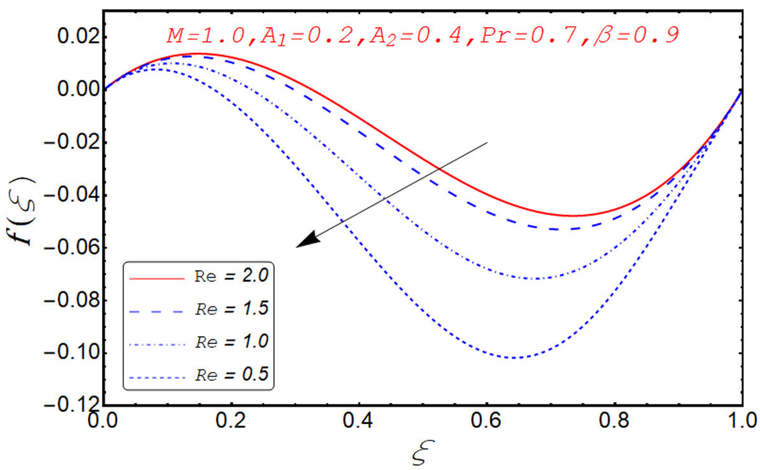

FIGURE 3 | Behavior of $f(\xi)$ for different *Re*.

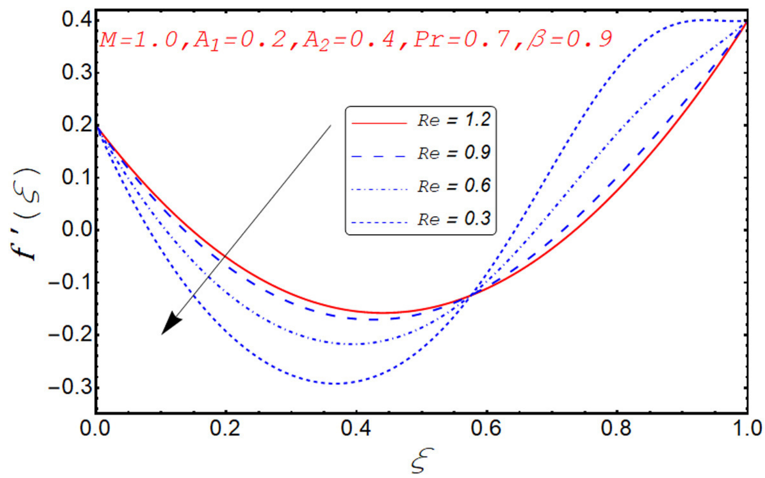

FIGURE 4 | Behavior of $f'(\xi)$ for different *Re*.

$$\rho C_p\left(\hat{u}\frac{\partial \hat{T}}{\partial r}+\hat{w}\frac{\partial \hat{T}}{\partial z}\right) = -\nabla\cdot\vec{q}, \quad (5)$$

with boundary conditions:

$$\begin{aligned}&\hat{u}=ra_1,\ \hat{v}=r\Omega_1, \hat{w}=0, \hat{T}=\hat{T}_1 \text{ at } z=0,\\ &\hat{u}=ra_2,\ \hat{v}=r\Omega_2, \hat{w}=0, \hat{T}=\hat{T}_2 \text{ at } z=h,\end{aligned} \quad (6)$$

where Equations (3–5) are referred to Hayat et al. [25], also pressure is expressed as $\hat{p}$, $\hat{T}_1 and\ \hat{T}_2$ are the temperatures of upper and lower disks, and flux of heat $\vec{q}$ satisfies:

$$\vec{q}+\gamma\left(\frac{\partial\vec{q}}{\partial t}+\mathbf{V}.\nabla\vec{q}-\vec{q}.\nabla\mathbf{V}+(\nabla.\mathbf{V})\vec{q}\right)=-k\nabla\hat{T}, \quad (7)$$

where γ is the thermal relaxation parameter (It is defined as the parameter that controls the speed of heat waves produced within the system and makes them move with finite speed to follow the principle of causality), and k is the thermal conductivity. Now, we omit q from the Equations (5, 7) and obtain:

$$\begin{aligned}\left(\hat{u}\frac{\partial\hat{T}}{\partial r}+\hat{w}\frac{\partial\hat{T}}{\partial z}\right)&=\frac{k}{\rho C_p}\left(\frac{\partial^2\hat{T}}{\partial r^2}+\frac{1}{r}\frac{\partial\hat{T}}{\partial r}+\frac{\partial^2\hat{T}}{\partial z^2}\right)\\ &-\gamma\left(\hat{u}^2\frac{\partial^2\hat{T}}{\partial r^2}+\hat{w}^2\frac{\partial^2\hat{T}}{\partial z^2}+2\hat{u}\hat{w}\frac{\partial^2\hat{T}}{\partial r\partial z}\right.\\ &\left.+\left(\hat{u}\frac{\partial\hat{u}}{\partial r}+\hat{w}\frac{\partial\hat{u}}{\partial z}\right)\frac{\partial\hat{T}}{\partial r}+\left(\hat{u}\frac{\partial\hat{w}}{\partial r}+\hat{w}\frac{\partial\hat{w}}{\partial z}\right)\frac{\partial\hat{T}}{\partial z}\right). \quad (8)\end{aligned}$$

Equations (2–5) and Equation (8) are transformed into ordinary differential equations by obliging Von Karman transformations [1]:

$$\hat{u}=r\Omega_1 f'(\zeta), \hat{v}=r\Omega_1 g(\zeta), \hat{w}=-2h\Omega_1 f(\zeta),$$

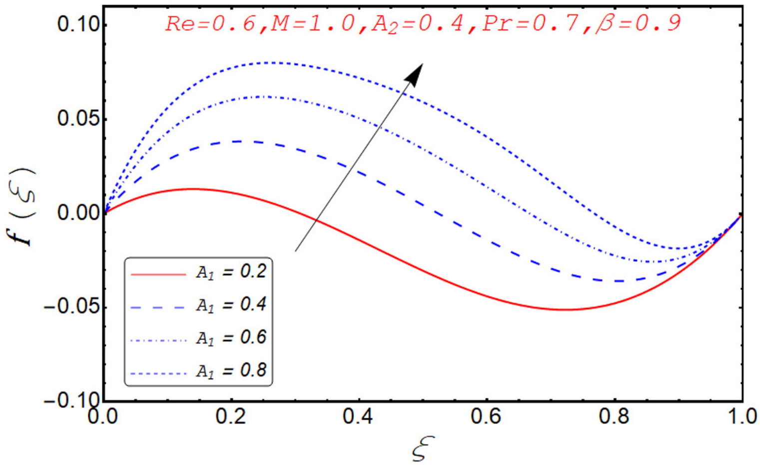

FIGURE 5 | Behavior of $f(\xi)$ for different A_1.

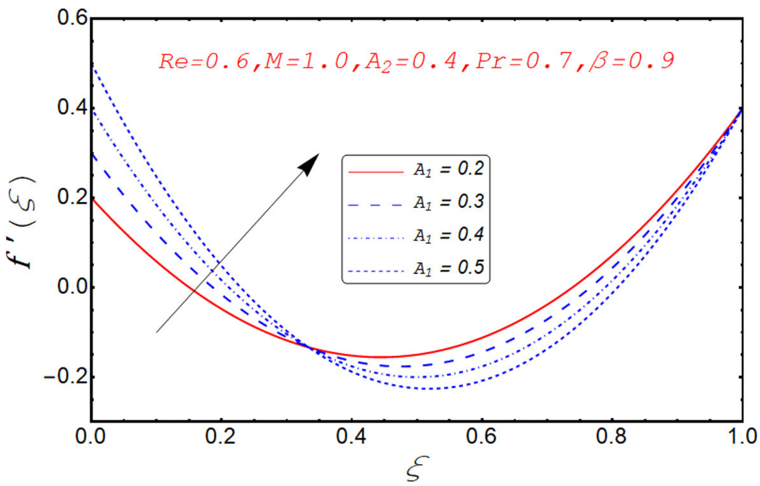

FIGURE 6 | Behavior of $f'(\xi)$ for different $A1$.

$$\theta = \frac{\hat{T} - \hat{T}_2}{\hat{T}_1 - \hat{T}_2},$$
$$\hat{p} = \rho_f \Omega_1 \nu_f \left(P(\zeta) + \frac{1}{2}\frac{r^2}{h^2}\epsilon \right), \zeta = \frac{z}{h}. \quad (9)$$

Mass conservation is identically satisfied, and Equations (2–4, 6, 8) take the following form:

$$f''' + Re\left(2ff'' - f'^2 + g^2 - \frac{1}{\beta}f' + Mf'\right) - \epsilon = 0, \quad (10)$$
$$Re\left(2f'g - 2fg' + \frac{1}{\beta}g + Mg\right) - g'' = 0, \quad (11)$$
$$P' = Re\left(\frac{2}{\beta}f - 4ff'\right) - 2f'', \quad (12)$$
$$\frac{1}{Pr}\theta'' + 2Ref\theta' - 4\lambda Re\left(f^2\theta'' + ff'\theta'\right) = 0, \quad (13)$$

with

$$f(0) = 0, f(1) = 0, f'(0) = A_1, f'(1) = A_2, g(0) = 1,$$
$$g(1) = \tau, \theta(0) = 1, \theta(1) = 0, P(0) = 0, \quad (14)$$

where

$$Re = \frac{\Omega_1 h^2}{\nu_f}, Pr = \frac{(\rho C_p)_f \nu_f}{k_f}, \lambda = \gamma\Omega_1,$$
$$A_1 = \frac{a_1}{\Omega_1}, A_2 = \frac{a_2}{\Omega_2}, \tau = \frac{\Omega_2}{\Omega_1}, \beta = \frac{k_0\Omega_1}{\nu}, \quad (15)$$

where Re denotes Reynolds number, Pr is the Prandtl number, A_1 and A_2 are scaled stretching parameters, λ is the thermal relaxation, τ and β are rotational number and porosity parameter.

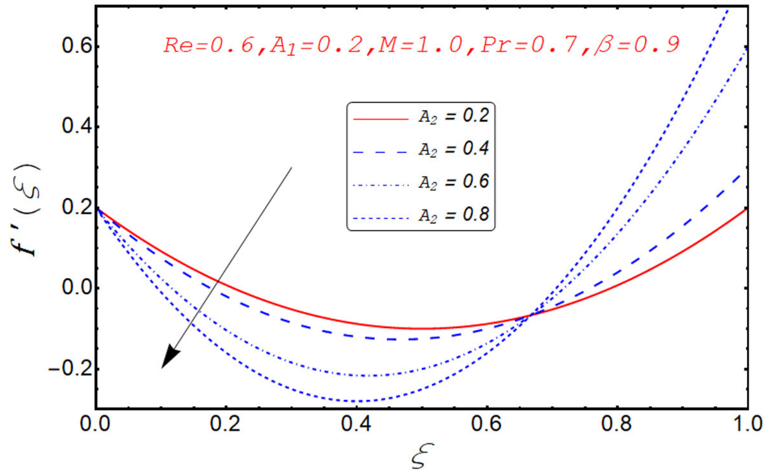

FIGURE 7 | Behavior of $f'(\xi)$ for different A_2.

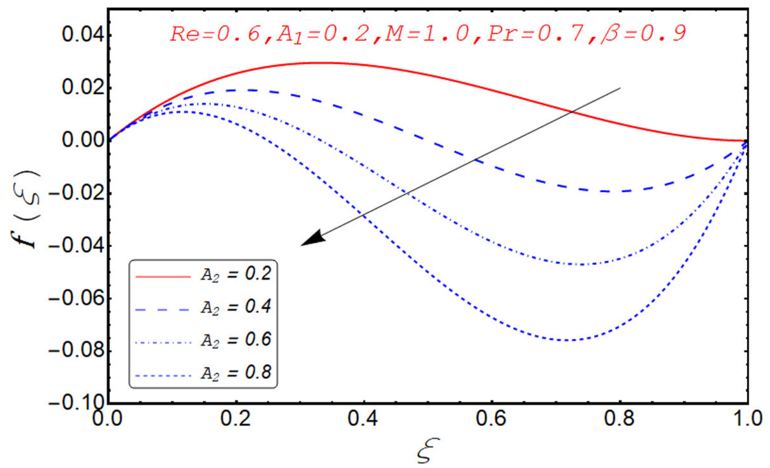

FIGURE 8 | Behavior of $f(\xi)$ for different A_2.

To make a simpler form of Equation (10), we removed ϵ.

$$f^{(iv)} + Re\left(2ff''' + 2gg' - \frac{1}{\beta}f'' - Mf''\right) = 0. \tag{16}$$

The pressure parameter ϵ can be found by using Equations (10 and 14) as:

$$\epsilon = f''(0) - Re\left(\left(f'(0)\right)^2 - \left(g(0)\right)^2 + \frac{1}{\beta}f'(0) - Mf'(0)\right). \tag{17}$$

Equation (17) vanishes due to the given initial conditions in Equation (14).

The radial and tangential components of shear stress at lower disk are τ_{zr} and $\tau_{z\theta}$

$$\tau_{zr} = \mu\left.\frac{\partial\hat{u}}{\partial z}\right|_{z=0} = \frac{\mu r\Omega_1 f''(0)}{h},\ \tau_{z\theta} = \mu\left.\frac{\partial\hat{v}}{\partial z}\right|_{z=0}$$

$$= \frac{\mu r\Omega_1 g'(0)}{h}. \tag{18}$$

where τ_w is the total shear stress, which is defined as:

$$\tau_w = \sqrt{\tau_{zr}^2 + \tau_{z\theta}^2}. \tag{19}$$

C_{f1} and C_{f2} are the skin friction coefficients at lower and upper disks defined as:

$$C_{f1} = \frac{\tau_w|_{z=0}}{\rho(r\Omega_1)^2} = \frac{1}{Re_r}\left(\left(f''(0)\right)^2 + \left(g'(0)\right)^2\right)^{1/2}, \tag{20}$$

$$C_{f2} = \frac{\tau_w|_{z=h}}{\rho(r\Omega_1)^2} = \frac{1}{Re_r}\left(\left(f''(1)\right)^2 + \left(g'(1)\right)^2\right)^{1/2}, \tag{21}$$

where $Re_r = \frac{r\Omega_1 h}{\nu}$ is the local Reynolds number.

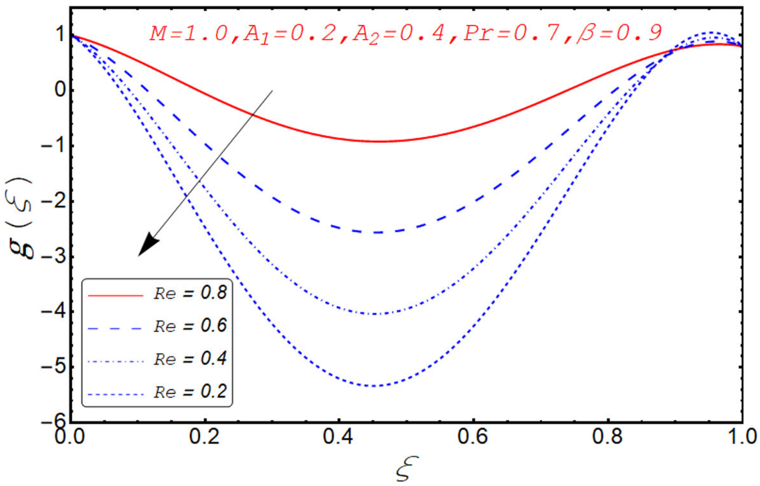

FIGURE 9 | Behavior of $g(\xi)$ for different Re.

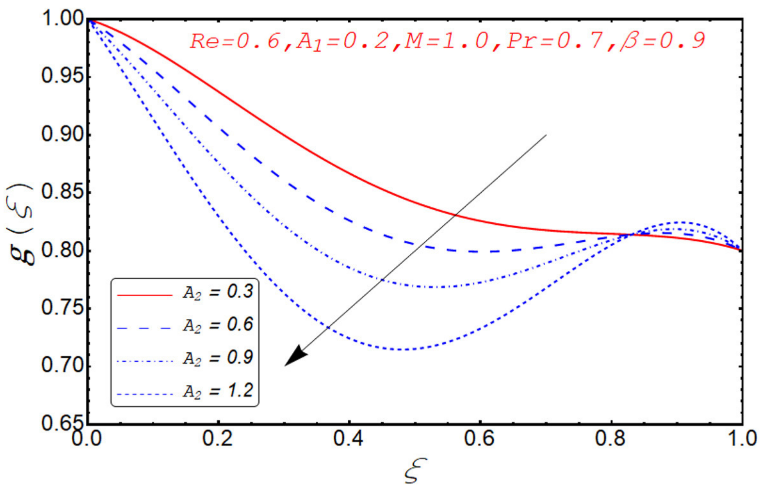

FIGURE 10 | Behavior of $g(\xi)$ for different A_2.

NUMERICAL PROCEDURE

Manipulation of accurate solution is necessary for physical interpretation of current work. Initially, equations are modeled by using Karman approximation and afterward, we have attained an intricate system of ordinary differential Equations (10–13) along with boundary conditions in Equation (14). We have applied Keller-box scheme referred to [40, 44–46], that is, the implicit finite difference scheme. For the implementation of this technique, first, we have to transform it into a system of first-order equations and define new variables $u(y,\zeta)$, $v(y,\zeta)$,

$$w(y,\zeta),\ s(y,\zeta),\ t(y,\zeta)\ and\ \theta(y,\zeta) = q(y,\zeta) \text{ are}$$
$$f' = u,\ u' = v,\ v' = w,\ g' = s \text{ and } q' = t, \quad (22)$$

and Equations (11–13, 16) are reduced to

$$s' - Re\left(2ug - 2fs + Mg + \frac{1}{\beta}g\right) = 0, \quad (23)$$

$$t' + 2PrReft - 4Pr\lambda Re\left(f^2t' + fut\right) = 0, \quad (24)$$

$$w' + Re\left(2fw + 2gs - Mv - \frac{1}{\beta}v\right) = 0. \quad (25)$$

Similarly, the boundary conditions are converted into the following forms

$$\begin{aligned} &f(0) = 0,\ u(0) = A_1,\ g(0) = 1, q(0) = 1, \\ &f(1) = 0,\ u(1) = A_2, g(1) = \tau,\ q(1) = 0. \end{aligned} \quad (26)$$

Average and center difference gradients at the point of net derivatives are demarcated in **Figure 2** and mathematically

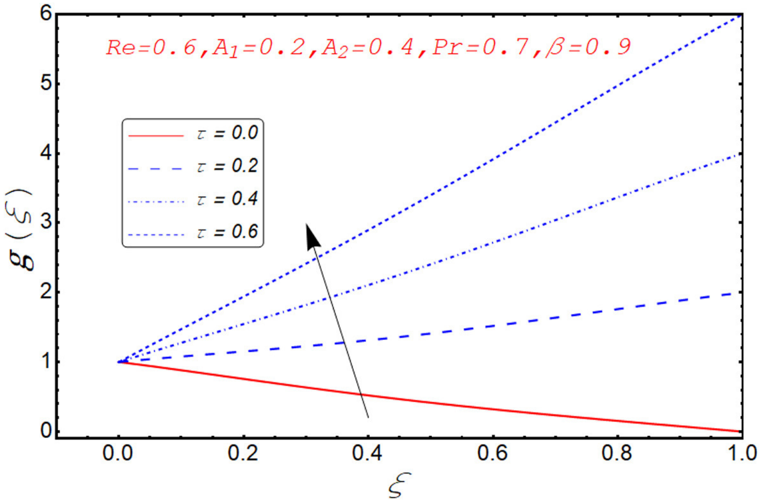

FIGURE 11 | Behavior of $g(\xi)$ for different τ.

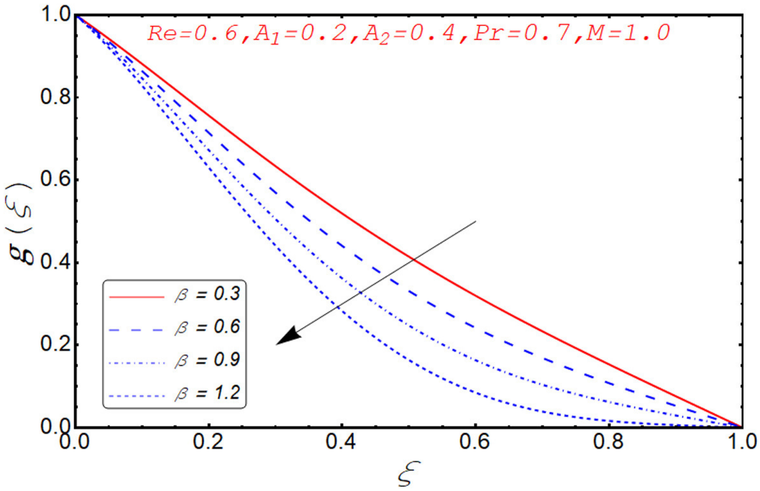

FIGURE 12 | Behavior of $g(\xi)$ for different β.

as below

$$\eta_o = 0, \eta_k = \eta_{k-1} + \eta_k, \quad k = 1, 2, 3, \ldots, k \quad \eta_k = \eta_\infty.$$

Applying the Newton iteration $f_{k+1} = f_k + \delta f_k$, for all dependent variables involved in linearized non-linear algebraic equations and substituting these expressions in non-linear equations and neglecting quadratic and higher order terms in δ, a linear tridiagonal system is presented as follows:

$$\delta f_k - \delta f_{k-1} - \frac{h_k}{2}\left(\delta u_k + \delta u_{k-1}\right) = (r_1)_{k-\frac{1}{2}},$$

$$\delta u_k - \delta u_{k-1} - \frac{h_k}{2}\left(\delta v_k + \delta v_{k-1}\right) = (r_5)_{k-\frac{1}{2}},$$

$$\delta v_k - \delta v_{k-1} - \frac{h_k}{2}\left(\delta w_k + \delta w_{k-1}\right) = (r_6)_{k-\frac{1}{2}},$$

$$\delta g_k - \delta g_{k-1} - \frac{h_k}{2}\left(\delta s_k + \delta s_{k-1}\right) = (r_7)_{k-\frac{1}{2}},$$

$$\delta q_k - \delta q_{k-1} - \frac{h_k}{2}\left(\delta t_k + \delta t_{k-1}\right) = (r_8)_{k-\frac{1}{2}},$$

$$(a_1)_k \delta f_k + (a_2)_k \delta f_{k-1} + (a_3)_k \delta u_k + (a_4)_k \delta u_{k-1} + (a_5)_k \delta g_k + (a_6)_k \delta g_{k-1} + (a_7)_k \delta s_k + (a_8)_k \delta s_{k-1} = (r_2)_{k-1/2},$$

$$\left(b_1\right)_k \delta f_k + \left(b_2\right)_k \delta f_{k-1} + \left(b_3\right)_k \delta u_k + \left(b_4\right)_k \delta u_{k-1} + \left(b_5\right)_k \delta t_k + \left(b_6\right)_k \delta t_{k-1} = (r_3)_{k-1/2},$$

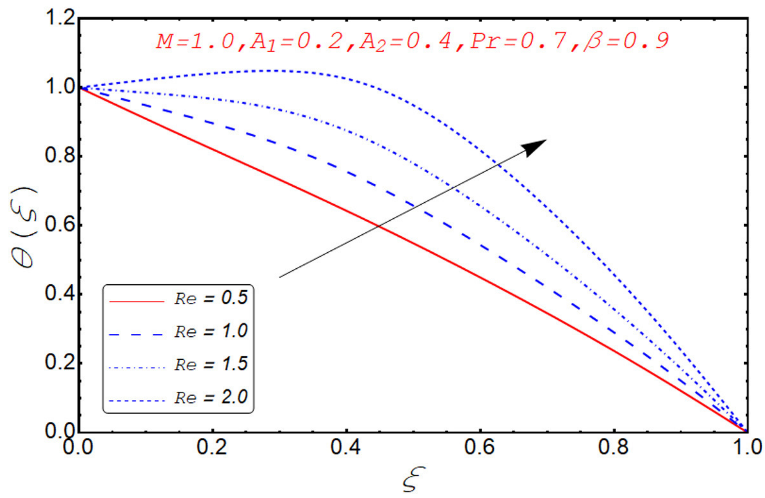

FIGURE 13 | Behavior of $\theta(\xi)$ for different *Re*.

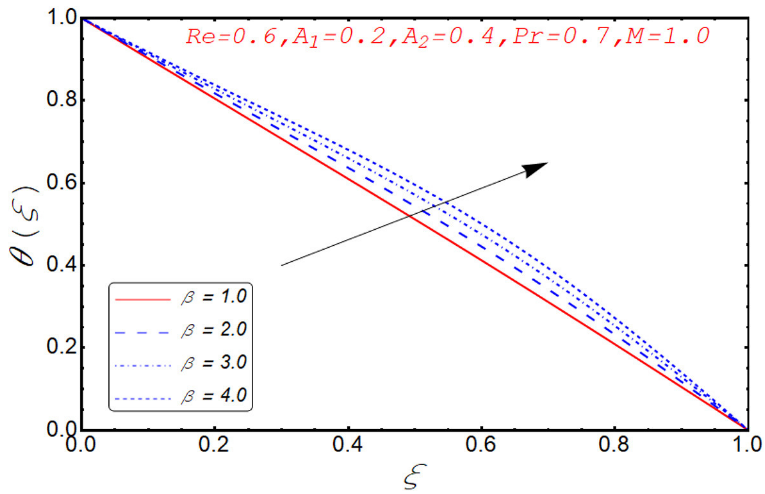

FIGURE 14 | Behavior of $\theta(\xi)$ for different β.

$$(c_1)_k\,\delta f_k + (c_2)_k\,\delta f_{k-1} + (c_3)_k\,\delta v_k + (c_4)_k\,\delta v_{k-1} + (c_5)_k\,\delta w_k + (c_6)_k\,\delta w_{k-1} + (c_7)_k\,\delta g_k + (c_8)_k\,\delta g_{k-1} + (c_7)_k\,\delta s_k + (c_8)_k\,\delta s_{k-1} = (r_4)_{k-1/2},$$

with boundary conditions are:

$$\delta f_o = 0, \delta u_o = A_1, \delta g_o = 1, \delta q_o = 1,$$
$$\delta f_k = 0, \delta u_k = A_2, \delta g_k = \tau, \delta q_k = 1,$$

where

$$(a_1)_k = (a_2)_k = hRe\left(s_{k-1/2}\right),$$
$$(a_3)_k = (a_4)_k = hRe\left(g_{k-1/2}\right),$$
$$(a_5)_k = (a_6)_k = hRe\left(u_{k-1/2} + \frac{1}{\beta} + M\right),$$
$$(a_7)_k = 1 + 2hRe\left(f_{k-1/2}\right),$$
$$(a_8)_k = -1 + 2hRe\left(f_{k-1/2}\right),$$
$$(b_1)_k = (b_2)_k = hRe\left(w_{k-1/2}\right),$$
$$(b_3)_k = (b_4)_k = hRe\left(M + \frac{1}{\beta}\right),$$
$$(b_5)_k = 1 + 2hRe\left(f_{k-1/2}\right),$$
$$(b_6)_k = -1 + 2hRe\left(f_{k-1/2}\right),$$
$$(b_7)_k = (b_8)_k = 2hRe\left(s_{k-1/2}\right),$$
$$(b_9)_k = (b_{10})_k = 2hRe\left(g_{k-1/2}\right),$$
$$(c_1)_k = (c_2)_k = 2hRePr\left(t_{k-1/2} - 2\lambda f_{k-1/2}\right),$$
$$(c_3)_k = (c_4)_k = 2hRePr\lambda\left(t_{k-1/2}\right)\left(f_{k-1/2}\right),$$
$$(c_5)_k = 1 + 2hRePr\Big(t_{k-1/2} - 2\lambda\left(f_{k-1/2}\right)^2$$

$$+\left(u_{k-1/2}\right)\left(f_{k-1/2}\right)\Big),$$

$$(c_6)_k = -1 + 2hRePr\Big(t_{k-1/2} - 2\lambda\left(f_{k-1/2}\right)^2 + \left(u_{k-1/2}\right)\left(f_{k-1/2}\right)\Big),$$

and

$$\begin{aligned}
(r_1)_k &= f_{k-1} - f_k + h\left(u_{k-1/2}\right),\\
(r_5)_k &= u_{k-1} - u_k + h\left(v_{k-1/2}\right),\\
(r_6)_k &= v_{k-1} - v_k + h\left(w_{k-1/2}\right),\\
(r_7)_k &= g_{k-1} - g_k + h\left(s_{k-1/2}\right),\\
(r_8)_k &= q_{k-1} - q_k + h\left(t_{k-1/2}\right),\\
(r_2)_k &= s_{k-1} - s_k + hRe\left(2u_{k-1/2}g_{k-1/2} - 2f_{k-\frac{1}{2}}s_{k-\frac{1}{2}} + \left(M + \frac{1}{\beta}\right)g_{k-1/2}\frac{1}{2}s_{k-\frac{1}{2}}\right),\\
(r_3)_k &= w_{k-1} - w_k + hRe\Big(2f_{k-1/2}w_{k-1/2} + 2g_{k-1/2}s_{k-1/2} - \left(M + \frac{1}{\beta}\right)v_{k-1/2}\Big),\\
(r_4)_k &= t_{k-1} - t_k + hRePr\Big(2f_{k-1/2}t_{k-1/2} - 4\lambda\left(f_{k-1/2}f_{k-1/2} + f_{k-1/2}u_{k-1/2}t_{k-1/2}\right)\Big).
\end{aligned}$$

Now, we consist the tridiagonal block matrices of given linearized equations in the form:

$$\mathbf{A}\delta = \mathbf{r} \tag{27}$$

where

$$\begin{pmatrix}
[A_1] & [C_1] & & & & \\
[B_1] & [A_2] & & & & \\
 & & [C_2] & \ddots & \ddots & \\
 & & \ddots & \ddots & \ddots & \\
 & & \ddots & \ddots & [B_{k-1}] & \\
 & & & & [A_{k-1}] & [C_{k-1}] \\
 & & & & [B_k] & [A_k]
\end{pmatrix}
\begin{pmatrix}[\delta_1]\\ [\delta_2]\\ \vdots \\ [\delta_{k-1}] \\ [\delta_k]\end{pmatrix}
=
\begin{pmatrix}[r_1]\\ [r_2]\\ \vdots \\ [r_{k-1}] \\ [r_k]\end{pmatrix} \tag{28}$$

In Equation (28), the elements are defined as:

$$[A_1] = \begin{pmatrix}
1 & 0 & 0 & 0 & 0 & 0 & 0 & 0\\
0 & 1 & 0 & 0 & 0 & 0 & 0 & 0\\
0 & 0 & 0 & 0 & 1 & 0 & 0 & 0\\
0 & 0 & 0 & 0 & 0 & 0 & 1 & 0\\
0 & -1 & -e_k & 0 & 0 & 0 & 0 & 0\\
0 & 0 & -1 & -e_k & 0 & 0 & 0 & 0\\
0 & 0 & 0 & 0 & -1 & -e_k & 0 & 0\\
0 & 0 & 0 & 0 & 0 & 0 & -1 & -e_k
\end{pmatrix}, e_k = \tfrac{1}{2}h_k$$

$$[\alpha_k] = \begin{pmatrix}
1 & -e_k & 0 & 0 & 0 & 0 & 0 & 0\\
(a_1)_k & 0 & (a_3)_k & (a_5)_k & (a_7)_k & (a_9)_k & 0 & 0\\
(b_1)_k & (b_3)_k & 0 & 0 & (b_5)_k & (b_7)_k & 0 & 0\\
(c_1)_k & (c_3)_k & 0 & 0 & 0 & 0 & 0 & (c_5)_k\\
0 & -1 & -e_k & 0 & 0 & 0 & 0 & 0\\
0 & 0 & -1 & -e_k & 0 & 0 & 0 & 0\\
0 & 0 & 0 & 0 & -1 & -e_k & 0 & 0\\
0 & 0 & 0 & 0 & 0 & 0 & -1 & -e_k
\end{pmatrix}, \quad 2 < k < K-1,$$

$$[\alpha_K] = \begin{pmatrix}
1 & -e_k & 0 & 0 & 0 & 0 & 0 & 0\\
(a_1)_k & 0 & (a_3)_k & (a_5)_k & (a_7)_k & (a_9)_k & 0 & 0\\
(b_1)_k & (b_3)_k & 0 & 0 & (b_5)_k & (b_7)_k & 0 & 0\\
(c_1)_k & (c_3)_k & 0 & 0 & 0 & 0 & 0 & (c_5)_k\\
1 & 0 & 0 & 0 & 0 & 0 & 0 & 0\\
0 & 1 & 0 & 0 & 0 & 0 & 0 & 0\\
0 & 0 & 0 & 0 & 1 & 0 & 0 & 0\\
0 & 0 & 0 & 0 & 0 & 0 & 1 & 0
\end{pmatrix},$$

$$[\beta_k] = \begin{pmatrix}
-1 & -e_k & 0 & 0 & 0 & 0 & 0 & 0\\
(a_2)_k & 0 & (a_4)_k & (a_6)_k & (a_8)_k & (a_{10})_k & 0 & 0\\
(b_2)_k & (b_4)_k & 0 & 0 & (b_6)_k & (b_8)_k & 0 & 0\\
(c_2)_k & (c_4)_k & 0 & 0 & 0 & 0 & 0 & (c_6)_k\\
0 & 0 & 0 & 0 & 0 & 0 & 0 & 0\\
0 & 0 & 0 & 0 & 0 & 0 & 0 & 0\\
0 & 0 & 0 & 0 & 0 & 0 & 0 & 0\\
0 & 0 & 0 & 0 & 0 & 0 & 0 & 0
\end{pmatrix}, \quad 2 < k < K$$

$$[C_k] = \begin{pmatrix}
0 & 0 & 0 & 0 & 0 & 0 & 0 & 0\\
0 & 0 & 0 & 0 & 0 & 0 & 0 & 0\\
0 & 0 & 0 & 0 & 0 & 0 & 0 & 0\\
0 & 0 & 0 & 0 & 0 & 0 & 0 & 0\\
0 & 1 & -e_k & 0 & 0 & 0 & 0 & 0\\
0 & 0 & 1 & -e_k & 0 & 0 & 0 & 0\\
0 & 0 & 0 & 0 & 1 & -e_k & 0 & 0\\
0 & 0 & 0 & 0 & 0 & 0 & 1 & -e_k
\end{pmatrix}, 1 < k < K-1,$$

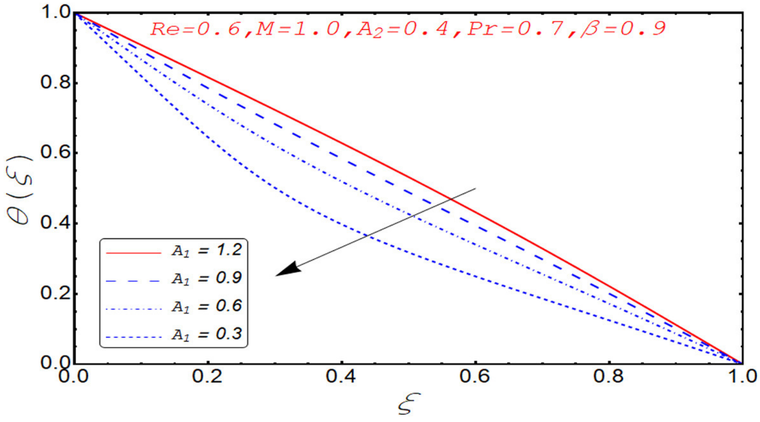

FIGURE 15 | Behavior of $\theta(\xi)$ for different A_1.

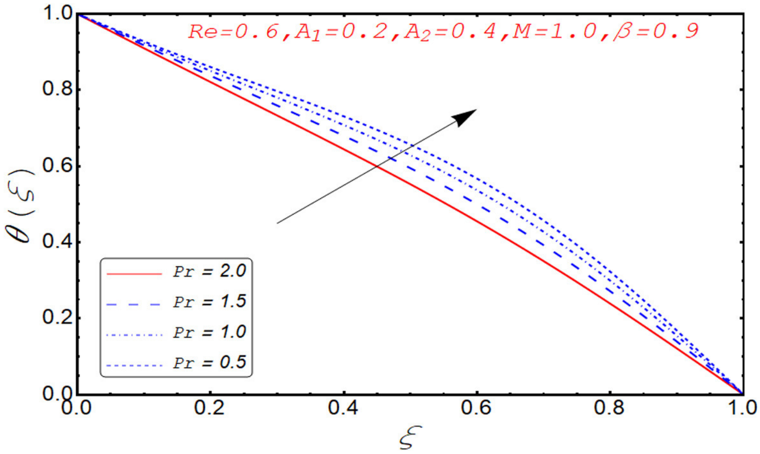

FIGURE 16 | Behavior of $\theta(\xi)$ for different Pr.

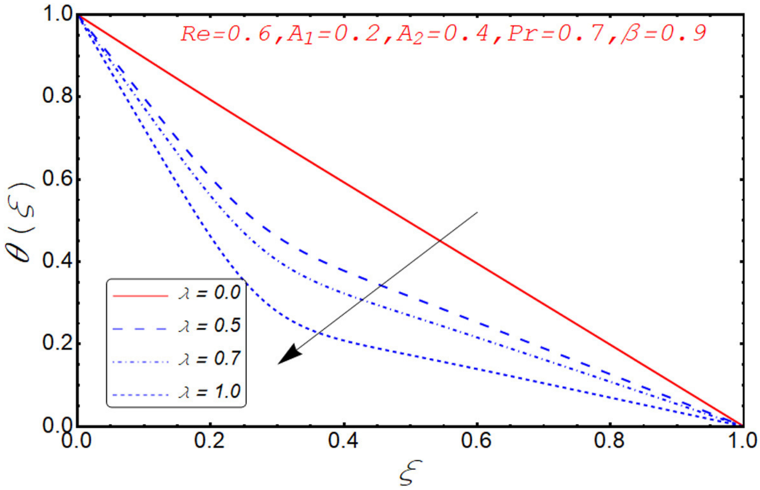

FIGURE 17 | Behavior of $\theta(\xi)$ for different λ.

$$[\delta_k] = \begin{pmatrix} \delta f_k \\ \delta u_k \\ \delta v_k \\ \delta w_k \\ \delta g_k \\ \delta s_k \\ \delta q_k \\ \delta t_k \end{pmatrix}, [r_k] = \begin{pmatrix} (r_1)_{k-(\frac{1}{2})} \\ (r_2)_{k-(\frac{1}{2})} \\ (r_3)_{k-(\frac{1}{2})} \\ (r_4)_{k-(\frac{1}{2})} \\ (r_5)_{k-(\frac{1}{2})} \\ (r_6)_{k-(\frac{1}{2})} \\ (r_7)_{k-(\frac{1}{2})} \\ (r_8)_{k-(\frac{1}{2})} \end{pmatrix}, 1 < k < K,$$

$$\mathbf{A} = \mathbf{LU}, \tag{29}$$

These computations are repeated until some convergence criteria are satisfied.

RESULTS AND DISCUSSION

Current segment is dedicated to elucidate the numerical and graphical impact of velocity parameters involved and temperature profile and coefficient of skin friction. Variation in axial velocity against Reynolds number is adorned in **Figure 3**. It is found that axial velocity at lower disk decays with increment in *Re*. The reason behind this fact is that *Re* has direct relation with inertial forces. Therefore, with increase of *Re*, inertial effects dominate and cause the velocity of lower disk to decelerate. **Figure 4** expresses the impact of *Re* on radial component of velocity. It is explored that with the increase of Re, velocity of lower disk diminishes and upper disk uplifts. It is seen from the picture that half of its portion from 0.0 to 0.6 represents velocity pattern of lower disk and from 0.6 to 1.0, it discloses radial velocity for upper plate. Impact of scaled stretching parameter on axial component of velocity at lower disk is exemplified in **Figure 5**. It is evidenced that with the increment of A_1, $f(\xi)$ mounts at lower disk because stretching rate is decreasing continuously. **Figure 6** is portrayed to manifest the variation in radial against A_1 velocity for lower and upper disks. It is found that radial component of velocity increases for the lower disk as compared to upper disk. This is due to the stretching rate of the lower disk that is continuously increasing and upper disk decrements. It is exhibited in **Figure 7** that $f'(\xi)$ decays with A_2 for lower disk and mounts in the case of upper disk. The justification behind this impact is that stretching rate of the upper disk is more than that of the lower disk. The behavior of axial velocity with stretching scaled parameter A_1 of upper disk is depicted in **Figure 8**. For larger values of A_2, the axial velocity of fluid decrements near the upper disk and upsurging behavior is noticed at the lower disk. By increasing A_2, velocity magnitude along radial direction in the vicinity of the upper disk increases, so velocity along axial direction as an outcome depreciates. The impact of *Re* on tangential component of velocity $g(\xi)$ is disclosed in **Figure 9**. It is fond that with increase of *Re*, $g(\xi)$ suppresses. By increasing *Re*, inertial forces increase so more velocity is induced by the inertial forces. Behavior of tangential velocity $g(\xi)$ against A_2 is stretched in **Figure 10**. It is found that $g(\xi)$ decrements and $f'(\xi)$ uplifts for A_2. With increase of A_2, stretching rate of the upper disk increases, and as an outcome, axial velocity increases and tangential velocity decreases. The variation in $g(\xi)$ with rotational parameter is revealed in **Figure 11**. Positive attribute in $g(\xi)$ is observed against τ. With the increase of rotational parameter τ, centrifugal force is induced, which as an outcome uplifts the tangential component of velocity. Curves investigating the aspects of β on tangential component of velocity are adorned in **Figure 12**. It is justified by the fact that momentum equation $\frac{1}{\beta}$ is a dimensionless parameter, so with the increase of β, momentum profile is tangential and its direction diminishes. Positive impact on thermal distribution against *Re* is observed in **Figure 13**. With increase of Re, viscous forces decrement and velocity of fluid particle increases. Thus, the temperature is defined as average motion of fluid molecules so thermal field molecules due to uplifts of movement of particles. The impact of $\theta(\xi)$ against β is anticipated and shown in **Figure 14**. Increase in thermal magnitude is observed if β is increased. Since increase in β raises the rotation of disks, by increasing the rotation of disk, more rotational motion in fluid is generated and as a consequence kinetic energy of fluid molecule increases. The increase in kinetic motion raises the temperature profile. Variation in thermal profile by varying A_1 in the range of $(0.0 \leq A_1 \leq 1.5)$ is revealed in **Figure 15**. It is observed that temperature of fluid boosts against the values of A_1. As we increase the A_1, the stretching rate increases, the fluid particles between disks exceeds, and hence temperature boosts up. The impact of Prandtl number *Pr* on $\theta(\xi)$ is exhibited in **Figure 16**. It is found that thermal distribution decreases with *Pr*. This is due to the fact that *Pr* is the ratio of viscous diffusion to thermal diffusion. Thus, by increasing *Pr*, thermal diffusion decreases so temperature decreases. **Figure 17** is adorned to study the impact of thermal relaxation parameter on thermal distribution. Declined attribute in temperature against thermal relaxation parameter λ is depicted. It is because of the fact that with the

TABLE 1 | Influence of skin friction coefficient at wall of upper and lower disks.

β	A_2	Re	A_1	τ	Cf_0	Cf_1
0.9					2.408192	2.408998
1	0.4	0.01	0.4	0.8	2.408139	2.409217
1.1					2.408104	2.409237
	0.5				2.607267	2.808388
0.9	0.6	0.01	0.4	0.8	2.806343	3.207760
	0.4				2.408201	2.418441
		0.1			2.40905	2.42920
0.9	0.4	0.2	0.4	0.8	2.409095	2.4292
		0.01			2.807079	2.608925
			0.5		3.2062	2.808669
0.1	0.5	0.2	0.6		2.401948	2.403120
			0.4		2.399815	2.401084
				0.7	2.399815	2.401084
0.1	0.5	0.2	0.4	0.9	2.399810	2.401089
				1	2.399560	2.401093

TABLE 2 | Comparison of $f''(0)$ and $g'(0)$ with Stewartson [4], Hayat et al. [24], and Hayat et al. [25] when $\phi = A1 = A2 = 0$ and $Re = 1$.

τ	$f''(0)$	$-g'(0)$	$f''(0)$	$-g'(0)$	$f''(0)$	$-g'(0)$	$f''(0)$	$-g'(0)$
	Stewartson [4]		**Hayat et al. [23]**		**Hayat et al. [25]**		**Present**	
−1	0.06666	2.00095	0.06666	2.00095	0.06666	2.00095	0.06666	2.00094
−0.8	0.08394	1.80259	0.08394	1.80259	0.08399	1.80259	0.08396	1.80257
−0.3	0.10395	1.30442	0.10395	1.30442	0.10395	1.30443	0.10395	1.30445
0	**0.09997**	**1.00428**	**0.09997**	**1.00428**	**0.09997**	**1.00428**	**0.09997**	**1.0043**
0.5	0.0663	0.50261	0.06663	0.50261	0.06667	0.50261	0.06668	0.50265

increase of λ, fluid particles will take more time to transfer heat to its neighboring particles, thus the temperature decreases.

Table 1 numerically discloses the influence of porosity parameter β, stretching parameters A_1 and A_2, and Reynolds number Re. The skin friction coefficient increases for greater value of Re and stretching parameters A_1 and A_2, whereas it decreases for increasing values of porosity parameter β and rotating parameter τ at the upper and lower disks. **Table 2** gives assurance of present work by constructing comparison with previously published literature for skin friction coefficient along radial and tangential components. Here, $\tau \geq 0$ shows the rotation of both disks in the same direction, $\tau \leq 0$ represents the direction of rotation of both disks in opposite direction, and $\tau = 0$ means upper disk is fixed.

CONCLUSIONS

Current exertion is devoted to analyze the impact of Cattaneo-Christov heat flux theory on fluid flow between the two parallel rotating disks. Equations are modeled in the form of partial differential equations and then transformed into ordinary differential expressions. These ODE (ordinary differential equations) are tackled by Keller-box scheme. The key findings are summarized as follows:

- At the lower disk, the radial and axial velocity profile increases for maximum value of $A1$ while the same effects at upper disk for greater A_2.
- For rotational and stretching parameters, the tangential velocity profile increases at disk with variation of parameters.
- Thermal effects are reduced for both thermal relaxation and Prandtl number.
- The skin friction coefficient at both disks is less for greater value of rotational parameter.

DATA AVAILABILITY STATEMENT

All datasets generated for this study are included in the article/supplementary material.

AUTHOR CONTRIBUTIONS

All authors listed have made a substantial, direct and intellectual contribution to the work, and approved it for publication.

ACKNOWLEDGMENTS

The authors extend their appreciation to the Deanship of Scientific Research at Majmaah University for funding this work under Project Number (RGP-2019-28).

REFERENCES

1. Karman TV. Uber laminare and turbulente Reibung. *Zeit Angew Math Mech.* (1921) **1**:233–52. doi: 10.1002/zamm.19210010401
2. Cochran WG. The flow due to a rotating disk. *Proc Cambridge Philos Soc.* (1934) **30**:365–75. doi: 10.1017/S0305004100012561
3. Batchelor GK. Note on a class of solutions of the Navier-Stokes equations representing steady rotationally symmetric flow. *The Quart J Mech App Maths.* (1951) **4**:29–41. doi: 10.1093/qjmam/4.1.29
4. Stewartson K. On the flow between two rotating coaxial disks. *Proc Combridge Philos Soc.* (1951) **49**:33–41.
5. Chapple PJ, Stokes VK. *On the Flow Between a Rotating and a Stationary Disk.* Department Mechanics Enginerring, Princeton University, Report No. FLD (1952). p. 8.
6. Mellor GL, Chapple PJ, Stokes VK. On the flow between a rotating and a stationary disk. *J Fluid Mech.* (1968) **31**:95–112. doi: 10.1017/S0022112068000054
7. Arora RC, Stokes VK. On the heat transfer between two rotating disks. *Int J Heat Mass Transf.* (1972) **15**:2119–32. doi: 10.1016/0017-9310(72)90036-1
8. Kumar SK, Tacher WI, Watson LT. Magnetohydrodynamic flow between a solid rotating disk and a porous stationary disk. *Appl Math Model.* (1989) **13**:494–500. doi: 10.1016/0307-904X(89)90098-X
9. Xun S, Zhao J, Zheng L, Chen X, Zhang X. Flow and heat transfer of Ostwald-de Waele fluid over a variable thickness rotating disk with index decreasing. *Int J Heat Mass Transf.* (2016) **103**:1214–24. doi: 10.1016/j.ijheatmasstransfer.2016.08.066
10. Das S, Maji SL, Guria M, Jana RN. Hall effects on unsteady MHD flow between two disks with non-coincident parallel axes of rotation. *Int J Appl Mech Eng.* (2010) **15**:5–18. doi: 10.1007/s40010-012-0049-1
11. Asgher S, Jalil M, Hussan, M, Turkyimazoglu M. Lie group analysis of flow and heat transfer over a stretching rotating disk. *Int J Heat Mass Transf.* (2014) **69**:140–6. doi: 10.1016/j.ijheatmasstransfer.2013.09.061

12. Elmaboud YA, Abdelsalam, SI, Mekheimer KS. Couple stress fluid flow in a rotating channel with peristalsis. *J Hyrdynamics*. (2018) **13**:307–16. doi: 10.1007/s42241-018-0037-2
13. Fourier JBJ. *Theorie Analytique De La Chaleur*. Paris: Chez Firmin Didot (1822).
14. Cattaneo C. Sulla conduzionedelcalore. In: *Atti del Seminario Maermatico e Fisico dell Universita di Modena e Reggio Emilia, Vol III*. (1948). p. **83**–101.
15. Christov CI. On frame indifferent formulation of the Maxwell–Cattaneo model of finite-speed heat conduction. *Mech Res Commun*. (2009) **36**:481–6. doi: 10.1016/j.mechrescom.2008.11.003
16. Straughan B. Thermal convection with the Cattaneo–Christov model. *Int J Heat Mass Transf*. (2010) **53**:95–8. doi: 10.1016/j.ijheatmasstransfer.2009.10.001
17. Ciarletta M, Straughan B. Uniqueness and structural stability for the Cattaneo–Christov equations. *Mech Res Commun*. (2010) **37**:445–7. doi: 10.1016/j.mechrescom.2010.06.002
18. Tibullo V, Zampoli V. A uniqueness result for the Cattaneo–Christov heat conduction model applied to incompressible fluids. *Mech Res Commun*. (2011) **38**:77–99. doi: 10.1016/j.mechrescom.2010.10.008
19. Aqsa, Malik M, Imtiaz A, Awais M. Rheology of Burgers' model with Cattaneo-Christov heat flux in the presence of heat source/sink and magnetic field. *Scientia Iranica*. (2019) **26**:323–30. doi: 10.24200/sci.2018.20165
20. Haddad SAM. Thermal instability in Brinkman porous media with Cattaneo–Christov heat flux. *Int J Heat Mass Transf*. (2014) **68**:659–68. doi: 10.1016/j.ijheatmasstransfer.2013.09.039
21. Mekheimer KS, Elmaboud YA. Simultaneous effects of variable viscosity and thermal conductivity on peristaltic flow in a vertical asymmetric channel. *Cand J Physc*. (2014) **92**:1541–55. doi: 10.1139/cjp-2013-0465
22. Mekheimer KS. Thermal properties of couple-stress fluid flow in an asymmetric channel with peristalsis. *J Heat Transf*. (2013) **135**:044502–1. doi: 10.1115/1.4023127
23. Hayat T, Qayyum S, Imtiaz M, Alsaedi A. Impact of Cattaneo-Christov heat flux in Jeffrey fluid flow with homogeneous-heterogeneous reactions. *PLoS ONE*. (2017) **6**:11201. doi: 10.1063/1.4942091
24. Hayat T, Khan MI, Farooq M, Alsaedi A, Waqas M, Yasmeen T. Impact of Cattaneo-Christov heat flux model in flow of variable thermal conductivity fluid over a variable thicked surface. *Int J Heat Mass Transf*. (2016) **66**:702–10. doi: 10.1016/j.ijheatmasstransfer.2016.04.016
25. Hayat T, Qayyum S, Imtiaz M, Alsaedi A. Flow between two stretchable rotating disks with Cattaneo-Christov heat flux model. *Results Phys*. (2017) **126**–33. doi: 10.1016/j.rinp.2016.12.007
26. Mustafa M. Cattaneo-Christov heat flux model for rotating flow and heat transfer of upper-convected Maxwell fluid. *AIP Adv*. (2015) **5**:047109. doi: 10.1063/1.4917306
27. Darcy H. *Les Fontaines Publiques de la Volle de Dijon*. Paris: Vector Dalmont (1856).
28. Khaled ARA, Vafai K. The role of porous media in modeling flow and heat transfer in biological tissues. *Int J Heat Mass Transf*. (2003) **46**:4989–5003. doi: 10.1016/S0017-9310(03)00301-6
29. Chen D, Mioshi H, Akai T, Yazawa Y. Colorless transparent fluorescence material: sintered porous glass containing rare-earth and transition-metal ions. *Appl Phys Lett*. (2005) **86**:231–8. doi: 10.1063/1.1946897
30. Muhammad T, Alsaedi A, Shahzad SA, Hayat T. A revised model for Darcy-Forchheimer flow of Maxwell nanofluid subject to convective boundary condition. *Chin J Phys*. (2017) **55**:963–76. doi: 10.1016/j.cjph.2017.03.006
31. Seddeek MA. Influence of viscous dissipation and thermophoresis on Darcy-Forchheimer mixed convection in a fluid saturated porous media. *J Colloids Interface Sci*. (2006) **293**:137–42. doi: 10.1016/j.jcis.2005.06.039
32. Jha BK, Kaurangini ML. Approximate analytical solutions for the non-linear Brinkman-Forchheimer-extended Darcy flow model. *Appl Math*. (2011) **21**:1432–6. doi: 10.4236/am.2011.212202
33. Aziz T, Mabood FM, Shahzad A. Travelling wave solutions for the unsteady flow of a third grade fluid induced due to impulsive motion of flat porous plate embedded in a porous medium. *J Mech*. (2017) **30**:527–35. doi: 10.1017/jmech.2014.17
34. Andersson HI. An exact solution of the Navier-Stokes equations for MHD flow. *Acta Mech*. (1995) **113**:241–4. doi: 10.1007/BF01212646
35. Liu IC. A note on heat and mass transfer for hydromagnetic flow over a stretching sheet. *Int Comm Heat Mass Transf*. (2005) **32**:1075–84. doi: 10.1016/j.icheatmasstransfer.2005.02.003
36. Kumaran V, Banerjee AK, Kumar AV, Vajravelu K. MHD flow past a stretching permeable sheet. *Appl Math Comp*. (2009) **210**:26–32. doi: 10.1016/j.amc.2008.10.025
37. Yirga Y, Tesfay D. Magnetohydrodynamic flow of viscous fluid over a non-linearly stretching sheet. *Open Access Library J*. (2014) **1**:1–11. doi: 10.4236/oalib.1101030
38. Yasin MHM, Ishak A, Pop I. MHD heat and mass transfer flow over a permeable stretching/shrinking sheet with radiation effect. *J Magnet Mag Mater*. (2016) **407**:235–40. doi: 10.1016/j.jmmm.2016.01.087
39. Mabood F, Khan WA, Ismail AIM. MHD flow over exponential radiating stretching sheet using homotopy analysis method. *J King Saud Univ*. (2017) **29**:68–74. doi: 10.1016/j.jksues.2014.06.001
40. Khalid A, Khan I, Khan A, Shafie S. Unsteady MHD free convection flow of Casson fluid past over an oscillating vertical plate embedded in a porous medium. *Eng Sci Tech Int J*. (2015) **18**:307–19. doi: 10.1016/j.jestch.2014.12.006
41. Abro KA, Khan I, Nisar KS. Novel technique of Atangana and Baleanu for heat dissipation in transmission line of electrical circuit. *Chaos Solit Fractals*. (2017) **129**:40–5. doi: 10.1016/j.chaos.2019.08.001
42. Saqib M, Ali F, Khan I, Sheikh NA, Aftab S, Jan SAA, et al. Exact solutions for free convection flow of generalized Jeffrey fluid: a Caputo-Fabrizio fractional model. *Alex Eng J*. (2017) **57**:1849–58. doi: 10.1016/j.aej.2017.03.017
43. Saqib M, Khan I, Shafie S. Natural convection channel flow of CMC-based CNTs nanofluid. *Europ Phys J Plus*. (2018) **133**:549. doi: 10.1140/epjp/i2018-12340-3
44. Keller HB, Cebeci T. Accurate numerical methods for boundary layer flows. II: two-dimensional turbulent flows. *AIAA J*. (1972) **10**:1193–9. doi: 10.2514/3.50349
45. Na TY. *Computational Methods in Engineering Boundary Value Problem*. Academic Press (1979).
46. Cebeci T, Bradshaw P. *Physical and Computational Aspects of Convective Heat Transfer*. Springer (1984). doi: 10.1007/978-3-662-02411-9

Conflict of Interest: The authors declare that the research was conducted in the absence of any commercial or financial relationships that could be construed as a potential conflict of interest.

Copyright © 2020 Bilal, Tassaddiq, Majeed, Nisar, Ali and Malik. This is an open-access article distributed under the terms of the Creative Commons Attribution License (CC BY). The use, distribution or reproduction in other forums is permitted, provided the original author(s) and the copyright owner(s) are credited and that the original publication in this journal is cited, in accordance with accepted academic practice. No use, distribution or reproduction is permitted which does not comply with these terms.

NOMENCLATURE

$(\hat{u},\hat{v},\hat{w})$	Dimensional velocity components	(f,g,h)	Dimensionless velocity components
C_p	Specific heat	C_{f1}	Local radial skin friction coefficient on the lower disk
C_{f2}	Local tangential skin friction coefficient on upper disk	Pr	Prandtl number
p	Fluid pressure	q	Heat flux
(r,φ,z)	Thermophoresis parameter	Re	Reynolds number
$\hat{T}_1$	Temperature in lower disk	$\hat{T}_2$	Temperature at the upper disk
Greek Symbols			
A_1,A_2	Scaled stretching parameters	ϵ	Pressure parameter
ζ	Dimensionless similarity variable	λ	Thermal conductivity
τ	Rotational number	β	Porosity
a_1,a_2	Stretching rate	θ	Dimensionless temperature
ρ	Fluid density	Ω_1,Ω_2	Angular velocity on the disks

frontiers in Physics

ORIGINAL RESEARCH
published: 15 January 2020
doi: 10.3389/fphy.2019.00219

Check for updates

A Numerical Simulation for Darcy-Forchheimer Flow of Nanofluid by a Rotating Disk With Partial Slip Effects

Malik Zaka Ullah[1]*, *Stefano Serra-Capizzano*[2,3] and *Dumitru Baleanu*[4,5]

[1] Department of Mathematics, Faculty of Science, King Abdulaziz University, Jeddah, Saudi Arabia, [2] Department of Science and High Technology, University of Insubria, Como, Italy, [3] Department of Information Technology, Uppsala University, Uppsala, Sweden, [4] Department of Mathematics, Cankaya University, Ankara, Turkey, [5] Institute of Space Sciences, Bucharest, Romania

This study examines Darcy-Forchheimer 3D nanoliquid flow caused by a rotating disk with heat generation/absorption. The impacts of Brownian motion and thermophoretic are considered. Velocity, concentration, and thermal slips at the surface of the rotating disk are considered. The change from the non-linear partial differential framework to the non-linear ordinary differential framework is accomplished by utilizing appropriate variables. A shooting technique is utilized to develop a numerical solution of the resulting framework. Graphs have been sketched to examine how the concentration and temperature fields are affected by several pertinent flow parameters. Skin friction and local Sherwood and Nusselt numbers are additionally plotted and analyzed. Furthermore, the concentration and temperature fields are enhanced for larger values of the thermophoresis parameter.

Keywords: rotating disk, Darcy-Forchheimer flow, nanoparticles, heat absorption/generation, slip conditions, numerical solution

OPEN ACCESS

Edited by:
Ahmed Zeeshan, International Islamic University, Islamabad, Pakistan

Reviewed by:
Nasir Shehzad, Govt. College Khayaban-E-Sir Syed, Pakistan
Mustafa Turkyilmazoglu, Hacettepe University, Turkey

***Correspondence:**
Malik Zaka Ullah
zmalek@kau.edu.sa

Specialty section:
This article was submitted to Mathematical Physics, a section of the journal Frontiers in Physics

Received: *01 November 2019*
Accepted: *28 November 2019*
Published: *15 January 2020*

Citation:
Ullah MZ, Serra-Capizzano S and Baleanu D (2020) A Numerical Simulation for Darcy-Forchheimer Flow of Nanofluid by a Rotating Disk With Partial Slip Effects. Front. Phys. 7:219. doi: 10.3389/fphy.2019.00219

1. INTRODUCTION

Flow due to a rotating disk plays an indispensable role in numerous modern items encompassing rotating machinery, apparatuses, rotors, and flywheels. As of late, rotating disks have become a significant component of many pieces of machinery, for example, thermal power-creation frameworks, rotor-stator turning circle reactors, electrical controls, stopping mechanisms, pivoting sawing machines, and rotational air cleaning systems. Close investigations of laminar boundary layer flow were carried out by Von Karman [1]. Turkyilmazoglu and Senel [2] examined the linked features of heat and mass exchange arising from the revolution of a hard and permeable disk. Entropy generation in slip flow by the turning of a permeable disk with MHD and variable properties was clarified by Rashidi et al. [3]. Nanofluid flow because of the revolution of a disk was explored by Turkyilmazoglu [4]. Hatami et al. [5] investigated the impacts of the contraction, turning, and heat of disks on the movement of nanofluids. They utilized a least-square strategy for solution development. Mustafa et al. [6] deciphered the three-dimensional rotating flow of nanofluids over a stationary disk. Sheikholeslami et al. [7] created numerical models of nanofluid splashing on a slanted turning disk. Transient thermophoretic molecule deposition through the constrained convective flow of micropolar liquid over a pivoting disk was examined by Doh and Muthtamilselvan [8]. Hayat et al. [9] discussed Darcy-Forchheimer flow of carbon nanotubes in response to a turning disk. Aziz et al. [10] gave a numerical report on nanofluid flow from the pivoting of a disk, looking at the impacts of slip and heat absorption/generation. Synthetically responsive flow of third-grade nanofluid over a stretchable turning disk with heat generation was broken down by Hayat et al. [11]. The radiative flow of a suspension of nanoparticles and gyrotactic microorganisms by the variably thick surface of a turning disk was clarified by Qayyum et al. [12]. Hayat et al. [13] presented a numerical simulation of the radiative flow of carbon nanotubes due to the revolution of a disk with partial slip.

The low thermal productivity of working fluids is a guideline problem for several heat transport components in engineering applications. For this reason, some researchers are making efforts to develop an innovative course for the improvement of the thermal efficiency of working fluids. Various measures have been proposed by experts to improve the thermal efficiency of fluids. Accordingly, the incorporation of nanomaterial into the working fluid, making what is termed a nanofluid, is extremely promising. Recent assessments of nanofluids reveal that working fluid has totally different features with the addition of nanomaterial. This is because the thermal efficiency of the working liquid is lower than that of the nanomaterial. Nanofluid is suspension of fluids containing standard fluid with the particles of nano-measure. Such nanomaterials are utilized in materials, MHD control generators, oil stores, cooling of nuclear reactors, vehicle transformers, and various others [14–18]. Choi and Eastman [19] coined the term nanofluid. They proposed that nanomaterials are a groundbreaking contender for the development of heat transport via the customary fluids. Buongiorno proposed a numerical model of convective transport by nanofluid [20]. Here, thermophoresis and Brownian motion are viewed as the most important slip mechanisms. Heat transfer increase by nanofluids in a two-sided top-driven heated square hole was considered by Tiwari and Das [21]. The significance of a CuO-water nanomaterial on the outside of heat exchangers was tentatively examined by Pantzali et al. [22]. Few ongoing studies on nanofluid flow can be found in the literature [23–45].

Motivated by the above-mentioned articles, the objective here is to examine the impacts of heat absorption/generation in Darcy-Forchheimer 3D nanofluid flow caused by a rotating disk and the impacts of slip. Both Brownian diffusion and thermophoretic phenomena occur in view of the existence of nanoparticles. Velocity, concentration, and thermal slips are accounted for. The obtained framework is solved numerically by the shooting technique. Concentration, temperature, skin friction, and local Sherwood and Nusselt numbers are also analyzed through plots.

2. MATHEMATICAL MODELING

Let us examine steady Darcy-Forchheimer 3D nanoliquid flow caused by a rotating disk with slip and heat absorption/generation. A disk at $z = 0$ rotates with constant angular velocity Ω (see **Figure 1**). The impacts of Brownian motion and thermophoretis are accounted for. The velocities are (u, v, w) in the directions of increase in (r, φ, z), respectively. The resulting boundary layer expressions are [45, 46]:

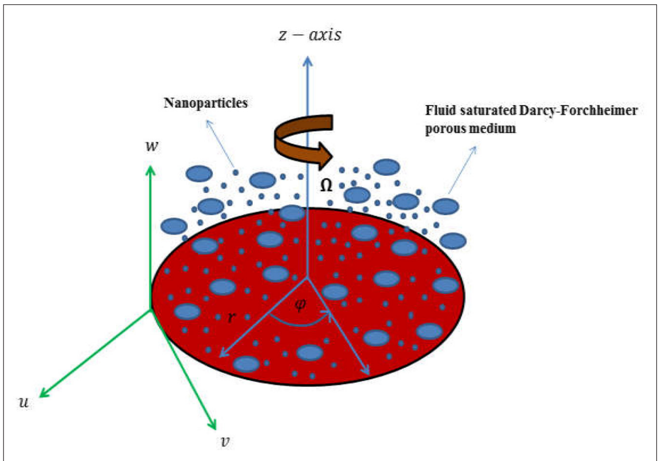

FIGURE 1 | Flow model and coordinate system.

$$\frac{\partial u}{\partial r} + \frac{u}{r} + \frac{\partial w}{\partial z} = 0, \tag{1}$$

$$u\frac{\partial u}{\partial r} - \frac{v^2}{r} + w\frac{\partial u}{\partial z} = \nu\left(\frac{\partial^2 u}{\partial z^2} + \frac{\partial^2 u}{\partial r^2} + \frac{1}{r}\frac{\partial u}{\partial r} - \frac{u}{r^2}\right) - \frac{\nu}{k^*}u - Fu^2, \tag{2}$$

$$u\frac{\partial v}{\partial r} + \frac{uv}{r} + w\frac{\partial v}{\partial z} = \nu\left(\frac{\partial^2 v}{\partial z^2} + \frac{\partial^2 v}{\partial r^2} + \frac{1}{r}\frac{\partial v}{\partial r} - \frac{v}{r^2}\right) - \frac{\nu}{k^*}v - Fv^2, \tag{3}$$

$$u\frac{\partial w}{\partial r} + w\frac{\partial w}{\partial z} = \nu\left(\frac{\partial^2 w}{\partial z^2} + \frac{\partial^2 w}{\partial r^2} + \frac{1}{r}\frac{\partial w}{\partial r}\right) - \frac{\nu}{k^*}w - Fw^2, \tag{4}$$

$$\begin{aligned} u\frac{\partial T}{\partial r} + w\frac{\partial T}{\partial z} &= \alpha^*\left(\frac{\partial^2 T}{\partial z^2} + \frac{\partial^2 T}{\partial r^2} + \frac{1}{r}\frac{\partial T}{\partial r}\right) + \frac{Q}{(\rho c)_f}(T - T_\infty) \\ &+ \frac{(\rho c)_p}{(\rho c)_f}\left(D_B\left(\frac{\partial T}{\partial r}\frac{\partial C}{\partial r} + \frac{\partial T}{\partial z}\frac{\partial C}{\partial z}\right)\right. \\ &\left.+ \frac{D_T}{T_\infty}\left(\left(\frac{\partial T}{\partial z}\right)^2 + \left(\frac{\partial T}{\partial r}\right)^2\right)\right), \end{aligned} \tag{5}$$

$$\begin{aligned} u\frac{\partial C}{\partial r} + w\frac{\partial C}{\partial z} &= D_B\left(\frac{\partial^2 C}{\partial z^2} + \frac{\partial^2 C}{\partial r^2} + \frac{1}{r}\frac{\partial C}{\partial r}\right) \\ &+ \frac{D_T}{T_\infty}\left(\frac{\partial^2 T}{\partial z^2} + \frac{\partial^2 T}{\partial r^2} + \frac{1}{r}\frac{\partial T}{\partial r}\right). \end{aligned} \tag{6}$$

It is subject to the boundary conditions [10] :

$$u = L_1\frac{\partial u}{\partial z},\ v = r\Omega + L_1\frac{\partial v}{\partial z},\ w = 0,\ T = T_w + L_2\frac{\partial T}{\partial z},$$

$$C = C_w + L_3 \frac{\partial C}{\partial z} \text{ at } z = 0, \quad (7)$$

$$u \to 0, \quad v \to 0, \quad T \to T_\infty, \quad C \to C_\infty \quad \text{as } z \to \infty. \quad (8)$$

Here u, v, and w represent the velocity components in the directions r, φ, and z while ρ_f, μ and, $\nu \left(= \mu/\rho_f\right)$ depict the fluid density, dynamic, and kinematic viscosities respectively, C_b the drag factor, L_1 the velocity slip factor, L_2 the thermal slip factor $(\rho c)_p$, the effective heat capacity of nanoparticles, T the fluid temperature, k^* the permeability of porous space, C the concentration $(\rho c)_f$, the heat capacity of the liquid, L_3 the concentration slip factor, C_∞ the ambient concentration, D_T the thermophoretic factor, $F = C_b/rk^{*1/2}$ the non-uniform inertia factor, k and $\alpha^* = k/(\rho c)_f$ the thermal conductivity and thermal diffusivity, respectively, D_B the Brownian factor, Q the heat generation/absorption factor and T_∞ the ambient temperature. Selecting [10]:

$$\left.\begin{array}{l} u = r\Omega f'(\zeta),\ w = -(2\Omega\nu)^{1/2} f(\zeta),\ v = r\Omega g(\zeta), \\ \phi(\zeta) = \frac{C-C_\infty}{C_w-C_\infty},\ \zeta = \left(\frac{2\Omega}{\nu}\right)^{1/2} z,\ \theta(\zeta) = \frac{T-T_\infty}{T_w-T_\infty}. \end{array}\right\} \quad (9)$$

Continuity Equation (1) is trivially verified, while Equations (2)–(8) yield

$$2f''' + 2ff'' - f'^2 + g^2 - \lambda f' - Frf'^2 = 0, \quad (10)$$

$$2g'' + 2fg' - 2f'g - \lambda g - Frg^2 = 0, \quad (11)$$

$$\frac{1}{\Pr}\theta'' + f\theta' + N_b\theta'\phi' + N_t\theta'^2 + \delta\theta = 0, \quad (12)$$

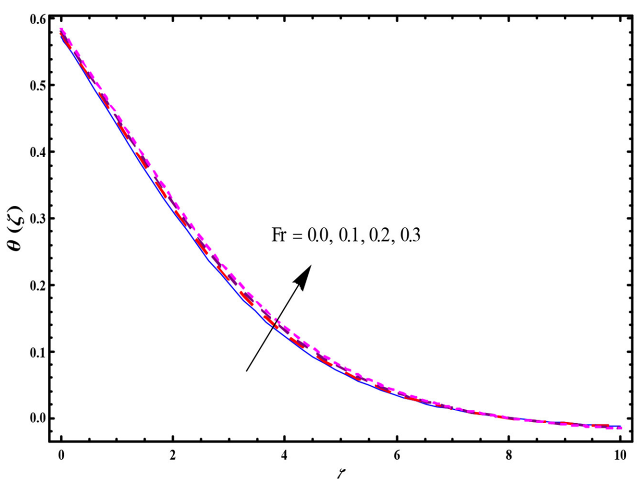

FIGURE 2 | Variations of $\theta(\zeta)$ for Fr.

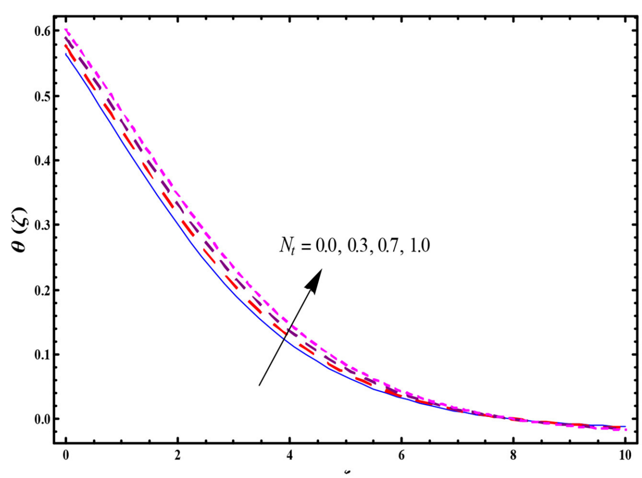

FIGURE 4 | Variations of $\theta(\zeta)$ for N_t.

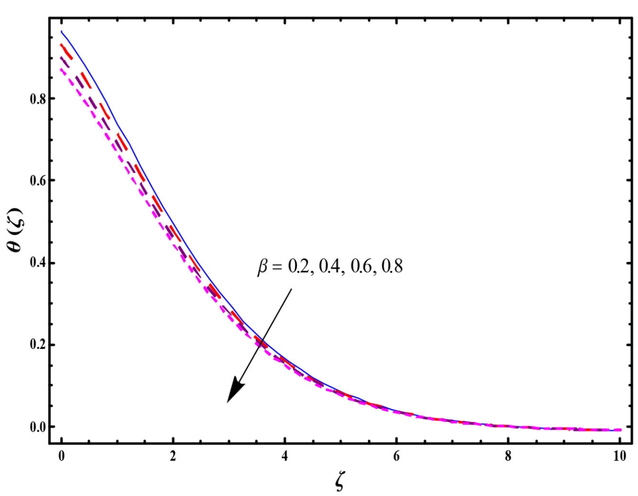

FIGURE 3 | Variations of $\theta(\zeta)$ for β.

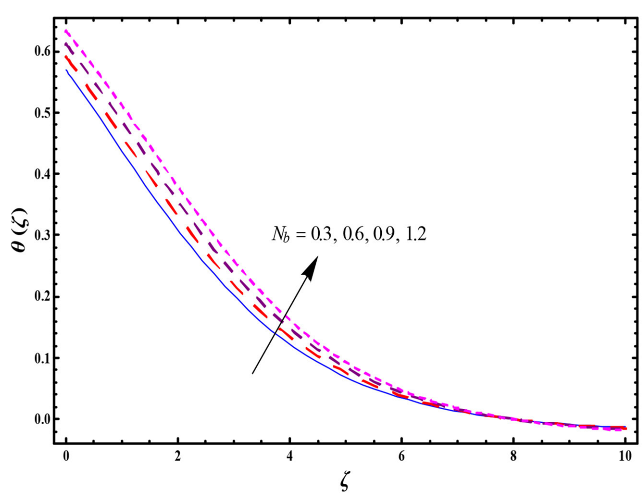

FIGURE 5 | Variations of $\theta(\zeta)$ for N_b.

$$\frac{1}{Sc}\phi'' + f\phi' + \frac{1}{Sc}\frac{N_t}{N_b}\theta'' = 0, \quad (13)$$

$$f(0) = 0,\ f'(0) = \alpha f''(0),\ g(0) = 1 + \alpha g'(0),$$
$$\theta(0) = 1 + \beta\theta'(0),\ \phi(0) = 1 + \gamma\phi'(0), \quad (14)$$

$$f'(\infty) \to 0,\ g(\infty) \to 0,\ \theta(\infty) \to 0,\ \phi(\infty) \to 0. \quad (15)$$

Here, Fr stands for the Forchheimer number, α for the velocity slip parameter, λ for the porosity parameter, N_t for the thermophoresis parameter, β for the thermal slip parameter, Pr for the Prandtl number, N_b for Brownian motion, δ for the heat absorption/generation parameter, γ for the concentration slip parameter, and Sc for the Schmidt number. Non-dimensional variables are defined by

$$\left.\begin{array}{c} \lambda = \frac{\nu}{k^*\Omega},\ \alpha = L_1\sqrt{\frac{2\Omega}{\nu}},\ Fr = \frac{C_b}{k^{*1/2}},\ N_b = \frac{(\rho c)_p D_B (C_w - C_\infty)}{(\rho c)_f \nu}, \\ \delta = \frac{Q}{2\Omega(\rho c)_f}, \\ \beta = L_2\sqrt{\frac{2\Omega}{\nu}},\ \Pr = \frac{\nu}{\alpha^*},\ N_t = \frac{(\rho c)_p D_T (T_w - T_\infty)}{(\rho c)_f \nu T_\infty},\ \gamma = L_3\sqrt{\frac{2\Omega}{\nu}}, \\ Sc = \frac{\nu}{D_B}. \end{array}\right\} \quad (16)$$

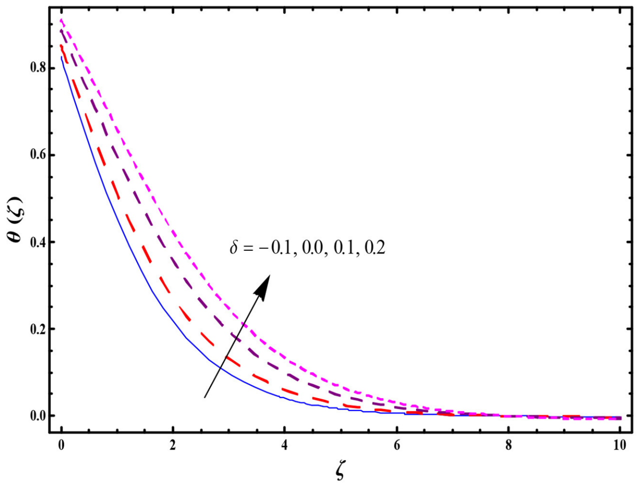

FIGURE 6 | Variations of $\theta(\zeta)$ for δ.

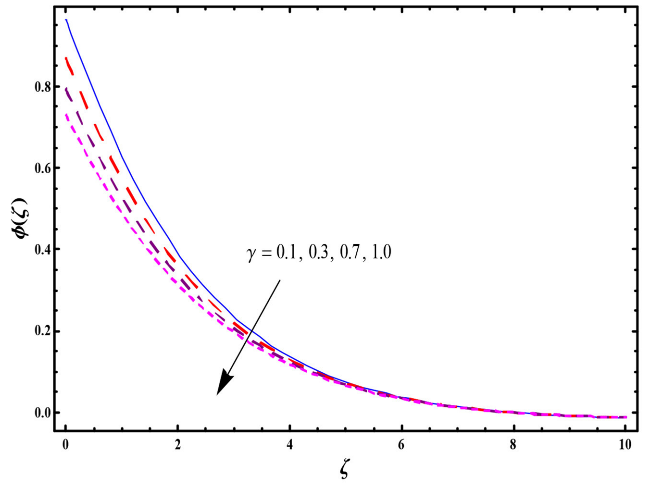

FIGURE 8 | Variations of $\phi(\zeta)$ for γ.

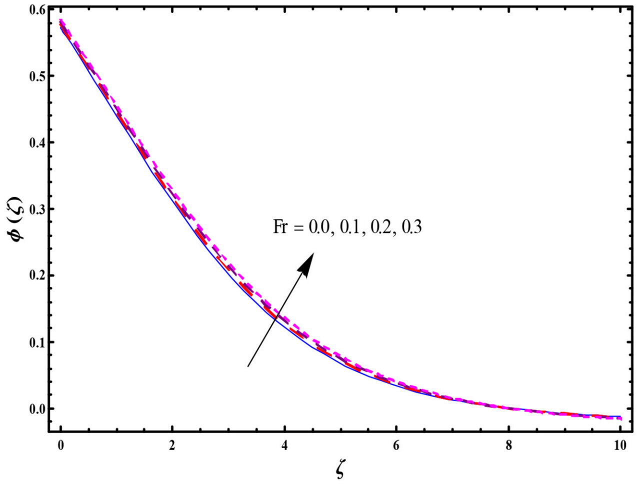

FIGURE 7 | Variations of $\phi(\zeta)$ for Fr.

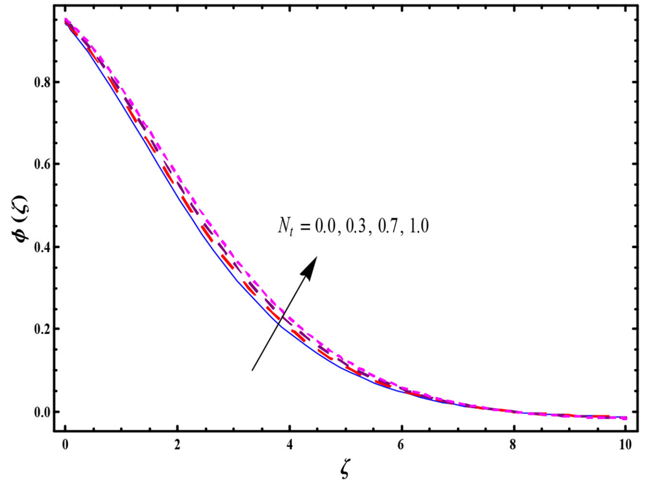

FIGURE 9 | Variations of $\phi(\zeta)$ for N_t.

The coefficients of skin friction and the Nusselt and Sherwood numbers are

$$Re_r^{1/2}C_f = f''(0),\ Re_r^{1/2}C_g = g'(0),\ Re_r^{-1/2}Nu = -\theta'(0),$$
$$Re_r^{-1/2}Sh = -\phi'(0), \tag{17}$$

where $Re_r = 2(\Omega r)r/\nu$ represents the local rotational Reynolds number.

3. NUMERICAL RESULTS AND DISCUSSION

This section depicts the contributions of various physical variables like thermophoresis parameter N_t, Forchheimer number Fr, thermal slip parameter β, heat generation/absorption parameter δ, Brownian number N_b, and concentration slip number γ on The concentration $\phi(\zeta)$ and temperature $\theta(\zeta)$ distributions. The effect of Forchheimer variable Fr on $\theta(\zeta)$ is portrayed in **Figure 2**. A larger value for Fr shows expanding behavior of $\theta(\zeta)$ and the related thermal layer. **Figure 3** shows the impact of thermal slip β on temperature $\theta(\zeta)$. Temperature is reduced by increasing thermal slip β. **Figure 4** demonstrates the effect of N_t on the temperature field $\theta(\zeta)$. A larger thermophoresis parameter N_t value leads to a higher temperature field and thicker dynamically warm layer. The reason for this conflict is that growth in N_t yields high grounded thermophoresis control, which further allows movement of the nanoparticles in the fluid zone. A long way from the surface, a more grounded temperature scattering $\theta(\zeta)$ and continuously warm layer is thus created. The impact of N_b on the temperature profile $\theta(\zeta)$ is portrayed in **Figure 5**. Physically, the irregularity of nanoparticle movement increases by enhancing Brownian motion, due to which collision of particles occurs. Thus, kinetic energy is converted into heat energy, which produces an increase in the temperature field. **Figure 6** shows how heat generation/absorption δ influences

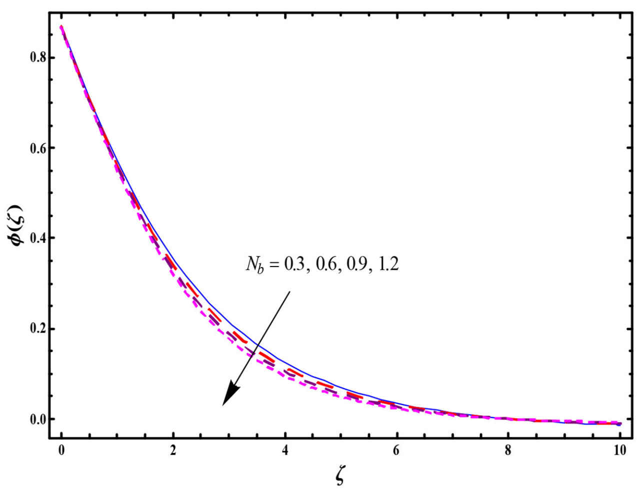

FIGURE 10 | Variations of $\phi(\zeta)$ for N_b.

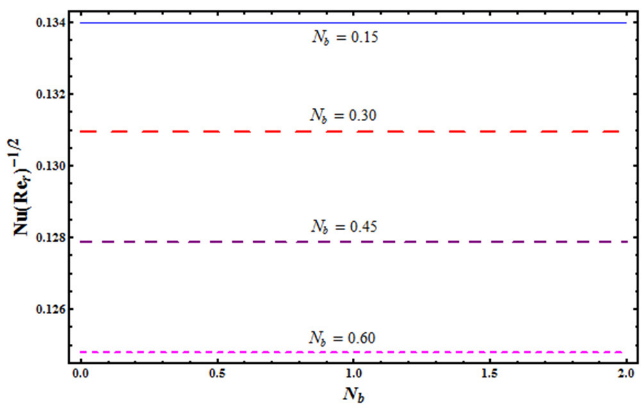

FIGURE 12 | Variations of $Nu(Re_r)^{-1/2}$ for N_b.

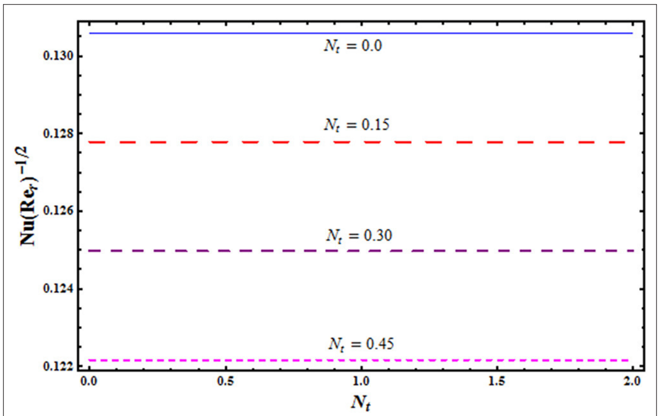

FIGURE 11 | Variations of $Nu(Re_r)^{-1/2}$ for N_t.

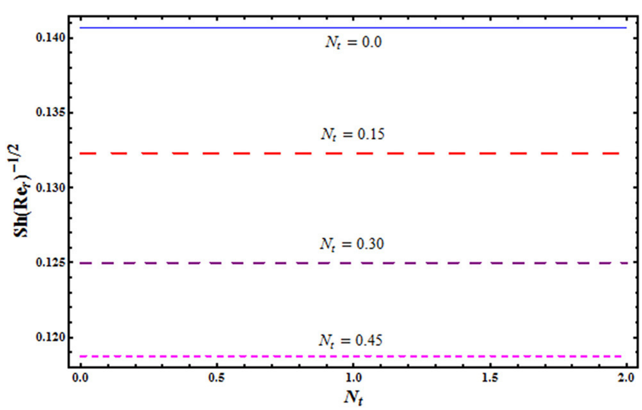

FIGURE 13 | Variations of $Sh(Re_r)^{-1/2}$ for N_t.

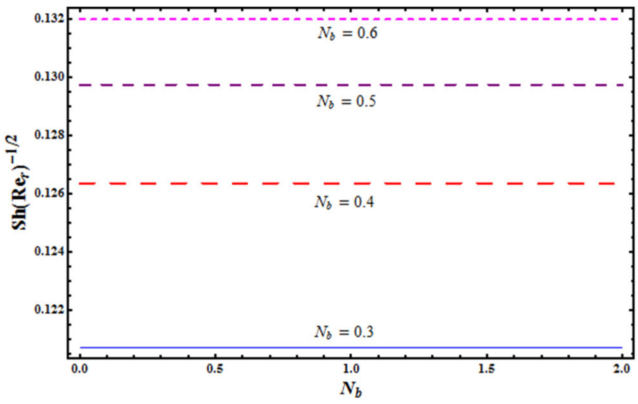

FIGURE 14 | Variations of $Sh(Re_r)^{-1/2}$ for N_b.

TABLE 1 | Comparative values of $f''(0)$ and $g'(0)$ for value of Fr when $\lambda = 0.2$ and $\alpha = 0$.

	Present results		Naqvi et al. [45]	
Fr	$f''(0)$	$g'(0)$	$f''(0)$	$g'(0)$
0.2	0.43478	−0.78139	0.4347813	−0.7813904

temperature dispersion $\theta(\zeta)$. Here, $\delta > 0$ portrays heat generation and $\delta < 0$ for heat absorption. Both temperature $\theta(\zeta)$ and the warm layer are upgraded with increasing δ. **Figure 7** shows that concentration $\phi(\zeta)$ is higher for larger values of the Forchheimer variable Fr. **Figure 8** shows how concentration $\phi(\zeta)$ is influenced by concentration slip γ. Concentration is reduced at higher estimations of γ. **Figure 9** demonstrates how the thermophoresis parameter N_t influences the concentration $\phi(\zeta)$. By improving thermophoresis parameter N_t, the concentration $\phi(\zeta)$ is increased. **Figure 10** depicts the impact of Brownian motion N_b on concentration $\phi(\zeta)$. It has been noted that a stronger concentration $\phi(\zeta)$ is developed by utilizing greater N_b. **Figures S1**, **S2** display the impacts of Fr on $C_f Re_r^{1/2}$ and $C_g Re_r^{1/2}$, respectively. It is noted that $C_f Re_r^{1/2}$ is a decaying function of Fr, while the reverse situation is observed for $C_g Re_r^{1/2}$. The effects of N_t and N_b on $Nu(Re_r)^{-1/2}$ are highlighted in **Figures 11**, **12**, respectively. Here, $Nu(Re_r)^{-1/2}$ reduces for N_t and N_b. The effects of N_t and N_b on $Sh(Re_r)^{-1/2}$ are portrayed in **Figures 13**, **14**, respectively. Here, $Sh(Re_r)^{-1/2}$ is an increasing factor of N_t, while the opposite trend is seen for N_b. The figures in **Table 1** were computed to validate the present results with previously published results in a limiting sense. Here, we see that the present numerical solution is in good agreement with the previous solution by Naqvi et al. [45] in a limiting sense.

4. CONCLUSIONS

In this paper, Darcy-Forchheimer 3D nanofluid flow caused by a rotating disk with heat generation/absorption is studied. Brownian motion and thermophoretic phenomena occur with the existence of nanoparticles. Velocity, concentration, and thermal slips are accounted for. A higher Forchheimer number Fr depicts similar behavior for concentration and temperature. A larger β corresponds to a lower temperature field. Higher γ depicts decreasing behavior for the concentration field. A stronger temperature field is observed for N_b and N_t. Concentration $\phi(\zeta)$ displays the reverse behavior for N_b and N_t.

DATA AVAILABILITY STATEMENT

The datasets generated for this study are available on request to the corresponding author.

AUTHOR CONTRIBUTIONS

All authors listed have made a substantial, direct and intellectual contribution to the work, and approved it for publication.

ACKNOWLEDGMENTS

This project was funded by the Deanship of Scientific Research (DSR), King Abdulaziz University, Jeddah, Saudi Arabia under grant no. KEP-16-130-40. The authors, therefore, acknowledge with thanks DSR technical and financial support.

SUPPLEMENTARY MATERIAL

The Supplementary Material for this article can be found online at: https://www.frontiersin.org/articles/10.3389/fphy.2019.00219/full#supplementary-material

Figure S1 | Variations of $C_f Re_r^{1/2}$ for Fr.

Figure S2 | Variations of $CgRe_r^{1/2}$ for Fr.

REFERENCES

1. Von Karman T. Uber laminare and turbulente Reibung. *Z Angew Math Mech.* (1921) **1**:233–52. doi: 10.1002/zamm.19210010401
2. Turkyilmazoglu M, Senel P. Heat and mass transfer of the flow due to a rotating rough and porous disk. *Int J Therm Sci.* (2013) **63**:146–58. doi: 10.1016/j.ijthermalsci.2012.07.013
3. Rashidi MM, Kavyani N, Abelman S. Investigation of entropy generation in MHD and slip flow over rotating porous disk with variable properties. *Int J Heat Mass Transf.* (2014) **70**:892–917. doi: 10.1016/j.ijheatmasstransfer.2013.11.058
4. Turkyilmazoglu M. Nanofluid flow and heat transfer due to a rotating disk. *Comput Fluids.* (2014) **94**:139–46. doi: 10.1016/j.compfluid.2014.02.009
5. Hatami M, Sheikholeslami M, Gangi DD. Laminar flow and heat transfer of nanofluids between contracting and rotating disks by least square method. *Powder Technol.* (2014) **253**:769–79. doi: 10.1016/j.powtec.2013.12.053
6. Mustafa M, Khan JA, Hayat T, Alsaedi A. On Bödewadt flow and heat transfer of nanofluids over a stretching stationary disk. *J Mol Liquid.* (2015) **211**:119–25. doi: 10.1016/j.molliq.2015.06.065

7. Sheikholeslami M, Hatami M, Ganji DD. Numerical investigation of nanofluid spraying on an inclined rotating disk for cooling process. *J Mol Liquid.* (2015) **211**:577–83. doi: 10.1016/j.molliq.2015.07.006
8. Doh DH, Muthtamilselvan M. Thermophoretic particle deposition on magnetohydrodynamic flow of micropolar fluid due to a rotating disk. *Int J Mech Sci*. (2017) **130**:350–9. doi: 10.1016/j.ijmecsci.2017.06.029
9. Hayat T, Haider F, Muhammad T, Alsaedi A. On Darcy-Forchheimer flow of carbon nanotubes due to a rotating disk. *Int J Heat Mass Transf.* (2017) **112**:248–54. doi: 10.1016/j.ijheatmasstransfer.2017.04.123
10. Aziz A, Alsaedi A, Muhammad T, Hayat T. Numerical study for heat generation/absorption in flow of nanofluid by a rotating disk. *Results Phys*. (2018) **8**:785–92. doi: 10.1016/j.rinp.2018.01.009
11. Hayat T, Ahmad S, Khan MI, Alsaedi A. Modeling and analyzing flow of third grade nanofluid due to rotating stretchable disk with chemical reaction and heat source. *Phys B*. (2018) **537**:116–26. doi: 10.1016/j.physb.2018.01.052
12. Qayyum S, Imtiaz M, Alsaedi A, Hayat T. Analysis of radiation in a suspension of nanoparticles and gyrotactic microorganism for rotating disk of variable thickness. *Chin J Phys*. (2018) **56**:2404–23. doi: 10.1016/j.cjph.2018.06.020
13. Hayat T, Khalid H, Waqas M, Alsaedi A. Numerical simulation for radiative flow of nanoliquid by rotating disk with carbon nanotubes and partial slip. *Comput Methods Appl Mech Eng.* (2018) **341**:397–408. doi: 10.1016/j.cma.2018.06.018
14. Mabood F, Ibrahim SM, Lorenzini G. Chemical reaction effects on MHD rotating fluid over a vertical plate embedded in porous medium with heat source. *J Eng Thermophys.* (2017) **26**:399–415. doi: 10.1134/S1810232817030109
15. Mabood F, Lorenzini G, Pochai N, Shateyi S. Homotopy analysis method for radiation and hydrodynamic-thermal slips effects on MHD flow and heat transfer impinging on stretching sheet. *Defect Diffusion Forum*. (2018) **388**:317–27. doi: 10.4028/www.scientific.net/DDF.388.317
16. Mabood F, Das K. Outlining the impact of melting on MHD Casson fluid flow past a stretching sheet in a porous medium with radiation. *Heliyon.* (2019) **5**:e01216. doi: 10.1016/j.heliyon.2019.e01216
17. Mabood F, Nayak MK, Chamkha AJ. Heat transfer on the cross flow of micropolar fluids over a thin needle moving in a parallel stream influenced by binary chemical reaction and Arrhenius activation energy. *Eur Phys J Plus*. (2019) **134**:427. doi: 10.1140/epjp/i2019-12716-9
18. Imtiaz M, Mabood F, Hayat T, Alsaedi A. Homogeneous-heterogeneous reactions in MHD radiative flow of second grade fluid due to a curved stretching surface. *Int J Heat Mass Transf.* (2019) **145**:118781. doi: 10.1016/j.ijheatmasstransfer.2019.118781
19. Choi SUS, Eastman JA. Enhancing thermal conductivity of fluids with nanoparticles. *ASME Int Mech Eng Cong Exp*. (1995) **66**:99–105.
20. Buongiorno J. Convective transport in nanofluids. *ASME J Heat Transf.* (2006) **128**:240–50. doi: 10.1115/1.2150834
21. Tiwari RK, Das MK. Heat transfer augmentation in a two-sided lid-driven differentially heated square cavity utilizing nanofluid. *Int J Heat Mass Transf*. (2007) **50**:2002–18. doi: 10.1016/j.ijheatmasstransfer.2006.09.034
22. Pantzali MN, Mouza AA, Paras SV. Investigating the efficacy of nanofluids as coolants in plate heat exchangers (PHE). *Chem Eng Sci.* (2009) **64**:3290–300. doi: 10.1016/j.ces.2009.04.004
23. Sheikholeslami M, Bandpy MG, Ganji DD, Soleimani S. Effect of a magnetic field on natural convection in an inclined half-anulus enclosure filled with Cu-water nanofluid using CVFEM. *Adv Powder Technol*. (2013) **24**:980–91. doi: 10.1016/j.apt.2013.01.012
24. Togun H, Safaei MR, Sadri R, Kazi SN, Badarudin A, Hooman K, et al. Numerical simulation of laminar to turbulent nanofluid flow and heat transfer over a backward-facing step. *Appl Math Comput.* (2014) **239**:153–70. doi: 10.1016/j.amc.2014.04.051
25. Hayat T, Aziz A, Muhammad T, Ahmad B. Influence of magnetic field in three-dimensional flow of couple stress nanofluid over a nonlinearly stretching surface with convective condition. *PLoS ONE*. (2015) **10**:e0145332. doi: 10.1371/journal.pone.0145332
26. Lin Y, Zheng L, Zhang X, Ma L, Chen G. MHD pseudo-plastic nanofluid unsteady flow and heat transfer in a finite thin film over stretching surface with internal heat generation. *Int J Heat Mass Transf.* (2015) **84**:903–11. doi: 10.1016/j.ijheatmasstransfer.2015.01.099
27. Hayat T, Muhammad T, Alsaedi A, Alhuthali MS. Magnetohydrodynamic three-dimensional flow of viscoelastic nanofluid in the presence of nonlinear thermal radiation. *J Magn Mater*. (2015) **385**: 222–9. doi: 10.1016/j.jmmm.2015.02.046
28. Gireesha BJ, Mahanthesh B, Shivakumara IS Eshwarappa KM. Melting heat transfer in boundary layer stagnation-point flow of nanofluid toward a stretching sheet with induced magnetic field. *Int J Eng Sci Technol.* (2016) **19**:313–21. doi: 10.1016/j.jestch.2015.07.012
29. Hayat T, Aziz A, Muhammad T, Alsaedi A. On magnetohydrodynamic three-dimensional flow of nanofluid over a convectively heated nonlinear stretching surface. *Int J Heat Mass Transf.* (2016) **100**:566–72. doi: 10.1016/j.ijheatmasstransfer.2016.04.113
30. Goshayeshi HR, Safaei MR, Goodarzi M, Dahari M. Particle size and type effects on heat transfer enhancement of Ferro-nanofluids in a pulsating heat pipe. *Powder Technol.* (2016) **301**:1218–26. doi: 10.1016/j.powtec.2016.08.007
31. Eid MR, Alsaedi A, Muhammad T, Hayat T. Comprehensive analysis of heat transfer of gold-blood nanofluid (Sisko-model) with thermal radiation. *Results Phys.* (2017) **7**:4388–93. doi: 10.1016/j.rinp.2017.11.004
32. Hayat T, Muhammad T, Shehzad SA, Alsaedi A. An analytical solution for magnetohydrodynamic Oldroyd-B nanofluid flow induced by a stretching sheet with heat generation/absorption. *Int J Therm Sci*. (2017) **111**:274–88. doi: 10.1016/j.ijthermalsci.2016.08.009
33. Hayat T, Sajjad R, Muhammad T, Alsaedi A, Ellahi R. On MHD nonlinear stretching flow of Powell-Eyring nanomaterial. *Results Phys.* (2017) **7**:535–43. doi: 10.1016/j.rinp.2016.12.039
34. Bhatti MM, Zeeshan A, Ellahi R. Simultaneous effects of coagulation and variable magnetic field on peristaltically induced motion of Jeffrey nanofluid containing gyrotactic microorganism. *Microvasc Res.* (2017) **110**:32–42. doi: 10.1016/j.mvr.2016.11.007
35. Muhammad T, Alsaedi A, Shehzad SA, Hayat T. A revised model for Darcy-Forchheimer flow of Maxwell nanofluid subject to convective boundary condition. *Chinese J Phys*. (2017) **55**:963–76. doi: 10.1016/j.cjph.2017.03.006
36. Muhammad T, Alsaedi A, Hayat T, Shehzad SA. A revised model for Darcy-Forchheimer three-dimensional flow of nanofluid subject to convective boundary condition. *Results Phys*. (2017) **7**:2791–7. doi: 10.1016/j.rinp.2017.07.052
37. Muhammad T, Lu DC, Mahanthesh B, Eid MR, Ramzan M, Dar A. Significance of Darcy-Forchheimer porous medium in nanofluid through carbon nanotubes. *Commun Theor Phys*. (2018) **70**:361. doi: 10.1088/0253-6102/70/3/361
38. Hayat T, Hussain Z, Alsaedi A, Muhammad T. An optimal solution for magnetohydrodynamic nanofluid flow over a stretching surface with constant heat flux and zero nanoparticles flux. *Neural Comp. Appl.* (2018) **29**:1555–62. doi: 10.1007/s00521-016-2685-x
39. Shehzad N, Zeeshan A, Ellahi R, Rashidi S. Modelling study on internal energy loss due to entropy generation for non-Darcy Poiseuille flow of silver-water nanofluid: an application of purification. *Entropy*. (2018) **20**:851. doi: 10.3390/e20110851
40. Ellahi R, Zeeshan A, Shehzad N, Alamri SZ. Structural impact of kerosene-Al_2O_3 nanoliquid on MHD Poiseuille flow with variable thermal conductivity: application of cooling process. *J Mol Liquid*. (2018) **264**:607–15. doi: 10.1016/j.molliq.2018.05.103
41. Shehzad N, Zeeshan A, Ellahi R. Electroosmotic flow of MHD Power law Al_2O_3-PVC nanofluid in a horizontal channel: Couette-Poiseuille flow model. *Commun Theor Phys*. (2018) **69**:655–66. doi: 10.1088/0253-6102/69/6/655
42. Zeeshan A, Shehzad N, Abbas T, Ellahi R. Effects of radiative electro-magnetohydrodynamics diminishing internal energy of pressure-driven flow of titanium dioxide-water nanofluid due to entropy generation. *Entropy*. (2019) **21**:236. doi: 10.3390/e21030236
43. Mabood F, Ibrahim SM, Khan WA. Effect of melting and heat generation/absorption on Sisko nanofluid over a stretching surface with nonlinear radiation. *Phys Scripta*. (2019) **94**:065701. doi: 10.1088/1402-4896/ab1164

44. Zeeshan A, Ellahi R, Mabood F, Hussain F. Numerical study on bi-phase coupled stress fluid in the presence of Hafnium and metallic nanoparticles over an inclined plane. *Int J Numer Methods Heat Fluid Flow*. (2019) **29**:2854–69. doi: 10.1108/HFF-11-2018-0677
45. Naqvi SMRS, Muhammad T, Kim HM, Mahmood T, Saeed A, Khan BS. Numerical treatment for Darcy-Forchheimer flow of nanofluid due to a rotating disk with slip effects. *Can J Phys*. (2019) **97**:856–63. doi: 10.1139/cjp-2018-0553
46. Turkyilmazoglu M. Direct contact melting due to a permeable rotating disk. *Phys Fluids*. (2019) **31**:023603. doi: 10.1063/1.5086724

Conflict of Interest: The authors declare that the research was conducted in the absence of any commercial or financial relationships that could be construed as a potential conflict of interest.

Copyright © 2020 Ullah, Serra-Capizzano and Baleanu. This is an open-access article distributed under the terms of the Creative Commons Attribution License (CC BY). The use, distribution or reproduction in other forums is permitted, provided the original author(s) and the copyright owner(s) are credited and that the original publication in this journal is cited, in accordance with accepted academic practice. No use, distribution or reproduction is permitted which does not comply with these terms.

frontiers in Physics

ORIGINAL RESEARCH
published: 17 January 2020
doi: 10.3389/fphy.2019.00244

Check for updates

Fractional View Analysis of Third Order Kortewege-De Vries Equations, Using a New Analytical Technique

Rasool Shah [1†], ***Umar Farooq*** [1†], ***Hassan Khan*** [1†], ***Dumitru Baleanu*** [2,3†], ***Poom Kumam*** [4,5*†] ***and Muhammad Arif*** [1†]

[1] Department of Mathematics, Abdul Wali Khan University Mardan, Mardan, Pakistan, [2] Department of Mathematics, Faculty of Arts and Sciences, Cankaya University, Ankara, Turkey, [3] Institute of Space Sciences, Măgurele, Romania, [4] Center of Excellence in Theoretical and Computational Science (TaCS-CoE) and KMUTTFixed Point Research Laboratory, Room SCL 802 Fixed Point Laboratory, Departments of Mathematics, Faculty of Science, King Mongkut's University of Technology Thonburi (KMUTT), Bangkok, Thailand, [5] Department of Medical Research, China Medical University Hospital, China Medical University, Taichung, Taiwan

OPEN ACCESS

Edited by:
*Ahmed Zeeshan,
International Islamic University,
Islamabad, Pakistan*

Reviewed by:
*Marin I. Marin,
Transilvania University of Braşov,
Romania
Aaqib Majeed,
Bacha Khan University, Pakistan
Ilyas Khan,
Ton Duc Thang University, Vietnam*

***Correspondence:**
*Poom Kumam
poom.kum@kmutt.ac.th*

† These authors have contributed equally to this work

Specialty section:
This article was submitted to Mathematical Physics, a section of the journal Frontiers in Physics

Received: *04 September 2019*
Accepted: *19 December 2019*
Published: *17 January 2020*

Citation:
Shah R, Farooq U, Khan H, Baleanu D, Kumam P and Arif M (2020) Fractional View Analysis of Third Order Kortewege-De Vries Equations, Using a New Analytical Technique. Front. Phys. 7:244. doi: 10.3389/fphy.2019.00244

In the present article, fractional view of third order Kortewege-De Vries equations is presented by a sophisticated analytical technique called Mohand decomposition method. The Caputo fractional derivative operator is used to express fractional derivatives, containing in the targeted problems. Some numerical examples are presented to show the effectiveness of the method for both fractional and integer order problems. From the table, it is investigated that the proposed method has the same rate of convergence as compare to homotopy perturbation transform method. The solution graphs have confirmed the best agreement with the exact solutions of the problems and also revealed that if the sequence of fractional-orders is approaches to integer order, then the fractional order solutions of the problems are converge to an integer order solution. Moreover, the proposed method is straight forward and easy to implement and therefore can be used for other non-linear fractional-order partial differential equations.

Keywords: analytical solution, Mohand transform, Adomian decomposition, caputo derivatives, third order Kortewege-De Vries equations

1. INTRODUCTION

The class of partial differential equations known as Korteweg-De Vries (KDV) equation which play a vital role in the diverse field of physics such as fluid mechanics, signal processing, hydrology, viscoelasticity and fractional kinetics [1, 2]. The KDV equation was first time derived by Korteweg and Vries in 1895. The KDV equation used to model long waves, tides, solitary waves, and wave propagating in a shallow canal. A partial differential Kortewege-De Vries equation of third order is also applied to study the non-linear model of water waves in superficial canal certain namely canal [3], in the time when wave in water was of important concentration in applications in navigational design and also for the awareness of flood and tides [4, 5]. The applications in numerous areas of physics, applied science and other scientific applications, therefore the excessive amount of investigation as a research work has been capitalized in the study of KDV equations [6–10]. We considered the third order time fractional KDV equation in the form [1]

$$\frac{\partial^{\gamma} u(\chi,\Im)}{\partial \Im^{\gamma}} + \kappa u(\chi,\Im)\frac{\partial u(\chi,\Im)}{\partial \chi} + \lambda \frac{\partial^{3} u(\chi,\Im)}{\partial \chi^{3}} + \psi(\chi,\Im), \quad 0 < \gamma \leq 1, \tag{1}$$

with initial source

$$u(\chi,0) = u(\chi),$$

where, κ and λ are real numbers.

The KdV equations of fractional order can be applied to examine the influence of the higher-order wave dispersion. The KdV-Burgers equation defines the waves on lower water surfaces. The strength of fractional KdV equation is the non-local property [11–21]. For a higher order Korteweg-de Vries equation, which is a natural extension of the Korteweg-de Vries equation written in a bilinear form, a Bcklund conversion in bilinear forms is provided. For this higher-order equation the Bcklund transition is given in ordinary forms and the inverse scattering scheme [22], Korteweg-de Vries type of equations 3rd order coefficient variable [23] and Solution of the third order Korteweg-De Vries homotopy perturbation approach using elzaki transform [24].

In few decades, integral transform of various types such as Fourier transform, Laplace transform, Hankel transform, Mellin transform, Z-transform, Wavelet transform, Elzaki transform, Kamal transform, Mahgoub transform, Aboodh transform, Mohand transform, Sumudu transform, Hermite transform etc., gained a enormous importance in solving advanced model in the field mathematics, physics and engineering [25–36].

In the current article, we have applied the Mohand transform with decomposition procedure for the analytical treatment of time fractional KDV equation. The Mohand Transform is one of the new integral transform use for the analytical treatment of different physical phenomena are molded by Differential Equations (DEs) of integer order or Fractional Partial Differential Equations (FPDEs). Recently, Kumar and Viswanathan used Mohand transform and solved the mechanics and electrical circuit problems [37]. Aggarwal have Comparatively Studied Mohand and Aboodh transforms for the solution of differential equations. The numerical applications reflect that both the transforms (Mohand and Aboodh transforms) are closely related to each other [38]. Sudhanshu Aggarwal have also discussed the comparative study of Mohand and Laplace transforms, Mohand and Sumudu transforms, Mohand and Mahgoub transforms [39–41]. Sudhanshu Aggarwal have successfully discussed the Mohand transform of Bessels functions of zero, one and two orders, which is very useful for solving many equations in cylindrical or spherical coordinates such as heat equation, wave equation etc. [42]. The exact solution of second kinds of linear Volterra integral equations get by using Mohand transform. It is claimed that Mohand transform take very little time and has no large computational work [43]. Mohand transform have also used the for solution of Abel's integral equation. The obtained results show that Mohand transform is a powerful integral transform for handling Abel's integral equation [44]. The remaining section of the paper are managed as follows. In the second section, we present some related definitions of fractional calculus and basic concepts of Mohand transform. The third section presents the implementation the proposed methodology. The four section represent different models of KDV equation are examined separately and plotted. Finally, we depict our conclusions.

PRELIMINARIES CONCEPTS

In this section, we present some basic necessary definitions and preliminaries concepts related to fractional calculus and Mohand transform.

DEFINITION

Mohand transform first time was define by Mohand and Mahgoub of the function $u(\Im)$ for $\Im \geq 0$ in the year 2017. The Mohand transform which is represented by $M(.)$ for a function $u(\tau)$ is define as [45]

$$M\{u(\Im)\} = R(\upsilon) = \upsilon^2 \int_0^\infty u(\Im)e^{-\upsilon\Im}d\Im, \ \ k_1 \leq \upsilon \leq k_2, \quad (2)$$

The Mohand transform of a function $u(\Im)$ is $R(\upsilon)$ then $u(\Im)$ is called the inverse of $R(\upsilon)$ which is expressed as.

$$M^{-1}\{R(\upsilon)\} = u(\Im), \ \ M^{-1} \ \textit{is inverse Mohand operator}. \quad (3)$$

DEFINITION

Mohand transform for nth derivatives [46]

$$M\{u^n(\Im)\} = \upsilon^n R(\upsilon) - \upsilon^{n+1}u(0) - \upsilon^n u'(0) - \cdots - \upsilon^2 u^{n-1}(0), \quad (4)$$

DEFINITION

Mohand transform for fractional order derivatives [46]

$$R\{u^\gamma(\Im)\} = \upsilon^\gamma R(\upsilon) - \sum_{k=0}^{n-1} \frac{u^k(0)}{\upsilon^{k-(\gamma+1)}}, \quad 0 < \gamma \leq n, \quad (5)$$

DEFINITION

Caputo operator of fractional partial derivative [47]

$$D_\tau^\gamma g(\chi,\Im) = \begin{cases} \dfrac{\partial^n g(\chi,\Im)}{\partial\Im^n}, & \gamma = n \in N, \\ \dfrac{1}{\Gamma(n-\gamma)} \int_0^\Im (\Im-\phi)^{n-\gamma-1} g^n(\phi)\partial\phi, & n-1 < \gamma < n \end{cases} \quad (6)$$

2. IMPLEMENTATION OF MOHAND TRANSFORM

In this section we have considered the time fractional KDV model in the form

$$\frac{\partial^\gamma u(\chi,\Im)}{\partial\Im^\gamma} + \kappa u(\chi,\Im)\frac{\partial u(\chi,\Im)}{\partial\chi} + \lambda\frac{\partial^3 u(\chi,\Im)}{\partial\chi^3} = \psi(\chi,\Im), \quad 0 < \gamma \leq 1, \quad (7)$$

with initial source

$$u(\chi,0) = u(\chi).$$

where, κ *and* λ are real numbers.

Applying Mohand transform [45]

$$M\left\{\frac{\partial^\gamma u(\chi,\Im)}{\partial\Im^\gamma} + \kappa u(\chi,\Im)\frac{\partial u(\chi,\Im)}{\partial\chi} + \lambda\frac{\partial^3 u(\chi,\Im)}{\partial\chi^3}\right\} = M\left\{\psi(\chi,\Im)\right\},\ 0<\gamma\le 1, \tag{8}$$

by using the transform property, we can simplify as

$$\upsilon^\gamma\{R(\upsilon)-\upsilon u(0)\} + M\left\{\kappa u(\chi,\Im)\frac{\partial u(\chi,\Im)}{\partial\chi} + \lambda\frac{\partial^3 u(x,\tau)}{\partial x^3}\right\} = M\left\{\psi(x,\tau)\right\}, \tag{9}$$

after some evaluation, Equation (8) simplified as

$$R(\upsilon) = \upsilon u(0) + \frac{1}{\upsilon^\gamma}M\left\{-\kappa u(x,\tau)\frac{\partial u(x,\tau)}{\partial x} - \lambda\frac{\partial^3 u(\chi,\Im)}{\partial\chi^3}\right\} + \frac{1}{\upsilon^\gamma}M\left\{\psi(\chi,\Im)\right\}, \tag{10}$$

by applying inverse Mohand transform

$$u(\chi,\Im) = \upsilon u(0) + M^{-1}\left\{\frac{1}{\upsilon^\gamma}M\left\{-\kappa u(\chi,\Im)\frac{\partial u(\chi,\Im)}{\partial\chi} - \lambda\frac{\partial^3 u(\chi,\Im)}{\partial\chi^3}\right\} + \frac{1}{\upsilon^\gamma}M\left\{\psi(\chi,\Im)\right\}\right\}. \tag{11}$$

Finally we obtain the recursive general relation as

$$u_0(\chi,\Im) = u(0) + M^{-1}\left\{\frac{1}{\upsilon^\gamma}M\left\{\psi(\chi,\Im)\right\}\right\} \quad m=0$$
$$u_{m+1}(\chi,\Im) = M^{-1}\left\{\frac{1}{\upsilon^\gamma}M\left\{-\kappa u_m(\chi,\Im)\frac{\partial u_m(\chi,\Im)}{\partial\chi} - \lambda\frac{\partial^3 u_m(\chi,\Im)}{\partial\chi^3}\right\}\right\}, \quad m\ge 0. \tag{12}$$

THEOREM

Let χ and $\mathcal{Y}$ be two Banach spaces and $T:\chi\to\mathcal{Y}$ be a contractive nonlinear operator, such that for all u; $u^*\in$; $\chi, ||T(u)-T(u^*)||\le K||u-u^*||,\quad 0<K<1$ [48].

Then, in view of Banach contraction theorem, T has a unique fixed point u, such that $Tu=u$: Let us write the generated series (12), by the Mohand decomposition method as

$$\chi_m = T(\chi_{m-1}),\quad \chi_{m-1} = \sum_{j=1}^{m-1} u_j,\quad j=0,1,2,\cdots$$

and supposed that $\chi_0 = u_0 \in \mathcal{S}_p(u)$, where $\mathcal{S}_p(u) = \{u^*\in \chi: ||u-u^*||<p\}$ then, we have

$$(B_1)\chi_m \in \mathcal{S}_p(u)$$
$$(B_2)\lim_{m\to\infty}\chi_n = u.$$

Proof

(B_1) In view of mathematical induction for $m=1$, we have

$$||\chi_1-u_1|| = ||T(\chi_0-T(u))|| \le K||u_0-u||.$$

Let the result is true for $m-1$, then

$$||\chi_{m-1}-u|| \le K^{m-1}||u_0-u||.$$

We have

$$||\chi_m-u|| = ||T(\chi_{m-1}-T(u))|| \le K||\chi_{m-1}-u|| \le K^m||u_0-u||.$$

Hence, using (B_1), we have

$$||\chi_m-u|| \le K^m||u_0-u|| \le K^m p < p,$$

which implies that $\chi_m\in\mathcal{S}_p(u)$.

(B_2): Since $||\chi_m-u|| \le K^m||u_0-u||$ and as a $\lim_{m\to\infty} K^m=0$.

Therefore; we have $\lim_{m\to\infty}||u_n-u||=0 \Rightarrow \lim_{m\to\infty} u_n=u$.

3. APPLICATIONS AND DISCUSSION

Here, we have implemented the Mohand transform on some time fractional KVD equations.

Example 4.1: Consider the third order time fractional KVD equation [49]

$$\frac{\partial^\gamma u(\chi,\Im)}{\partial\Im^\gamma} + 6u(\chi,\Im)\frac{\partial u(\chi,\Im)}{\partial\chi} + \frac{\partial^3 u(\chi,\Im)}{\partial\chi^3} = 0,\quad 0<\gamma\le 1, \tag{13}$$

with initial source

$$u(\chi,0)=\chi.$$

Taking Mohand transform of Equation (12), we get

$$\upsilon^\gamma\{R(\upsilon)-\upsilon u(0)\} = M\left\{-6u(\chi,\Im)\frac{\partial u(\chi,\Im)}{\partial\chi} - \frac{\partial^3 u(\chi,\Im)}{\partial\chi^3}\right\}, \tag{14}$$

after some evaluation, Equation (13) is simplified as

$$R(\upsilon) = \upsilon u(0) + \frac{1}{\upsilon^\gamma}\left\{M\left\{-6u(\chi,\Im)\frac{\partial u(\chi,\Im)}{\partial\chi} - \frac{\partial^3 u(\chi,\Im)}{\partial\chi^3}\right\}\right\}, \tag{15}$$

by applying inverse Mohand transform, we get

$$u(\chi,\Im) = u(0) + M^{-1}\left\{\frac{1}{\upsilon^\gamma}M\left\{-6u(\chi,\Im)\frac{\partial u(\chi,\Im)}{\partial\chi} - \frac{\partial^3 u(\chi,\Im)}{\partial\chi^3}\right\}\right\}, \tag{16}$$

thus, by using recursive scheme of Equation (11), we get

$$u_0(\chi,\Im) = u(0) = \chi, \tag{17}$$

$$u_{m+1}(\chi,\Im) = M^{-1}\left\{\frac{1}{\upsilon^{\gamma}}M\left\{-6u_m(\chi,\Im)\frac{\partial u_m(\chi,\Im)}{\partial\chi} - \frac{\partial^3 u_m(\chi,\Im)}{\partial\chi^3}\right\}\right\}, \quad m = 0,1,\cdots. \tag{18}$$

From the recursive formula (17),
for $m = 0$

$$u_1(\chi,\Im) = M^{-1}\left\{\frac{1}{\upsilon^{\gamma}}M\left\{-6u_0(\chi,\Im)\frac{\partial u_0(\chi,\Im)}{\partial\chi} - \frac{\partial^3 u_0(\chi,\Im)}{\partial\chi^3}\right\}\right\},$$

$$u_1(\chi,\Im) = -6\chi\frac{\Im^{\gamma}}{\gamma!}, \tag{19}$$

for $m = 1$

$$u_2(\chi,\Im) = M^{-1}\left\{\frac{1}{\upsilon^{\gamma}}M\left\{-6u_0(\chi,\Im)\frac{\partial u_1(\chi,\Im)}{\partial\chi} - 6u_1(\chi,\Im)\frac{\partial u_0(\chi,\Im)}{\partial\chi} - \frac{\partial^3 u_1(\chi,\Im)}{\partial\chi^3}\right\}\right\},$$

$$u_2(\chi,\Im) = 72\chi\frac{\Im^{2\gamma}}{(2\gamma)!}, \tag{20}$$

for $m = 2$

$$u_3(\chi,\Im) = M^{-1}\left\{\frac{1}{\upsilon^{\gamma}}M\left\{-6u_0(\chi,\Im)\frac{\partial u_2(\chi,\Im)}{\partial\chi} - 6u_1(\chi,\Im)\frac{\partial u_1(\chi,\Im)}{\partial\chi} - 6u_2(\chi,\Im)\frac{\partial u_0(\chi,\Im)}{\partial\chi} - \frac{\partial^3 u_2(\chi,\Im)}{\partial\chi^3}\right\}\right\},$$

$$u_3(\chi,\Im) = -864\chi\frac{\Im^{3\gamma}}{(3\gamma)!} - 216\chi(2\gamma)!\frac{\Im^{3\gamma}}{(3\gamma)!\gamma!\gamma!}, \tag{21}$$

Similarly for $m = 3$, we can get

$$u_4(\chi,\Im) = 10368\chi\frac{\Im^{4\gamma}}{(4\gamma)!} + 2592\chi(2\gamma)!\frac{\Im^{4\gamma}}{(4\gamma)!\gamma!} + 5184\chi(3\gamma)!\frac{\Im^{4\gamma}}{(4\gamma)!(2\gamma)!\gamma!}, \tag{22}$$

$$\vdots$$

The Mohand transform solution for example 4.1 is

$$u(\chi,\Im) = u_0(\chi,\Im) + u_1(\chi,\Im) + u_2(\chi,\Im) + u_3(\chi,\Im) + u_4(\chi,\Im) + \cdots. \tag{23}$$

$$u(\chi,\Im) = \chi - 6x\frac{\Im^{\gamma}}{\gamma!} + 72\chi\frac{\Im^{2\gamma}}{(2\gamma)!} - 864\chi\frac{\Im^{3\gamma}}{(3\gamma)!} - 216\chi(2\gamma)!\frac{\Im^{3\gamma}}{(3\gamma)!\gamma!\gamma!} + 10368\chi\frac{\Im^{4\gamma}}{(4\gamma)!} + 2592\chi(2\gamma)!\frac{\Im^{4\gamma}}{(4\gamma)!\gamma!} + 5184\chi(3\gamma)!\frac{\Im^{4\gamma}}{(4\gamma)!(2\gamma)!\gamma!} + \cdots. \tag{24}$$

For particular case $\gamma = 1$, the Mohand transform solution become as

$$u(x,\tau) = \chi(1 - 6\Im + 36\Im^2 - 216\Im^3 + 1296\Im^4 + \cdots). \tag{25}$$

The calculated result provide the exact solution in the close form

$$u(\chi,\Im) = \frac{\chi}{1+6\Im}. \tag{26}$$

Example 4.2: Consider the third order time fractional KVD equation [50]

$$\frac{\partial^{\gamma} u(\chi,\Im)}{\partial\Im^{\gamma}} + u(\chi,\Im)\frac{\partial u(\chi,\Im)}{\partial\chi} + \frac{\partial^3 u(\chi,\Im)}{\partial\chi^3} = 0, \quad 0 < \gamma \le 1, \tag{27}$$

with initial source

$$u(\chi,0) = 1 - \chi.$$

Taking Mohand transform of Equation (26)

$$\upsilon^{\gamma}\{R(\upsilon) - \upsilon u(0)\} = M\left\{-u(\chi,\Im)\frac{\partial u(\chi,\Im)}{\partial\chi} - \frac{\partial^3 u(\chi,\Im)}{\partial\chi^3}\right\}, \tag{28}$$

after some evaluation, Equation (27) is simplified as

$$R(\upsilon) = \upsilon u(0) + \frac{1}{\upsilon^{\gamma}}\left\{M\left\{-u(\chi,\Im)\frac{\partial u(\chi,\Im)}{\partial\chi} - \frac{\partial^3 u(\chi,\Im)}{\partial\chi^3}\right\}\right\}, \tag{29}$$

taking inverse Mohand transform of Equation (28)

$$u(\chi,\Im) = u(0) + M^{-1}\left\{\frac{1}{\upsilon^{\gamma}}M\left\{-u(\chi,\Im)\frac{\partial u(\chi,\Im)}{\partial\chi} - \frac{\partial^3 u(\chi,\Im)}{\partial\chi^3}\right\}\right\}, \tag{30}$$

by using the recursive scheme Equation (11), we get

$$u_0(\chi,\Im) = u(0) = 1 - \chi, \tag{31}$$

$$u_{m+1}(\chi,\Im) = M^{-1}\left\{\frac{1}{\upsilon^{\gamma}}M\left\{-u_m(\chi,\Im)\frac{\partial u_m(\chi,\Im)}{\partial\chi} - \frac{\partial^3 u_m(\chi,\Im)}{\partial\chi^3}\right\}\right\}, \tag{32}$$

From the recursive formula (31),
for $m = 0$

$$u_1(\chi,\Im) = M^{-1}\left\{\frac{1}{\upsilon^{\gamma}}M\left\{-u_0(\chi,\Im)\frac{\partial u_0(\chi,\Im)}{\partial\chi} - \frac{\partial^3 u_0(\chi,\Im)}{\partial\chi^3}\right\}\right\},$$

$$u_1(\chi,\Im) = (1-\chi)\frac{\Im^{\gamma}}{\gamma!}, \tag{33}$$

for $m = 1$

$$u_2(\chi,\Im) = M^{-1}\left\{\frac{1}{\upsilon^{\gamma}}M\left\{-u_0(\chi,\Im)\frac{\partial u_1(\chi,\Im)}{\partial\chi} - u_1(\chi,\Im)\frac{\partial u_0(\chi,\Im)}{\partial\chi} - \frac{\partial^3 u_1(\chi,\Im)}{\partial\chi^3}\right\}\right\},$$

$$u_2(\chi,\Im) = 2(1-\chi)\frac{\Im^{2\gamma}}{(2\gamma)!}, \tag{34}$$

for $m = 2$

$$u_3(\chi,\Im) = M^{-1}\left\{\frac{1}{\upsilon^\gamma}M\left\{-u_0(\chi,\Im)\frac{\partial u_2(\chi,\Im)}{\partial\chi} - u_1(\chi,\Im)\frac{\partial u_1(\chi,\Im)}{\partial\chi} - u_2(\chi,\Im)\frac{\partial u_0(\chi,\Im)}{\partial\chi} - \frac{\partial^3 u_2(\chi,\Im)}{\partial\chi^3}\right\}\right\},$$

$$u_3(\chi,\Im) = 6(1-\chi)\frac{\Im^{3\gamma}}{(3\gamma)!}. \tag{35}$$

$$\vdots$$

The Mohand transform solution for example 3.2 is

$$u(\chi,\Im) = u_0(\chi,\Im) + u_1(\chi,\Im) + u_2(\chi,\Im) + u_3(\chi,\Im) + .. \tag{36}$$

$$u(\chi,\Im) = 1-\chi+(1-\chi)\frac{\Im^\gamma}{\gamma!} + 2(1-\chi)\frac{\Im^{2\gamma}}{(2\gamma)!} + 6(1-\chi)\frac{\Im^{3\gamma}}{(3\gamma)!} + \cdots. \tag{37}$$

For particular case $\gamma = 1$, the Mohand transform solution become as

$$u(\chi,\Im) = 1-\chi(1+\Im+\Im^2+\Im^3+\cdots). \tag{38}$$

The calculated result provide the exact solution in the close form

$$u(\chi,\Im) = \frac{1-\chi}{1-\Im}. \tag{39}$$

Example 4.3 Consider the third order time fractional KVD equation [6]

$$\frac{\partial^\gamma u(\chi,\Im)}{\partial\Im^\gamma} - 6u(\chi,\Im)\frac{\partial u(\chi,\Im)}{\partial\chi} + \frac{\partial^3 u(\chi,\Im)}{\partial\chi^3} = 0, \quad 0<\gamma\leq 1, \tag{40}$$

with initial source

$$u(\chi,0) = 6\chi.$$

Taking Mohand transform of Equation (39)

$$\upsilon^\gamma\{R(\upsilon) - \upsilon u(0)\} = M\left\{6u(\chi,\Im)\frac{\partial u(\chi,\Im)}{\partial\chi} - \frac{\partial^3 u(\chi,\Im)}{\partial\chi^3}\right\}, \tag{41}$$

after some evaluation, Equation (40) is simplified as

$$R(\upsilon) = \upsilon u(0) + \frac{1}{\upsilon^\gamma}\left\{M\left\{6u(\chi,\Im)\frac{\partial u(\chi,\Im)}{\partial\chi} - \frac{\partial^3 u(\chi,\Im)}{\partial\chi^3}\right\}\right\}, \tag{42}$$

by applying inverse Mohand transform, we get

$$u(\chi,\Im) = u(0) + M^{-1}\left\{\frac{1}{\upsilon^\gamma}M\left\{6u(\chi,\Im)\frac{\partial u(\chi,\Im)}{\partial\chi} - \frac{\partial^3 u(\chi,\Im)}{\partial\chi^3}\right\}\right\}, \tag{43}$$

thus, by using recursive scheme of Equation (11), we get

$$u_0(\chi,\Im) = u(0) = 6\chi \tag{44}$$

$$u_{m+1}(\chi,\Im) = M^{-1}\left\{\frac{1}{\upsilon^\gamma}M\left\{6u_m(\chi,\Im)\frac{\partial u_m(\chi,\Im)}{\partial\chi} - \frac{\partial^3 u_m(\chi,\Im)}{\partial\chi^3}\right\}\right\}, \quad m = 0,1,\cdots. \tag{45}$$

From the recursive formula (44),
for $m = 0$

$$u_1(\chi,\Im) = M^{-1}\left\{\frac{1}{\upsilon^\gamma}M\left\{6u_0(\chi,\Im)\frac{\partial u_0(\chi,\Im)}{\partial\chi} - \frac{\partial^3 u_0(\chi,\Im)}{\partial\chi^3}\right\}\right\},$$

$$u_1(\chi,\Im) = 216\chi\frac{\Im^\gamma}{\gamma!}, \tag{46}$$

for $m = 1$

$$u_2(\chi,\Im) = M^{-1}\left\{\frac{1}{\upsilon^\gamma}M\left\{6u_0(\chi,\Im)\frac{\partial u_1(\chi,\Im)}{\partial\chi} + 6u_1(\chi,\Im)\frac{\partial u_0(\chi,\Im)}{\partial\chi} - \frac{\partial^3 u_1(\chi,\Im)}{\partial\chi^3}\right\}\right\},$$

$$u_2(\chi,\Im) = 15552\chi\frac{\Im^{2\gamma}}{(2\gamma)!}, \tag{47}$$

for $m = 2$

$$u_3(\chi,\Im) = M^{-1}\left\{\frac{1}{\upsilon^\gamma}M\left\{6u_0(\chi,\Im)\frac{\partial u_2(\chi,\Im)}{\partial\chi} + 6u_1(\chi,\Im)\frac{\partial u_1(\chi,\Im)}{\partial\chi} + 6u_2(\chi,\Im)\frac{\partial u_0(\chi,\Im)}{\partial\chi} - \frac{\partial^3 u_2(\chi,\Im)}{\partial\chi^3}\right\}\right\},$$

$$u_3(\chi,\Im) = 1119744\chi\frac{\Im^{3\gamma}}{(3\gamma)!} + 279936\chi(2\gamma)!\frac{\Im^{3\gamma}}{(3\gamma)!\gamma!\gamma!}, \tag{48}$$

$$\vdots$$

The Mohand transform solution for example 4.3 is

$$u(\chi,\Im) = u_0(\chi,\Im) + u_1(\chi,\Im) + u_2(\chi,\Im) + u_3(\chi,\Im) + \cdots. \tag{49}$$

$$u(\chi,\Im) = 6\chi + 216\chi\frac{\Im^\gamma}{\gamma!} + 15552\chi\frac{\Im^{2\gamma}}{(2\gamma)!} + 1119744\chi\frac{\Im^{3\gamma}}{(3\gamma)!} + 279936\chi(2\gamma)!\frac{\Im^{3\gamma}}{(3\gamma)!\gamma!\gamma!} + \cdots. \tag{50}$$

For particular case $\gamma = 1$, the Mohand transform solution become as

$$u(\chi,\Im) = 6\chi(1+36\Im+1296\Im^2+46656\Im^3+\cdots). \tag{51}$$

The calculated result provide the exact solution in the close form

$$u(\chi,\Im) = \frac{6\chi}{1-36\Im}. \tag{52}$$

Example 4.4 Consider the third order time fractional KVD equation [6]

$$\frac{\partial^{\gamma} u(\chi,\Im)}{\partial \Im^{\gamma}} - 6u(\chi,\Im)\frac{\partial u(\chi,\Im)}{\partial \chi} + \frac{\partial^3 u(\chi,\Im)}{\partial \chi^3} = 0, \quad 0<\gamma\le 1, \tag{53}$$

with initial source

$$u(\chi,0) = \frac{6}{\chi^2}.$$

Taking Mohand transform of Equation (52)

$$\upsilon^{\gamma}\{R(\upsilon) - \upsilon u(0)\} = M\left\{6u(\chi,\Im)\frac{\partial u(\chi,\Im)}{\partial \chi} - \frac{\partial^3 u(\chi,\Im)}{\partial \chi^3}\right\}, \tag{54}$$

after some evaluation, Equation (53) is simplified as

$$R(\upsilon) = \upsilon u(0) + \frac{1}{\upsilon^{\gamma}}\left\{M\left\{6u(\chi,\Im)\frac{\partial u(\chi,\Im)}{\partial \chi} - \frac{\partial^3 u(\chi,\Im)}{\partial \chi^3}\right\}\right\}, \tag{55}$$

by applying inverse Mohand transform, we get

$$u(\chi,\Im) = u(0) + M^{-1}\left\{\frac{1}{\upsilon^{\gamma}}M\left\{6u(\chi,\Im)\frac{\partial u(\chi,\Im)}{\partial \chi} - \frac{\partial^3 u(\chi,\Im)}{\partial \chi^3}\right\}\right\}. \tag{56}$$

Thus, by using recursive scheme of Equation (11), we get

$$u_0(\chi,\Im) = u(0) = \frac{6}{\chi^2}, \tag{57}$$

$$u_{m+1}(\chi,\Im) = M^{-1}\left\{\frac{1}{\upsilon^{\gamma}}M\left\{6u_m(\chi,\Im)\frac{\partial u_m(\chi,\Im)}{\partial \chi} - \frac{\partial^3 u_m(\chi,\Im)}{\partial \chi^3}\right\}\right\}, \quad m = 0, 1, \cdots. \tag{58}$$

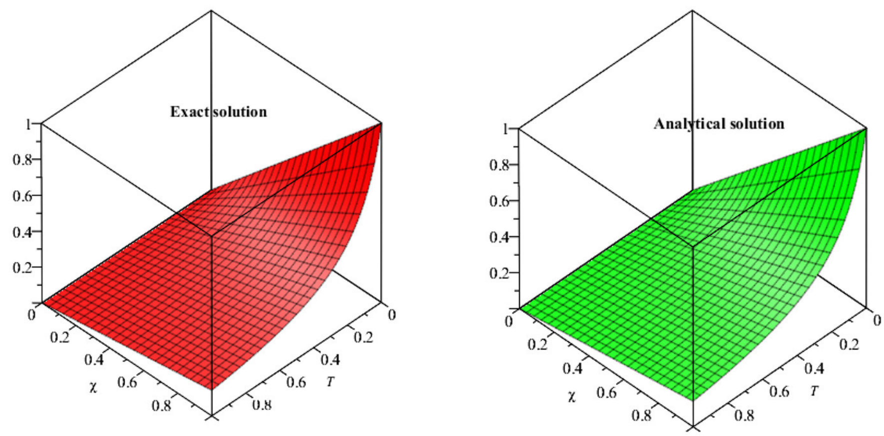

FIGURE 1 | Represents the exact and analytical solution of example 4.1.

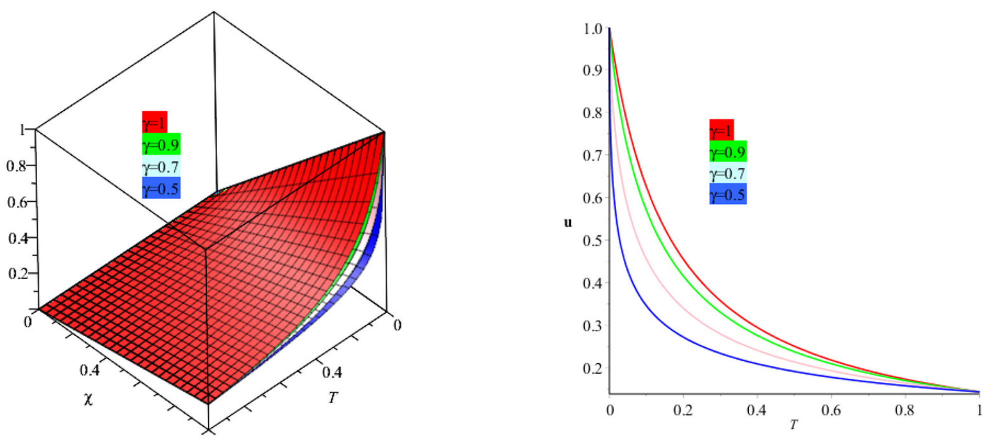

FIGURE 2 | Represents the solution at different fractional order.

From the recursive formula (44),
for $m = 0$

$$u_1(\chi,\Im) = M^{-1}\left\{\frac{1}{\upsilon^{\gamma}}M\left\{6u_0(\chi,\Im)\frac{\partial u_0(\chi,\Im)}{\partial\chi} - \frac{\partial^3 u_0(\chi,\Im)}{\partial\chi^3}\right\}\right\},$$

$$u_1(\chi,\Im) = \frac{-288}{\chi^5}\frac{\Im^{\gamma}}{\gamma!}, \tag{59}$$

for $m = 1$

$$u_2(\chi,\Im) = M^{-1}\left\{\frac{1}{\upsilon^{\gamma}}M\left\{6u_0(\chi,\Im)\frac{\partial u_1(\chi,\Im)}{\partial\chi} + 6u_1(\chi,\Im)\frac{\partial u_0(\chi,\Im)}{\partial\chi} - \frac{\partial^3 u_1(\chi,\Im)}{\partial\chi^3}\right\}\right\},$$

$$u_2(\chi,\Im) = \frac{12096}{\chi^8}\frac{\Im^{2\gamma}}{(2\gamma)!}, \tag{60}$$

for $m = 2$

$$u_3(\chi,\Im) = M^{-1}\left\{\frac{1}{\upsilon^{\gamma}}M\left\{6u_0(\chi,\Im)\frac{\partial u_2(\chi,\Im)}{\partial\chi} + 6u_1(\chi,\Im)\frac{\partial u_1(\chi,\Im)}{\partial\chi} + 6u_2(\chi,\Im)\frac{\partial u_0(\chi,\Im)}{\partial\chi} - \frac{\partial^3 u_2(\chi,\Im)}{\partial\chi^3}\right\}\right\},$$

$$u_3(\chi,\Im) = \frac{4354560}{\chi^{11}}\frac{\Im^{3\gamma}}{(3\gamma)!} - \frac{2488320}{\chi^{11}}(2\gamma)!\frac{\Im^{3\gamma}}{(3\gamma)!\gamma!\gamma!}, \tag{61}$$

$$\vdots$$

The Mohand transform solution for example 4.3 is

$$u(\chi,\Im) = u_0(\chi,\Im) + u_1(\chi,\Im) + u_2(\chi,\Im) + u_3(\chi,\Im) + .. \tag{62}$$

$$u(\chi,\Im) = \frac{6}{\chi^2} - \frac{288}{\chi^5}\frac{\Im^{\gamma}}{\gamma!} + \frac{12096}{\chi^8}\frac{\Im^{2\gamma}}{(2\gamma)!} + \frac{4354560}{\chi^{11}}\frac{\Im^{3\gamma}}{(3\gamma)!} - \frac{2488320}{\chi^{11}}(2\gamma)!\frac{\Im^{3\gamma}}{(3\gamma)!\gamma!\gamma!}. \tag{63}$$

For particular case $\gamma = 1$, the Mohand transform solution become as

$$u(\chi,\Im) = \frac{6}{\chi^2} - \frac{288}{\chi^5}\Im + \frac{6048}{\chi^8}\Im^2 - \frac{103680}{\chi^{11}}\Im^3 + \cdots. \tag{64}$$

The calculated result converge to the exact solution in the close form

$$u(\chi,\Im) = \frac{6\chi(\chi^3 - 24\Im)}{(\chi^3 + 12\Im)^2}. \tag{65}$$

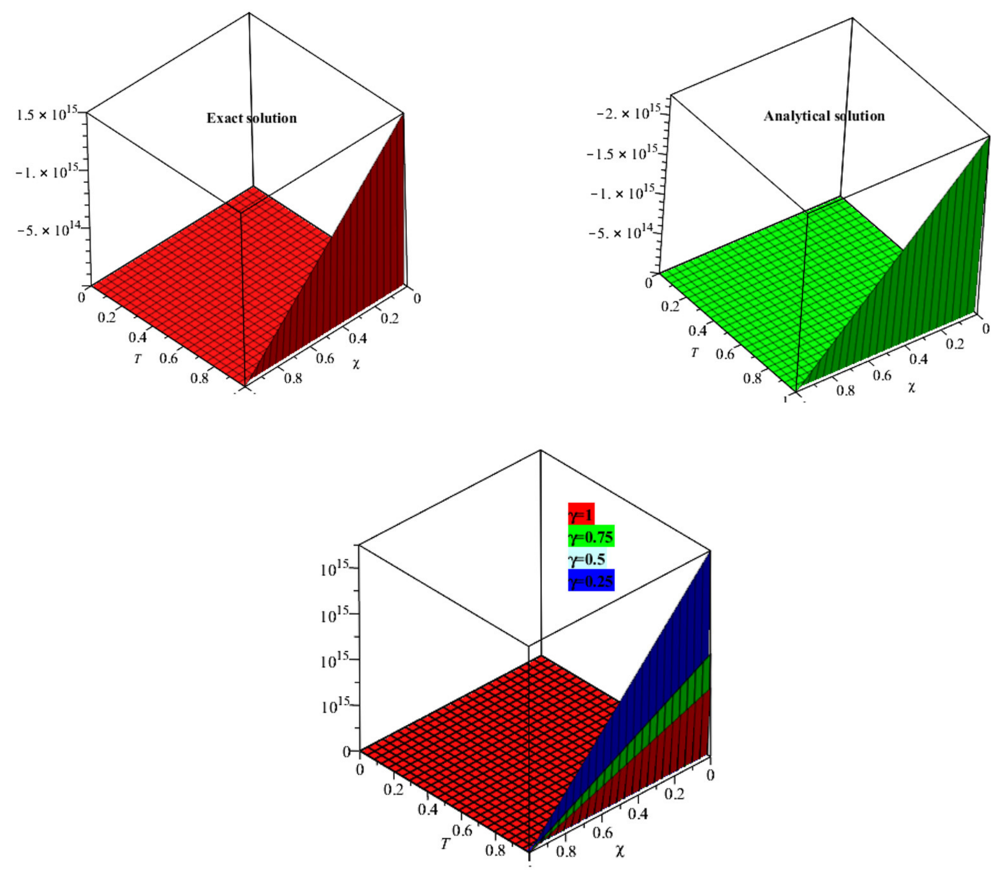

FIGURE 3 | Represents the exact and analytical solution of example 4.2.

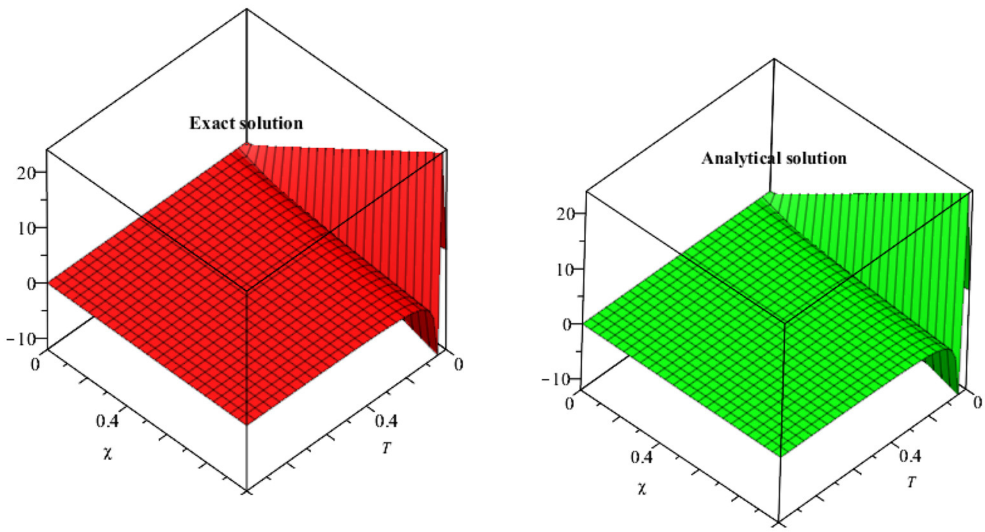

FIGURE 4 | Represents the exact and analytical solution of example 4.3.

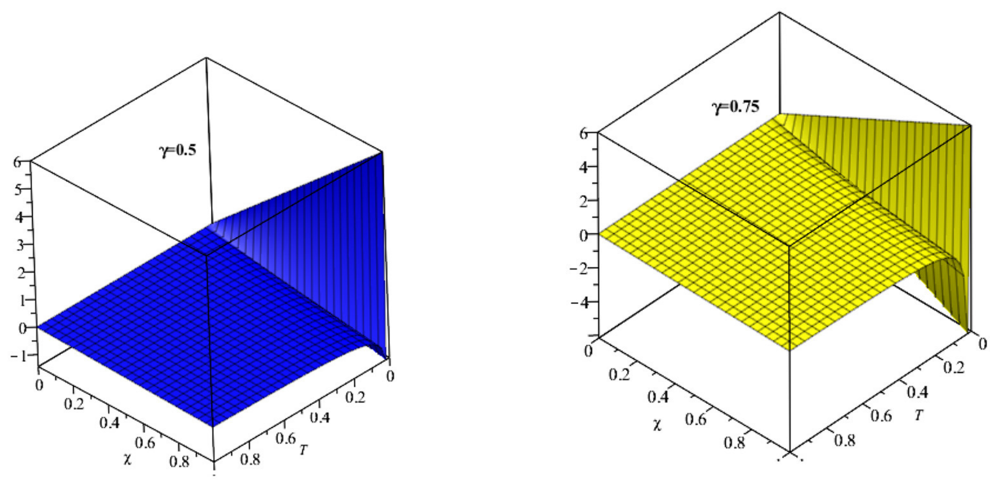

FIGURE 5 | Represents the solution of example 4.3 at $\gamma = 0.75$, $\gamma = 0.5$.

4. RESULTS AND DISCUSSION

In **Figure 1**, the exact and analytical solutions of example 4.1 are presented. The solution-graph have confirmed that the obtained results are in good contact with the exact solutions of example 4.1. In **Figure 2**, the fractional-order solutions are calculated at fractional-order $\gamma = 1, 0.9, 0.7$, and 0.5. The solutions graphs are expressed in both two and three dimensions. The convergence phenomena can be observed from **Figure 2**. The similar implementation and results can be seen in **Figures 3–7** for example 4.3 and 4.4 also. In **Table 1**, the results of MDM are compared with the results of HPTM which provide identical results. It is observed that the proposed method has the sufficient accuracy and rate of convergence to the exact solutions of the problems. It is also investigated that the proposed method provided the simple and straightforward implementation for all examples 1, 2, 3, and 4. These investigations of results have confirmed that the present method can be extended to other fractional-order problems arising in science and engineering.

5. CONCLUSION

The proposed method is considered to be one of the pre-eminent and new analytical technique, to solve fractional order partial differential equation. In current research article, the proposed method is applied to solve fractional-order kortewege-De Vries equations. The current method is constructed by using Mohand transformation along with Adomian decomposition method. The new hybrid method is very useful to handle the analytical

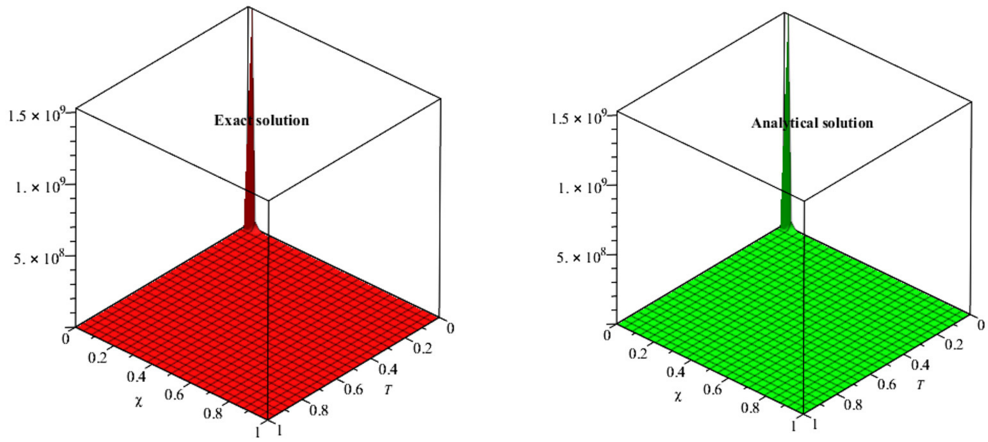

FIGURE 6 | Represents the exact and analytical solution of example 4.4.

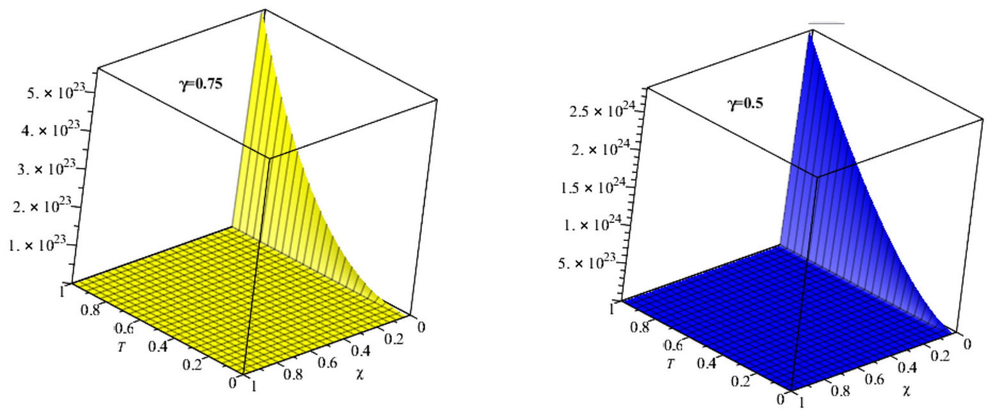

FIGURE 7 | Represents the solution of example 4.4 at $\gamma = 0.75$, $\gamma = 0.5$.

TABLE 1 | Comparison of MDM and HPTM [49] of example 1 at $\Im = 0.5$.

	MDM	MDM	MDM	Absolute error	Absolute error
χ	$\gamma = 0.55$	$\gamma = 0.75$	$\gamma = 1$	*HPTM* ($\gamma = 1$)	*MDM* ($\gamma = 1$)
0.1	0.0712628292	0.0893256192	0.0970873	7.86E-08	7.85E-08
0.2	0.1425256585	0.1786512385	0.1941746	1.57E-07	1.56E-07
0.3	0.2137884877	0.2679768577	0.2912619	2.35E-07	2.35E-07
0.4	0.2850513169	0.3573024770	0.3883492	3.14E-07	3.14E-07
0.5	0.3563141462	0.4466280962	0.4854365	3.93E-07	3.93E-07
0.6	0.4275769754	0.5359537154	0.5825238	4.71E-07	4.71E-07
0.7	0.4988398046	0.6252793347	0.6796111	5.50E-07	5.50E-07
0.8	0.5701026338	0.7146049539	0.7766984	6.29E-07	6.29E-07
0.9	0.6413654631	0.8039305732	0.8737857	7.07E-07	7.07E-07
1	0.7126282923	0.8932561924	0.9708730	7.86E-07	7.86E-07

solutions of fractional-order partial differential equations. To verify, the validity of the suggested method some numerical examples of time fractional third order KdV equations are considered to solve it analytically. The solution graphs have confirmed the validity and reliability of the suggested method toward the solutions of other fractional-order non-linear partial differential equations.

DATA AVAILABILITY STATEMENT

The datasets generated for this study are available on request to the corresponding author.

AUTHOR CONTRIBUTIONS

HK, RS, and UF has the primary contribution to produce this manuscript. PK has provided the financial support to publish this article. DB and MA have provided their expert opinion and writing draft of the paper.

FUNDING

The research grant for this manuscript was provided by PK, Center of Excellence in Theoretical and Computational Science

(TaCS-CoE) and KMUTTFixed Point Research Laboratory, Room SCL 802 Fixed Point Laboratory, Science Laboratory Building, Departments of Mathematics, Faculty of Science, King Mongkut's University of Technology Thonburi (KMUTT), 126 Pracha-Uthit Road, Bang Mod, Thrung Khru, Bangkok 10140, Thailand.

REFERENCES

1. Miura RM, editor. Bäcklund transformations, the inverse scattering method, solitons, and their applications: In: *Proceedings of the NSF Research Workshop on Contact Transformations*. Nashville, TN: Springer (2006).
2. Asif M, Ul Haq S, Islam S, Abdullah Alkanhal T, Khan ZA, Khan I, et al. Unsteady flow of fractional fluid between two parallel walls with arbitrary wall shear stress using caputofabrizio derivative. *Symmetry*. (2019) **11**:449. doi: 10.3390/sym11040449
3. Whitham GB. *Linear and nonlinear waves, Vol. 42*. John Wiley & Sons (2011). doi: 10.1002/9781118032954
4. Ali F, Murtaza S, Khan I, Sheikh NA, Nisar KS. AtanganaBaleanu fractional model for the flow of Jeffrey nanofluid with diffusion-thermo effects: applications in engine oil. *Adv Diff Equat*. (2019) **2019**:346. doi: 10.1186/s13662-019-2222-1
5. Lund LA, Omar Z, Alharbi SO, Khan I, Nisar KS. Numerical investigation of multiple solutions for caputo fractional-order-two dimensional magnetohydrodynamic unsteady flow of generalized viscous fluid over a shrinking sheet using the Adams-type predictor-corrector method. *Coatings*. (2019) **9**:548. doi: 10.3390/coatings9090548
6. Kaya D, Aassila M. An application for a generalized KdV equation by the decomposition method. *Phys Lett A*. (2002) **299**:201–6. doi: 10.1016/S0375-9601(02)00652-7
7. Drazin PG, Robin SJ. *Solitons: An Introduction*. Vol. 2. Cambridge: Cambridge University Press (1989).
8. Saucez P, Vande Wouwer A, Schiesser WE. An adaptive method of lines solution of the Korteweg-de Vries equation. *Comput Math Appl*. (1998) **35**:13–25. doi: 10.1016/S0898-1221(98)00093-5
9. Abassy TA, El-Tawil MA, El-Zoheiry H. Exact solutions of some nonlinear partial differential equations using the variational iteration method linked with Laplace transforms and the Pad technique. *Comput Math Appl*. (2007) **54**:940–54. doi: 10.1016/j.camwa.2006.12.067
10. Kangalgil F, Ayaz F. Solitary wave solutions for the KdV and mKdV equations by differential transform method. *Chaos Solit Fract*. (2009) **41**:464–72. doi: 10.1016/j.chaos.2008.02.009
11. Ganji DD, Mirmohammadsadeghi SE, Safari M. Application fo He's variational iteration method and Adomian's decomposition method to prochhammer-chree equation. *Int J Mod Phys B*. (2009) **23**:435–46. doi: 10.1142/S0217979209049656
12. Marin M. On the domain of influence in thermoelasticity of bodies with voids. *Arch Math (Brno)*. (1997) **33**:301–8.
13. Shah R, Khan H, Arif M, Kumam P. Application of Laplace Adomian decomposition method for the analytical solution of third-order dispersive fractional partial differential equations. *Entropy*. (2019) **21**:335. doi: 10.3390/e21040335
14. Othman MIA, Marin M. Effect of thermal loading due to laser pulse on thermoelastic porous medium under GN theory. *Results Phys*. (2017) **7**:3863–72. doi: 10.1016/j.rinp.2017.10.012
15. Momani S, Odibat Z, Alawneh A. Variational iteration method for solving the space and time fractional KdV equation. *Numer Methods Part Diff Equat*. (2008) **24**:262–71. doi: 10.1002/num.20247
16. Wang Q. Homotopy perturbation method for fractional KdV equation. *Appl Math Comput*. (2007) **190**:1795–802. doi: 10.1016/j.amc.2007.02.065
17. Wang Q. Homotopy perturbation method for fractional KdV-Burgers equation. *Chaos Solit Fract*. (2008) **35**:843–50. doi: 10.1016/j.chaos.2006.05.074
18. Momani S. An explicit and numerical solutions of the fractional KdV equation. *Math Comput Simulat*. (2005) **70**:110–8. doi: 10.1016/j.matcom.2005.05.001
19. Song L, Zhang H. Application of homotopy analysis method to fractional KdVBurgersKuramoto equation. *Phys Lett A*. (2007) **367**:88–94. doi: 10.1016/j.physleta.2007.02.083
20. Shah R, Khan H, Farooq U, Baleanu D, Kumam P, Arif M. A new analytical technique to solve system of fractional-order partial differential equations. *IEEE Access*. (2019) **7**:150037–50. doi: 10.1109/ACCESS.2019.2946946
21. Jeffrey A. *Applied Partial Differential Equations: An Introduction*. San Diego, CA: Academic Press (2003).
22. Satsuma J, Kaup DJ. A Bcklund transformation for a higher order Korteweg-de Vries equation. *J Phys Soc Jpn*. (1977) **43**:692–7. doi: 10.1143/JPSJ.43.692
23. Grses M, Karasu A. Variable coefficient third order Kortewegde Vries type of equations. *J Math Phys*. (1995) **36**:3485–91. doi: 10.1063/1.530974
24. Chavan SS, Panchal MM. Solution of third order Korteweg-De Vries equation by homotopy perturbation method using Elzaki transform. *Int J Res Appl Sci Eng Technol*. (2014) **2**:366–9.
25. Debnath L, Bhatta D. *Integral Transforms and Their Applications*. New York, NY: Chapman and Hall/CRC Press (2014).
26. Mahgoub, MAM. The new integral transform "Mahgoub Transform". *Adv Theor Appl Math*. (2016) **11**:391–8.
27. Abdelilah K, Hassan S. The new integral transform "Kamal Transform". *Adv Theor Appl Math*. (2016) **11**:451–8.
28. Elzaki TM. The new integral transform "Elzaki transform". *Glob J Pure Appl Math*. (2011) **7**:57–64.
29. Aboodh KS. The new integral transform "Aboodh Transform". *Glob J Pure Appl Math*. (2013) **9**:35–43.
30. Mohand M, Mahgoub A. The new integral transform Mohand Transform. *Adv Theor Appl Math*. (2017) **12**:113–20.
31. Watugala GK. Sumudu transform: a new integral transform to solve differential equations and control engineering problems. *Integr Educ*. (1993) **24**:35–43. doi: 10.1080/0020739930240105
32. Khan H, Shah R, Baleanu D, Kumam P, Arif M. Analytical solution of fractional-order hyperbolic telegraph equation, using natural transform decomposition method. *Electronics*. (2019) **8**:1015. doi: 10.3390/electronics8091015
33. Eltayeb H, Klman A. A note on the Sumudu transforms and differential equations. *Appl Math Sci*. (2010) **4**:1089–98.
34. Aggarwal S, Singh GP. *Shehu Transform of Error Function (probability integral). Int J Res Advent Technol*. (2019) **7**:54–60. doi: 10.32622/ijrat.76201932
35. Shah R, Khan H, Baleanu D, Kumam P, Arif M. A novel method for the analytical solution of fractional ZakharovKuznetsov equations. *Adv Diff Equat*. (2019) **2019**:1–14. doi: 10.1186/s13662-019-2441-5
36. Aggarwal S, Gupta AR. Solution of linear Volterra integro-differential equations of second kind using Kamal transform. *J Emerg Technol Innovat Res*. (2019) **6**:741–7.
37. Kumar PS, Viswanathan A. Applications of Mohand transform to mechanics and electrical circuit problems. *Int J Res Adv Technol*. (2018) **6**:2838–40.
38. Aggarwal S, Chauhan R. A comparative study of Mohand and Aboodh transforms. *Int J Res Adv Technol*. (2019) **7**:520–9. doi: 10.32622/ijrat.712019107
39. Shah R, Khan H, Baleanu D. Fractional WhithamBroerKaup Equations within Modified Analytical Approaches. *Axioms*. (2019) **8**:125. doi: 10.3390/axioms8040125
40. Aggarwal S, Sharma SD. A comparative study of Mohand and Sumudu transforms. *J Emerg Technol Innovat Res*. (2019) **6**:145–53.
41. Aggarwal S. A comparative study of Mohand and Mahgoub transforms. *Stat*. (2019) **4**:1–7.
42. Aggarwal S, Raman C, Nidhi S. Mohand transform of Bessels functions. *Int J Res Adv Technol*. (2018) **6**:3034–8.

43. Aggarwal S, Sharma N, Chauhan RŚolution of linear Volterra integral equations of second kind using Mohand transform. *Int J Res Adv Technol.* (2018) **6**:3098–102.
44. Srivastava HM, Shah R, Khan H, Arif M. Some analytical and numerical investigation of a family of fractional order Helmholtz equations in two space dimensions. *Math Methods Appl Sci.* (2020) **43**:199–212. doi: 10.1002/mma.5846
45. Mohand M, Mahgoub A. The new integral transform Mohand Transform. *Adv Theor Appl Math.* (2017) **12**:113–20.
46. Aggarwal S, Mishra R, Chaudhary A. A comparative study of Mohand and Elzaki transforms. *Glob J Eng Sci Res.* (2019) **6**: 203–13.
47. Hilfer R, editor. *Applications of Fractional Calculus in Physics*. Singapore: World Scientific (2000).
48. Shah K, Khalil H, Ali Khan R. Analytical solutions of fractional order diffusion equations by natural transform method. *Iran J Sci Technol Trans A*. (2018) **42**:1479–90. doi: 10.1007/s40995-016-0136-2
49. Eljaily MH, Elzaki TM. Homotopy perturbation transform method for solving korteweg-devries (kdv) equation. *Pure Appl Math J.* (2015) **4**:264–8. doi: 10.11648/j.pamj.20150406.17
50. Sedeeg AKH. Homotopy perturbation transform method for solving third order Korteweg De-Vries (KDV) Equation. *AJAM*. (2016) **4**:247–51. doi: 10.11648/j.ajam.20160405.16

Conflict of Interest: The authors declare that the research was conducted in the absence of any commercial or financial relationships that could be construed as a potential conflict of interest.

Copyright © 2020 Shah, Farooq, Khan, Baleanu, Kumam and Arif. This is an open-access article distributed under the terms of the Creative Commons Attribution License (CC BY). The use, distribution or reproduction in other forums is permitted, provided the original author(s) and the copyright owner(s) are credited and that the original publication in this journal is cited, in accordance with accepted academic practice. No use, distribution or reproduction is permitted which does not comply with these terms.

ORIGINAL RESEARCH
published: 27 January 2020
doi: 10.3389/fphy.2019.00215

Marangoni Driven Boundary Layer Flow of Carbon Nanotubes Toward a Riga Plate

Anum Shafiq[1], *Islam Zari*[2], *Ilyas Khan*[3]*, *Tahir Saeed Khan*[2], *Asiful H. Seikh*[4] and *El-Sayed M. Sherif*[4,5]

[1] School of Mathematics and Statistics, Nanjing University of Information Science and Technology, Nanjing, China, [2] Department of Mathematics, University of Peshawar, Peshawar, Pakistan, [3] Faculty of Mathematics and Statistics, Ton Duc Thang University, Ho Chi Minh City, Vietnam, [4] Centre of Excellence for Research in Engineering Materials, King Saud University, Riyadh, Saudi Arabia, [5] Electrochemistry and Corrosion Laboratory, Department of Physical Chemistry, National Research Centre, Cairo, Egypt

The objective of this article is to explore radiative Marangoni boundary layer flow of carbon nanotubes along a surface that is an electromagnetic actuator, such as a Riga surface. A comparative study is conducted to investigate the behavior of Lorentz forces on the basis of nanoparticle temperature fluxes with two different types of carbon nanotubes, namely single-wall carbon nanotube and multi-wall carbon nanotubes saturated into water as the base fluid. The proposed schemes of governing equations are then converted into ordinary differential equations by similarity transformation. One of best analytical methods, the homotopy analytical method, is utilized for the solution of the governing equations and the convergence of the control parameters. Embedded dimensionless parameters of the flow fields are examined via graphical illustrations. It is observed that an increase in the modified Hartmann number increases the velocity field but reduces the temperature distribution.

Keywords: Marangoni boundary layer flow, carbon nanotubes, Riga plate, thermal radiation, series solutions

OPEN ACCESS

Edited by:
Muhammad Mubashir Bhatti, Shanghai University, China

Reviewed by:
Arshad Riaz, University of Education Lahore, Pakistan
Anwar Shahid, International Islamic University, Islamabad, Pakistan

***Correspondence:**
Ilyas Khan
ilyaskhan@tdtu.edu.vn

Specialty section:
This article was submitted to Mathematical Physics, a section of the journal Frontiers in Physics

Received: *13 September 2019*
Accepted: *26 November 2019*
Published: *27 January 2020*

Citation:
Shafiq A, Zari I, Khan I, Khan TS, Seikh AH and Sherif E-SM (2020) Marangoni Driven Boundary Layer Flow of Carbon Nanotubes Toward a Riga Plate. Front. Phys. 7:215. doi: 10.3389/fphy.2019.00215

1. INTRODUCTION

Marangoni boundary layer flow phenomena are characterized by gradients in surface tension due to variations in surfactant concentration, concentration of solute, and variations in temperature along the interface. In light of the enhanced significance of surface forces and greater interface extensions, Marangoni boundary layer flows become pertinent in microgravity and in earth gravity. On the other hand, for a duly defined sufficient large Reynolds number, Marangoni boundary layers are edge dissipative flows and form thin dissipative films near unrestricted surfaces [1]. These types of flows have widespread application in diverse fields of engineering and practical projects such as for stabilizing soap films, drying silicon wafers after wrap processing steps, growing crystals, spreading thin films, nucleating vapor bubbles, processing semiconductors, and welding and for use in packed distillation columns, falling film spectator, artificial rain, and materials science. In view of their importance, many researchers have studied and reported results for these types of flows. The first contribution to this research area was by Napolitano [2] during his survey of steady dissipative layers. Lin and Zheng [3] theoretically investigated the problem of Marangoni boundary layer flow and heat transfer of copper-water nanofluid over a porous medium disk. They concluded that the Marangoni parameter has a destabilizing effect on all the other parameters such as temperature, shear stress, velocity, and boundary layer velocity. Moreover, to achieve an analytical solution of the said model, they employed the Homotopy Analysis Method (HAM). Recently, Tiwari et al. [4] presented a mathematical model for electrically conducting Marangoni MHD flow saturated with carbon nanotubes (CNTs) as the nanoparticles in a base fluid over a porous medium. An analytical method was adopted to achieve a solution for this project. A similarity solution of Marangoni convection boundary layer flow, taking into account the impacts of gravitational and external pressure, has been studied by Zhang and Zheng [5]. They showed that flow and heat transfer phenomena were substantially affected by the Marangoni convection parameter and the Prandtl number. A numerical method was adopted by Mehdi et al. to investigate the influence of different nanoparticles on Marangoni convection boundary layer flow [6]. The study showed that some nanoparticles with low thermal conductivity have a greater amplification effect on heat transfer phenomena than other recommended particles. Sheikholeslami and Ganji [7] considered Marangoni boundary layer flow to investigate the effect of the magnetic field on various nanofluids. The results illustrated that a Lorentz force increase causes the velocity of nanofluid to decrease. Remeli et al. [8] investigated suction and injection in a nanofluid via Marangoni-driven boundary layer flow. The effect of the injection parameter is to decrease the velocity profile, while the suction parameter increases the velocity profile and delays the separation of the boundary layer. The effects of particle shape on Marangoni convection boundary layer flow of a nanofluid were addressed by Ellahi et al. [9]. They considered different types of nanoparticles, such as needle-shaped, disc-shaped, and sphere-shaped. They discussed the said flow model in the context of nanoparticles and found that with an increase in the volume fraction and size of the particles, the surface temperature gradient fluctuated correspondingly. The maximum heat transfer rate at the surface was found in the case of sphere-shaped particles. Further, numerous studies on Marangoni boundary layer flow of several types can be found in the literature [10–12].

The characteristic of nanofluid of tremendously intensifying heat transfer and thermal convection has led to its broad application in innumerable fields, such as in biomedical devices and in highly advanced technical contexts such as the cooling of microchips, nanodrug delivery, nuclear reactions and radiators, etc. To reconcile the issues associated with high-temperature mixtures and to improve thermal conductivity in practice, nanoparticles are soaked into a base fluid. Many contributions have been made to the literature on nanoparticles that disseminate in the base fluid to attain excellent thermal properties [13–15]. According to Tiwari et al. [16], the adding of nanoparticles within a base fluid alone is not enough. CNTs had a six-times improved thermal conductivity compared to other nanomaterials [17]. Through the enhancement of various models of CNTs, these tubes have a wide span of properties such as thermal and electronic [18]. Similarly, solid nanoparticles have higher conductivity than do liquids. Therefore, CNTs are a topic of interest for advanced technology due to their electrical and isolated structure. In recent years, different applications of CNTs [19–21] have been investigated to develop ideal materials ranging from ultra-strong fibers to field emission. These tubes have extensive uses and applications in various fields such as providing increased energy density for capacitors, modeling the structures of catalysts, detecting proteins that indicate the existence of oral cancer, for gas storage, for water purification devices, for detecting bacteria in drinking water, for minimizing the weight of coaxial cable in aerospace applications, for improving battery lifetime, as an extra powerful fiber, etc. In this regard, Hayat et al. [22] utilized carbon nanotubes in water flow under homogenous-heterogeneous reactions and with melting heat transfer effects. Two different types of CNTs, i.e., SWCNT and MWCNT, were incorporated in water for the flow model. It was found that, in comparison with other nanofluids, the minimum thermal resistance and maximum heat transfer was achieved when MWCNT was disseminated in the base fluid. Moreover, the surface thickness of carbon nanotubes with heat transfers in stagnation point flow was examined by Hayat et al. [23].

From the last few decades, many researchers have turned their attention toward the study of flow fields with different configurations. One of the new geometries devised by Gailitis and Lielausis [24] for weakly conducting fluids is the so-called Riga plate. The novelty of this plate is that it incorporates and imposes magnetic and electric fields, which properly instigates Lorentz forces parallel to the wall to constrain the flow of weakly conducting fluid. Avoiding boundary layer separation, it may be utilized as an efficient agent for submarine pressure drag, skin friction, and radiation. The related theory has important features and is employed in many areas such as engineering, geophysics, astrophysics, industrial procedures, and MHD generators. Pantokratoras et al. [25] addressed boundary layer flow based on a weakly conducting fluid passing through a Riga plate. Their analysis demonstrated that by keeping quality, suitable size of nanoparticles, and adjusting the magnitude of flow, aiding and opposing Lorentz force due to the Riga plate in order to control the skin friction. Magyari and Pantokratoras [26] carried out an investigation to extend the idea of opposing and aiding mixed convection flows through a Riga plate. Further, Pantokratoras [27] addressed Blasius and Sakiadis type flows over a Riga plate. Hayat et al. [28] explored the flow of nanofluid through a convectively heated Riga plate with variable thickness. The results demonstrated that for larger values of the modified Hartman number, the velocity distribution exhibited decreasing behavior. Shafiq et al. [29] analyzed the impact of radiation in stagnation point flow of Walters' B fluid through a Riga plate. Their observations indicated that due to enhancement of the strength of Newtonian heating, the temperature and surface heat transfer significantly increased. Theoretical and numerical discussion by Bhatti et al. has shown the effects of thermal radiation with EMD through a Riga plate [30]. Further, a Cattaneo-Christov model for third-grade nanofluid flow toward a Riga plate has been developed by Naseem et al. [31] by using a semi-analytical method, i.e., the optimal homotopy analysis method (OHAM). The proposed theory was adopted together with the newly esteemed zero nanoparticles mass flux condition to investigate mass and thermal diffusions. Thermal radiation and heat transfer phenomena play a central role in advanced technological systems through boundary layer flow. The important applications of this flow in the aforementioned fields can be seen in the literature [32–34]. Henceforth, in various flow fields, the importance of thermal radiation cannot be overlooked. Non-linear radiation and Joule heating in Marangoni mixed convection flow were demonstrated by Hayat et al. [35]. The impact of exponential temperature on radiation effects and particle shape was examined by Lin et al. by utilizing heat transfer of copper water-based nanofluid and Marangoni boundary layer flow [36]. Hayat et al. [37] reported the effect of Joule heating and thermal radiation in the flow of third-grade fluid over a radiative surface. They studied whether the presence of an electric field and the radiation parameter caused the temperature and velocity to increase. A revised model of second-grade nanofluid magnetohydrodynamic Falkner Skan flow was examined by Hayat et al. [38]. A few other interesting investigations are given in Ellahi et al. [39–44], Bhatti et al. [30, 45, 46], Ellahi and Riaz [47], and Waqas et al. [48].

The main intention of the present study is to interpret radiative Marangoni-driven boundary layer flow utilizing different types of CNTs (SWCNTs and MWCNTs) over a Riga plate. To the best of our knowledge, such a study does not yet exist in the literature. Suitable transformations are utilized to establish a non-linear system of equations. The homotopy analysis method (HAM) is utilized for convergent series solutions. The impacts of several influential parameters on the physical quantities of interest are analyzed through tables and graphs. The upcoming sections illustrate the mathematical model and explore the effects of the different physical parameters on the velocity and temperature profiles, respectively.

2. MATHEMATICAL SCHEME OF THE PROBLEM

We consider Marangoni boundary layer flow of carbon-nanoliquids (SWCNTs and MWCNTs) toward a Riga surface along with radiation phenomenon. The Riga plate comprises a spanwise connected array of permanent magnets and irregular electrodes attached to a horizontal surface. Lorentz forces generated by the Riga plate and directed along the free stream are responsible for optimally controlling the proposed flow field. The base fluid, water, is packed with SWCNTs and MWCNTs. Further, the governing equations for the flow form may be expressed as (1–5):

$$\frac{\partial \breve{u}}{\partial \breve{x}} + \frac{\partial \breve{v}}{\partial \breve{y}} = 0, \tag{1}$$

$$\breve{u}\frac{\partial \breve{u}}{\partial \breve{x}} + \breve{v}\frac{\partial \breve{u}}{\partial \breve{y}} = \breve{u}_e \frac{d\breve{u}_e}{d\breve{x}} + \frac{\mu_{nf}}{\rho_{nf}}\frac{\partial^2 \breve{u}}{\partial \breve{y}^2} + \frac{\pi M_0 J_0 \, Exp[-\frac{\pi}{b}\breve{y}]}{8\rho_{nf}} - g\,\breve{\beta}(T - T_w), \tag{2}$$

$$\breve{u}\frac{\partial T}{\partial \breve{x}} + \breve{v}\frac{\partial T}{\partial \breve{y}} = \alpha_{nf}\frac{\partial^2 T}{\partial \breve{y}^2} - \frac{1}{(\rho c_p)_{nf}}\frac{\partial q_r}{\partial \breve{y}} + \frac{\mu}{(\rho c_p)_{nf}}\left(\frac{\partial \breve{u}}{\partial \breve{y}}\right)^2, \tag{3}$$

and the boundary conditions are set as

$$\breve{v} = 0, \quad T = T_0, \quad \frac{\mu_{nf}}{\mu_f}\frac{\partial \breve{u}}{\partial \breve{y}} = \frac{\partial T}{\partial \breve{x}} \quad \text{at } \breve{y} = 0,$$
$$\breve{u} = \breve{u}_e, \quad T = T_e \quad \text{at } \breve{y} \to \infty\,. \tag{4}$$

The velocity components in the $\breve{x}$ and $\breve{y}$ directions mentioned in the expressions are $\breve{u}$ and $\breve{v}$, the fluid density is denoted by ρ, the velocity of external flow is $\breve{u}_e(x)$, ρ_{nf} indicates the nanofluid density, μ_{nf} is the nanofluid dynamic viscosity, j_0 stands for the applied current density within the electrodes, M_0 is the magnetization of the permanent magnets, b indicates the width of the magnets and electrode, the constant temperature of the Riga plate is denoted by T_w where $T_w > 0$, K is the thermal conductivity, c_p represents the specific heat, μ is the dynamic viscosity, and T is the nanofluid temperature. The boundary temperature distribution is $T_0(x)$, and $(\rho c_p)_{nf}$ is the nanofluid heat capacity. The nanofluid effective density is α_{nf}. The radiative heat flux q_r is defined as

$$q_r = -\frac{4\sigma^*}{3k_1}\frac{\partial T^4}{\partial \breve{y}}, \tag{5}$$

where σ^* is the Stefan-Boltzmann constant and k_1 is the mean absorption coefficient. Through Taylor's series, we have $T^4 \cong 4T_e^3 T - 3T_e^4$, where T_e is the ambient temperature, and then energy equation now reduces to the following expression:

$$(\rho c_p)_{nf}\left(\breve{u}\frac{\partial T}{\partial \breve{x}} + \breve{v}\frac{\partial T}{\partial \breve{y}}\right) = \left(\frac{16\sigma^* T_\infty^3}{3k_1} + K\right)\frac{\partial^2 T}{\partial \breve{y}^2} + \mu\left(\frac{\partial \breve{u}}{\partial \breve{y}}\right)^2. \tag{6}$$

Moreover, the mathematical properties of CNTs are demonstrated by the following Equation (19–22)

$$\alpha_{nf} = \frac{k_{nf}}{(\rho c_p)_{nf}}, \; \mu_{nf} = \frac{\mu_f}{(1-\phi)^{2.5}}, \; \breve{v}_{nf} = \frac{\mu_{nf}}{\rho_{nf}},$$
$$\frac{k_{nf}}{k_f} = \frac{2\phi\frac{\breve{k}_{CNT}}{k_{CNT} - k_f}\ln\frac{\breve{k}_{CNT} + \breve{k}_f}{2\breve{k}_f} + (1-\phi)}{2\phi\frac{\breve{k}_f}{k_{CNT} - k_f}\ln\frac{\breve{k}_{CNT} + \breve{k}_f}{2\breve{k}_f} + (1-\phi)},$$
$$\rho_{nf} = \rho_f(1-\phi) + \rho_s(c_p)_{CNT}\,\phi\,, \tag{7}$$

where $\breve{k}_f$ is the fluid thermal conductivity, k_{nf} is the nanofluid thermal conductivity, the nanofluid solid volume fraction is ϕ, and μ_f is the fluid dynamic viscosity. $\frac{\hat{\mu}_{nf}}{\hat{\mu}_f}\frac{\partial u}{\partial y}\Big|_{y=0} = \frac{\partial T}{\partial x}\Big|_{y=0}$ denotes Marangoni condition at the interface. The linear relation of surface tension σ is given as:

$$\sigma = \sigma_0\left[1 - \gamma_1\left(T - T_e\right)\right]\,, \tag{8}$$

where $\gamma_1 = -\frac{1}{\sigma_0}\frac{\partial \sigma}{\partial T} > 0$ represents the surface tension temperature coefficient, and σ_0 represents surface tension. The directions of the driving forces depend on the orientation of the temperature gradients in nanoliquids ∇T.

The similarity transformation is introduced:

$$u(x,y) = u_0 x^{(2r-1)/3} f'(\eta),$$
$$v(x,y) = \frac{1}{3} u_0 l_0 x^{(r-2)/3}\left[(2-r)\eta f'(\eta) - (1+r) f(\eta)\right],$$
$$T(x,y) = T_e - h_0 x^r \theta(\eta), \quad \eta = x^{(r-2)/3}\frac{y}{l_0}, \tag{9}$$

where h_0, u_0, and l_0 represent constants. The values of u_0 and l_0 take the following form when $h_0 = 1$:

$$u_0 = \left(\frac{3}{1+r}\right)^{1/3} r^{2/3}, \quad l_0 = \left(\frac{3}{1+r}\right)^{1/3} r^{-1/3}, \tag{10}$$

after the above-mentioned transformations, Equations (1)–(6) take the following form:

$$\frac{1}{(1-\phi)^{2.5}(1-\phi+\frac{\rho_{CNT}}{\rho_f}\phi)} f''' + ff'' - (\frac{2r-1}{1+r})[(f')^2 - 1] + \frac{3}{1+r}\lambda\theta(\eta) + \frac{3}{1+r} Q\, Exp[-c\eta] = 0, \tag{11}$$

$$\left(1+\frac{4}{3}R\right)\frac{\frac{k_{nf}}{k_f}}{[(1-\phi)+\frac{(\rho c_p)_{CNT}}{(\rho c_p)_f}\phi]}\theta'' - \frac{3}{1+r}\Pr\left[rf'\theta - \frac{1+r}{3} f\,\theta'\right] - \Pr\ Ec\,(f'')^2 = 0, \tag{12}$$

in which

$$Q = \frac{\pi M_0 J_0 \breve{x}}{8\rho_{nf}\breve{u}_e^2}, \quad R = \frac{4\sigma^3 T_\infty^3}{3k_{nf}k^*}, \quad \Pr = \frac{c_p\mu}{k}, \quad Ec = \frac{\breve{u}_e^2\ \breve{x}^{\frac{1}{3}(r-2)}}{\rho\ c_p^2 h_0}, \tag{13}$$

where Q denotes the modified Hartmann number, R represents the radiation parameter, Pr indicates the Prandtl number, and Ec symbolizes the Eckert number.

3. SOLUTION METHODOLOGY

To find the series solution of the underlying problem, the Homotopy Analysis Method is adopted. Therefore, the auxiliary linear operators $(\mathcal{I}_f, \mathcal{I}_\theta)$ and the initial guess $(\left(\breve{f}_0, \breve{\theta}_0\right))$ may be defined as:

$$\breve{f}_0(\eta) = \eta + (1-\phi)^{2.5}(1-e^{-\eta}), \quad \breve{\theta}_0(\eta) = e^{-\eta}, \tag{14}$$

$$\mathcal{I}_\theta(\breve{\theta}) = \frac{d^2\breve{\theta}}{d\eta^2} - \breve{\theta}, \quad \mathcal{I}_f(\breve{f}) = \frac{d^3\breve{f}}{d\eta^3} - \frac{d\breve{f}}{d\eta}, \tag{15}$$

$$\mathcal{I}_f[K_1 + K_2 Exp(\eta) + K_3 Exp(-\eta)] = 0,$$
$$\mathcal{I}_\theta[K_4 Exp(\eta) + K_5 Exp(-\eta)] = 0, \tag{16}$$

where K_h $(h = 1-5)$ are arbitrary constants.

The zeroth-order problem design is

$$(1-\breve{p})\mathcal{I}_f[\breve{f}(\eta,\breve{p}) - \breve{f}_0(\eta)] = \breve{p}\hbar_f \mathcal{M}_f\left[\breve{f}(\eta,\breve{p})\right], \tag{17}$$

$$\left.\frac{\partial\breve{f}(\eta;\breve{p})}{\partial\eta}\right|_{\eta=0} = 0, \quad \frac{1}{(1-\phi)^{2.5}}\left.\frac{\partial^2\breve{f}(\eta;\breve{p})}{\partial\eta^2}\right|_{\eta=0} = -1, \quad \left.\frac{\partial\breve{f}(\eta;\breve{p})}{\partial\eta}\right|_{\eta\to\infty} = 1, \tag{18}$$

$$(1-\breve{p})\mathcal{I}_\theta[\breve{\theta}(\eta,\breve{p}) - \breve{\theta}_0(\eta)] = \breve{p}\hbar_\theta \mathcal{M}_\theta\left[\breve{\theta}(\eta,\breve{p}), \breve{f}(\eta,\breve{p})\right], \tag{19}$$

$$\left.\breve{\theta}(\eta;\breve{p})\right|_{\eta=0} = 1, \quad \left.\breve{\theta}(\eta;\breve{p})\right|_{\eta\to\infty} = 0, \tag{20}$$

The non-linear operators are

$$\mathcal{M}_f\left[\breve{f}(\eta;\breve{p})\right] = \frac{1}{(1-\phi)^{2.5}[1-\phi+\frac{(\tilde{\rho}c_p)_{CNT}}{(\tilde{\rho}c_p)_f}\phi]}\frac{\partial^3\breve{f}(\eta,\breve{p})}{\partial\eta^3} + \breve{f}(\eta,\breve{p})\frac{\partial^2\breve{f}(\eta,\breve{p})}{\partial\eta^2} - \frac{2r-1}{1+r}\left(\frac{\partial\breve{f}(\eta,\breve{p})}{\partial\eta}\right)^2 + \frac{2r-1}{1+r} + \frac{3}{1+r}\lambda\theta(\eta) + \frac{3}{1+r} Q\, Exp[-c\eta\ ], \tag{21}$$

$$\mathcal{M}_\theta\left[\breve{f}(\eta;\breve{p}), \breve{\theta}(\eta;\breve{p})\right] = \left(1+\frac{4}{3}R_d\right)\frac{\frac{k_{nf}}{k_f}}{[1-\phi+\frac{(\tilde{\rho}c_p)_{CNT}}{(\tilde{\rho}c_p)_f}\phi]}\frac{\partial^2\breve{\theta}(\eta,\breve{p})}{\partial\eta^2} - \frac{3}{1+r}\Pr\left[r\frac{\partial\breve{f}(\eta,\breve{p})}{\partial\eta}\breve{\theta}(\eta,\breve{p})\right] - \frac{3}{1+r}\Pr\left[-\frac{1+r}{3}\breve{f}(\eta,\breve{p})\frac{\partial\breve{\theta}(\eta,\breve{p})}{\partial\eta}\right] - \Pr\ Ec\left(\frac{\partial^2\breve{f}(\eta,\breve{p})}{\partial\eta^2}\right)^2, \tag{22}$$

where, $0 \le \breve{p} \le 1$ and $\hbar_f$ and $\hbar_\theta$ designate zero free auxiliary parameters.

The mth-order deformation problem is

$$\mathcal{I}_f\left[\breve{f}_m(\eta) - \breve{\chi}_m\breve{f}(\eta)\right] = \hbar_f\mathcal{P}_m^{\breve{f}}(\eta), \tag{23}$$

$$\left.\frac{\partial^2\breve{f}_m(\eta,\breve{p})}{\partial\eta^2}\right|_{\eta=0} = 0, \quad \left.\frac{\partial\breve{f}_m(\eta,\breve{p})}{\partial\eta}\right|_{\eta\to\infty} = 0, \quad \left.\breve{f}_m(\eta;\breve{p})\right|_{\eta=0} = 0, \tag{24}$$

$$\mathcal{I}_\theta\left[\breve{\theta}_m(\eta) - \breve{\chi}_m\breve{\theta}_{m-1}(\eta)\right] = \hbar_\theta\mathcal{P}_m^{\breve{\theta}}(\eta), \tag{25}$$

$$\left.\breve{\theta}_m(\eta;\breve{p})\right|_{\eta=0} = 0, \quad \left.\breve{\theta}_m(\eta;\breve{p})\right|_{\eta\to\infty} = 0, \tag{26}$$

$$\mathcal{P}_m^{\breve{f}}(\eta) = \frac{1}{(1-\phi)^{2.5}[1-\phi+\frac{\rho_{CNT}}{\rho_f}\phi]} f'''_{m-1}(\eta) - \sum_{k=0}^{m-1} f_{m-1-k} f''_k - \frac{2r-1}{1+r}\left[\sum_{k=0}^{m-1} f_k f'_{m-1-k} - (1-\chi_m)\right] + \frac{3}{1+r}\lambda\theta_{m-1}(\eta) + \frac{3}{1+r} Q\, Exp[-c\eta], \quad (27)$$

$$\mathcal{P}_m^{\breve{\theta}}(\eta) = \left(1+\frac{4}{3}R_d\right)\frac{\frac{\tilde{k}_{nf}}{k_f}}{[1-\phi+\frac{(\rho c_p)_{CNT}}{(\rho c_p)_f}\phi]}\theta''_{m-1}(\eta) - \frac{3}{1+r}\Pr\sum_{k=0}^{m-1}\left[r f'_k\theta_{m-1-k} - \frac{1+r}{3} f_{m-1-k}\theta'_k\right] - \Pr Ec\sum_{k=0}^{m-1} f'_{m-1-k} f'_k, \quad (28)$$

where

$$\breve{\chi}_m = \begin{cases} 0, m \le 1 \\ 1, m > 1 \end{cases}. \quad (29)$$

For $\breve{p} = 0$ and $\breve{p} = 1$, we have

$$\breve{f}(\eta, 0) = \breve{f}_0(\eta), \quad \breve{f}(\eta, 1) = \breve{f}(\eta), \quad (30)$$

$$\breve{\theta}(\eta, 0) = \breve{\theta}_0(\eta), \quad \breve{\theta}(\eta, 1) = \breve{\theta}(\eta). \quad (31)$$

The solutions $\breve{f}(\eta;\breve{p})$ and $\breve{\theta}(\eta;\breve{p})$ vary from the primary solutions $\breve{f}_0(\eta)$ and $\breve{\theta}_0(\eta)$ to the final solutions $\breve{f}(\eta)$ and $\breve{\theta}(\eta)$, respectively, where $\breve{p}$ differs from 0 to 1. The Taylor series expansion follows:

$$\breve{f}(\eta, \breve{p}) = \breve{f}_0(\eta) + \sum_{m=1}^{\infty}\breve{f}_m(\eta)\breve{p}^m, \ \breve{f}_m(\eta) = \frac{1}{m!}\left.\frac{\partial^m \breve{f}_m(\eta, \breve{p})}{\partial\breve{p}^m}\right|_{\breve{p}=0}, \quad (32)$$

$$\breve{\theta}(\eta, \breve{p}) = \breve{\theta}_0(\eta) + \sum_{m=1}^{\infty}\theta_m(\eta)\breve{p}^m, \ \breve{\theta}_m(\eta) = \frac{1}{m!}\left.\frac{\partial^m \breve{\theta}(\eta, \breve{p})}{\partial\breve{p}^m}\right|_{\breve{p}=0}. \quad (33)$$

The above series solutions converge if the auxiliary parameters are properly nominated. Therefore,

$$\breve{f}(\eta) = \breve{f}_0(\eta) + \sum_{m=1}^{\infty}\breve{f}_m(\eta), \quad (34)$$

$$\breve{\theta}(\eta) = \breve{\theta}_0(\eta) + \sum_{m=1}^{\infty}\breve{\theta}_m(\eta), \quad (35)$$

The general solutions $\left(\breve{f}_m, \breve{\theta}_m\right)$ via special solutions $\left(f_m^{\times}, \theta_m^{\times}\right)$ are

$$\breve{f}_m(\eta) = f_m^{\times}(\eta) + K_1 + K_2 Exp(\eta) + K_3 Exp(-\eta), \quad (36)$$

$$\breve{\theta}_m(\eta) = \theta_m^{\times}(\eta) + K_4 Exp(\eta) + K_5 Exp(-\eta), \quad (37)$$

where K_h $(h = 1-5)$ are the elaborated constants.

4. CONVERGENCE OF SERIES SOLUTIONS

The convergence phenomenon of HAM solution is dependent on auxiliary parameters $\hbar_f$ and $\hbar_\theta$, which control and adjust the convergence of the derived series solution. Therefore, $\hbar-$ curves are portrayed in **Figures 2A,B** for different values of the physical parameters in terms of SWCNT and MWCNT. The suitable values of these parameters $\hbar_f$ and $\hbar_\theta$ are $-0.78 \le \hbar_f < -0.19$, $-0.19 \le \hbar_\theta < -0.03$ for SWCNT and $-0.66 \le \hbar_f < -0.1$, $-0.22 \le \hbar_\theta < -0.01$ for MWCNT.

5. DISCUSSION

The major contribution of this section is to explore the physical influence of different dimensionless parameters on the velocity and temperature profiles. A physical sketch of the problem is given in **Figure 1**. The graphs in **Figures 3–11** depict the results of the comprehensive analysis. We divide this section into three subsections for simplicity and clarity. In the first subsection, exploration is made of the physical impact of various parameters on the velocity profile. A discussion of the effects of the same parameters along with the radiation parameter on the temperature profile is given in the next subsection. The third subsection is based on the performance of the Nusselt number under the influence of different parameters.

The impact of fluid parameter r on the velocity profile is illustrated in **Figure 3** for both SWCNT and MWCNT. The velocity distribution is noted to decrease with the intensification of parameter r. Further, the velocity profile is seen to be higher in the case of MWCNT with a base fluid of water. **Figure 4** is plotted to indicate the effect of the nanofluid solid volume fraction ϕ for both SWCNT and MWCNT. It is shown that the velocity distribution increases with the enhancement of the nanofluid volume fraction. In addition, a stronger response is seen with MWCNT than with SWCNT. This is due to the low density of MWCNT. **Figures 5**, **6** display the effects of variation in the convection parameter λ on the velocity profile in both opposing ($\lambda < 0$) and assisting ($\lambda > 0$) flows. Under these circumstances, the velocity profile and the momentum boundary layer thickness exhibit increasing behavior with the buoyancy

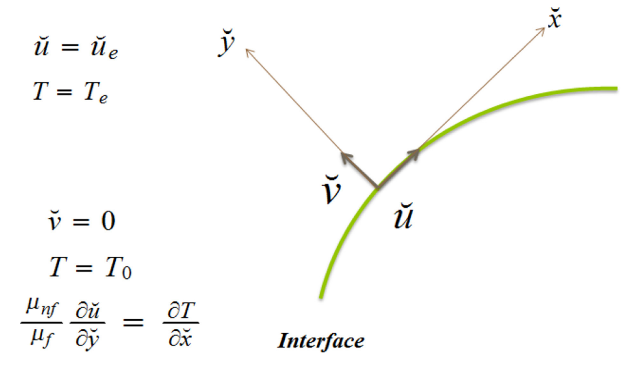

FIGURE 1 | Physical model of the problem.

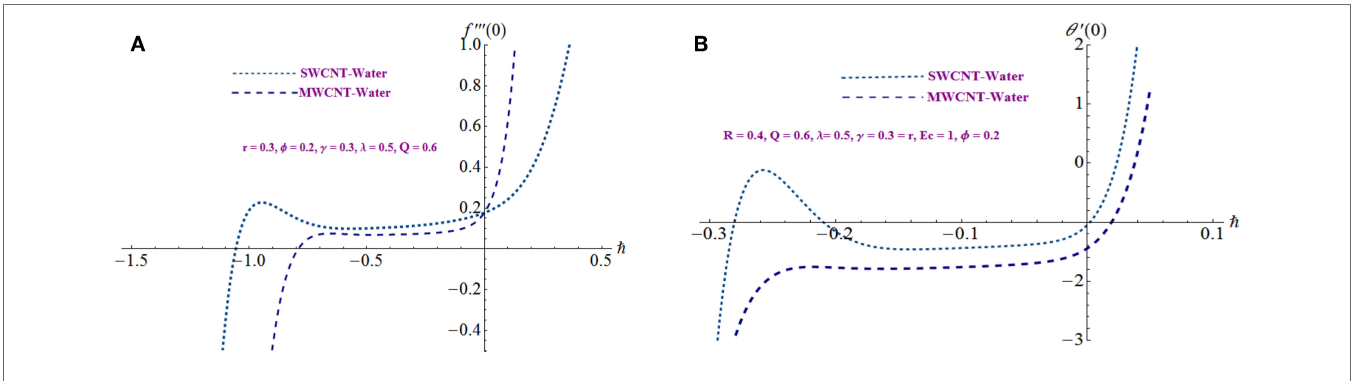

FIGURE 2 | (A) $\hbar$−curve for $f'''(0)$. **(B)** $\hbar$−curve for $\theta'(0)$.

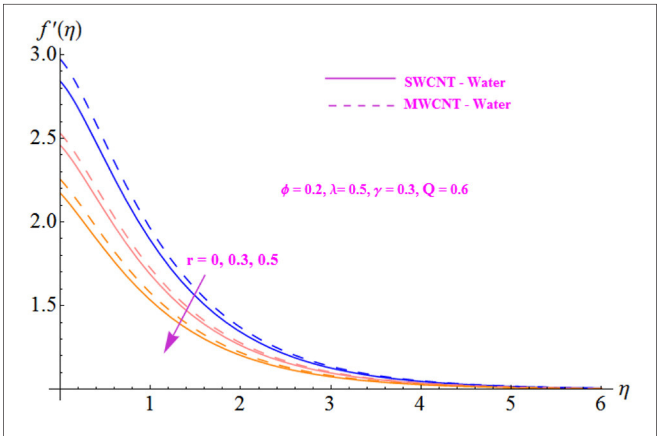

FIGURE 3 | Significance of r on $f'(\eta)$.

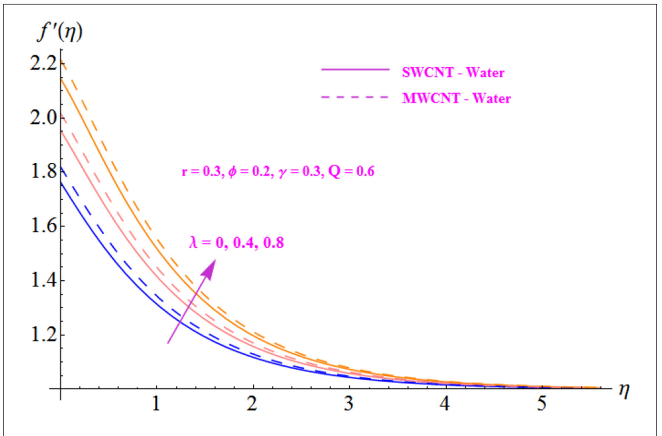

FIGURE 5 | Significance of λ on $f'(\eta)$.

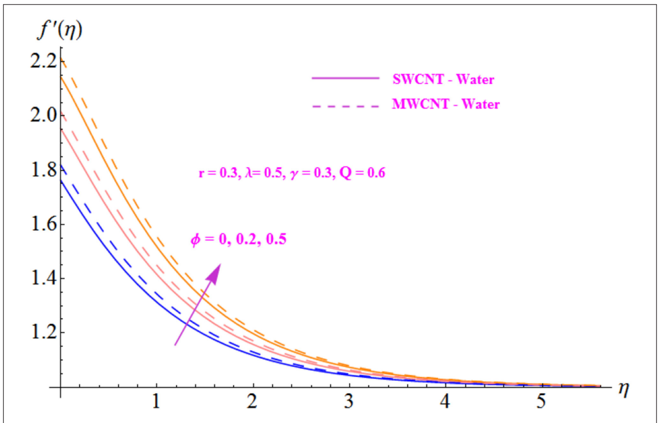

FIGURE 4 | Significance of ϕ on $f'(\eta)$.

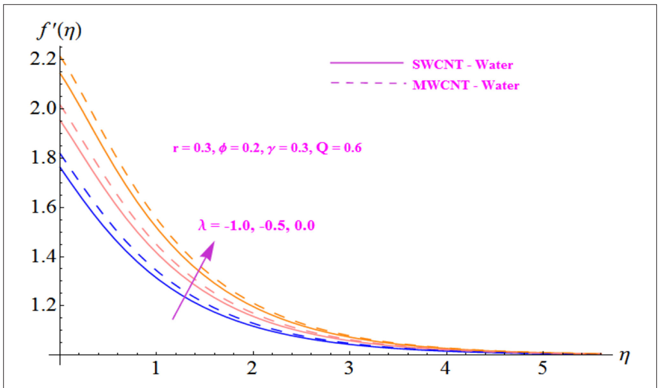

FIGURE 6 | Significance of λ on $f'(\eta)$.

parameter for both SWCNT and MWCNT. Basically, the mixed convection may be defined as the ratio of buoyancy forces to inertial forces. The reason behind enhancement in the velocity of the fluid is the buoyancy force, which influences the inertial force, increasing the value of the mixed convection parameter. Moreover, MWCNT shows an increasing trend throughout the field in comparison to SWCNT. The effect of the Hartmann number Q on the velocity profile is shown in **Figure 7** for both SWCNT and MWCNT. Physically, an increase in the modified Hartmann number increases the velocity field. The structure of the Hartmann number is the ratio of electromagnetic force to viscous force. Since the increasing phenomenon of the velocity profile is dependent on an increase in Q, this indicates development in the Lorentz force, which is generated by the presence of a magnetic field in the flow field and acts against the flow if the magnetic field is applied in the normal direction. The significance of the modified Hartmann number Q is exhibited in **Figure 8** for both SWCNT and MWCNT. An increment in the Hartmann number correlates with a reduction in the temperature distribution.

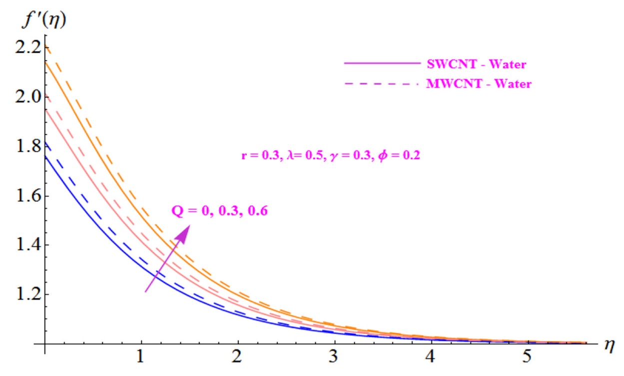

FIGURE 7 | Significance of Q on $f'(\eta)$.

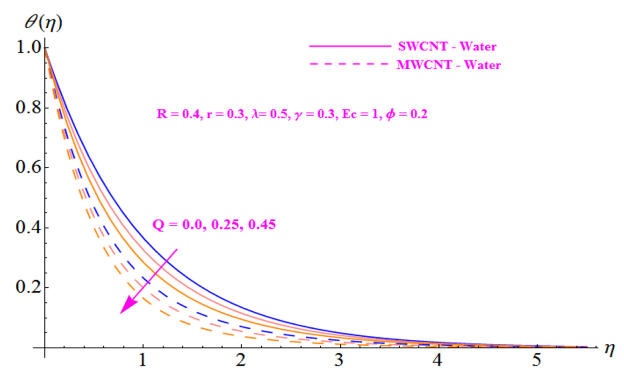

FIGURE 8 | Significance of Q on $\theta(\eta)$.

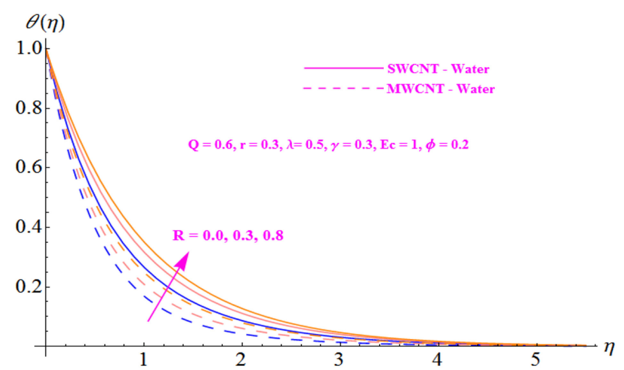

FIGURE 9 | Significance of R on $\theta(\eta)$.

The effect of variation of radiative parameter R on temperature profile $\theta(\eta)$ is plotted in **Figure 9** for both MWCNT and SWCNT. The behavior inferred from this figure is that there is an enhancement in temperature distribution and in the related boundary layer thickness due to the increment in R. Hence, the temperature profile is an increasing function of the radiative parameter. Hence, the enhancement in the temperature profile due to an increase in the radiative parameter causes a reduction in the absorption coefficient. Further, SWCNT shows a stronger response compared with MWCNT.

The physical effect of fluid parameter r on the velocity field is depicted in **Figure 10** for both SWCNT and MWCNT. The velocity profile is noted to increase with escalation in parameter

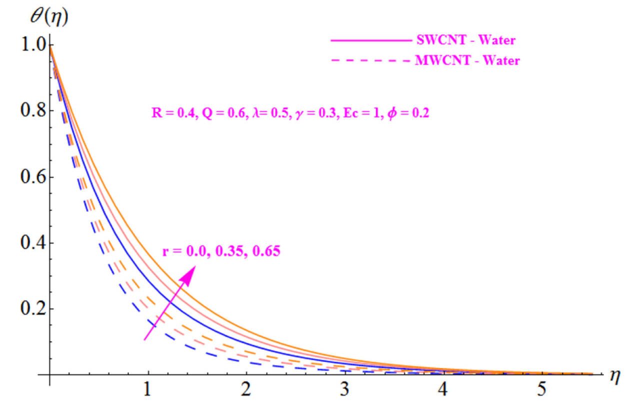

FIGURE 10 | Significance of r on $\theta(\eta)$.

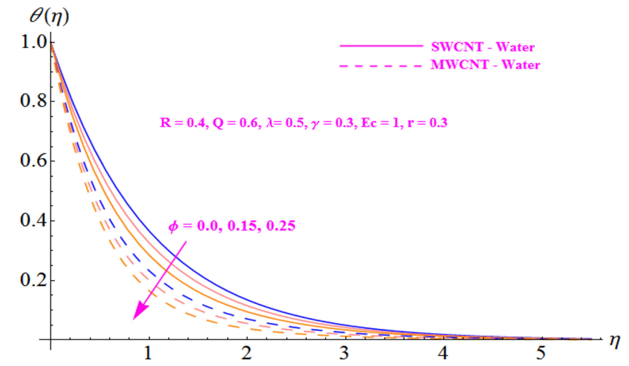

FIGURE 11 | Significance of ϕ on $\theta(\eta)$.

TABLE 1 | Thermophysical characteristics of base fluid and nanoparticles (SWCNT and MWCNT).

Physical properties	Base fluid	Nanoparticle	
	Water	SWCNT	MWCNT
ρ (kg/m^3)	997	2,600	1,600
c_p (J/kgK)	4,179	425	796
k (W/mK)	0.613	6,600	3,000

TABLE 2 | Convergence of homotopy solutions when $\alpha = 0.01$, $\beta = 0.1$, $\gamma = 0.1$, $\delta = 0.3$, $M = 0.1$, $Re = 2$, $\Pr = 6.2$, $Ec = 0.1$, and $\hbar_f = \hbar_\theta = -0.7$.

Order of approximation	$-f'''(0)$		$-\theta'(1)$	
	SWCNT	MWCNT	SWCNT	MWCNT
1	0.6233	0.6377	0.8953	0.8222
2	1.5232	1.5591	0.9254	0.8660
5	1.6222	1.6602	0.9465	0.8824
10	1.7655	2.5195	1.5623	0.9520
15	1.7863	2.5195	1.5832	1.0323
20	2.5462	2.5195	1.6322	1.0323
27	2.5462	2.5195	1.6322	1.0323
30	2.5462	2.5195	1.6322	1.0323
40	2.5462	2.5195	1.6322	1.0323

TABLE 3 | Numerical values of the Nusselt number for both SWCNT and MWCNT at different values of other parameters.

r	λ	Q	ϕ	R	γ	$Re_x Nu$	
						SWCNT	MWCNT
0.1	0.2	0.5	0.5	0.5	0.3	3.0955	5.2872
0.2						2.8231	3.7121
0.3						1.8597	2.2123
0.2	0.0	0.5	0.5	0.5	0.3	2.5732	2.3426
	0.1					1.4831	1.3842
	0.2					1.1492	0.9625
0.3	0.4	0.0	0.5	0.5	0.3	0.4428	0.5424
		0.2				1.4074	1.5421
		0.4				1.5945	1.6442
0.2	0.2	0.2	0.1	0.5	0.3	5.1262	4.2354
			0.2			3.5624	3.3298
			0.3			2.5121	2.2133
0.1	0.2	0.2	0.5	0.0	0.3	3.8691	2.9894
				0.2		5.4701	4.3278
				0.5		6.0772	5.9985
0.1	0.2	0.2	0.5	0.5	0.0	1.8691	2.3287
					0.1	2.1682	2.8652
					0.2	3.6253	3.7536

r. **Figure 11** depicts the influence of the nanofluid solid volume fraction ϕ for both SWCNT and MWCNT. It is observed that with the augmentation of the nanofluid volume fraction, the velocity profile shows a reduction.

Table 1 presents the thermophysical properties (density, specific heat, and thermal conductivity) of the base fluid (water) and carbon nanotubes (SWCNT and MWCNT). **Table 2** shows that the series solutions are convergent up to four decimal places for the velocity profile at the 10th order of approximation for MWCNT and at the 20th order of approximation for SWCNT. Similarly, for the case of the temperature field, the 20th order of approximation for SWCNT and 15th order of approximation for MWCNT were observed for convergence. Further, **Table 3** displays the behavior of the local Nusselt number for different values of physical parameters such as fluid parameter r, convection parameter λ, Hartman number Q, volume fraction ϕ, radiative parameter R , and parameter γ. The desired results were observed for both SWCNT and MWCNT. It is concluded that the Nusselt number shows decreasing behavior for larger values of r, λ, and ϕ in the cases of both SWCNT and MWCNT. On the other hand, the Nusselt number shows stronger behavior for larger values of Q, R , and γ for both SWCNT and MWCNT.

6. FINAL OBSERVATION

The key points are as follows:

- Increment in the velocity profile is based on increases in the modified Hartmann number, buoyancy-assisting flow parameter, and solid volume fraction.
- The velocity profile for water-based MWCNT is higher than that for SWCNT for all of the discussed fluid parameters.
- Enhancement in parameter r results in a reduction in the velocity distribution.
- Augmentation in the temperature field is based on increment in the radiative parameter, whereas the Hartmann number, buoyancy-assisting flow parameter, and solid volume fraction have the opposite effect on the temperature profile to the radiative parameter.
- SWCNT shows excellent agreement with the temperature distribution than MWCNT for all proposed fluid parameters.
- For larger values of Q, R , and γ, the local Nusselt number increases for both SWCNT and MWCNT.
- The Nusselt number illustrates decreasing behavior for larger values of r, λ, and ϕ in the cases of SWCNT and MWCNT.

DATA AVAILABILITY STATEMENT

The raw data supporting the conclusions of this article will be made available by the authors, without undue reservation, to any qualified researcher.

AUTHOR CONTRIBUTIONS

AS formulated the problem. IZ solved the problem. TK computed the results. IK discussed the results with the conclusion. All authors contributed to writing the manuscript.

ACKNOWLEDGMENTS

The authors would like to extend their sincere appreciation to the Deanship of Scientific Research at King Saud University for its funding of this research through Researchers Supporting Project number (RSP-2019/33), King Saud University, Riyadh, Saudi Arabia. AS was supported by the Talented Young Scientist Program of Ministry of Science and Technology of China (Pakistan-19-007).

REFERENCES

1. Pop I, Postelnicu A, Grosan T. Thermasolutal marangoni forced convection boundary layers. *Meccanica*. (2001) **36**:555–71. doi: 10.1023/A:1017431224943
2. Napolitano LG. Marangoni boundary layers. *Mater Sci Space*. (1979) 349–58.
3. Lin Y, Zheng L. Marangoni boundary layer flow and heat transfer of copper-water nanofluid over a porous medium disk. *AIP Adv*. (2015) **5**:107225. doi: 10.1063/1.4934932
4. Tiwari AK, Raza F, Akhtar J. Mathematical model for Marangoni convection MHD flow of CNTs through a porous medium. *J Adv Res Appl Sci*. (2017) **4**:216–22.
5. Zhang Y, Zheng L. Similarity solutions of Marangoni convection boundary layer flow with gravity and external pressure. *Chin J Chem Eng*. (2014) **22**:365–9. doi: 10.1016/S1004-9541(14)60040-9
6. Mehdi M, Hosein M, Samareh R, Poor HM. Numerical study on the effects of Marangoni driven boundary layer flow for different nanoparticales with variable based fluids. *J Int Acad Res Multidiscip*. (2014) **2**:2320–5083.
7. Sheikholeslami M, Ganji DD. Influence of magnetic field on Cu Oe H2O nanofluid flow considering Marangoni boundary layer. *Int J Hydr Energy*. (2017) **42**:821–9. doi: 10.1016/j.ijhydene.2016.09.121
8. Remeli A, Arifin NM, Nazar R, Ismail F, Pop I. Marangoni-driven boundary layer flow in a nanofluid with suction and injection. *World Appl Sci J*. (2012) **17**:21–6. doi: 10.1186/2251-7456-6-21
9. Ellahi R, Zeeshan A, Hassan M. Particle shape effects on Marangoni convection boundary layer flow of a nanofluid. *Int J Numer Methods Heat Fluid Flow*. (2016) **26**:2160–74. doi: 10.1108/HFF-11-2014-0348
10. Christopher DM, Wang B. Prandtl number effects for Marangoni convection over a flat surface. *Int J Ther Sci*. (2001) **40**:564–70. doi: 10.1016/S1290-0729(01)01244-3
11. Mudhaf A, Chamkha AJ. Similarity solutions for MHD thermosolutal Marangoni convection over a flat surface in the presence of heat generation or absorption effects. *Heat Mass Transf*. (2005) **42**:112–21. doi: 10.1007/s00231-004-0611-8
12. Magyari E, Chamkha AJ. Exact analytical results for the thermosolutal MHD marangoni boundary layers. *Int J Ther Sci*. (2008) **47**:848–57. doi: 10.1016/j.ijthermalsci.2007.07.004
13. Hayat T, Qayyum S, Alsaedi A, Shafiq A. Inclined magnetic field and heat source/sink aspects in flow of nanofluid with nonlinear thermal radiation. *Int J Heat Mass Transf*. (2016) **103**:99–107. doi: 10.1016/j.ijheatmasstransfer.2016.06.055
14. Hayat T, Mumtaz M, Shafiq A, Alsaedi A. Stratified magnetohydrodynamic flow of tangent hyperbolic nanofluid induced by inclined sheet. *Appl Math Mech*. (2017) **38**:271–88. doi: 10.1007/s10483-017-2168-9
15. Shafiq A, Hammouch Z. Bioconvective MHD flow of tangent hyperbolic nanofluid with newtonian heating. *Int J Mech Sci*. (2017) **133**:759–66. doi: 10.1016/j.ijmecsci.2017.07.048
16. Khan A, Khan D, Khan I, Ali F, Karim F, Nisar KS. MHD flow of brinkman type H_2O-Cu, Ag, TiO_2 and Al_2O_3 nanofluids with chemical reaction and heat generation effects in a porous medium. *J Magnet*. (2019) **24**:262–70. doi: 10.4283/JMAG.2019.24.2.262
17. Murshd SMS, Leong KC, Yang C. Enhanced thermal conductivity of TiO2- Water based nanofluid. *Int J Ther Sci*. (2005) **4**:367–73. doi: 10.1016/j.ijthermalsci.2004.12.005
18. Oberlin A, Endo M, Koyama T. Filamentous growth of carbon though benzene decomposition. *J Cryst Growth*. (1976) **32**:335–9. doi: 10.1016/0022-0248(76)90115-9
19. Baughman RH, Zakhidov AA, Heer WA. Carbon nanotubes- the route toward applications. *Science*. (2002) **297**:787–92. doi: 10.1126/science.1060928
20. Ericson LM, Fan H, Peng H, Davis VA, Zhou W. Macroscopic neat single-walled carbon nanotube fibers. *Science*. (2004) **305**:1447–50. doi: 10.1126/science.1101398
21. Milne IW, Teo KB, Amaratunga GA, Legagneux P, Gangloff L, Schnell P. Carbon nanotubes as field emission sources. *J Mat Chem*. (2004) **14**:933–43. doi: 10.1039/b314155c
22. Hayat T, Hussain Z, Alsaedi A, Ahmad A. Heterogeneous-homogeneous reactions and melting heat transfer effects in flow with carbon nanotubes. *J Mol Liquids*. (2016) **220**:200–7. doi: 10.1016/j.molliq.2016.04.012
23. Hayat T, Khursheed M, Farooq M, Alsaedi A. Melting heat transfer in stagnation point flow of carbon nanotubes towards variable thickness surface. *AIP Adv*. (2016) **6**:015214. doi: 10.1063/1.4940932
24. Gailitis A, Lielausis O. On a possibility to reduce the hydrodynamic resistance of a plate in an electrolyte. *Appl Magnetohydrodyn*. (1961) **12**:143–6.
25. Pantokratoras A, Magyari E. EMHD free-convection boundary-layer flow from a Riga-plate. *J Eng Math*. (2009) **64**:303–15. doi: 10.1007/s10665-008-9259-6
26. Magyari E, Pantokratoras A. Aiding and opposing mixed convection flows over the Riga plate. *Commun Nonlin Sci Numer Simulat*. (2011) **16**:3158–67. doi: 10.1016/j.cnsns.2010.12.003
27. Pantokratoras A. The Blasius and Sakiadis flow along a Riga-plate. *Prog Comput Fluid Dyn*. (2011) **11**:329–33. doi: 10.1504/PCFD.2011.042184
28. Hayat T, Abbas M, Ayub M, Farooq M, Alsaedi A. Flow of nanofluid due to convectively heated Riga plate with variable thickness. *J Mol Liquids*. (2016) **222**:854–62. doi: 10.1016/j.molliq.2016.07.111
29. Shafiq A, Hammouch Z, Turab A. Impact of radiation in a stagnation point flow of Walters' B fluid towards a Riga plate. *Ther Sci Eng Prog*. (2017) **6**:27–33. doi: 10.1016/j.tsep.2017.11.005
30. Bhatti MM, Abbas T, Rashidi MM. Effects of thermal radiation and electromagnetohydrodynamics on viscous nanofluid through a Riga plate. *Multidiscip Model Mater Struct*. (2016) **12**:605–18. doi: 10.1108/MMMS-07-2016-0029
31. Naseem A, Shafiq A, Zhao L, Farooq MU. Analytical investigation of third grade nanofluidic flow over a Riga plate using Cattaneo-Christov model. *Results Phys*. (2018) **9**:961–9. doi: 10.1016/j.rinp.2018.01.013
32. Hayat T, Jabeen S, Shafiq A, Alsaedi A. Radiative squeezing flow of second grade fluid with convective boundary conditions. *PLoS ONE*. (2016) **11**:e0152555. doi: 10.1371/journal.pone.0152555
33. Sheikholeslamia M, Hayat T, Alsaedi A. MHD free convection of Al_2 O_3 – water nanofluid considering thermal radiation: a numerical study. *Int J Heat Mass Transf*. (2016) **96**:513–24. doi: 10.1016/j.ijheatmasstransfer.2016.01.059
34. Hayat T, Shehzad SA, Qasim M. Mixed convection flow of a micropolar fluid with radiation and chemical reaction. *Int J Numer Methods Fluids*. (2011) **67**:1418–36. doi: 10.1002/fld.2424
35. Hayat T, Shaheen U, Shafiq A, Alsaedi A, Asghar S. Marangoni mixed convection flow with Joule heating and nonlinear radiation. *AIP Adv*. (2015) **5**:077140. doi: 10.1063/1.4927209
36. Lin Y, Li B, Zheng L, Chen G. Particle shape and radiation effects on marangoni boundary layer flow and heat transfer of copper-water nanofluid driven by an exponential temperature. *Powder Technol*. (2016) **301**:379–86. doi: 10.1016/j.powtec.2016.06.029
37. Hayat T, Shafiq A, Alsaedi A. Effect of Joule heating and thermal radiation in flow of third-grade fluid over radiative surface. *PLoS ONE*. (2014) **9**:e83153. doi: 10.1371/journal.pone.0083153
38. Hayat T, Shafiq A, Imtiaz M, Alsaedi A. Impact of melting phenomenon in the Falkner-Skan wedge flow of second grade nanofluid: a revised model. *J Mol Liquids*. (2016) **215**:664–70. doi: 10.1016/j.molliq.201 6.01.004
39. Ellahi R, Fetecau C, Sheikholeslami M. Recent advances in the application of differential equations in mechanical engineering problems. *Math Prob Eng*. (2018) **2018**:1584920. doi: 10.1155/2018/1584920
40. Ellahi R, Zeeshan A, Hussain F, Abbas T. Study of shiny film coating on multi-fluid flows of a rotating disk suspended with nano-sized silver and gold particles: a comparative analysis. *Coatings*. (2018) **8**:422. doi: 10.3390/coatings8120422
41. Ellahi R, Alamri SZ, Basit A, Majeed A. Effects of MHD and slip on heat transfer boundary layer flow over a moving plate based on specific entropy generation. *J Taibah Univ Sci*. (2018) **12**:476–82. doi: 10.1080/16583655.2018.1483795
42. Ellahi R, Riaz A, Abbasbandy S, Hayat T, Vafai K. A study on the mixed convection boundary layer flow and heat transfer over a vertical slender cylinder. *Ther Sci*. (2014) **18**:1247–58. doi: 10.2298/TSCI11092 3097E
43. Ellahi R, Tariq MH, Hassan M, Vafai K. On boundary layer magnetic flow of nano-Ferroliquid under the influence of low oscillating over stretchable rotating disk. *J Mol Liquids*. (2017) **229**:339–45. doi: 10.1016/j.molliq.2016.12.073

44. Ellahi R, Raza M, Akbar NS. Study of peristaltic flow of nanofluid with entropy generation in a porous medium. *J Porous Media*. (2017) **20**:461–78. doi: 10.1615/JPorMedia.v20.i5.70
45. Bhatti MM, Abbas MA, Rashidi MM. Entropy generation for peristaltic blood flow with casson model and consideration of magnetohydrodynamics effects. *Walailak J Sci Technol*. (2016) **14**:451–61.
46. Bhatti MM, Mishra SR, Abbas T, Rashidi MM. A mathematical model of MHD nanofluid flow having gyrotactic microorganisms with thermal radiation and chemical reaction effects. *Neural Comput Appl*. (2018) **30**:1237–49. doi: 10.1007/s00521-016-2768-8
47. Ellahi R, Riaz A. Analytical solutions for MHD flow in a third-grade fluid with variable viscosity. *Math Comput Model*. (2010) **52**:1783–93. doi: 10.1016/j.mcm.2010.07.005
48. Waqas H, Khan SU, Imran M, Bhatti MM. Thermally developed Falkner–Skan bioconvection flow of a magnetized nanofluid in the presence of a motile gyrotactic microorganism: Buongiorno's nanofluid model. *Phys Script*. (2019) **94**:1–15. doi: 10.1088/1402-4896/ab2ddc

Conflict of Interest: The authors declare that the research was conducted in the absence of any commercial or financial relationships that could be construed as a potential conflict of interest.

Copyright © 2020 Shafiq, Zari, Khan, Khan, Seikh and Sherif. This is an open-access article distributed under the terms of the Creative Commons Attribution License (CC BY). The use, distribution or reproduction in other forums is permitted, provided the original author(s) and the copyright owner(s) are credited and that the original publication in this journal is cited, in accordance with accepted academic practice. No use, distribution or reproduction is permitted which does not comply with these terms.

NOMENCLATURE

$\check{u}_e$	External flow velocity
(h_0, u_0, l_0)	constants
b	Width of magnets and electrode
μ_{nf}	Nanofluid dynamic viscosity
j_0	Applied current density within electrodes
$(c_p)_{nf}$	Nanofluid heat capacity
ρ_{nf}	Nanofluid density
α_{nf}	Nanofluid effective density
T_0	Temperature at boundary
T_e	Temperature of external fluid
T_w	Temperature of fluid at Riga plate
Γ	Buoyancy force parameter
β	Nanoparticle thermal parameter
q_r	Radiative heat flux
$\check{k}_f$	Fluid thermal conductivity
k_{nf}	Nanofluid thermal conductivity
ρ_{nf}	Nanofluid density
ρ_{CNT}	Carbon nanotube density
ϕ	Nanofluid solid volume fraction
λ	Convective parameter
Q	Modified Hartman number
R	Radiation parameter
Pr	Prandtl number
Ec	Eckert number
M_0	Magnetic parameter

frontiers in Physics

ORIGINAL RESEARCH
published: 07 February 2020
doi: 10.3389/fphy.2019.00250

Entropy Generation in $C_6H_9NAO_7$ Fluid Over an Accelerated Heated Plate

Tarek Nabil Ahmed[1,2] and Ilyas Khan[1,3]**

[1] Basic Engineering Sciences Department, College of Engineering Majmaah University, Al-Majmaah, Saudi Arabia,
[2] Mathematics Department, Faculty of Science, Beni-Suef University, Beni-Suef, Egypt, [3] Department of Mathematics, College of Science Al-Zulfi, Majmaah University, Al-Majmaah, Saudi Arabia

This study considers sodium-alginate ($C_6H_9NaO_7$) fluid over an accelerated vertical plate. The plate is heated from the bottom. A non-Newtonian model of $C_6H_9NaO_7$ is considered. The convection term in the momentum equations is also considered. The dimensionless form of the problem is constructed based on dimensionless variables. The integral transformation of Laplace is used to develop the exact solution to the problem. Explicit expressions are obtained for the velocity field and temperature distribution. The corresponding skin-friction and Nusselt number results are computed based on this. Equations for entropy generation (EG) and Bejan number (BN) are developed. The results are plotted and discussed for embedded parameters. Most significantly, the results for EG and BN are computed and discussed.

Keywords: heat transfer, entropy generation, Casson fluid, exact solutions, integral transform

OPEN ACCESS

Edited by:
Sara I. Abdelsalam, National Autonomous University of Mexico, Mexico

Reviewed by:
Kh S. Mekheimer, Al-Azhar University, Egypt
Abdullah Zaher, Benha University, Egypt
Hina Sadaf, National University of Sciences and Technology, Pakistan

***Correspondence:**
Tarek Nabil Ahmed
t.ahmed@mu.edu.sa
Ilyas Khan
i.said@mu.edu.sa

Specialty section:
This article was submitted to Mathematical Physics, a section of the journal Frontiers in Physics

Received: 20 October 2019
Accepted: 23 December 2019
Published: 07 February 2020

Citation:
Ahmed TN and Khan I (2020) Entropy Generation in $C_6H_9NAO_7$ Fluid Over an Accelerated Heated Plate. Front. Phys. 7:250. doi: 10.3389/fphy.2019.00250

INTRODUCTION

Entropy generation (EG) is a tool that helps to assess improved results, enhance achievements, and reduce the loss of energy in thermal engineering systems (TES) [1]. Recently, this technique has been applied to TES operating with nanofluids [2]. The EG method is used to develop performance standards for thermal engineering equipment. In the literature, Bejan is considered to be the first to point out the various factors behind EG [3, 4] in TES. Bejan [5] introduced the EG number, referred to as the Bejan number, which is the ratio of EG due to heat transfer to the total EG of the system. Moreover, he indicated the conditions of the second law of thermodynamics related to the convection problems of nanofluids. Selimefendigil et al. [6] demonstrated the magnetic-resistive convection flow of nanofluids (CuO-water and Al_2O_3-water) in a restricted trapezoidal cavity. Quing et al. [7] investigated EG in radiative flow of Casson nanofluids over permeable stretchable sheets. A detailed review of EG in nanofluid flow was presented by Mahian et al. [8], who collected and critically discussed recent studies with a wide range of applications. The study organized different aspects of heat-transfer problems and EG in the current state of the art, making suggestions for useful future directions.

Darbari et al. used the response surface method (RSM) to conduct a numerical sensitivity analysis of the effect of nanoparticles (Al_2O_3) in water-based nanofluids on EG [9]. The results indicated that the total EG comprised EG due to friction and due to heat conduction. The sensitivity analysis of EG highlighted the influence of the Reynolds number, particle size, and solid-volume fraction. Ellahi et al. [10] mathematically analyzed EG in natural-convection boundary-layer flow of nanofluids near an inverted cone. It was found that EG was produced because of nanoparticles. Sheikholislami et al. [11] revealed that the EG and heat-transfer rate were enhanced by volume friction and Rayleigh number during the flow of various types of nanofluids in a cavity containing square-shell rectangular heated objects. Saqib et al. [12] developed a Caputo-type fractional model for the mixed-convection flow of different types of nanofluids. The exact analytical results for velocity, temperature, EG, and Bejan number were obtained via the Laplace-transform technique and presented in figures and tables with physical explanations. Khan et al. [13] described the EG in unsteady magnetic fluid dynamics (MHD) flow through porous media, combining the effects of mass and heat transfer. The effects of several factors on EG, Bejan number, and velocity distribution were reported in numerous figures. Bhatti et al. [14] analyzed the EG of Eyeling-Powell nanofluids through a permeable stretchable surface. The effects of magnetohydrodynamics (MHD) and non-linear thermal radiation were also considered. Li et al. [15] considered EG in forced-convection flow of Al_2O_3-water nanofluids. They reported the impact of Reynolds number (Re), height ratio, and pitch ratio on EG.

Khan et al. [16] obtained an exact solution for the problem of convection-MHD flow of sodium-alginate-based Casson-type nanofluids with the effects of MHD and Newtonian heating. Haq et al. [17] used an exact analysis and developed an exact solution for the free-convection problem of viscous fluid, which depends strongly on time and the slippage condition. Khan et al. [18] generated exact solutions for a rotating viscous fluid such that the fluid exhibits eccentric-concentric rotation. Ahmed and Khan [19] examined the mixed-convection flow of SA-NaAlg nanofluids such that the base fluid is taken as MoS_2. Khater et al. [20, 21] studied two different problems using the magnetohydrodynamics effect with a Hall current. In this problem, the analysis of entropy generation is considered for Casson fluid over an accelerated plate. The problem in dimensionless form is solved by using the Laplace transform technique, and the results are plotted and discussed.

DESCRIPTION OF THE PROBLEM

Consider the unsteady, incompressible mixed-convection flow of a Casson fluid near an infinite vertical plate. It is assumed that, at $\tau \leq 0$, the system is at rest at a temperature of θ_∞. At $\tau = 0^+$, the plate starts moving with a variable velocity of $v(0,\tau) = A\tau$, and the temperature of the plate increases from $\theta(\eta,0) = \theta_\infty$ to $\theta(0,\tau) = \theta_w$. At this stage, mixed convection occurs owing to the change in temperature and the motion of the plate. The initial fluid motion is in the vertical direction and is governed by the following partial differential equations (momentum and energy equations) [16, 19].

$$\rho \frac{\partial v(\eta,\tau)}{\partial \tau} = \mu\left(1+\frac{1}{\beta}\right)\frac{\partial^2 v}{\partial \eta^2} + \rho g \beta_\theta \left(\theta(\eta,\tau) - \theta_\infty\right), \quad (1)$$

$$\rho c_p \frac{\partial \theta(\eta,\tau)}{\partial \tau} = k\frac{\partial^2 \theta(\eta,\tau)}{\partial \eta^2}, \quad (2)$$

These are associated with the following physical initial and boundary conditions.

$$\left.\begin{array}{l} V(\eta,0) = 0, \quad \theta(\eta,0) = \theta_\infty \\ v(0,\tau) = A\tau, \; v(\infty,\tau) = 0 \\ \theta(0,\tau) = \theta_w, \; \theta(\infty,\tau) = \theta_\infty \end{array}\right\}, \quad (3)$$

where ρ is the density, $v(\eta,\tau)$ the x-component of the velocity vector, μ the dynamic viscosity, g the gravitational acceleration, β_θ the volumetric thermal expansion, $\theta(\eta,\tau)$ the x-component of the temperature vector, c_p the heat capacitance, and k the thermal conductivity of the fluid. To remove the units, the following dimensionless variables are introduced into Equations (1)–(3).

$$v^* = \frac{v}{(\nu A)^{\frac{1}{3}}}, \; \eta^* = \frac{\eta A^{\frac{1}{3}}}{\nu^{\frac{2}{3}}}, \; \tau^* = \frac{\tau A^{\frac{2}{3}}}{\nu^{\frac{1}{3}}}, \; \theta^*(\eta,\tau) = \frac{\theta - \theta_\infty}{\theta_w - \theta_\infty},$$

This yields the following form.

$$\frac{\partial v}{\partial \tau} = \left(1+\frac{1}{\beta}\right)\frac{\partial^2 v}{\partial \eta^2} + Gr\theta, \quad (4)$$

$$\Pr \frac{\partial \theta}{\partial \tau} = \frac{\partial^2 \theta}{\partial \eta^2}, \quad (5)$$

$$\left.\begin{array}{l} V(\eta,0) = 0, \; v(0,\tau) = \tau, \quad v(\infty,\tau) = 0 \\ \theta(0,\tau) = 1, \; \theta(\infty,\tau) = 0, \quad \theta(\eta,0) = 0 \end{array}\right\}, \quad (6)$$

where $Gr = \frac{g\beta_\theta \Delta\theta}{A}$,$\Pr = \frac{\mu c_p}{k}$.

Entropy Generation

The following entropy-generation relation is developed to optimize the heat transfer and minimize the energy loss in the system defined in Equations (4)–(6) [3–5, 12, 13].

$$s_{gen} = \frac{k}{\theta_\infty^2}\left(\frac{\partial \theta}{\partial \eta}\right)^2 + \frac{\mu}{\theta_\infty}\left(1+\frac{1}{\beta}\right)\left(\frac{\partial v}{\partial \eta}\right)^2. \quad (7)$$

Using the non-similarity variable, $\partial\theta/\partial\eta = \Delta\theta A^{\frac{1}{3}} \nu^{-\frac{2}{3}} \partial\theta^*/\partial\eta^*$ and $\partial v/\partial\eta = A^{\frac{2}{3}} \nu^{-\frac{1}{3}} \partial v^*/\partial\eta^*$ are derived and incorporated into Equation (7), which yields

$$N_s = \left(\frac{\partial \theta}{\partial \eta}\right)^2 + \frac{Br}{\Omega}\left(1+\frac{1}{\beta}\right)\left(\frac{\partial v}{\partial \eta}\right)^2, \quad (8)$$

where

$$N_s = \frac{s_{gen}\nu^{\frac{4}{3}}\theta^2{}_\infty}{kA^{2/3}(\Delta\theta)^2}, \; Br = \frac{\mu A^{\frac{2}{3}}\nu^{\frac{2}{3}}}{k\Delta\theta}, \; \Omega = \frac{\Delta\theta}{\theta_\infty} = \frac{\theta_w - \theta_\infty}{\theta_\infty}.$$

Bejan Number

Bejan is generally considered in the literature to be the first person to point out various factors for optimizing the performance of thermal systems. He developed Bejan's number, which is the ratio of heat-transfer entropy production to total entropy production, and proposed aspects of the second law of thermodynamics that consider various problems associated with mixed convection. The Bejan number is given by

$$Be=\frac{\frac{k}{\theta_\infty^2}\left(\frac{\partial\theta}{\partial\eta}\right)^2}{\frac{k}{\theta_\infty^2}\left(\frac{\partial\theta}{\partial\eta}\right)^2+\frac{\mu}{\theta_\infty}\left(1+\frac{1}{\beta}\right)\left(\frac{\partial v}{\partial\eta}\right)^2} \tag{9}$$

and

$$Be=\frac{\left(\frac{\partial\theta}{\partial\eta}\right)^2}{\left(\frac{\partial\theta}{\partial\eta}\right)^2+\frac{Br}{\Omega}\left(1+\frac{1}{\beta}\right)\left(\frac{\partial v}{\partial\eta}\right)^2}. \tag{10}$$

EXACT SOLUTIONS

In the literature, mixed-convection problems are handled using numerical or approximate methods, and exact solutions are limited. Here, the exact solutions are obtained using the Laplace transform method. Applying the Laplace transform to Equations (4)–(6) gives

$$q\bar{v}(\eta,q)=\left(1+\frac{1}{\beta}\right)\frac{\partial^2\bar{v}(\eta,q)}{\partial\eta^2}+Gr\bar{\theta}(\eta,q) \tag{11}$$

$$\bar{v}(0,q)=\frac{1}{q^2},\quad \bar{v}(\infty,q)=0 \tag{12}$$

$$\Pr q\bar{\theta}(\eta,q)=\frac{\partial^2\bar{\theta}(\eta,q)}{\partial\eta^2} \tag{13}$$

$$\bar{\theta}(0,q)=\frac{1}{q},\quad \bar{\theta}(\infty,q)=0 \tag{14}$$

The second-order partial differential Equation (13) is solved using the transform boundary conditions (14) as follows.

$$\bar{\theta}(\eta,q)=\frac{e^{-\eta\sqrt{\Pr q}}}{q} \tag{15}$$

Inverting the Laplace transform yields

$$\theta(\eta,\tau)=erfc\left(\frac{\eta\sqrt{\Pr}}{2\sqrt{\tau}}\right) \tag{16}$$

Similarly, the solution of Equation (11) using Equations (12) and (15) is given by

$$\bar{v}(\eta,q)=\frac{a_1}{q^2}e^{-\eta\sqrt{\gamma q}}+\frac{a_0}{q^2}e^{-\eta\sqrt{\Pr q}} \tag{17}$$

where

$$\left(1+\frac{1}{\beta}\right)=\frac{1}{\gamma},\quad a_0=\frac{Gr\gamma}{\gamma-\Pr},\quad a_1=1-a_0.$$

With the inverse Laplace transform,

$$v(\eta,\tau)=a_1\left[\left(\frac{1}{2}\eta^2\gamma+\tau\right)erfc\left(\frac{\eta\sqrt{\gamma}}{2\sqrt{\tau}}\right)-\eta\sqrt{\frac{\tau\gamma}{\pi}}e^{\frac{\eta^2\gamma}{4\tau}}\right]+a_0\left[\left(\frac{1}{2}\eta^2\Pr+\tau\right)erfc\left(\frac{\eta\sqrt{\Pr}}{2\sqrt{\tau}}\right)-\eta\sqrt{\frac{\tau\Pr}{\pi}}e^{\frac{\eta^2\Pr}{4\tau}}\right]. \tag{18}$$

Special Case: Note that Equation (18) is reduced to the following form for Newtonian fluid ($\frac{1}{\beta}\rightarrow 0$):

$$v(\eta,\tau)=\left(1-\frac{Gr}{1-\Pr}\right)\left[\left(\frac{1}{2}\eta^2+\tau\right)erfc\left(\frac{\eta}{2\sqrt{\tau}}\right)-\eta\sqrt{\frac{\tau}{\pi}}e^{\frac{\eta^2}{4\tau}}\right]+\frac{Gr}{1-\Pr}\left[\left(\frac{1}{2}\eta^2\Pr+\tau\right)erfc\left(\frac{\eta\sqrt{\Pr}}{2\sqrt{\tau}}\right)-\eta\sqrt{\frac{\tau\Pr}{\pi}}e^{\frac{\eta^2\Pr}{4\tau}}\right]. \tag{19}$$

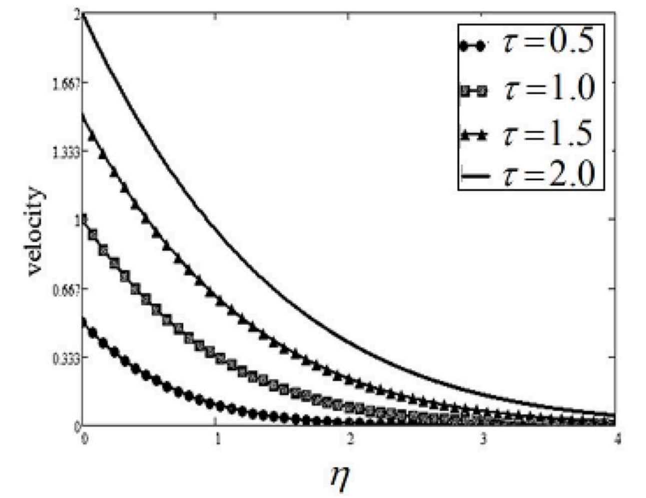

FIGURE 1 | Velocity plot for τ.

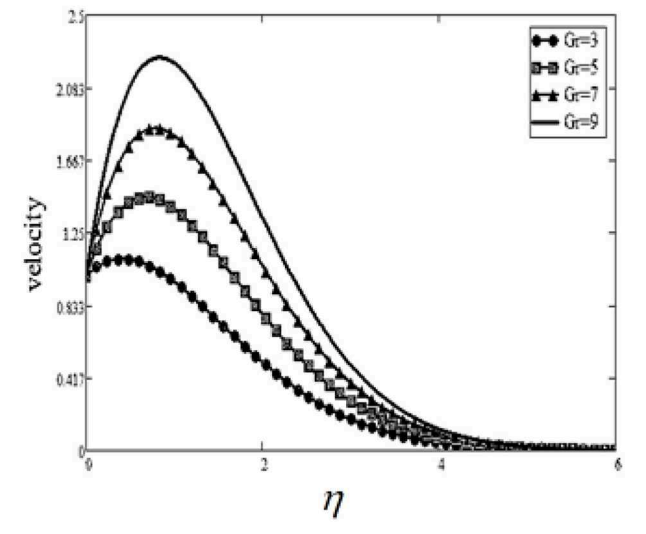

FIGURE 2 | Velocity plot for Gr.

Skin Friction

In the dimensionless form, skin friction is defined as

$$c_f = \left(1 + \frac{1}{\beta}\right) \left. \frac{\partial v(\eta, \tau)}{\partial \eta} \right|_{\eta=0} \tag{20}$$

Nusselt Number

The heat-transfer rate in the dimensionless form is given by

$$Nu = \left. \frac{\partial \theta(\eta, \tau)}{\partial \eta} \right|_{\eta=0} \tag{21}$$

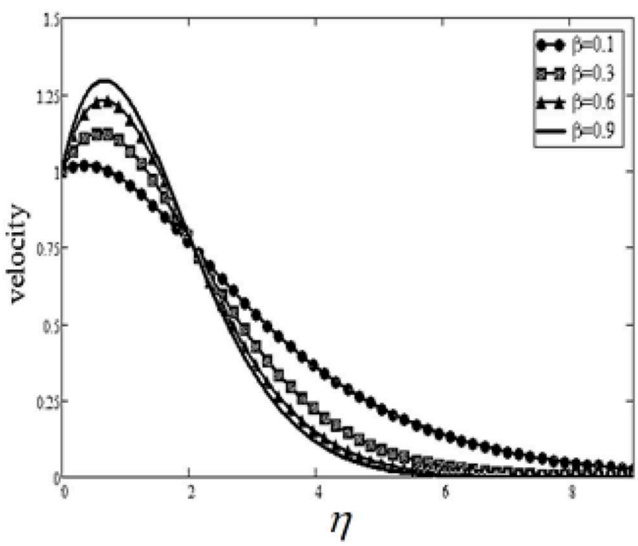

FIGURE 3 | Velocity plot for β.

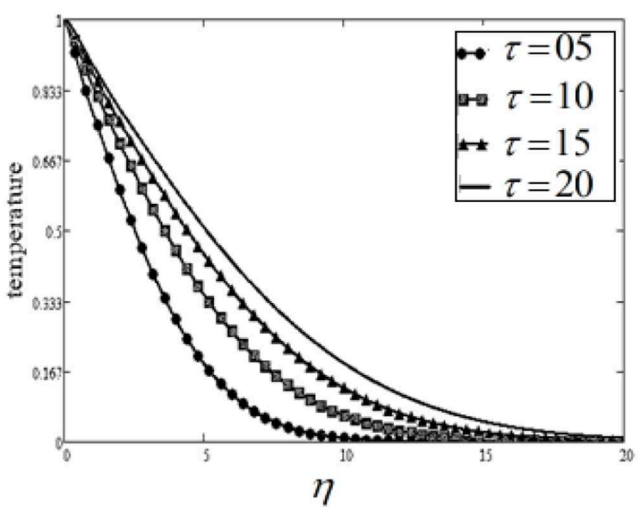

FIGURE 4 | Temperature plot for τ.

RESULTS AND DISCUSSION

In this paper, we conducted an entropy generation (EG) analysis for accelerated flow of non-Newtonian fluid. EG, also known as the second law of thermodynamics, is quite useful in heat transfer problems such as in analyzing heat exchangers. This section highlights the influence of different parameters on velocity, temperature, entropy generation, and Bejan number. Since, in this work, sodium-alginate is taken as a counter-example of a Casson fluid, the Prandtl number (Pr) value is taken as 13.09

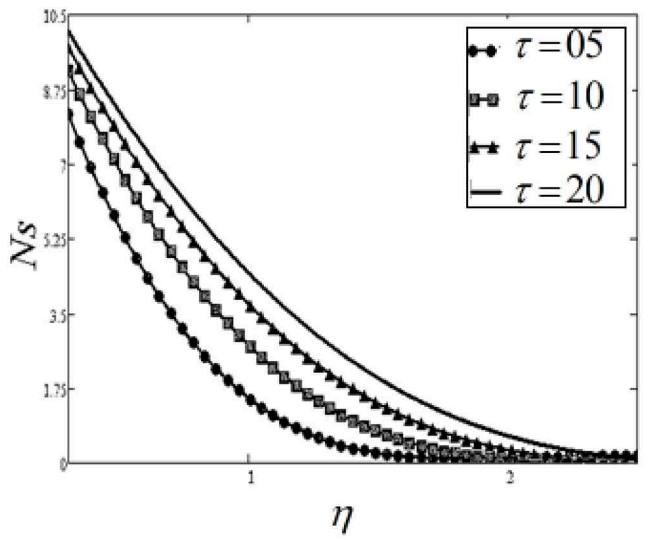

FIGURE 5 | Entropy generation plot for τ.

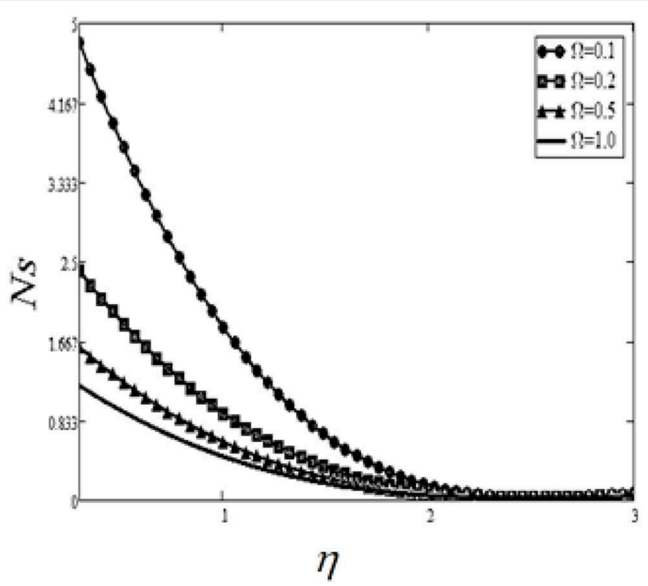

FIGURE 6 | Entropy generation plot for Ω.

in all of these figures. This value of Pr is computed from $\Pr = \mu c_p/k$, $\mu = 0.002;\ k = 0.6376;\ c_p = 4175$.

Figure 1 shows the effects of time τ on velocity. It is found that an increase in time results in an increase in the velocity profile. Physically, the fluid is considered to be unsteady, and thus velocity increases with time. **Figure 2** highlights the effect of *Gr*: the velocity profile increases with increasing *Gr* Value. The increase in *Gr* enhances the buoyancy force, causing the velocity to increase. The physical interpretation indicates that positive values of Gr show heating of the fluid or cooling of the boundary surface. The effect of the Casson parameter, β, is highlighted in **Figure 3**; a dual effect is generated. Initially, near the plate, the velocity is found to increase, and then away from the plate, it decreases for large values of β. This is because an increase in β reduces the boundary-layer thickness. **Figure 4** shows the influence of time τ on the temperature profile, where the maximum values of time τ lead to an increase in temperature.

The impact of EG (*Ns*) for dissimilar values of τ is highlighted in **Figure 5**. An increase in time τ leads to an increase in EG. **Figure 6** presents the EG values for different values of Ω. Ω is defined as the temperature difference, and an increase in temperature difference decreases entropy generation. **Figure 7** presents the influence of unlike values of *Gr* on EG. The buoyancy forces increase with increasing *Gr* values, which results in an

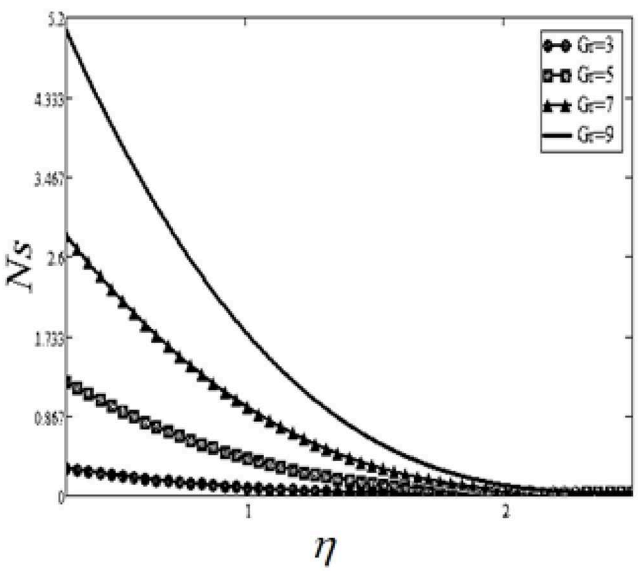

FIGURE 7 | Entropy generation plot for *Gr*.

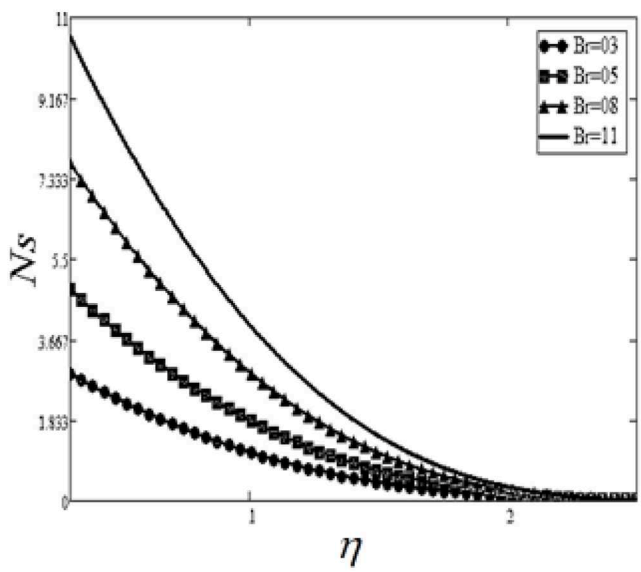

FIGURE 9 | Entropy generation plot for *Br*.

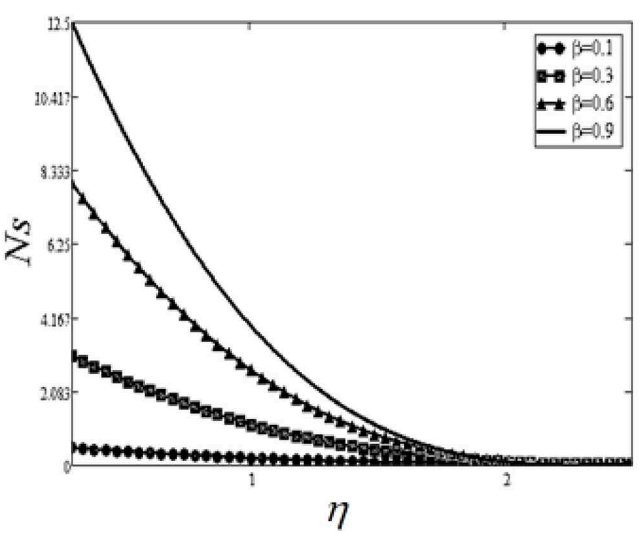

FIGURE 8 | Entropy generation plot for β.

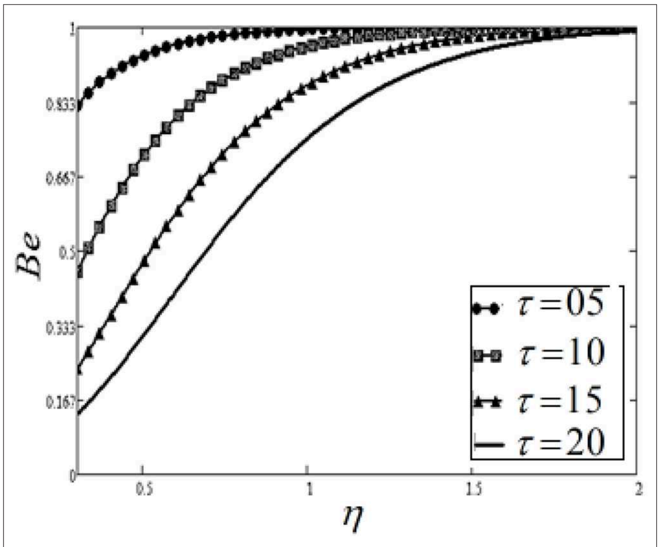

FIGURE 10 | Bejan number plot for t.

increase in entropy generation. In addition, an increase in *Gr* could save energy in the system.

The effect of β is shown in **Figure 8**; it is significant to note that the thickness of the velocity boundary layer decreases with increasing Casson parameter value, and hence EG increases. Furthermore, at high values of β, i.e., $\beta \rightarrow \infty$, Newtonian fluid behavior is observed. The decrease in the Casson parameter leads to an increase in fluid plasticity. The influence of Brickman's number, *Br*, is investigated in **Figure 9**. A large value of Brickman's number produces a high amount of heat via viscous dissipation and vice versa. Therefore, high values of Brickman's number increase entropy generation.

The influence of time parameter τ on Bejan number variation is highlighted in **Figure 10**. The influence of time τ leads to a decrease in Bejan number. **Figure 11** shows the effect of the temperature difference, Ω, on the Bejan number; the maximum value of Ω corresponds with an increase in the Bejan number. **Figure 12** highlights the change in Bejan number with respect to *Gr*. It is detected that a greater *Gr* value decreases the Bejan number. This is because heat-transfer reunification becomes dominant in the region near the plate with increasing *Gr* value. In **Figure 13**, the Bejan number can be seen to decrease with increasing Casson parameter β. The Bejan number variation for different *Br* values is reported in **Figure 14**. Larger values of *Br* are associated with decreasing Bejan number.

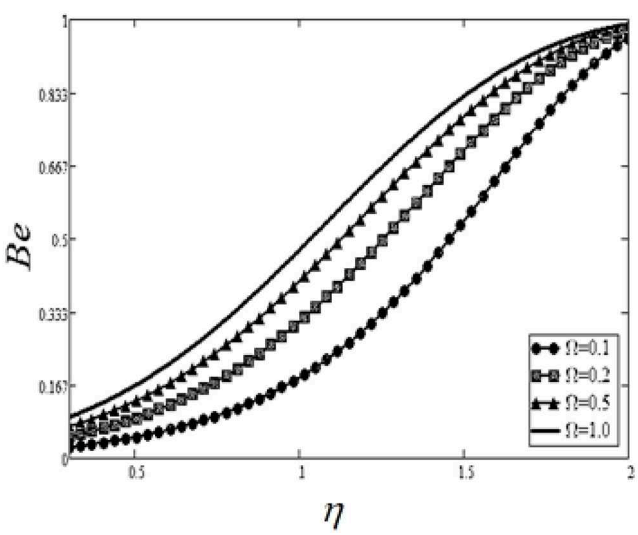

FIGURE 11 | Bejan number plot for Ω.

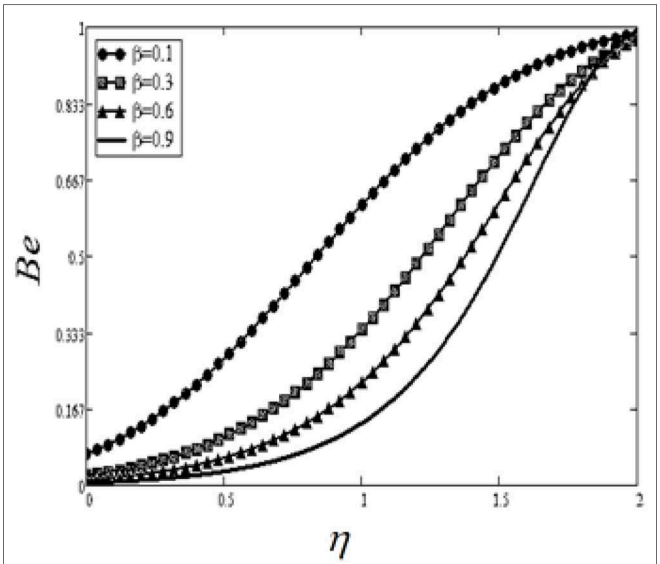

FIGURE 13 | Bejan number plot for β.

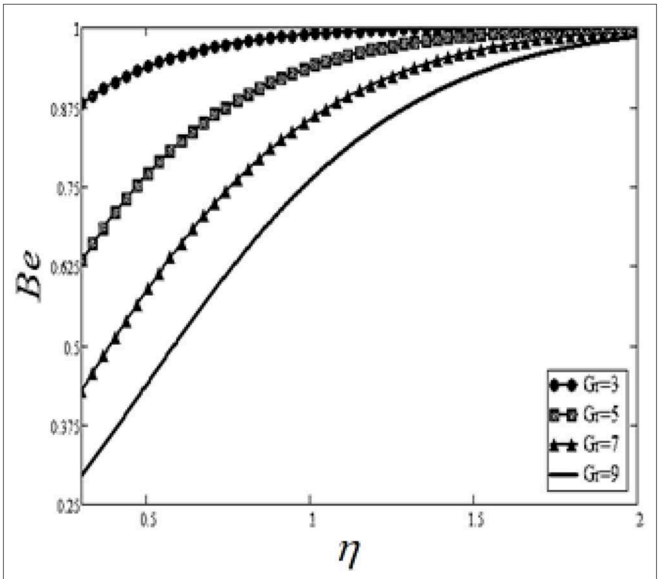

FIGURE 12 | Bejan number plot for *Gr*.

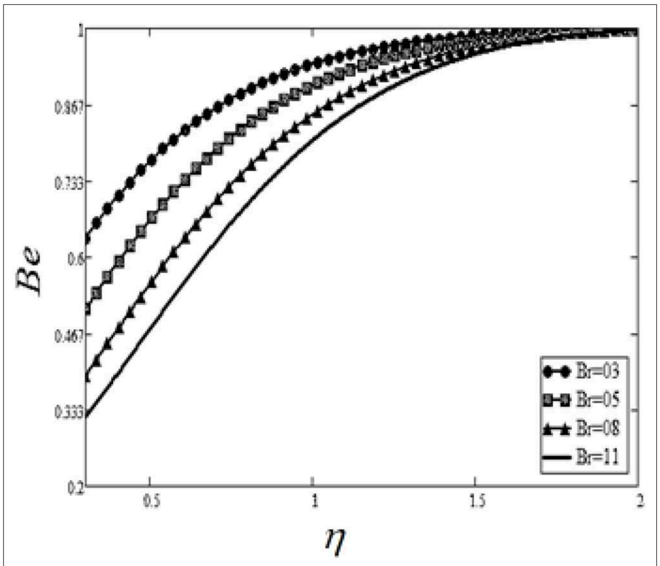

FIGURE 14 | Bejan number plot for *Br*.

TABLE 1 | Effect of variation of different variables on C_f.

t	*β*	*Gr*	Pr	C_f
1	0.1	5	0.6	1.5
2				1.811
3				2.05
	0.3			2.147
	0.5			2.219
		7		3.598
		9		5.695
			0.7	1.215
			0.8	0.975

TABLE 2 | Effect of variation of different variables on Nu.

τ	Pr	*Nu*
1	0.6	0.219
2		0.077
3		0.042
	1.2	0.309
	2.2	0.418

Table 1 examines the effect of different factors on skin friction. It is observed that the skin friction increases with increasing τ, β, and Gr values. **Table 2** highlights the effect of the variation in τ and Pr on Nusselt number. The Nusselt number decreases up to the maximum value of τ and increases for the maximum value of Pr.

CONCLUDING REMARKS

An exact analysis of entropy generation in sodium-alginate fluid over an accelerated heated plate is conducted via Laplace-transform methods. The Bejan number Be and local entropy generation Ns are discussed for various parameters. The effects are displayed for different embedded parameters. The main conclusions are:

- For maximum entropy generation Ns, we need to maximize the t, Gr, β, and Br values. In contrast, for minimum values, we need to minimize the Pr and Ω values.
- For the maximum Bejan number, Be, we need to maximize the Pr and Ω values. In contrast, for minimum values, we need to minimize the t, Gr, β, and Br values.
- The Casson parameter, β, exhibits dual effects.

AUTHOR CONTRIBUTIONS

TA formulated and solved the problem. IK plotted and discussed the results and revised the manuscript. TA and IK wrote the manuscript.

ACKNOWLEDGMENTS

The authors acknowledge with thanks the Deanship of Scientific Research (DSR) at Majmaah University, Majmaah, Saudi Arabia, for technical and financial support through vote number 38/107 for this research project.

REFERENCES

1. Mahian O, Kianifar A, Sahin AZ, Wongwises S. Entropy generation during Al2O3/water nanofluid flow in a solar collector: effects of tube roughness, nanoparticle size, and different thermophysical models. *Int J Heat Mass Transf*. (2014) **78**:64–75. doi: 10.1016/j.ijheatmasstransfer.2014.06.051
2. Mahian O, Mahmud S, Heris SZ. Effect of uncertainties in physical properties on entropy generation between two rotating cylinders with nanofluids. *J Heat Transf*. (2012) **134**:101704. doi: 10.1115/1.4006662
3. Bejan A. Second-law analysis in heat transfer and thermal design. *Adv Heat Transf*. (1982) **15**:1–58. doi: 10.1016/S0065-2717(08)70172-2
4. Bejan A. *Entropy Generation Minimization: The Method of Thermodynamic Optimization of Finite-Size Systems and Finite-Time Processes*. Boca Raton: CRC Press (1995).
5. Bejan A. A study of entropy generation in fundamental convective heat transfer. *ASME J Heat Transf*. (1979) **101**:718–25. doi: 10.1115/1.3451063
6. Selimefendigil F, Öztop HF, Abu-Hamdeh N. Natural convection and entropy generation in nanofluid filled entrapped trapezoidal cavities under the influence of magnetic field. *Entropy*. (2016) **18**:43. doi: 10.3390/e18020043
7. Qing J, Bhatti MM, Abbas MA, Rashidi MM, Ali MES. *Entropy* generation on MHD Casson nanofluid flow over a porous stretching/shrinking surface. *Entropy*. (2016) **18**:123. doi: 10.3390/e18040123
8. Mahian O, Kianifar A, Kleinstreuer C, Moh'd AAN, Pop I, Sahin AZ, et al. A review of entropy generation in nanofluid flow. *Int J Heat Mass Transf*. (2013) **65**:514–32. doi: 10.1016/j.ijheatmasstransfer.2013.06.010
9. Darbari B, Rashidi S, Abolfazli Esfahani J. Sensitivity analysis of entropy generation in nanofluid flowinside a channel by response surface methodology. *Entropy*. (2016) **18**:52. doi: 10.3390/e18020052
10. Ellahi R, Hassan M, Zeeshan A. Shape effects of nanosize particles in Cu–H2O nanofluid on entropy generation. *Int J Heat Mass Transf*. (2015) **81**:449–56. doi: 10.1016/j.ijheatmasstransfer.2014.10.041
11. Sheikholeslami M, Ashorynejad HR, Rana P. Lattice Boltzmann simulation of nanofluid heat transfer enhancement and entropy generation. *J Mol Liquids*. (2016) **214**:86–95. doi: 10.1016/j.molliq.2015.11.052
12. Saqib M, Ali F, Khan I, Sheikh NA, Khan A. Entropy generation in different types of fractionalized nanofluids. *Arab J Sci Eng*. (2019) **44**:531–40. doi: 10.1007/s13369-018-3342-8
13. Khan A, Khan I, Alkanhal TA, Ali F, Khan D, Nisar KS. Entropy generation in MHD conjugate flow with wall shear stress over an infinite plate: exact analysis. *Entropy*. (2019) **21**:359. doi: 10.3390/e21040359
14. Bhatti M, Abbas T, Rashidi M, Ali M, Yang Z. Entropy generation on MHD Eyring–Powell nanofluid through a permeable stretching surface. *Entropy*. (2016) **18**:224. doi: 10.3390/e18060224
15. Li Z, Sheikholeslami M, Jafaryar M, Shafee A, Chamkha AJ. Investigation of nanofluid entropy generation in a heat exchanger with helical twisted tapes. *J Mol Liquids*. (2018) **266**:797–805. doi: 10.1016/j.molliq.2018.07.009
16. Khan A, Khan D, Khan I, Ali F, ul Karim F, Imran M. MHD flow of Sodium Alginate-based Casson type nanofluid passing through a porous medium with Newtonian heating. *Sci Rep*. (2018) **8**:8645. doi: 10.1038/s41598-018-26994-1
17. Haq SU, Khan I, Ali F, Abdelhameed TN. Influence of slip condition on unsteady free convection flow of viscous fluid with ramped wall temperature. *Abst Appl Anal*. (2015) **2015**:327975. doi: 10.1155/2015/327975
18. Khan I, Abdelhameed TN, Dennis LC. Heat transfer in eccentric-concentric rotation of a disk and fluid at infinity. *J Comp Theor Nanosci*. (2016) **13**:6482–7. doi: 10.1166/jctn.2016.5590

19. Ahmed TN, Khan I. Mixed convection flow of sodium alginate (SA-NaAlg) based molybdenum disulphide (MoS2) nanofluids: Maxwell Garnetts and Brinkman models. *Results Phys.* (2018) **8**:752–7. doi: 10.1016/j.rinp.2018.01.004
20. Khater AH, Callebaut DK, Abdul-Aziz SF, Abdelhameed TN. Potential symmetry and invariant solutions of Fokker–Planck equation modelling magnetic field diffusion in magnetohydrodynamics including the Hall current. *Phys A.* (2004) **341**:107–22. doi: 10.1016/j.physa.2004.04.118
21. Khater AH, Callebaut DK, Abdelhameed TN. Potential symmetry and invariant solutions of Fokker-Planck equation in cylindrical coordinates related to magnetic field diffusion in magnetohydrodynamics including the Hall current. *Eur Phys J B Condens Matter Complex Syst.* (2006) **50**:17. doi: 10.1140/epjb/e2006-00138-5

Conflict of Interest: The authors declare that the research was conducted in the absence of any commercial or financial relationships that could be construed as a potential conflict of interest.

Copyright © 2020 Ahmed and Khan. This is an open-access article distributed under the terms of the Creative Commons Attribution License (CC BY). The use, distribution or reproduction in other forums is permitted, provided the original author(s) and the copyright owner(s) are credited and that the original publication in this journal is cited, in accordance with accepted academic practice. No use, distribution or reproduction is permitted which does not comply with these terms.

NOMENCLATURE

u -Velocity of the fluid, $[ms^{-1}]$
θ -Temperature of the fluid, $[K]$
g -Acceleration due to gravity, $[ms^{-2}]$
c_p -Specific heat at a constant pressure, $[jkg^{-1}K^{-1}]$
Gr -Thermal Grasshof number, $(= \beta T_w)$
k -Thermal conductivity of the fluid, $[Wm^{-2}K^{-1}]$
Nu -Nusselt number, $[-]$
Pr -Prandtl number, $(= \mu c_p/k)$
θ_∞ -Fluid temperature far away from the plate, $[K]$
q -Laplace transforms parameter
A -Arbitrary constant $[ms^{-2}]$

GREEK SYMBOLS

ν -Kinematic viscosity of the fluid, $[m^2 s^{-1}]$
μ -Dynamic viscosity, $[kgm^{-1}s^{-1}]$
ρ -Fluid density, $[kgms^{-3}]$
β_θ -Volumetric coefficient of thermal expansion,$[K^{-1}]$
β -Casson fluid parameter
B_γ -Brinkman number
Ω -Dimensionless temperature function

ORIGINAL RESEARCH
published: 08 April 2020
doi: 10.3389/fphy.2020.00095

Swimming of Motile Gyrotactic Microorganisms and Nanoparticles in Blood Flow Through Anisotropically Tapered Arteries

Muhammad M. Bhatti[1,2*], *Marin Marin*[3], *Ahmed Zeeshan*[4], *R. Ellahi*[4,5,6] and *Sara I. Abdelsalam*[7]

[1] College of Mathematics and Systems Science, Shandong University of Science and Technology, Qingdao, China, [2] Shanghai Institute of Applied Mathematics and Mechanics, Shanghai University, Shanghai, China, [3] Department of Mathematics and Computer Science, Transilvania University of Brasov, Brasov, Romania, [4] Department of Mathematics and Statistics, Faculty of Basic and Applied Sciences (FBAS), International Islamic University (IIU), Islamabad, Pakistan, [5] Department of Mechanical Engineering, University of California, Riverside, Riverside, CA, United States, [6] Center for Modeling and Computer Simulation, Research Institute, King Fahd University of Petroleum and Minerals, Dhahran, Saudi Arabia, [7] Basic Science, Faculty of Engineering, The British University in Egypt, Cairo, Egypt

OPEN ACCESS

Edited by:
Dumitru Baleanu,
University of Craiova, Romania

Reviewed by:
Amin Jajarmi,
University of Bojnord, Iran
Jordan Yankov Hristov,
University of Chemical Technology and Metallurgy, Bulgaria

***Correspondence:**
Muhammad M. Bhatti
muhammad09@shu.edu.cn;
mmbhatti@sdust.edu.cn

Specialty section:
This article was submitted to Mathematical Physics, a section of the journal Frontiers in Physics

Received: 15 November 2019
Accepted: 13 March 2020
Published: 08 April 2020

Citation:
Bhatti MM, Marin M, Zeeshan A, Ellahi R and Abdelsalam SI (2020) Swimming of Motile Gyrotactic Microorganisms and Nanoparticles in Blood Flow Through Anisotropically Tapered Arteries. Front. Phys. 8:95. doi: 10.3389/fphy.2020.00095

In the present article, we have presented a theoretical study on the swimming of migratory gyrotactic microorganisms in a non-Newtonian blood-based nanofluid via an anisotropically narrowing artery. Sutterby fluid model is used in order to understand the rheology of the blood as a non-Newtonian fluid model. This fluid pattern has the ability to show Newtonian and non-Newtonian features. The mathematical formulation is performed via continuity, temperature, motile microorganism, momentum, and concentration equation. The series solutions are obtained using the perturbation scheme up to the third-order approximation. The resulting solutions are discussed with the help of graphs for all the leading parameters. The graphical results are also presented for non-tapered, diverging, and converging artery. We further discuss the velocity, temperature, swimming microorganism and temperature distribution. Moreover, the variation of impedance and the impact of wall shear stress are discussed and presented through the graphs.

Keywords: Sutterby fluid, wall shear stress, motile microorganism, anisotropically tapered artery, nanoparticles, perturbation solutions

INTRODUCTION

Throughout the previous decade, nanofluids have gained essential importance due to their extensive fields of applications especially in the biomedical sciences. Different theoretical and experimental studies have been presented based on the formulation of nanofluids [1–4]. Nanofluids are beneficial in improving the thermo-physical features i.e., thermal diffusivity, convection, and conductivity of the governing fluid. In biomedical science, nanofluids are helpful for the bacteriostatic activity, nano-drug delivery, labeling of cancerous tissues, magnetic resonance imaging (MRI), localized therapy, cancer therapeutics, production of ferrofluids and magnetic resonance imaging, etc. Further, they are also beneficial in nano-cryosurgery. Ferrofluids can be utilized as contrast agents for MRI and are helpful in cancer detection. In this case, the ferrofluids are made up of iron oxide nanoparticles and are recognized as *superparamagnetic iron oxide nanoparticles* (SPIONs). Recently, the localized delivery of cancer medicine to the cancer patient at the affected part. With the help of the heat transfer process, it can also be used for detergency. Because of these significant applications, different authors examined the behavior of nanofluids in different situations. Bég and Tripathi [5] presented a Mathematica simulation of the bioengineering model with the help of peristaltic configuration and nanofluids. Tripathi and Bég [6] analyzed the drug delivery systems using a peristaltic flow of nanofluids and presented the exact mathematical solutions. Kothandapani and Prakash [7] explored the behavior of a heat source on an MHD non-Newtonian hyperbolic tangent nanofluid model in an asymmetric tapered conduit. El-Dabe et al. [8] discussed the influence of slip in mild stenosis tapered artery using peristaltic simulation. Akbar [9] addressed the blood flow with thermal conductivity in a non-tapered stenosis artery filled with blood. She further discussed the shape properties of the nanoparticles. Abbas et al. [10] presented a blood flow model using nanofluids and explained the applications of drug delivery and magnetic field phenomena. Akbar [11] studied the metal-based nanomaterials suspended in the blood propagating via a tapered stenotic artery and explained the applications of Nanomedicines. Bhatti et al. [12] discussed the heat transfer properties and the applications of the blood clot model with variable viscosity. They considered the two-phase model with peristalsis. Bhatti et al. [13] also discussed the behavior of titanium magneto-nanoparticles suspended in Sisko fluid. Some more essential studies on the blood flow and nanofluids can be found from Shit et al. [14], Riaz et al. [15], Ijaz and Nadeem [16], and Abdelsalam and Bhatti [17] and in the references therein.

The macroscopic movement of the fluid as a result of the spatial variation of density over an area causes additive mobility in the swimming microorganisms known as bioconvection. The self-driven motile microorganisms tend to improve the base fluid in a particular direction producing a bio-convective stream. The moving microorganisms are divided into various types i.e., chemotaxis or oxytactic, gyrotactic microorganisms, and negative gravitaxis. The nanoparticles are not self-driven as compared with motile microorganisms, and their motion is due to the impact of the Brownian motion and the thermophoresis effect. Bioconvection in the nanofluids is anticipated to be feasible if the concentration of nanoparticles is small and as a result it won't be able to produce an essential enhancement in the base fluid viscosity. Bioconvection in the presence of nanoparticles was initially considered in Kuznetsov and Avramenko [18, 19]. Later, Kuznetsov [20] presented the suspension of nanoparticles with gyrotactic microorganisms using the Buongiorno's theory. Bég et al. [21] investigated the bioconvection flow with nanofluids through a porous medium numerically. Akbar [22] considered the bioconvection flow through a symmetric channel filled with nanoparticles and presented a bio nano-engineering model. Bhatti et al. [23] also inspected the behavior of a varying magnetic field and clot blood model using Jeffrey fluid model with nanoparticles and microorganisms. Ahmed et al. [24] considered the magnetized laminar flow of nanofluid and gyrotactic microorganisms through a non-Darcy porous medium. Chakraborty et al. [25] researched the extrinsic magnetic influence and bioconvection flow with nanoparticles with convective boundary conditions. Few important studies on the motile gyrotactic microorganisms and nanofluids can be found in Shahid et al. [26], Waqas et al. [27], Waqas et al. [28], and Sohail et al. [29].

From the above survey, it is observed that blood flow in the presence of nanoparticles has been discussed, but no attention has been devoted to discussing the simulation of motile gyrotactic microorganisms and nanoparticles suspended in the blood propagating through an anisotropically tapered artery. In most of the aforementioned studies, work has been done with nanoparticles propagating through tapered artery, however, no one considered the presence of gyrotactic microorganism in blood. Mathematical modeling has been performed on the basis of temperature, momentum, concentration and motile microorganism equations followed by an approximation in wavelength being long with and inertia-free flow. The Homotopy perturbation scheme is employed to obtain the series results. The governing equations are nonlinear and coupled and the exact solutions are not possible, whereas some other numerical/analytical methods [30–32] are beneficial to solve these kinds of problems. All the outcomes are presented graphically and plotted against the leading parameters. The behavior of temperature, velocity, concentration, and motile microorganism profile have been considered. Furthermore, wall shear and variation of impedance are also investigated and presented graphically. According to the results, it is found that the flow behavior through converging, diverging and non-tapered arteries are uniform throughout the whole channel.

MATHEMATICAL MODELING

We consider a tube having finite length "L" filled with nanofluids and motile gyrotactic microorganisms. We present here the theoretical model of the swimming of nanoparticles with motile gyrotactic microorganisms in non-Newtonian blood flow propagating in an anisotropically tapered artery. A Sutterby fluid model is used to represent the rheology of the blood. The governing fluid is incompressible and having constant density. Let (r, θ, z) be the cylinderical polar coordinates while z lies along the axis, whereas r, θ are considered along the radial and circumferential direction (see **Figure 1**). We consider the temperature and concentration at the wall of the tube as T_1 and C_1, respectively. The anisotropically tapered stenosed artery with time-variant stenosis is geometrically defined as

$$\frac{R(z)}{R_0} = \begin{cases} \tau(t)\Big[\xi z + R_0 - \frac{\delta \cos\Psi}{L_0}\Big(11 - \frac{94}{3L_0}(z-d) \\ \quad + \frac{32}{L_0^2}(z-d)^2 - \frac{32}{L_0^3}(z-d)^3\Big)\Big]; & d \le z \le \frac{3}{2}L_0, \\ \tau(t)(1+\xi z); & otherwise \end{cases} \quad (1)$$

where $R(z)$ denotes the tapered arterial segment and the artery radius with composite stenosis, t the time, L_0 the stenosis length,

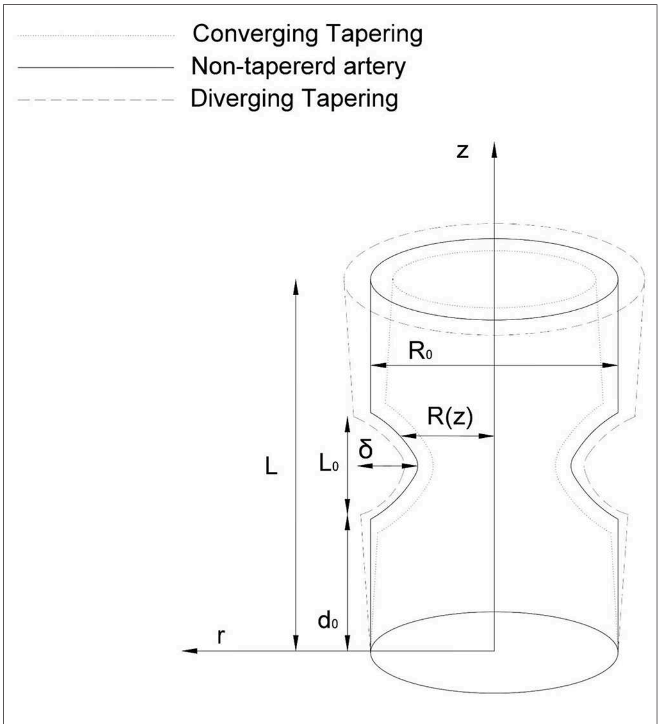

FIGURE 1 | Flow structure.

δ is the stenosis height, R_0 is the normal artery radius in the non-stenotic zone, Ψ is the tapering angle, and $\xi = \tan\Psi$ shows the slope of the tapered vessel i.e.,

$$\Psi = \begin{cases} < 0, \text{ converging artery} \\ = 0, \text{ non-tapered artery} \\ > 0, \text{ diverging artery} \end{cases} \tag{2}$$

The time-variant, $\tau(t)$, is defined as

$$\tau(t) = 1 + \frac{\alpha(1-\cos\omega t)}{e^{\alpha\omega t}}, \tag{3}$$

where α is constant and ω is the radial frequency of the forced oscillation.

The equations governing the flow model can then be written as

$$\nabla\cdot\tilde{\mathbf{V}} = 0, \tag{4}$$

$$\begin{aligned}\rho_f\left(\frac{\partial\tilde{\mathbf{V}}}{\partial t} + \tilde{\mathbf{V}}\cdot\nabla\tilde{\mathbf{V}}\right) &= -\nabla\cdot p + \nabla^2\cdot\tilde{\mathbf{V}} \\ &+ \left[\rho_f T_e(1-C_1)(T-T_1)\right. \\ &- \left(\rho_p-\rho_f\right)T_e(C-C_1) \\ &- \left.(n-n_1)\,\Theta\left(\rho_m-\rho_f\right)\right]\mathbf{g},\end{aligned} \tag{5}$$

where $\tilde{\mathbf{V}} = [U, V]$ are the components of velocity, T is the nanofluid temperature, T_1 is the reference temperature, p is the pressure, Θ is the average volume of a microorganism, n is the concentration of microorganisms, ρ_f is the density basefluid at the reference temperature, ρ_p is the nanoparticles' density, ρ_m is the density of microorganisms, $\mathbf{g}$ is the gravity vector, T_e is the base fluid volumetric coefficient of thermal expansion, and μ the viscosity of the suspension (the suspension contains the nanoparticles, microorganisms, and base fluid).

The temperature equation reads as

$$\begin{aligned}(\rho c)_f\left(\frac{\partial T}{\partial t} + \tilde{\mathbf{V}}\cdot\nabla T\right) &= \nabla\cdot\left(k_f\nabla T\right) \\ &+ (\rho c)_p\left[D_B\nabla C\cdot\nabla T + \frac{D_T}{T_1}\nabla T\cdot\nabla T\right],\end{aligned} \tag{6}$$

where D_T and D_B, k_f, $(\rho c)_f$ and $(\rho c)_p$ are the thermophoretic diffusion and Brownian coefficient, thermal conductivity, volumetric heat capacities for the nanofluid and nanoparticles, respectively.

The concentration equation with no chemical reaction reads as

$$\left(\frac{\partial C}{\partial t} + \tilde{\mathbf{V}}\cdot\nabla C\right) = D_B\nabla^2 C + \frac{D_T}{T_1}\nabla T\cdot\nabla T, \tag{7}$$

The conservation of microorganisms' reads as

$$\left(\frac{\partial n}{\partial t} + \tilde{\mathbf{V}}\cdot\nabla n\right) + \frac{bW_c}{C_0 - C_1}\nabla(n\cdot\nabla C) = -D_{\text{mo}}\nabla^2 n, \tag{8}$$

where b is the chemotaxis constant, W_c is the maximum cell swimming speed, and D_{mo} is the diffusivity of microorganisms.

The stress tensor for Sutterby fluid reads as

$$\mathbf{S} = \frac{\mu}{2}\left[\frac{\sinh^{-1}B\varsigma}{B\varsigma}\right]^m\mathbf{A}_1. \tag{9}$$

where A, B are material constants and

$$\varsigma = \sqrt{\frac{\text{trac }\mathbf{A}_1^2}{2}}, \tag{10}$$

$\mathbf{A}_1 = \text{grad }\mathbf{V} + \left(\text{grad }\mathbf{V}\right)^{\mathrm{T}}$.
The boundary conditions are given by

$$\begin{aligned}\frac{\partial u}{\partial r} &= \frac{\partial T}{\partial r} = \frac{\partial C}{\partial r} = \frac{\partial n}{\partial r} = 0, \text{ at } r = 0 \\ u &= 0, T = T_1, C = C_1, n = n_1, \text{ at } r = R(z)\end{aligned} \tag{11}$$

The non-dimensional quantities are defined as

$$\begin{aligned}\hat{r} &= \frac{r}{R_0}, \hat{z} = \frac{z}{R_0}, \hat{v} = \frac{L_0}{U_a\delta}v, \hat{R} = \frac{R}{R_0}, \hat{p} = \frac{R_0^2}{U_a L_0 \mu}p, T \\ &= (1-\theta)\, T_1 + T_0, \\ C &= (1-\phi)\, C_1 + C_0, n = (1-\chi)\, n_1 + n_0, \hat{\delta} = \frac{\delta}{R_0}, \hat{L} \\ &= \frac{L}{L_0}, \hat{\xi} = \frac{L_0 \xi}{R_0}. \end{aligned} \tag{12}$$

where U_a is the averaged velocity over a section of the whole tube.

Substituting with Equation (12) into the governing mathematical model assuming the case of mild stenosis and creeping flow yields (after dropping the hat)

$$\frac{\partial p}{\partial r} = 0, \tag{13}$$

$$\frac{\partial p}{\partial z} = \frac{1}{r}\frac{\partial}{\partial r}\left[r S_{rz}\right] + T_g\theta + N_g\phi - R_b\chi, \tag{14}$$

$$\frac{1}{r}\frac{\partial}{\partial r}\left(\frac{\partial \theta}{\partial r}r\right) + \frac{\partial \theta}{\partial r}\left[T_b\frac{\partial \Phi}{\partial r} + T_t\left(\frac{\partial \theta}{\partial r}\right)\right] = 0, \tag{15}$$

$$\frac{1}{r}\frac{\partial}{\partial r}\left(\frac{\partial \phi}{\partial r}r\right) + \frac{T_t}{T_b}\frac{1}{r}\frac{\partial}{\partial r}\left(\frac{\partial \theta}{\partial r}r\right) = 0, \tag{16}$$

$$\frac{1}{r}\frac{\partial}{\partial r}\left(\frac{\partial \chi}{\partial r}r\right) = P_l\left[\frac{\partial \chi}{\partial r}\frac{\partial \phi}{\partial r} + \left(\bar{\Theta} + \chi\right)\frac{\partial^2 \phi}{\partial r^2}\right], \tag{17}$$

and

$$S_{rz} = \left[1 - \beta\left(\frac{\partial u}{\partial r}\right)^2\right]\left(\frac{\partial u}{\partial r}\right), \tag{18}$$

whereas for *Newtonian fluid* the results can be achieved by taking $\beta = 0$.

The parameters used above are defined as

$$\begin{aligned}\beta &= \frac{mB^2U_a^2}{6R_0^2}, T_b = \frac{D_B\left(C_0 - C_1\right)(\rho c)_p}{k_f(\rho c)_f}, \\ T_t &= \frac{D_B\left(T_0 - T_1\right)(\rho c)_p}{k_f T_1(\rho c)_f}, \\ N_g &= -\frac{T_e g\left(\rho_p - \rho_f\right)R_0^2\left(T_0 - T_1\right)}{\mu U_a}, \\ P_l &= \frac{bW_c}{D_{mo}}, \bar{\Theta} = \frac{n_1}{n_0 - n_1}, \\ T_g &= \frac{T_e g \rho_f R_0^2\left(1 - C_1\right)\left(T_0 - T_1\right)}{\mu U_a}, \\ R_b &= \frac{\left(n - n_1\right)\Theta\left(\rho_m - \rho_f\right)gR_0^2}{\mu U_a}. \end{aligned} \tag{19}$$

In the above equation, T_g is the local temperature Grashof number, N_g is the local particle Grashof number, R_b is the bioconvection Rayleigh number, T_b is the Brownian motion parameter, T_t is the thermophoresis parameter, P_l is the Peclet number, $\bar{\Theta}$ is a constant, and β is the fluid parameter.

The boundary conditions read.

$$\begin{aligned} &u' = 0,\ \theta' = 0, \phi' = 0, \chi' = 0, \quad \text{at } r = 0, \\ &u = 0,\ \theta = 0, \phi = 0, \chi = 0, \quad \text{at } r = R. \end{aligned} \tag{20}$$

SERIES SOLUTIONS

The solutions of Equations (13) to (17) can be obtained using a Homotopy perturbation method. And thus, the Homotopy P_s for Equations (13) to (17) are defined as

$$\begin{aligned} P_s\left(\bar{u}, \zeta\right) &= (1-\zeta)\left[\ell\left(\bar{u}\right) - \ell\left(\bar{u}_0\right)\right] \\ &+ \zeta\left[\ell\left(\bar{u}\right) - 3\beta\frac{\partial^2 \bar{u}}{\partial r^2}\left(\frac{\partial \bar{u}}{\partial r}\right)^2 - \frac{\beta}{r}\left(\frac{\partial \bar{u}}{\partial r}\right)^3\right. \\ &+ \left. T_g\bar{\theta} + N_g\bar{\phi} - R_b\bar{\chi} - \frac{\partial p}{\partial z}\right], \end{aligned} \tag{21}$$

$$\begin{aligned} P_s\left(\bar{\theta}, \zeta\right) &= (1-\zeta)\left[\ell\left(\bar{\theta}\right) - \ell\left(\bar{\theta}_0\right)\right] \\ &+ \zeta\left[\ell\left(\bar{\theta}\right) + T_b\frac{\partial \bar{\phi}}{\partial r}\frac{\partial \bar{\theta}}{\partial r} + T_t\left(\frac{\partial \bar{\theta}}{\partial r}\right)^2\right], \end{aligned} \tag{22}$$

$$\begin{aligned} P_s\left(\bar{\phi}, \zeta\right) &= (1-\zeta)\left[\ell\left(\bar{\phi}\right) - \ell\left(\bar{\phi}_0\right)\right] \\ &+ \zeta\left[\ell\left(\bar{\phi}\right) + \frac{T_t}{T_b}\frac{1}{r}\frac{\partial}{\partial r}\left(\frac{\partial \bar{\theta}}{\partial r}r\right)\right], \end{aligned} \tag{23}$$

$$\begin{aligned} P_s\left(\bar{\chi}, \zeta\right) &= (\zeta - 1)\left[\ell\left(\bar{\chi}_0\right) - \ell\left(\bar{\chi}\right)\right] \\ &+ \zeta\left[\ell\left(\bar{\chi}\right) - P_l\frac{\partial}{\partial r}\left(\left(\bar{\chi} + \bar{\Theta}\right)\frac{\partial \bar{\phi}}{\partial r}\right)\right], \end{aligned} \tag{24}$$

where $\zeta \in [0, 1]$the embedding parameter.

The linear operator reads as

$$\ell = \frac{\partial^2}{\partial r^2} + \frac{1}{r}\frac{\partial}{\partial r}, \tag{25}$$

and the initial guesses read as

$$\bar{w}_0 = \bar{\theta}_0 = \bar{\phi}_0 = \bar{\chi}_0 = \frac{r^2 - R^2}{c^2}, \tag{26}$$

where $c\,(\neq 0)$ is a constant.

The above initial guess is chosen in such a way that the following initial guess satisfied the linear operator as given in Equation (25) as well as satisfy all the governing boundary conditions as given in Equation (20).

Defining the following expansions

$$\bar{u} = \bar{u}_0 + \zeta\,\bar{u}_1 + \zeta^2\bar{u}_2 + \ldots, \tag{27}$$

$$\bar{\theta} = \bar{\theta}_0 + \zeta\bar{\theta}_1 + \zeta^2\bar{\theta}_2 + \ldots., \tag{28}$$

$$\bar{\phi} = \bar{\phi}_0 + \zeta\bar{\phi}_1 + \zeta^2\bar{\phi}_2 + \ldots., \tag{29}$$

$$\bar{\chi} = \bar{\chi}_0 + \zeta\,\bar{\chi}_1 + \zeta^2\,\bar{\chi}_2 + \ldots., \tag{30}$$

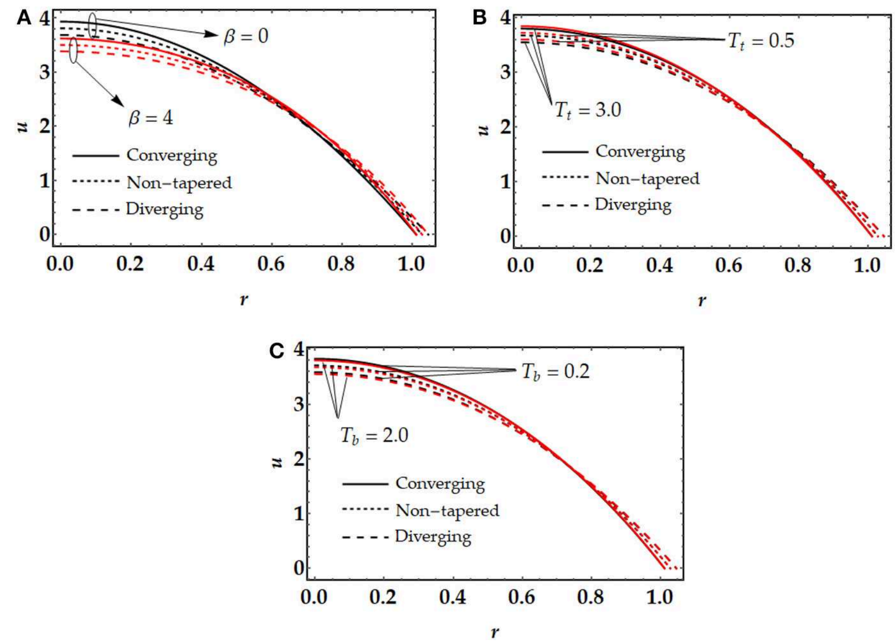

FIGURE 2 | Velocity curves for multiple values of **(A)** β, **(B)** T_t, **(C)** T_b.

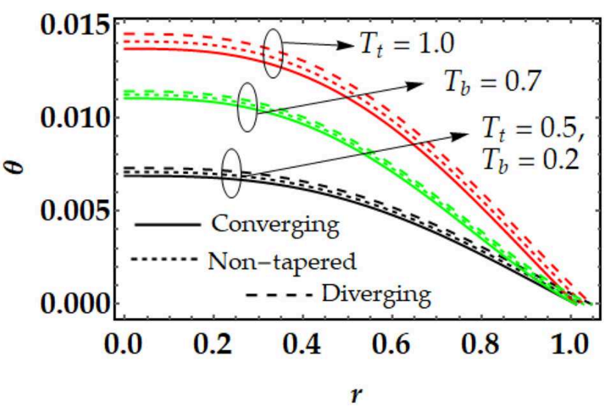

FIGURE 3 | Temperature curves for multiple values of T_b, T_t.

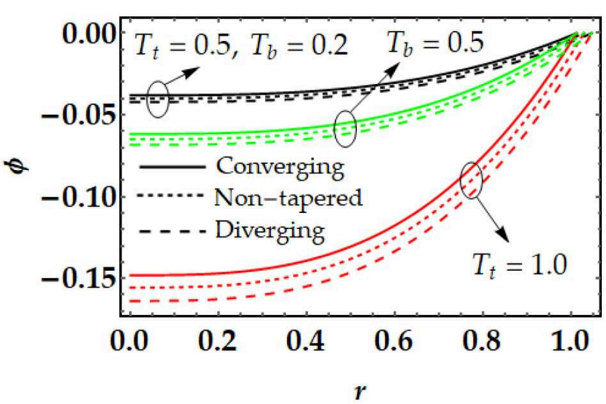

FIGURE 4 | Concentration curves for multiple values of T_b, T_t.

Using the series expansions in Equations (27–30) in the Homotopy equations [see Equations (21) to (24)], we get the set of linear differential equations, after comparing the powers of ζ. By applying the property of Homotopy perturbation method, i.e., $\zeta \to 1$, we get

$$u = \bar{u} = \bar{u}_0 + \bar{u}_1 + \bar{u}_2 + \ldots, \tag{31}$$

$$\theta = \bar{\theta} = \bar{\theta}_0 + \bar{\theta}_1 + \bar{\theta}_2 + \ldots., \tag{32}$$

$$\phi = \bar{\phi} = \bar{\phi}_0 + \bar{\phi}_1 + \bar{\phi}_2 + \ldots., \tag{33}$$

$$\chi = \bar{\chi} = \bar{\chi}_0 + \bar{\chi}_1 + \bar{\chi}_2 + \ldots., \tag{34}$$

The final results for all the governing equations are obtained as

$$u\,(r) = u_0 + r^2 u_1 + r^4 u_2 + r^5 u_3 + r^6 u_4 + \cdots, \tag{35}$$

$$\theta\,(r) = \theta_0 + r^3\theta_1 + r^4\theta_2 + r^5\theta_3 + r^6\theta_4 + \cdots, \tag{36}$$

$$\phi\,(r) = \phi_0 + r^3\phi_1 + r^4\phi_2 + \cdots, \tag{37}$$

$$\chi\,(r) = \chi_0 + r^2\chi_1 + r^4\chi_2 + r^6\chi_4 + \cdots. \tag{38}$$

where $u_n, \theta_n, \phi_n, \chi_n$, with $n = 1, 2, 3\ldots$ are the constants which can be found using the calculations through a computational software Mathematica 10.3v.

The flux Q can be determined as

$$Q = \int_0^R 2ru\,(r,z)\,\mathrm{d}r. \tag{39}$$

$$Q = \frac{\wp}{f\,(z)}, \tag{40}$$

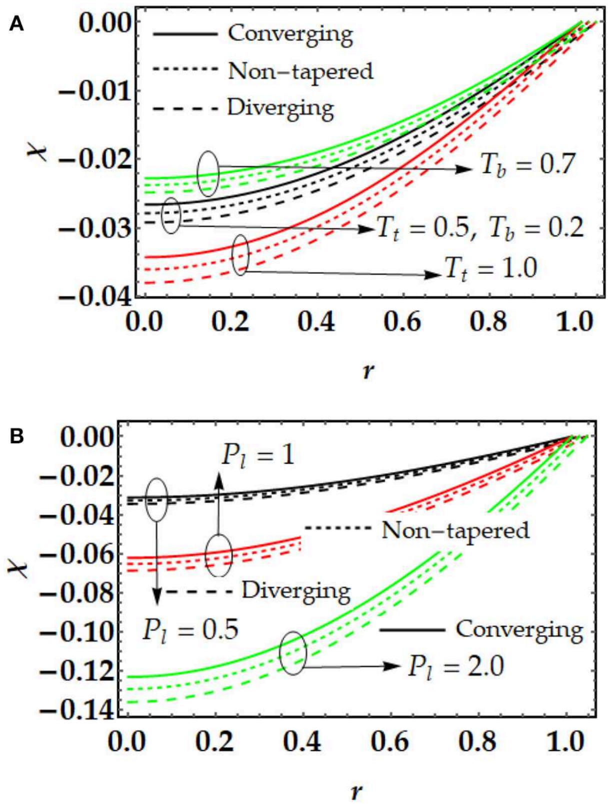

FIGURE 5 | Motile microorganism curves for multiple values of **(A)** T_t and T_b, **(B)** P_l.

where $\wp = -\frac{dp}{dz}$.

The impedance can be determined as

$$\lambda = \frac{1}{Q}\int_0 \wp dz, \tag{41}$$

The wall shear stress is calculated as.

$$S_{rz} = \frac{1}{2}\wp R\bigg|_{r=R}. \tag{42}$$

DISCUSSION

We have discussed the graphical behavior of all the leading parameters for the temperature, velocity, motile microorganism and concentration profiles. The effects of wall shear stress and the variation of impedance are also investigated to see the behavior of blood during the swimming of microorganisms and the movement of nanoparticles. With the aid of said perturbation scheme, we obtained the third order approximation against each profile. All the numerical computations have been performed using computational software Mathematica. **Figures 2–7** are plotted for different profiles with all the emerging parameters i.e., Peclet number P_l, height of stenosis δ, angular frequency ω, fluid parameter β, local temperature Grashof number T_g, local particle Grashof number N_g, bioconvection Rayleigh number R_b, thermophoresis parameter T_t, and Brownian motion T_b. All three cases i.e., diverging, converging, and non-tapered artery, have been plotted with the help of Equation (2).

Figure 2 presents the behavior of the velocity profile against the fluid parameter β, thermophoresis parameter T_t, and

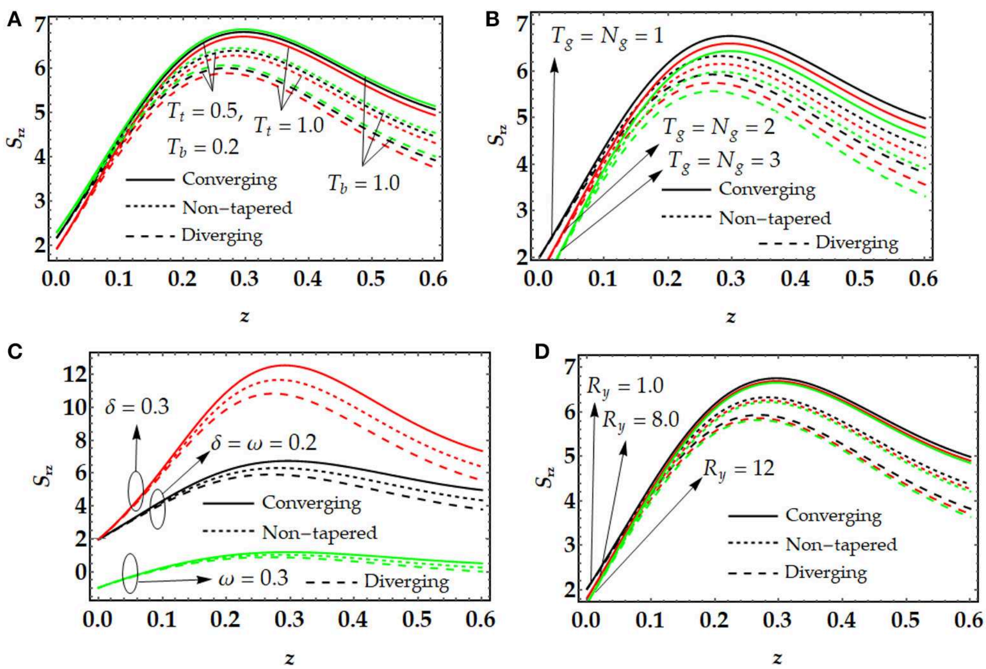

FIGURE 6 | Wall shear stress for multiple values of **(A)** T_t and T_b, **(B)** T_g and N_g, **(C)** δ and ω, **(D)** R_y.

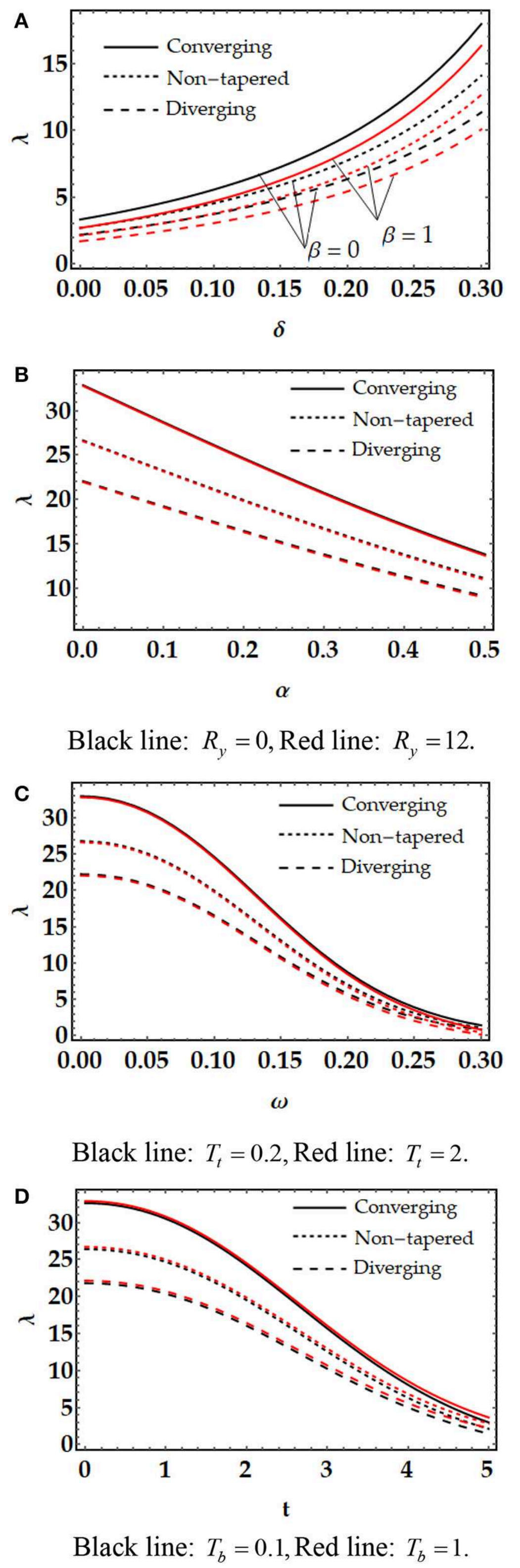

FIGURE 7 | Impedance profile for various values of **(A)** β; Black line: $\beta = 0$, Red line: $\beta = 1$. **(B)** R_y; Black line: $R_y = 0$, Red line: $R_y = 12$. **(C)** T_t; Black line: $T_t = 0.2$, Red line: $T_t = 2$. **(D)** T_b; Black line: $T_b = 0.1$, Red line: $T_b = 1$.

Brownian motion parameter T_b. In order to understand the behavior of hemodynamics in a specific artery or lesion, it is necessary to have a knowledge of blood velocity within the flow pattern. The hemodynamic velocity in the artery is not the same at all the points [33]. We can see from **Figure 2A** that the distribution of velocity at the center of the channel is maximum while it attains a minimum value when it gets close to the wall. Further, we can notice that in the case of non-Newtonian fluid, $\beta = 4$, the velocity of the blood diminishes. However, we can see a turning point between $r \in (0.6, 0.8)$ the artery where the velocity turns opposite as compared with the core of the channel and decreases as it gets closer to the wall of the artery. The significant change in the velocity gradient among different points in the artery exists because of the friction forces that play an essential role among the fluid at the walls and the flowing fluid. The friction forces occur because of the viscosity features. The viscosity represents the resistance to the flow, and it attains a minimum value if the trivial force on the fluid layer generates a velocity higher than that layer associated with the adjoining layer, and the converse is true [34, 35]. **Figure 2B** shows the behavior of the thermophoresis parameter T_t on the velocity profile. It is noticed from this figure that by enhancing the thermophoresis parameter, the nanoparticles start moving quickly and tends to repel from the hotter to a colder area. But it doesn't affect the velocity of the fluid. However, it causes resistance in the velocity of the fluid. Brownian motion plays a simultaneous role with thermophoresis. However, both parameters similarly affect the velocity profile (see **Figure 2C**). Brownian motion occurs due to the collision of suspended particles in random direction in the working fluid. Higher values of Brownian motion reveals that the particles collide very quickly which causes the resistance in the motion of the base fluid.

Figures 3, **4** are plotted for temperature and concentration distributions for multiple values of T_t and T_b. In **Figure 3**, we can see that the temperature profile rises with the increment in T_t and T_b. The enhancement of both parameters tends to repel the particles quickly. Therefore, the particles start moving from one region to the other area (i.e., hotter to colder part). Both parameters produce a force i.e., thermophoretic force and random movement of suspended particles which resist the fluid motion and as result the temperature profile increases. **Figure 4** shows that the concentration profile that is shown to be inversely proportional to the temperature profile. By increasing both parameters, the concentration profile tends to diminish remarkably. **Figure 5** is plotted to judge the variation of motile microorganisms with P_l, T_t, and T_b. It can be noticed from **Figure 5A** that the motile microorganisms 'distribution rises due to the strong influence of the Brownian motion parameter. However, a converse behavior has been observed for the thermophoresis parameter. In **Figure 5B**, we can see that the Peclet number produces resistance in the motile microorganism profile. By increasing Peclet number, it is noticed that advection propagation transport in more dominant as compared with diffusion propagation rate, which suppress the motile microorganism profile.

Figure 6 shows that the behavior of wall shear stress, that has been plotted using Equation (42), with δ, ω, T_g, N_g, R_b, T_t, and T_b. The wall shear stress is an essential part of the blood flow, and it can be described as the fluid flowing over the surface of the conduit artery. From Equation (42) we can see that wall shear stress is directly proportional to the velocity gradient close to the wall of the artery. That shows how quickly the velocity of the fluid is when propagating from one point on the artery wall to another point adjacent to the point in the perpendicular direction of the wall. However, low wall shear stress belongs to low velocities, accordingly, the higher residence time of the fluid closer to the wall. And as a result, this velocity gradient close to the wall is known as the wall shear rate. We can see from **Figure 6A** that wall shear stress is reduced due to the strong influence of the thermophoresis parameter, however, an inverse behavior has been noticed with a variation of T_b. In **Figure 6B**, we can see that local temperature Grashof number and local particle Grashof number suppress the wall shear stress remarkably. However, we noticed that the height of the clot enhances the wall shear stress, whereas the angular frequency tends to diminish the wall shear stress as shown in **Figure 6C**. In **Figure 6D**, we found that bioconvection Rayleigh number doesn't affect the wall shear stress significantly and the effect is minimal.

Figure 7 is schemed to judge the variation of impedance distribution for multiple values of β, R_b, $\mathbf{T_t}$, and T_b. **Figure 7A** is sketched for impedance vs. height of the clot for various values of the fluid parameter. We can see from this figure that impedance profile rises with an increase in the height of the clot, whereas it decreases simultaneously due to an enhancement in the fluid parameter. In **Figure 7B**, the effect of bioconvection Rayleigh number is shown incrementally decreasing. Further, it is noticed that an increase in the angular frequency ω implies to a decrease in the impedance profile. Also, it is seen in the whole domain that the thermophoresis parameter tends to suppress the impedance profile, as shown in **Figure 7C**. In **Figure 7D**, the impedance profile rises due to the strong influence of the Brownian motion parameter. However, it is seen that the impedance profile tends to reduce with an increment in time.

CONCLUDING REMARKS

A theoretical study on the swimming of nanoparticles with motile gyrotactic microorganisms in non-Newtonian blood flow propagating in an anisotropically tapered artery has been presented. Sutterby fluid model is presented to understand the rheology of the blood. The mathematical modeling is formulated using continuity, temperature, motile microorganism, momentum and concentration equation. The Homotopy perturbation method is applied to obtain the series solutions. All the graphical results are presented for diverging, converging, and non-tapered artery. The main results from the present study has been summarized below:

i. The non-Newtonian effects tends to resist in the fluid motion.
ii. Thermophoresis and Brownian motion parameter oppose the fluid motion.
iii. Temperature profile increases as the artery changes from converging to diverging shape with an increase in the thermophoresis parameter and Brownian motion.
iv. The concentration profile tends to diminish due to the strong impact of Brownian motion and thermophoresis parameter.
v. The Peclet number significantly opposes the motile microorganism profile.
vi. Thermal Grashof number opposes the wall shear stress profile and similar behavior is observed due to an increment in nanoparticle Grashof number.
vii. The shear stress at the wall is reduced due to an increment in the height of stenosis and the bioconvection Rayleigh number.
viii. The impedance profile decreases due to with an increase in bioconvection Rayleigh number, fluid parameter, and thermophoresis parameter, whereas it increases with an increase in the Brownian motion parameter.

AUTHOR CONTRIBUTIONS

MB and MM performed mathematical formulation, AZ and RE made the analysis and wrote the paper. SA made the geometry of problem and arranged the setting of the paper.

REFERENCES

1. Trisaksri V, Wongwises S. Critical review of heat transfer characteristics of nanofluids. *Renew Sust Energ Rev*. (2007) **11**:512–23. doi: 10.1016/j.rser.2005.01.010
2. Özerinç S, Kakaç S, Yazicioglu AG. Enhanced thermal conductivity of nanofluids: a state-of-the-art review. *Microfluid Nanofluid*. (2010) **8**:145–70. doi: 10.1007/s10404-009-0524-4
3. Abdelsalam SI, Bhatti MM. New insight into AuNP applications in tumour treatment and cosmetics through wavy annuli at the nanoscale. *Sci Rep*. (2019) **9**:260. doi: 10.1038/s41598-018-36459-0
4. Abdelsalam SI, Bhatti MM. The study of non-Newtonian nanofluid with hall and ion slip effects on peristaltically induced motion in a non-uniform channel. *RSC Adv*. (2018) **8**:7904–15. doi: 10.1039/C7RA13188G
5. Bég OA, Tripathi D. Mathematica simulation of peristaltic pumping with double-diffusive convection in nanofluids: a bio-nano-engineering model. *Proc Inst Mech Eng N*. (2011) **225**:99–114. doi: 10.1177/1740349912437087
6. Tripathi D, Bég OA. A study on peristaltic flow of nanofluids: application in drug delivery systems. *Int J Heat Mass Transf.* (2014) **70**:61–70. doi: 10.1016/j.ijheatmasstransfer.2013.10.044
7. Kothandapani M, Prakash J. Influence of heat source, thermal radiation, and inclined magnetic field on peristaltic flow of a hyperbolic tangent nanofluid in a tapered asymmetric channel. *IEEE T Nanobiosci*. (2014) **14**:385–92. doi: 10.1109/TNB.2014.2363673

8. El-dabe NT, Moatimid GM, Hassan MA, Mostapha DR. Analytical solution of the peristaltic flow of a Jeffrey nanofluid in a tapered artery with mild stenosis and slip condition. *Int J Innov Appl Stud*. (2015) **12**:1.
9. Akbar NS. A new thermal conductivity model with shaped factor ferromagnetism nanoparticles study for the blood flow in non-tapered stenosed arteries. *IEEE T Nanobiosci*. (2015) **14**:780–9. doi: 10.1109/TNB.2015.2462755
10. Abbas MA, Bai YQ, Rashidi MM, Bhatti MM. Application of drug delivery in magnetohydrodynamics peristaltic blood flow of nanofluid in a non-uniform channel. *J Mech Med Biol*. (2016) **16**:1650052. doi: 10.1142/S0219519416500524
11. Akbar NS. Metallic nanoparticles analysis for the blood flow in tapered stenosed arteries: Application in nanomedicines. *Int J Biomath*. (2016) **9**:1650002. doi: 10.1142/S1793524516500029
12. Bhatti MM, Zeeshan A, Ellahi R. Heat transfer analysis on peristaltically induced motion of particle-fluid suspension with variable viscosity: clot blood model. *Comput Meth Prog Bio*. (2016) **137**:115–24. doi: 10.1016/j.cmpb.2016.09.010
13. Bhatti MM, Zeeshan A, Ellahi R. Endoscope analysis on peristaltic blood flow of Sisko fluid with Titanium magneto-nanoparticles. *Comput Biol Med*. (2016) **78**:29–41. doi: 10.1016/j.compbiomed.2016.09.007
14. Shit GC, Ranjit NK, Sinha A. Electro-magnetohydrodynamic flow of biofluid induced by peristaltic wave: a non-Newtonian model. *J Bionic Eng*. (2016) **13**:436–48. doi: 10.1016/S1672-6529(16)60317-7
15. Riaz A, Bhatti MM, Ellahi R, Zeeshan A, Sait SM. Mathematical analysis on an asymmetrical wavy motion of blood under the influence entropy generation with convective boundary conditions. *Symmetry*. (2020) **12**:102. doi: 10.3390/sym12010102
16. Ijaz S, Nadeem S. A biomedical solicitation examination of nanoparticles as drug agents to minimize the hemodynamics of a stenotic channel. *Eur Phys J Plus*. (2017) **132**:448. doi: 10.1140/epjp/i2017-11703-6
17. Abdelsalam SI, Bhatti MM. The impact of impinging TiO2 nanoparticles in Prandtl nanofluid along with endoscopic and variable magnetic field effects on peristaltic blood flow. *Multidiscip Model Mater Struct*. (2018) **14**:530–48. doi: 10.1108/MMMS-08-2017-0094
18. Kuznetsov AV, Avramenko AA. Effect of small particles on this stability of bioconvection in a suspension of gyrotactic microorganisms in a layer of finite depth. *Int Commun Heat Mass*. (2004) **31**:1–10. doi: 10.1016/S0735-1933(03)00196-9
19. Geng P, Kuznetsov AV. Settling of bidispersed small solid particles in a dilute suspension containing gyrotactic microorganisms. *Int J Eng Sci*. (2005) **43**:992–1010. doi: 10.1016/j.ijengsci.2005.03.002
20. Kuznetsov AV. Non-oscillatory and oscillatory nanofluid bio-thermal convection in a horizontal layer of finite depth. *Eur J Mech B Fluids*. (2011) **30**:56–165. doi: 10.1016/j.euromechflu.2010.10.007
21. Bég OA, Prasad VR, Vasu B. Numerical study of mixed bioconvection in porous media saturated with nanofluid containing oxytactic microorganisms. *J Mech Med Biol*. (2013) **13**:1350067. doi: 10.1142/S021951941350067X
22. Akbar NS. Bioconvection peristaltic flow in an asymmetric channel filled by nanofluid containing gyrotactic microorganism: bio nano engineering model. *Int J Num Method H*. (2015) **25**:214–24. doi: 10.1108/HFF-07-2013-0242
23. Bhatti MM, Zeeshan A, Ellahi R. Simultaneous effects of coagulation and variable magnetic field on peristaltically induced motion of Jeffrey nanofluid containing gyrotactic microorganism. *Microvasc Res*. (2017) **110**:32–42. doi: 10.1016/j.mvr.2016.11.007
24. Ahmed SE, Mahdy A. Laminar MHD natural convection of nanofluid containing gyrotactic microorganisms over vertical wavy surface saturated non-Darcian porous media. *Appl Math Mech*. (2016) **37**:471–84. doi: 10.1007/s10483-016-2044-9
25. Chakraborty T, Das K, Kundu PK. Framing the impact of external magnetic field on bioconvection of a nanofluid flow containing gyrotactic microorganisms with convective boundary conditions. *Alex Eng J*. (2018) **57**:61–71. doi: 10.1016/j.aej.2016.11.011
26. Shahid A, Zhou Z, Hassan M, Bhatti MM. Computational study of magnetized blood flow in the presence of Gyrotactic microorganisms propelled through a permeable capillary in a stretching motion. *Int J Multiscale Com*. (2018) **16**:409–26. doi: 10.1615/IntJMultCompEng.2018026030
27. Waqas H, Khan SU, Hassan M, Bhatti MM, Imran M. Analysis on the bioconvection flow of modified second-grade nanofluid containing gyrotactic microorganisms and nanoparticles. *J Mol Liq*. (2019) **291**:111231. doi: 10.1016/j.molliq.2019.111231
28. Waqas H, Khan SU, Imran M, Bhatti MM. Thermally developed Falkner-Skan bioconvection flow of a magnetized nanofluid in the presence of a motile gyrotactic microorganism: Buongiorno's nanofluid model. *Phys Scr*. (2019) **94**:115304. doi: 10.1088/1402-4896/ab2ddc
29. Sohail M, Naz R, Abdelsalam SI. On the onset of entropy generation for a nanofluid with thermal radiation and gyrotactic microorganisms through 3D flows. *Physica Scripta*. (2020) **95**:045206. doi: 10.1088/1402-4896/ab3c3f
30. Bhatti MM, Khalique CM, Bég TA, Bég OA, Kadir A. Numerical study of slip and radiative effects on magnetic Fe3O4-water-based nanofluid flow from a nonlinear stretching sheet in porous media with Soret and Dufour diffusion. *Mod Phys Lett B*. (2020) **34**:2050026. doi: 10.1142/S0217984920500268
31. Marin M. Lagrange identity method for microstretch thermoelastic materials. *J Math Anal Appl*. (2010) **363**:275–86. doi: 10.1016/j.jmaa.2009.08.045
32. Marin M, Agarwal RP, Mahmoud SR. Nonsimple material problems addressed by the Lagrange's identity. *Bound Value Probl*. (2013) **2013**:135. doi: 10.1186/1687-2770-2013-135
33. Strackee J, Westerhof N. *The Physics of Heart and Circulation*. Bristol: Institute of Physics Publishing (1993).
34. Rowan JO. *Physics and the Circulation*, Vol. 9. Bristol: Adam Hilger Ltd (1981).
35. Pearson TC, Path FRC. Hemorheology in the erythrocytoses. *Mt Sinai J Med*. (2001) **68**:182–91.

Conflict of Interest: The authors declare that the research was conducted in the absence of any commercial or financial relationships that could be construed as a potential conflict of interest.

The handling editor declared a past co-authorship with the author MM.

Copyright © 2020 Bhatti, Marin, Zeeshan, Ellahi and Abdelsalam. This is an open-access article distributed under the terms of the Creative Commons Attribution License (CC BY). The use, distribution or reproduction in other forums is permitted, provided the original author(s) and the copyright owner(s) are credited and that the original publication in this journal is cited, in accordance with accepted academic practice. No use, distribution or reproduction is permitted which does not comply with these terms.

frontiers in Physics

ORIGINAL RESEARCH
published: 08 April 2020
doi: 10.3389/fphy.2020.00066

A New Computational Technique Design for EMHD Nanofluid Flow Over a Variable Thickness Surface With Variable Liquid Characteristics

Muhammad Irfan, Muhammad Asif Farooq and Tousif Iqra*

Department of Mathematics, School of Natural Sciences (SNS), National University of Sciences and Technology (NUST), Islamabad, Pakistan

The objective of this paper comprises two key aspects: to establish descriptive mathematical models for constant and variable fluid flows over a variable thickness sheet by inducting applied electric and magnetic fields, porosity, radiative heat transfer, and heat generation/absorption, and to seek their solution by constructing a novel numerical method, the Simplified Finite Difference Method (SFDM). We resort to similarity transformations to implicate partial differential equations (PDEs) into a set of ordinary differential equations (ODEs). Optimal results for a pair of ODEs obtained from SFDM are assessed by drawing a comparison with *bvp4c* and existing literature values. SFDM has been implemented in MATLAB for both constant and variable fluid properties. Tabulated numerical values of the skin friction coefficient and local Nusselt and Sherwood numbers are measured and analyzed against different parameters. The influence of distinct parameters on velocity, temperature, and nanoparticle volume fraction are explained in great detail via diagrams. The skin friction coefficient for variable fluid properties is greater than for constant fluid properties. However, the local Nusselt number is lower for variable fluid properties than with constant fluid properties. Surprisingly, high-precision computational results are achieved from the SFDM.

Keywords: electrical magnetohydrodynamics (EMHD), variable thicked surface, nanofluid, simplified finite difference method (SFDM), variable fluid properties

OPEN ACCESS

Edited by:
Muhammad Mubashir Bhatti, Shanghai University, China

Reviewed by:
Rahmat Ellahi, University of California, Riverside, United States
Muhammad Ibrahim, University of Science and Technology Beijing, China

****Correspondence:***
Muhammad Asif Farooq
asiffarooq.2007@gmail.com

Specialty section:
This article was submitted to Mathematical Physics, a section of the journal Frontiers in Physics

Received: *02 December 2019*
Accepted: *28 February 2020*
Published: *08 April 2020*

Citation:
Irfan M, Farooq MA and Iqra T (2020) A New Computational Technique Design for EMHD Nanofluid Flow Over a Variable Thickness Surface With Variable Liquid Characteristics. Front. Phys. 8:66. doi: 10.3389/fphy.2020.00066

1. INTRODUCTION

Fluid mechanics has many applications in contexts from the human biological system to the manufacturing industry. For example, the study of breathing in biological systems uses bio-fluid dynamics. Cooling is another such phenomenon, which is important in electronics and the automobile industry. Investigating stretching sheet flows is relevant to many significant applications. All of this plays a vital role in technological advances such as those of polymer manufacturing and cooling processes in glass and paper production Hayat et al. [1]. Having variable thickness becomes useful in minimizing the weight of architectural elements Hayat et al. [1].

Hayat et al. [1, 2] analyzed the consequences of Cattaneo-Christov heat flux and a temperature-dependent fluid thermal conductivity on fluid flow over a variable thickness sheet and showed that variable conductivity enhances the temperature distribution. They also maintained that the temperature profile decreases with the thermal relaxation parameter. Mabood et al. [3] discussed the non-Darcian MHD convective flow and claimed that temperature rise depends on the Eckert number. In the context of a stretching sheet for variable thickness, Fang et al. [4] has tackled the boundary layer flow and analyzed multiple solutions. Khader and Ahmed [5] computed a numerical solution for variable sheet thickness with slip velocity and pointed out that the skin friction coefficient increases with the wall thickness parameter. Daniel et al. [6] discussed the thermal stratification effects on MHD radiative flow of nanofluid for a variable thickness sheet. They submitted that the thermal stratification effect reduces temperature. Reddy et al. [7] investigated the MHD flow and heat transfer of Williamson nanofluid over a variable thickness sheet with variable thermal conductivity and identified that the velocity profile decreases with the wall thickness parameter when $m < 1$. Daniel et al. [8] examined the effect of thermal radiation on electrical MHD flow of nanofluid over a stretching sheet with variable thickness and concluded that the thermal radiation did impact the nanofluid temperature.

Magnetohydrodynamics is the study of the flow of electrically conducting fluids in an electro-magnetic-field. The study of MHD flow is of considerable interest in modern metallurgical and metal-working processes. Noreen et al. [9] examined the numerical solutions of magnetohydrodynamic boundary layer flow of tangent hyperbolic fluid toward a stretching sheet. They showed that the skin friction coefficient increases with an increase in M. Mukhopadhyay et al. [10] conducted a study to assess the effects of fluid flow with constant and changeable viscosity on a heated surface. They noticed that a decrease in viscosity causes the velocity to decrease with increasing distance along the stretching sheet. Nadeem et al. [11] examined MHD three-dimensional Casson fluid flow through a porous linear stretching plate and concluded that the stretching parameter resulted in decreasing behavior of the velocity profile. Mabood et al. [12] investigated MHD boundary layer flow and heat transfer of nanofluid over a non-linear stretching sheet. They note that the boundary layer thickness grows with Brownian motion. Zhang et al. [13] discussed the MHD flow and radiation heat transfer of nanofluids in porous media with variable surface heat flux and chemical reaction. They examined three types of nanoparticles. Popley et al. [14] addressed the overall impact of varying liquid characteristics upon hydro-magnetic motion and heat transfer across a non-linear stretching surface. They demonstrated that the free stream velocity induces a reduction in the boundary layer thickness. Mohsen et al. [15] discussed nanofluid flow with convective heat transfer considering Lorentz forces and showed that heat transfer rises with the Hartmann number. Patel [16] studied the effects of heat generation, thermal radiation, and Hall current on MHD Casson fluid flow past an osculating plate in a porous medium. They stated that the Hall current boosts mobility in both directions. Farooq et al. [17] discussed the MHD flow of Maxwell fluid with nanomaterials due to an exponentially stretching surface. The influence of the thermophoresis parameter on the temperature distribution is negligible. Magnetohydrodynamic (MHD) boundary layer flow past a wedge with heat transfer and viscous effects of nanofluid embedded in porous media was investigated by Ibrahim and Tulu [18]. They discover that the pressure gradient influences the boundary layer thickness. The impact of 3D Maxwell nanofluid flow over an exponentially stretching surface in terms of heat and mass transfer was explored by Ali et al. [19]. They showed that the skin friction coefficient decreases with the Deborah number.

Nanofluids solid-liquid suspensions consisting of solid nanoparticles of size 1-100 nm and liquid Mabood et al. [3]. Due to reports of their having significantly enhanced thermal properties, nanofluids have drawn great interest recently Mabood et al. [3]. The term nanofluid was proposed by Choi and Eastman [20], who demonstrated that the introduction of a small number of nanoparticles ($<$ 1 percent by volume fraction) to traditional liquids increased the fluid thermal conductivity by approximately two times Nadeem et al. [11]. The numerical simulation of nanofluid flow with convective boundary conditions was studied by Das et al. [21], who demonstrated that the surface convection parameter enhances the heat transfer rate. Mabood and Das [22], in their analysis, communicated melting heat transfer of hydromagnetic nanofluid flow with a second-order slip condition. Cao et al. [23] discussed the MHD flow and heat transfer of fractional Maxwell viscoelastic nanofluid over a moving plate by using a finite difference method and found that the average Nusselt number is higher with a rise in the fractional derivative parameter. Das et al. [24] studied the effects of a magnetic field on an unsteady mixed convection flow of nanofluids containing spherical and cylindrical nanoparticles. Narayana et al. [25] discussed the effects of thermal radiation and a heat source on an MHD nanofluid past a vertical plate in a rotating system with a porous medium. They used three different nanoparticles and showed that they enhance the heat transfer rate, a result that can be used in heat exchanger technology. The influences on stagnation-point flow toward a stretching/shrinking sheet in a nanofluid were discussed by Mansur et al. [26] using the Buongiorno model. They proved that the thermophoresis parameter reduces the heat transfer rate. Makinde [27] studied viscous dissipation and Newtonian heating over a flat plate in a nanofluid. The heat transfer rate rises with the nanoparticle volume fraction and the Biot number. Ali et al. [28] discussed a numerical study of unsteady MHD Couette flow and heat transfer of nanofluids in a rotating system with convective cooling and indicated that the rotation has a significant effect on velocity and heat transfer. Ashwinkumar and Sulochana [29] investigated the effect of radiation absorption and buoyancy force on the MHD mixed convection flow of Casson nanofluid. They noticed that the volume fraction of nanoparticles governs the temperature distribution. Under temperature control, Andersson and Aarseth [30] revisited the fluid properties of a liquid. The effect of variable fluid properties on the hydromagnetic flow and heat transfer over a non-linearly stretching sheet was discussed by Prasad et al. [31]. Hayat et al. [32] discussed mixed convection flow across a porous sheet and reported that the thermal boundary layer thickness is lowered with Pr. Reddy et al. [33] probed the effect of variable thermal conductivity on MHD flow of nanofluid over a stretching sheet. They considered convective boundary conditions. Zaka et al. [34] applied numerical simulation for Darcy-Forchheimer flow of nanofluid by considering a rotating disk. They reported that the temperature distribution is enhanced with the thermophoresis parameter. Shah et al. [35] discussed the nanofluid flow for different shape factors. They managed to show that the shape factor causes stronger convection. Zeeshan et al. [36] reported the effect of radiative nanofluid flow under a pressure gradient due to entropy generation and observed an increase in entropy with an increase in the pressure gradient. Ellahi et al. [37] investigated flow of a power-law nanofluid with entropy generation and noted that the skin friction coefficient increases at the heated wall. Yousif et al. [38] analyzed the momentum and heat transfer of MHD Carreau nanofluid over an exponentially stretching surface and used the shooting method to compute the solution. Sarafraz et al. [39] discussed the pool boiling heat transfer characteristics of an iron oxide nano-suspension considering a constant magnetic field and found that bubble formation is intensified due to the magnetic field. Fujimoto [40] described multi-scale simulation on adaptive meshes.

This paper is arranged in the following way. A mathematical formalism of the physical model is explained in section Problem Formulation. Section Fluid Properties Analysis addresses constant as well as varying liquid characteristics. Section Physical Quantities provides physical quantities, and an overview of the numerical process has been given in section Numerical Procedure. Results and discussion are presented in section Result and Discussion. In section Conclusions, the conclusion is drawn.

2. PROBLEM FORMULATION

We assume an electrical magnetohydrodynamic (EMHD), two-dimensional, steady, laminar flow of nanofluid over a non-linear stretching sheet with variable thickness. A variable magnetic field $B(x) = B_o(x+b)^{\frac{n-1}{2}} (n \neq 1)$ and variable electrical field $E(x) = E_o(x+b)^{\frac{n-1}{2}} (n \neq 1)$ are applied normal to the direction of flow. The sheet is stretching with non-linear velocity $U_w = U_o(x+b)^n (n \neq 1)$, where b is the dimensional constant and U_o is the reference velocity. Therefore, the surface is considered not to be flat, and its thickness varies as $y = A(x+b)^{\frac{1-n}{2}} (n \neq 1)$, where A is a very small constant to hold the sheet thin enough. We also observe that for $n = 1$, the current problem reduces to a flat sheet. The geometry of the problem is shown in **Figure 1**, where the x-axis has been taken along the sheet and y-axis is normal to it.

The induced magnetic field has been neglected under the assumption of a small magnetic Reynolds number. The boundary layer equations governing this flow are Daniel et al. [6, 8] and Irfan et al. [41]

$$\frac{\partial u}{\partial x} + \frac{\partial v}{\partial y} = 0, \quad (1)$$

$$u\frac{\partial u}{\partial x} + v\frac{\partial u}{\partial y} = \frac{1}{\rho}\frac{\partial}{\partial y}\left(\frac{\mu \partial u}{\partial y}\right) + \frac{\sigma}{\rho}(E(x)B(x) - B^2(x)u) - \frac{\mu}{\rho K(x)}u \quad (2)$$

$$u\frac{\partial T}{\partial x} + v\frac{\partial T}{\partial y} = \frac{1}{\rho C_p}\frac{\partial}{\partial y}\left(\frac{k\partial T}{\partial y}\right) + \tau\left(D_B\frac{\partial T}{\partial y}\frac{\partial C}{\partial y} + \frac{D_T}{T_\infty}\left(\frac{\partial T}{\partial y}\right)^2\right)$$
$$-\frac{1}{\rho C_p}\frac{\partial q_r}{\partial y} + \frac{\sigma}{\rho C_p}(uB(x) - E(x))^2 + \frac{Q(x)}{\rho C_p}(T - T_\infty), \quad (3)$$

$$u\frac{\partial C}{\partial x} + v\frac{\partial C}{\partial y} = D_B\frac{\partial^2 C}{\partial y^2} + \frac{D_T}{T_\infty}\frac{\partial^2 T}{\partial y^2}, \quad (4)$$

Here, u and v are the velocity components parallel to the $x-$ and $y-$ axis, respectively. Further, μ is the viscosity, ρ is the density, ν is the kinematic viscosity, C_p is the specific heat capacity, B is the magnetic field. T and C are the fluid temperature and nanoparticle fraction, respectively. The temperature of the fluid at the wall and ambient temperature are denoted by T_w and T_∞, respectively. D_B and D_T are the Brownian diffusion coefficient and thermophoretic diffusion coefficient, respectively. $\tau = \frac{(\rho c)_p}{(\rho c)_f}$ is the ratio of the effective heat capacity of the nanoparticle material to the heat capacity of the fluid, q_r is the radiative heat flux, $Q(x) = Q_0(x+b)^{\frac{n-1}{2}}$ is the volumetric rate of heat generation, and $K(x) = K_0(x+b)^{n-1}$ is a variable permeability.

The above system is completed with the following appropriate boundary conditions, taking to view of [32] and [33]:

$$u = U_w(x) = U_o(x+b)^n,\ v = 0,\ -k\frac{\partial T}{\partial y} = h_s(T_f - T),$$
$$D_B\frac{\partial C}{\partial y} + D_T\frac{\partial T}{\partial y} = 0 \text{ at } y = A(x+b)^{\frac{1-n}{2}}$$
$$u \longrightarrow 0, \quad T \longrightarrow T_\infty, \quad C \longrightarrow C_\infty \quad \text{as} \quad y \longrightarrow \infty \quad (5)$$

To the above equations, (1)-(4), the following relevant transformations will be utilized:

$$\psi = \sqrt{\frac{2}{n+1}\nu U_o(x+b)^{n+1}} f(\eta),$$
$$\xi = y\sqrt{\left(\frac{n+1}{2}\right)\frac{U_o(x+b)^{n-1}}{\nu}}, \alpha = A\left(\frac{(n+1)U_0}{2\nu}\right)^{\frac{1}{2}}$$
$$\eta = \xi - \alpha = y\sqrt{\left(\frac{n+1}{2}\right)\frac{U_o(x+b)^{n-1}}{\nu}} - \alpha$$
$$\theta = \frac{T - T_\infty}{T_w - T_\infty}, \quad \phi = \frac{C - C_\infty}{C_w - C_\infty}, \quad u = U_o(x+b)^n f'(\eta),$$
$$v = -\sqrt{\frac{2}{n+1}\nu U_o(x+b)^{n-1}}\left(f(\eta) + \eta\frac{n-1}{n+1}f'(\eta)\right). \quad (6)$$

Equation (1) is identically satisfied. In addition, when the above similarity variables are applied to Eqations (2), (3), and (4), it yields:

$$\left(\frac{\mu}{\mu_o}f''\right)' - \frac{2n}{n+1}f'^2 + ff'' + M(E_1 - f') - Kp\frac{\mu}{\mu_o}f' = 0, \quad (7)$$

$$\left(1 + \frac{4}{3}Rd\right)\left(\frac{k}{k_o}\theta'\right)' + Pr_o(f\theta' + Nb\theta'\phi' + Nt(\theta')^2$$
$$+MEc(f' - E_1)^2 + \frac{2}{n+1}s\theta) = 0, \quad (8)$$

$$\phi'' + \frac{Nt}{Nb}\theta'' + LePr_o f\phi' = 0. \quad (9)$$

The equivalent boundary conditions in terms of similarity variables are specified as:

$$f(0) = \alpha\left(\frac{1-n}{1+n}\right),\ f'(0) = 1,\ ,f'(\infty) = 0,\ \theta'(0) = -B_i(1 - \theta(0))$$
$$\theta(\infty) = 0, \quad Nb\phi'(0) + Nt\theta'(0) = 0, \quad \phi(\infty) = 0, \quad (10)$$

where $M = \frac{2\sigma B_o^2}{\rho U_o(n+1)}$ is a magnetic parameter, α is the wall thickness parameter, $E_1 = \frac{E_o}{B_o U_o(x+b)^n}$ is the electric field, and

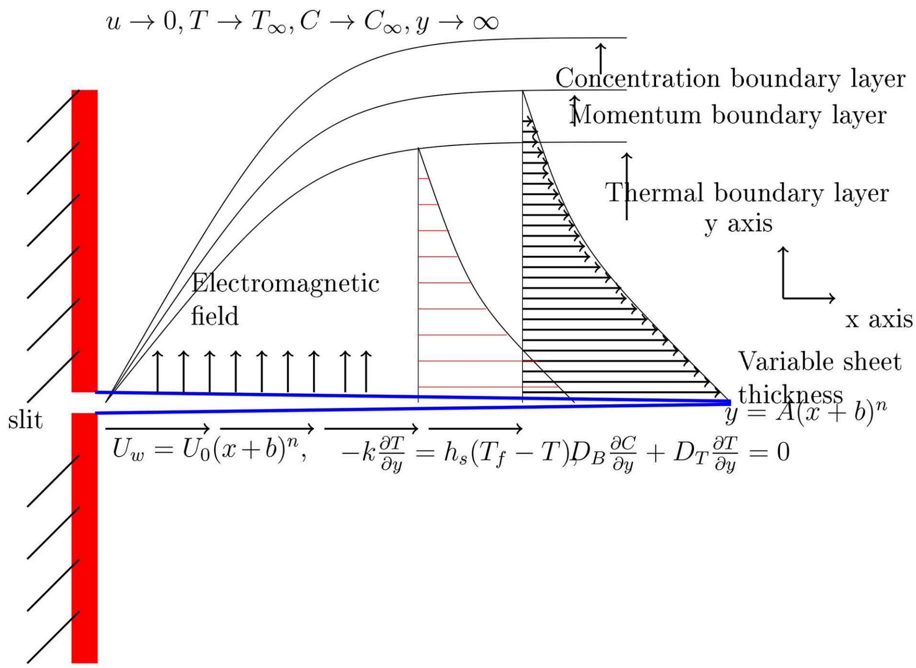

FIGURE 1 | Schematic diagram of the problem.

$Kp = \frac{2\nu}{K_o U_o(n+1)}$ is the permeability constant. $Pr_o = \frac{\mu_o C_p}{k_o}$ is the Prandtl number, $Nb = \frac{\tau D_B(C_w - C_\infty)}{\nu}$ is the Brownian motion parameter, $Nt = \frac{\tau D_T(T_w - T_\infty)}{T_\infty \nu}$ is the thermophoresis parameter, $Ec = \frac{U_w^2}{C_p(T_w - T_\infty)}$ is the local Eckert number, $Rd = \frac{4\sigma^* T_\infty^3}{k_o k^*}$ denotes the radiation parameter, $s = \frac{Q_o(x+b)}{\rho u_w C_p}$ is the heat source parameter, B_i is the Biot number, and $Le = \frac{\nu}{D_B}$ is Lewis number Irfan et al. [41].

3. FLUID PROPERTIES ANALYSIS

We illustrate the main theme of this work through the following two subsections.

3.1. Case A: Constant Fluid Characteristics

For this case, we rewrite Equations (7), (8), and (9) into the following set of equations Irfan et al. [41]:

$$f''' - \frac{2n}{n+1}f'^2 + ff'' + M(E_1 - f') - Kpf' = 0 \tag{11}$$

$$\left(1 + \frac{4}{3}Rd\right)\theta'' + Pr_o(f\theta' + Nb\theta'\phi' + Nt(\theta')^2 + MEc(f' - E_1)^2 + \frac{2}{n+1}s\theta) = 0 \tag{12}$$

$$\phi'' + \frac{Nt}{Nb}\theta'' + Pr_o Lef\phi' = 0 \tag{13}$$

3.2. Case B: Variable Fluid Properties

In this case, we express viscosity and thermal conductivity as a function of temperature Andersson and Aarseth [30]

$$\mu(T) = \frac{\mu_{ref}}{1 + \gamma(T - T_{ref})} \tag{14}$$

In (14), above, γ is a property of a fluid. Assuming $T_o \approx T_{ref}$, we get

$$\mu = \frac{\mu_o}{1 - \frac{T - T_o}{\theta_r(T_w - T_o)}} = \frac{\mu_o}{1 - \frac{\theta(\eta)}{\theta_r}} \tag{15}$$

Here, $\theta_r = \frac{-1}{\gamma(T_w - T_o)}$. Inserting Equation (15) into Equation (7), we get

$$\frac{\theta_r}{(\theta r - \theta)}f''' + \frac{f''\theta'\theta_r}{(\theta_r - \theta)^2} - \frac{2n}{n+1}f'^2 + ff'' + M(E_1 - f') - Kp\frac{\theta_r}{\theta_r - \theta}f' = 0 \tag{16}$$

Following Prasad et al. [31], the changeable thermal conductivity is expressed as

$$k(T) = k_o(1 + \epsilon\theta) \tag{17}$$

Using Equation (17) in Equation (8), we get.

$$\left(1 + \frac{4}{3}Rd\right)((1 + \epsilon\theta)\theta'' + \epsilon(\theta')^2) + Pr_o(f\theta' + Nb\theta'\phi' + Nt(\theta')^2 + MEc(f' - E_1)^2 + \frac{2}{n+1}s\theta) = 0 \tag{18}$$

4. PHYSICAL QUANTITIES

The important physical parameters are defined as follows.

4.1. Skin Friction Coefficient

The wall friction coefficients for case A and case B are defined as

$$C_f = \frac{\tau_w}{\rho u_w^2} = \sqrt{\frac{1+n}{2Re_x}} f''(0)\ (\textbf{CASE A})$$

$$C_f = \frac{\tau_w}{\rho u_w^2} = \frac{\theta_r}{\theta_r - \theta(0)} \sqrt{\frac{1+n}{2Re_x}} f''(0)\ (\textbf{CASE B})$$

4.2. Local Nusselt Number

The local Nusselt numbers for Cases A and B are the same and can be written as

$$Nu_x = -\frac{(x+b)q_w}{k_o(T_w - T_\infty)} = -(1 + \frac{4}{3}Rd)\sqrt{\frac{(1+n)Re_x}{2}}\theta'(0)$$

4.3. Local Sherwood Number

The local Sherwood number for both Case A and Case B is

$$Sh_x = -\frac{(x+b)j_w}{C_w - C_\infty} = -\sqrt{\frac{(1+n)Re_x}{2}}\phi'(0) \quad (19)$$

5. NUMERICAL PROCEDURE

The system of ODEs for Case A and Case B, along with the boundary conditions, are first transformed into a system of first-order ODEs. We use two numerical methods to find the solution of these ODEs. The first method is the SFDM [42], and the second is implemented through MATLAB's built-in solver *bvp4c*. The details of the methods and the implications are described below.

5.1. Simplified Finite Difference Method (SFDM)

The algorithm and necessary details for the simplified FDM are as follows:

1. We first reduce the third-order ODE into a group of first- and second-order ODEs. This reduction of order simplifies the process of finite difference approximation. The ODE already written in second order cannot be reduced.
2. For further simplification, we use a Taylor series to linearize the system of nonlinear ODEs.
3. We replace the derivatives in linear ODEs with the corresponding finite difference approximation formulas.
4. In the end, we reach an algebraic system of equations that can be solved efficiently by the Thomas algorithm.
5. The process will be repeated for energy and concentration equations.

An explanation of SFDM has been illustrated in the flowchart. Generally, we find the results when $N = 1,000$ grid points in the η direction. The domain to achieve steady state varies due to the effects of different parameters, but the domain $\eta = 7$ seems sufficient for our results. To initiate, we assume $f' = F$ in (11), and then we get

$$\frac{d^2F}{d\eta^2} = \frac{2n}{n+1}F^2 - f\frac{dF}{d\eta} - M(E_1 - F) + KpF \quad (20)$$

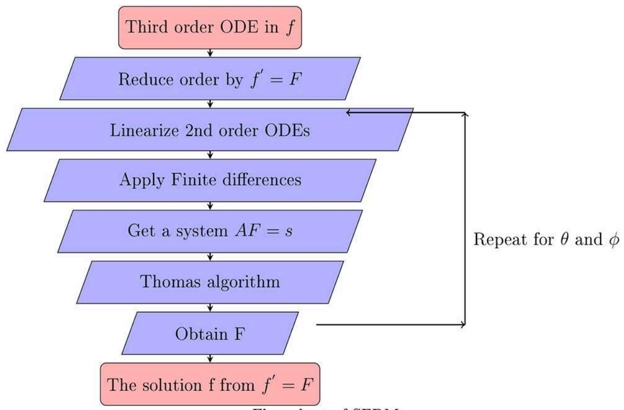

Flow chart of SFDM.

We can write this expression for the function f as

$$\chi_1(\eta, F, F') = \frac{2n}{n+1}F^2 - f\frac{dF}{d\eta} - M(E_1 - F) + KpF \quad (21)$$

Let us approximate $\frac{dF}{d\eta}$ in the above equation by forward difference approximation

$$\chi_1(\eta, F, F') = \frac{2n}{n+1}F_i^2 - f_i(\frac{F_{i+1} - F_i}{h}) - M(E_1 - F_i) + KpF_i \quad (22)$$

The coefficients of second-order ODE read as

$$A_n = -\frac{\partial \chi_1}{\partial F'} = -(-f) = f = f_i \quad (23)$$

$$B_n = -\frac{\partial \chi_1}{\partial F} = -(\frac{4n}{n+1}F + M + Kp) = -(\frac{4n}{n+1}F_i + M + Kp) \quad (24)$$

$$D_n = \chi_1(\eta, F, F') + B_nF_i + A_n\frac{F_{i+1} - F_i}{h} \quad (25)$$

After some manipulation, (25) becomes

$$a_iF_{i-1} + b_iF_i + c_iF_{i+1} = r_i, \qquad i = 1, 2, 3...., N \quad (26)$$

where

$$a_i = 2 - hA_n, \quad b_i = 2h^2B_n - 4, \quad c_i = 2 + hA_n, \quad r_i = 2h^2D_n \quad (27)$$

In matrix-vector form, it is written compactly as

$$AF = s \quad (28)$$

where

$$A = \begin{bmatrix} b_1 & c_1 & & & \\ a_2 & b_2 & c_2 & & \\ & & .... & & \\ & & a_{N-2} & b_{N-2} & c_{N-2} \\ & & & a_{N-1} & b_{N-1} \end{bmatrix} \quad (29)$$

$$F = \begin{bmatrix} F_1 \\ F_2 \\ . \\ . \\ F_{N-1} \end{bmatrix} \qquad s = \begin{bmatrix} s_1 \\ s_2 \\ . \\ . \\ s_{N-1} \end{bmatrix} \quad (30)$$

The matrix A is a tridiagonal matrix and is written in LU-Factorization as [43]

$$A = LU \quad (31)$$

where

$$L = \begin{bmatrix} \beta_1 & & & \\ a_2 & \beta_2 & & \\ & .... & & \\ & a_{N-2} & \beta_{N-2} & \\ & & a_{N-1} & \beta_{N-1} \end{bmatrix} \quad (32)$$

and

$$U = \begin{bmatrix} 1 & \gamma_1 & & \\ & 1 & \gamma_2 & \\ & & .... & \\ & & 1 & \gamma_{N-2} \\ & & & 1 \end{bmatrix} \quad (33)$$

where L and U are the lower and upper triangular matrices, respectively. Here the unknowns $(\beta_i, \gamma_i), i = 1, 2, ..., N-1$ are to be related as [43]

$$\beta_1 = -1 - \frac{\lambda}{h}, \quad \gamma_1 = \frac{\lambda}{\beta_1 h} \quad (34)$$

$$\beta_i = b_i - a_i\gamma_{i-1}, \quad i = 2, 3, ..., N-1 \quad (35)$$

$$\beta_i\gamma_i = c_i, \quad i = 2, 3, ..., N-2 \quad (36)$$

After defining these relations, (31) becomes

$$LUF = s, \quad UF = z, \quad \text{and} \quad Lz = s \quad (37)$$

and we have

$$\begin{bmatrix} \beta_1 & & & \\ a_2 & \beta_2 & & \\ & .... & & \\ & a_{N-2} & \beta_{N-2} & \\ & & a_{N-1} & \end{bmatrix} \begin{bmatrix} z_1 \\ z_2 \\ z_3 \\ . \\ . \\ . \\ z_{N-2} \\ z_{N-1} \end{bmatrix} = \begin{bmatrix} s_1 \\ s_2 \\ s_3 \\ . \\ . \\ . \\ s_{N-2} \\ s_{N-1} \end{bmatrix} \quad (38)$$

The unknown elements of z can be found by

$$z_1 = s_1/\beta_1, z_i = \frac{s_i - a_i z_{i-1}}{\beta_i}, i = 2, 3, ..., N-1 \quad (39)$$

and

$$\begin{bmatrix} 1 & \gamma_1 & & \\ & 1 & \gamma_2 & \\ & & .... & \\ & & 1 & \gamma_{N-2} \\ & & & 1 \end{bmatrix} \begin{bmatrix} F_1 \\ F_2 \\ . \\ . \\ . \\ F_{N-2} \\ F_{N-1} \end{bmatrix} = \begin{bmatrix} z_1 \\ z_2 \\ . \\ . \\ . \\ z_{N-2} \\ z_{N-1} \end{bmatrix} \quad (40)$$

We then get

$$F_{i-1} = z_{i-1}, \quad F_i = z_i - \gamma_i F_{i+1}, \quad i = N-2, N-3, ..., 3, 2, 1 \quad (41)$$

which is a solution of (20). We can easily find f from $f' = F$, which in discretization form

$$\frac{f_{i+1} - f_i}{h} = F_i \quad (42)$$

gives a required solution of (11). A similar procedure can also adopted for solutions θ and ϕ. For the sake of brevity, we only present coefficients for these ODEs and leave out the details that follow on the same line as presented above. For example, the energy equation (12) is

$$\frac{d^2\theta}{d\eta^2} = -(\frac{Pr_o}{(1+\frac{4}{3}Rd)}(f\frac{d\theta}{d\eta} + Nb\frac{d\theta}{d\eta}\frac{d\phi}{d\eta} + Nt(\frac{d\theta}{d\eta})^2 + MEc(\frac{df}{d\eta} - E_1)^2 + \frac{2}{n+1}s\theta)) \quad (43)$$

$$\chi_2(\eta, \theta, \theta') = -(\frac{Pr_o}{(1+\frac{4}{3}Rd)}(f_i(\frac{\theta_i - \theta_{i-1}}{h}) + Nb(\frac{\theta_i - \theta_{i-1}}{h})(\frac{\phi_i - \phi_{i-1}}{h}) + Nt(\frac{\theta_i - \theta_{i-1}}{h})^2 + MEc(F_i - E_1)^2 + \frac{2}{n+1}s\theta_i)) \quad (44)$$

$$A_{nn} = -\frac{\partial\chi}{\partial\theta'} = -(-\frac{Pr_o}{(1+\frac{4}{3}Rd)}(f + Nb\phi' + (2Nt\theta') \quad (45)$$

$$A_{nn} = \frac{Pr_o}{(1+\frac{4}{3}Rd)}(f_i + Nb(\frac{\phi_i - \phi_{i-1}}{h}) + 2N_t(\frac{\theta_i - \theta_{i-1}}{h})) \quad (46)$$

$$B_{nn} = \frac{2Pr_o}{(n+1)(1+4/3Rd)}s \quad (47)$$

$$\frac{d^2\phi}{d\eta^2} = \frac{-Nt}{Nb}\frac{d^2\theta}{d\eta^2} - LePr_o f\phi' \quad (48)$$

$$\chi_3(\eta, \phi, \phi') = \frac{-Nt}{Nb}\frac{\theta_{i-1} - 2\theta_i + \theta_{i+1}}{h^2} - LePr_o(f_i\frac{\phi_i - \phi_{i-1}}{h}) \quad (49)$$

Similarly, the coefficients for (13) are written as

$$A_{nnn} = Pr_o Lef_i, \quad B_{nnn} = 0 \quad (50)$$

Boundary conditions can easily be discretized by following the above procedure.

5.2. bvp4c

To solve the system of ODEs for Case A and Case B, we first transformed the system into first-order ODEs to compute the solution using *bvp4c*. For Case A it gives,

(a) Case A:

$$f = v_1, f' = v_2, f'' = v_3, f''' = v_3' = \frac{2n}{n+1}v_2^2 - v_1 v_3 - M(E_1 - v_2) + Kpv_2,$$

TABLE 1 | Resemblance of $-f''(0)$ from the literature for various n values (**CASE A**).

n	α	Fang et al. [4]	Khader and Ahmed [5]	Present result (bvp4c)	Present result (SFDM)
10	0.25	1.1433	1.1433	1.1433	1.1433
9		1.1404	1.1404	1.1404	1.1404
7		1.1323	1.1322	1.1323	1.1323
5		1.1186	1.1186	1.1186	1.1186
3		1.0905	1.0904	1.0905	1.0905
1		1.0000	1.0000	1.0000	1.0000
0.5		0.9338	0.9337	0.9338	0.9338
0		0.7843	0.7843	0.7843	0.7843
−1/3		0.5000	0.5000	0.5000	0.5025
−0.5		0.0833	0.0833	0.0833	0.0867
10	0.5	1.0603	1.0603	1.0603	1.0603
9		1.0589	1.0588	1.0589	1.0589
7		1.0550	1.0551	1.0551	1.0551
5		1.0486	1.0486	1.0486	1.0486
3		1.0359	1.0358	1.0359	1.0359
2		1.0234	1.0234	1.0234	1.0234
1		1.0000	1.0000	1.0000	1.0000
0.5		0.9799	0.9798	0.9799	0.9798
0.00		0.9576	0.9577	0.9576	0.9577
−0.5		1.1667	1.1667	1.1667	1.1669

TABLE 2 | Resemblance of the values of $-f''(0)$ for different values of parameters M, n, α, E_1, and θ_r.

						Case B		Case A	
M	n	α	E_1	Kp	θ_r	$-f''(0)$(*bvp4c*)	$-f''(0)$ (SFDM)	$-f''(0)$(*bvp4c*)	$-f''(0)$ (SFDM)
0	0.5	0.3	0.1	0.1	−5	1.075408	1.075408	0.996308	0.996308
0.3						1.184031	1.184031	1.097247	1.097247
0.7						1.335487	1.335487	1.236298	1.236298
0.1	0					0.983771	0.987475	0.907889	0.907889
	0.5					1.106245	1.106245	1.025923	1.025923
	1					1.160763	1.160763	1.078835	1.078835
	0.5	0.4				1.125682	1.125682	1.043448	1.043448
		0.7				1.185376	1.185376	1.097515	1.097515
		1				1.247097	1.247097	1.153791	1.153791
		0.3	0.5			1.025633	1.025633	0.954581	0.954581
			1			0.940761	0.940761	0.877466	0.877466
			1.5			0.864007	0.864007	0.807036	0.807036
			0.1	0.1		1.106245	1.106245	1.025923	1.025923
				0.3		1.205899	1.205899	1.12657	1.12657
				0.5		1.294325	1.294325	1.216757	1.216757
				0.1	−10	1.066455	1.066455		
					−1	1.391356	1.391356		
					−0.5	1.703479	1.703479		

TABLE 3 | Comparison of the values of $-\theta^{'}(0)$ and $\phi^{'}(0)$ for different values of Rd, Ec, Le, Nb, Nt, n, Pr_o, s, α, and ϵ for Case B with Case A, respectively.

										Case B		Case A	
Rd	**Ec**	**Le**	**Nb**	**Nt**	**n**	**Pr_o**	**s**	**α**	**ϵ**	**$-\theta^{'}(0)$**	**$-\phi^{'}(0)$**	**$-\theta^{'}(0)$**	**$-\phi^{'}(0)$**
0.4	0.1	1	0.1	0.2	0.5	1	0.1	0.3	0.2	0.2125241	−0.4250431	0.2477734	−0.4955469
0.7										0.1682977	−0.3365954	0.2047175	−0.409435
1										0.1331988	−0.2663976	0.1704	−0.3407401
0.2	0.2									0.2450324	−0.4900648	0.2790463	−0.5580926
	0.6									0.2263721	−0.4527441	0.2603162	−0.5206325
	1									0.2077006	−0.4154012	0.2415691	−0.4831381
	0.1	0.7								0.2507037	−0.5014074	0.2847274	−0.5694548
		1								0.2496957	−0.4993915	0.2837261	−0.5674523
		1.3								0.2489893	−0.4979786	0.283001	−0.566002
		1	0.2							0.2496958	−0.2496958	0.2837261	−0.2837261
			0.5							0.2496958	−0.0998783	0.2837261	−0.1134905
			0.7							0.2496958	−0.07134165	0.2837261	−0.08106461
			0.1	0.1						0.2532452	−0.2532452	0.2869886	−0.2869886
				0.2						0.249657	−0.4993915	0.2837261	−0.5674523
				0.4						0.2424194	−0.969777	0.2770397	−1.108159
				0.2	0					0.28097	−0.5619401	0.3176236	−0.6352471
					0.5					0.2496957	−0.4993915	0.2837261	−0.5674523
					1					0.236645	−0.4732899	0.268578	−0.5371561
					0.5	0.7				0.1808165	−0.361633	0.2169344	−0.4338689
						1				0.2496957	−0.4993915	0.2837261	−0.5674523
						1.3				0.3014584	−0.6029168	0.3334471	−0.6668941
						1	0			0.3226349	−0.6452698	0.3492327	−0.6984654
							0.1			0.2496957	−0.4993915	0.2837261	−0.5674523
							0.1	0.4		0.2597021	−0.5194042	0.2935494	−0.5870988
								0.7		0.2886493	−0.5772986	0.3219052	−0.6438104
								1		0.3160671	−0.6321342	0.3486554	−0.6973109
								0.3	0.3	0.2380814	−0.4761629		
									0.5	0.2168179	−0.4336357		
									0.8	0.1892523	−0.3785047		

$$v_4=\theta, v_5=\theta^{'},\theta^{''}=v_5^{'}=-\frac{Pr_o}{(1+\frac{4}{3})Rd}(v_1v_5+Nbv_5v_7$$
$$+Ntv_5^2+MEc(v_2-E_1)^2+\frac{2}{n+1}sv_4),$$
$$v_6=\phi, v_7=\phi^{'},\phi^{''}=v_7^{'}=-LePr_ov_1v_7-\frac{Nt}{Nb}v_5^{'}.$$

(b) Case B: The transformed ODEs for Case B are,

$$f=u_1,f^{'}=u_2,f^{''}=u_3,f^{'''}=u_3^{'}=\frac{(u_3u_5)}{(u_4-\theta_r)}$$
$$+\frac{(u_4-\theta_r)}{\theta_r}(-\frac{2n}{n+1}u_2^2+u_1u_3+M(E_1-u_2)-Kpu_2),$$
$$u_4=\theta, u_5=\theta^{'},\theta^{''}=u_5^{'}=\frac{-\epsilon u_5^2}{1+\epsilon u_4}$$
$$-\frac{Pr_o}{(1+\epsilon u_4)(1+\frac{4}{3}Rd)}(u_1u_5+Nbu_5u_7+Ntu_5^2+$$
$$MEc(u_2-E_1)^2+\frac{2}{n+1}su_4),$$
$$u_6=\phi, u_7=\phi^{'},\phi^{''}=u_7^{'}=-LePr_ou_1u_7-\frac{Nt}{Nb}u_5^{'}.$$

6. RESULT AND DISCUSSION

In this section, we present the outcomes of our results both in tabulated and graphical forms.

In **Table 1**, we compare our results with the literature for the skin friction coefficient against different values of n while fixing $\alpha = 0.25$ and $\alpha = 0.5$. The SFDM shows an excellent agreement with *bvp4c* and the literature. In summary, the skin friction coefficient is higher for Case B and lower values for Case A.

In **Table 2** we calculate the skin friction coefficient for various parameters like magnetic parameter M, power law index n, electric field E_1, porosity parameter Kp, variable thickness α, and viscosity parameter θ_r. Its value goes up by changing M, n, α, Kp, and θ_r, while it gets lower by changing E_1. **Table 3** shows the heat and mass transfer rates for various parameters.

An electric field parameter, E_1, enhances the velocity of the fluid, as can be seen in **Figure 2**. Lorentz force is responsible for increasing velocity due to the fact that the skin friction coefficient (as shown in **Table 2**) decreases.

In **Figure 3**, we observe that the momentum boundary layer thickness thins with an increase in porosity parameter *Kp*. This decrease in velocity profile is due to an increase in skin friction for increasing values of porosity parameter *Kp*. Moreover, increasing

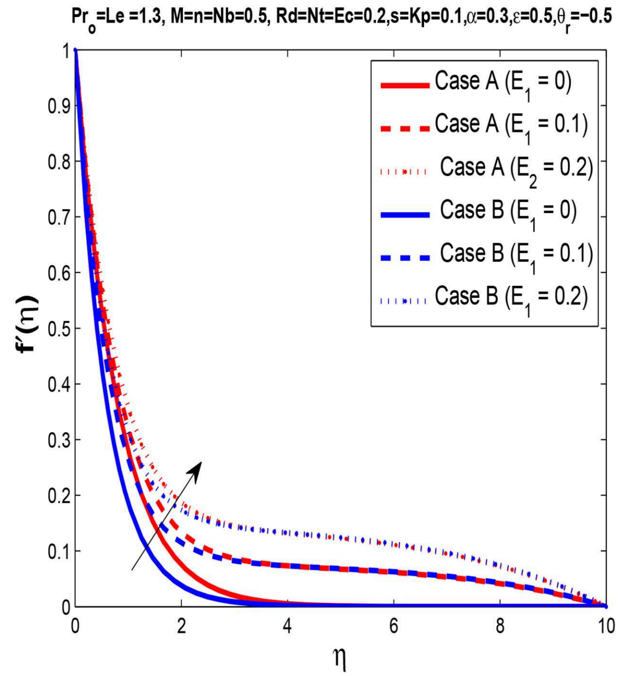

FIGURE 2 | Velocity $f'(\eta)$ for different values of E_1.

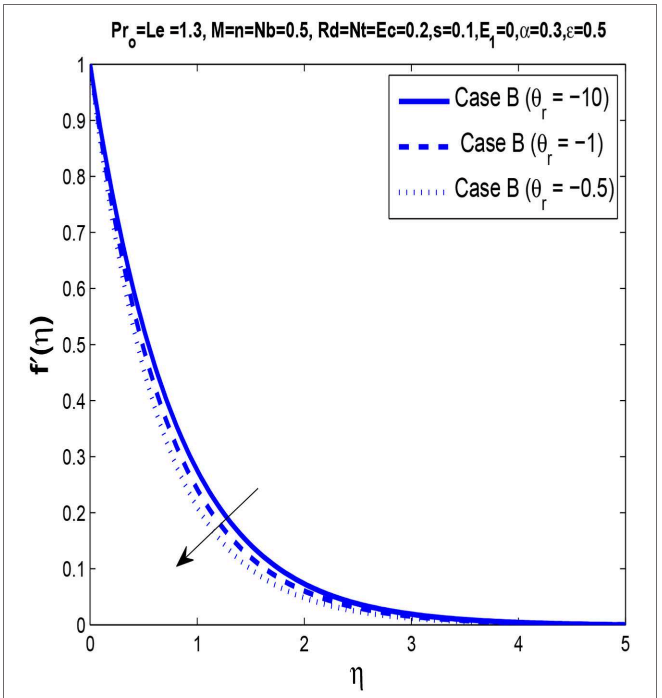

FIGURE 4 | Velocity profile $f'(\eta)$ for different values of θ_r.

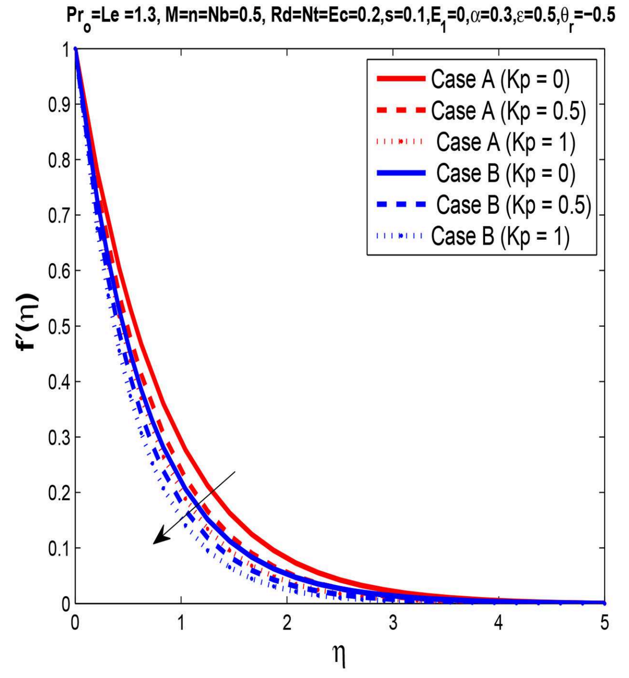

FIGURE 3 | Velocity $f'(\eta)$ for different values of *Kp*.

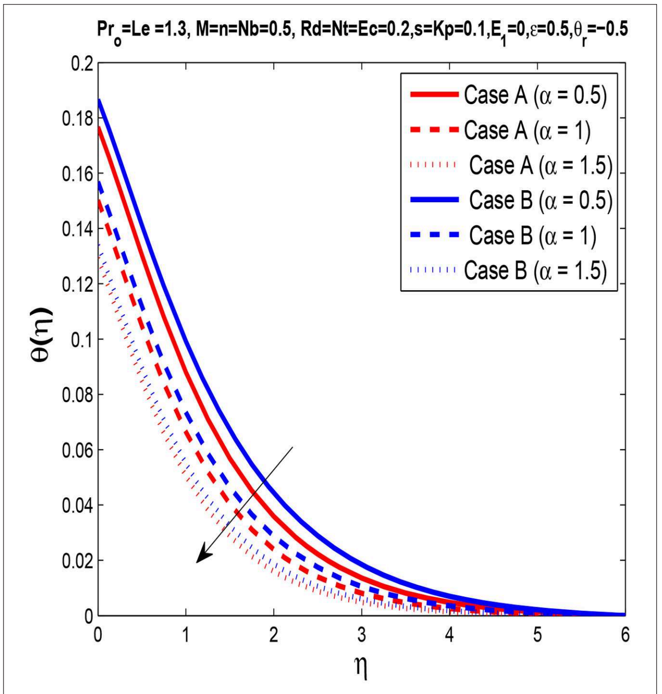

FIGURE 5 | Temperature profile $\theta(\eta)$ for different values of α.

porosity provides resistance to the flow, which ultimately reduces the velocity of the fluid.

Figure 4 describes the velocity profile for different values of viscosity parameter θ_r. It is observed that the momentum boundary layer thins with an increase in fluid viscosity parameter θ_r. This can be related to **Table 2**, where we can see that increasing viscosity parameter θ_r leads to the magnitude of the skin friction coefficient increasing, which causes the reduction in velocity. Increasing viscosity provides more resistance to the fluid motion since higher shear stress is required to move viscous fluids.

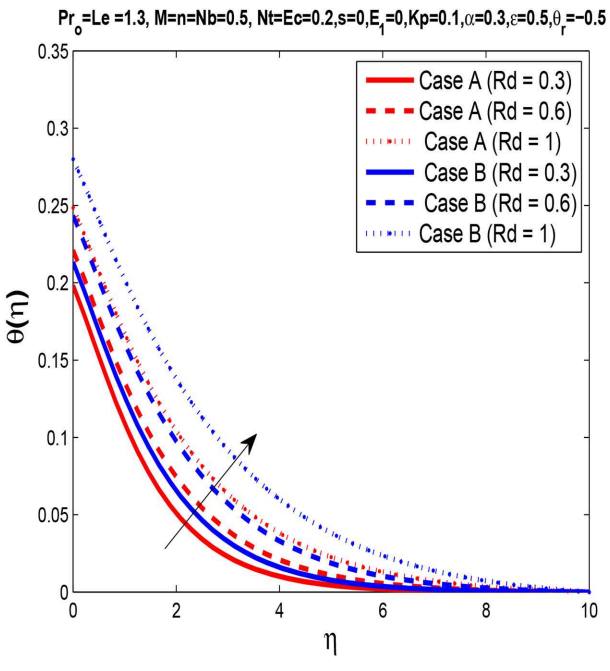

FIGURE 6 | Temperature profile $\theta(\eta)$ for different values of *Rd*.

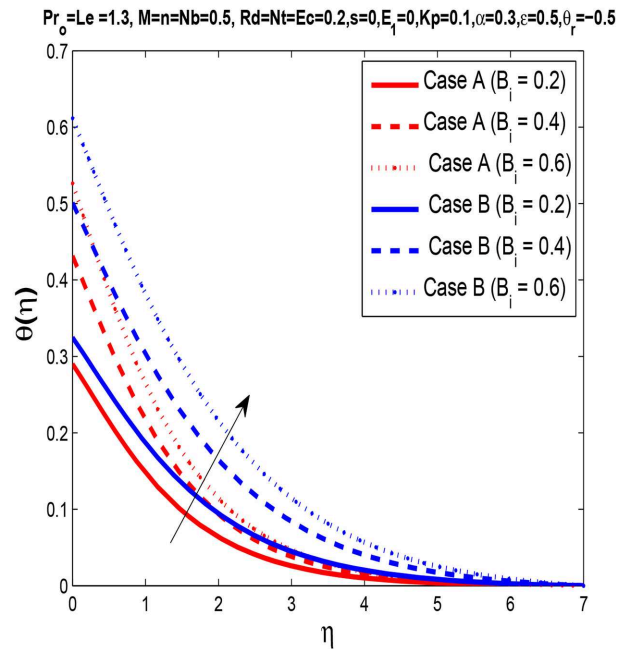

FIGURE 8 | Temperature profile $\theta(\eta)$ for different values of B_i.

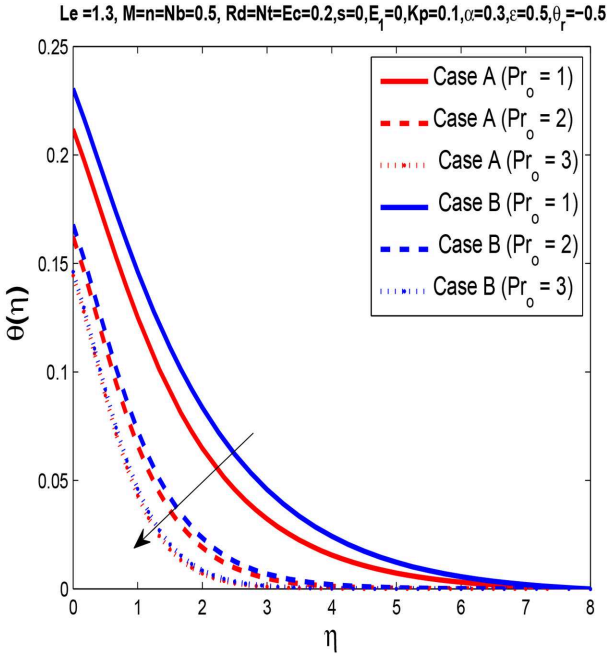

FIGURE 7 | Temperature profile $\theta(\eta)$ for different values of Pr_o.

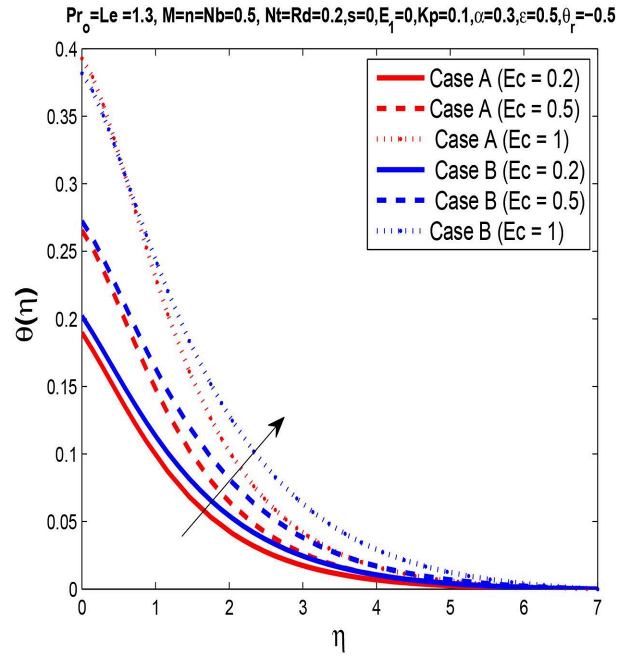

FIGURE 9 | Temperature profile $\theta(\eta)$ for different values of *Ec*.

The effect of variable thickness parameter α on temperature can be seen in **Figure 5**. It is observed that only some energy is transmitted from the surface to the liquid when we raise the wall thickness parameter. Physically, it shows that as we enhance wall thickness parameter α, less heat is transferred from the sheet to the fluid. The temperature profile therefore decreases.

Figure 6 is plotted to demonstrate the effect of thermal radiation parameter Rd on the temperature profile. It is found that with the rise in Rd, the temperature profile increases significantly, as an increase in the radiation parameter provides more energy to the fluid, which increases the thickness of the thermal boundary layer.

In **Figure 7**, it is observed that an increase in Prandtl number Pr_o causes a reduction in the temperature profile. The reason for this decrease is that smaller values of Prandtl number Pr_0 are equivalent higher thermal conductivity. Since the thermal conductivity of air is higher, ultimately, the temperature is higher. However, a high Prandtl number corresponds to low thermal conductivity and lower temperature flow.

In **Figure 8**, we illustrate the influence of Biot number B_i on the temperature profile. It is seen that for higher values of Biot number B_i, the thermal boundary layer thickness increases. This increase in temperature profile is due to the heat transfer rate, which enhances for higher values of Biot number B_i. Since the thermal conductivity is dominant compared to convection, heat transport increases as the Biot number increases.

To examine the effects of the Eckert number Ec on the temperature distribution, we plot **Figure 9**. For higher values of the Eckert number Ec, it is evaluated that somehow the temperature profile rises and the thermal boundary layer gets thinner. Eckert number Ec is the ratio of the kinetic energy of fluid and enthalpy. For increasing values of Eckert number Ec, the kinetic energy increases, which causes an enhancement in fluid temperature.

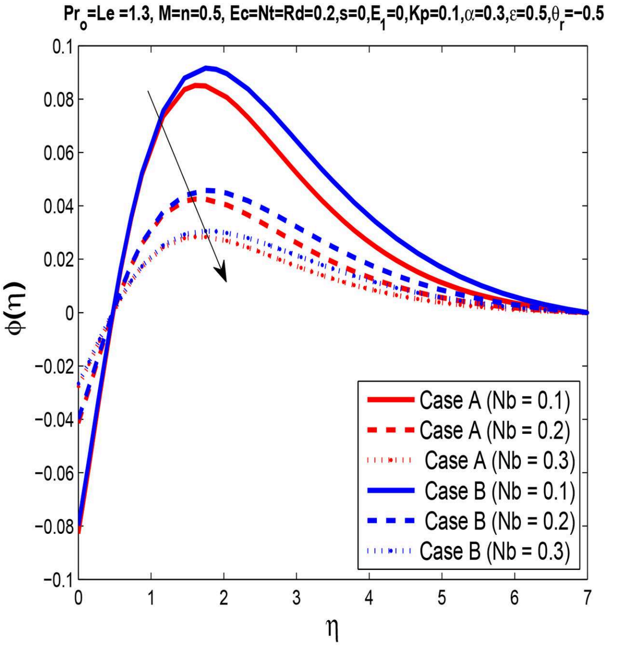

FIGURE 10 | Concentration profile $\phi(\eta)$ for different values of Nb.

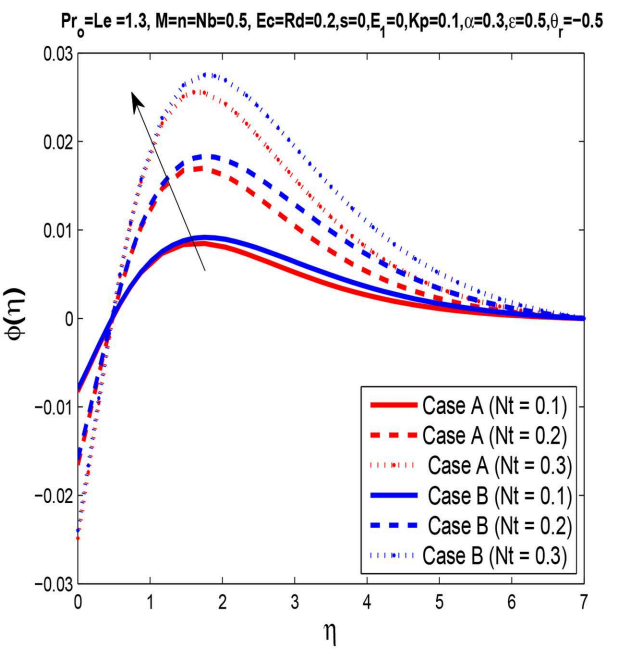

FIGURE 11 | Concentration profile $\phi(\eta)$ for different values of Nt.

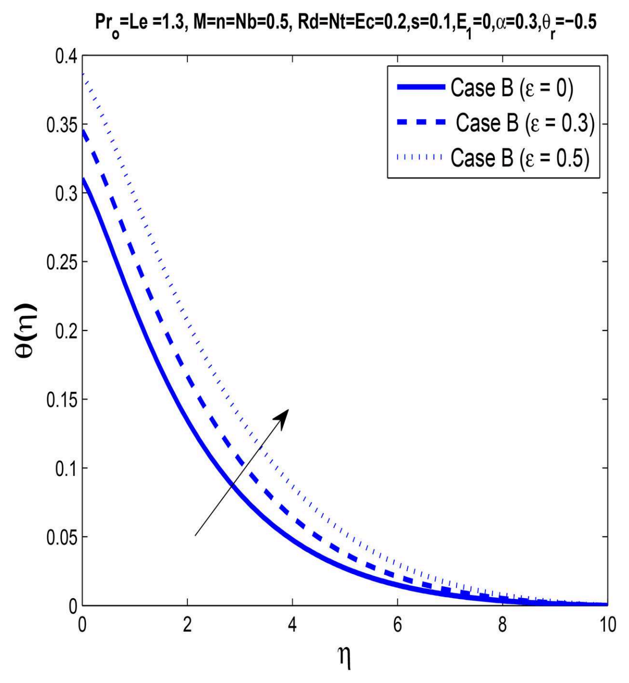

FIGURE 12 | Temperature profile $\theta(\eta)$ for different values of ϵ.

Figure 10 is plotted to illustrate the effect of the Brownian motion parameter on the concentration profile. It is concluded that higher values of Brownian motion parameter Nb cause a reduction in the nanoparticle concentration profile.

Figure 11 is presented to characterize the behavior of thermophoresis parameter Nt on the concentration profile. It is noted that by increasing the thermophoresis parameter, we find a reduction in the nanoparticle concentration profile.

In **Figure 12**, it is found that an increase in variable thermal conductivity parameter ϵ enhances the temperature profile. **Table 3** indicates that the Nusselt number decreases with increasing ϵ. Due to this, the heat transfer rate increases, and hence the temperature profile increases.

7. CONCLUSIONS

This analysis achieved two goals. Firstly, an assessment of distinctive features for constant and variable properties has been done. Secondly, we adopted a new numerical process, the SFDM, to compute solutions and compared its accuracy with *bvp4c*. The notable results for both cases, Case A and B, are as follows:

- The numerical technique, the SFDM, has produced excellent results with high accuracy, as shown in **Tables 1**, **2**.
- Momentum boundary layer thickness grows with an increase in the electric field E_1, whereas it decreases with increases in porosity parameter Kp and fluid viscosity parameter θ_r.
- The thermal boundary layer thickness rises when radiation parameter Rd, Biot number B_i, Eckert number Ec, or thermal conductivity parameter ϵ rises, while it decreases for higher values of variable thickness parameter α and Prandtl number Pr_o.
- The concentration boundary layer thickness decreases with increasing Nb and increases with increasing Nt.
- It is shown that the results are different for constant and variable fluid properties. For variable fluid properties, heat transfer and mass transfer rates are lower than with constant fluid properties. The skin friction coefficient is higher for variable fluid properties than for constant fluid properties.

AUTHOR CONTRIBUTIONS

MI and MF have jointly written the manuscript. The numerical part of bvp4c, as well as tables and graphs, have been completed by MI. TI investigated the SFDM for comparison. MF, MI, and TI have discussed results.

ACKNOWLEDGMENTS

MF would like to thank Research Scientist S. Hussain for his valuable contributions in the numerical part of this work.

REFERENCES

1. Hayat T, Ijaz Khan M, Farooq M, Alsaedi A, Waqas M, Yasmeen T. Impact of Cattaneo–Christov heat flux model in flow of variable thermal conductivity fluid over a variable thicked surface. *Int J Heat Mass Transfer.* (2016) 99:702–10. doi: 10.1016/j.ijheatmasstransfer.2016.04.016
2. Hayat T, Farooq M, Alsaedi A, Falleh Al-Solamy. Impact of Cattaneo-Christov heat flux in the flow over a stretching sheet with variable thickness. *AIP Adv.* (2015) 5:087159. doi: 10.1063/1.4929523
3. Mabood F, Ibrahim SM, Rashidi MM, Shadloo MS, Lorenzini G. Non-uniform heat source/sink and Soret effects on MHD non-Darcian convective flow past a stretching sheet in a micropolar fluid with radiation. *Int J Heat Mass Transfer.* (2016) 93:674–82. doi: 10.1016/j.ijheatmasstransfer.2015.10.014
4. Fang T, Zhang J, Zhong Y. Boundary layer flow over a stretching sheet with variable thickness. *Appl Math Comput.* (2012) 218:7241–52. doi: 10.1016/j.amc.2011.12.094
5. Khader MM, Megahed AM. Numerical solution for boundary layer flow due to a nonlinearly stretching sheet with variable thickness and slip velocity. *Eur Phys J Plus.* (2013) 128:100. doi: 10.1140/epjp/i2013-13100-7
6. Daniel YS, Abdul Aziz Z, Ismail Z, Salah F. Thermal stratification effects on MHD radiative flow of nanofluid over nonlinear stretching sheet with variable thickness. *J Comput Design Eng.* (2018) 5:232–42. doi: 10.1016/j.jcde.2017.09.001
7. Reddy S, Naikoti K, Rashidi MM. MHD flow and heat transfer characteristics of Williamson nanofluid over a stretching sheet with variable thickness and variable thermal conductivity. *Trans A Razmadze Math Inst.* (2017) 171:195–211. doi: 10.1016/j.trmi.2017.02.004
8. Daniel YS, Aziz ZA, Ismail Z, Salah F. Impact of thermal radiation on electrical MHD flow of nanofluid over nonlinear stretching sheet with variable thickness. *Alexandria Eng J.* (2018) 57:2187–97. doi: 10.1016/j.aej.2017.07.007
9. Akbar NS, Nadeem S, Ul Haq R, Khan ZH. Numerical solutions of Magnetohydrodynamic boundary layer flow of tangent hyperbolic fluid towards a stretching sheet. *Indian J Phys.* (2013) 87:1121–4. doi: 10.1007/s12648-013-0339-8
10. Mukhopadhyay S, Layek GC, Samad SA. Study of MHD boundary layer flow over a heated stretching sheet with variable viscosity. *Int J Heat Mass Transfer.* (2005) 48:4460–6. doi: 10.1016/j.ijheatmasstransfer.2005.05.027
11. Nadeem S, Ul Haq R, Akbar NS, Khan ZH. MHD three-dimensional Casson fluid flow past a porous linearly stretching sheet. *Alexandria Eng J.* (2013) 52:577–82. doi: 10.1016/j.aej.2013.08.005
12. Mabood F, Khan WA, Ismail AM. MHD boundary layer flow and heat transfer of nanofluids over a nonlinear stretching sheet: a numerical study. *J Magnet Magnet Mater.* (2015) 374:569–76. doi: 10.1016/j.jmmm.2014.09.013
13. Zhang C, Zheng L, Zhang X, Chen G. MHD flow and radiation heat transfer of nanofluids in porous media with variable surface heat flux and chemical reaction. *Appl Math Modell.* (2015) 39:165–81. doi: 10.1016/j.apm.2014.05.023
14. Poply V, Singh P, Yadav AK. A study of temperature-dependent fluid properties on MHD free stream flow and heat transfer over a non-linearly stretching sheet. *Proc Eng.* (2015) 127:391–7. doi: 10.1016/j.proeng.2015.11.386
15. Sheikholeslami M, Bandpy MG, Ellahi R, Zeeshan A. Simulation of MHD CuO-water nanofluid flow and convective heat transfer considering Lorentz forces. *J Magnet Magnet Mater.* (2014) 369:69–80. doi: 10.1016/j.jmmm.2014.06.017
16. Patel HR. Effects of heat generation, thermal radiation, and hall current on MHD Casson fluid flow past an oscillating plate in porous medium. *Multiphase Sci Technol.* (2019) 31:87–107. doi: 10.1615/MultScienTechn.2019029514
17. Farooq U, Lu D, Munir S, Ramzan M, Suleman M, Hussain S. MHD flow of Maxwell fluid with nanomaterials due to an exponentially stretching surface. *Sci Rep.* (2019) 9:7312. doi: 10.1038/s41598-019-43549-0
18. Ibrahim W, Tulu A. Magnetohydrodynamic (MHD) boundary layer flow past a wedge with heat transfer and viscous effects of nanofluid embedded in porous media. *Math Problems Eng.* (2019) 2019:4507852. doi: 10.1155/2019/4507852

19. Ali A, Shehzadi K, Sulaiman M, Asghar S. Heat and mass transfer analysis of 3D Maxwell nanofluid over an exponentially stretching surface. *Phys Script.* (2019) 94:065206. doi: 10.1088/1402-4896/ab07cf
20. Choi SUS, Eastman JA. *Enhancing Thermal Conductivity of Fluids With Nanoparticles.* Argonne National Lab., IL (1995).
21. Das K, Duari PR, Kundu PK. Numerical simulation of nanofluid flow with convective boundary condition. *J Egypt Math Soc.* (2015) 23:435–39. doi: 10.1016/j.joems.2014.05.009
22. Mabood F, Das K. Melting heat transfer on hydromagnetic flow of a nanofluid over a stretching sheet with radiation and second-order slip. *Eur Phys J Plus.* (2016) 131:3. doi: 10.1140/epjp/i2016-16003-1
23. Cao Z, Zhao J, Wang Z, Liu F, Zheng L. MHD flow and heat transfer of fractional Maxwell viscoelastic nanofluid over a moving plate. *J Mol Liquids*. (2016) 222:1121–7. doi: 10.1016/j.molliq.2016.08.012
24. Das K, Duari PR, Kundu PK. Effects of magnetic field on an unsteady mixed convection flow of nanofluids containing spherical and cylindrical nanoparticles. *J Heat Transfer*. (2016) 138:061901. doi: 10.1115/1.4032835
25. Satya Narayana PV, Venkateswarlu B, Venkataramana S. Thermal radiation and heat source effects on a MHD nanofluid past a vertical plate in a rotating system with porous medium. *Heat Transfer Asian Res.* (2015) 44:1–19. doi: 10.1002/htj.21101
26. Mansur S, Ishak A, Pop I. Stagnation-point flow towards a stretching/shrinking sheet in a nanofluid using Buongiorno's model. *Proc Inst Mech Eng : J Process Mech Eng.* (2017) 231:172–80. doi: 10.1177/0954408915585047
27. Makinde OD. Effects of viscous dissipation and Newtonian heating on boundary-layer flow of nanofluids over a flat plate. *Int J Num Methods Heat Fluid Flow.* (2013) 23:1291–303. doi: 10.1108/HFF-12-2011-0258
28. Ali AO, Makinde OD, Nkansah-Gyekye Y. Numerical study of unsteady MHD Couette flow and heat transfer of nanofluids in a rotating system with convective cooling. *Int J Num Methods Heat Fluid Flow.* (2016) 26:1567–79. doi: 10.1108/HFF-10-2014-0316
29. Ashwinkumar GP, Sulochana C. Effect of radiation absorption and buoyancy force on the MHD mixed convection flow of Casson nanofluid embedded with Al50Cu50 alloy nanoparticles. *Multidiscipl Model Mater Struct.* (2018) 14:1082–100. doi: 10.1108/MMMS-12-2017-0164
30. Andersson HI, Aarseth JB. Sakiadis flow with variable fluid properties revisited. *Int J Eng Sci.* (2007) 45:554–61. doi: 10.1016/j.ijengsci.2007.04.012
31. Prasad KV, Vajravelu K, Datti PS. The effects of variable fluid properties on the hydro-magnetic flow and heat transfer over a non-linearly stretching sheet. *Int J Thermal Sci.* (2010) 49:603–10. doi: 10.1016/j.ijthermalsci.2009.08.005
32. Hayat T, Shehzad SA, Qasim M, Alsaedi A. Mixed convection flow by a porous sheet with variable thermal conductivity and convective boundary condition. *Braz J Chem. Eng.* (2014) 31:109–17. doi: 10.1590/S0104-66322014000100011
33. Bhaskar Reddy N, Poornima T, Sreenivasulu P. Influence of variable thermal conductivity on MHD boundary layer slip flow of ethylene-glycol based Cu nanofluids over a stretching sheet with convective boundary condition. *Int J Eng Math.* (2014) 2014:905158. doi: 10.1155/2014/905158
34. Ullah MZ, Serra-Capizzano S, Baleanu D. A numerical simulation for Darcy-Forchheimer flow of nanofluid by a rotating disk with partial slip effects. *Front Phys.* (2019) 7:219. doi: 10.3389/fphy.2019.00219
35. Shah Z, Babazadeh H, Kumam P, Shafee A, Thounthong P. Numerical simulation of magnetohydrodynamic nanofluids under the influence of shape factor and thermal transport in a porous media using CVFEM. *Front Phys.* (2019) 7:164. doi: 10.3389/fphy.2019.00164
36. Zeeshan A, Shehzad N, Abbas T, Ellahi R. Effects of radiative electro-magnetohydrodynamics diminishing internal energy of pressure-driven flow of titanium dioxide-water nanofluid due to entropy generation. *Entropy*. (2019) 21:236. doi: 10.3390/e21030236
37. Ellahi R, Sait SM, Shehzad N, Mobin N. Numerical simulation and mathematical modeling of electro-osmotic Couette-Poiseuille flow of MHD power-law nanofluid with entropy generation. *Symmetry*. (2019) 11:1038. doi: 10.3390/sym11081038
38. Yousif MA, Ismael HF, Abbas T, Ellahi R. Numerical study of momentum and heat transfer of MHD Carreau nanofluid over an exponentially stretched plate with internal heat source/sink and radiation. *Heat Transfer Res.* (2019) 50:649–58. doi: 10.1615/HeatTransRes.2018025568
39. Sarafraz MM, Pourmehran O, Yang B, Arjomandi M, Ellahi R. Pool boiling heat transfer characteristics of iron oxide nano-suspension under constant magnetic field. *Int J Thermal Sci.* (2020) 147:106131. doi: 10.1016/j.ijthermalsci.2019.106131
40. Fujimoto K. Multi-scale kinetic simulation of magnetic reconnection with dynamically adaptive meshes. *Front Phys.* (2018) 6:119. doi: 10.3389/fphy.2018.00119
41. Irfan M, Farooq MA. Magnetohydrodynamic free stream and heat transfer of nanofluid flow over an exponentially radiating stretching sheet with variable fluid properties. *Front Phys.* (2019) 7:186. doi: 10.3389/fphy.2019.00186
42. Na TY, editor. *Computational Methods in Engineering Boundary Value Problems.* Academic Press (1980).
43. Thomas LH. *Elliptic Problems in Linear Difference Equations Over a Network.* New York, NY: Watson Sci. Comput. Lab. Rept., Columbia University (1949).

Conflict of Interest: The authors declare that the research was conducted in the absence of any commercial or financial relationships that could be construed as a potential conflict of interest.

Copyright © 2020 Irfan, Farooq and Iqra. This is an open-access article distributed under the terms of the Creative Commons Attribution License (CC BY). The use, distribution or reproduction in other forums is permitted, provided the original author(s) and the copyright owner(s) are credited and that the original publication in this journal is cited, in accordance with accepted academic practice. No use, distribution or reproduction is permitted which does not comply with these terms.

NOMENCLATURE

(u, v)	Velocity components
b	Positive constant
n	Power law index
$B(x)$	Applied magnetic field
$E(x)$	Applied electric field
μ	Coefficient of viscosity
ρ	Density of fluid
σ	Electrical conductivity of the fluid
M	Magnetic field parameter
E_1	Electric field parameter
Kp	Permeability parameter
T	Fluid temperature
k	Thermal conductivity
C_p	Specific heat capacity
q_r	Radiative heat flux
$Q(x)$	Heat generation/absorption parameter
C	Concentration
τ	Ratio of heat capacities of nanofluid to heat capacities of base fluid
$(\rho C)_p$	Heat capacities of nanofluid
$(\rho C)_f$	Heat capacities of base fluid
D_B	Brownian coefficients
D_T	Thermophoretic diffusion coefficients
T_∞	Ambient fluid temperature
T_w	Constant temperature at wall
C_∞	Ambient fluid concentration
C_w	Fluid concentration at wall
Pr_o	Prandtl number
Le	Lewis number
Nt	Thermophoresis number
Nb	Brownian motion parameter
α	Wall thickness parameter
Rd	Thermal radiation parameter
σ^*	Stefan-Boltzman constant
k^*	Mean absorption coefficient
ϵ	Thermal conductivity parameter of the fluid
θ_r	Fluid viscosity parameter
B_i	Biot number
Ec	Eckert number
s	Heat source parameter
Re_x	Local Reynolds number
τ_w	Surface shear stress
q_w	Wall heat flux
j_w	Wall mass flux
$C_f = \frac{\tau_w}{\rho u_w^2}$	Skin friction coefficient
$Nu_x = -\frac{(x+b)q_w}{k_o(T_w - T_\infty)}$	Nusselt parameter
$Sh_x = -\frac{(x+b)j_w}{C_w - C_\infty}$	Sherwood parameter
$K(x)$	Permeability

frontiers in Physics

ORIGINAL RESEARCH
published: 29 April 2020
doi: 10.3389/fphy.2020.00113

Check for updates

Heat Transfer Analysis for Non-linear Boundary Driven Flow Over a Curved Stretching Sheet With a Variable Magnetic Field

Kehinde M. Sanni, Qumar Hussain and Saleem Asghar*

Department of Mathematics, COMSATS University Islamabad, Islamabad, Pakistan

A 2-D boundary-layer flow induced by non-linear (quadratic) stretching of a curved surface of an incompressible MHD viscous fluid is investigated. Heat transfer analysis is presented including viscous dissipation and thermal radiation. A radially variable magnetic field is applied that satisfies Maxwell's equation and incorporates the curvature effects. A new similarity variable and similarity transformation are introduced to reduce the governing PDE's into ODE's. A numerical procedure is adopted to find the solution of momentum and energy equations. The numerical scheme is validated with the existing data. The results are illustrated graphically and discussed physically. Comparison with the literature shows a significant improvement compared to existing studies.

Keywords: curved surface, non-linear stretching, MHD, variable temperature, viscous dissipation, Joule heating, radiation, CST and PSVT

OPEN ACCESS

Edited by:
Sara I. Abdelsalam,
National Autonomous University of Mexico, Mexico

Reviewed by:
Abdullah Zaher,
Benha University, Egypt
Muhammad Sohail,
Institute of Space Technology, Pakistan

****Correspondence:***
Kehinde M. Sanni
km.sanni@outlook.com

Specialty section:
This article was submitted to Mathematical Physics, a section of the journal Frontiers in Physics

Received: *31 January 2020*
Accepted: *23 March 2020*
Published: *29 April 2020*

Citation:
Sanni KM, Hussain Q and Asghar S (2020) Heat Transfer Analysis for Non-linear Boundary Driven Flow Over a Curved Stretching Sheet With a Variable Magnetic Field. Front. Phys. 8:113. doi: 10.3389/fphy.2020.00113

INTRODUCTION

Stretching is one of the most important mechanisms for boundary driven flows. Crane [1] was the first to present an exact analytical solution for linear stretching on a flat plate. Since then a lot of theoretical and numerical studies have been conducted with applications in the polymer industry and engineering processes. Linear stretching was extended to non-linear and exponential stretching velocities for plane surfaces and tubes in Newtonian and non-Newtonian fluids [2–13]. The stretching of curved surfaces is now being studied for its mathematical interest as a method for solving non-linear governing equations in curvilinear coordinates and for understanding boundary driven flow behavior and generalized flow geometry. As the body of literature about stretching is so large it cannot be cited here, we will focus on curved surfaces only. Sajid et al. [14] was first to introduce the concept of flow due to the linear stretching of the curved surface in a Newtonian fluid. They concluded that the velocity decreases as the radius of curvature increases, or the velocity and the boundary layer thickness increase for the curved surface in comparison with the flat surface. In addition, the pressure gradient is variable contrary to the constant pressure gradient for the flat surface. Sanni et al. [15] discussed non-linear power law stretching velocity. Magnetohydrodynamic (MHD) flow over a curved linear stretching surface with heat transferred to an electrically conducting fluid in the presence of a transversely applied magnetic field was presented by Abbas et al. [16]. We observe that the studies for MHD flow in the curvilinear geometry are normally undertaken using a uniform magnetic field [17–24]. However, we find that the magnetic field must be such that it satisfies the solenoidal property $\left(div\,\mathbf{B}=0\right)$. Hence, the assumption of a uniform magnetic field is valid for a rectangular coordinate system but not for curvilinear coordinates. Variable magnetic fields are used for the treatment of peptic ulcers, medical diagnosis and in medical therapeutic techniques. In industry, the growing of pure crystal semiconductors can be controlled using a variable magnetic field [25, 26]. Some other papers about curved structures also include: Reddy et al. [27] which analyzed a dual solution of nanofluid flow due to a curved stretching surface under the influence of non-linear radiation. The flow of a nanofluid with carbon nanotubes caused by a curved stretching surface, with internal heat generation, is examined by Saba et al. [28]. Naveed et al. [29] documented dual solutions of MHD viscous fluid flow past a shrinking curved surface. Hayat et al. [30] discussed a numerical solution for hydromagnetic fluid flow under Soret and Dufour effects. In the presence of variable viscosity and carbon nanotubes, Nadeem et al. [31] investigated an MHD nanofluid over a curved stretching surface. For the solution methodology, new similarities have been defined which take into account the effects of both linear and non-linear stretching velocities. In the literature, the similarity for the non-linear stretching velocity is defined in a way that takes care of the linear part only. We believe that it results in incomplete governing equations and incomplete results missing out the effects of the non-linear part. This motivates us to define a new similarity transformation, resulting in the complete set of governing equations and improved results which addresses the non-linear part of the velocity as well. Mathematically, the objective of the present study has been to formulate the Lorentz force for variable magnetic field in the curvilinear coordinates and to redefine the similarity transformation to improve upon the results of the non-linear stretching velocity for a flat surface. This is accomplished for the flow and heat transfer analysis over the non-linear stretching of a curved surface in an electrically conducting viscous fluid in the presence of a variable magnetic field. The important observations are that the velocity induced by the boundary decreases as the the magnetic field and the radius of curvature increases. Thus, the flow field and the boundary layer thickness can be maintained with the help of these parameters. The non-linear contribution of the boundary velocity has more significant effect than the linear part. Detailed consequences of this study are discussed in the last section.

PROBLEM FORMULATION

Consider the steady two-dimensional boundary-layer flow and heat transfer for an incompressible hydromagnetic viscous fluid moving over a curved surface. The flow is induced by a non-linear (quadratic) stretching velocity of the form $ax + bx^2$ (a and b being the dimensional constants), and the energy equation includes the viscous dissipation and thermal radiation. A variable applied magnetic field, given as $\boldsymbol{B}(r) = RB_o(R+r)^{-1}\hat{\boldsymbol{e}}_{\boldsymbol{r}}$, is acting in the radial direction compared to the curved surface. The variable magnetic field is taken on purpose to make it consistent with Maxwell's equation ($\nabla.\boldsymbol{B} = 0$). The governing equations are modeled using curvilinear coordinates. The Lorentz force $\boldsymbol{F} = \boldsymbol{J} \times \boldsymbol{B}$ and the current density $\boldsymbol{J}$ in the absence of an electrical current ($\boldsymbol{E} = 0$) are expressed as:

$$\boldsymbol{J} = \sigma\,(\mathbf{V} \times \mathbf{B}) \tag{1}$$

$$\boldsymbol{F} = (-\sigma RB_o(R+r)^{-1}u, 0, 0). \tag{2}$$

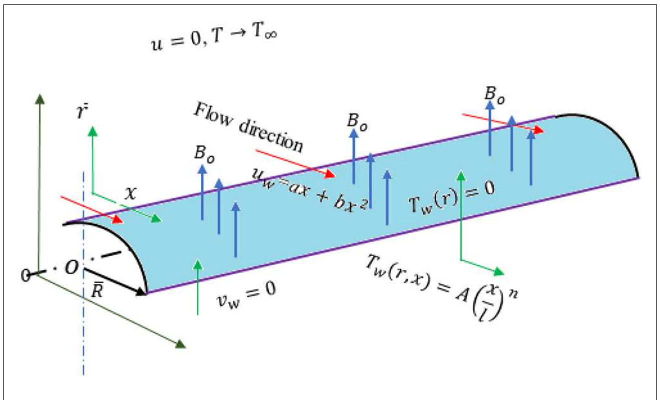

FIGURE 1 | Physical geometry of the problem.

We observe that an electrically conducting fluid transverses a curved path along the stretching surface (instead of in a linear direction), and the magnetic field is perpendicular to the flow direction. Using Equaion (1), the Lorentz force takes the form $\boldsymbol{F} = (-\sigma RB_o(R+r)^{-1}u, 0, 0)$ which takes a constant value as R goes to infinity. In the above equation, σ is the electrical conductivity of the fluid, $\hat{\boldsymbol{e}}_{\boldsymbol{r}}$ is the unit vector in the radial direction and B_o is the strength of the applied magnetic field; whereas u and v are the components of velocity field in the $x-$ and $r-$directions. The geometry of the flow is given in **Figure 1**.

The boundary layer equations [16] in the presence of a variable magnetic field can be given as follows:

$$\partial_r\left[(R+r)\,v\right] = -R\partial_x u \tag{3}$$

$$v\partial_r u + \tfrac{Ru}{R+r}\partial_x u + \tfrac{uv}{R+r} = -\tfrac{1}{\rho}\tfrac{R}{R+r}\partial_x P$$
$$+\upsilon\left\{\left(\tfrac{1}{R+r}\partial_r[(R+r)\,\partial_r u]\right) - \tfrac{u}{(R+r)^2}\right\} - \tfrac{\sigma B_0^2 R^2}{\rho(R+r)^2}u \tag{4}$$

$$\tfrac{u^2}{R+r} = \tfrac{1}{\rho}\partial_r P \tag{5}$$

$$v\partial_r T + \tfrac{Ru}{R+r}\partial_x T = \tfrac{K}{\rho C_p}\left\{\tfrac{1}{R+r}\partial_r[(R+r)\,\partial_r T\right\}$$
$$+\tfrac{u}{\rho C_p}\left(\partial_r u - \tfrac{u}{R+r}\right)^2 - \tfrac{1}{\rho C_p}\partial_r q_w + \tfrac{\sigma R^2}{\rho C_p(R+r)^2}u^2, \tag{6}$$

where u is the viscosity of the fluid, ρ is the fluid density, p is the pressure, T_w is the temperature of the surface at $\gamma = 0$, T_∞ is the ambient temperature, K is the thermal conductivity of the fluid, C_p is specific heat of the fluid at constant pressure, and q_w is the heat flux.

The boundary conditions for all a, $b \in \mathcal{R}$ satisfied by the velocity and the temperature fields are:

$$u_w = ax + bx^2, \quad v = v_w = 0, T = T_w \quad at \quad r = 0 \tag{7}$$

$$u = 0, \quad \partial_r u = 0, T \to T_\infty \quad as \quad r \to \infty. \tag{8}$$

In Equation (7), a and b determine the strength of the linear and non-linear parts of the stretching velocity, respectively.

The similarity variables given in [2–4] are revisited and modified for generalized curvilinear coordinates to include both a linear and non-linear part. These are now defined as:

$$\gamma = r\left\{\frac{a+bx}{\upsilon}\right\}^{\frac{1}{2}}, = axg'(\gamma) + bx^2h'(\gamma),$$

$$R = k\left\{\frac{\upsilon}{a+bx}\right\}^{\frac{1}{2}},\ p = \rho u_w^2 P(\eta) \tag{9}$$

$$v = -\frac{R}{R+r}\left\{\frac{\upsilon}{a+bx}\right\}^{\frac{1}{2}}\{[ag(\gamma)+2bxh(\gamma)] + \frac{d}{2(a+bx)}\{[\gamma[axg'(\gamma)+bx^2h'(\gamma)] - [axg(\gamma)+bx^2h(\gamma)]]\}\}. \tag{10}$$

Equation (3) is identically satisfied; however, Equations (4) and (5) together with Equations (9) and (10) yield

$$a^2x\left\{-\frac{k\left[gg''-(g')^2-2p_1(\gamma)\right]}{k+\gamma} - \frac{k(gg'-\frac{1}{k}g')}{(k+\gamma)^2} - \frac{g''}{k+\gamma} - g''' + \frac{Hak^2g'}{(k+\gamma)^2}\right\} + abx^2\left\{-\frac{k\left[h''g+2hg''-3h'g'-6p_2(\gamma)\right]}{k+\gamma} - \frac{k(2hg'+h'g)}{(k+\gamma)^2} - \frac{h''+g''}{k+\gamma} + \frac{h'+g'}{(k+\gamma)^2} - (h'''+g''') + \frac{Hak^2h'}{(k+\gamma)^2}\right\} + b^2x^3\left\{-\frac{2k\left[hh''-(g')^2+\frac{1}{k}h''-2p_3(\gamma)\right]}{k+\gamma} - \frac{k\left[hh'-\frac{1}{k}h'\right]}{(k+\gamma)^2} - h'''\right\} = 0 \tag{11}$$

$$a^2x\left[\frac{(g')^2}{k+\gamma} - p_i{}'(\gamma)\right] + abx^2\left[\frac{2h'g'}{k+\gamma} - 2p_j{}'(\gamma)\right] + b^2x^3\left[\frac{(h')^2}{k+\gamma} - p_k{}'(\gamma)\right] = 0 \tag{12}$$

where $\left(Ha = \sqrt{\sigma B_0{}^2a^2/\mu}\right)$ is the Hartman number.

The boundary conditions in the dimensionless form are:

$$g(0) = 0,\ g'(0) = 1,\ h(0) = 0,\ h'(0) = 1 \quad at \quad \gamma = 0 \tag{13}$$

$$h'(\infty) = 0,\ h''(\infty) = 0,\ g'(\infty) = 0,\ g''(\infty) = 0 \quad as\ \gamma \to \infty. \tag{14}$$

Equation (12) along with Equation (11) gives

$$\frac{2k}{k+\gamma}P_1(\gamma) = g''' + \frac{g''}{k+\gamma} - \frac{g'}{(k+\gamma)^2} + \frac{kgg''}{k+\gamma} + \frac{kgg'}{(k+\gamma)^2} - \frac{k(g')^2}{k+\gamma} - \frac{Hak^2}{(k+\gamma)^2}g' \tag{15}$$

$$\frac{6k}{k+\gamma}P_2(\gamma) = g''' + h''' + \frac{h''+g''}{k+\gamma} - \frac{h'+g'}{(k+\gamma)^2} + \frac{kh''g}{(k+\gamma)} + \frac{2khg''}{(k+\gamma)} - \frac{3kh'g'}{k+\gamma} + \frac{2khg'}{(k+\gamma)^2} + \frac{kh'g}{(k+\gamma)^2} - \frac{Hak^2}{(k+\gamma)^2}h' \tag{16}$$

$$\frac{4k}{k+\gamma}P_3(\gamma) = h''' + \frac{h''}{k+\gamma} - \frac{h'}{(k+\gamma)^2} + \frac{2khh''}{k+\gamma} + \frac{2khh'}{(k+\gamma)^2} - \frac{2k(h')^2}{k+\gamma}. \tag{17}$$

The pressure inside the boundary layer is now expressed as:

$$P(\gamma) = a^2p_1(\gamma) + abp_2(\gamma) + bp_3(\gamma). \tag{18}$$

Using the limit $\xi \to \infty$, Equations (15)–(17) reduce to

$$g''' + gg'' - (g')^2 - Ha^2g' = 0 \tag{19}$$

$$h''' + g''' + h''g + 2hg'' - 3h'g' - Ha^2h' = 0 \tag{20}$$

$$h''' + 2hh'' - 2(h')^2 = 0 \tag{21}$$

At this point, we make some observations of vital importance. One, the similarity transformation as defined in this paper considers the contribution of both linear and non-linear parts of the stretching velocity through the terms "a" and "b." The similarity used in the literature for non-linear stretching ($\eta = y\sqrt{\frac{a}{\upsilon}}$) is deficient in that its only involves a which only corresponds to the linear part of the stretching velocity [2–4]. This omission leads to the omission of terms in the momentum equations and consequently results in an incomplete solution.

Eliminating the pressure from Equations (15), (16), and (17), we obtain self-similar equations as given below:

$$g^{'v} + \frac{2g'''}{k+\gamma} - \frac{g''}{(k+\gamma)^2} + \frac{g'}{(k+\gamma)^3} + \frac{kgg'''}{k+\gamma} - \frac{kg'g''}{k+\gamma} + \frac{kgg''}{(k+\gamma)^2} - \frac{k(g')^2}{(k+\gamma)^2} - \frac{kgg'}{(k+\gamma)^3} - \frac{Ha^2k^2g''}{(k+\gamma)^2} + \frac{Ha^2k^2g'}{(k+\gamma)^3} = 0 \tag{22}$$

$$h^{'v} + g^{'v} + \frac{2(h'''+g''')}{k+\gamma} - \frac{h''+g''}{(k+\gamma)^2} + \frac{h'+g'}{(k+\gamma)^3} + \frac{k(gh'''+2hg'''-2h''g'-h'g'')}{k+\gamma} - \frac{k(2hg'+h'g)}{(k+\gamma)^3} + \frac{k(gh''-3h'g'+2hg'')}{(k+\gamma)^2} - \frac{Ha^2k^2h''}{(k+\gamma)^2} + \frac{Ha^2k^2h'}{(k+\gamma)^3} = 0 \tag{23}$$

$$h^{'v} + \frac{2h'''}{k+\gamma} - \frac{h''}{(k+\gamma)^2} + \frac{h'}{(k+\gamma)^3} + \frac{2khh'''}{k+\gamma} - \frac{2kh'h''}{k+\gamma} + \frac{2khh''}{(k+\gamma)^2} - \frac{2k(h')^2}{(k+\gamma)^2} - \frac{2khh'}{(k+\gamma)^3} = 0. \tag{24}$$

HEAT TRANSFER ANALYSIS

The thermal boundary layer Equation (6) is solved for a constant surface temperature and variable surface temperature, in sequence.

Constant Surface Temperature (CST)

In this case, $T = T(r)$ and the Equation (6) reduces to

$$v\partial_r T = \frac{K}{\rho C_p}\left\{\frac{1}{R+r}\partial_r\left[(R+r)\,\partial_r T\right]\right\} + \frac{\mathrm{u}}{\rho C_p}\left(\partial_r u - \frac{u}{R+r}\right)^2 - \frac{1}{\rho C_p}\partial_r q_w + \frac{\sigma R^2}{\rho C_p (R+r)^2}u^2 \quad (25)$$

The boundary conditions are

$$T = T_{\ w|_{r=0}} \text{ and } T_{|r\to\infty} = 0 \quad (26)$$

and the dimensionless temperature distributions is of the form,

$$\theta(\gamma) = \frac{T - T_\infty}{T_w - T_\infty}. \quad (27)$$

Variable Surface Temperature (PSVT)

Expressing $T = T(x,\ r)$ in the form

$$T\,(x, r) = T_\infty + A\left(\frac{x}{l}\right)^n \theta(\gamma) \quad (28)$$

and the boundary conditions

$$T_{\ w|_{r=0}} = T_\infty + A\left(\frac{x}{l}\right)^n \text{ and } T_{|r\to\infty} = 0 \quad (29)$$

in which $n \in \mathcal{R}$ is the index of wall temperature parameter, and A is the dimensional wall constant.

The radiative heat flux q_w under Rosseland's approximation is given by

$$q_w = -\frac{4\sigma^*}{3k^*}\partial_r T^4 \quad (30)$$

where k^* and σ^* are the mean absorption coefficient and the Stefan-Boltzmann constant, respectively.

Taylor's series is employed in the expansion of the temperature variation (T^4) about T_∞, and we get

$$T^4 \approx 4T_\infty^3 T - 3T_\infty^4. \quad (31)$$

Substituting Equation (31) in Equation (30), we have

$$\partial_r q_w = -\frac{16\sigma^* T_\infty^3}{3k^*}\partial_{rr} T. \quad (32)$$

After using Equation (32), the energy Equation (25) and (6) for CST and PSVT cases reduce to

$$v\partial_r T = \frac{K}{\rho C_p}\left(1 + \frac{16\sigma^* T_\infty^3}{3k^* K}\right)\partial_{rr} T + \frac{\mu}{\rho C_p}\left(\partial_r u - \frac{u}{R+r}\right)^2 + \frac{K}{\rho C_p}\partial_r T + \frac{\sigma R^2}{\rho C_p (R+r)^2}u^2 \quad (33)$$

$$v\partial_r T + \frac{Ru}{R+r}\partial_x T = \frac{K}{\rho C_p}\left(1 + \frac{16\sigma^* T_\infty^3}{3k^* K}\right)\partial_{rr} T + \frac{\mu}{\rho C_p}\left(\partial_r u - \frac{u}{R+r}\right)^2 + \frac{K}{\rho C_p}\partial_r T + \frac{\sigma R^2}{\rho C_p (R+r)^2}u^2. \quad (34)$$

Equations (33) and (34) after using Equation (9), (10), (27), and (28) give

$$\left(1 + Rd\right)\theta'' + \frac{\theta'}{(k+\gamma)} + \frac{Prk\left(g + 2h\right)\theta'}{(k+\gamma)} + \text{EcPr}\left(h'' + g'' - \frac{h' + g'}{k+\gamma}\right)^2 + \frac{wk^2\left(h' + g'\right)^2}{\left(k+\gamma\right)^2} = 0 \quad (35)$$

$$\left(1 + Rd\right)\theta'' + \frac{\theta'}{(k+\gamma)} + \frac{Prk\left[\left(g + 2h\right)\theta' - \ n\ \left(h' + g'\right)\theta\right]}{(k+\gamma)} + \text{EcPr}\left(h'' + g'' - \frac{h' + g'}{k+\gamma}\right)^2 + \frac{wk^2\left(h' + g'\right)^2}{\left(k+\gamma\right)^2} = 0 \quad (36)$$

The boundary conditions become

$$\theta|_{\gamma=0} = 1 \text{ and } \ \theta|_{\gamma\to\infty} = 0 \quad (37)$$

where Pr $\left(= C_p\mu/k_o\right)$, Ec $\left(= U^2/(C_p\left(T_w - T_\infty\right))\right)$, Ec $\left(= U^2/C_p A\,(x)^n\right)$, Rd $\left(= 16\sigma^* T_\infty^3/3k^* K\right)$ and $w\,(= H_a^2 EcPr)$ are Prandtl's number, Eckert's number, the modified Eckert number, Radiation and Joule heating parameters, respectively. Equation (36) is locally similar and corresponds to CST if $n = 0$.

The surface frictional drag and other important quantities experienced by the fluid flow at the surface are the skin-friction coefficients C_f, Nusselt number Nu and Local Nusselt Nu^*. These are defined as follows:

$$C_f = \frac{\tau_{rx}|_{r=0}}{\frac{1}{2}\rho u_w^2}, Nu = \frac{xq_w}{k^*(T - T_w)} \text{ and } Nu^* = \frac{xq_w}{k^* B\,(x)^\omega} \quad (38)$$

such that

$$\tau_{rx}|_{r=0} = \mu\left(\partial_r u - \frac{u}{R+r}\right)_{r=0};\ R_{e_x}^{\frac{1}{2}} = \sqrt{\left(\frac{c + dx}{\upsilon}\right)x^2};$$
$$q_w = -k^*\ \ \partial_r T|_{r=0} \quad (39)$$

Equations (38) and (39) give

$$-\frac{1}{2}R_{e_x}^{\frac{1}{2}} C_f = \left(f''\,(0) + g''\,(0) - \frac{2}{k}\right) \quad (40)$$

$$NuR_e^{\frac{1}{2}} = -\,\theta'(0), Nu^* R_{e_x}^{\frac{1}{2}} \quad (41)$$

We notice that Equation (41) is subjected to the heat conditions defined in Equation (37).

TABLE 1 | Comparison of the present results of the Skin-friction coefficient and the Local Nusselt number.

Curvature	Magnetic parameter	Abbas et al. (u = cx) [16]		Present results (u = cx), d = 0	
ξ	M	$-R_{e_s}^{\frac{1}{2}} C_f$	$-\theta'(0)$	$-R_{e_s}^{\frac{1}{2}} C_f$	$-\theta'(0)$
5	0.2	1.22881	0.43268	1.20372	0.42418
10	0.2	1.12311	0.41896	1.10709	0.41132
20	0.2	1.07541	0.41094	1.06389	0.40365
50	0.2	1.04849	0.40571	1.03958	0.39864
100	0.2	1.03982	0.40390	1.03175	0.39691
200	0.2	1.03553	0.40298	1.02788	0.39604
1,000	0.2	1.03212	0.40224	1.02480	0.39533
10	0.2	1.12311	0.41896	1.10709	0.41132
10	0.4	1.18306	0.40717	1.16408	0.39975
10	0.6	1.27633	0.38927	1.25344	0.38190
10	0.8	1.39562	0.36727	1.36870	0.35953
10	1.0	1.53419	0.34304	1.50358	0.33447

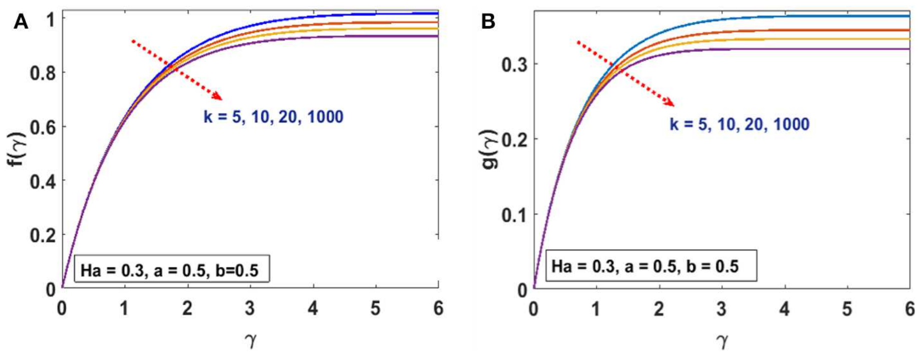

FIGURE 2 | (A) Effects of k on stream function $f(\gamma)$. **(B)** Effects of k on stream function $g(\gamma)$.

COMPUTATIONAL METHODOLOGY

In this present work, our focus is to present physical and plausible solutions for the three momentum equations in response to a curved structure through a numerical approach. Substituting Equation (22) into Equation (23), differentiating the resulting equation and accommodating Equation (24) gives

$$g^{'v} + \frac{2g''' + kgg''' - kg'g''}{(k+\gamma)} - \frac{g'' - kgg'' + k\left(g'\right)^2 + (Ha)^2 k^2 g''}{(k+\gamma)^2} + \frac{g' - kgg' - (Ha)^2 k^2 g'}{(k+\gamma)^3} = 0 \quad (42)$$

$$h^v - \frac{7h'''}{(k+\gamma)^2} + \frac{5h''}{(k+\gamma)^3} - \frac{5h'}{(k+\gamma)^4} + \frac{4khh'}{(k+\gamma)^4} - \frac{2k\left(2hh''' - 2h'h''\right)}{(k+\gamma)^2} - \frac{2k\left[2hh'' - 2\left(h'\right)^2\right]}{(k+\gamma)^3} + \frac{k\left[3gg'' - \left(g'\right)^2\right]}{(k+\gamma)^3} - \frac{3kgg'}{(k+\gamma)^4} - \frac{k\left[gg^{iv} - \left(g''\right)^2\right]}{(k+\gamma)}$$
$$+ \frac{k\left(2hg^{iv} + h'g''' - h'''g' - 3h''g''\right)}{(k+\gamma)} + \frac{kgh^{iv}}{(k+\gamma)} - \frac{k\left(3h''g + 6hg'' - 3h'g'\right)}{(k+\gamma)^3} + \frac{3k\left(2hg' + h'g\right)}{(k+\gamma)^4} - \frac{(Ha)^2 k^2\left(h''' + g'''\right)}{(k+\gamma)^2} - \frac{(Ha)^2 k^2\left(h'' + g''\right)}{(k+\gamma)^3} + \frac{(Ha)^2 k^2 (3h' + g')}{(k+\gamma)^4} = 0 \quad (43)$$

At this point, the solution of the non-linear coupled system of differential Equations (35), (36), (42), and (43) as subject to boundary conditions from Equations (13), (14), and (37), is obtained by using the shooting method with Runge-Kutta algorithms in MATLAB. The initial expression of the higher order system into first order differential equations are transformed into an initial value problem by considering $\left(g, g', g'', g''', h, h', h'', h''', h'v, \theta, \theta'\right)^T = \left(s_1, s_2, s_3, s_4, s_5, s_6 s_7, s_8, s_9, s_{10}, s_{11}\right)^T$. The implementation of our numerical technique into the above system of equations gives the following.

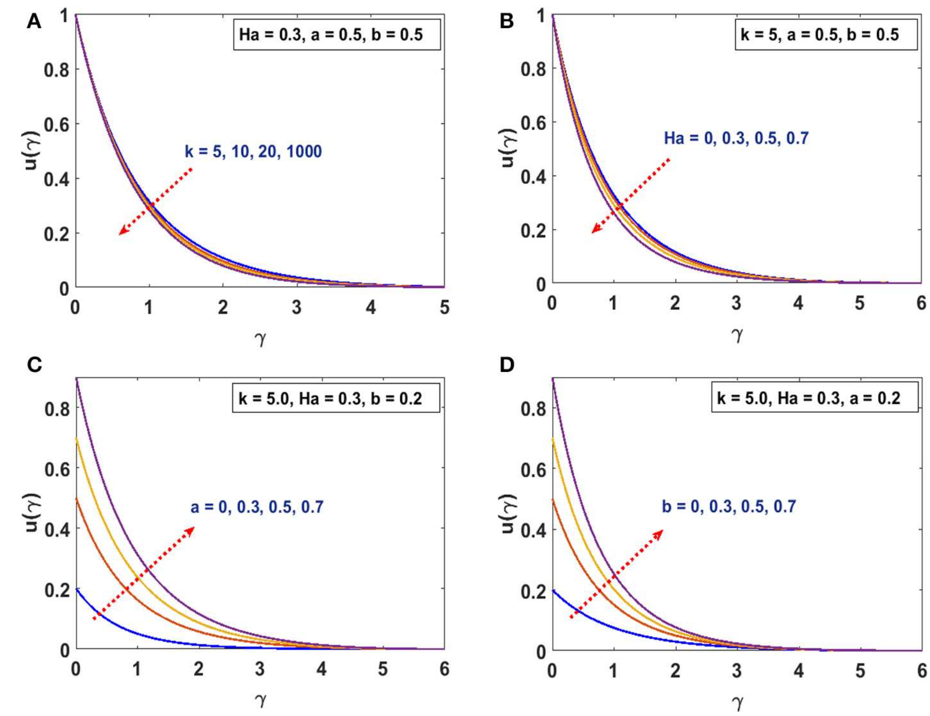

FIGURE 3 | (A) Effects of *k* on velocity field *u*(γ). **(B)** Effects of *Ha* on velocity field *u*(γ). **(C)** Effects of *a* on velocity field *u*(γ). **(D)** Effects of *b* on velocity field *u*(γ).

$$\begin{pmatrix} s_1{}' \\ s_2{}' \\ s_3{}' \\ s_4{}' \\ s_5{}' \\ s_6{}' \\ s_7{}' \\ s_8{}' \\ s_9{}' \\ s_{10}{}' \\ s_{11}{}' \end{pmatrix} = \left\{ \begin{matrix} s_2 \\ s_3 \\ s_4 \\ -\begin{bmatrix} z\left(2s_4 + ks_1s_4 - ks_2s_3\right) - z^2\left(s_3 - ks_1s_3 + ks_2^2 + (Ha)^2k^2s_3\right) \\ +z^3\left(s_2 - ks_1s_2 - (Ha)^2k^2s_2\right) \end{bmatrix} \\ s_6 \\ s_7 \\ s_8 \\ s_9 \\ -\begin{bmatrix} -7z^2s_8 + 5z^3s_7 - 5z^4s_6 + 4kz^4s_5s_6 - 4kz^2s_5s_8 + 4kz^2s_6s_7 \\ -4kz^3s_5s_7 + 4kz^3s_6^2 + 3kz^3s_1s_3 - kz^3s_2^2 - 3kz^4s_1s_2 - kzs_1s_4{}' \\ -kzs_3^2 + 2kzs_1s_4{}' + kzs_6s_4 - kzs_2s_8 - 3kzs_3s_7 + kzs_1s_9{}' - 3kz^3s_1s_7 \\ -6kz^3s_3s_5 + 3kz^3s_2s_6 + 6kz^4s_2s_5 + 3kz^4s_1s_6 - (Ha)^2k^2z^2(s_8 + s_4) \\ -(Ha)^2k^2z^3(s_7 + s_3) + (Ha)^2k^2z^4(3s_6 + s_2) \end{bmatrix} \\ s_{11} \\ -z_k\begin{bmatrix} zs_{11} + kzPr\left(s_1s_{10} + 2s_5s_{10} - ns_{10}\left[s_6 + s_2\right]\right) + EcPr\left(s_7 + s_3 - z\left[s_6 + s_2\right]\right) \\ +wk^2z^2(s_6 + s_2) \end{bmatrix} \end{matrix} \right\}, \tag{44}$$

$$\begin{pmatrix} s_1(0) \\ s_2(0) \\ s_3(0) \\ s_4(0) \\ s_5(0) \\ s_6(0) \\ s_7(0) \\ s_8(0) \\ s_9(0) \\ s_{10}(0) \\ s_{11}(0) \end{pmatrix} = \begin{pmatrix} 0 \\ 1 \\ N_1 \\ N_2 \\ 0 \\ 1 \\ N_3 \\ N_4 \\ N_5 \\ 1 \\ N_6 \end{pmatrix}, \tag{45}$$

where $z = \frac{1}{(k+\gamma)}$ and $z_k = \frac{1}{(1+Rd)}$. The unknown initial values N_1, N_2, N_3, N_4, N_5 and N_6 are approximated with the help of Newton's method till the required conditions ($h'(\gamma) = 0$, $h''(gamma) = 0$, $g'(\gamma) = 0, g''(\gamma) = 0$, $g'''(\gamma) = 0$, $\theta'(\gamma) = 0$) are satisfied as $\gamma \to \infty$. The initial guesses are given by

$$\left.\begin{matrix} g'' = N_1 \\ g''' = N_2 \\ h'' = N_3 \\ h''' = N_4 \\ h'v = N_5 \\ \theta' = N_6 \end{matrix}\right\}_{\eta=0}. \tag{46}$$

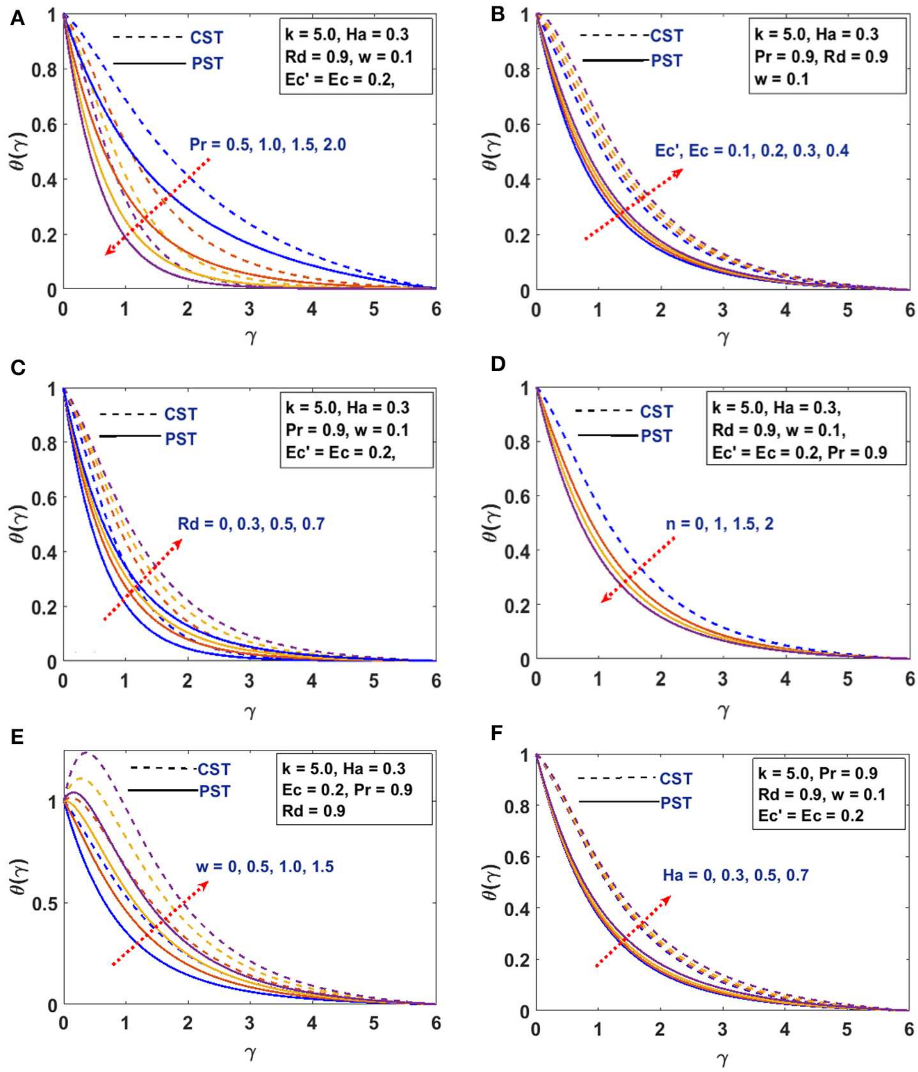

FIGURE 4 | (A) Effects of Pr on temperature field $\theta(\gamma)$. **(B)** Effects of Ec′, Ec on temperature field $\theta(\gamma)$. **(C)** Effects of *Rd* on temperature field $\theta(\gamma)$. **(D)** Effects of *n* on temperature field $\theta(\gamma)$. **(E)** Effects of *w* on temperature field $\theta(\gamma)$. **(F)** Effects of *Ha* on temperature field $\theta(\gamma)$.

Expanding Equation (46) about $\gamma = \infty$

$$\begin{aligned} & g''(\gamma,\ N_1 + \Delta N_1, N_2 + \Delta N_2, N_3 + \Delta N_3, N_4 \\ & \quad + \Delta N_4, N_5 + \Delta N_5, N_6 + \Delta N_6) \\ & = g''(\gamma,\ N_1, N_2, N_3, N_4, N_5, N_6) + \frac{\partial g''}{\partial N_1}\Delta N_1 + \frac{\partial g''}{\partial N_2}\Delta N_2 \\ & \quad + \frac{\partial g''}{\partial N_3}\Delta N_3 + \frac{\partial g''}{\partial N_4}\Delta N_4 + \frac{\partial g''}{\partial N_5}\Delta N_5 + \frac{\partial g''}{\partial N_6}\Delta N_6. \end{aligned} \quad (47)$$

The remaining conditions $(g''', h'', h''', h'v, \theta')$ are subsequently expressed in the form of Equation (47). The required Jacobian Matrix computed (for $\gamma = \infty$) after several processes is given as

$$\hat{A}\hat{X} = \hat{B}, \quad (48)$$

where $\hat{X} = (N_1, N_2, N_3, N_4, N_5, N_6)^T$, $\hat{B} = (B_1, B_2, B_3, B_4, B_5, B_6)^T$ and the iterations that generate the above Matrix takes the form:

$$\text{For } \left.\begin{matrix} i = 1\,(1)\,6 \\ j = 1(1)6 \end{matrix}\right\} \quad (49)$$

$$\begin{aligned} \hat{A}(i,j) = {} & s(11i+3) \\ & \times s(11j+3) + s(11i+4) \times s(11j+4) \\ & + s(11i+7) \times s(11j+7) \\ & + s(11i+8) \times s(11j+8) + s(11i+9) \\ & \times s(11j+9) + s(11i+11) \times s(11j+11) \end{aligned} \quad (50)$$

$$\begin{aligned} \hat{B}(i) = & -(s(3) \times s(11i+3) + s(4) \\ & \times s(11i+4) + s(7) \times s(11i+7) + s(8) \\ & \times s(11i+8) + s(9) \times s(11i+9) + s(11) \times s(11i+11)). \end{aligned} \quad (51)$$

The final point of the boundary layer region is determined successfully when no changes occur at $s = 1$ to a tolerance

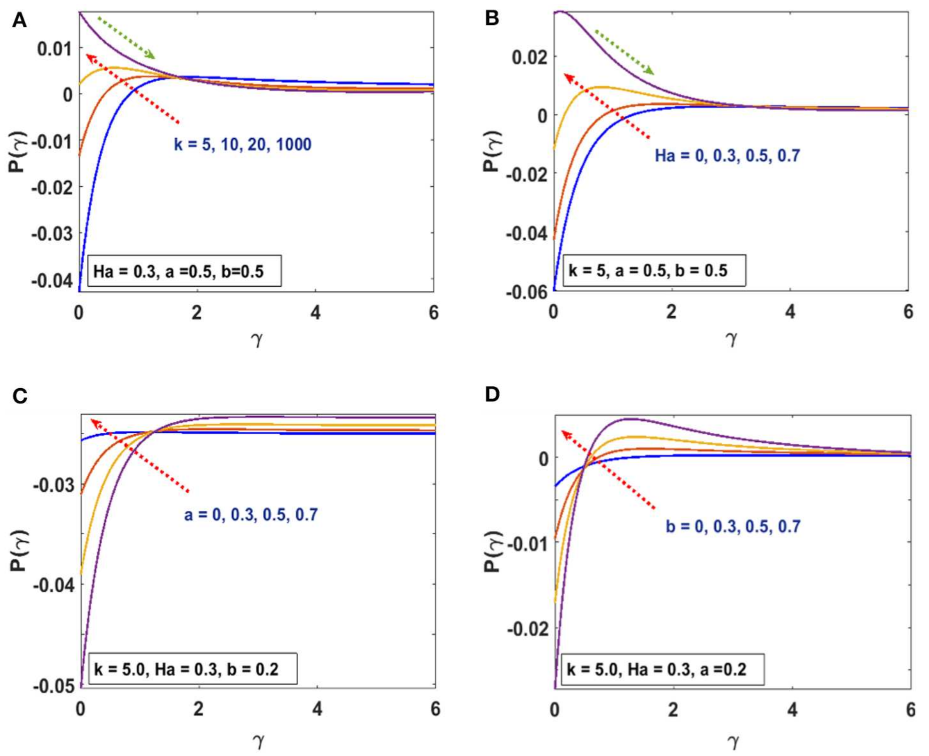

FIGURE 5 | (A) Effects of k on pressure profile $P(\gamma)$. **(B)** Effects of Ha on pressure profile $P(\gamma)$. **(C)** Effects of a on pressure profile $P(\gamma)$. **(D)** Effects of b on pressure profile $P(\gamma)$.

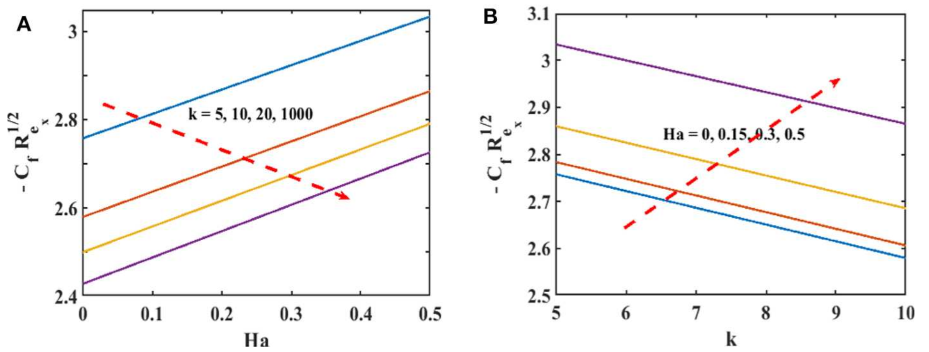

FIGURE 6 | (A) Effects of k on surface drage force. **(B)** Effect of Ha on surface drag force.

value of 10^{-8}. Our interest focuses in investigating the flow characteristics: velocity, temperature, momentum and thermal boundary layer thickness over a curved surface under certain physical parameters.

RESULT AND DISCUSSION

In this section, we present the effects of characterizing parameters on flow and thermal behavior. **Table 1** gives the surface drag force and heat transfer rate for CST/PSVT cases. **Figures 2A,B** establish the patterns of fluid trajectory which decreases as the radius of curvature, k, increases. **Figures 3A,B** examine the behavior of the velocity, $u(\gamma)$, and momentum boundary layer for an increasing radius of curvature, k, and the Lorentz force. The fluid velocity and the momentum boundary layer are found to decrease as these parameters increase. This helps to control the fluid flow by means of curvature (**Figure 3A**) and the Lorentz force (**Figure 3B**). Thus, besides the well-known behavior of the Lorentz force, the curvature plays an important role in reducing the velocity. This alternate way of reducing the velocity field through the radius of curvature (for curved structures) has been established for the first time. The effects of the linear, a, and non-linear, b, parts of the stretching velocity are presented in **Figures 3C,D**. It is noted that fixing either a

TABLE 2 | Numerical values of $-R_{e_x}^{\frac{1}{2}} C_f$ and rate of heat transfer at fixed $a = 0.5$, and $b = 0.5$.

k	Ha	Pr	Ec'	Ec	Rd	w	$-R_{e_x}^{\frac{1}{2}} C_f$	CST (n = 0) $-\theta'(0)$	PSVT (n = 0.3) $-\theta'(0)$
5	0.2	0.9	0.2	0.2	0.9	0.1	2.80246	0.25898	0.98254
–	0.3	–	–	–	–	–	2.85872	0.25055	0.97141
–	0.4	–	–	–	–	–	2.93584	0.23887	0.95599
–	0.2	0.7	–	–	–	–	2.80246	0.20943	0.82570
–	–	0.9	–	–	–	–	–	0.25898	0.98254
10	–	1.2	–	–	–	–	–	0.32758	1.18706
–	–	1.5	0.1	0.1	–	–	–	0.59220	1.52979
–	–	–	0.2	0.2	–	–	–	0.38709	1.36450
–	0.3	–	0.3	0.3	–	–	2.85872	0.16446	1.18024
–	–	–	0.2	0.2	0.5	–	–	0.45540	1.56950
20	–	2.0	–	–	0.7	–	–	0.48926	1.71391
–	–	–	–	–	0.9	–	–	0.45145	1.60176
–	0.4	–	0.3	0.3	1.2	0.1	2.93584	0.13874	1.24422
–	–	–	–	–	–	0.2	–	0.01932	1.14752
–	–	–	–	–	–	0.3	–	−0.10009	1.05083
–	0.5	–	–	–	–	0.4	3.03237	−0.24530	0.92318

or b and varying the other parameter increases the velocity field and the boundary layer thickness; inferring that both parameters are indispensable and equally important. The temperature profile is found to decrease/increase for increasing/decreasing Prandtl/Eckert numbers for both CST (**Figure 4A**) and PSVT (**Figure 4B**) according to the physics of heat flow. Increasing the radiation parameter, Rd, increases the fluid temperature and the thermal boundary layer thickness (radiation servers as additional source for heat generation) as shown in **Figure 4C**. This effect is more significant in CST than PSVT. **Figure 4D** gives a comparison of the temperature distribution between CST ($n = 0$) and PSVT ($n > 0$). It is observed that the thermal kinetics profile is maintained over the surface for CST. However, the temperature and thermal boundary layer decreases as the temperature index, n, increases. **Figure 4E** expresses the effect of Lorentz force in the generation of surface heating. Thus, the application of Lorentz force increases the heat flow characteristic in both CST/PSVT. The effects of a magnetic parameter on the temperature and thermal boundary layer thickness are presented in **Figure 4F** and show a slight increase with Ha. It is further observed that heat transfer from the surface to the fluid is more significant for a constant surface temperature than a variable surface temperature. This shows an additional effect of magnetic fields (hitherto unknown) is raising the temperature of the fluid flow over the curved surface. The pressure gradient $P(\gamma)$ in the boundary layer region for the curved surface cannot be neglected; whereas it is neglected for the straight surface. However, the effect of increasing curvature, k, and Ha on the pressure is shown in **Figures 5A,B**. We observe from **Figure 5A** that the pressure rises from the start of the curved surface and decreases subsequently. The observation conforms with the velocity behavior which decreases for large k, while the pressure approaches zero for the flat surface as ($k \rightarrow \infty$). In **Figure 5B** the pressure decreases significantly along the curved surface due to an opposing Lorentz force that suppresses the bulk movement of the fluid. This agrees with the behavior of the velocity as explained in the figure above. **Figures 5C,D** show the effects of stretching strengths a and b on the pressure. The pressure increases when either a (**Figure 5C**) or b (**Figure 5D**) is increased. This increase is more significant at the start of the curved surface for b, proving that the strength of non-linear stretching contributes more effectively compared to the linear strength of the stretching velocity. This phenomenal observation is presented for the first time. We further notice that the flow field characteristic decreases for linear stretching in **Figure 5C** while it increases for non-linear stretching in **Figure 5D**. The surface drag force for varying curvature and magnetic field parameters is shown in **Figures 6A,B**. **Figure 6A** shows that the drag force increases with k for increasing Ha, while in **Figure 6B** it decreases with Ha as a consequence of increasing k. **Table 1** is presented to show the impacts of a variable magnetic field in comparison with the constant magnetic input on surface drag force and heat transfer rate in view of possible engineering applications. The differences raise a slight concern due to improvements in the geometry (curvilinear) of the magnetic field rather that using a constantly applied field as in the existing literature. **Table 2** is computed to tabulate the numerical values of the skin friction coefficient and the heat transfer rate (Nusselt/local Nusselt numbers) for CST/PSVT under varying values of the characterizing parameters.

CONCLUSION

The flow and heat transfer analysis of a two-dimensional steady hydromagnetic viscous fluid flow due to non-linear (quadratic) stretching of the curved surface is investigated. The energy equation contains viscous dissipation, linear radiation and joule heating effects. The similarity transformation is improved to contain both the effects of the linear and non-linear parts of the stretching velocity on the velocity field. The expression of Lorentz force is modified for the curved surface. The heat flow is discussed for the cases of constant surface temperature (CST) and variable surface temperature (PSVT). The reduced boundary layer equations are solved numerically using Runge-Kutta (RK) fourth order algorithms. The salient features of this work are: (i) Correct modeling of the quadratic stretching is presented by redefining the similarity transformation. (ii) An accurate expression of the Lorentz force is obtained for an applied magnetic field on the curved structure by considering the variable magnetic field that depends on the radial direction. (iii) The velocity field and the momentum boundary layer thickness can be maintained by the curvature and the Lorentz force. (iv) The effects of the strengths of the linear and non-linear parts of the stretching velocity are investigated for controlling the flow over the curved surface. (v) For both CST/PSVT cases the magnetic field increases slightly due to quantum heat generation caused by the Lorentz force. (vi) A decrease of the dimensionless radius of curvature (increasing the curvature) gives a decrease in the heat transfer from the curved surface to the fluid as compared to a flat surface. (vii) Increasing the Eckert/Local Eckert number enhances the temperature field and thermal boundary layer thickness. (viii) Low thermal conductivity due to an increasing Prandtl number consequently diminishes the temperature field and thermal boundary layer thickness. (ix) A high radiation parameter increases the heat flow from the surface to the fluid. (x) Variation of the wall temperature (PSVT) index reduces the heat flow characteristics, consequently it helps in regulating the heat flow rate generated over a curved sheet. (xi) The pressure decreases for a large radius of curvature, k, and Ha and increases due to the non-linear part of the stretching velocity.

DATA AVAILABILITY STATEMENT

The datasets generated for this study are available on request to the corresponding author.

AUTHOR CONTRIBUTIONS

The corresponding author is a PhD student under supervision of SA and co-guidance QH. All authors work and mediated on, the technicality, physical intuition, and mathematical significance contributions of the manuscript content to the research world.

REFERENCES

1. Crane LJ. Flow past a stretching plate. *Z Angew Math Phys*. (1970) **7**:645–7. doi: 10.1007/BF01587695
2. Kumaran V, Ramanaiah G. A note on the flow over stretching sheet. *Acta Mech*. (1996) **116**:229–33. doi: 10.1007/BF01171433
3. Raptis, AA, Perdikis C. Viscous flow over a nonlinear stretching sheet in the presence of a chemical reaction and magnetic field. *Int. J. Nonlinear Mech*. (2006) **41**:527–9. doi: 10.1016/j.ijnonlinmec.2005.12.003
4. Cortell R. Further results on nonlinearly stretching permeable sheets. analytic solution for MHD flow and mass transfer. *Math Probl Eng*. (2012) **2012**:18. doi: 10.1155/2012/743130
5. Takhar HS, Raptis AA, Perdikis CP. MHD asymmetric flow past note a semi-infinte moving plate. *Acta Mech*. (1986) **65**:287–90. doi: 10.1007/BF01176888
6. Kelson NA. Note on similarity solutions for viscous flow over an impermeable and non-linearly (quadratic) stretching sheet. *Int J Nonlinear Mech*. (2011) **46**:1090–1. doi: 10.1016/j.ijnonlinmec.2011.04.025
7. Cortel R. MHD (magneto-hydrodynamic) flow and radiative nonlinear heat transfer of a viscoelastic fluid over a stretching sheet with heat generation/absorption. *Energ J*. (2014) **74**:896–905. doi: 10.1016/j.energy.2014.07.069
8. Magyari E, Keller B. Heat and mass transfer in the boundary layer on an exponentially stretching continuous surface. *J Phys D Appl Phys*. (1999) **32**:577–85. doi: 10.1088/0022-3727/32/5/012
9. Partha MK, Murthy PN, Rajasekhar GP. Effect of viscous dissipation on the mixed convection heat transfer from an exponentially stretching surface. *Heat Mass Transfer*. (2005) **41**:360–6. doi: 10.1007/s00231-004-0552-2
10. Abd-El-Aziz M. Viscous dissipation effect on mixed convection flow of a micropolar fluid over an exponentially stretching sheet. *Can J Phys*. (2009) **57**:359–3678. doi: 10.1139/P09-047
11. Ishak A. MHD boundary layer flow due to an exponentially stretching sheet with radiation effect. *Sains Malays*. (2011) **40**:391–5. Available online at: http://journalarticle.ukm.my/2406/1/17_Anuar_Ishak.pdf
12. Zeeshan A, Ellahi R. Series solutions for nonlinear partial differential equations with slip boundary conditions for non-Newtonian MHD fluid in porous space. *Appl Math Inform Sci*. (2013) **7**:257–65. doi: 10.12785/amis/070132
13. Magyari E, Ali ME, Keller B. Heat and mass transfer characteristics of self-similar boundary-layer flows induced continuous surface stretched with rapidly decreasing velocities. *Heat Mass Transfer*. (2010) **38**:65–74. doi: 10.1007/s002310000126
14. Sajid M, Ali N, Javed T, Abbas Z. Stretching a curved surface in a viscous fluid. *Chinese Phys Lett*. (2010) **27**:024703. doi: 10.1088/0256-307X/27/2/024703
15. Sanni KM, Asghar S, Jalil M, Okechi NF. Flow of viscous fluid along a nonlinearly stretching curved surface. *Results Phys*. (2017) **7**:1–7. doi: 10.1016/j.rinp.2016.11.058
16. Abbas Z, Naveed M, Sajid M. Heat transfer analysis for stretching flow over a curved surface with magnetic field. *J Eng Thermophys*. (2013) **22**:337–45. doi: 10.1134/S1810232813040061
17. Naveed M, Abbas Z, Sajid M. Hydromagnetic flow over an unsteady curved stretching surface. *Eng Sci Technol Int J*. (2016) **19**:841–5. doi: 10.1016/j.jestch.2015.11.009
18. Imtiaz M, Hayat T, Alsaedi A, Hobiny A. Homogeneous-heterogeneous reaction in MHD flow due to an unsteady curved stretching surface. *J Mol Liq*. (2016) **221**:245–53. doi: 10.1016/j.molliq.2016.05.060
19. Imtiaz M, Hayat T, Alsaedi A. MHD convective flow of jeffrey fluid due to a curved stretching surface with homogeneous-heterogeneous reactions. *PLoS ONE*. (2016) **11**:e0161641. doi: 10.1371/journal.pone.0161641
20. Imtiaz M, Hayat T, Alsaedi A. Convective flow of ferrofluid due to a curved stretching surface with homogeneous-heterogeneous reaction. *Powder Technol*. (2017) **310**:154–62. doi: 10.1016/j.powtec.2017.01.029
21. Abbas Z, Naveed M, Sajid M. Hydromagnetic Slip flow of nanofluid Over a Curved Surface with heat generation and thermal radiation. *J Mol Liq*. (2016) **215**:756–62. doi: 10.1016/j.molliq.2016.01.012
22. Hayat T, Rashid M, Imtiaz M, Alsaedi A. MHD Convective flow due to a curved surface with thermal radiation and chemical reaction. *J Mol Liq*. (2016) **225**:482–9. doi: 10.1016/j.molliq.2016.11.096
23. Hayat T, Sajjad R, Ellahi R, Alsaedi A, Muhammad T. Homogeneous-heterogeneous reaction in MHD flow of micropolar fluid by a curved stretching surface. *J Mol Liq*. (2017) **240**:209–20. doi: 10.1016/j.molliq.2017.05.054
24. Hayat T, Saif RS, Ellahi R, Muhammad T, Ahmad B. Numerical study of boundary layer flow due to a nonlinear curved stretching sheet

with convective heat and mass conditions. *Results Phys*. (2017) **7**:2601–6. doi: 10.1016/j.rinp.2017.08.030

25. Aleksander S, Grzegorz C. Application of variable magnetic fields in medicine—15 years' experience. *Wiad Lek (Warsaw, Poland: 1960)*. (2003) **56**:9–10. Available online at: https://europepmc.org/article/med/15049208
26. Hurley DP, Coey JMD. *Device for Generating a Variable Magnetic Field*. United State Patent US 6535092B1 (2003). Dublin: Magnetic Solution (Holdings) Limited.
27. Reddy JVR, Sugunamma V, Sandeep N. Dual solutions for nanofluid past a curved surface with nonlinear radiation, soret and Dufour effects. *IOP Conf Series J Phys Conf Series*. (2018) **1000**:012152. doi: 10.1088/1742-6596/1000/1/012152
28. Saba F, Ahmed N, Hussain S, Khan U, Mohyd-Din ST. Thermal analysis of nanofluid flow over a curved stretching surface suspended by carbon nanotubes with internal heat generation. *Appl Sci.* (2018) **8**:395. doi: 10.3390/app8030395
29. Naveed M, Abbas Z, Sajid M. Dual solutions in hydromagnetic viscous fluid flow past a shrinking curved surface. *Arab J Sci Eng*. (2018) **43**:1189–94. doi: 10.1007/s13369-017-2772-z
30. Hayat T, Nasir T, Ijaz MK, Alsaedi A. Numerical investigation of MHD flow with Soret and Dufour effect. *Results Phys*. (2018) **8**:1017–22. doi: 10.1016/j.rinp.2018.01.006
31. Nadeem S, Ahmed Z, Saleem S. Carbon nanotubes effect in magneto nanofluid flow over a curved stretching surface with variable viscosity. *Microsyst Technol*. (2019) **25**:2881–8. doi: 10.1007/s00542-018-4232-4

Conflict of Interest: The authors declare that the research was conducted in the absence of any commercial or financial relationships that could be construed as a potential conflict of interest.

Copyright © 2020 Sanni, Hussain and Asghar. This is an open-access article distributed under the terms of the Creative Commons Attribution License (CC BY). The use, distribution or reproduction in other forums is permitted, provided the original author(s) and the copyright owner(s) are credited and that the original publication in this journal is cited, in accordance with accepted academic practice. No use, distribution or reproduction is permitted which does not comply with these terms.

frontiers in Physics

ORIGINAL RESEARCH
published: 06 May 2020
doi: 10.3389/fphy.2020.00109

Particle–Fluid Suspension of a Non-Newtonian Fluid Through a Curved Passage: An Application of Urinary Tract Infections

Arshad Riaz[1]* *and Muhammad Adil Sadiq*[2]

[1] Department of Mathematics, Division of Science and Technology, University of Education, Lahore, Pakistan, [2] Department of Mathematics, Dammam Community College, King Fahd University of Petroleum and Minerals, Dhahran, Saudi Arabia

OPEN ACCESS

Edited by:
Muhammad Mubashir Bhatti,
Shanghai University, China

Reviewed by:
Maryiam Javed,
Institute of Space Technology, Pakistan
Noreen Akbar,
National University of Sciences and Technology (NUST), Pakistan
Arash Asadollahi,
Southern Illinois University Carbondale, United States
Anwar Shahid,
Nanjing University of Aeronautics and Astronautics, China

***Correspondence:**
Arshad Riaz
arshad-riaz@ue.edu.pk

Specialty section:
This article was submitted to Mathematical Physics, a section of the journal Frontiers in Physics

Received: 08 January 2020
Accepted: 23 March 2020
Published: 06 May 2020

Citation:
Riaz A and Sadiq MA (2020) Particle–Fluid Suspension of a Non-Newtonian Fluid Through a Curved Passage: An Application of Urinary Tract Infections. Front. Phys. 8:109. doi: 10.3389/fphy.2020.00109

The current investigation deals with the inclusion of solid particles in the flow of a non-Newtonian incompressible fluid passing through a symmetric, curved channel admitting flexible walls and exhibiting wavy characteristics for the passage of fluid. This analysis reflects the disease of white particles occurring in the flow of urine. The problem formulation is structured under the constraints of lubrication approach. The flow is considered to be laminar and steady by transforming the unsteady coordinates into wave frame coordinates. The governing equations have been formulated with the help of similarity transformations. The solution of boundary value problems has been handled by perturbation procedure. The analytical solutions for fluid and particulate phase velocities, mean flow rates, and pressure gradient profile have been presented, while a numerical treatment has been carried out for pressure rise. Analyses of fluid velocity and particulate suspension velocity, pressure gradient, and pressure rise curves under the variations of material parameters have been discussed by graphs. It is observed from this investigation that solid particles are curtailing the velocity and pressure of the liquid. It is also procured that the curvature of the channel also reduces the movement of the fluid and that the particulate suspension is occurring at the bottom of the container. It is very considerable that the increase in peristaltic pumping causes a decrease in the solid particle concentration. This theoretical analysis can help in curing the diseases like urinary tract infections (UTIs). The analysis may also be pertinent to the flow of other physiological liquids and industrial solicitation where peristaltic pumping is concerned.

Keywords: analytical solution, eyring-powell model, pumping phenomenon, solid particles, two-phase flow

INTRODUCTION

Peristaltic flows are produced by spreading waves along the exorable membranes of a conduit. These flows provide an efficient means for fluid transport and are therefore used in the physical simulation. In clinical and medical contexts, peristaltic flows are meant for the blood transport within tiny blood vessels or fabricated blood instruments. Fluid trapping and material reflux are the two wonderful aspects of peristaltic passages. They describe the development and flow of free transport, called bolus supply. These two factors are of major importance, as they can be responsible for blood circulation and transport of viruses. From the point of view of mechanical engineering, these phenomena highlight the complexity of the chosen apparatus, but also encourage the fundamental study of such flows. Studies of peristaltic phenomena have been reported in Bhatti et al. [1], Hussain et al. [2], and Riaz [3].

It is noticed that the instant flow studies are congested to Newtonian fluids. The non-Newtonian behavior of fluids is of greater concern in many areas of science and technology. In applications for electroosmosis, for example, test accumulation, discovery, blending, and division of different natural and synthetic species on a chip coordinated with fluidic siphons and valves, the liquid rheological conduct for the most part should be considered. Major comprehension of the non-Newtonian job in fluid transport through microchannels is imperative in accurately foreseeing the exhibition and qualities of microfluidic gadgets. Numerous specialists have researched the entry of non-Newtonian liquid through peristaltic component [4, 5].

The progression of particles in a liquid is a part of multiphase mechanism. Such studies are significant in different physical issues, for example, sedimentation, barometril aftermath, powder innovation, vaporized filtration, fluidization [6], debris and lunar streams, and so forth. Moreover, with the assistance of the continuum hypothesis of blends, it is anything but difficult to look at different assorted subjects, for example, the rheology of blood [7], dissemination of proteins, demeanor of particles in a respiratory tract, and swimming of microorganisms [8]. Besides, molecule portrayal is likewise a significant part in a generation of molecule, preparing, taking care of, producing, and in different modern scientific applications [9]. Molecule portrayal is an essential and starting approach that aids in a procedure concerning solid particles. Such a depiction not only includes the natural static parameters—for example, volume, morphology, recision, dimensions, and so on—but also their dynamic frame of mind related to the liquid stream for example maximum speed and drag constant. Yao et al. [10] considered the multiphase course across the penetrable porous passage with walls impact. He prepared the perturbation solutions by considering the slip boundary conditions and observed that the slip limit condition essentially improved the speed of the liquid and a reduction of slip factor will in general increase the speed through a channel. Additionally, with an augmentation in volume portion thickness, liquid axis speed climbs. Mekheimer and Abd Elmaboud [11] evaluated the viscous fluid and particle mixture in uniform and non-uniform inlets for peristaltic concept and exact solutions are structured. Kamel et al. [12] explored the wave stream of molecule liquid adultration considering a planar channel having boundary slip and exhibited an arrangement utilizing perturbation technique. Lozano et al. [13] presented the peristaltic flow of incompressible Newtonian fluid with alike, solid particles of spherical shape distribution. They have found that the pressure in the wrinkled part of the ureter is enhanced accordingly with larger particle volume fraction.

Experimental work demonstrates that there is no check on basic speed for a liquid coursing through a curved channel. If the channel is straight, the loss of the head increases suddenly as the speed reaches its base value. The head loss varies below the basic frequency of the speed, but over it approximately as the following energy. But, through a curved channel, there is no impression of such an unexpected change at any speed of the stream. One plausibility is that movement through a curved channel is streamlined at speeds much more noteworthy than the basic for a straight channel, however testing seems to indicate that the basic speed is less in a curved channel than in a straight one. The mathematical examination of the peristaltic flow of hyperbolic tangent liquid in a curved channel has been explored by Nadeem and Maraj [14]. Narla et al. [15] have disclosed the peristaltic transport of Jeffrey nanofluid in curved channels. They discussed the dissemination of velocity, temperature, and nanoparticles fixation for different parameters overseeing the stream with the concurrent impacts of Brownian movement and thermophoretic dispersion of nanoparticles.

The urinary mechanism explains the homeostatic regulation of water and ion content in the blood and the disposal of waste products of metabolism. The kidneys receive blood from the renal artery, process it, and return the processed blood to the body through the renal vein. Urine produced in the kidneys passes into the urethra. Under normal conditions, peristalsis in the upper urinary tract begins with the origin of electrical activity at pacemaker sites located in the proximal part of the urinary collecting system. This electrical activity spreads distally, triggering the mechanical event of peristalsis and renal pelvic and ureteral contractions, which push urine from the kidney into the bladder [16]. Urine is expelled through the urethra into the outer body. Likoudis and Roos [17] studied the fluid flow in the ureter under lubrication approximation and focused their analysis on the pressure profile in the contracted part. Griffiths [18] studied the ureter with a one-dimensional lubrication approach and emphasized the relationship between low and high flow rates, pressure fields, and peristaltic contractions. Peristaltic flow in the ureter presents as an important application of peristalsis; the parameters are reasonably known, and the fluid being transported is fundamentally non-neutron and incompressible. Geometrically, however, the problem is complex. Peristaltic waves in the ureter can occur in multiple forms, either isolated or periodic, with complete occlusion throughout the cycle. Although the ureter itself is a tubular duct, the configuration of the lumen during peristalsis can be altered because its inner layer is made up of mucosa lined by the transitional epithelium. In this study, the geometry of having a two-dimensional curved shape is considered as it is of immense importance in the sense of applications.

As far as we could possibly know, no endeavor is made for peristaltic system of Eyring—Powell tensor within the sight of solid particles coursing through a curved channel. This examination is uncovered to fill this void in the literature and present the analytical and numerical examination of the model chosen. Right off the bat, we have transformed the conservation of mass and momentum into segment structure of velocity field and afterward changed over them by presenting wave outline. After this progression, physical demonstrated conditions have been diminished into a dimensionless structure by receiving some new dimensionless parameters. We have assembled the problem more comprehensively by lubrication constraints. To assess the nonlinear coupled differential conditions, perturbation strategy is applied on Eyring–Powell parameter A. The outflows

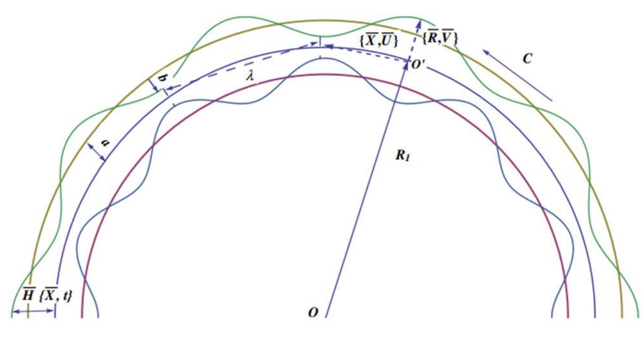

FIGURE 1 | Schematic diagram of the problem.

of liquid and particulate suspensions, stream rates, pressure slope, and pressure rise have been revealed. At last, physical ailments have been outlined in different diagrams under the changing estimations of appropriate parameters.

MODELING AND FORMATTING OF THE PROBLEM

Let us assume the creeping transport through a curved passage with small solid particles. We have adopted curvilinear cylindrical coordinates in a three-dimensional curved passage where $\bar{R}$ and $\bar{X}$ rays are selected to be normal and parallel to the flow, respectively. Moreover, the surfaces of the container are supposed to be flexible and executing sinusoidal waves propagating at the lower and upper surfaces at a fixed pace "c."

The boundary of the panel is expressed mathematically as

$$\bar{H}\left(\bar{X},\bar{t}\right) = \tilde{a} + \tilde{b}cos\left(\frac{2\pi}{\tilde{\lambda}}(\bar{X} - c\bar{t})\right). \tag{1}$$

The symbols, like $\tilde{a}$ and $\tilde{b}$, represent the radius of the channel and wave amplitude, accordingly. Moreover, $\tilde{\lambda}$ is the wavelength, and $\bar{t}$ executes time characteristics (see **Figure 1**). Here, we write the continuity and momentum conservation relations of the fluid and particle phases.

Fluid Phase

For fluid phase, the physical conservation laws of mass and momentum can be described in component form as

$$\frac{\partial}{\partial \bar{R}}\left((R_1+\bar{R})U_{2f}\right) + R_1\frac{\partial \overline{U}_{1f}}{\partial \bar{X}} = 0, \tag{2}$$

$$\rho\left(1-C\right)\left(\frac{\partial \overline{U}_{2f}}{\partial \bar{t}} + \overline{U}_{2f}\frac{\partial \overline{U}_{2f}}{\partial \overline{R}}R_1 + \frac{\overline{U}_{1f}R_1}{R_1+\overline{R}}\frac{\partial \overline{U}_{2f}}{\partial \overline{X}}R_1 - \frac{\overline{U}_{1f}^{\,2}R_1}{R_1+\overline{R}}\right) = -\left(1-C\right)\frac{\partial \overline{P}}{\partial \overline{R}}$$
$$+\mu_s\left(1-C\right)\left(\frac{R_1}{R_1+\overline{R}}\frac{\partial}{\partial \overline{R}}\left(\left(R_1+\overline{R}\right)\overline{\tau}_{11}\right) + \frac{R_1}{R_1+\overline{R}}\frac{\partial \overline{\tau}_{21}}{\partial \overline{X}}R_1 - \frac{R_1}{R_1+\overline{R}}\overline{\tau}_{22}\right) + CS\left(\overline{U}_{2p} - \overline{U}_{2f}\right), \tag{3}$$

$$\rho\left(1-C\right)\left(\frac{\partial \overline{U}_{1f}}{\partial \bar{t}} + \overline{U}_{2f}\frac{\partial \overline{U}_{1f}}{\partial \overline{R}}R_1 + \frac{\overline{U}_{1f}R_1}{R_1+\overline{R}}\frac{\partial \overline{U}_{1f}}{\partial \overline{X}}R_1 + \frac{\overline{U}_{2f}\overline{U}_{1f}R_1}{R_1+\overline{R}}\right) = \left(1-C\right)$$
$$\left(-\frac{R_1}{R_1+\overline{R}}\frac{\partial \overline{P}}{\partial \overline{X}} + \frac{\mu_s R_1}{R_1+\overline{R}}\frac{\partial \overline{\tau}_{22}}{\partial \overline{X}} + \frac{\mu_s}{R_1+\overline{R}}\left(R_1+\overline{R}\right)\frac{\partial \overline{\tau}_{12}}{\partial \overline{R}} + \overline{\tau}_{12}\right) + CS\left(\overline{U}_{1p} - \overline{U}_{1f}\right), \tag{4}$$

where C is the partial volume fraction parameter, μ_s is the solvent viscosity, $\overline{U}_{1f}$ and $\overline{U}_{2f}$ represent the fluid velocities, $\overline{\tau}_{ij}$ exhibits the stress tensor components whose general form is defined as [19]:

$$\bar{\tau} = \mu\,\partial_i\mathbf{V}_i + \frac{1}{\beta}\sinh^{-1}\left(\frac{\partial_i\mathbf{V}_i}{l}\right), \tag{5}$$

where $\partial_i\,\mathbf{V}_i$ gives the gradient tensor of velocity vector, the dynamic viscosity is measured by μ, and flow constants are represented by β and l.

Particulate Phase

For particle phase, the above defined equation will take the following form:

$$\frac{\partial \overline{U}_{1p}}{\partial \overline{R}} + \frac{R_1}{R_1+\overline{R}}\frac{\partial \overline{U}_{2p}}{\partial \overline{X}} + \frac{\overline{U}_{1p}}{R_1+\overline{R}} = 0, \tag{6}$$

$$\rho_p C\left(\frac{\partial \overline{U}_{2p}}{\partial \bar{t}} + \overline{U}_{2p}\frac{\partial \overline{U}_{2p}}{\partial \overline{R}} + \frac{\overline{U}_{1p}R_1}{R_1+\overline{R}}\frac{\partial \overline{U}_{2p}}{\partial \overline{X}} + \frac{\overline{U}_{1p}^{\,2}R_1}{R_1+\overline{R}}\right)$$
$$= -C\frac{\partial \overline{P}}{\partial \overline{R}} + CS\left(\overline{U}_{2f} - \overline{U}_{2p}\right), \tag{7}$$

$$\rho_p C\left(\frac{\partial \overline{U}_{1p}}{\partial \bar{t}} + \overline{U}_{2p}\frac{\partial \overline{U}_{1p}}{\partial \overline{R}} + \frac{\overline{U}_{1p}R_1}{R_1+\overline{R}}\frac{\partial \overline{U}_{1p}}{\partial \overline{X}} + \frac{\overline{U}_{2p}\overline{U}_{1p}R_1}{R_1+\overline{R}}\right)$$
$$= -C\frac{R_1}{R_1+\overline{R}}\frac{\partial \overline{P}}{\partial \overline{X}} + CS\left(\overline{U}_{1f} - \overline{U}_{1p}\right). \tag{8}$$

In above relations, ρ_p, $\overline{U}_{2p}$, $\overline{U}_{1p}$, and S represent the density of solid particles, their velocities and drag coefficient, respectively. The drag coefficient term and the empirical expression for the suspension viscosity are defined as [1]

$$S = \frac{4.5\mu'_0}{R_0^2}\bar{\lambda}(C),\ \mu_s = \frac{\mu'_0}{1-\bar{m}C},$$
$$\bar{\lambda}(C) = \frac{4+\left(8C-3C^2\right)^{1/2}+3C}{4+9C^2-12C},$$
$$\overline{m} = 0.70e^{\left[\frac{249}{100}C+\frac{1107}{T}\exp\left(-\frac{169}{100}C\right)\right]}.$$

Now suggesting the following lab and wave framework transformations

$$\bar{x}=\bar{X}-c\bar{t},\ \bar{r}=\bar{R},\ \bar{u}_{f,p}=\bar{U}_{1f,1p}-c,\ \bar{v}_{f,p}=\bar{U}_{2f,2p},\ \bar{p}=\bar{P}. \quad (9)$$

In new frame of reference, Equations (3), (4), (7), and (8) transformed into the subsequent form

$$\rho(1-C)\left(\bar{v}_f\frac{\partial\bar{v}_f}{\partial\bar{r}}R_1+\frac{(\bar{u}_f+c)\,R_1}{R_1+\bar{r}}\frac{\partial\bar{v}_f}{\partial\bar{x}}R_1-\frac{(\bar{u}_f+c)^2R_1}{R_1+\bar{r}}\right)=-(1-C)\,\frac{\partial\bar{p}}{\partial\bar{r}}R_1$$
$$+\mu_S(1-C)\left(\frac{R_1}{R_1+\bar{r}}\frac{\partial}{\partial\bar{r}}\left((R_1+\bar{r})\,\tau_{11}\right)+\frac{R_1}{R_1+\bar{r}}\frac{\partial\tau_{21}}{\partial\bar{x}}R_1-\frac{R_1}{R_1+\bar{r}}\bar{\tau}_{22}\right)+CS\left(\bar{v}_p-(\bar{v}_f)\right), \quad (10)$$

$$\rho(1-C)_{\rho f}\left(\bar{v}_f\frac{\partial\bar{u}_f}{\partial\bar{r}}R_1+\frac{(\bar{u}_f+c)\,R_1}{R_1+\bar{r}}\frac{\partial\bar{u}_f}{\partial\bar{x}}R_1+\frac{\bar{v}_f(\bar{u}_f+c)\,R_1}{R_1+\bar{r}}\right)=(1-C)$$
$$\left(-\frac{R_1}{R_1+\bar{r}}\frac{\partial\bar{p}}{\partial\bar{x}}+\frac{\mu_sR_1}{R_1+\bar{r}}\frac{\partial\bar{\tau}_{22}}{\partial\bar{x}}+\frac{\mu_s}{R_1+\bar{r}}\left((R_1+\bar{r})\,\frac{\partial\bar{\tau}_{12}}{\partial\bar{r}}+\bar{\tau}_{12}\right)\right)+CS\left(\bar{u}_p-\bar{u}_f\right), \quad (11)$$

$$\rho_\rho C\left(\bar{v}_p\frac{\partial\bar{v}_p}{\partial\bar{r}}+\frac{(\bar{u}_p+c)\,R_1}{R_1+\bar{r}}\frac{\partial\bar{v}_p}{\partial\bar{x}}-\frac{(\bar{u}_p+c)^2R_1}{R_1+\bar{r}}\right)=-C\frac{\partial\bar{p}}{\partial\bar{r}}+CS\left(\bar{v}_f-\bar{v}_p\right), \quad (12)$$

$$\rho_\rho C\left(\bar{v}_p\frac{\partial\bar{u}_p}{\partial\bar{r}}+\frac{(\bar{u}_p+c)\,R_1}{R_1+\bar{r}}\frac{\partial\bar{u}_p}{\partial\bar{x}}+\frac{\bar{v}_p(\bar{u}_p+c)\,R_1}{R_1+\bar{r}}\right)=-C\frac{R_1}{R_1+\bar{r}}\frac{\partial\bar{p}}{\partial\bar{x}}+CS\left(\bar{u}_f-\bar{u}_p\right), \quad (13)$$

Now we introduce the following dimensionless quantities for further simplification

$$\begin{aligned}u_{f,p}&=\frac{\bar{u}_{f,p}}{c},\ v_{f,p}=\frac{\bar{v}_f}{c\delta},\ h=\frac{\bar{H}}{\tilde{a}},\ p=\frac{\tilde{a}^2}{\tilde{\lambda}\bar{c}\mu_s}\bar{p},\\ R_e&=\frac{\rho\tilde{a}c}{\mu_s},\ y=\frac{\bar{r}}{\tilde{a}},\ x=\frac{2\pi\bar{x}}{\tilde{\lambda}},\ k_1=\frac{R_1}{\tilde{a}},\\ h'&=\frac{H'}{\tilde{a}},\ \varphi=\frac{\tilde{b}}{\tilde{a}},\ \tau_{ij}=\frac{\tilde{a}}{\mu c}\bar{\tau}_{ij},\ B=\frac{1}{\beta\mu l},\\ A&=\frac{Bc^2}{6l^2\tilde{a}^2},\ \delta=\frac{2\pi\tilde{a}}{\tilde{\lambda}},N_1=\frac{S\tilde{a}^2}{\mu_s}.\end{aligned} \quad (14)$$

Injecting the above revealed factors, Equations (10) through (13) become

$$R_e\delta(1-C)\left(v_f\frac{\partial v_f}{\partial y}+\frac{k_1v_f}{k_1+y}\delta\frac{\partial v_f}{\partial x}-\frac{(u_f+1)^2}{k_1+y}\right)=-(1-C)\,\frac{\partial p}{\partial y}$$
$$+(1-C)\left(\frac{\delta}{k_1+y}\tau_{11}+\delta\frac{\partial\tau_{21}}{\partial x}-\delta\frac{\tau_{22}}{k_1+y}\right)+\delta CN_1\left(u_p-u_f\right), \quad (15)$$

$$R_e(1-C)\left(v_f\frac{\partial u_f}{\partial y}+\delta\frac{k_1(u_f+1)}{k_1+y}\frac{\partial u_f}{\partial x}-\frac{v_f(u_f+1)}{k_1+y}\right)=-(1-C)\,\frac{k_1}{k_1+y}\frac{\partial p}{\partial x}$$
$$+(1-C)\left(\delta\frac{k_1}{k_1+y}\frac{\partial\tau_{22}}{\partial x}+\frac{1}{k_1+y}\frac{\partial}{\partial y}\left((k_1+y)\,\tau_{12}\right)\right)+N_1C\left(u_p-u_f\right), \quad (16)$$

$$R_e\delta C\left(\delta^2v_p\frac{\partial v_p}{\partial y}+\frac{\delta^2}{\lambda}\frac{k_1}{k_1+y}v_p\frac{\partial v_p}{\partial x}-\frac{u_p+1}{k_1+y}\right)=-C\frac{\partial p}{\partial y}+CN_1\delta\left(v_p-v_f\right), \quad (17)$$

$$R_eC\left(\delta v_p\frac{\partial u_p}{\partial y}+\frac{1}{\lambda}\frac{k_1(u_p+1)}{k_1+y}\frac{\partial u_p}{\partial x}+\delta\frac{v_p(u_p+1)}{k_1+y}\right)=-C\frac{k_1}{k_1+y}\frac{\partial p}{\partial x}+N_1C\left(u_f-u_p\right). \quad (18)$$

Now inserting assumptions of long wavelength ($\delta\approx 0$) and low Reynolds number ($R_e\approx 0$), we arrive at

$$\frac{\partial p}{\partial y}=0, \quad (19)$$

$$-\frac{\partial p}{\partial x}+\frac{1}{k_1}\frac{\partial}{\partial y}\left((k_1+y)\,\tau_{12}\right)+\frac{N_1C\,(k_1+y)\,(u_p-u_f)}{(1-C)\,k_1}=0, \quad (20)$$

$$u_p=u_f-\frac{1}{N_1}\frac{k_1}{k_1+y}\frac{\partial p}{\partial x}, \quad (21)$$

where the stress component τ_{12} for Eyring–Powell fluid is found as [19]

$$\tau_{12}=-(1+B)\left(u_{fy}+\frac{1+u_f}{k_1+y}\right)+A\left(u_{fy}+\frac{1+u_f}{k_1+y}\right)^3. \quad (22)$$

After proper substitution, Equation (22) becomes

$$-\frac{dp}{dx}+\frac{1}{k_1}\frac{\partial}{\partial y}\left((k_1+y)\left(-(1+B)\left(u_{fy}+\frac{1+u_f}{k_1+y}\right)+A\left(u_{fy}+\frac{1+u_f}{k_1+y}\right)^3\right)\right)$$
$$+\frac{N_1C}{1-C}\left(\frac{k_1+y}{k_1}\right)\left(-\frac{1}{N_1}\frac{k_1}{k_1+y}\frac{\partial p}{\partial x}\right)=0. \quad (23)$$

We apply no-slip at the walls and the corresponding boundary conditions are manufactured as

$$U_f\left(H'\right)=0 \text{ and } U_f\left(-H'\right)=0. \tag{24}$$

In dimensionless form, using wave frame, we have

$$u_f\left(h'\right)=-1 \text{ and } u_f\left(-h'\right)=-1, \tag{25}$$

where dimensionless form of the channel height in wave frame is disclosed as $\pm h'=\pm\left(1+\varphi\cos x\right)$.

METHODS AND RESULTS

This section has produced regular perturbation solutions for small values of A. So, we will use the following series expansion as a proposed solution for u_f

$$u_f=\sum_{i=0}^{\infty}A^i u_i. \tag{26}$$

The system generated by equating coefficients of exponent A^0

$$\frac{dp}{dx}+\frac{1}{k_1}\frac{\partial}{\partial y}\left(\left(k_1+y\right)\left(-\left(1+B\right)\left(u_{0y}+\frac{1+u_0}{k_1+y}\right)\right)\right)+\frac{N_1C}{1-C}\left(\frac{k_1+y}{k_1}\right)\left(u_p-u_0\right)=0, \tag{27}$$

with corresponding B.Cs

$$u_0\left(h'\right)=-1 \text{ and } u_0\left(-h'\right)=-1 \tag{28}$$

and the first order system (comparing coefficients of A^1) is achieved as

$$\frac{1}{k_1}\frac{\partial}{\partial y}\left(\left(k_1+y\right)\left(-\left(1+B\right)\left(u_{1y}+\frac{1+u_1}{k_1+y}\right)+\left(u_{0y}+\frac{1+u_0}{k_1+y}\right)^3\right)\right)\frac{N_1C}{1-C}\left(\frac{k_1+y}{k_1}\right)+\left(u_p-u_1\right)=0, \tag{29}$$

with

$$u_1\left(h'\right)=0 \text{ and } u_1\left(-h'\right)=0. \tag{30}$$

After handling the above obtained problems by executing built-in commands of the computer software, Mathematica, we finally get the following results

$$u_0=-1+\frac{k_1(-h'^2+y^2)\,dp/dx}{2(1+B)\,(C-1)\,(k_1+y)}. \tag{31}$$

$$\begin{aligned}u_1=&\frac{k_1^3\left(-h'\left(h'-y\right)\left(h'+y\right)\left(h'^2\left(k_1+y\right)-k_1^2\left(3k_1+y\right)\right)\right)\left(\frac{dp}{dx}\right)^3}{2(1+B)^4(-1+C)^3h'\left(h'-k_1\right)\left(h'+k_1\right)\left(k_1+y\right)^2}\\&-\frac{1}{2(1+B)^4(-1+C)^3h'\left(h'-k_1\right)\left(h'+k_1\right)\left(k_1+y\right)^2}(3k_1^3\left(\left(h'-k_1\right)\right.\\&k_1^2\left(h'+k_1\right)\left(k_1+y\right)\left(\left(h'-y\right)\log\left(-h'+k_1\right)+\left(h'+y\right)\log\left(h'+k_1\right)\right)\left.\right)\left(\frac{dp}{dx}\right)^3\\&-\frac{k_1^3\left(2h'\log\left(k_1+y\right)\right)\left(\frac{dp}{dx}\right)^3}{2(1+B)^4(-1+C)^3h'\left(h'-k_1\right)\left(h'+k_1\right)\left(k_1+y\right)^2}.\end{aligned} \tag{32}$$

Hence,

$$\begin{aligned}u_f=&-1+\frac{k_1\left(-h'^2+y^2\right)\frac{dp}{dx}}{2\left(1+B\right)\left(-1+C\right)\left(k_1+y\right)}\\&+\frac{Ak_1^3\left(-h'\left(h'-y\right)\left(h'+y\right)\left(h'^2\left(k_1+y\right)-k_1^2\left(3k_1+y\right)\right)\right)}{2(1+B)^4(-1+C)^3h'\left(h'-k_1\right)\left(h'+k_1\right)\left(k_1+y\right)^2}\\&\left(\frac{dp}{dx}\right)^3-\frac{1}{2(1+B)^4(-1+C)^3h'\left(h'-k_1\right)\left(h'+k_1\right)\left(k_1+y\right)^2}\\&(3Ak_1^3\left(\left(h'-k_1\right)k_1^2\left(h'+k_1\right)\left(k_1+y\right)\right.\\&\left(\left(h'-y\right)\log\left(-h'+k_1\right)+\left(h'+y\right)\log\left(h'+k_1\right)\right)\left.\right)\\&\left.\left(\frac{dp}{dx}\right)^3\right)-\frac{Ak_1^3\left(2h'\log\left(k_1+y\right)\right)\left(\frac{dp}{dx}\right)^3}{2(1+B)^4(-1+C)^3h'\left(h'-k_1\right)\left(h'+k_1\right)\left(k_1+y\right)^2}.\end{aligned} \tag{33}$$

From Equation (21), we get the solution of particulate velocity, u_p, which is displayed below

$$\begin{aligned}u_p=&-1+\frac{k_1\left(-h'^2+y^2\right)\frac{dp}{dx}}{2\left(1+B\right)\left(-1+C\right)\left(k_1+y\right)}\\&+\frac{Ak_1^3\left(-h'\left(h'-y\right)\left(h'+y\right)\left(h'^2\left(k_1+y\right)-k_1^2\left(3k_1+y\right)\right)\right)}{2(1+B)^4(-1+C)^3h'\left(h'-k_1\right)\left(h'+k_1\right)\left(k_1+y\right)^2}\\&\left(\frac{dp}{dx}\right)^3-\frac{1}{2(1+B)^4(-1+C)^3h'\left(h'-k_1\right)\left(h'+k_1\right)\left(k_1+y\right)^2}\\&(3Ak_1^3\left(\left(h'-k_1\right)k_1^2\left(h'+k_1\right)\right.\\&\left(k_1+y\right)\left(\left(h'-y\right)\log\left(-h'+k_1\right)+\left(h'+y\right)\log\left(h'+k_1\right)\right)\left.\right)\left.\left(\frac{dp}{dx}\right)^3\right)\\&-\frac{Ak_1^3\left(2h'\log\left(k_1+y\right)\right)\left(\frac{dp}{dx}\right)^3}{2(1+B)^4(-1+C)^3h'\left(h'-k_1\right)\left(h'+k_1\right)\left(k_1+y\right)^2}-\frac{k_1\frac{dp}{dx}}{\left(k_1+y\right)N_1}.\end{aligned} \tag{34}$$

Mathematical form of total mean volume flow rate due to fluid and particles is recognized as

$$Q=Q_f+Q_p, \tag{35}$$

where

$$Q_f=\left(1-C\right)\int u_f dy, \tag{36}$$

$$Q_f=\frac{4\left(1+B\right)\left(-1+C\right)h'-h'\left(h'-2k_1\right)k_1\frac{dp}{dx}+2k_1\left(-h'^2+k_1^2\right)\frac{dp}{dx}\left(\log\left(k_1\right)-\log\left(h'+k_1\right)\right)}{4\left(1+B\right)} \tag{37}$$

and

$$Q_p=C\int u_p dy, \tag{38}$$

$$Q_p = \frac{4(1+B)(-1+C)\,Ck_1\frac{dp}{dx}\left(\log(k_1)-\log(h'+k_1)\right)}{4(1+B)(-1+C)N_1} + \frac{C\left(-4(1+B)(-1+C)h'\right)}{4(1+B)(-1+C)N_1}$$
$$\frac{-4\left(h'(h'-2k_1)\,k_1\frac{dp}{dx} + 2(h'-k_1)\,k_1(h'+k_1)\frac{dp}{dx}\left(\log(k_1)-\log(h'+k_1)\right)\right)}{4(1+B)(-1+C)}. \quad (39)$$

Hence, we conclude

$$Q = \frac{4(1+B)(-1+C)h' - h'(h'-2k_1)\,k_1\frac{dp}{dx} + 2k_1\left(-h'^2+k_1^2\right)\frac{dp}{dx}\left(\log(k_1)-\log(h'+k_1)\right)}{4(1+B)(-1+C)N_1}$$
$$+\frac{4(1+B)(-1+C)\,Ck_1\frac{dp}{dx}\left(\log(k_1)-\log(h'+k_1)\right)}{4(1+B)(-1+C)N_1} + \frac{C\left(-4(1+B)(-1+C)h'\right)}{4(1+B)(-1+C)N_1} +$$
$$\frac{-4\left(h'(h'-2k_1)\,k_1\frac{dp}{dx} + 2(h'-k_1)\,k_1(h'+k_1)\frac{dp}{dx}\left(\log(k_1)-\log(h'+k_1)\right)\right)}{4(1+B)(-1+C)}. \quad (40)$$

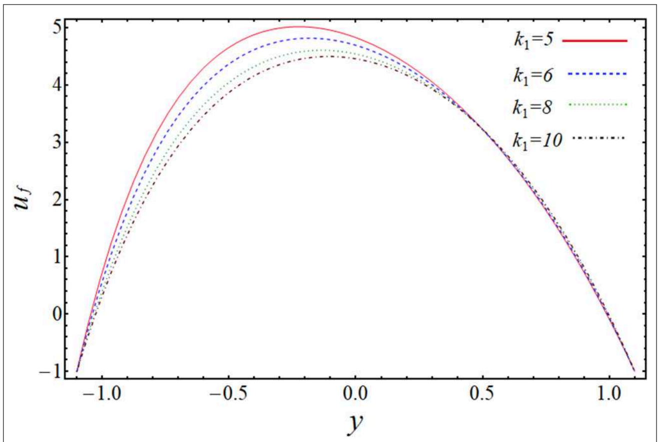

FIGURE 2 | Change of velocity u_f for k_1 when $Q = 1$, $x = 1$, $\phi = 0.1$, $N_1 = 0.9$, $B = 0.02$, $A = 0.01$, $C = 0.12$.

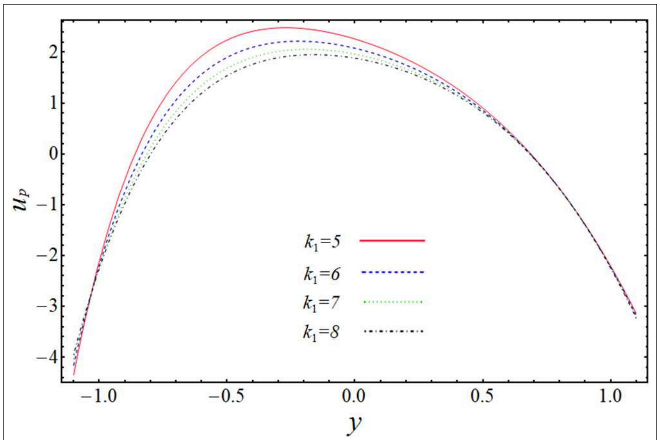

FIGURE 4 | Change of velocity u_p for k_1 when $Q = 1$, $x = 1$, $\phi = 0.1$, $N_1 = 2$, $B = 0.02$, $A = 0.05$, $C = 0.01$.

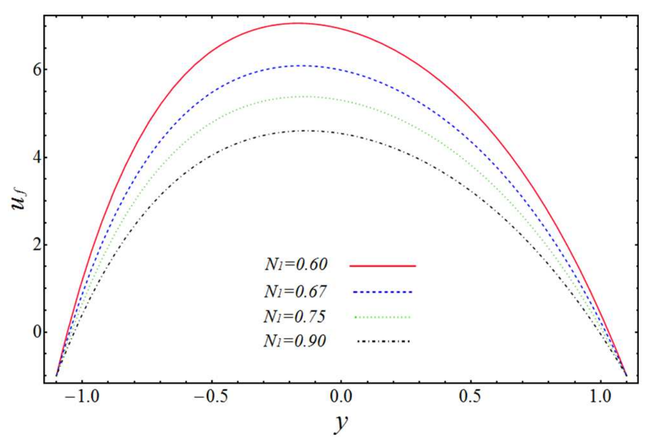

FIGURE 3 | Change of velocity u_f for N_1 when $Q = 1$, $x = 1$, $\phi = 0.1$, $k_1 = 8$, $B = 0.02$, $A = 0.01$, $C = 0.12$.

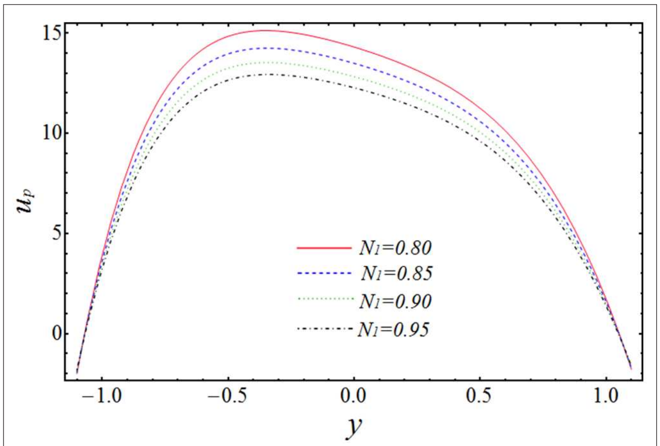

FIGURE 5 | Change of velocity u_p for N_1 when $Q = 1$, $x = 1$, $\phi = 0.1$, $k_1 = 9$, $B = 0.02$, $A = 0.1$, $C = 0.9$.

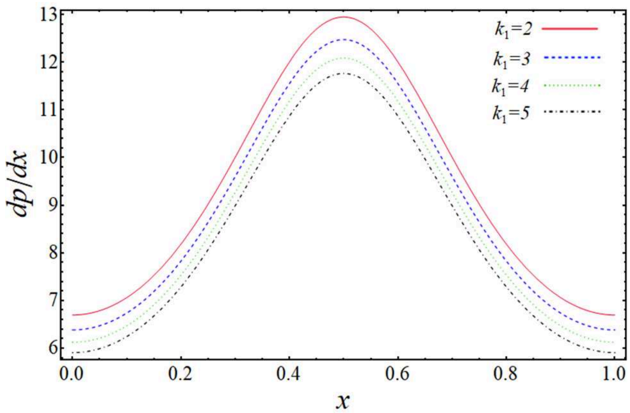

FIGURE 6 | Change of pressure gradient for k_1 when $Q = 1$, $\phi = 0.1$, $N_1 = 1$, $B = 0.01$, $C = 0.12$.

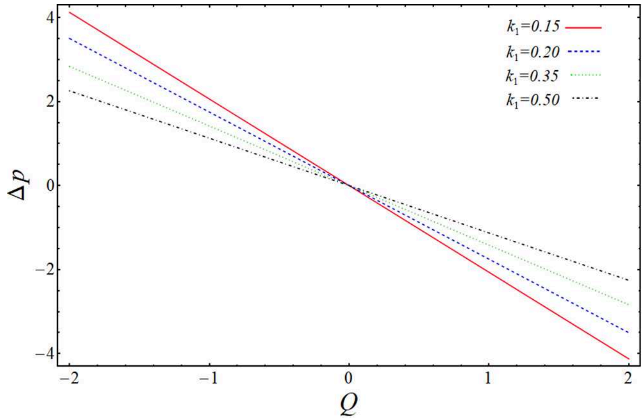

FIGURE 8 | Change of pressure rise for k_1 when $\phi = 0.1$, $N_1 = 0.05$, $B = 0.1$, $C = 0.1$.

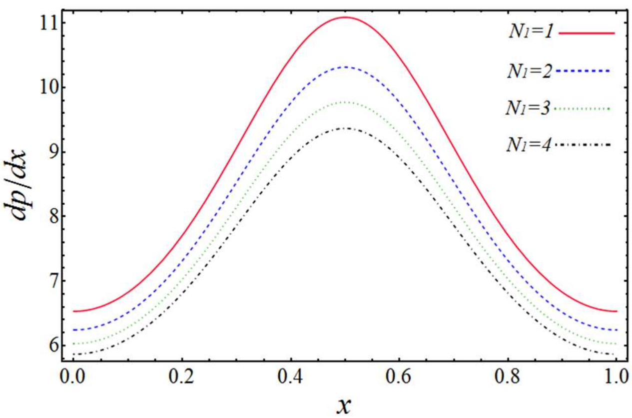

FIGURE 7 | Change of pressure gradient for N_1 when $Q = 1$, $\phi = 0.1$, $k_1 = 1$, $B = 0.01$, $C = 0.12$.

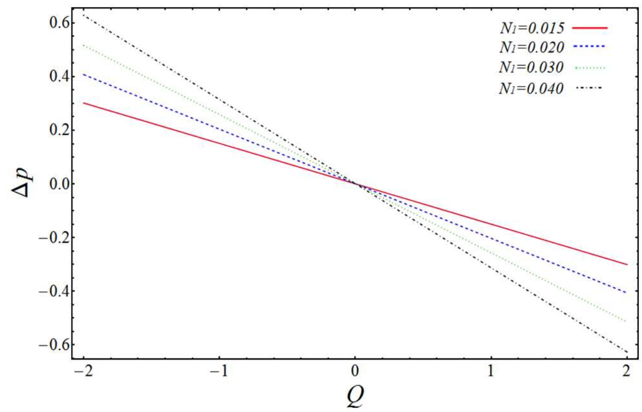

FIGURE 9 | Change of pressure rise for N_1 when $\phi = 0.1$, $k_1 = 1$, $B = 0.1$, $C = 0.15$.

From the above described Equations (35) through (40), we can find the value of pressure gradient dp/dx, which is achieved as shown below:

$$\frac{dp}{dx} = \frac{4\,(1+B)\,(-1+C)\,\left(h'+Q\right)\,N_1}{4\,(1+B)\,(-1+C)\,Ck_1\left(\log\left(k_1\right)-\log\left(h'+k_1\right)\right)+k_1} \frac{1}{\left(h'\left(h'-2k_1\right)+2\left(h'-k_1\right)\,\left(h'+k_1\right)\,\left(\log\left(k_1\right)-\log\left(h'+k_1\right)\right)\right)\,N_1}. \tag{41}$$

GRAPHICAL ANALYSIS

In the above section, we have solved the obtained governing equations for velocity, pressure gradient, and pressure rise by regular perturbation technique. The observing systems of differential equations have been handled on a mathematical software, Mathematica, via built-in DSolve commands. The more clarified results can be shown by plotting the graphs of above-obtained important quantities to see the effect of various physical parameters on them. The graphs will give a clearer picture of what is happening to the velocity, pressure gradient, and pressure rise when changes are made to the values of affecting parameters. To imagine these theoretical aspects, we have plotted the profiles of velocities u_f and u_p against the radial coordinate y in **Figures 2–5**, the pressure gradient $\frac{dp}{dx}$ vs. the coordinate x in **Figures 6**, **7**, and pressure rise along the flow rate Q in **Figures 8**, **9**. The trapping bolus mechanism has been provoked in **Figures 10**, **11**. It is observed from **Figures 2**, **3** that when we increase the numerical values of curvature parameter, k_1, and solid particle concentration, N_1, the fluid velocity, u_f, is decreasing its height in most part of the channel for both the parameters expect the lower part where the velocity is showing almost a constant behavior with k_1. They are usually included in systems that allow solids to settle to the bottom of the channel without any interruption. This is showing the physical fact that when channel is more curved and there are some solid particles placed in front of fluid flow,

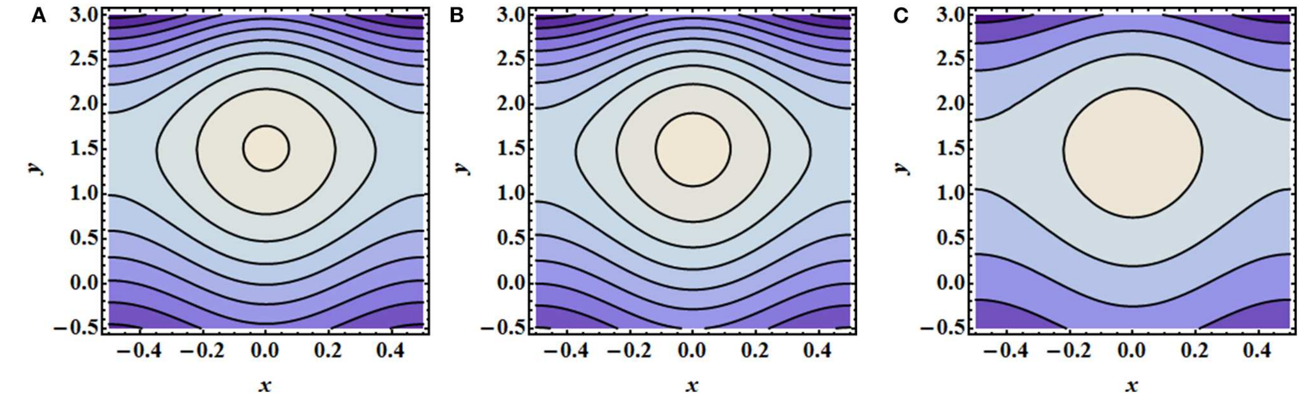

FIGURE 10 | Trapping variation for fluid phase when $N_1 = 3$, $\phi = 0.04$, $Q = 1$, $B = 0.1$, $A = 0.1$, $C = 0.03$. **(A)** $k = 3.1$, **(B)** $k = 3.2$, and **(C)** $k = 3.3$.

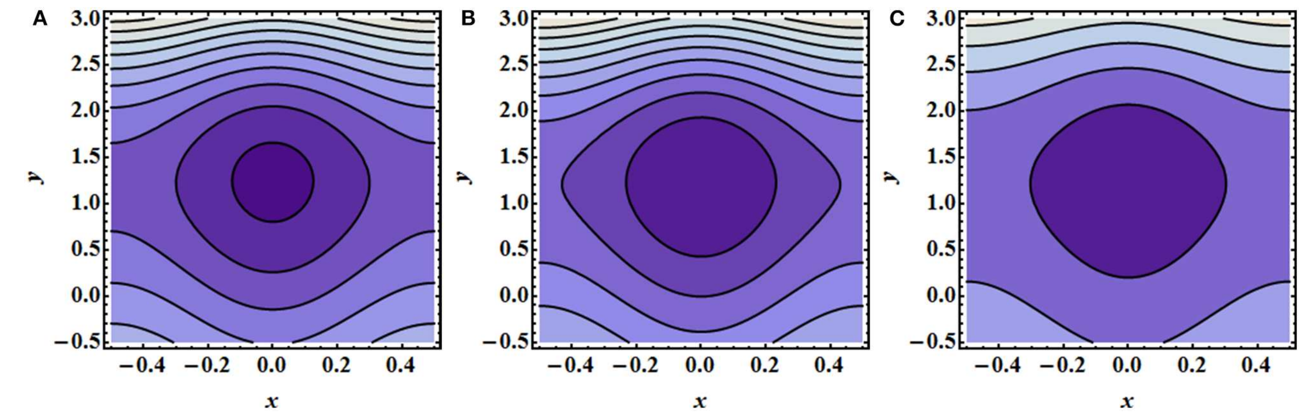

FIGURE 11 | Trapping variation for particulate phase when $N_1 = 3$, $\phi = 0.04$, $Q = 1$, $B = 0.1$, $A = 0.1$, $C = 0.03$. **(A)** $k = 3.1$, **(B)** $k = 3.2$, and **(C)** $k = 3.3$.

the velocity lowers, which is very much in agreement with the true experimental and physical facts. **Figures 4**, **5** are plotted for velocity of solid particles, u_p, with the variation of parameters k_1 and N_1. From these figures, it is captured that the velocity of solid particles, u_p, is showing almost a similar character as we have measured in the graphs of fluid velocity, u_f, but the height of the parabolic path of velocity is less than that of fluid velocity, which admits that the velocity of particulate phase is less than that of the fluid phase. This is because the increase in curvature will slow down the particle's movement and because the large amount of particles will affect the motion and suppresses the fluid. **Figures 6**, **7** have been drawn to estimate the behavior of pressure gradient $\frac{dp}{dx}$ for different values of curvature parameter, k_1 and N_1. It is very obvious from these figures that pressure gradient profile is decreasing with the increasing magnitudes of both the parameters, and maximum change in axial pressure is depicted at the central part of the channel as compared to the both side corners. **Figures 8**, **9** shows the variation of pressure rise quantity, Δp, against the flow rate parameter, Q, to find the influence of k_1 and N_1. These two plots can be divided into two portions, namely Region-I $\left(\Delta p > 0,\ \eta < 0\right)$ and Region-II $\left(\Delta p < 0,\ \eta > 0\right)$, and we can observe that point of intersection of all the lines is almost, the origin. In Region-I, it can be seen that pressure rise curves are showing inverse behavior with the variation of k_1, but in Region-II, the situation is completely opposite (see **Figure 8**). From **Figure 9**, it is quite clear that Δp rises proportionally to the increasing values of N_1 in Region-I, while in Region-II, the curves are showing inverse relation.

The most important phenomenon of peristaltic flows is circulating bolus trapping. The scenario is mentioned in **Figures 10**, **11**. **Figure 10** is developed for fluid phase under the variation of curvature parameter, k_1. It is measured here that boluses expand against the increasing values of curvature, which shows that curvature affects the bolus shape directly. **Figure 11** also depicts the same results for particulate phase streamlines, but, in this case, the number of boluses has been reduced to one.

CONCLUSIONS

In the above study, we have obtained the analytical solutions of peristaltic flow Eyring–Powell fluid model in a curved two-dimensional channel in the presence of solid particles. This study can contribute to the curing of diseases like urinary tract infections (UTIs). The problem is maintained simple under the implementation of lubrication approach. Analytical solutions have been achieved by applying the perturbation technique. The graphs have been plotted to show the behavior of some prominent quantities under the variation of pertinent parameters. From all of the above discussion, the following key points have been measured:

1. It is noted that both the curvature of the channel and the presence of solid particles slow the flow velocity, as compared with the flow in a straight channel and without solid particles.
2. It is observed that the curvature of the channel also affects the solid suspension velocity in the same manner as fluid velocity.
3. It is noticed that pressure gradient curves are getting lower as we increase the curvature of the channel and the amount of solid particles.
4. It is seen that the curvature of the channel decreases the peristaltic pressure on the negative side of the flow rate domain and increases on the other side.
5. It is examined from the above analysis that solid particles affect the pressure rise curves in quite the opposite manner when compared to the curvature parameter.

DATA AVAILABILITY STATEMENT

The datasets generated for this study are available on request to the corresponding author.

AUTHOR CONTRIBUTIONS

AR produced the methodology and formal analysis. MS wrote and edited the paper.

FUNDING

The authors wish to express their thanks for the financial support received from King Fahd University of Petroleum and Minerals, Saudi Arabia.

ACKNOWLEDGMENTS

The authors are grateful to the University of Education, Lahore Pakistan for providing suitable facilities to perform this research.

REFERENCES

1. Bhatti MM, Zeeshan A, Tripathi D, Ellahi R. Thermally developed peristaltic propulsion of magnetic solid particles in biorheological fluids. *Indian J Phys.* (2018) **92**:423–30. doi: 10.1007/s12648-017-1132-x
2. Hussain F, Ellahi R, Zeeshan A, Vafai K. Modelling study on heated couple stress fluid peristaltically conveying gold nanoparticles through coaxial tubes: a remedy for gland tumors and arthritis. *J Mol Liq.* (2018) **268**:149–55. doi: 10.1016/j.molliq.2018.07.034
3. Riaz A, Alolaiyan H, Razaq A. Convective heat transfer and magnetohydrodynamics across a peristaltic channel coated with nonlinear nanofluid. *Coatings*. (2019) **9**:816. doi: 10.3390/coatings9120816
4. Abbas MA, Bai YQ, Bhatti MM, Rashidi MM. Three dimensional peristaltic flow of hyperbolic tangent fluid in non-uniform channel having flexible walls. *Alexandria Eng J.* (2016) **55**:653–62. doi: 10.1016/j.aej.2015.10.012
5. Akbar NS, Butt AW. Entropy generation analysis in convective ferromagnetic nano blood flow through a composite stenosed arteries with permeable wall. *Commun Theor Phy.* (2017) **67**:554. doi: 10.1088/0253-6102/67/5/554
6. Enwald H, Peirano E, Almstedt AE. Eulerian two-phase flow theory applied to fluidization. *Int J Multiph.* (1996) **22**:21–66. doi: 10.1016/S0301-9322(96)90004-X
7. Mekheimer KS, Kot ME. Suspension model for blood flow through arterial catheterization. *Chem Eng Commun.* (2010) **197**:1195–214. doi: 10.1080/00986440903574883
8. Matousek P, Morris M. (Eds.). *Emerging Raman Applications and Techniques in Biomedical and Pharmaceutical Fields*. New York, NY: Springer Science & Business Media.
9. Beddow JK. *Particle Characterization in Technology: Volume II: Morphological Analysis*. Boca Raton, FL: CRC Press. (2018).
10. Yao J, Tao K, Huang Z. Flow of particulate-fluid suspension in a channel with porous walls. *Transport Porous Med.* (2013) **98**:147–72. doi: 10.1007/s11242-013-0137-y
11. Mekheimer KS, Abd Elmaboud Y. Peristaltic transport of a particle–fluid suspension through a uniform and non-uniform annulus. *Appl Bionics Biomech.* (2008) **5**:47–57. doi: 10.1080/11762320802376183
12. Kamel MH, Eldesoky IM, Maher BM, Abumandour RM. Slip effects on peristaltic transport of a particle-fluid suspension in a planar channel. *Appl Bionics Biomech*. (2015) **2015**:703574. doi: 10.1155/2015/703574
13. Jiménez-Lozano J, Sen, M. Corona, E. Analysis of peristaltic two-phase flow with application to ureteral biomechanics. *Acta Mech.* (2011) **219:**91–109. doi: 10.1007/s00707-010-0438-y
14. Nadeem S, Maraj EN. The mathematical analysis for peristaltic flow of hyperbolic tangent fluid in a curved channel. *Commun Theor Phy.* (2013) **59**:729. doi: 10.1088/0253-6102/59/6/14
15. Narla VK, Prasad KM, Ramanamurthy JV. Peristaltic transport of Jeffrey nanofluid in curved channels. *Procedia Eng.* (2015) **127**:869–76. doi: 10.1016/j.proeng.2015.11.424
16. Weiss RM, Tamarkin FJ, Wheeler MA. Pacemaker activity in the upper urinary tract. *J Smooth Muscle Res.* (2006) **42**:103–15. doi: 10.1540/jsmr.42.103
17. Lykoudis PS, Roos R. The fluid mechanics of the ureter from a lubrication theory point of view. *J Fluid Mech.* (1970) **43**:661–74.
18. Griffiths DJ. Flow of urine through the ureter: a collapsible, muscular tube undergoing peristalsis. *J Biomech Eng.* (1989) **111**:206–11.
19. Noreen S, Qasim M. Peristaltic flow of MHD Eyring-Powell fluid in a channel. *Eur Phy J.* (2013) **128**:91. doi: 10.1140/epjp/i2013-13091-3

Conflict of Interest: The authors declare that the research was conducted in the absence of any commercial or financial relationships that could be construed as a potential conflict of interest.

Copyright © 2020 Riaz and Sadiq. This is an open-access article distributed under the terms of the Creative Commons Attribution License (CC BY). The use, distribution or reproduction in other forums is permitted, provided the original author(s) and the copyright owner(s) are credited and that the original publication in this journal is cited, in accordance with accepted academic practice. No use, distribution or reproduction is permitted which does not comply with these terms.

frontiers in Physics

ORIGINAL RESEARCH
published: 12 May 2020
doi: 10.3389/fphy.2020.00075

Check for updates

A Novel Investigation and Hidden Effects of MHD and Thermal Radiations in Viscous Dissipative Nanofluid Flow Models

Naveed Ahmed [1], Adnan [2], Umar Khan [3], Syed Tauseef Mohyud-Din [4], Ilyas Khan [5]*, Rashid Murtaza [2], Iftikhar Hussain [2] and El-Sayed M. Sherif [6,7]

[1] Department of Mathematics, Faculty of Sciences, HITEC University, Taxila, Pakistan, [2] Department of Mathematics, Mohi-ud-Din Islamic University, Nerian Sharif, Pakistan, [3] Department of Mathematics and Statistics, Hazara University, Mansehra, Pakistan, [4] Department of Mathematics, University of Multan, Multan, Pakistan, [5] Faculty of Mathematics and Statistics, Ton Duc Thang University, Ho Chi Minh City, Vietnam, [6] Center of Excellence for Research in Engineering Materials (CEREM), King Saud University, Riyadh, Saudi Arabia, [7] Electrochemistry and Corrosion Laboratory, Department of Physical Chemistry, National Research Centre, Cairo, Egypt

OPEN ACCESS

Edited by:
Ahmed Zeeshan,
International Islamic University,
Islamabad, Pakistan

Reviewed by:
Taseer Muhammad,
King Khalid University, Saudi Arabia
Usman Masud,
University of Engineering and Technology, Pakistan

***Correspondence:**
Ilyas Khan
ilyaskhan@tdtu.edu.vn

Specialty section:
This article was submitted to Mathematical Physics, a section of the journal Frontiers in Physics

Received: 04 October 2019
Accepted: 03 March 2020
Published: 12 May 2020

Citation:
Ahmed N, Adnan, Khan U, Mohyud-Din ST, Khan I, Murtaza R, Hussain I and Sherif E-SM (2020) A Novel Investigation and Hidden Effects of MHD and Thermal Radiations in Viscous Dissipative Nanofluid Flow Models. Front. Phys. 8:75. doi: 10.3389/fphy.2020.00075

Hidden effects of MHD and thermal radiations for a viscous dissipative nanofluids ($Al_2O_3 - H_2O$ and $\gamma Al_2O_3 - H_2O$) are taken under consideration. The models are formulated by implementing the suitable similarity transformations. Then, two models are discussed mathematically by using RK scheme together with shooting method. The results for flow regimes, coefficient of skin friction, thermophysical characteristics, and heat transfer coefficient are pictured and discussed comprehensively by changing the pertinent flow parameters. It is observed that the nanofluids velocity increases abruptly for higher Hartree pressure gradient. For assisting flow situation, the velocity $F'(\eta)$ increases and abrupt decreasing behavior is examined for opposing flow case. The composition of $Al_2O_3 - H_2O$, and $\gamma Al_2O_3 - H_2O$ becomes more dense for high volume fraction therefore, drops in the velocity field is noted. The temperature of $Al_2O_3 - H_2O$, and $\gamma Al_2O_3 - H_2O$ rises rapidly by varying opposing flow parameter $\gamma < 0$ and high volume fraction ϕ. Also, the temperature $\beta(\eta)$ declines abruptly for parameter λ.

Keywords: wedge, host fluid, magnetic field, thermal radiation, viscous dissipation, γAl_2O_3 nanoparticles, RK scheme

INTRODUCTION

The analysis of the host fluids saturated by various sort of nanoparticles over a wedge geometry is of the essential and interesting topic in fluid dynamics and heat transfer phenomena. Currently, the hidden effects of significant flow parameters like magnetic number, thermal radiation, and viscous dissipation for regular and nanofluids models becomes important.

The flow and entropy generation analysis in magnetized nanofluid by considering the impacts of porosity described in Ellahi et al. [1]. The study of effective dynamic viscosity in non-Newtonian fluids in porous medium reported in Eberhard et al. [2]. The analysis of Roselands heat flux over non-linear stretchable surface with slip flow conditions was examined in Majeed et al. [3].

Keeping in mind the importance and popularity of the wedge type flow, Falkner and Skan [4, 5] focused on this particular direction of fluid mechanics and presented earlier study. They analyzed the boundary layer model mathematically and extend the case for stretching walls of the wedge. The work of Falkner and Skan provided a new direction in the fluid dynamics. Rajagopal et al. [6]

inspired by the work of Falkner and Skan [4, 5] and extended the boundary layer model for non-Newtonian fluid and found fascinating results. They analyzed the flow characteristics over a fixed wedge in the fluid. Later on, Lin et al. [7] inspired by the concept forced convection and extend the model by incorporating the various Prandtl values. Hartree [8] discussed the boundary layer model for approximate solutions and highlighted important results. Watanabe [9] and Watanabe and Pop [10] extended the Falkner Skan model by considering the phenomena of free and forced convection and explored the hidden effects on the flow characteristics, respectively. They presented the impacts of magnetic field, suction and injection in the flow field.

The porosity of the wedge walls affects the flow characteristics significantly. In the light of this fact, Koh and Hartnett [11] explored the results for skin friction and local coefficient of heat transfer and observed significant variations due to porosity parameter. Similarly, Kumari et al. [12] discussed the phenomena of mixed convection over a porous wedge. In 2003, Chamkha et al. [13] reported the radiative Falkner Skan flow and presented its characteristics over a semi-infinite domain. El-Dabe et al. [14] prolonged the Falkner Skan model for Casson fluid and treated the respective non-linear flow model numerically and incorporated the influences of magnetic field in the flow behavior and the heat transfer phenomena. The flow characteristics of Casson fluid over a symmetric wedge was presented by Mukhopadhyay et al. [15] in 2013. A novel analysis comprising the impacts of ohmic heating, applied magnetic field, and mixed convection on radiative flow over a stretchable wedge reported in Su et al. [16]. The alterations in the flow pattern of micropolar and Newtonian fluids over a wedge moving in the fluid and Viscoelastic fluid flow in the presence Lorentz force reported in Ishak et al. [17, 18] and Rashidi et al. [19], respectively.

Kandasamy et al. [20] prolonged the Falkner Skan flow by comprising the impacts of chemical reaction and found the results for suction or blowing on the radiative flow over a porous wedge. Hussanan et al. [21] highlighted the influences of Joule heating in the flow past over an oscillating plate. They also highlighted the alterations in the flow characteristics due to convective flow condition and resistive heat phenomena. A comprehensive analysis of Falkner Skan flow in the presence of velocity slip phenomena and applied Lorentz force described by Su et al. [22]. Recently, Ullah et al. [23] contributed the Falkner Skan model for non-Newtonian nature of the fluid.

A prominent fact that the regular fluids have less heat transfer characteristics. For many productions in various industries required considerable level of heat transfer and base liquids fail to provide such amount heat. However, researchers focused and thought to overcome this issue. Finally, a new class of the fluid developed and titled as Nanofluid. Basically, the nanofluid is a compound fluid composed by base liquid with the nanoparticles. These nanoparticles obtained from various metals and their oxides. In nanofluids, the volume fraction of the nanoparticles plays the role of back bone for the heat transfer enhancement. The development of the nanofluids reduces the problems and issues faced by the industrialist and engineers. Thus, the analysis of the nanofluids became an orbit for the researchers and engineers and explored new and fascinating characteristics of the nanofluids.

Recently, Rafique et al. [24] reported the numerical study of Casson nanofluid over an inclined surface and found the results for flow field. Impact of magnetic field by considering second slip flow condition on the flow Casson nanofluid explored by Majeed et al. [25]. In 2019, Bibi et al. [26] examined the flow model in the presence of convective boundary condition. The significant analysis for different sort of nanofluids under various flow conditions are examined in Saba et al. [27] and Srinivasacharya et al. [28].

The nanofluid models ($Al_2O_3 - H_2O$ and $\gamma Al_2O_3 - H_2O$) considering the phenomena of magnetic field, thermal radiation, and viscous dissipation is taken over a wedge geometry in the Cartesian coordinates. Two types of thermal conductivities are incorporated in the energy equation to enhance the heat transfer rate in $Al_2O_3 - H_2O$ and $\gamma Al_2O_3 - H_2O$ nanofluids. The model is described in section Model Formulation and treated mathematically in section Mathematical Analysis. The fascinating role of magnetic field and thermal radiation in the flow regimes explored and explain in section Physical Interpretation of Results. The quantities related to engineering interest (Skin friction and local Nusselt number) are presented and analyzed for varying flow parameters. In the end, major effects of under consideration model are incorporated.

MODEL FORMULATION

Statement and Geometry

Steady, laminar and viscous incompressible flow of H_2O saturated by Al_2O_3 and γAl_2O_3 nanoparticles is taken over a wedge. The effects of magnetic field and thermal radiation are taken into account. The velocity at the wedge surface is $\breve{u}_w = \breve{U}_w x^m$ and at the free stream is $\breve{U}_e = \breve{U}_\infty x^m$ and are functions of x. Here, $\breve{U}_w$ and $\breve{U}_\infty$ are constants at the surface and away from the surface. Furthermore, corresponding to wedge angle $\lambda = \Omega/\pi$, the Hartree pressure parameter is $\lambda = 2m/(m+1)$. Induced magnetic field produced due to the motion of $Al_2O_3 - H_2O$ and $\gamma Al_2O_3 - H_2O$ nanofluids is neglected through the analysis. The temperature at the wedge surface is $\hat{T}_w = \hat{T}_\infty + A/x^{2m}$ and is a function of x. The temperature at the surface and at the free stream is T_w and T_∞, respectively. The physical theme of the model comprising the role of Al_2O_3 and γAl_2O_3 nanoparticles is demonstrated in **Figure 1** over a semi-infinite region.

Governing Equations and Non-dimensionalization

In the light of above highlighted assumptions, the following is the model which govern the flow of nanofluids over a wedge [23, 28]:

$$\frac{\partial \hat{u}}{\partial x} + \frac{\partial \hat{v}}{\partial y} = 0 \tag{1}$$

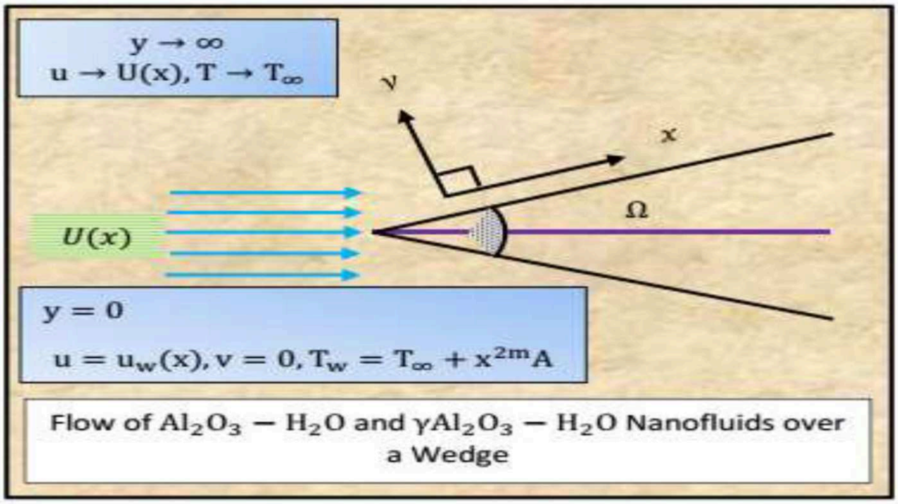

FIGURE 1 | Physical Theme of the Flow.

$$\hat{u}\frac{\partial \hat{u}}{\partial x}+\hat{v}\frac{\partial \hat{u}}{\partial y} = \breve{U}_e(x)\frac{d\breve{U}_e(x)}{dx}+\frac{\hat{\mu}_{nf}}{\hat{\rho}_{nf}}\left(\frac{\partial^2 \hat{u}}{\partial y^2}\right) - \frac{\hat{\sigma}_{nf}}{\hat{\rho}_{nf}}B_0^2(x)\left(u-\breve{U}_e(x)\right) \tag{2}$$

$$\hat{u}\frac{\partial \hat{T}}{\partial x}+\hat{v}\frac{\partial \hat{T}}{\partial y} = \frac{\hat{k}_{nf}}{\left(\hat{\rho}c_p\right)_{nf}}\left(\frac{\partial^2 \hat{T}}{\partial y^2}\right)+\frac{1}{\left(\hat{\rho}c_p\right)_{nf}}\left(\frac{\partial \hat{u}}{\partial y}\right)^2 - \frac{16\sigma^* T_\infty^3}{3k\left(\hat{\rho}C_p\right)_{nf}}\left(\frac{\partial^2 \hat{T}}{\partial y^2}\right) \tag{3}$$

The law of conservation of mass, momentum and energy shown in Equations (1–3), respectively. The velocities in x and y directions are $\hat{u}$ and $\hat{v}$, respectively. The velocity at the free stream, temperature, effective dynamic viscosity, density, electrical conductivity, thermal conductivity, and heat capacity are represented by $\breve{U}_e$, $\hat{T}$, $\hat{\mu}_{nf}$, $\hat{\rho}_{nf}$, $\hat{\sigma}_{nf}$, $\hat{k}_{nf}$, and $\left(\rho c_p\right)_{nf}$, respectively. Mean absorption coefficient and Stefan Boltzmann constants are denoted by k and σ^*, respectively.

The conditions on the flow at the boundaries are defined as Ullah et al. [23]:

$$\left.\begin{array}{c}\text{At the surface}\\ \hat{u}=\hat{u}_w(x),\\ \hat{v}=0,\\ \hat{T}=\hat{T}_\infty+\frac{A}{x^{-2m}}\\ \text{At the free stream}\\ \hat{u}\to\breve{U}_e(x),\\ \hat{T}\to\hat{T}_\infty\end{array}\right\} \tag{4}$$

The similarity variables defined in the following way for the non-dimensionalization of the governing flow model [23]:

$$\left.\begin{array}{r}\hat{u}=\frac{\partial\hat{\psi}}{\partial y}\\ \hat{v}=-\frac{\partial\hat{\psi}}{\partial x}\\ \hat{\psi}=\sqrt{\frac{2\nu_f x\hat{U}_e(x)}{(m+1)}}\,F(\eta)\\ \eta=\sqrt{\frac{(m+1)\hat{U}_e(x)}{2\nu_f x}}\,y\\ \beta(\eta)=\frac{\hat{T}-\hat{T}_\infty}{\hat{T}_w-\hat{T}_\infty}\end{array}\right\} \tag{5}$$

The following models are used to enhance the performance of the particular model [29]:

$$\hat{\rho}_{nf}=\left\{(1-\phi)+\frac{\phi\hat{\rho}_s}{\hat{\rho}_f}\right\}\hat{\rho}_f \tag{6}$$

$$\left.\begin{array}{l}\hat{\mu}_{nf}=\hat{\mu}_f(1-\phi)^{-2.5}\\ \hat{\mu}_{nf}=\hat{\mu}_f(123\phi^2+7.3\phi+1)\end{array}\right\}$$

For $Al_2O_3-H_2O$ and $\gamma Al_2O_3-H_2O$, (7)

$$\left(\hat{\rho}c_p\right)_{nf}=\left\{(1-\phi)+\frac{\phi\left(\hat{\rho}c_p\right)_s}{\left(\hat{\rho}c_p\right)_f}\right\}\left(\hat{\rho}c_p\right)_f$$

$$\left.\begin{array}{l}\hat{k}_{nf}=\hat{k}_f\left\{\frac{\hat{k}_s+2\hat{k}_f-2\phi\left(\hat{k}_f-\hat{k}_s\right)}{\hat{k}_s+2\hat{k}_f+\phi\left(\hat{k}_f-\hat{k}_s\right)}\right\}\\ \hat{k}_{nf}=\hat{k}_f(4.97\phi^2+2.72\phi+1)\end{array}\right\} \tag{8}$$

For $Al_2O_3-H_2O$ and $\gamma Al_2O_3-H_2O$ (9)

$$\hat{\sigma}_{nf}=\hat{\sigma}_f\left\{1+\frac{3\left(\frac{\hat{\sigma}_s}{\hat{\sigma}_f}-1\right)\phi}{\left(\frac{\hat{\sigma}_s}{\hat{\sigma}_f}+2\right)-\left(\frac{\hat{\sigma}_s}{\hat{\sigma}_f}-1\right)\phi}\right\}. \tag{10}$$

The particular values of thermophysical characteristics embedded in Equations (6–10) are given in **Table 1**.

TABLE 1 | Thermal and Physical Properties [29].

Host fluid and nanoparticles	$\hat{\rho}$(kg/m^3)	$\hat{c}_p$(kg^{-1}K^{-1})	$\hat{k}$(Wm^{-1}K^{-1})	$\hat{\sigma}$(S/m)	Pr
H_2O	997.1	4,179	0.613	0.005	6.96
Al_2O_3	3,970	765	40	3.5 × 10^7	-

After performing the suitable differentiation and incorporating the effective nanofluids models given in Equations (6–10) in the dimensional model, the following two models of nanofluids are obtained:

$Al_2O_3 - H_2O$ Model

$$F''' + \frac{1-\phi+\frac{\phi\hat{\rho}_s}{\hat{\rho}_f}}{(1-\phi)^{-2.5}}\left(FF'' + \lambda\left(1-F'2\right)\right) + \frac{(1-\phi)^{2.5}}{\left(1+\frac{3\left(\frac{\hat{\sigma}_s}{\hat{\sigma}_f}-1\right)\phi}{\left(\frac{\hat{\sigma}_s}{\hat{\sigma}_f}+2\right)-\left(\frac{\hat{\sigma}_s}{\hat{\sigma}_f}-1\right)\phi}\right)^{-1}} M^2(1-F') = 0, \tag{11}$$

$$\left[1+\frac{Rd}{\frac{\hat{k}_s+2\hat{k}_f-2\phi\left(\hat{k}_f-\hat{k}_s\right)}{\hat{k}_s+2\hat{k}_f+\phi\left(\hat{k}_f-\hat{k}_s\right)}}\right]\beta'' + \frac{1}{\frac{\hat{k}_s+2\hat{k}_f-2\phi\left(\hat{k}_f-\hat{k}_s\right)}{\hat{k}_s+2\hat{k}_f+\phi\left(\hat{k}_f-\hat{k}_s\right)}}\left[\frac{\left(PrF\beta' - 2\lambda PrF'\beta\right)}{\left\{(1-\phi)+\frac{\phi(\rho c_p)_s}{(\rho c_p)_f}\right\}^{-1}} + PrEcF''2\right] = 0. \tag{12}$$

$\gamma Al_2O_3 - H_2O$ Model

$$F''' + \frac{\left(1-\phi+\frac{\phi\hat{\rho}_s}{\hat{\rho}_f}\right)}{123\phi^2+7.3\phi+1}\left(FF''+\lambda\left(1-F'2\right)\right) + \frac{\left(1+\frac{3\left(\frac{\hat{\sigma}_s}{\hat{\sigma}_f}-1\right)\phi}{\left(\frac{\hat{\sigma}_s}{\hat{\sigma}_f}+2\right)-\left(\frac{\hat{\sigma}_s}{\hat{\sigma}_f}-1\right)\phi}\right)}{123\phi^2+7.3\phi+1} M^2(1-F') = 0, \tag{13}$$

$$\left[1+\frac{Rd}{4.97\phi^2+2.72\phi+1}\right]\beta'' + \frac{1}{4.97\phi^2+2.72\phi+1}\left[\frac{\left(PrF\beta' - 2\lambda PrF'\beta\right)}{\left\{(1-\phi)+\frac{\phi(\hat{\rho} c_p)_s}{(\hat{\rho} c_p)_f}\right\}^{-1}} + PrEcF''2\right] = 0. \tag{14}$$

The conditions at the boundaries at the surface and at the free stream are as under:

$$\left.\begin{array}{c} At\ the\ surface\ \eta = 0 \\ F(\eta) = 0 \\ F'(\eta) = \gamma \\ \beta(\eta) = 1 \\ At\ the\ free\ surface\ \eta \to \infty \\ F'^{(\eta)} \to 1 \\ \beta(\eta) \to 0 \end{array}\right\} \tag{15}$$

The parameters embedded in the models are Eckert number,

$$\frac{\hat{U}^2(x)}{(c_p)_f(T_w - T_\infty)}, \Pr = \frac{\hat{\mu}_f(\hat{c}_p)_f}{\hat{k}_f}, M^2 = \frac{\hat{\sigma}_f B_0^2 \nu_f}{\breve{U}_\infty(m+1)},$$

$$Rd = \frac{16\sigma^* T_\infty^3}{3\hat{k}_f k}, and \gamma = \frac{\breve{U}_w}{\breve{U}_\infty}.$$

Quantities of Engineering Interest

Skin friction and local heat transfer phenomena are of great importance from engineering point of view. Mathematical dimensional expressions for these quantities are as under:

$$\breve{C}_F = \frac{\hat{\mu}_{nf}}{\hat{\rho}_{nf}\hat{U}^2(x)}\left(\frac{\partial\hat{u}}{\partial y}\right)\downarrow_{y=0} \tag{16}$$

$$\breve{N}u_x = \left[\frac{-x\hat{k}_{nf}}{\hat{k}_f\left(\hat{T}_w - \hat{T}_\infty\right)}\right]\left(\frac{\partial\hat{T}}{\partial y}\right)\downarrow_{y=0}, \tag{17}$$

These expressions reduced in the following non-dimensional form by implementing the suitable differentiation and nanofluids models:

$$\breve{C}_F\sqrt{Re_x} = \frac{123\phi^2+7.3\phi+1}{\left((1-\phi)+\frac{\phi\hat{\rho}_s}{\hat{\rho}_f}\right)}F''(0), \tag{18}$$

$$\breve{N}u_x(Re_x)^{-\frac{1}{2}} = \left.\begin{array}{ll} -\frac{\hat{k}_s+2\hat{k}_f-2\phi\left(\hat{k}_f-\hat{k}_s\right)}{\hat{k}_s+2\hat{k}_f+\phi\left(\hat{k}_f-\hat{k}_s\right)}\beta'(0) & \text{For } Al_2O_3 - H_2O \\ -\left(4.97\phi^2+2.72\phi+1\right)\beta'(0) & \text{For } \gamma Al_2O_3 - H_2O \end{array}\right\} \tag{19}$$

here, $Re_x = \frac{x\breve{U}(x)}{\breve{\nu}_f}$ is denotes the local Reynold number.

MATHEMATICAL ANALYSIS

Shooting technique [30, 31] is adopted for the mathematical analysis of the particular nanofluids flow models. The reason behind this choice is the non-linearity (for instance see [32–40]) of the models over semi-infinite region. To initiate the technique, the following substitution are made:

$$\overbrace{y}_1 = F, \overbrace{y}_2 = F', \overbrace{y}_3 = F'', \overbrace{y}_4 = \beta, \overbrace{y}_5 = \beta'. \tag{20}$$

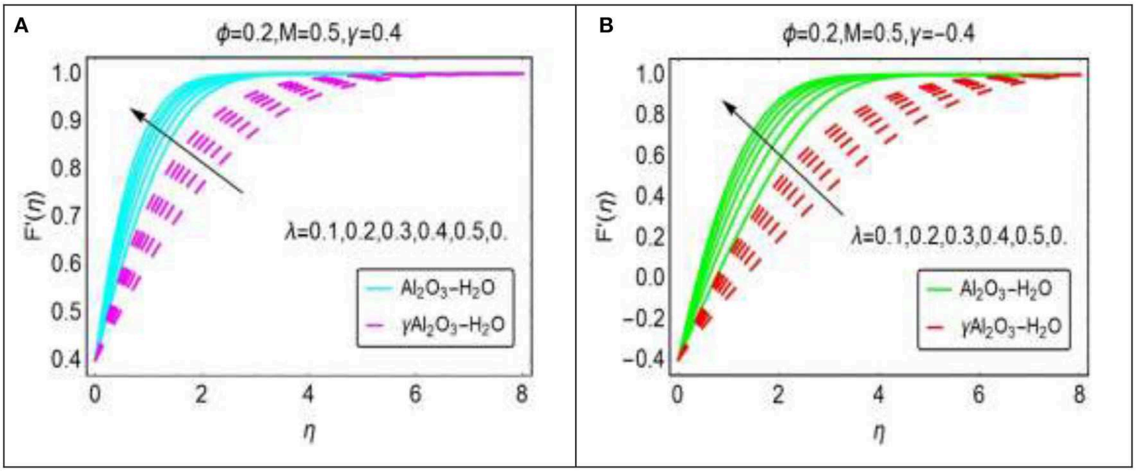

FIGURE 2 | The effects of λ on dimensionless velocity $F'(\eta)$ for **(A)** $\gamma = 0.4$, **(B)** $\gamma = -0.4$.

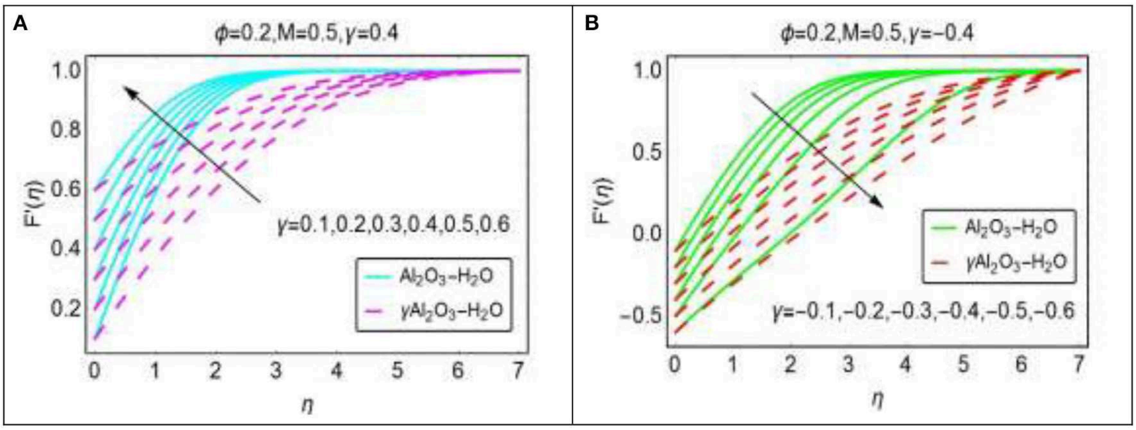

FIGURE 3 | The effects of **(A)** γ positive, **(B)** γ negative on dimensionless ϕ on dimensionless velocity $F'(\eta)$.

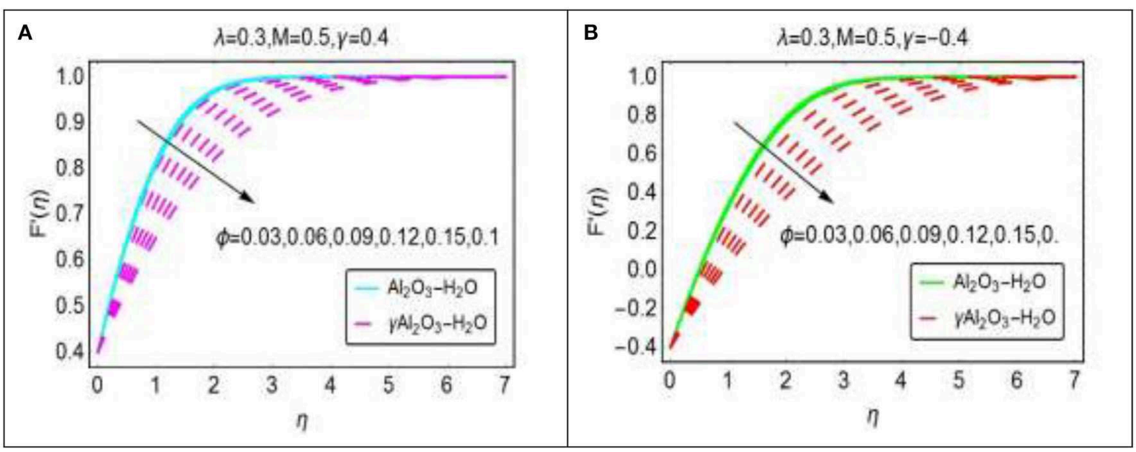

FIGURE 4 | The effects of ϕ on dimensionless velocity $F'(\eta)$ for **(A)** $\gamma = 0.4$, **(B)** $\gamma = -0.4$.

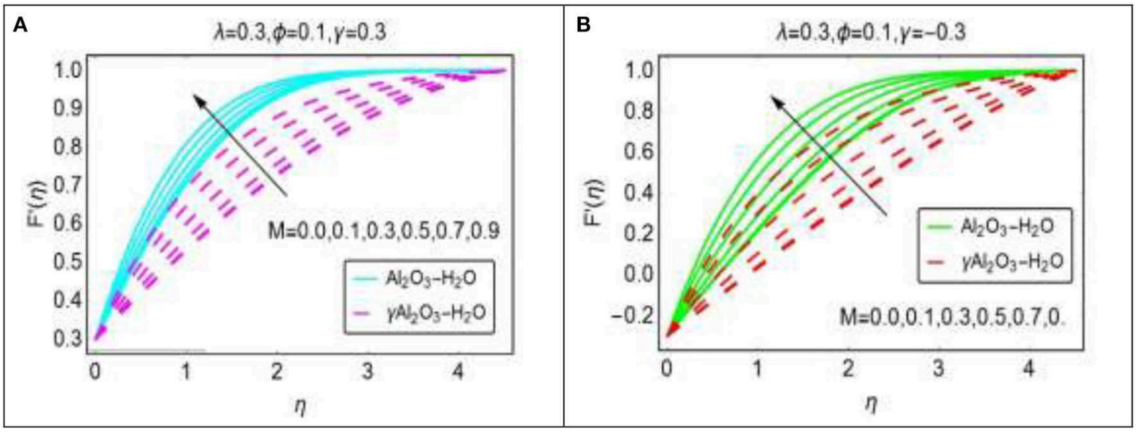

FIGURE 5 | The effects of M on dimensionless velocity $F'(\eta)$ for **(A)** $\gamma = 0.3$, **(B)** $\gamma = -0.3$.

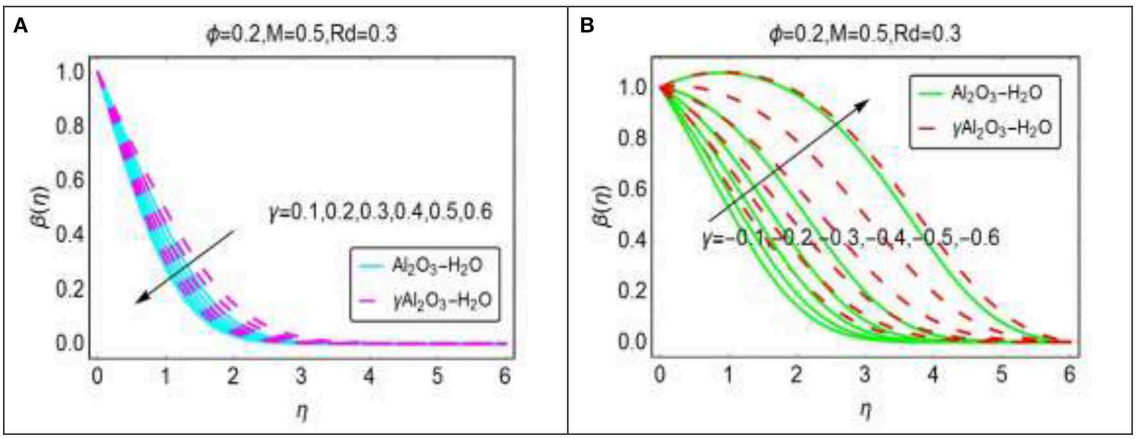

FIGURE 6 | The effects of **(A)** γ positive, **(B)** γ negative on dimensionless temperature $\beta(\eta)$.

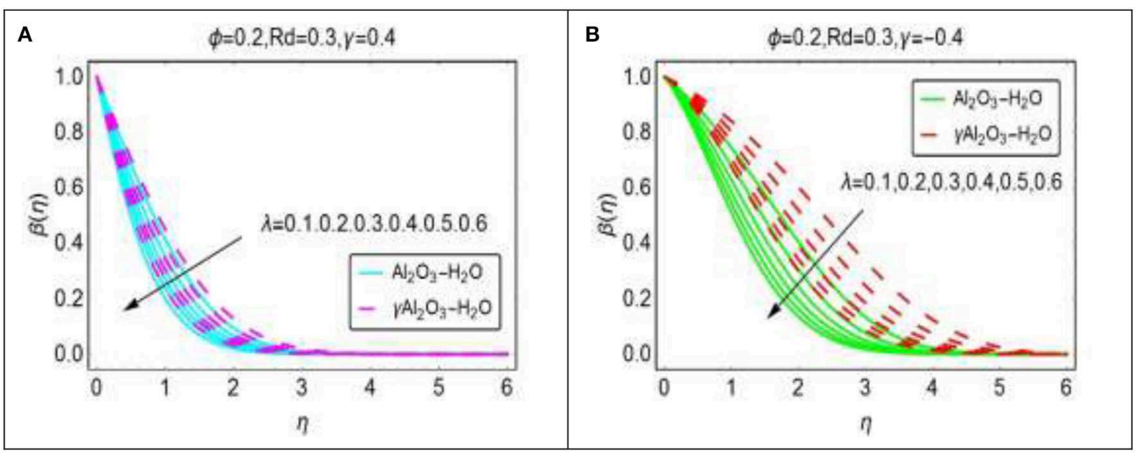

FIGURE 7 | The effects of λ on dimensionless temperature $\beta(\eta)$ for **(A)** $\gamma = 0.4$, **(B)** $\gamma = -0.4$.

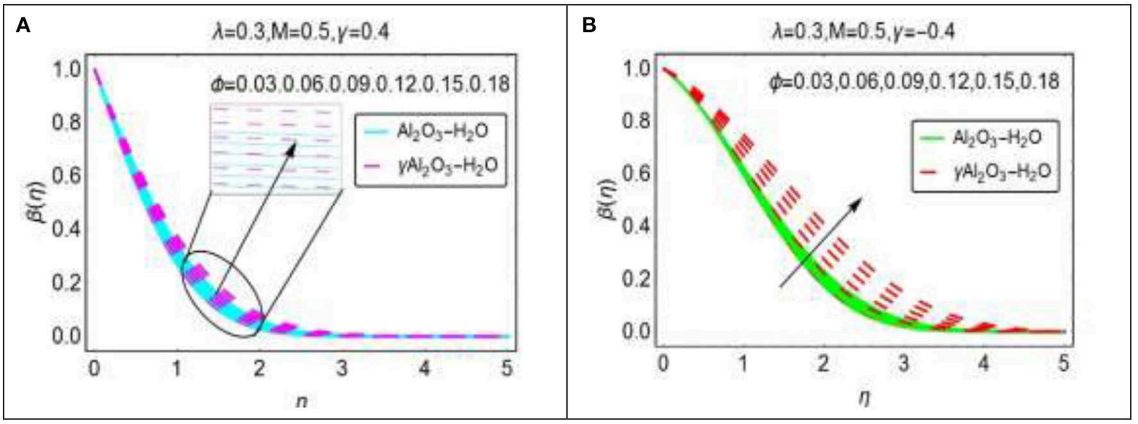

FIGURE 8 | The effects of ϕ on dimensionless temperature $\beta(\eta)$ for **(A)** $\gamma = 0.4$, **(B)** $\gamma = -0.4$.

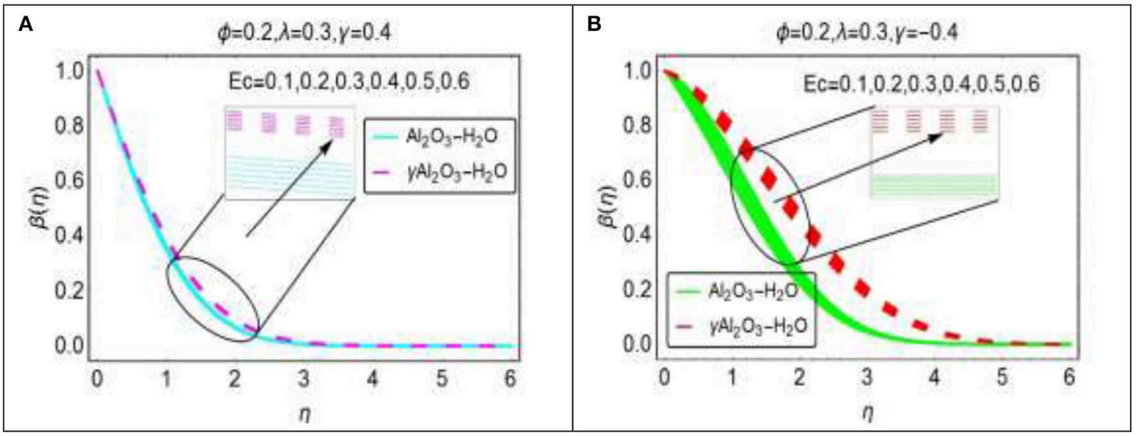

FIGURE 9 | The effects of Ec on dimensionless temperature $\beta(\eta)$ for **(A)** $\gamma = 0.4$, **(B)** $\gamma = -0.4$.

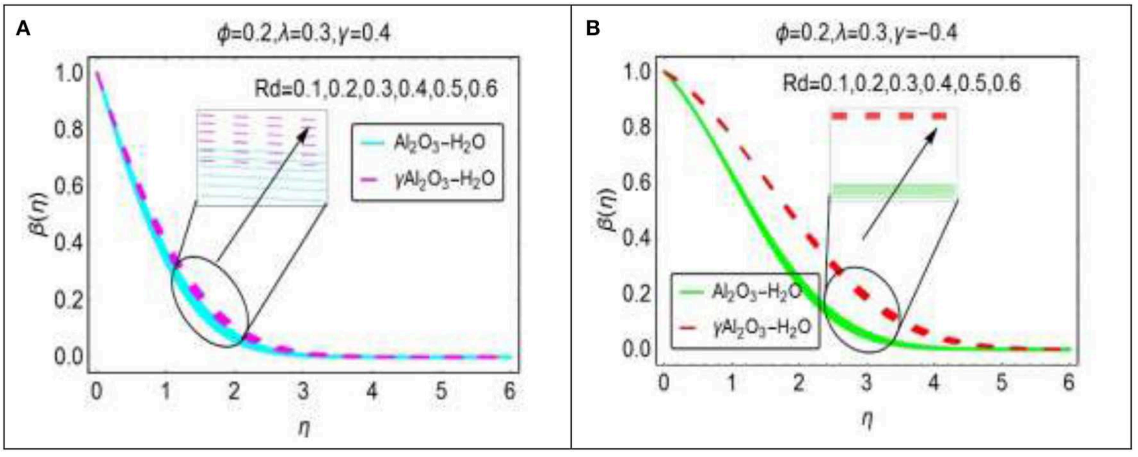

FIGURE 10 | The effects of Rd on dimensionless temperature $\beta(\eta)$ for **(A)** $\gamma = 0.4$, **(B)** $\gamma = -0.4$.

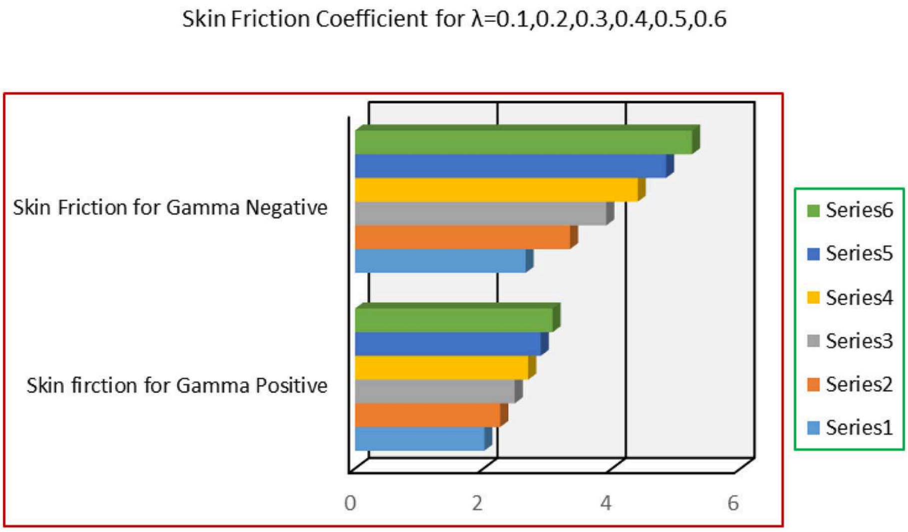

FIGURE 11 | The effects of λ on skin friction coefficient.

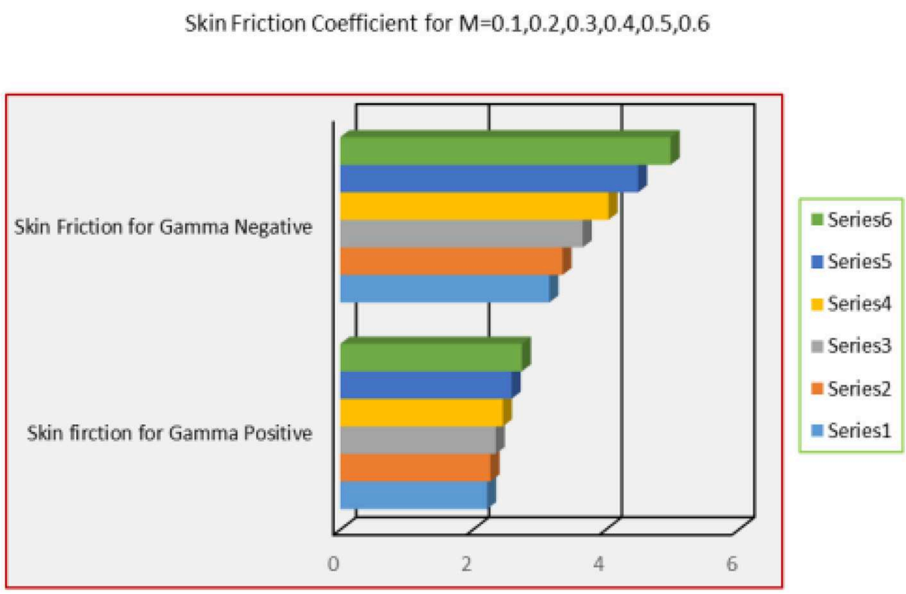

FIGURE 12 | The effects of *M* on skin friction coefficient.

$Al_2O_3 - H_2O$ Model

The flow model $Al_2O_3 - H_2O$ can be reduced into the following form:

$$F''' = -\frac{1-\phi+\frac{\phi\hat{\rho}_s}{\hat{\rho}_f}}{(1-\phi)^{-2.5}}\left(FF''+\lambda\left(1-F'2\right)\right) - \frac{(1-\phi)^{2.5}}{\left(1+\frac{3\left(\frac{\hat{\sigma}_s}{\hat{\sigma}_f}-1\right)\phi}{\left(\frac{\hat{\sigma}_s}{\hat{\sigma}_f}+2\right)-\left(\frac{\hat{\sigma}_s}{\hat{\sigma}_f}-1\right)\phi}\right)^{-1}} M^2(1-F'), \quad (21)$$

$$\beta'' = \frac{-1}{1+\frac{Rd}{\frac{\hat{k}_s+2\hat{k}_f-2\phi\left(\hat{k}_f-\hat{k}_s\right)}{\hat{k}_s+2\hat{k}_f+\phi\left(\hat{k}_f-\hat{k}_s\right)}}}$$

$$\left[\frac{1}{\frac{\hat{k}_s+2\hat{k}_f-2\phi\left(\hat{k}_f-\hat{k}_s\right)}{\hat{k}_s+2\hat{k}_f+\phi\left(\hat{k}_f-\hat{k}_s\right)}}\left(\frac{\left(PrF\beta'-2\lambda PrF'\beta\right)}{\left\{(1-\phi)+\frac{\phi\left(\hat{\rho}c_p\right)_s}{(hat\rho c_p)_f}\right\}^{-1}}+PrEcF''2\right)\right].(22)$$

By implementing the transformations made in Equation (19), the system of Equations. (21, 22)

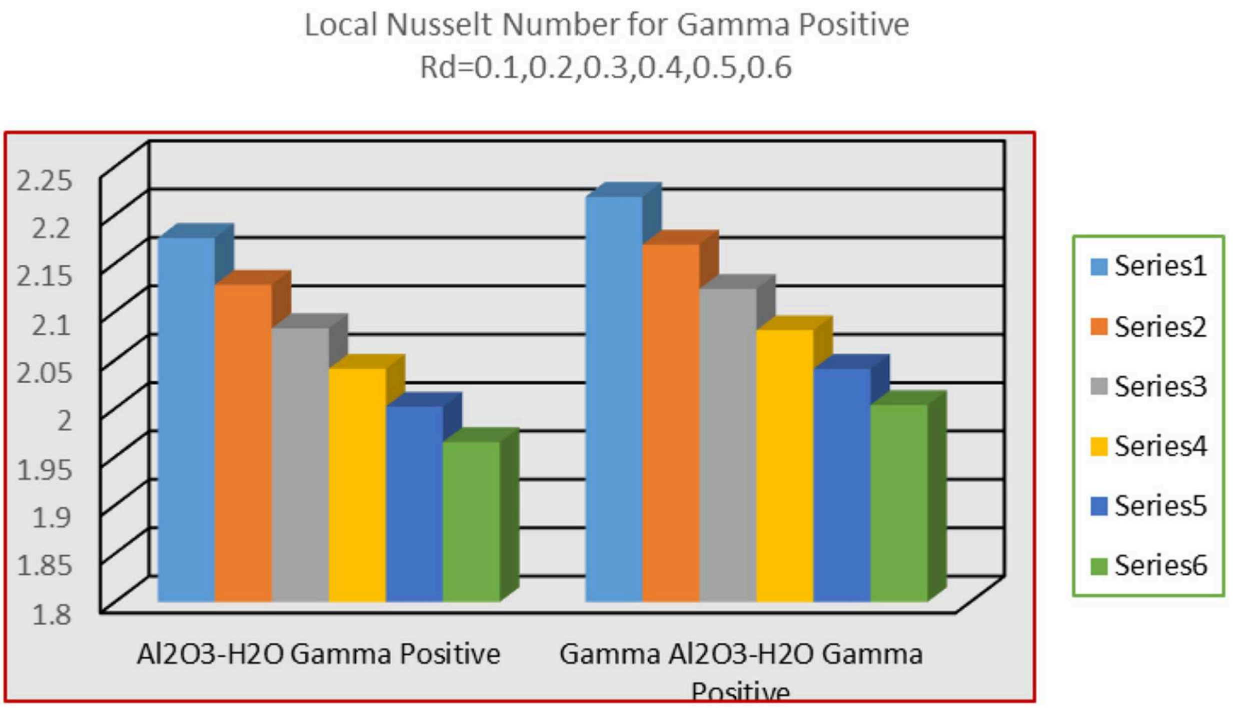

FIGURE 13 | The effects of *Rd* on local Nusselt number ($\gamma > 0$).

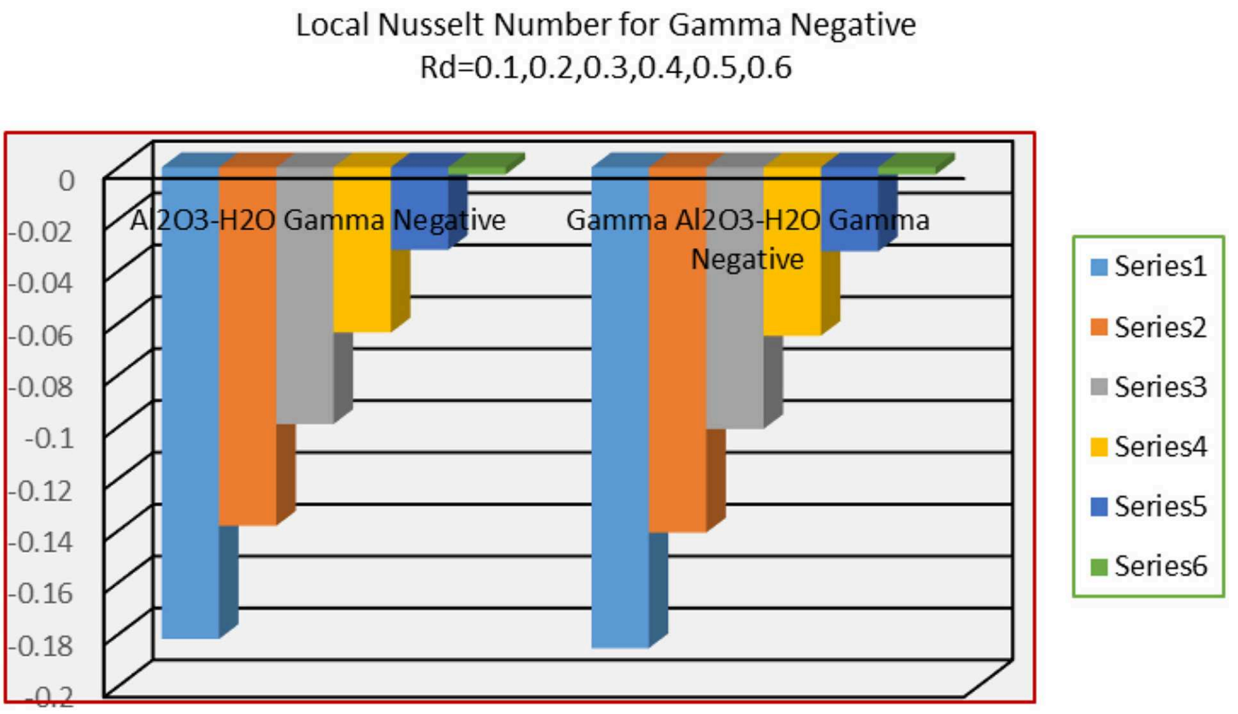

FIGURE 14 | The effects of *Rd* on local Nusselt number ($\gamma < 0$).

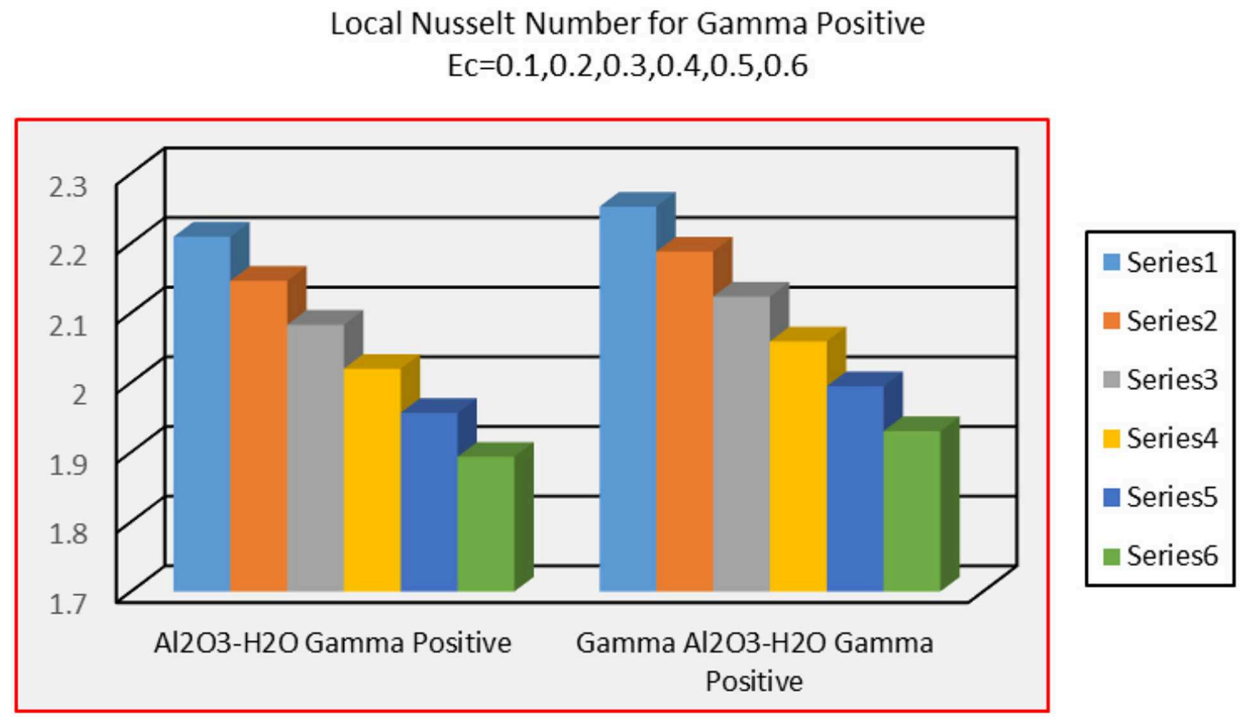

FIGURE 15 | The effects of *Ec* on local Nusselt number ($\gamma > 0$).

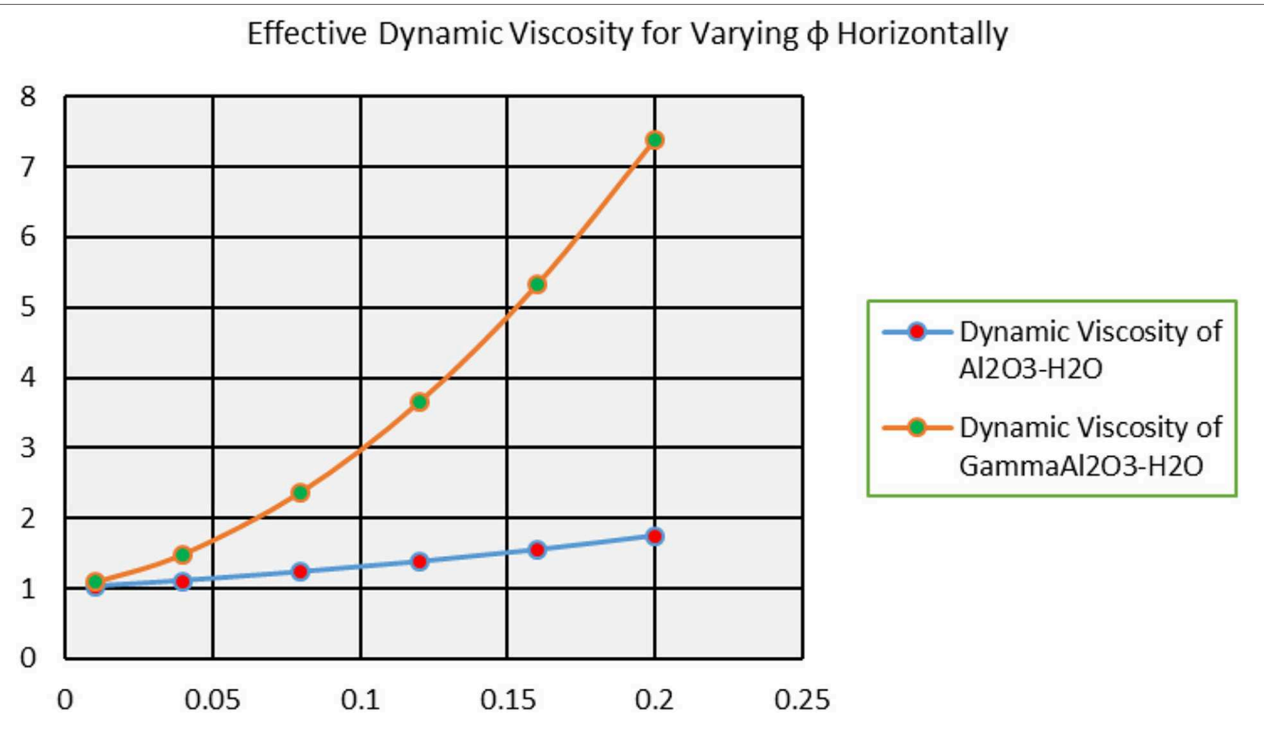

FIGURE 16 | The effects of ϕ on Effective Dynamic viscosity.

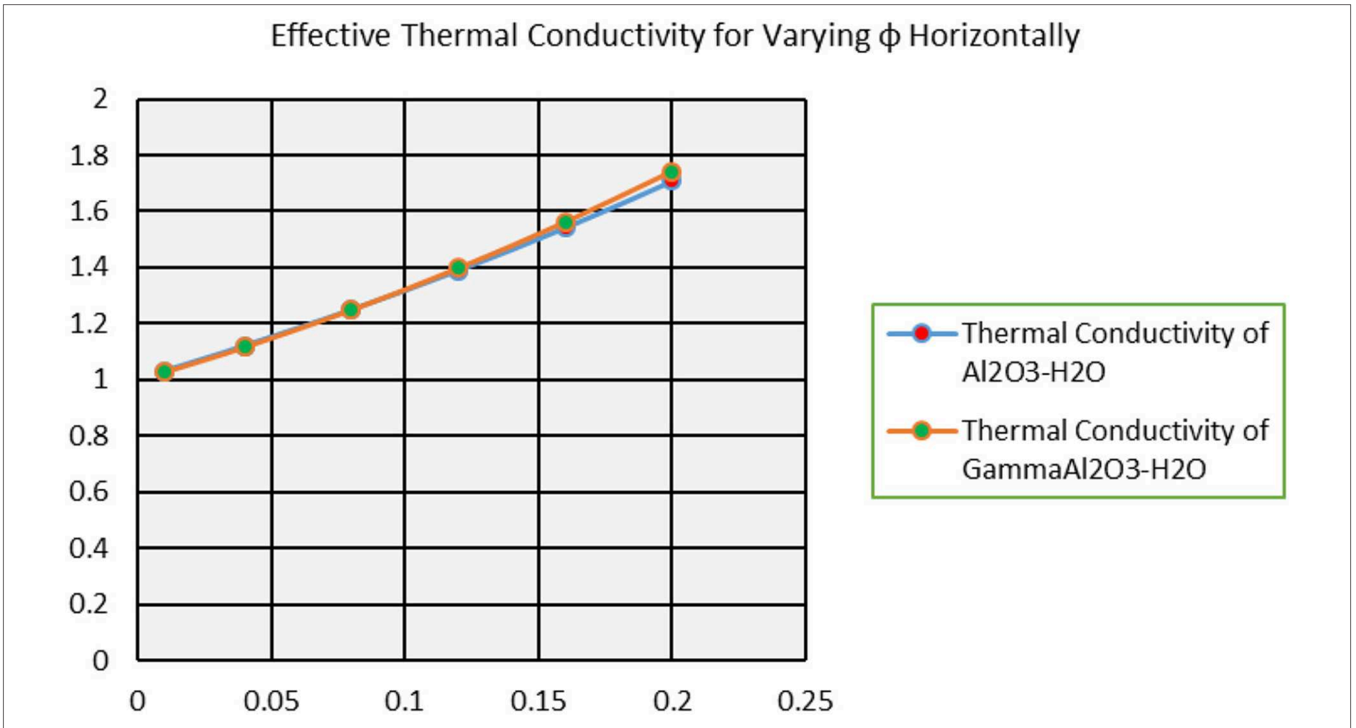

FIGURE 17 | The effects of ϕ on Thermal conductivity.

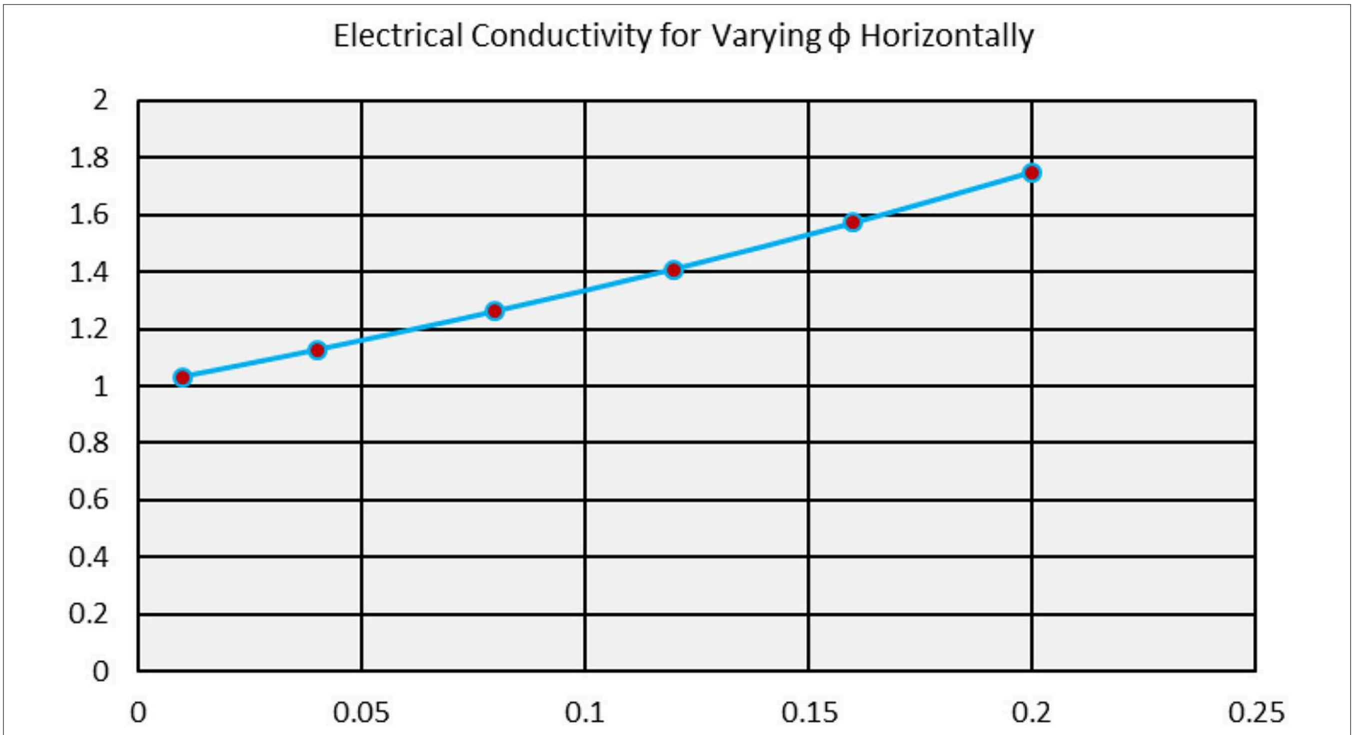

FIGURE 18 | The effects of ϕ on Electrical conductivity.

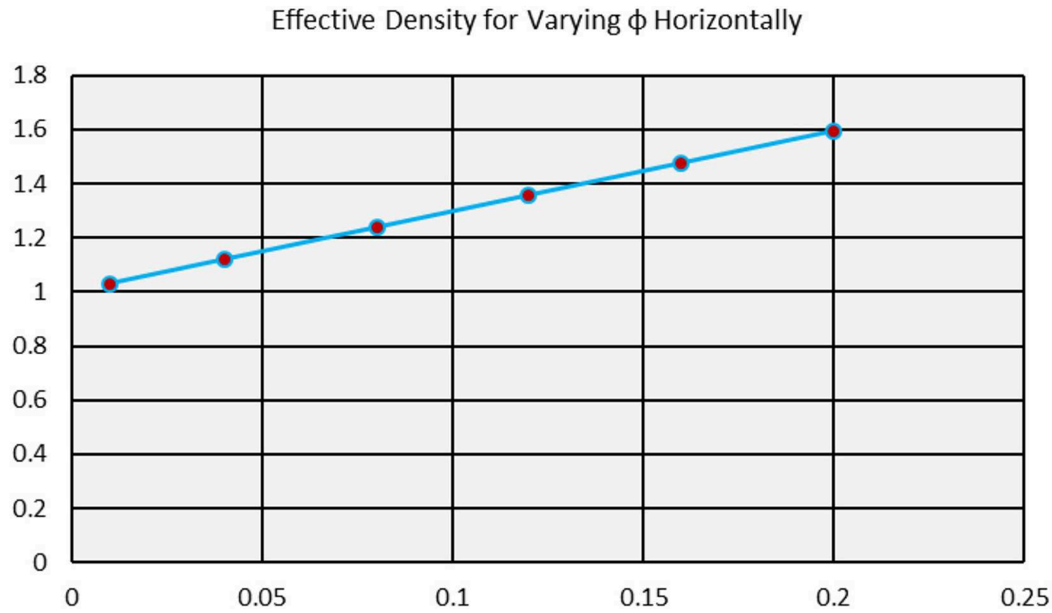

FIGURE 19 | The effects of ϕ on Effective density.

TABLE 2 | Reliability of the study by comparing with existing scientific literature for $F''(0)$.

$\phi = 0, M = 0, Rd = 0, Ec = 0, \gamma = 0, Pr = 0.73, \lambda = \frac{2m}{m+1}$

m	Current results	Existing scientific literature
0.0000	0.46959	0.46960
0.0141	0.5046143	−−
0.0435	0.5689777	0.56898
0.0909	0.6549788	0.65498
0.1429	0.7319985	0.73200
0.2000	0.8021256	0.80213
0.3333	0.9276536	0.92765
0.5000	1.0389035	1.03890

transformed into the following initial value problem:

$$\begin{bmatrix} \overbrace{y}'_1 \\ \overbrace{y}'_2 \\ \overbrace{y}'_3 \\ \overbrace{y}'_4 \\ \overbrace{y}'_5 \end{bmatrix} = \begin{bmatrix} \overbrace{y}_2 \\ \overbrace{y}_3 \\ -\dfrac{\left(\overbrace{y}_1 \overbrace{y}_3 + \lambda\left(1 - \left(\overbrace{y}_2\right)^2\right)\right)}{\left[1-\phi+\frac{\phi\rho_s}{\rho_f}\right]^{-1}(1-\phi)^{-2.5}} - \dfrac{\left[1+\dfrac{3\left(\frac{\hat{\sigma}_s}{\hat{\sigma}_f}-1\right)\phi}{\left(\frac{\hat{\sigma}_s}{\hat{\sigma}_f}+2\right)-\left(\frac{\hat{\sigma}_s}{\hat{\sigma}_f}-1\right)\phi}\right]}{(1-\phi)^{-2.5}} M^2\left(1-\overbrace{y}_2\right) \\ \overbrace{y}_5 \\ -\breve{A}_1\left[\breve{A}_2\left[\dfrac{\left(\Pr \overbrace{y}_1 \overbrace{y}_5 - 2\lambda Pr \overbrace{y}_2 \overbrace{y}_4\right)}{\left\{(1-\phi)+\frac{\phi(\hat{\rho}c_p)_s}{(\hat{\rho}c_p)_f}\right\}^{-1}} + Ec\left(\overbrace{y}_3\right)^2\right]\right] \end{bmatrix}, \quad (23)$$

Where, $\breve{A}_1 = \dfrac{-1}{1+\dfrac{Rd}{\frac{\hat{k}_s+2\hat{k}_f-2\phi\left(\hat{k}_f-\hat{k}_s\right)}{\hat{k}_s+2\hat{k}_f+\phi\left(\hat{k}_f-\hat{k}_s\right)}}}$

$$\breve{A}_2 = \dfrac{1}{\dfrac{\hat{k}_s+2\hat{k}_f-2\phi\left(\hat{k}_f-\hat{k}_s\right)}{\hat{k}_s+2\hat{k}_f+\phi\left(\hat{k}_f-\hat{k}_s\right)}}$$

and the set of conditions at $\eta = 0$ are as:

$$\begin{bmatrix} \overbrace{y}_1 \\ \overbrace{y}_2 \\ \overbrace{y}_3 \\ \overbrace{y}_4 \\ \overbrace{y}_5 \end{bmatrix} = \begin{bmatrix} 0 \\ \gamma \\ \breve{n}_1 \\ 1 \\ \breve{n}_2 \end{bmatrix} \quad (24)$$

Here, $\breve{n}_1$ and $\breve{n}_2$ are unknown and the accuracy is set as 10^{-6}.

$\gamma Al_2O_3 - H_2O$ Model

The model $\gamma Al_2O_3 - H_2O$ reduced into the following pattern:

$$F''' = -\frac{\left(1-\phi+\frac{\phi\hat{\rho}_s}{\hat{\rho}_f}\right)}{123\phi^2+7.3\phi+1}\left(FF''+\lambda\left(1-F'2\right)\right)-\frac{\left(1+\frac{3\left(\frac{\hat{\sigma}_s}{\hat{\sigma}_f}-1\right)\phi}{\left(\frac{\hat{\sigma}_s}{\hat{\sigma}_f}+2\right)-\left(\frac{\hat{\sigma}_s}{\hat{\sigma}_f}-1\right)\phi}\right)}{123\phi^2+7.3\phi+1}M^2(1-F'), \tag{25}$$

$$\beta'' = \frac{-1}{1+\frac{Rd}{4.97\phi^2+2.72\phi+1}}\left[\frac{1}{4.97\phi^2+2.72\phi+1}\left(\frac{\left(PrF\beta'-2\lambda PrF'\beta\right)}{\left\{(1-\phi)+\frac{\phi(\hat{\rho}c_p)_s}{(\hat{\rho}c_p)_f}\right\}^{-1}}+PrEcF''2\right)\right]. \tag{26}$$

By using transformations, the following system is obtained:

$$\begin{bmatrix}\overset{\frown}{y}'_1\\ \overset{\frown}{y}'_2\\ \overset{\frown}{y}'_3\\ \overset{\frown}{y}'_4\\ \overset{\frown}{y}'_5\end{bmatrix} = \begin{bmatrix}\overset{\frown}{y}_2\\ \overset{\frown}{y}_3\\ -\frac{(1-\phi+\frac{\phi\rho_s}{\rho_f})\left(\overset{\frown}{y}_1\overset{\frown}{y}_3+\lambda\left(1-\left(\overset{\frown}{y}_2\right)^2\right)\right)}{123\phi^2+7.3\phi+1}-\frac{\left[1+\frac{3\left(\frac{\hat{\sigma}_s}{\hat{\sigma}_f}-1\right)\phi}{\left(\frac{\hat{\sigma}_s}{\hat{\sigma}_f}+2\right)-\left(\frac{\hat{\sigma}_s}{\hat{\sigma}_f}-1\right)\phi}\right]}{123\phi^2+7.3\phi+1}M^2(1-\overset{\frown}{y}_2)\\ \overset{\frown}{y}_5\\ -\breve{A}_{11}\left[\breve{A}_{12}\left[\frac{\left(\Pr\overset{\frown}{y}_1\overset{\frown}{y}_5-2\lambda Pr\overset{\frown}{y}_2\overset{\frown}{y}_4\right)}{\left\{(1-\phi)+\frac{\phi(\hat{\rho}c_p)_s}{(\hat{\rho}c_p)_f}\right\}^{-1}}+Ec\left(\overset{\frown}{y}_3\right)^2\right]\right]\end{bmatrix}, \tag{27}$$

where, $\breve{A}_{11} = \frac{1}{1+\frac{Rd}{4.97\phi^2+2.72\phi+1}}$

$$\breve{A}_{12} = \frac{1}{4.97\phi^2+2.72\phi+1} \tag{28}$$

The initial conditions are same as in Equation (24).

PHYSICAL INTERPRETATION OF RESULTS

The flow parameters like magnetic parameter, thermal radiation, and viscous dissipation play fascinating role in the flow regimes. The influences of afore mentioned flow parameters on the flow field explored graphically and discussed comprehensively in this section. Moreover, the results for the quantities of engineering interest are taken into account and discussed. The results plotted for two cases of the wedge according to the wedge movement. It is important to mention the cases of flow depending on the value of parameter γ. The wedge and fluid move in opposite direction for negative γ and move in alike direction for positive γ.

Velocity Field

Figure 2 interprets the behavior of the nanofluids velocity ($Al_2O_3 - H_2O$ and $\gamma Al_2O_3 - H_2O$) for $\gamma > 0$ and $\gamma < 0$, respectively. From **Figure 2A**, it is obvious that the velocity increases when the wedge and the nanofluids move in alike way ($\gamma > 0$). The velocity of $Al_2O_3 - H_2O$ nanofluids increases abruptly in comparison with $\gamma Al_2O_3 - H_2O$ nanofluid. The reason behind this is the difference between the effective models of dynamic viscosity for Al_2O_3 and γAl_2O_3. The nanofluid $\gamma Al_2O_3 - H_2O$ becomes more dense due to the dynamic viscosity containing high volume fraction of the nanoparticles and the momentum of the fluid drops. Due to drop in momentum, the velocity starts decreasing. Near the wedge surface, momentum of the nanofluids declines due to the friction between the wedge surface and the nanofluids. The effects of the pressure parameter are very prominent in the region $2 \leq \eta \leq 4$. These effects are elaborated in **Figure 2A**. **Figure 2B** highlights the alterations in the nanofluids velocity for opposing case. The negative values of γ shows that the nanofluids and wedge move in opposite direction. For opposing case, the asymptotic region increases for $\gamma Al_2O_3 - H_2O$ nanofluid.

Figure 3 elaborates the alterations in the velocity $F'(\eta)$ for varying wedge parameter γ. Due to altering wedge parameter, very interesting variations in the velocity field are observed. For assisting case $\gamma > 0$, the velocity upturns abruptly. When the nanofluids and wedge move in alike direction then the movement of wedge in the direction of nanofluids provide extra momentum to the nanofluids. Therefore, the velocity positively increases. In the vicinity of the wedge, the velocity increase abruptly for both sort of nanofluids. For $Al_2O_3 - H_2O$ nanofluid, the velocity shows asymptotic behavior quickly in comparison with $\gamma Al_2O_3 - H_2O$. These results are plotted in **Figure 3A**. **Figure 3B** shows that the velocity of the nanofluids drops very quickly over the domain of interest. The opposite movement of the wedge and the nanofluids cause the declines in the velocity profile. Due to the opposite movement, friction between the wedge surface and the nanofluids slow down the momentum of the nanofluids. Consequently, the velocity drops.

The volume fraction of the nanoparticles is very key ingredients which alters the nanofluid characteristics affectively. These effects are portrayed in **Figures 4A,B** for assisting and opposing case, respectively. The behavior of the velocity for assisting case elaborated in **Figure 4A**. For increasing ϕ, the nanofluids velocity drops rapidly. For $\gamma Al_2O_3 - H_2O$, the prompt decrement in the velocity occurs due to high volume fraction incorporated in the dynamic viscosity. The velocity vanishes asymptotically beyond $\eta \geq 4$. **Figure 4B** portrays the velocity profile for opposing flow case. For opposing flow, the velocity declines very abruptly in comparison with assisting flow. The opposite movement and high volume fraction of the nanoparticles opposes the opposes the motion. Therefore, the velocity rapidly drops and asymptotically vanishes beyond $\eta \geq 6$.

The influences in the velocity behavior by altering the magnetic parameter are depicted in **Figure 5**. From **Figure 5A**, it is observed that the velocity of the nanofluids $F'(\eta)$ positively increases for assisting flow. Due to less dense composition of $Al_2O_3 - H_2O$ nanofluid, the velocity profile increases promptly as compared to $\gamma Al_2O_3 - H_2O$ nanofluid. Similarly, for opposing case, the velocity field portrayed in **Figure 5B**. **Figure 5B** shows the prompt increasing behavior of the velocity for both sort of nanofluids. In the region $1 \leq \eta \leq 3.5$, these effects of M on the velocity $F'(\eta)$ are very rapid.

Temperature Field

The alterations in temperature fields of $Al_2O_3 - H_2O$ and $\gamma Al_2O_3 - H_2O$ nanofluids by varying the wedge parameter γ presented in **Figure 6**. **Figure 6A** shows that for assisting flow, the temperature $\beta(\eta)$ drops. The drops in the temperature is due to the alike motion of the nanofluids and wedge. For $Al_2O_3 - H_2O$ nanofluids, decreasing pattern of the temperature is quite rapid and prominent in the region $1 \leq \eta \leq 3$. The temperature $\beta(\eta)$ vanishes asymptotically at the free stream. An interesting impacts of γ are observed for opposing flow case. These alterations are depicted in **Figure 6B**. When the wedge moves in the opposite direction of the nanofluids, then due to the force of friction between the wedge surface and the molecules of the nanofluids heat produces which favors the temperature $\beta(\eta)$. The temperature increases abruptly near the wedge. The reason is that the more friction between the molecules of the nanofluids and the wedge surface. For $\gamma Al_2O_3 - H_2O$ nanofluids, the temperature arises rapidly than $Al_2O_3 - H_2O$ nanofluid.

Figure 7 highlights the influences of pressure parameter λ on the temperature of $Al_2O_3 - H_2O$ and $\gamma Al_2O_3 - H_2O$ nanofluids. The pressure parameter λ opposes the nanofluids temperature. For assisting flow, the temperature is decreasing function of λ and the decrement in $Al_2O_3 - H_2O$ nanofluid is rapid. Due to high dynamic viscosity of $\gamma Al_2O_3 - H_2O$ nanofluid, the temperature drops slowly than $Al_2O_3 - H_2O$ nanofluid. It is observed that the temperature vanishes at the thermal boundary layer which starts beyond $\eta > 3$. These influences are shown in **Figure 7A**. It is investigated that the opposite motion of the wedge and nanofluids reduces the temperature very rapidly. Due to opposite motion, the velocity of the momentum drops. Consequently, the velocity declines which cause the rapid decrement in the temperature. The role of λ on $\beta(\eta)$ is very cleared. Moreover, for opposing case, thermal boundary layer increases and the temperature decreases beyond $\eta > 5$. This behavior of the temperature is portrays in **Figure 7B**.

Figures 8–10 depicted the behavior of temperature $\beta(\eta)$ for volumetric fraction ϕ, Eckert number Ec and thermal radiation parameter Rd, respectively. The temperature patterns for both assisting and opposing case are plotted.

In the study of nanofluids, the importance of volume fraction cannot be neglected. The volume fraction alters the temperature effectively and plays vibrant role. The variations in the temperature for assisting and opposing flow due to altering ϕ are plotted in **Figures 8A,B**, respectively. From these, it is inspected that the volume fraction favors the temperature positively. For $\gamma > 0$, the increasing pattern of the temperature is quite slow than $\gamma < 0$. The main reason of this phenomena is the force of friction produces between the wedge surface and molecules of the nanofluids. For assisting case, thermal boundary layer decrease and in the case of opposing flow it starts increases and the temperature is vanishes beyond $\eta > 3$ and $\eta > 4$, respectively. For $\gamma Al_2O_3 - H_2O_3$ the temperature $\beta(\eta)$ increases very promptly due to the dynamic viscosities of $Al_2O_3 - H_2O_3$ and $\gamma Al_2O_3 - H_2O_3$ nanofluids.

The effects of Eckert number which appears due to the viscous dissipation are plotted in **Figures 9A,B** for alike and opposing flow cases, respectively. The temperature varies almost inconsequentially for $\gamma > 0$ for both sort of nanofluids. On the other hand, it is inspected that for more dissipative nanofluids, the temperature $\beta(\eta)$ arises rapidly. Thermal boundary layer decreases for $Al_2O_3 - H_2O$ nanofluid and increases for $\gamma Al_2O_3 - H_2O$ nanofluid. From **Figures 10A,B**, it is obvious that thermal radiation parameter increases the nanofluids temperature for both the cases. For opposing case, the temperature $\beta(\eta)$ arises quite rapid than alike flow case.

Skin Friction and Local Nusselt Number

This subsection highlights the behavior of skin friction and local Nusselt number for different values of the flow parameters for assisting and opposing flow. It is observed that the skin friction is directly proportional to the pressure parameter λ. For opposing flow, skin friction increases slowly in comparison with opposing flow case. These are depicted in **Figure 11**. **Figure 12** shows that the magnetic parameter M favors the skin friction for both assisting and opposing flows. For assisting case, it varies very slowly for assisting case while abrupt alterations are observed for opposing flow.

The alterations in local heat transfer coefficient (Nusselt number) for different parameters incorporating in **Figures 13–15** for alike and opposing flow cases. It is observed that heat transfer decreases at the wedge surface for alike flow case for radiative flow. The heat transfers for $\gamma Al_2O_3 - H_2O$ nanofluids is rapidly drops than $Al_2O_3 - H_2O$ nanofluids. On the other hand, decrement in the heat transfer is observed for opposing flow. The heat transfer drops abruptly for $\gamma Al_2O_3 - H_2O$ nanofluid. These variations are portrayed in **Figure 14**. **Figure 15** depicts the influences of dissipation phenomena on the heat transfer. The heat transfer drops abruptly for more dissipative $\gamma Al_2O_3 - H_2O$ nanofluid and in $Al_2O_3 - H_2O$ nanofluid, these effects are quite slow.

Thermophysical Properties

Thermophysical characteristics contribute vibrantly in the flow regimes of nanofluids. These properties effectively alter the nanofluid characteristics. The effects of volume fraction ϕ on the effective dynamic viscosity, thermal conductivity, electrical conductivity and density are plotted in **Figures 16–19**. From **Figure 16**, it is clear that the dynamic viscosity of $\gamma Al_2O_3 - H_2O$ increases exponentially. The for $Al_2O_3 - H_2O$ nanofluids, these are very slow. Due to this improvement in the dynamic viscosity, the characteristics of the nanofluids affects. Similarly, thermal conductivity of $\gamma Al_2O_3 - H_2O$ nanofluid is quite rapid. However, no major difference between thermal conductivities of $Al_2O_3 - H_2O$ and $\gamma Al_2O_3 - H_2O$ nanofluids is observed. Furthermore, electrical conductivity and density of the nanofluid arises by increasing the volume fraction in feasible domain. These are elaborated in **Figures 18**, **19**, respectively.

Comparison With Scientific Literature

Table 2 elaborating the reliability of the presented results with existing scientific literature for $F''(0)$. It is detected that by setting different physical parameters equal to zero, our results meets the existing scientific results in the literature that show the reliability of the presented physical results and applied numerical technique.

CONCLUSIONS

A novel radiative and dissipative study on $Al_2O_3 - H_2O$ and $\gamma Al_2O_3 - H_2O$ nanofluids heat transfer model in the presence of applied magnetic field is considered over wedge. Two nanofluids models are obtained corresponding to two different sort of nanoparticles together with host liquid water. Then the models are treated mathematically by implementing RK scheme coupled with shooting method. Finally, the results for the flow regimes, heat transfer and thermophysical characteristics are plotted and found the following major outcomes:

i. The velocity of $\gamma Al_2O_3 - H_2O$ nanofluid increases for higher Hartree pressure gradient parameter.
ii. The assisting flow of nanofluid over wedge favors the velocity field $F'(\eta)$ and the velocity drops for opposing flow.
iii. The velocity profile $F'(\eta)$ drops for higher volume fraction factor ϕ of the nanoparticles.
iv. The temperature of the nanofluids arises for opposing flow.
v. The temperature $\beta(\eta)$ arises for more dissipative and radiative nanofluids.
vi. The temperature field $\beta(\eta)$ declines for higher Hartree pressure gradient parameter.
vii. The parameter λ and strength of magnetic field favors the skin friction coefficient.
viii. For more radiative and dissipative nanofluids, the heat transfer coefficient drops.
ix. Dynamic viscosity increases abruptly for $\gamma Al_2O_3 - H_2O$ than $Al_2O_3 - H_2O$ nanofluid which alters the flow characteristics effectively.
x. Thermal and electrical conductivities increases by increasing the nanoparticles volume fraction ϕ.
xi. From comparison of presented results with existing scientific literature, it is observed that the presented physical results are valid.

DATA AVAILABILITY STATEMENT

The datasets generated for this study are available on request to the corresponding author.

AUTHOR CONTRIBUTIONS

The formulation of the problem was done by UK, A and SM-D. Non-dimensionalization of the nanofluid models by using invertible transformations done by RM, IH, E-SS, and NA. Mathematical analysis and the graphical results plotted and discussed by SM-D and IK. The revision and editing was done by UK, E-SS, SM-D, and IK. All the authors have equal contributions.

ACKNOWLEDGMENTS

Researchers Supporting Project number (RSP-2019/33), King Saud University, Riyadh, Saudi Arabia.

REFERENCES

1. Ellahi R, Sait S, Shehzad S, Ayaz Z. A hybrid investigation on numerical and analytical solutions of electro-magnetohydrodynamics flow of nanofluid through porous media with entropy generation *Int J Numer Methods Heat Fluid Flow*. (2019) **30**:834–54. doi: 10.1108/HFF-06-2019-0506
2. Eberhard U, Seybold HJ, Floriancic M, Bertsch P, Martínez JJ, Andrade JJS, et al. Determination of the effective viscosity of non-newtonian fluids flowing through porous media. *Front Phys*. (2019) **7**:71. doi: 10.3389/fphy.2019.00071
3. Majeed A, Zeeshan A, Xu H, Kashif M, Masud U. Heat transfer analysis of magneto-eyring–powell fluid over a nonlinear stretching surface with multiple slip effects: application of roseland's heat flux. *Can J Phys*. (2019) **97**:1253–61. doi: 10.1139/cjp-2018-0732
4. Falkner VM, Skan SW. Some approximate solutions of the boundary layer equations. *Philos Mag*. (1931) **12**:865–96.
5. Falkner VM, Skan SW. Some approximate solutions of the boundary-layer for flow past a stretching boundary. *SIAM J Appl Math*. (1931) **49**:1350–8. doi: 10.1137/0149081
6. Rajagopal KR, Gupta AS, Na TY. A note on the falkner-skan flows of a non-newtonian fluid. *Int J NonLin Mech*. (1983) **18**:313–20. doi: 10.1016/0020-7462(83)90028-8
7. Lin HT, Lin LK. Similarity solutions for laminar forced convection heat transfer from wedges to fluids of any prandtl number. *Int J Heat Mass Trans*. (1987) **30**:1111–8. doi: 10.1016/0017-9310(87)90041-X
8. Hartree DH. On an equation occurring in falkner and skan's approximate treatment of the equations of the boundary layer. *Proc Camb Phil Soc*. (1973) **33**:223–39. doi: 10.1017/S0305004100019575
9. Watanabe T. Thermal boundary layer over wedge with uniform suction or injection in force flow. *Acta Mech*. (1990) **83**:119–26. doi: 10.1007/BF01172973

10. Watanabe T, Pop I. Magnetohydrodynamic free convection flow over a wedge in the presence of a transverse magnetic field. *Int Com Heat Mass Trans*. (1993) **20**:871–81. doi: 10.1016/0735-1933(93)90040-3
11. Koh JCY, Hartnett JP. Skin-friction and heat transfer for incompressible laminar flow over porous wedges with suction and variable wall temperature. *Int J Heat Mass Trans*. (1961) **2**:185–98. doi: 10.1016/0017-9310(61)90088-6
12. Kumari M, Takhar HS, Nath G. Mixed convection flow over a vertical wedge embedded in a highly porous medium. *Heat Mass Trans*. (2001) **37**:139–46. doi: 10.1007/s002310000154
13. Chamkha AJ, Mujtaba M, Quadri A, Issa C. Thermal radiation effects on MHD forced convection flow adjacent to a non-isothermal wedge in the presence of a heat source or sink. *Heat Mass Trans*. (2003) **39**:305–12. doi: 10.1007/s00231-002-0353-4
14. El-dabe NT, Ghaly AY, Rizkallah RR, Ewis KM. Numerical solution of MHD boundary layer flow of non-newtonian casson fluid on a moving wedge with heat and mass transfer and induced magnetic field. *J Appl Math Phys*. (2015) **3**:649–63. doi: 10.4236/jamp.2015.36078
15. Mukhopadhyay S, Mondal IC, Chamkha AJ. Casson fluid flow and heat transfer past a symmetric wedge. *Heat Trans. Res*. (2013) **42**:665–75. doi: 10.1002/htj.21065
16. Su X, Zheng L, Zhang X, Zhang J. MHD mixed convective heat transfer over a permeable stretching wedge with thermal radiation and ohmic heating. *Chem Eng Sci*. (2012) **78**:1–8. doi: 10.1016/j.ces.2012.04.026
17. Ishak A, Nazar R, Pop I. Falkner-Skan equation for flow past a moving wedge with suction or injection. *J Appl Math Comp*. (2007) **25**:67–83. doi: 10.1007/BF02832339
18. Ishak A, Nazar R, Pop I. Moving wedge and flat plate in a micropolar fluid. *Int J Eng Sci*. (2006) **44**:1225–36. doi: 10.1016/j.ijengsci.2006.08.005
19. Rashidi MM, Ali M, Freidoonimehr N, Rostami B, Hossain MA. Mixed convective heat transfer for MHD viscoelastic fluid flow over a porous wedge with thermal radiation. *Adv Mechl Eng*. (2014) **6**:735939. doi: 10.1155/2014/735939
20. Kandasamy R, Raji AWBM, Khamis AB. Efiects of chemical reaction, heat and mass transfer on boundary layer flow over a porous wedge with heat radiation in the presence of suction or injection. *Theo Appl Mech*. (2006) **33**:123–48. doi: 10.2298/TAM0602123K
21. Hussanan A, Anwar MI, Ali F, Khan I, Shafie S. Natural convection flow past an oscillating plate with newtonian heating. *Heat Trans Res*. (2014) **45**:119–35. doi: 10.1615/HeatTransRes.2013006385
22. Su X, Xiaohong L. Hall effect on MHD flow and heat transfer of nanofluids over a stretching wedge in the presence of velocity slip and joule heating. *Cen Eur J Phys*. (2013) **11**:1694–703. doi: 10.2478/s11534-013-0331-0
23. Ullah I, Khan I, Shafie S. Hydromagnetic falkner-skan flow of casson fluid past a moving wedge with heat transfer. *Alex Eng J*. (2016) **55**:2139–48. doi: 10.1016/j.aej.2016.06.023
24. Rafique K, Anwar MI, Misiran M, Khan I, Alharbi OS, Thounthong P, et al. Numerical solution of casson nanofluid flow over a non-linear inclined surface with soret and dufour effects by keller-box method. *Front Phys*. (2019) **7**:139. doi: 10.3389/fphy.2019.00139
25. Majeed A, Zeeshan A, Mahmood T, Rahman SU. Impact of magnetic field and second-order slip flow of casson liquid with heat transfer subject to suction/injection and convective boundary condition. *J Mag*. (2010) **24**:181–89. doi: 10.4283/JMAG.2019.24.1.081
26. Bibi M, Zeeshan A, Malik MY, Rehman KU. Numerical investigation of the unsteady solid-particle flow of a tangent hyperbolic fluid with variable thermal conductivity and convective boundary. *Eur Phy J Plus*. (2019) **137**:298. doi: 10.1140/epjp/i2019-12651-9
27. Saba F, Ahmed N, Khan U, Waheed A, Rafiq M, Mohyud-Din ST. Thermophysical analysis of water based ($Cu–Al_2O_3$) hybrid nanofluid in an asymmetric channel with dilating/squeezing walls considering different shapes of nanoparticles. *Appl Sci*. (2018) **8**:1549. doi: 10.3390/app8091549
28. Srinivasacharya D, Mendu U, Venumadhav K. MHD boundary layer flow of a nanofluid past a wedge. *Proc Eng*. (2015) **127**:1064–70. doi: 10.1016/j.proeng.2015.11.463
29. Rashidi MM, Ganesh NV, Hakeem AAK, Ganga B, Lorenzini G. Influences of an effective prandtl number model on nano boundary layer flow of gamma-Al_2O_3-H_2O and gamma-Al_2O_3-$C_2H_6O_2$ over a vertical stretching sheet. *Int J Heat Mass Trans*. (2016) **98**:616–23. doi: 10.1016/j.ijheatmasstransfer.2016.03.006
30. Khan U, Ahmed N, Mohyud-Din ST. Numerical investigation for three dimensional squeezing flow of nanofluid in a rotating channel with lower stretching wall suspended by carbon nanotubes. *Appl Ther Eng*. (2017) **113**:1107–17. doi: 10.1016/j.applthermaleng.2016.11.104
31. Khan JA, Mustafa M, Hayat T, Alsaedi A. On three-dimensional flow and heat transfer over a non-linearly stretching sheet: analytical and numerical solutions. *PLoS ONE*. (2014) **9**:e107287. doi: 10.1371/journal.pone.0107287
32. Yasutomi M. Thermodynamic mechanism of the density anomaly of liquid water. *Front Phys*. (2015) **3**:8. doi: 10.3389/fphy.2015.00008
33. Dhar A, Kundu A, Kundu A. Anomalous heat transport in one dimensional systems: a description using non-local fractional-type diffusion equation. *Front Phys*. (2019) **7**:159. doi: 10.3389/fphy.2019.00159
34. Hayat T, Nadeem S. Heat transfer enhancement with Ag–CuO/water hybrid nanofluid. *Res Phys*. (2017) **7**:2317–24. doi: 10.1016/j.rinp.2017.06.034
35. Alamri SZ, Khan AA, Azeez M, Ellahi R. Effects of mass transfer on MHD second grade fluid towards stretching cylinder: a novel perspective of cattaneo–christov heat flux model. *Phys Lett A*. (2019) **383**:276–81. doi: 10.1016/j.physleta.2018.10.035
36. Manjunatha S, Kuttan BA, Jayanthi S, Chamkha A, Gireesha BJ. Heat transfer enhancement in the boundary layer flow of hybrid nanofluids due to variable viscosity and natural convection. *Heliyon*. (2019) **5**:e01469. doi: 10.1016/j.heliyon.2019.e01469
37. Yasutomi M. Which shape characteristics of the intermolecular interaction of liquid water determine its compressibility? *Front Phys*. (2016) **4**:21. doi: 10.3389/fphy.2016.00021
38. Khan AA, Bukhari SR, Marin M, Ellahi R. Effects of chemical reactio on third-grade MHD fluid under the influence of heat and mass transfer with variable reactive index. *Heat Trans Res*. (2019) **50**:1061–80. doi: 10.1615/HeatTransRes.2018028397
39. Chamkha AJ, Dogonchi AS, Ganji DD. Magneto-hydrodynamic flow and heat transfer of a hybrid nanofluid in a rotating system among two surfaces in the presence of thermal radiation and joule heating. *AIP Adv*. (2019) **9**:025103. doi: 10.1063/1.5086247
40. Ellahi R, Sait SM, Shehzad N, Mobin N. Numerical simulation and mathematical modeling of electro-osmotic couette–poiseuille flow of MHD power-law nanofluid with entropy generation. *Symmetry*. (2019) **11**:1038. doi: 10.3390/sym11081038

Conflict of Interest: The authors declare that the research was conducted in the absence of any commercial or financial relationships that could be construed as a potential conflict of interest.

Copyright © 2020 Ahmed, Adnan, Khan, Mohyud-Din, Khan, Murtaza, Hussain and Sherif. This is an open-access article distributed under the terms of the Creative Commons Attribution License (CC BY). The use, distribution or reproduction in other forums is permitted, provided the original author(s) and the copyright owner(s) are credited and that the original publication in this journal is cited, in accordance with accepted academic practice. No use, distribution or reproduction is permitted which does not comply with these terms.

NOMENCLATURE

Parameter	Description	SI Unit
Ec	Eckert number	Dimensionless
$F'(\eta)$	Dimensionless velocity	Dimensionless
k_{nf}	Effective thermal conductivity	$Wm^{-1}K^{-1}$
k_f	Thermal conductivity of the fluid	$Wm^{-1}K^{-1}$
k_s	Thermal conductivity of the nanoparticles	$Wm^{-1}K^{-1}$
M	Hartmann number	Dimensionless
Pr	Prandtl number	Dimensionless
$q(x)$	Wall heat flux	W/m^2
Rd	Thermal radiation parameter	Dimensionless
T	Temperature	K
$\hat{U}(x,t)$	Main stream velocity	m/s
$\hat{u}$	Velocity in x direction	m/s
$\hat{v}$	Velocity in y direction	m/s
$\beta(\eta)$	Dimensionless temperature	Dimensionless
γ	Wedge parameter	Dimensionless
η	Similarity variable	Dimensionless
μ_{nf}	Effective dynamic viscosity	kg/ms
μ_f	Dynamic viscosity of the fluid	kg/ms
ρ_{nf}	Effective density	kg/m^3
ρ_f	Density of the fluid	kg/m^3
ρ_s	Density of the solid particles	kg/m^3
$(c_p)_{nf}$	Effective heat capacity of the nanofluid	$kg^{-1}K^{-1}$
$(c_p)_f$	Heat capacity of the fluid	$kg^{-1}K^{-1}$
$(c_p)_s$	Heat capacity of the nanoparticles	$kg^{-1}K^{-1}$
σ_m^*	Electrical conductivity	S/m

NOMENCLATURE

u, v, w	Velocity components	x, y, z	Coordinate axes
Ω	Angular velocity	B_0	Magnetic field strength
μ	Dynamic viscosity	ρ	Fluid density
ν	Kinematic viscosity	p	Pressure
σ	Electrical conductivity	V_0	Suction/blowing velocity
T	Temperature	C	Concentration
α_m^*	Thermal diffusivity	D	Mass diffusion coefficient
c_s	Concentration susceptibility	c_p	Specific heat
k_T	Thermal-diffusion	T_m	Fluid mean temperature
a	Stretching rate	t	Time
T_0	Temperature at lower plate	C_0	Concentration at lower plate
F', G	Dimensionless velocities	η	Dimensionless variable
θ	Dimensionless temperature	ϕ	Dimensionless concentration
S_q	Squeezing number	Ec	Eckert number
S	Suction/blowing parameter	M	Magnetic number
Ω	Rotation parameter	Pr	Prandtl number
Sc	Schmidt number	Sr	Soret number
Df	Dufour number	Nu_x	Local Nusselt number
τ_{wx}, τ_{wz}	Wall shear stresses	Sh_x	Local Sherwood number
C_{fx}, C_{fz}	Skin friction coefficients	Re_x	Local Reynolds number

frontiers in Physics

ORIGINAL RESEARCH
published: 09 June 2020
doi: 10.3389/fphy.2020.00178

Check for updates

Novel Microstructural Features on Heat and Mass Transfer in Peristaltic Flow Through a Curved Channel

Raheel Ahmed[1†], Nasir Ali[1†], Sami Ullah Khan[2†], A. M. Rashad[3†], Hossam A. Nabwey[4,5†] and Iskander Tlili[6,7*†]

[1] Department of Mathematics and Statistics, International Islamic University Islamabad, Islamabad, Pakistan, [2] Department of Mathematics, COMSATS University Islamabad, Sahiwal, Pakistan, [3] Department of Mathematics, Faculty of Science, Aswan University, Aswan, Egypt, [4] Department of Mathematics, College of Science and Humanities in Al-Kharj, Prince Sattam bin Abdulaziz University, Al-Kharj, Saudi Arabia, [5] Department of Basic Engineering Science, Faculty of Engineering, Menoufia University, Shebin El-Kom, Egypt, [6] Department for Management of Science and Technology Development, Ton Duc Thang University, Ho Chi Minh City, Vietnam, [7] Faculty of Applied Sciences, Ton Duc Thang University, Ho Chi Minh City, Vietnam

OPEN ACCESS

Edited by:
Sara I. Abdelsalam,
National Autonomous University of Mexico, Mexico

Reviewed by:
Abdullah Zaher,
Benha University, Egypt
Sohail Nadeem,
Quaid-i-Azam University, Pakistan

***Correspondence:**
Iskander Tlili
iskander.tlili@tdtu.edu.vn

† These authors have contributed equally to this work

Specialty section:
This article was submitted to Mathematical Physics, a section of the journal Frontiers in Physics

Received: 10 March 2020
Accepted: 27 April 2020
Published: 09 June 2020

Citation:
Ahmed R, Ali N, Khan SU, Rashad AM, Nabwey HA and Tlili I (2020) Novel Microstructural Features on Heat and Mass Transfer in Peristaltic Flow Through a Curved Channel. Front. Phys. 8:178. doi: 10.3389/fphy.2020.00178

Recently, significant interest has been developed by researchers toward the peristaltic transport of fluid, as this phenomenon involves a variety of applications in the biomechanics, bioengineering, and biomedical industries. In the present contribution, we investigate the effect of heat and mass transfer on magnetically influenced micropolar flow induced by peristaltic waves. The fundamental laws regarding current flow problem are employed by using curvilinear coordinates. A reduction of these equations is made based on lubrication approximation. The solution algorithm is based on the implementation of the famous finite difference method. The fundamental impacts of coupling number, micropolar parameter, Hartmann number, Brinkman number, rate of chemical reaction, and curvature parameter on longitudinal velocity, pressure rise, temperature, and mass concentration are analyzed in detail. The flow patterns in the channel illustrating the effects of several involved parameters are also displayed.

Keywords: micropolar fluid, hartmann number, heat and mass transfer, curved channel, implicit finite difference method

INTRODUCTION

The theory of fluids has gained the attention of scientists, engineers, biologists, and mathematicians in recent times. Generally, fluids are categorized as Newtonian or non-Newtonian. Newtonian fluids are those in which viscous stresses sustain a linear relationship between strain rates at every point. The viscous fluids are referred to as a simple linear model that reports the viscosity. Examples of Newtonian fluids are water, glycerol, alcohol, thin motor oil, and air. Another class of fluids is defined as a fluid which fails to follow Newton's viscosity model. A number of fluids are non-Newtonian in nature. Examples are custard, ketchup, shampoo, starch, paint, blood, and suspension. Recently, many researchers have been concentrating on the flows of non-Newtonian fluids. This is due to the applications of non-Newtonian fluids in polymer processing, biofluid mechanics, and complex mathematical non-linear constitutive equations.

The motivating implication of the Peristalsis phenomenon has attained a valuable attraction of scientists in the last few years as it involves fundamental industrial and bioscience applications. Several investigations are reported regarding the peristaltic transport of non-Newtonian materials which encountered many physiology applications. Raju and Devanathan [1] worked on the peristaltic study of the power law model configured by a tube, where it was assumed that a sinusoidal with lower amplitude traveled down along the channel wall. Mekheimer [2] studied the transport of magnetohydrodynamic viscous and incompressible peristaltic flow in an inclined planar channel. Hakeem et al. [3] modeled the peristaltic flow motion equations for Carreau fluid by using long wavelength assumptions in a uniform tube. The peristaltic study of Johnson–Segalman liquid influenced by magnetic force in a 2D flexible channel has been depicted by Elshahed and Haroun [4]. Hakeem et al. [5] examined the significance of magnetic force in trapping evolved regarding the peristaltic flow generalized viscous fluid. The rheological justification of non-Newtonian Burger's fluid due to peristaltic movement encountered by a planar channel was reported by Hayat et al. [6]. The reported flow model was based on long wavelength theory, and later on, an exact solution is developed for a formulated problem. The theoretical model developed by Haroun [7] signified the rheological consequences in third-order liquid for a peristaltic phenomenon configured by the asymmetric channel. Wang et al. [8] studied the magnetohydrodynamic peristaltic motion of a Sisko fluid in a symmetric or asymmetric channel. An investigation with peristaltic aspects for third-grade fluid encountered by a circular cylindrical tube was performed by Ali et al. [9]. The peristaltic mechanism of Prandtl–Eyring fluid along with heat transfer features in a curved channel was evaluated by Hayat et al. [10]. Rafiq et al. [11] investigated ion-slip and Hall features in the peristaltic flow of nanoparticles with biomedical applications. Ahmed and Javed [12] used finite element technique to model Navier–Stokes expressions for the peristaltic phenomenon in the presence of a porous medium. The influence of electromagnetic features in the peristaltic flow of Eyring-Powell nanofluid. Asha and Sunitha [13] involved the Hall effects in peristaltic transport of nanoparticles in the asymmetric channel.

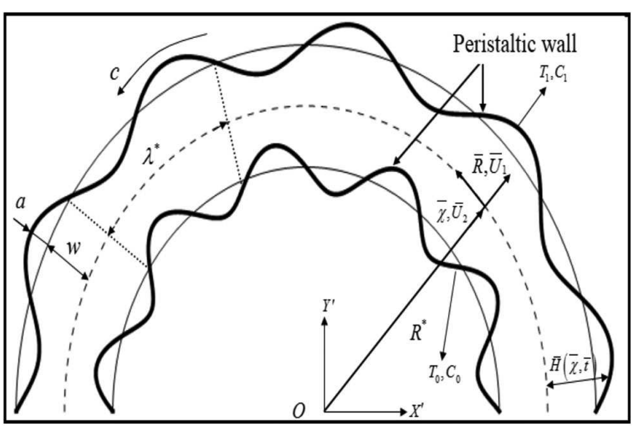

FIGURE 1 | Physical problem of the peristaltic flow regime.

Non-Newtonian fluids are characterized through a number of models due to their complexity. Among these models, a micropolar fluid model has been gaining attention of a number of researchers. In this model, stiff particles cramped into a relatively minute-volume element are able to move about the center of the element. The rotational attribute of fluid particles is carried out through a vector called micro-rotation expressions. It is not worth remarking that those intrinsic rotation features of the fluid are associated with rigid body movement for a whole-volume element which depends upon various factors. Such features are referred to the micro-rotational effects, and the role of these factors at macro-scale cannot be taken into account. However, such effects become important when flow is considered in narrow gaps, i.e., when geometric dimensions of the flow domain are very small [14]. In peristaltic flows, fluid is usually pushed through nano-size vessels, and therefore, it is expected that micro-rotation of particles reflects some diverse and distinguished flow characteristics. Important effects cannot be captured by the Navier–Stokes theory. The fundamental work on the micropolar fluid theory was first introduced by Eringen [15, 16] to describe the suspensions of neutrally buoyant rigid particles in a viscous fluid. The work on micropolar fluid was initiated by Eringen by involving the micro-rotation features in the classical Navier–Stokes theory. Ariman et al. [17] studied the application of micro-continuum fluid mechanics in a broader prospect. The assessment of a boundary layer for the micropolar fluid has been successfully examined by Na and Pop [18]. Srinivasacharya et al. [19] reported a closed-form relation for peristaltic aspects of micropolar fluid flow due to a circular tube. The model problem was based on the famous long wavelength and small Reynolds number assumptions. The peristaltic movement under the influence of wall properties in 2D flow of micropolar liquid has been revealed by Muthu et al. [20]. Lok et al. [21] investigated the steady mixed convective due to vertical moving geometry for flow of micropolar fluid. Hayat et al. [22] examined the impact of different waveforms in a peristaltic flow of a micropolar fluid. The flow of micropolar liquid followed by a peristaltic pattern in the asymmetric channel has been focused by Ali and Hayat [23]. Another continuation made by Hayat and Ali [24] reported the endoscope consequences for micropolar fluid flow in a concentric tube. Another peristaltic phenomenon based on an exploration for micropolar liquid with implementation of magnetic field impact was estimated by Mekheimer [25]. Ishak et al. [26] studied the magnetohydrodynamic flow of a micropolar fluid toward a stagnation point on a vertical surface. Mekheimer and El Kot [27] used the micropolar fluid model for blood flow through a stenosed tapered artery. Sajid et al. [28] employed the homotopy analysis method to discuss boundary layer flow micropolar fluid through a porous channel. Ashraf et al. [29] examined numerical solutions portraying the appliance of micropolar material in a channel having porous walls. Rashidi et al. [30] applied the differential transform method to get a semi-analytical solution of micropolar flow in a porous channel with mass injection. Ali et al. [31] comprehensively studied the peristaltic flow of a micropolar fluid in a curved channel. The unsteady peristaltic prospective for 2D channel flow of micropolar fluid in the presence of heat and mass transportation has been examined by El-Dabe and Zeid [32]. The investigation for micropolar fluid in contacting a wall channel additionally featuring an isotropic porous space was assessed by Abd Elmaboud [33]. Sui et al. [34] reported a constitutive diffusion model to investigate the heat transfer performances in micropolar fluid encountered by a moving geometry. Waqas et al. [35] numerically predicted the join

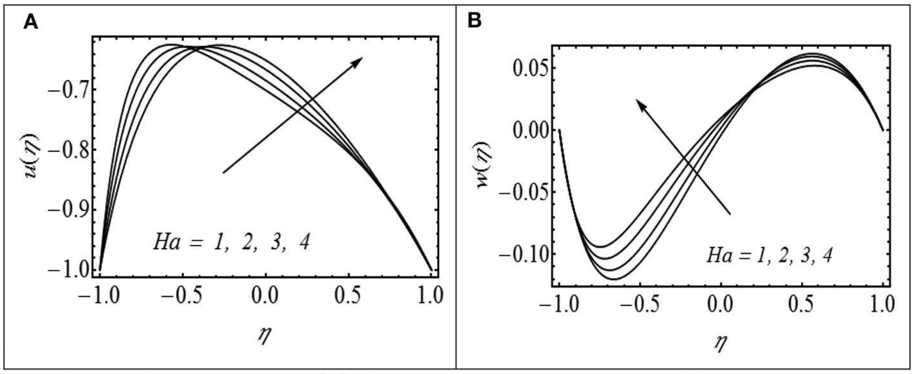

FIGURE 2 | (A,B) Impact of *Ha* on $u(\eta)$ with $\gamma = 2.5$, $N_1 = 0.5$, $N_2 = 1.2$, $\lambda = 0.4$, and $\Theta = 1.5$. **(B)** Impact of *Ha* on $w(\eta)$ with $\gamma = 2.5$, $N_1 = 0.5$, $N_2 = 1.2$, $\lambda = 0.4$, and $\Theta = 1.5$.

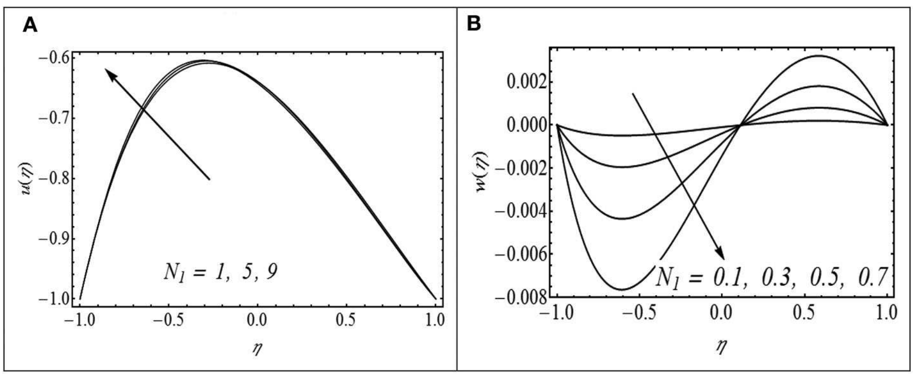

FIGURE 3 | (A,B) Impact of N_1 on $u(\eta)$ with $\gamma = 2.5$, $Ha = 2$, $N_2 = 0.2$, $\lambda = 0.4$, and $\Theta = 1.5$. **(B)** Impact of N_1 on $w(\eta)$ with $\gamma = 2.5$, $N_2 = 0.2$, $\lambda = 0.4$, and $\Theta = 1.5$.

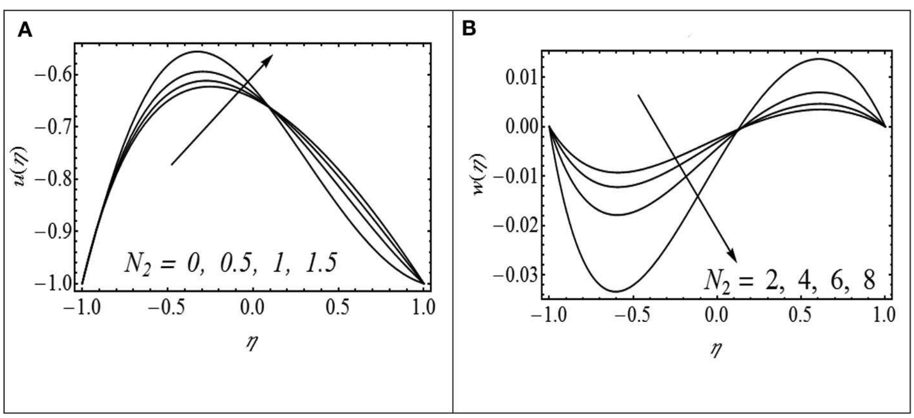

FIGURE 4 | (A,B) Impact of N_2 on $u(\eta)$ with $\gamma = 2.5$, $Ha = 2$, $N_1 = 0.5$, $\lambda = 0.4$, and $\Theta = 1.5$. **(B)** Impact of N_2 on $w(\eta)$ with $\gamma = 2.5$, $N_1 = 0.5$, $\lambda = 0.4$, and $\Theta = 1.5$.

features of Maxwell viscoelasticity–based nanofluid additionally featuring a porous medium. In another contribution, Waqas and co-workers [36] utilized the bioconvection phenomenon in the flow of micropolar nanofluid with additional thermal radiation features. Ali et al. [37] intended the micropolar liquid rheological significance compiled in calendaring geometry. Ahmed et al. [38] examined the effects of heat and mass transfer on peristaltic flow of Sisko fluid through a curved channel. Mekheimer et al.

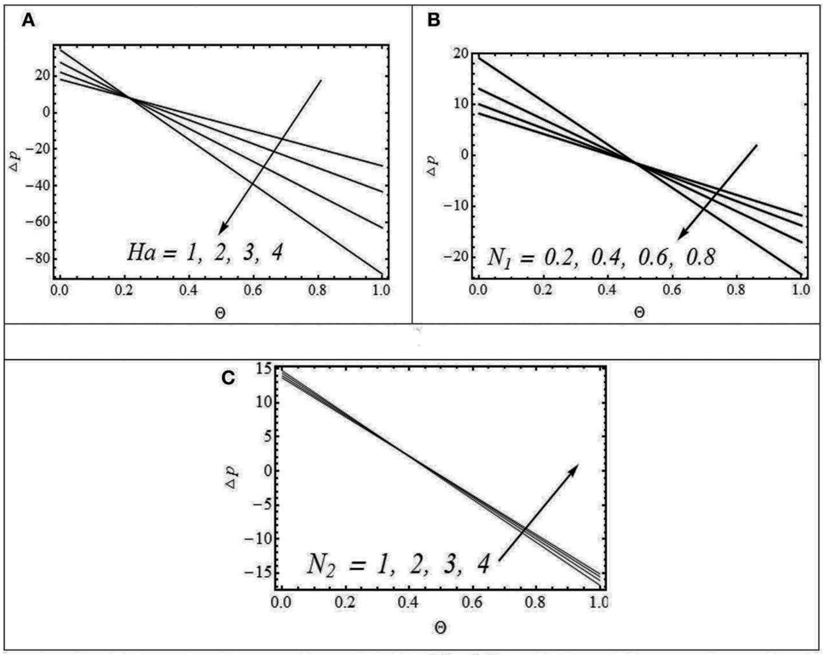

FIGURE 5 | (A) Impact of Ha on Δp with $N_1 = 0.5, N_2 = 1.2$, $\gamma = 2.5$, and $\lambda = 0.4$. **(B)** Impact of N_1 on Δp with $\gamma = 2.5$, $N_2 = 1.2$, and $\lambda = 0.4$. **(C)** Impact of N_2 on Δp with $N_1 = 0.5$, $\gamma = 2.5$, and $\lambda = 0.4$.

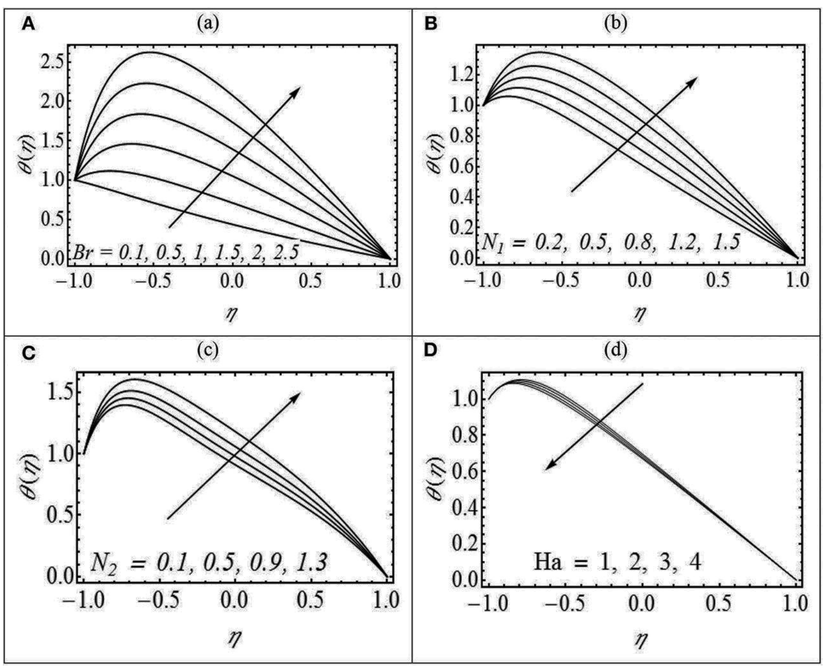

FIGURE 6 | (A–D) Variation in θ for various values of **(A)** Br with $N_1 = 0.5$, $N_2 = 1.2$, $\lambda = 0.4$, and $\gamma = 2$; **(B)** N_1 with $Br = 2$, $N_2 = 1.2$, $\lambda = 0.4$, and $\gamma = 2$; **(C)** N_2 with $Br = 2$, $N_1 = 0.5$, $\lambda = 0.4$, and $\gamma = 2$; and **(D)** Ha with $N_1 = 0.5$, $N_2 = 1.2$, $\lambda = 0.4$, and $\gamma = 2$.

[39] studied the effect of gold nanoparticle third-grade fluid on peristaltic blood flow. Elkhair et al. [40] considered the impact of heat transfer on oscillatory flow of a dielectric fluid through a porous medium. Recently, Mekheimer et al. [41] investigated the behavior of a blood confined by stenotic arterial walls. In another useful attempt, Mekheimer et al. [42] performed the features of heat transfer additionally featuring AC current. Nadeem et al. [43, 44] studied hybrid-based nanofluid flow over a curved surface in different scenarios. Abbas et al. [45] observed transportation of micropolar hybrid nanomaterial which was externally impacted by magnetic influence. Sadaf et al. [46] discussed the effect of heat transfer on fluid motion generated by cilia and a pressure gradient in a curved channel. In a most recent study, Nadeem et al. [47] investigated the effect of heat transfer on micropolar fluid flow over a Riga plate. Some more recent investigations on this topic are seen in references [48–50].

From the literature cited above, it is noted that the hydrodynamic flow of micropolar fluid through a curved channel with peristalsis is studied but less attention is paid to hydromagnetic aspects of micropolar liquid along with heat and mass transportation aspects. The prime objective of this study is to investigate the effects of coupling number, micropolar parameter, Hartmann number, Brinkman number, and dimensionless radius of curvature on flow, heat, and mass transfer characteristics. To this end, the associated equations for velocity, temperature, and mass concentration are constituted. The modeled system is numerically interpolated with assistance of finite difference scheme. The fluid velocity, temperature, and concentration fields are analyzed for several values of the involved parameters. It is important to mention that governing equations for heat and mass transfer for the flow of micropolar fluid in a curved peristaltic channel are derived for the first time in the literature.

GOVERNING EQUATIONS

For micropolar fluid, the mathematical expressions in presence of heat/mass influences are given by [37].

Continuity equation:

$$U_{i,i}=0 \tag{1}$$

Momentum equation:

$$\rho\dot{U}_k=\tau_{lk,l}+\rho f_k \tag{2}$$

Moment of momentum equation:

$$\rho j\dot{w}_k=m_{lk,l}+e_{kij}\tau_{ij} \tag{3}$$

Energy equation:

$$\rho c_p\dot{T}=kT_{,ii}+\tau_{kl}a_{kl}-m_{kl}b_{kl} \tag{4}$$

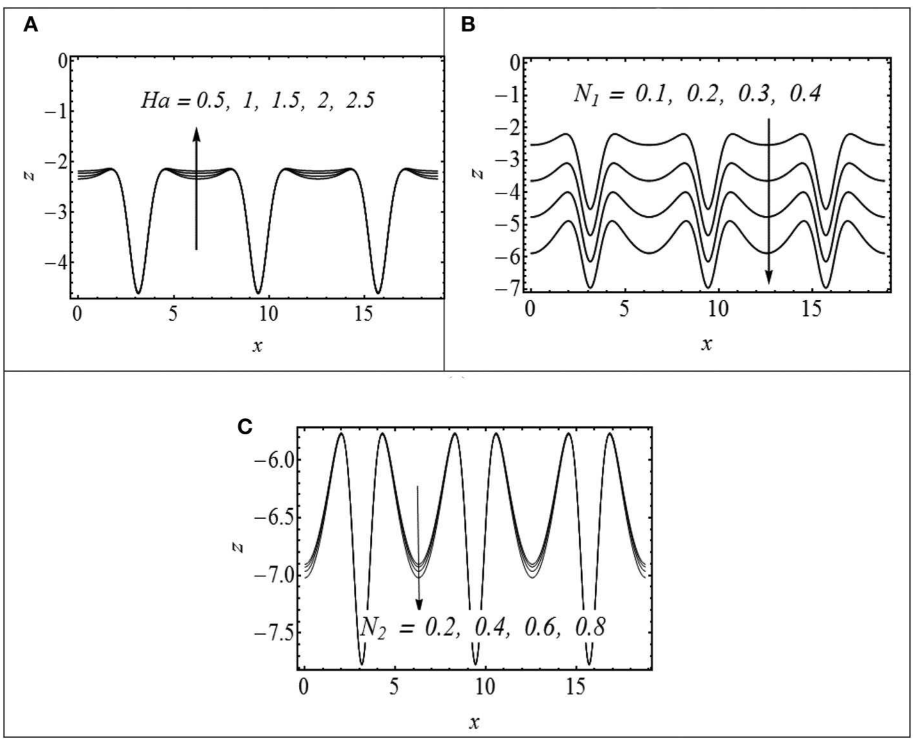

FIGURE 7 | (A–C) Variation in z at the upper wall for **(A)** Ha with $N_1 = 0.5$, $N_2 = 1.2$, $\lambda = 0.4$, and $\gamma = 2$; **(B)** N_1 with $Br = 2$,, $N_2 = 1.2$, $\lambda = 0.4$, and $\gamma = 2$; and **(C)** N_2 with $Br = 2$, $N_1 = 0.5$, $\lambda = 0.4$, and $\gamma = 2$.

Concentration equation:

$$\dot{C} = DC_{,ii} + \frac{Dk_T}{T_m} T_{,ii} - k_1 C \tag{5}$$

In the above equations, U_k is the velocity, C is the mass concentration, f_k is the body force, T is the symbolized temperature, τ_{kl} is the Cauchy stress tensor, m_{kl} is the moment stress tensor, p is the pressure, ρ is the fluid density, w_k is the micro-rotation vector, c_p is the specific heat at constant pressure, D is the coefficient of mass diffusivity, K_T is the thermal diffusivity, T_m is the mean temperature, k_1 is the rate of chemical reaction, k is the thermal conductivity, j is the micro moment of inertia, and dot indicates the material time derivative. Moreover, $\tau_{kl}, m_{kl}, a_{kl}$ and b_{kl} are given by

$$\left.\begin{array}{l} \tau_{kl} = -p\delta_{kl} + \left(\mu + k_2\right) a_{kl} + \mu a_{lk}, \\ m_{kl} = \alpha\, tr(b_{mm})\delta_{kl} + \beta b_{kl} + \gamma^* b_{lk}, \\ a_{kl} = v_{l,k} + e_{lkm} w_m, \\ b_{kl} = w_{k,l}, \end{array}\right\} \tag{6}$$

where μ is the viscosity, k_2 is the dynamic micro-rotation viscosity, e_{lkm} is the permutation symbol, and α, β, γ^* are the constants called coefficient of angular viscosity. It is remarked that Equation (2) has been diminished into a Navier–Stokes expression when $k_2 = \alpha = \beta = \gamma^* = 0$. It is further emphasized that if $k_2 = 0$, both micro-rotation and velocity are unyoked and micro-rotation does not play to alter the global motion. Following Eringen [51], the following relations hold for μ, k_2,α, β, and γ^*

$$2\mu + k_2 \geq 0, k_2 \geq 0, 3\alpha + \beta + \gamma^* \geq 0, \alpha \geq |\beta|.$$

MATHEMATICAL MODELING

Consider a curved channel of width $2w$ coiled in circle having radius R_0 and center O. An incompressible micropolar fluid flows inside the channel. The fluid flows due to the wall of the channel which deforms uniformly. Let T_0, T_1, C_0, and C_1 represent the upper wall temperature, lower wall temperature, upper

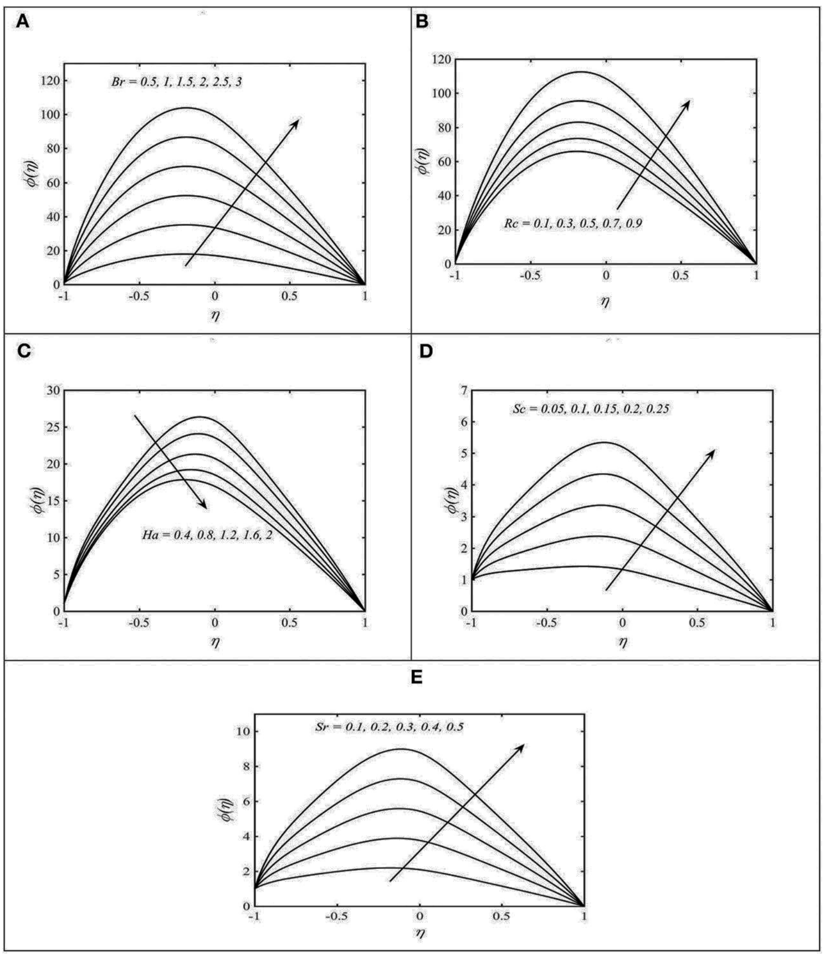

FIGURE 8 | (A–D) Change in φ for various values of **(A)** *Br* with $N_1 = 0.5$, $N_2 = 1.2$, $\lambda = 0.4$, and $\gamma = 2$; **(B)** R_c with $Br = 2$, $N_1 = 0.5$, $N_2 = 1.2$, $\lambda = 0.4$, and $\gamma = 2$; **(C)** *Ha* with $Br = 2$,$N_1 = 0.5$, $N_2 = 1.2$, $\lambda = 0.4$, and $\gamma = 2$; **(D)** *Sc* with $Br = 2$, $N_1 = 0.5$, $N_2 = 1.2$, $\lambda = 0.4$, and $\gamma = 2$; and **(E)** *Sr* with $Br = 2$,$N_1 = 0.5$, $N_2 = 1.2$,$\lambda = 0.4$, and $\gamma = 2$.

wall concentration, and lower wall concentration, respectively. The fluid movement is described by following the curvilinear coordinate system (R, χ, Z). It is emphasized that χ is specified in the flow direction and R is radially oriented while Z is assumed normal to the plane. The flow visualization for the current problem can be described by sketching **Figure 1**. The shape of both walls is described mathematically as [31, 38]

$$H_1(\chi, t) = w + a\sin\left(\left(\frac{2\pi}{\lambda^*}\right)(\chi - ct)\right), \quad \text{Upper wall,} \tag{7}$$

$$H_2(\chi, t) = -w - a\sin\left(\left(\frac{2\pi}{\lambda^*}\right)(\chi - ct)\right), \quad \text{Lower wall,} \tag{8}$$

where λ^* is the wavelength, c is the wave speed, a is the amplitude, and t is the time. The present work is based on the following assumptions:

(1) The fluid is assumed as a continuum.
(2) Fluid is incompressible.
(3) The solid matrix is in a local thermal equilibrium with the fluid.
(4) The walls of the channel are non-compliant.
(5) Flow is laminar with negligible gravitational effects.
(6) The magnetic Reynolds number is assumed small, and hence, effects of induced magnetic field are negligible.
(7) Soret and chemical effects are taken into account.

It is further assumed that the flow is subjected to the radial magnetic field of the form

$$\mathbf{B} = \left(\frac{B^*\tilde{R}}{R+\tilde{R}}\right)\mathbf{e}_R,$$

where B^* is the limiting value of B when $\tilde{R} \to \infty$. Thus, by generalizing Ohm's law, the body force term in Equation (2) becomes

$$\rho f_k = (\mathbf{J} \times B)_{\mathbf{k}},$$

where $J = \sigma(V \times B)$. Here, we neglect the electric field and invoke the low magnetic Reynolds number assumption. Using the velocity, temperature, concentration, and micro-rotation fields defined by

$$\mathbf{U} = [U_1(\chi, R, t), U_2(\chi, R, t), 0], \; T = T(\chi, R, t),$$
$$C = C(\chi, R, t), \mathbf{w} = [0, 0, -w(x, r)]$$

the set of Equations (1)–(5) in component form becomes [31, 38]

$$\frac{\partial}{\partial R}\left\{(R+\tilde{R})U_1\right\} + \tilde{R}\frac{\partial U_2}{\partial \chi} = 0, \tag{9}$$

$$\frac{\partial U_1}{\partial t} + (U_1.\nabla)U_1 - \frac{{U_2}^2}{R+\tilde{R}} = -\frac{1}{\rho}\frac{\partial P}{\partial R} + \frac{1}{\rho}(\mu + k_2)\left[\nabla^2 U_1 - \frac{U_1}{(R+\tilde{R})^2} - \frac{2\tilde{R}}{(R+\tilde{R})^2}\frac{\partial U_2}{\partial \chi}\right] + \frac{k_2\tilde{R}}{\rho(R+\tilde{R})}\frac{\partial w}{\partial \chi}, \tag{10}$$

$$\frac{\partial U_2}{\partial t} + (U_1.\nabla)U_2 + \frac{U_1U_2}{R+\tilde{R}} = -\frac{\tilde{R}}{\rho(R+\tilde{R})}\frac{\partial P}{\partial \chi} + \frac{1}{\rho}(\mu + k_2)\left[\nabla^2 U_2 - \frac{U_2}{(R+\tilde{R})^2} + \frac{2\tilde{R}}{(R+\tilde{R})^2}\frac{\partial U_1}{\partial \chi}\right] - \frac{k_2}{\rho}\frac{\partial w}{\partial R} - \frac{\sigma {B^*}^2\tilde{R}^2}{\rho(R+\tilde{R})^2}U_2, \tag{11}$$

$$(U_1.\nabla)\, w = -\frac{\gamma^*}{\rho j}\left[\frac{\partial^2 w}{\partial R^2} + \frac{1}{R+\tilde{R}}\frac{\partial w}{\partial R} + \left(\frac{\tilde{R}}{R+\tilde{R}}\right)^2\frac{\partial^2 w}{\partial \chi^2}\right] + \frac{k_2}{\rho j}\left[2w - \frac{\tilde{R}}{R+\tilde{R}}\frac{\partial U_1}{\partial \chi} + \frac{\partial U_2}{\partial R} + \frac{U_2}{R+\tilde{R}}\right], \tag{12}$$

$$\begin{aligned}
\rho c_p\left(\frac{\partial T}{\partial t} + U_1\frac{\partial T}{\partial R} + \frac{U_2\tilde{R}}{R+\tilde{R}}\frac{\partial T}{\partial \chi}\right) &= k\left(\frac{\partial^2 T}{\partial R^2} + \frac{1}{R+\tilde{R}}\frac{\partial T}{\partial R} + \frac{\tilde{R}^2}{(R+\tilde{R})^2}\frac{\partial^2 T}{\partial \chi^2}\right) + \frac{\partial U_1}{\partial R}\left(-p + 2\mu\frac{\partial U_1}{\partial R} + k_2\frac{\partial U_1}{\partial R}\right) \\
&+ \left(\frac{\tilde{R}}{R+\tilde{R}}\frac{\partial U_1}{\partial \chi} - \frac{U_2}{R+\tilde{R}} - w\right)\left(\frac{\mu\tilde{R}}{R+\tilde{R}}\frac{\partial U_1}{\partial \chi} + \mu\frac{\partial U_2}{\partial R} - \frac{\mu U_2}{R+\tilde{R}} + \frac{k\tilde{R}}{R+\tilde{R}}\frac{\partial U_1}{\partial \chi} - \frac{kU_2}{R+\tilde{R}} - k_2 w\right) + \left(\frac{\partial U_2}{\partial R} + w\right) \\
&\left(\frac{\mu\tilde{R}}{R+\tilde{R}}\frac{\partial U_1}{\partial \chi} + \mu\frac{\partial U_2}{\partial R} - \frac{\mu U_2}{R+\tilde{R}} + k_2\frac{\partial U_2}{\partial R} + k_2 w\right) + \left(\frac{\tilde{R}}{R+\tilde{R}}\frac{\partial U_2}{\partial \chi} + \frac{U_1}{R+\tilde{R}}\right)\left(-p + \frac{2\mu\tilde{R}}{R+\tilde{R}}\frac{\partial U_2}{\partial \chi} + \frac{2\mu U_1}{R+\tilde{R}} + \frac{k\tilde{R}}{R+\tilde{R}}\frac{\partial U_2}{\partial \chi} + \frac{kU_1}{R+\tilde{R}}\right) \\
&+ \gamma^*\left(\left(\frac{\partial w}{\partial R}\right)^2 + \left(\frac{\tilde{R}}{R+\tilde{R}}\frac{\partial w}{\partial \chi}\right)^2\right),
\end{aligned} \tag{13}$$

$$\frac{\partial C}{\partial t} + (U_1.\nabla)C = D\nabla^2 C + \frac{DK_T}{T_m}\left(\frac{\partial^2 T}{\partial R^2} + \frac{\tilde{R}}{R+\tilde{R}}\frac{\partial T}{\partial R} + \left(\frac{\tilde{R}}{R+\tilde{R}}\right)^2\frac{\partial^2 T}{\partial \chi^2}\right) - k_1 C, \tag{14}$$

where

$$U_1.\nabla = U_1\frac{\partial}{\partial R} + \frac{\tilde{R}U_2}{R+\tilde{R}}\frac{\partial}{\partial \chi}, \tag{15}$$

and

$$\nabla^2 = \frac{1}{R+\tilde{R}}\frac{\partial}{\partial R}\left\{(R+\tilde{R})\frac{\partial}{\partial R}\right\} + \left(\frac{\tilde{R}}{R+\tilde{R}}\right)^2\frac{\partial^2}{\partial \chi^2} \tag{16}$$

The boundary conditions associated with Equations (9)–(14) are [8]

$$U_2 = 0,\; U_1 = \frac{\partial H_1}{\partial t},\; w = 0, T = T_o,\; C = C_o \text{ at } R = H_1(\chi, t), \tag{17}$$

$$U_2 = 0, U_1 = \frac{\partial H_2}{\partial t},\; w = 0, T = T_1,\; C = C_1 \text{ at } R = H_2(\chi, t). \tag{18}$$

The following transformations are suggested to transmute the fixed wave from (R, χ) to new wave from (r, x)

$$x = \chi - ct,\ r = R,\ p = P,\ u_1 = U_1,\ u_2 = U_2 - c. \quad (19)$$

The governing flow equation is transmuted into a wave frame while defining the following appropriate variables [31, 38]:

$$\bar{x} = {}^{2\pi x}\!/_{\lambda^*},\ \eta = {}^{r}\!/_{a},\ \gamma = \frac{\tilde{R}}{a},\ \bar{u}_1 = {}^{u_1}\!/_{c},\ \bar{u}_2 = {}^{u_2}\!/_{c},$$
$$\bar{w} = {}^{aw}\!/_{c},\ \bar{p} = {}^{2\pi a^2 p}\!/_{\lambda^* \mu c},\ \mathrm{Re} = {}^{\rho ca}\!/_{\mu},\ \theta = {}^{(T-T_1)}\!/_{(T_0-T_1)},$$
$$\phi = {}^{(C-C_1)}\!/_{(C_0-C_1)},\ \delta = {}^{2\pi a}\!/_{\lambda^*},\ \bar{j} = {}^{j}\!/_{a^2},\ N_1 = {}^{k_2}\!/_{\mu},\ N_2 = {}^{\gamma^*}\!/_{a^2\mu}$$

Moreover, invoking the lubrication approximations ($\delta \approx 0, \mathrm{Re} \approx 0$) reduces to

$$\frac{\partial p}{\partial \eta} = 0, \quad (20)$$

$$-\frac{\partial p}{\partial x} - \frac{1}{\gamma(1-N_1)}\left[\frac{\partial}{\partial \eta}\left\{(\eta+\gamma)\frac{\partial^2 \psi}{\partial \eta^2}\right\} + \frac{1}{\eta+\gamma}\left(1-\frac{\partial \psi}{\partial \eta}\right) - N_1(\eta+\gamma)\frac{\partial w}{\partial \eta}\right] - \frac{\gamma Ha^2}{\eta+\gamma}\left(1-\frac{\partial \psi}{\partial \eta}\right) = 0, \quad (21)$$

$$\left(\frac{2-N_1}{N_2}\right)\left[\frac{\partial^2 w}{\partial \eta^2} + \frac{1}{\eta+\gamma}\frac{\partial w}{\partial \eta}\right] - 2w + \frac{\partial^2 \psi}{\partial \eta^2} - \frac{1}{\eta+\gamma}\left(1-\frac{\partial \psi}{\partial \eta}\right) = 0, \quad (22)$$

$$\frac{\partial^2 \theta}{\partial \eta^2} + \frac{1}{(\eta+\gamma)}\frac{\partial \theta}{\partial \eta} + Br\left(\frac{1}{\eta+\gamma}\left(1-\frac{\partial \psi}{\partial \eta}\right) + w\right)$$
$$\left(\frac{\partial^2 \psi}{\partial \eta^2} + \frac{1}{\eta+\gamma}\left(1-\frac{\partial \psi}{\partial \eta}\right)(1+N_1) + N_1 w\right) + \quad (23)$$
$$Br\left(\frac{\partial^2 \psi}{\partial \eta^2} - w\right)\left(\frac{\partial^2 \psi}{\partial \eta^2} + \frac{1}{\eta+\gamma}\left(1-\frac{\partial \psi}{\partial \eta}\right) + N_1\left(\frac{\partial^2 \psi}{\partial \eta^2} - w\right)\right) + N_2 Br\left(\frac{\partial w}{\partial \eta}\right)^2 = 0,$$

$$\frac{\partial^2 \phi}{\partial \eta^2} + \frac{1}{(\eta+\gamma)}\frac{\partial \phi}{\partial \eta} - R_c\phi = -SrSc\left(\frac{\partial^2 \theta}{\partial \eta^2} + \frac{1}{(\eta+\gamma)}\frac{\partial \theta}{\partial \eta}\right) + R_c. \quad (24)$$

In the above equations $N_1,\ N_2,\ \mathrm{Re},\ \delta,\ \gamma,\ K^*$, and R_c represent the coupling number, micropolar constant, Reynolds number, wave number, radius of curvature, dimensionless permeability parameter, and dimensionless rate of the chemical reaction parameter, respectively. Here, the coupling number presents the coupling between the vortex viscosity and shear viscosity coefficients, while micropolar parameter is the ratio between the coefficient of angular viscosity and the shear viscosity coefficient. Further, the stream function ψ and velocity components u_1 and u_2 are related through the expressions

$$u_1 = \delta\frac{\gamma}{\eta+\gamma}\frac{\partial \psi}{\partial x},\quad u_2 = -\frac{\partial \psi}{\partial \eta}. \quad (25)$$

Combining Equation (20) with Equation (21), one gets $\frac{1}{1-N_1}\left[\frac{\partial^2}{\partial \eta^2}\left\{(\eta+\gamma)\frac{\partial^2 \psi}{\partial \eta^2}\right\} + \frac{\partial}{\partial \eta}\left(\frac{1}{\eta+\gamma}\left(1-\frac{\partial \psi}{\partial \eta}\right)\right) - N_1\frac{\partial}{\partial \eta}\left((\eta+\gamma)\frac{\partial w}{\partial \eta}\right)\right] - \frac{\gamma^2 Ha^2}{\eta+\gamma}\left(1-\frac{\partial \psi}{\partial \eta}\right) = 0. \quad (26)$

The transmuted boundary assumptions (17)–(18) are

$$\psi = -\frac{q}{2},\ \frac{\partial \psi}{\partial \eta} = 1,\ w = 0, \theta = 0,\ \phi = 0,\ \text{at}$$
$$\eta = h_1 = 1 + \lambda \sin x, \quad (27)$$
$$\psi = \frac{q}{2},\ \frac{\partial \psi}{\partial \eta} = 1,\ w = 0,\ \theta = 1,\ \phi = 1,\ \text{at}$$
$$\eta = h_2 = -1 - \lambda \sin x. \quad (28)$$

In the above set of equations, $\lambda = {}^{a}\!/_{w}$ symbolizes the amplitude ratio. Our objective is to compute the solution of Equations (22)–(24) and (26) subject to boundary conditions (27) and (28).

We summarized the following relations for pressure rise per wavelength (Δp), heat transfer coefficients $z_i (i = 1, 2)$, and expressions for Sherwood number $Sh_i (i = 1, 2)$ at the upper and lower wall surfaces in the following forms:

$$\Delta p = \int_0^{2\pi} \frac{dp}{dx} dx, \quad (29)$$

$$z_i = \left.\frac{\partial h_i}{\partial x}\frac{\partial \theta}{\partial \eta}\right|_{\eta = h_i},\ i = 1, 2. \quad (30)$$

$$Sh = \left.\frac{\partial h_i}{\partial x}\frac{\partial \phi}{\partial \eta}\right|_{\eta = h_i}.\ i = 1, 2. \quad (31)$$

NUMERICAL SOLUTION

In this, we numerically address the solution procedure of Equations (27), (28), and (30) subject to boundary conditions given in Equations (31) and (32). On this end, we adopted a famous finite difference procedure to perform such numerical simulations [52–54]. According to this method, simulations are performed by the following steps:

(i) As a first step, an iterative procedure has been compiled by transmuting non-linear flow equations into linear equations at the $(m+1)$th iterative step. Adopting such iterative process, we get

$$\frac{\partial^4\psi^{(m+1)}}{\partial\eta^4}+\frac{2}{(\eta+\gamma)}\frac{\partial^3\psi^{(m+1)}}{\partial\eta^3}-\frac{1}{(\eta+\gamma)^2}\frac{\partial^2\psi^{(m+1)}}{\partial\eta^2}+\left\{\frac{1}{(\eta+\gamma)^3}+\frac{\gamma^2Ha^2(1-N_1)}{(\eta+\gamma)^2}\right\}\frac{\partial\psi^{(m+1)}}{\partial\eta}$$
$$-N_1\frac{\partial^2w^{(m+1)}}{\partial\eta^2}-\frac{N_1}{(\eta+\gamma)}\frac{\partial w^{(m+1)}}{\partial\eta}-\frac{1}{(\eta+\gamma)^3}-\frac{\gamma^2Ha^2(1-N_1)}{(\eta+\gamma)^2}=0. \tag{32}$$

$$\frac{\partial^2\theta^{(m+1)}}{\partial\eta^2}+\frac{1}{(\eta+\gamma)}\frac{\partial\theta^{(m+1)}}{\partial\eta}+Br\left(\frac{1}{\eta+\gamma}\left(1-\frac{\partial\psi^{(m)}}{\partial\eta}\right)+w^{(m)}\right)\left(\frac{\partial^2\psi^{(m)}}{\partial\eta^2}+\frac{1}{\eta+\gamma}\left(1-\frac{\partial\psi^{(m)}}{\partial\eta}\right)(1+N_1)+N_1w^{(m)}\right)+$$
$$Br\left(\frac{\partial^2\psi^{(m)}}{\partial\eta^2}-w^{(m)}\right)\left(\frac{\partial^2\psi^{(m)}}{\partial\eta^2}+\frac{1}{\eta+\gamma}\left(1-\frac{\partial\psi^{(m)}}{\partial\eta}\right)+N_1\left(\frac{\partial^2\psi^{(m)}}{\partial\eta^2}-w^{(m)}\right)\right)+N_2Br\left(\frac{\partial w^{(m)}}{\partial\eta}\right)^2=0, \tag{33}$$

$$\frac{\partial^2\phi^{(m+1)}}{\partial\eta^2}+\frac{1}{\eta+\gamma}\frac{\partial\phi^{(m+1)}}{\partial\eta}-R_c\phi^{(m+1)}=-SrSc\left(\frac{\partial^2\theta^{(m)}}{\partial\eta^2}+\frac{1}{(\eta+\gamma)}\frac{\partial\theta^{(m)}}{\partial\eta}\right)+R_c\,, \tag{34}$$

$$\psi^{m+1}=-\frac{q}{2},\ \frac{\partial\psi^{m+1}}{\partial\eta}=1,\ w^{m+1}=0,\ \theta^{(m+1)}=0,\ \phi^{(m+1)}=0,\ at\eta=h_1, \tag{35}$$

$$\psi^{(m+1)}=\frac{q}{2},\ \frac{\partial\psi^{(m+1)}}{\partial\eta}=1,\ w^{m+1}=0,\theta^{(m+1)}=1,\ \phi^{(m+1)}=1,\ at\eta=h_2. \tag{36}$$

In the above expression, m is the iterative step index. It is emphasized that the above transmuted set of equations is linear in $\psi^{(m+1)}$.

(ii) This step deals with utilization of finite difference approximations of $\psi^{(m+1)}$, $w^{(m+1)}$, $\theta^{(m+1)}$, and $\phi^{(m+1)}$ along with their derivatives into Equations (36)–(38), which results in a linear set of algebraic equations at each iterative step.

(iii) The solution of the algebraic set of equation constructed above gives the numerical results for $\psi^{(m+1)}$, $w^{(m+1)}$, $\theta^{(m+1)}$, and $\phi^{(m+1)}$. In order to develop the iterative process, we need initial guesses for $\psi^{(m)}$, $w^{(m)}$, $\theta^{(m)}$, and $\phi^{(m)}$ as each cross section. The simulations are performed up to a desirable accuracy of solution. The fast convergence solution has been obtained by employing a successive under-relaxation technique. The values at of $\tilde{\psi}^{(m+1)}$, $\tilde{w}^{(m+1)}$,$\tilde{\theta}^{(m+1)}$ and $\tilde{\phi}^{(m+1)}$ at the (m+1)th iterative step are determined as

$$\begin{aligned}\psi^{(m+1)}&=\psi^{(m)}+\tau(\tilde{\psi}^{(m+1)}-\psi^{(m)}),\\ w^{(m+1)}&=w^{(m)}+\tau(\tilde{w}^{(m+1)}-w^{(m)}),\\ \theta^{(m+1)}&=\theta^{(m)}+\tau(\tilde{\theta}^{(m+1)}-\theta^{(m)}),\\ \phi^{(m+1)}&=\phi^{(m)}+\tau(\tilde{\phi}^{(m+1)}-\phi^{(m)}),\end{aligned}$$

where τ denotes the under relaxation parameter. For excellent accuracy of the solution, the values of τ should be taken small. In

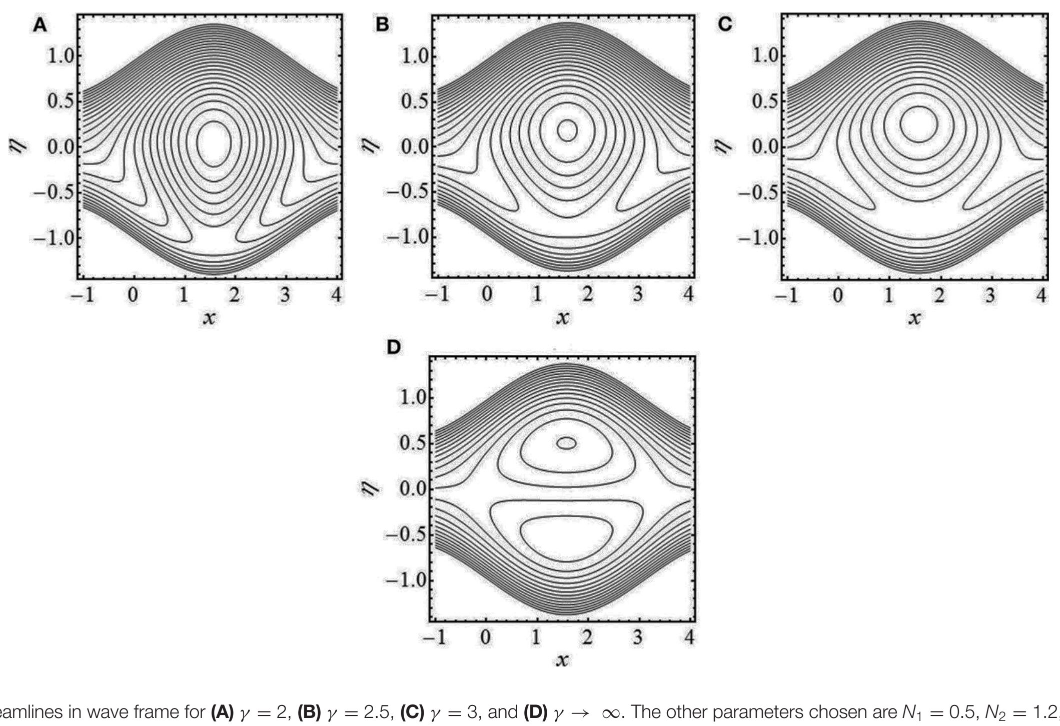

FIGURE 9 | Streamlines in wave frame for **(A)** $\gamma=2$, **(B)** $\gamma=2.5$, **(C)** $\gamma=3$, and **(D)** $\gamma\to\infty$. The other parameters chosen are $N_1=0.5$, $N_2=1.2$, and $\lambda=0.8$.

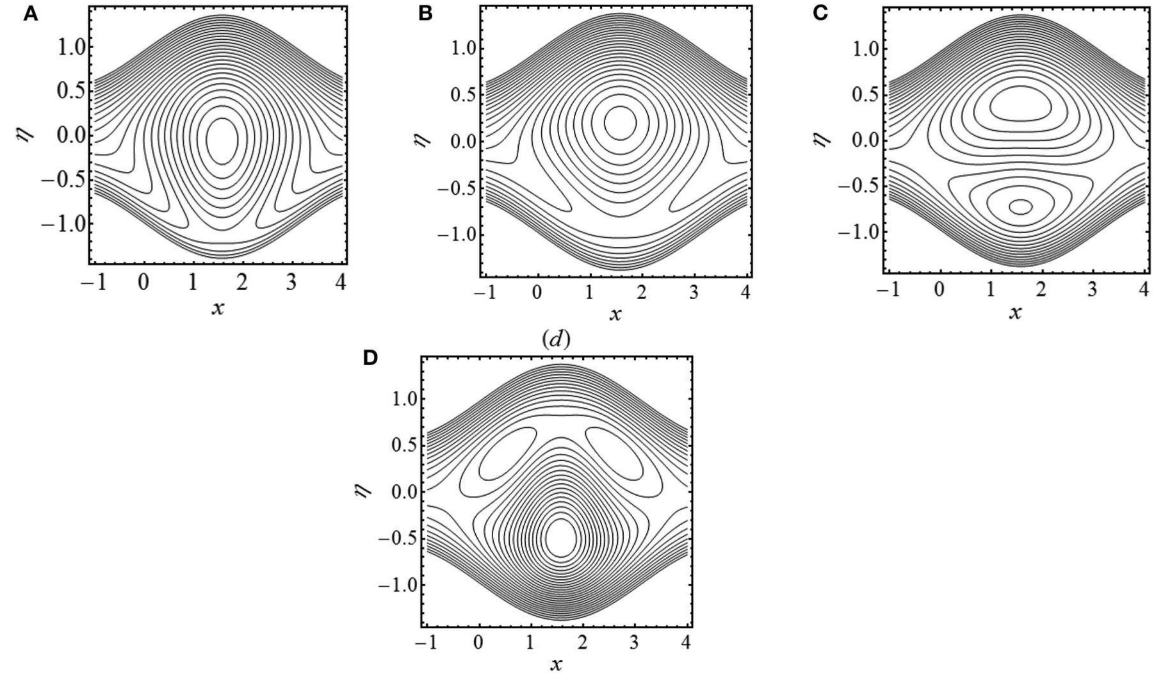

FIGURE 10 | Streamlines in wave frame for **(A)** $N_1 = 0.8$, **(B)** $N_1 = 1$, **(C)** $N_1 = 1.2$, and **(D)** $N_1 = 1.4$. The other parameters chosen are $Ha = 2$, $N_2 = 1.2$, $\gamma = 2.5$, and $\lambda = 0.8$.

the current situation, the convincing accuracy of 10^{-8} has been achieved for ψ, w, θ, and ϕ.

RESULTS AND DISCUSSION

To understand some momentous consequences of peristaltic aspects of flow features, pumping phenomenon, temperature distribution and trapping phenomenon for various values of coupling number (N_1), micropolar parameter (N_2), Brinkman number (Br) , Hartmann number (Ha), and curvature parameter (γ), various graphs are provided in **Figures 2–5** with relevant consequences. The heat transfer characteristics at both wall surfaces are also visualized.

The effects of Hartmann number (Ha) on axial velocity $u(\eta)$ and micro rotation $w(\eta)$ are shown in **Figures 2A,B**. **Figure 2A** shows that $u(\eta)$ reached at peak level with a larger variation of Ha at the upper channel level in contrast to the lower wall channel. **Figure 2B** exhibits the effect of Hartmann number (Ha) on micro-rotation $w(\eta)$. In the lower channel region, $w(\eta)$ boosted up with the increment of Ha while its behavior is reversed in the upper part. The decrease in velocity with increasing Ha in the lower part of the channel is attributed to the resistive nature of the Lorentz force due to the applied magnetic field. In order to maintain the prescribed flux, the velocity attained a peak variation in the upper channel portion due to Ha. **Figure 3A** displays the effects of N_1 on axial velocity. The parameter N_1 reflects the vortex to the dynamic viscosity ratio of the fluid. In fact, it is a measure of which viscosity dominates the flow under consideration. Larger values of N_1 correspond to the situation in which vortex viscosity due to spinning motion of fluid particles dominates the flow, and as a result, axial velocity $u(\eta)$ decreases in the upper channel region. In order to preserve the prescribed flow rate, the axial velocity $u(\eta)$ increases in the lower part of the channel with increasing N_1. **Figure 3B** shows an enhancement in the magnitude of micro-rotation component $w(\eta)$ with increasing N_1 in both parts of the channel. **Figure 4A** shows the impact of micropolar parameter (N_2) on $u(\eta)$. It is observed that $u(\eta)$ increases with increasing N_2 in the lower part of the channel. In contrast, $u(\eta)$ decreases with increasing (N_2) in the upper part of the channel. **Figure 4B** shows the effect of N_2 on $w(\eta)$. It is observed that $w(\eta)$ decreases in the lower portion of the channel while it increases in the upper portion with increasing N_2.

Figures 5A–C exhibit the effect of Hartmann number (Ha), coupling number (N_1), micropolar parameter (N_2), and curvature parameter (γ) on pressure rise per wavelength (Δp). The profiles of the pressure rise per wavelength for different values of Ha (Hartmann number) and coupling number (N_1) are shown in **Figures 5A,B**. It is observed that in pumping region $\left(\Theta > 0,\ \Delta p > 0\right)$, the pressure rise per wavelength increases with increasing Ha and N_1. The situation is different in the free pumping ($\Delta p = 0$) and co-pumping regions ($\Theta > 0$, $\Delta p < 0$). Here, Δp decreases by increasing Ha and N_1. **Figure 5C** shows the effects of micropolar parameter (N_2) on Δp. In the case of the micropolar parameter, an opposite trend is observed as seen in the figure.

The profiles of the temperature field for different values of the Brinkman number (Br), Hartmann number (Ha), coupling number (N_1), and micropolar parameter (N_2) are shown in **Figures 6A–D**. It is noted that θ increases over the entire cross section with each increase in Br,N_1, and N_2. The increase in θ with increasing N_1 and N_2 is due to the retarding effect of these parameters on velocity $u(\eta)$. The Brinkman number is a parameter which is the ratio of viscous heat to the heat transported by conduction. Larger values of Brinkman correspond to the scenario when heat generated due to viscous dissipation is dominant. In such situation, an enhanced temperature distribution in the channel has been justified. **Figure 6D** shows that θ decreases with increasing Ha. In order to determine how heat transfer coefficient z is altered for diverse values of Ha, N_1 and N_2 are displayed in **Figures 7A–C**. The behavior of z is clearly oscillating which is attributed to the oscillatory nature of the channel walls. A damping in amplitude of oscillations is observed with increasing Ha. The effects of Br (Brinkman number), R_c (rate of chemical reaction), Ha (Hartmann number), Sc (Schmidt number), and Sr (Soret number) on mass concentration ($\phi(\eta)$) can be observed in **Figures 8A–E**. It is observed that $\phi(\eta)$ is enhanced with increasing Br, R_c, Sc, and Sr. On the contrary, $\phi(\eta)$ turns down by varying Ha. The streamlines of flow inside the channel for different values of curvature parameter (γ) and coupling number (N_1) are shown in **Figures 9**, **10**. The objective is to investigate the trapping phenomenon. **Figure 9** shows the effect of the curvature parameter on streamlines. We noticed that for minimum values of γ, the fluid bolus has been concentrated in the upper channel region which is divided into symmetric parts due to increment in γ. The physical consequences of coupling number N_1 on streamlines are investigated by preparing **Figure 10**. Similar to earlier observations, the fluid bolus concentrated in the upper channel portion exists for lesser variation of coupling number ($N_1 = 0.8, 1$). The bolus has been ripped into two shapes as N_1 gets maximum values. However, the upper part is relatively bigger as compared to the lower part. The lower part of the bolus increases in size with increasing N_1 to 1.4. It is strongly anticipated that the upper part of the bolus vanishes with further increasing N_1 and the channel is only filled with a single bolus concentrated in the lower part.

CONCLUDING REMARKS

We have reported the transportation of the heat/mass phenomenon in the peristaltic study of micropolar liquid in a curved channel. The flow model is constructed via relevant equations which are treated numerically by employing the finite difference procedure. We summarized important observations from the current analysis in the following points:

- ❖ The axial velocity increases with impact of the micropolar parameter in the vicinity of the lower boundary whereas it shows an opposite behavior in the upper channel surface.
- ❖ The axial component of velocity attained the same trend due to variation of coupling number and Hartmann number.
- ❖ The pressure rise per wavelength increases with increasing Ha and N_1 in the pumping region.
- ❖ The temperature inside the channel follows an increasing trend with increasing N_1 and N_2. However, it shows a declining variation due to the impact of Ha.
- ❖ The concentration of fluid attained maximum variation with Br and R_c.
- ❖ The fluid bolus in the upper wall surface is split up into two parts as $\boldsymbol{N_1}$ assigned leading numerical values.
- ❖ The streamline symmetry trend has been visualized when $\gamma \to \infty$.

DATA AVAILABILITY STATEMENT

The datasets generated for this study are available on request to the corresponding author.

AUTHOR CONTRIBUTIONS

All authors listed have made a substantial, direct and intellectual contribution to the work, and approved it for publication.

REFERENCES

1. Raju KK, Devanathan R. Peristaltic motion of non-Newtonian fluid, Part-I. *Rheol Acta.* (1972) **11**:170–8. doi: 10.1007/BF01993016
2. Mekheimer S. Non-linear peristaltic transport of magnetohydrodynamic flow in an inclined planar channel. *Arab J Sci Eng.* (2003) **28**:183–201.
3. Abd El Hakeem Abd El Naby, El Misery AEM, Abd El Kareem FM. Separation in the flow through peristaltic motion of a carreau fluid in uniform tube. *Phys A.* (2004) **343**:1–14. doi: 10.1016/j.physa.2004.05.072
4. Elshahed M, Haroun MH. Peristaltic transport of Johnson-Segalman fluid under effect of a magnetic field. *Math Prob Eng.* (2005) **6**:663–77. doi: 10.1155/MPE.2005.663
5. Abd El Hakeem Abd El Naby, El Misery AEM, Abd El Kareem FM. Effects of a magnetic field on trapping through peristaltic motion for generalized Newtonian fluid in channel. *Phys A.* (2006) **367**:79–92. doi: 10.1016/j.physa.2005.10.045
6. Hayat T, Ali N, Asghar S. Peristaltic motion of a Burger's fluid in a planar channel. *Appl Math Comput.* (2007) **186**:309–29. doi: 10.1016/j.amc.2006.07.098
7. Haroun MH. Effect of Deborah number and phase difference on peristaltic transport of a third order fluid in an asymmetric channel. *Commun Nonlin Sci Numerical Simul.* (2007) **12**:1464–80. doi: 10.1016/j.cnsns.2006.03.002
8. Wang Y, Hayat T, Ali N, Oberlack M. Magnetohydrodynamic peristaltic motion of a Sisko fluid in a symmetric or asymmetric channel. *Phys A.* (2008) **387**:347–62. doi: 10.1016/j.physa.2007.10.020
9. Ali N, Wang Y, Hayat T, Oberlack O. Slip effects on the peristaltic flow of a third grade fluid in a circular cylindrical tube. *J Appl Mech.* (2009) **76**:1–10. doi: 10.1115/1.2998761
10. Hayat T, Bibi S, Alsaadi F, Rafiq M. Peristaltic transport of Prandtl-Eyring liquid in a convectively heated curved channel. *PLoS ONE.* (2016) **11**:e0156995. doi: 10.1371/journal.pone.0156995
11. Maimona Rafiq, H.Yasmin, Hayat T, Alsaadi F. Effect of Hall and ion-slip on the peristaltic transport of nanofluid: a biomedical application. *Chin J Phys.* (2019) **60**:208–27. doi: 10.1016/j.cjph.2019.04.016
12. Ahmed B, Javed T. A study of full Navier-Stokes equations of peristaltic flow in a porous-saturated tube under the inducement of magnetic field: finite element analysis. *Chaos Solitons Fractals.* (2019) **125**:79–87. doi: 10.1016/j.chaos.2019.05.012
13. Asha SK, Sunitha G. Thermal radiation and Hall effects on peristaltic blood flow with double diffusion in the presence of nanoparticles. *Case Stud Therm Eng.* (2020) **17**:100560. doi: 10.1016/j.csite.2019.100560
14. Pietal AK. Flow past a sphere moving towards a wall in micropolar fluid. *J Theoret Appl Mech.* (1999) **37**:2.

15. Eringen AC. Some micro fluids. *Int J Eng Sci*. (1964) **2**:205–17. doi: 10.1016/0020-7225(64)90005-9
16. Eringen AC. *Microcontinuum Field Theories. II Fluent Media*. New York, NY: Springer Verlag (2001).
17. Ariman T, Turk MA, Sylvester N. Application of microcontinum fluid mechanics. *Int J Eng Sci*. (1974) **12**:273–93. doi: 10.1016/0020-7225(74)90059-7
18. Na TY, Pop I. Boundary-layer flow of a micropolar fluid due to a stretching wall. *Arch Appl Mech*. (1997) **67**:229–36. doi: 10.1007/s004190050113
19. Srinivasacharya D, Mishra M, Rao RA. Peristaltic pumping of a micropolar fluid in a tube. *Acta Mech*. (2003) **161**:165–78. doi: 10.1007/s00707-002-0993-y
20. Muthu P, Rathish Kumar BV, Chandra P. On the influence of wall properties in the peristaltic motion of micropolar fluid. *ANZIAM J*. (2003) **2**:245–60. doi: 10.1017/S1446181100013304
21. Lok YY, Amin N, Pop I. Steady mixed convection flow of a micropolar fluid near the stagnation point on a vertical surface. *Int J Numerical Methods Heat Fluid Flow*. (2005) **15**: 654–70. doi: 10.1108/09615530510613861
22. Hayat T, Ali N, Abbas Z. Peristaltic flow of a micropolar fluid in a channel with different wave forms. *Phys Lett A*. (2007) **370**:331–44. doi: 10.1016/j.physleta.2007.05.099
23. Ali N, Hayat T. Peristaltic flow of a micropolar fluid in an asymmetric channel. *Comp Math Appl*. (2008) **55**:589–608. doi: 10.1016/j.camwa.2007.06.003
24. Hayat T, Ali N. Effects of an endoscope on peristaltic flow of a micropolar fluid. *Math Comp Model*. (2008) **48**:721–33. doi: 10.1016/j.mcm.2007.11.004
25. Mekheimer Kh S. Peristaltic flow of a magneto-micropolar fluid: effect of induced magnetic field. *J Appl Math*. (2008) **23**:570825. doi: 10.1155/2008/570825
26. Ishak A, Nazar R, Pop I. Magnetohydrodynamic (MHD) flow of a micropolar fluid towards a stagnation point on a vertical surface. *Comput Math Appl*. (2008) **56**:3188–94. doi: 10.1016/j.camwa.2008.09.013
27. Kh. Mekheimer S, El Kot MA. The micropolar fluid model for blood flow through a tapered artery with a stenosis. *Acta Mech Sin*. (2008) **24**:637–44. doi: 10.1007/s10409-008-0185-7
28. Sajid M, Abbas Z, Hayat T. Homotopy analysis for boundary layer flow of a micropolar fluid through a porous channel. *Appl Math Model*. (2009) **33**:4120–5. doi: 10.1016/j.apm.2009.02.006
29. Ashraf M, Anwar Kamala M, Syeda KS. Numerical study of asymmetric laminar flow of micropolar fluids in a porous channel. *Comput Fluids*. (2009) **38**:1895–902. doi: 10.1016/j.compfluid.2009.04.009
30. Rashidi MM, Mohimanian Pour SA, Laraqi N. A semi-analytical solution of micropolar flow in a porous channel with mass injection by using differential transform method. *Nonlin Anal Model*. (2010) **15**:341–50. doi: 10.15388/NA.15.3.14329
31. Ali N. Sajid M. Javed T. Abbas Z. An analysis of peristaltic flow of a micropolar fluid in a curved channel. *Chin Phys Lett*. (2010) **28**:0147041–4. doi: 10.1088/0256-307X/28/1/014704
32. El–Dabe NT, Abou-zeid MY. The wall properties effect on peristaltic transport of micropolar non-Newtonian fluid with heat and mass transfer. *Math Prob Eng*. (2010) **2010**:898062. doi: 10.1155/2010/898062
33. Abd Elmaboud Y. Thermo micropolar fluid flow in a porous channel with peristalsis. *Porous Media J*. (2011) **14**:1033–45. doi: 10.1615/JPorMedia.v14.i11.70
34. Sui J, Zhao P, Cheng Z, Zheng L, Zhang X. A novel investigation of a micropolar fluid characterized by nonlinear constitutive diffusion model in boundary layer flow and heat transfer. *Phys Fluids*. (2017) **29**:023105. doi: 10.1063/1.4976642
35. Waqas H, Imran M, Khan SU, Shehzad SA, Meraj MA. Slip flow of Maxwell viscoelasticity-based micropolar nano particles with porous medium: a numerical study. *Appl Math Mech*. (2019) **40**:1255–68. doi: 10.1007/s10483-019-2518-9
36. Waqas H, Khan SU, Shehzad SA, Imran M. Radiative flow of Maxwell nanofluids containing gyrotactic microorganism and energy activation with convective Nield conditions. *Heat Transf Asian Res*. (2019) **48**:1663–87. doi: 10.1002/htj.21451
37. Ali N, Atif HM, Javed MA, Sajid M. A mathematical model of the calendered exiting thickness of micropolar sheet. *Polym Eng Sci*. (2018) **58**:327–34. doi: 10.1002/pen.24578
38. Ahmed R, Ali N, Javid K. Heat and mass transfer effects on the peristaltic flow of Sisko fluid in a curved channel. *Therm Sci*. (2017) **23**:331–45. doi: 10.2298/TSCI161018115A
39. Mekheimer Kh S, Hasona WM, Zaher AZ. Peristaltic blood flow with gold nanoparticles as a third grade nanofluid in catheter: application of cancer therapy. *Phys Lett A*. (2018) **382**:85–93. doi: 10.1016/j.physleta.2017.10.042
40. Abo-Elkhair R, Mekheimer Kh S, Zaher AZ. Electro-Magnetohydrodynamic oscillatory flow of a dielectric fluid through a porous medium with heat transfer: Brinkman model. *Bionanoscience*. (2018) **8** 596–608. doi: 10.1007/s12668-018-0515-6
41. Mekheimer Kh S, Zaher AZ, Abdellateef AI. Entropy hemodynamics particle-fluid suspension model through eccentric catheterization for time-variant stenotic arterial wall: Catheter injection. *Int J Geometric Methods Modern Phys*. (2019) **16**:1950164. doi: 10.1142/S0219887819501640
42. Mekheimer Kh S, Hassona WM, El-Shekhipy AA, Zaher AZ. Electrokinetics of dielectric non-newtonian bio fluids with heat transfer through a flexible channel: numerical study. *Comput Methods Sci Technol*. (2017) **23**:331–41. doi: 10.12921/cmst.2017.0000020
43. Nadeem S, Abbas N, Malik MY. Inspection of hybrid based nanofluid flow over a curved surface. *Comp Methods Prog Biomed*. (2020) **189**: 105193. doi: 10.1016/j.cmpb.2019.105193
44. Nadeem S, Abbas N, Elmasry Y, Malik MY. Numerical analysis of water based CNTs flow of micropolar fluid through rotating frame. *Comp Methods Prog Biomed*. (2019) **186**:105194. doi: 10.1016/j.cmpb.2019.105194
45. Abbas N, Malik MY, Nadeem S. Transportation of magnetized micropolar hybrid nanomaterial fluid flow over a Riga curface surface. *Comput Methods Prog Biomed*. (2020) **185**:105136. doi: 10.1016/j.cmpb.2019.105136
46. Sadaf H, Nadeem S. Fluid flow analysis of cilia beating in a curved channel in the presence of magnetic field and heat transfer. *Can J Phys*. (2020) **98**:191. doi: 10.1139/cjp-2018-0715
47. Nadeem S, Malik MY, Abbas N. Heat transfer of three-dimensional micropolar fluid on a Riga plate. *Can J Phys*. (2019) **98**:32–8. doi: 10.1139/cjp-2018-0973
48. Muhammad N, Nadeem S, Issakhov A. Finite volume method for mixed convection flow of Ag–ethylene glycol nanofluid flow in a cavity having thin central heater. *Phys A*. (2020) **537**:122738. doi: 10.1016/j.physa.2019.122738
49. Abbas N, Malik MY, Nadeem S. Stagnation flow of hybrid nanoparticles with MHD and slip effects. *Heat Trnasf Asian Res*. (2020) 180–96. doi: 10.1002/htj.21605
50. Hayat T, Khan WA, Abbas SZ, Nadeem S, Ahmad S. Impact of induced magnetic field on second-grade nanofluid flow past a convectively heated stretching sheet. *Appl Nanosci*. (2020). doi: 10.1007/s13204-019-01215-x. [Epub ahead of print].
51. B. Mallick J, Misra C. Peristaltic flow of Eyring-Powell nanofluid under the action of an electromagnetic field. *Eng Sci Technol Int J*. (2019) **22**:266–81. doi: 10.1016/j.jestch.2018.12.001
52. Ali N, Khan SU, Abbas Z. Hydromagnetic flow and heat transfer of a Jeffrey fluid over an oscillatory stretching surface. *Z Naturforsch*. (2015) **70**:567–76. doi: 10.1515/zna-2014-0273
53. Khan SU, Ali N, Abbas Z. Hydromagnetic flow and heat transfer over a porous oscillating stretching surface in a viscoelastic fluid with porous medium. *PLoS ONE*. (2015) **10**:e0144299. doi: 10.1371/journal.pone.0144299
54. Ali N, Khan SU, Abbas Z, Sajid M. Slip effects in the hydromagnetic flow of a viscoelastic fluid through porous medium over a porous oscillatory stretching sheet. *J Porous Media*. (2017) **20**:249–62. doi: 10.1615/JPorMedia.v20.i3.50

Conflict of Interest: The authors declare that the research was conducted in the absence of any commercial or financial relationships that could be construed as a potential conflict of interest.

Copyright © 2020 Ahmed, Ali, Khan, Rashad, Nabwey and Tlili. This is an open-access article distributed under the terms of the Creative Commons Attribution License (CC BY). The use, distribution or reproduction in other forums is permitted, provided the original author(s) and the copyright owner(s) are credited and that the original publication in this journal is cited, in accordance with accepted academic practice. No use, distribution or reproduction is permitted which does not comply with these terms.

NOMENCLATURE

j	micro moment of inertia	$[ML^2]$	B^*	magnetic field	$[Wbm^{-2}]$
λ, λ'	amplitude ratio	$[m]$	T	temperature	$[K]$
ρ	density	$[kgm^{-3}]$	k^*	thermal conductivity	$[Wm^{-1}K^{-1}]$
Φ	dissipation function	$[kgm^{-1}s^{-3}]$	u_1, u_2	velocity component	$[ms^{-1}]$
C	mass concentration	$[kg]$	μ	viscosity parameter	$[kgm^{-1}s^{-1}]$
T_m	mean fluid temperature	$[K]$	c	wave speed	$[ms^{-1}]$
D	coefficient of mass diffusivity	$[m^2s^{-1}]$	$\alpha^*, \beta^*, \gamma,^*$	coefficient of angular velocity	$[MLT^{-1}]$

frontiers in Physics

ORIGINAL RESEARCH
published: 24 July 2020
doi: 10.3389/fphy.2020.00246

Triple Diffusive Unsteady Flow of Eyring–Powell Nanofluid Over a Periodically Accelerated Surface With Variable Thermal Features

*Sami Ullah Khan[1], Hanumesh Vaidya[2], Wathek Chammam[3], Sa'ed A. Musmar[4], K. V. Prasad[2] and Iskander Tlili[5,6]**

[1] Department of Mathematics, COMSATS University Islamabad, Sahiwal, Pakistan, [2] Department of Mathematics, Vijayanagara Sri Krishnadevaraya University, Karnataka, India, [3] Department of Mathematics, College of Science Al-Zulfi, Majmaah University, Al Majma'ah, Saudi Arabia, [4] Industrial Engineering Department, The University of Jordan, Amman, Jordan, [5] Department for Management of Science and Technology Development, Ton Duc Thang University, Ho Chi Minh City, Vietnam, [6] Faculty of Applied Sciences, Ton Duc Thang University, Ho Chi Minh City, Vietnam

This research communicates the triple diffusion perspective of Eyring–Powell nano-materials configured by a periodically moving configuration. The thermal consequences of variable natures are utilized as a novelty. Combined magnetic and porous medium effects are also involved, which result in a magneto-porosity parameter. The thermophoretic and Brownian motion aspects are reported by using Buongiorno's nanofluid theory. The formulated flow equations in non-dimensional forms are tackled with the implementation of a homotopy analysis algorithm. A detailed physical investigation against derived parameters is presented graphically. Due to periodically accelerated surface, the oscillations in velocity and wall shear stress have been examined.

Keywords: eyring–powell nanofluid, triple diffusion, variable thermal conductivity, oscillatory stretching sheet, homotopy analysis method

OPEN ACCESS

Edited by:
Muhammad Mubashir Bhatti, Shanghai University, China

Reviewed by:
Kh S. Mekheimer, Al-Azhar University, Egypt
Mohammad Rahimi Gorji, Ghent University, Belgium

Correspondence:
Iskander Tlili
iskander.tlili@tdtu.edu.vn

Specialty section:
This article was submitted to Mathematical and Statistical Physics, a section of the journal Frontiers in Physics

Received: *28 March 2020*
Accepted: *04 June 2020*
Published: *24 July 2020*

Citation:
Khan SU, Vaidya H, Chammam W, Musmar SA, Prasad KV and Tlili I (2020) Triple Diffusive Unsteady Flow of Eyring–Powell Nanofluid Over a Periodically Accelerated Surface With Variable Thermal Features. Front. Phys. 8:246. doi: 10.3389/fphy.2020.00246

INTRODUCTION

Recent advances in nanotechnology have discovered an advanced source of energy based on utilization nanoparticles. Nanofluids have been interacted for the impressive thermal properties that turn into enhancement of energy transportation. The enhancement of thermo-physical features of conventional base liquids with the addition of micro-sized metallic particles is a relatively new and interesting development in nanotechnology. Nanoparticles attain microscopic size, having a range between 1 and 100 nm. Recently, the investigations on nano-materials become a new class of intense engineering research due to inherent significances in biomedical, chemical, and mechanical industries, electronic field, nuclear reactors, power plants, cooling systems, diagnoses, diseases, etc. The primary investigation on this topic was reported by Choi [1], which was further worked out by several scientists, especially in the current century. The convective features for nano-materials based on thermophoresis and Brownian movement phenomenon were notified by Buongiorno [2]. This investigation revealed that the role of thermophoresis and Brownian motion factors was quite essential for convective slip mechanism. Khan and Pop [3] discussed the feature of nanofluid immersed in base material confined by moving configuration. Sheikholeslami et al. [4] reported the features of thermal radiation in magneto-nanoparticle flow between circular cylinders. The slip flow in nano-material due to porous surface has been reported by

Shahzadi et al. [5]. Khan et al. [6] directed their investigation regarding stability prospective of nanoliquids in a curved geometry and successfully estimated a dual solution for the formulated problem. Turkyilmazoglu [7] imposed zero mass flux constraints regarding asymmetric channels filled by nanoparticles. Vaidya et al. [8] enrolled the fundamental thermal characteristics in the three-dimensional (3D) flow of Maxwell nanofluid where analytical expressions were developed by using optimal homotopic procedure. Hayat et al. [9] focused on the thermal properties and developed the 3D flow of Oldroyd-B fluid featuring mixed convection effects. Some valuable closed-form expressions for a nanofluid flow problem in porous space have been computed by Turkyilmazoglu [10]. Krishna and Chamkha [11] investigated the ion and hall slip effects in the rotating flow of nanofluid configured by a vertical porous plate. The enhancement of heat transfer by using hybrid nanofluids having variable thermal viscosity was reported by Manjunatha et al. [12]. Sardar et al. [13] used non-Fourier's expressions for Carreau nanofluid and suggested some useful multiple numerical solutions successfully. Alwatban et al. [14] performed a numerical analysis to examine the rheological consequences in Eyring–Powell fluid subjected to the second-order slip along with activation energy. The stability analysis for bioconvection flow of nanofluid was reported by Zhao et al. [15]. Alkanhal et al. [16] involved thermal radiation and external heat source for nanofluid enclosed by a wavy shaped cavity. Kumar et al. [17] discussed the thermo-physical properties of hybrid ferrofluid in thin-film flow impacted by uniform magnetic field. Bhattacharyya et al. [18] evaluated the characteristics of different carbon nanotubes for coaxial movement of disks. Mekheimer and Ramdan [19] investigated the flow of Prandtl nanofluid in the presence of gyrotactic microorganisms over a stretching/shrinking surface.

Recently, researchers specified their attention toward the complex and interesting properties of non-Newtonian meterials due to their miscellaneous application in many industries and technologies. The non-Newtonian materials due to convoluted features attracted special attention especially in the current century. The novel physical importance of such non-Newtonian liquids in various engineering and physical processes, biological sciences, physiology, and manufacturing industries is associated due to complex rheological features. Some useful applications associated with the non-Newtonian fluids include polymer solutions, certain oil, petroleum industries, blood, honey, lubricants, and many more. It is commonly observed that distinctive features of such non-Newtonian fluid cannot be pointed out via single relation. Therefore, different non-Newtonian fluid models are suggested by investigators according to their rheology. Among these, Eyring–Powell fluid is inferred from kinetic laws of gases instead of any empirical formulas. This model reduces the viscous fluid at both low and high shear rates (see Powell and Eyring [19]). Gholinia et al. [20] carried out the homogenous and heterogeneous impact in flow of Powell–Eyring liquid due to rotating. Khan et al. [21] focused on viscosity-dependent mixed convection flow of Eyring–Powell nanofluid encountered by inclined surface. Salawu and Ogunseye [22] reported the entropy generation prospective in Eyring–Powell nanofluid featuring variable thermal consequences and electric field. Another useful continuation performed by Abegunrin et al. [23] examined the change in the boundary layer for the flow of Eyring–Powell fluid subjected by the catalytic surface reaction. Rahimi et al. [24] adopted a numerical technique to compute the numerical solution of a boundary value problem modeled due to the flow of Eyring–Powell fluid. Reddy et al. [25] involved some interesting thermal features, like activation energy, chemical reaction, and non-linear thermal radiation in the 3D flow of Eyring–Powell nanofluid induced via slandering surface. Hayat and Nadeem [26] examined the flow of Eyring–Powell fluid and suggested modification in energy and concentration expressions by using generalized Fourier's law. Ghadikolaei et al. [27] reported the Joule heating and thermal radiation features inflow of Eyring–Powell non-Newtonian fluid in a stretching walls channel.

The double diffusion convection is a natural phenomenon that encountered multiple novel applications in area soil sciences, groundwater, oceanography, petroleum engineering, food processing, etc. The double-diffusive convection refers to the intermixing of components of two fluid having different diffuse rates. However, the situation becomes quite interesting when double-diffusive convection depends upon more than two components of fluids. Examples of such multiple diffusive phenomenons include seawater, molten alloy solidification, and geothermally heated lakes. The triple diffusion flow appears in diverse engineering and scientific fields like geology, astrophysics, disposals of nuclear waste, deoxyribonucleic acid (DNA), chemical engineering, etc. [28–30].

After careful observation of the previously cited work, it is claimed that no efforts have been made to report the triple diffusion flow of Eyring–Powell nanofluid induced by an oscillatory stretching surface with variable thermal features. Although some investigations on flow that is due to periodical acceleration have been available in the literature, thermodiffusion features for Eyring–Powell nanofluid are not studied yet. Therefore, our prime objective of this contribution is to report the triple diffusion aspects of Eyring–Powell nanofluid flow by using variable thermal properties. The most interesting convergent technique homotopy analysis procedure is followed to simulate the solution [31–35]. The graphs are prepared to see the impact of different flow parameters with relevant physical consequence.

FLOW PROBLEM

To develop governing equations for unsteady flow of Eyring–Powell nanofluid, we have considered a periodically stretching surface where x-axis is assumed along with the stretched configuration, whereas y-axis is taken normally. The source of induced flow is based on the periodically moving surface where amplitude of oscillations are assumed to be small. Let velocity of the moving surface as $u = u_\omega = bx \sin \omega t$, b as stretching rate, ω being angular frequency, whereas t represent time. The uniform features of the magnetic field are reported by implementing it vertically. Let T represent the temperature, C solutal concentration, whereas Φ report the nanoparticle volume fraction. Furthermore, T_∞, C_∞, and Φ_∞ denote free stream nanoparticle temperature, free stream solutal concentration, and volume fraction of nanofluid, respectively. After using such assumptions, the flow problem is modeled through the following equations [22, 33]:

$$\frac{\partial u}{\partial x}+\frac{\partial v}{\partial y}=0, \tag{1}$$

$$u\left(\frac{\partial u}{\partial x}\right)+v\left(\frac{\partial u}{\partial y}\right)+\frac{\partial u}{\partial t}=\left(\nu+\frac{1}{\rho_f\beta^* C}\right)\left(\frac{\partial^2 u}{\partial y^2}\right)-\frac{1}{2\rho\beta^* C^3}\left[\left(\frac{\partial u}{\partial y}\right)^2\frac{\partial^2 u}{\partial y^2}\right]-\left(\frac{\sigma B_0^2}{\rho_f}+\frac{\nu\vartheta}{k'}\right)u, \tag{2}$$

$$u\left(\frac{\partial T}{\partial x}\right)+\left(\frac{\partial T}{\partial y}\right)+\frac{\partial T}{\partial t}=\frac{1}{(\rho c)_p}\frac{\partial}{\partial y}\left(K(T)\frac{\partial T}{\partial y}\right)+\tau_T\left[D_T\frac{\partial\phi}{\partial y}\frac{\partial T}{\partial y}+\frac{D_T}{T_\infty}\left(\frac{\partial T}{\partial y}\right)^2\right]+DK_{TC}\left(\frac{\partial^2 C}{\partial y^2}\right), \tag{3}$$

$$u\left(\frac{\partial C}{\partial x}\right)+v\left(\frac{\partial C}{\partial y}\right)+\frac{\partial C}{\partial t}=D_s\left(\frac{\partial^2 C}{\partial y^2}\right)+DK_{CT}\left(\frac{\partial^2 T}{\partial y^2}\right), \tag{4}$$

$$u\left(\frac{\partial \Phi}{\partial x}\right)+v\left(\frac{\partial \Phi}{\partial y}\right)+\frac{\partial \Phi}{\partial t}=D_B\left(\frac{\partial^2 \Phi}{\partial y^2}\right)+\frac{D_T}{T_\infty}\left(\frac{\partial^2 T}{\partial y^2}\right), \tag{5}$$

where ν is viscosity, ρ_f fluid density, (β^*, C) fluid parameters, ϑ permeability of porous medium, σ_e electrical conductivity, α_1 thermal diffusivity, DK_{TC} Dufour diffusivity, $\tau_T = (\rho c)_p/(\rho c)_f$ ratio of heat capacity of nanoparticles to heat capacity of fluid, D_B Brownian diffusion coefficients, D_s solutal diffusivity, D_T thermophoretic diffusion coefficient, whereas DK_{CT} Soret diffusivity.

Following boundary assumptions are articulated for current flow problem

$$u = u(x,t) = u_w \sin\omega t = bx\sin\omega t,\quad v = 0,$$
$$T = T_w,\ C = C_w, \Phi = \Phi_w \text{ at } y = 0, \tag{6}$$
$$u \to 0,\ v \to 0,\ T \to T_\infty,\ C \to C_\infty, \Phi \to \Phi_\infty \text{ at } y \to \infty. \tag{7}$$

In order to suggest modification in energy equation (3), we used the following relations for variable thermal conductivity [33, 34]

$$K(T) = K_\infty\left[1+\varepsilon\frac{(T-T_\infty)}{\Delta T}\right], \tag{8}$$

where K_∞ ambient fluid conductivity and ε thermal dependence conductivity constant. Now, before perfume analytical simulations, first, we reduce the number of independent variables in the governing equations by using the following variables:

$$\xi = \left(\frac{b}{\nu}\right)^{1/2} y,\ \tau = t\omega,\ u = u_w f_y(\xi,\tau),$$
$$v = -\sqrt{\nu b} f(\xi,\tau), \tag{9}$$
$$\theta(\xi,\tau) = \frac{(T-T_\infty)}{(T_w-T_\infty)}, \varphi(\xi,\tau) = \left(\frac{(C-C_\infty)}{C_w-C_\infty}\right), \phi(\xi,\tau) = \frac{(\Phi-\Phi_\infty)}{(\Phi_w-\Phi_\infty)}, \tag{10}$$

The dimensionless set of equations in view of the previously mentioned transformations is

$$(1+K) f_{\xi\xi\xi} - Sf_{\xi\tau} - f_\xi^2 + ff_{\xi\xi} - \Omega f_\xi - \Gamma K f_{\xi\xi}^2 f_{\xi\xi\xi} = 0, \tag{11}$$

$$(1+\delta\theta)\theta_{\xi\xi} + \delta(\theta_\xi)^2 + \Pr\left[f\phi_\xi - S\phi_\tau + Nb\theta_\xi\phi_\xi + Nt(\theta_\xi)^2 + (Nd)\varphi_{\xi\xi}\right] = 0, \tag{12}$$

$$\varphi_{\xi\xi} - S\varphi_\tau + Le(f\varphi_\xi) + Ld\theta_{\xi\xi} = 0, \tag{13}$$

$$\phi_{\xi\xi} - S\phi_\tau + Ln(f\phi_\xi) + \frac{Nt}{Nb}\theta_{\xi\xi} = 0, \tag{14}$$

The boundary constraints in the non-dimensional form are

$$f_\xi(0,\tau) = \sin\tau,\ f(0,\tau) = 0,$$
$$\theta(0,\tau) = 1,\ \varphi(0,\tau) = 1, \phi(0,\tau) = 1, \tag{15}$$
$$f_y(\infty,\tau) \to 0, \theta(\infty,\tau) \to 0, \varphi(\infty,\tau) \to 0, \phi(\infty,\tau) \to 0, \tag{16}$$

where $K = 1/\mu\beta^* C$ and $\Gamma = u_w{}^2 b/2\nu C^2$ denote the material parameters, $\Omega = \sigma B_0^2/\rho_f b + \nu\vartheta/k' b$ is magneto-porosity constant, $S = \omega/b$ oscillating frequency-to-stretching rate ratio, $N_t = (\rho c)_p D_T (T_w - T_\infty)/(\rho c)_f T_\infty \nu$ thermophoresis parameter, $\Pr = \nu/\alpha_m$ is Prandtl number, $N_b = (\rho c)_p D_B (C_w - C_\infty)/(\rho c)_f \nu$ Brownian motion constant, $Nd = D_{TC}(C_w - C_\infty)/\alpha_m (T_w - T_\infty)$ modified Dufour number, $Ld = D_{CT}(T_w - T_\infty)/\alpha_m(C_w - C_\infty)$ Dufour Lewis number, $Le = \nu/D_s$ regular Lewis number, whereas $Ln = \nu/D_B$ nano-Lewis number.

We define the following relations associated with the definitions of wall shear stress, local Nusselt number, Sherwood

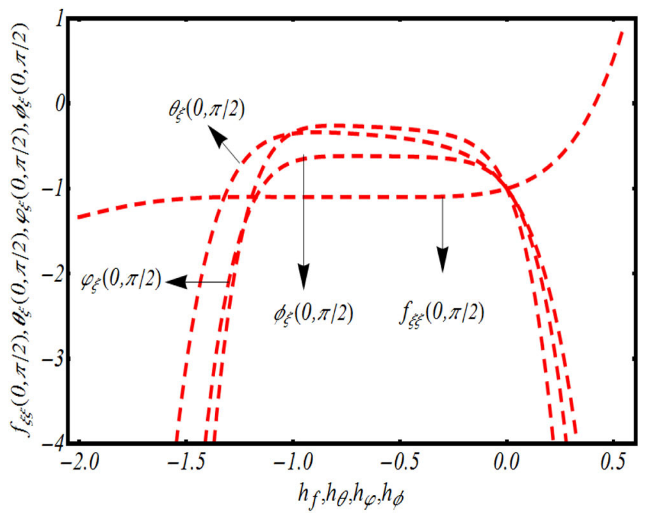

FIGURE 1 | $h-$ curves for $f_{\xi\xi}(0,\pi/2)$, $\theta_\xi(0,\pi/2)$, $\varphi_\xi(0,\pi/2)$, and $\phi_\xi(0,\pi/2)$ temperature, solutal concentration, and nanoparticle concentration.

number, and nano-Sherwood number:

$$C_f = \frac{\tau_w}{\rho u_w^2}, Nu_x = \frac{xq_s}{k(T_w - T_\infty)}, Sh_x = \frac{xj_s}{D_B(C_w - C_\infty)},$$
$$Sh_{xn} = \frac{xq_m}{D_s(\varphi_w - \varphi_\infty)}, \tag{17}$$

where q_s, j_s, and g_s stand for surface heat flux, surface mass flux, and motile microorganisms flux, respectively. The dimensionless forms of the previously mentioned physical quantities are

$$\left.\begin{aligned} \mathrm{Re}_x^{1/2} C_f &= (1+K) f_{\xi\xi} - \tfrac{K}{3}\beta\left(f_{\xi\xi}\right)_{\xi=0}, \\ Nu_x \mathrm{Re}_x^{-1/2} &= -\theta_\xi(0,\tau), \\ Sh_x \mathrm{Re}_x^{-1/2} &= -\varphi_\xi(0,\tau), \\ Sh_n \mathrm{Re}_x^{-1/2} &= -\phi_\xi(0,\tau). \end{aligned}\right\} \tag{18}$$

TABLE 1 | Comparison of $f_{\xi\xi}(0,\tau)$ for τ with Abbas et al. [35] when $S = 1$, $\Omega = 12$, $\Gamma = 0$, and $K = 0$.

τ	Abbas et al. [35]	Present results
$\tau = 1.5\pi$	11.678656	11.6786560
$\tau = 5.5\pi$	11.678707	11.678708
$\tau = 9.5\pi$	11.678656	11.678656

where $\mathrm{Re}_x = u_w\bar{x}/\nu$ is mentioned for local Reynolds number.

SOLUTION METHODOLOGY

The structured set of non-linear partial differential equations (12–16) with boundary conditions (17–18) are simulated analytically via homotopy analysis technique. Due to efficient and convincing accuracy, various physical problems in recent years have been solved by following this procedure. The initial guesses for the present flow problem are

$$f_0(\xi,\tau) = \sin\tau\left(1 - e^{-\xi}\right), \ \theta_0(\xi) = e^{-\xi}, \ \varphi_0(\xi) = e^{-\xi},$$
$$\phi_0(\xi) = e^{-\xi}, \tag{19}$$

Following auxiliary linear operators that are followed to precede the solution

$$\pounds_f = \frac{\partial^3}{\partial\xi^3} - \frac{\partial}{\partial\xi}, \pounds_\theta = \frac{\partial^2}{\partial\xi^2} - 1, \pounds_\varphi = \frac{\partial^2}{\partial\xi^2} - 1,$$
$$\pounds_\phi = \frac{\partial^2}{\partial\xi^2} - 1, \tag{20}$$

satisfying

$$\pounds_f\left[a_1 + a_2 e^{\xi} + a_3 e^{-\xi}\right] = 0, \tag{21}$$

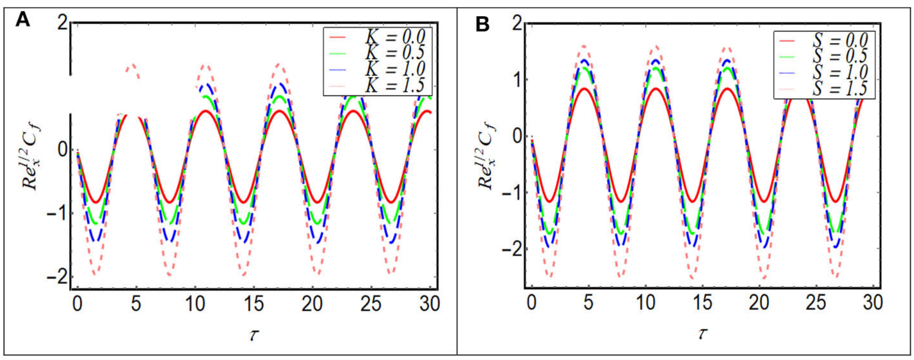

FIGURE 2 | Impact of **(A)** K **(B)** S on skin friction coefficient.

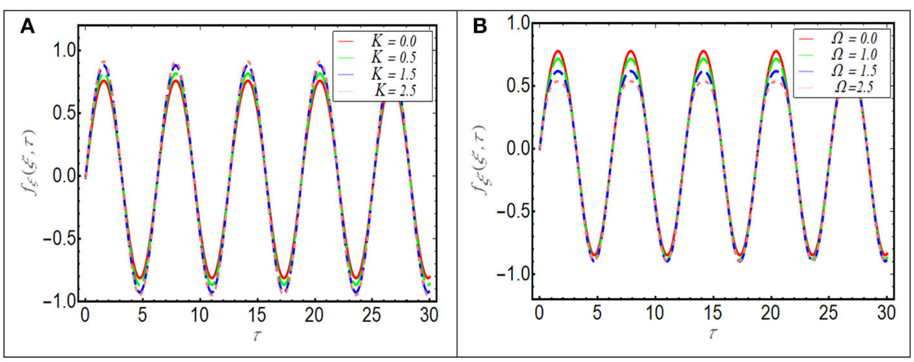

FIGURE 3 | Impact of **(A)** K **(B)** Ω on velocity.

$$\pounds_{\theta}\left[a_4e^{\xi}+a_5e^{-\xi}\right]=0, \tag{22}$$

$$\pounds_{\varphi}\left[a_6e^{\xi}+a_7e^{-\xi}\right]=0, \tag{23}$$

$$\pounds_{\phi}\left[a_8e^{\xi}+a_9e^{-\xi}\right]=0, \tag{24}$$

where $a_1, \ldots a_9$ are arbitrary constants.

CONVERGENT REGION

The convergence procedure in homotopic solution is regulated with auxiliary parameters h_f, h_θ, h_φ, and h_ϕ. On this end, we prepare $h-$curves to report the convincible range of such parameters. It is obvious from **Figure 1** that the preferable range of these such parameters can be utilized from $-2 \leq h_f \leq 0$, $-1.2 \leq h_\theta \leq -0.2$, $-1.4 \leq h_\varphi \leq 0$ and $-1.2 \leq h_\phi \leq -0.2$.

VALIDATION OF RESULTS

Table 1 shows the comparison of present results with Abbas et al. [35] as a limiting case. An excellent accuracy of results is noted with these reported investigations.

DISCUSSION

This section aims to manifest the features of some interesting flow parameters that appeared in the dimensionless equations, where material parameter K, magneto-porosity constant Ω, oscillating frequency-to-rate of stretching ratio S, Brownian motion Nb, thermophoresis constant Nt, variable thermal conductivity δ, Prandtl number Pr, Dufour Lewis number Ld, modified Dufour constant Nd, regular Lewis number Le, and nano-Lewis number Ln. During variation of each flow parameter, we fixed some numerical values to remaining parameters, like K=0.2, $\Omega = 0.4$, $S = 0.2$, $Nt = 0.3$, $\Pr = 0.7$, $Nb = 0.4$, $Nd, = 0.5$, $Ld = 0.3$, $Le = 0.2$, and $Ln = 0.3$.

Skin Friction Coefficient

The impact of the skin friction coefficient against time τ for diverse variation of K and S is evaluated in **Figures 2A,B**. An interesting periodic oscillation in the wall shear stress is evaluated by both figures. Furthermore, the growing values of both parameters increase the amplitude of oscillation sufficiently. Due to no-slip conditions at the surface, the fluid particles accelerated together with surface in same amplitude and phase. However, the occurrence of a phase shift in both curves is almost negligible.

Velocity Profile

The results reported in **Figures 3A,B** show the change in velocity f_ξ, verse time τ and leading values of material constant K, and magneto-porosity parameter Ω. **Figure 3A** characterized the influence of K on f_ξ, which shows that an increment in K leads to higher velocity amplitude. The physical justification of such enhancing velocity distribution is attributed to the lower viscosity of fluid associated with the higher values of K. However, reverse observations are predicated for Ω. In fact, magneto-porosity

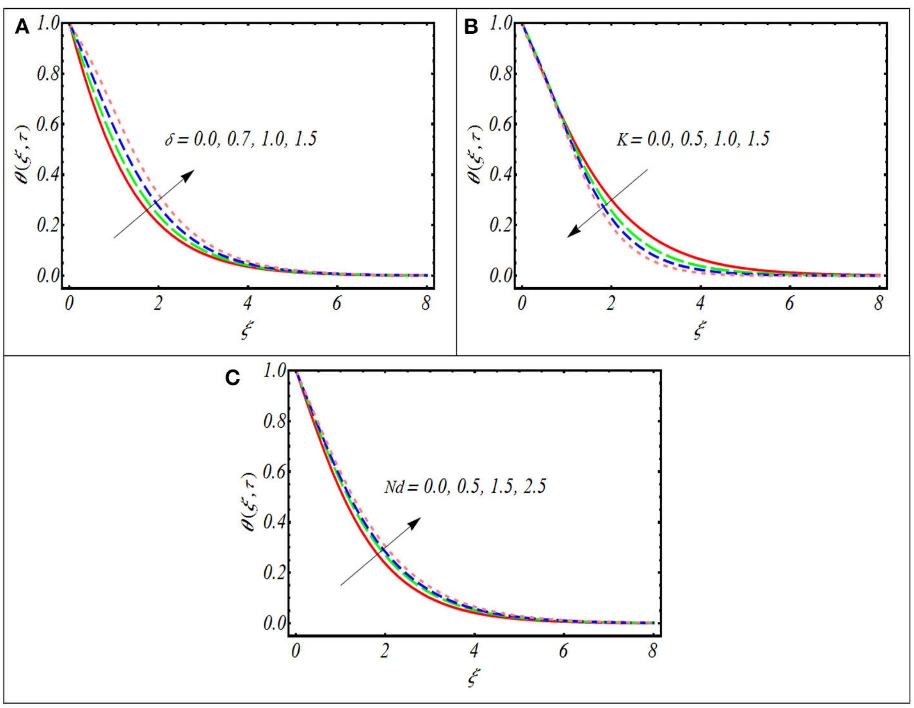

FIGURE 4 | Impact of **(A)** δ, **(B)** K, **(C)** Nd.

constant is the combination of magnetic field and porous space. The existence of a magnetic force encountered the effects of Lorentz force, in which a declining oscillation behavior is noticed. Similarly, the permeability of a porous medium also retards the velocity amplitude due to the loss of fluid. Moreover, the utilization of magnetic force enhances the apparent viscosity of fluid up to a certain point of becoming an elastic solid, and subsequently, the fluid stress can be managed upon changing the magnetic force. These interesting observations can be used in various processes, like magnetohydrodynamic drive ion propulsion, magnetohydrodynamic drive power generators, electromagnetic material casting, etc.

Temperature Distribution

To visualize the alter profile of nanoparticle temperature θ due to δ, K, and Nd, **Figures 4A–C** are prepared. **Figure 4A** reveals that temperature distribution θ increases with variable thermal conductivity constant δ. **Figure 4B** is constituted to observe the change in θ due to material parameter K. A fall in θ is associated with leading variation of K. An increment in viscosity would yield for arising values of K that increases the fluid velocity but a decline in the temperature of fluid. The change in θ with effect of modified Dufour number Nd has been reported in **Figure 4C**. A slightly dominant variation in θ is seen with larger values of Nd.

Solutal Concentration Profile

Now, we observe the variation in solutal concentration profile φ by varying regular Lewis number (Le), Dufour Lewis constant (Ld), and material constant (K). **Figure 5A** is designed to observe the impact of Le on φ. A decreasing solutal concentration profile φ is notified due to Le. Physical explanation of such decling variation of φ can be justified on the fact that Le captures reverse relation with species diffusion, which means that when Le is maximum, species diffusion is lower, which leads to the decrement of the resulting solutal concentration. From **Figure 5B**, φ increases with the growth of Ld. Physically, Ld depends upon the Lewis number due to lower mass diffusivity. **Figure 5C** presents change in φ due to material constant K. Again, an enhanced distribution of solutal concentration profile φ has resulted for maximum values of K.

Nanoparticle Concentration

The physical consequences of Ln, Nt, and Nb on concentration distribution ϕ are deliberated in **Figures 6A–C**. **Figure 6A** specified the input of Ln on ϕ. A declining concentration distribution ϕ is examined in the peak values of Ln. This decreasing behavior of ϕ is attributed to the fact that Ln is associated with the Brownian diffusion coefficient because Ln expresses the thermal diffusivity-to-mass diffusivity ratio. This parameter that is referred to the fluid flow in a

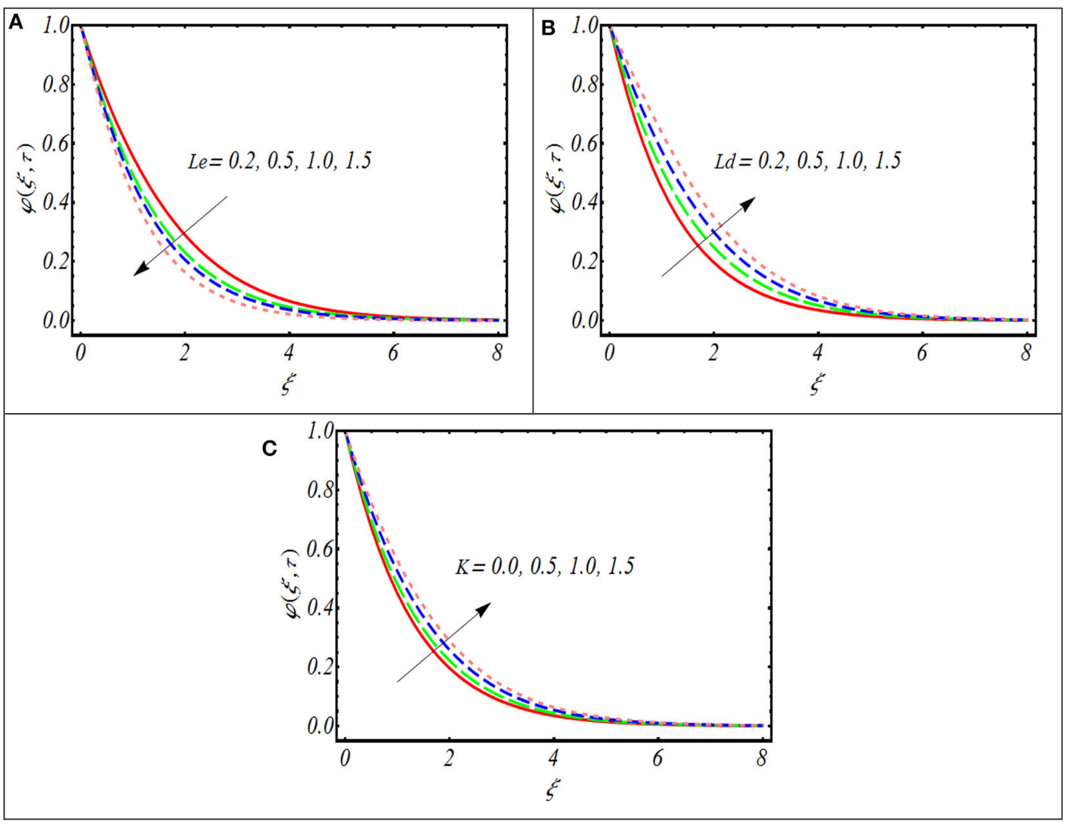

FIGURE 5 | Impact of **(A)** *Le*, **(B)** *Ld*, and **(C)** *K* on solutal concentration.

phenomenon of heat and mass transfer occurs due to convection. The consequences for another important parameter, namely thermophoresis constant *Nt*, are analyzed in **Figure 6B**. As expected, a larger concentration distribution ϕ is reported due to involvement of *Nt*. The larger variation of *Nt* helps to improve the thermal conductivity of fluid. Physically, the thermophoretic process is based on collective migrated heat particles in the region of low temperature and plays a momentous role in many physical

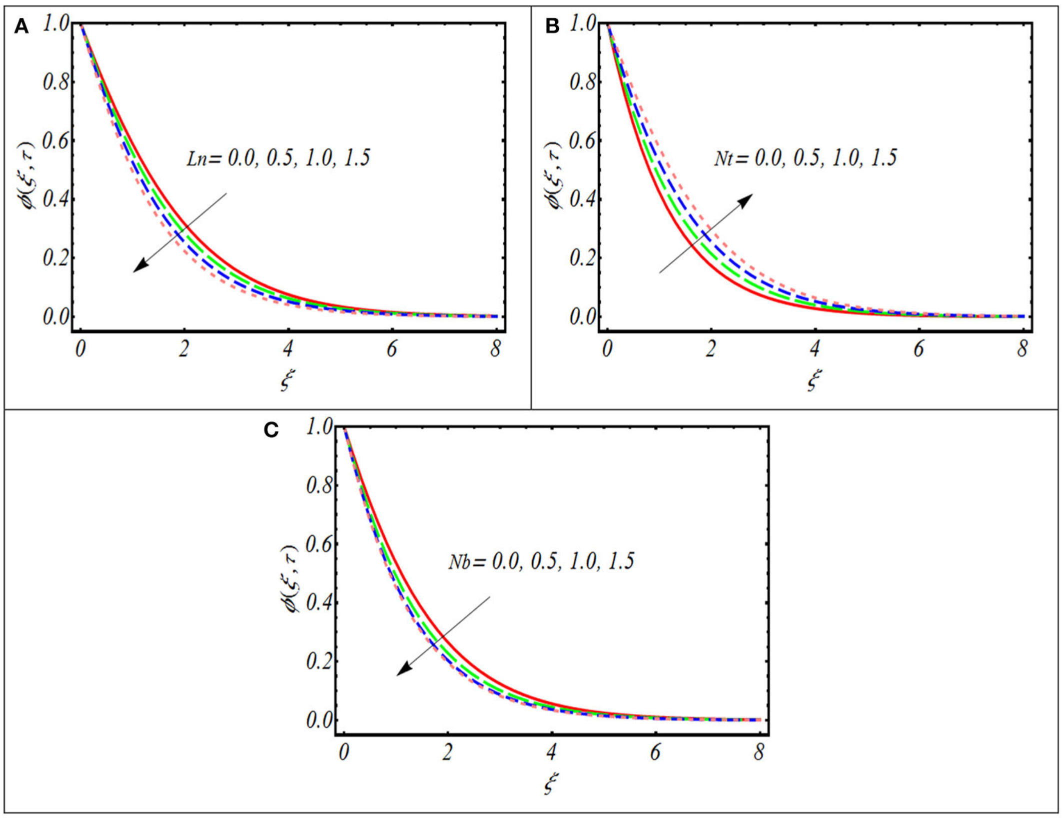

FIGURE 6 | Impact of **(A)** *Ln*, **(B)** *Nt*, and **(C)** *Nb*.

TABLE 2 | Numerical values of $-\theta_\xi(0,\tau)$, $-\varphi_\xi(0,\tau)$, and $-\phi_\xi(0,\tau)$, when $\tau = \pi/2$.

Ω	Pr	*Nt*	*Nb*	ε	*K*	$-\theta_\xi(0,\tau)$	$-\varphi_\xi(0,\tau)$	$-\phi_\xi(0,\tau)$
0.0	0.7	0.3	0.3	0.1	0.1	0.62231	0.55537	0.54652
0.5						0.60854	0.53876	0.51828
1.0						0.59654	0.50535	0.49632
0.2	0.2					0.48896	0.44689	0.42658
	0.5					0.55658	0.47598	0.46485
	1.0					0.57875	0.49535	0.50280
	0.7	0.0				0.58029	0.60986	0.62384
		0.4				0.53531	0.56154	0.57567
		0.5				0.51189	0.519856	0.53878
		0.3	0.2			0.49598	0.455454	0.43562
			0.5			0.44357	0.44543	0.50635
			0.7			0.42637	0.43045	0.57420
			0.3	0.2		0.48351	0.44659	0.50015
				0.4		0.46743	0.42798	0.48243
				0.6		0.44092	0.40659	0.44564
				0.1	0.0	0.49359	0.44659	0.52658
					0.4	0.46578	0.42298	0.50256
					0.6	0.43395	0.41326	0.47559

phenomenons. The curve of ϕ attained maximum level due to *Nt*. However, a reduced concentration distribution ϕ is associated with *Nb*, as shown in **Figure 6C**. The Brownian movement is based on random pattern moving fluid particles in flow surface. It is further justified from Equation (16), which clearly shows that reverse relation is developed between *Nb* and ϕ. In fact, the specified numerical values of *Nb* are associated to the more prominent nanoparticle moments that are being pushed back from accelerated plate to quiescent, which resulted in a retarded concentration distribution.

Physical Quantities

To perform the numerical simulations for local Nusselt number $-\theta_\xi\,(0,\tau)$, local Sherwood Number $-\varphi_\xi\,(0,\tau)$ and nanofluid Sherwood number $-\phi_\xi\,(0,\tau)$, **Table 2** is designed. It is observed that when Ω, ε, and K assigned larger numerical values, a decreasing trend in $-\theta_\xi\,(0,\tau)$, $-\varphi_\xi\,(0,\tau)$, and $-\phi_\xi\,(0,\tau)$ is reported. However, these physical quantities increase with the variation of Pr.

CONCLUSIONS

We have focused on periodically accelerated unsteady flow of Eyring–Powell nanofluid with utilization of thermal diffusive features. The variable impact of thermal conductivity, porous medium, and magnetic field consequences are also utilized. The important observations from current flow problem are summarized as:

- ➢ The magneto-porosity parameter declined the periodic oscillation in the velocity, and subsequently, the magnitude of velocity declined.
- ➢ The wall shear stress oscillates periodically with time that increases by varying material parameter.
- ➢ The thermal conductivity with the variable nature is more effective in enhancing the nanoparticle temperature.
- ➢ The modified Dufour number increases the temperature distribution.
- ➢ It is noted that solutal concentration increases subject to Dufour Lewis number and material constant.
- ➢ An increasing change in nanoparticle concentration determined with nano-Lewis number and a material parameter.

The observation based on the reported results can be used to improve thermal extrusion processes, heat exchangers, solar technology, energy production, cooling processes, etc.

DATA AVAILABILITY STATEMENT

The original contributions presented in the study are included in the article/supplementary materials, further inquiries can be directed to the corresponding author/s.

AUTHOR CONTRIBUTIONS

All authors listed have made a substantial, direct and intellectual contribution to the work, and approved it for publication.

ACKNOWLEDGMENTS

The authors extend their appreciation to the Deanship of Scientific Research at Majmaah University for funding this work under project number: RGP-2019-1.

REFERENCES

1. Choi S. Enhancing thermal conductivity of fluids with nanoparticles, development and applications of non-newtonian flow ASME. *MD*. (1995) **66**:99–105.
2. Buongiorno J. Convective transport in nanofluids. *J Heat Transfer*. (2010) **128**:240–50. doi: 10.1115/1.2150834
3. Khan WA, Pop I. Boundary layer flow of a nanofluid past a stretching sheet. *Int J Heat Mass Transfer*. (2010) **53**:2477–83. doi: 10.1016/j.ijheatmasstransfer.2010.01.032
4. Sheikholeslami M, Nimafar M, Ganji DD. Nanofluid heat transfer between two pipes considering brownian motion using AGM. *Alexandria Eng J*. (2017) **56**:277–83. doi: 10.1016/j.aej.2017.01.032
5. Shahzadi I, Nadeem S. Impinging of metallic nanoparticles along with the slip effects through a porous medium with MHD. *J Braz Soc Mech Sci Eng*. (2017) **39**:2535. doi: 10.1007/s40430-017-0727-7
6. Khan AU, Hussain ST, Nadeem S. Existence and stability of heat and fluid flow in the presence of nanoparticles along a curved surface by mean of dual nature solution. *Appl Math Comput*. (2019) **353**:66–81. doi: 10.1016/j.amc.2019.01.044
7. Turkyilmazoglu M. Buongiorno model in a nanofluid filled asymmetric channel fulfilling zero net particle flux at the walls. *Int J Heat Mass Transfer*. (2018) **126**:974–9. doi: 10.1016/j.ijheatmasstransfer.2018.05.093
8. Vaidya H, Prasad KV, Vajravelu K, Shehzad SA, Basha H. Role of variable liquid properties in 3d flow of maxwell nanofluid over convectively heated surface: optimal solutions. *J Nanofluids*. (2019) **8**:1133–46. doi: 10.1166/jon.2019.1658
9. Hayat T, Ullah I, Muhammad T, Alsaedi A. Thermal and solutal stratification in mixed convection three- dimensional flow of an oldroyd-B nanofluid. *Result Phys*. (2017) **7**:3797–805. doi: 10.1016/j.rinp.2017.09.051
10. Turkyilmazoglu M. MHD natural convection in saturated porous media with heat generation/absorption and thermal radiation: closed-form solutions. *Arch Mech*. (2019) **71**:49–64. doi: 10.24423/aom.3049
11. Krishna MV, Chamkha AJ. Hall and ion slip effects on MHD rotating boundary layer flow of nanofluid past an infinite vertical plate embedded in a porous medium. *Results Phys*. (2019) **15**:102652. doi: 10.1016/j.rinp.2019.102652
12. Manjunatha S, Kuttan A, Jayanthi S, Chamkha A, Gireesha BJ. Heat transfer enhancement in the boundary layer flow of hybrid nanofluids due to variable viscosity and natural convection. *Heliyon*. (2019) **5**:e01469. doi: 10.1016/j.heliyon.2019.e01469
13. Sardar H, Khan M, Alghamdi M. Multiple solutions for the modified Fourier and Fick's theories for Carreau nanofluid. *Ind J Phys*. (2019) doi: 10.1007/s12648-019-01628-y
14. Alwatban AM, Khan SU, Waqas H, Tlili I. Interaction of Wu's slip features in bioconvection of Eyring Powell nanoparticles with activation energy. *Processes*. (2019) **7**:859. doi: 10.3390/pr7110859
15. Zhao M, Xiao Y, Wang S. Linear stability of thermal-bioconvection in a suspension of gyrotactic micro-organisms. *Int J Heat Mass Transfer*. (2018) **126**:95–102. doi: 10.1016/j.ijheatmasstransfer.2018.05.030
16. Alkanhal TA, Sheikholeslami M, Usman M, Haq R-U, Shafee A, SaadAl-Ahmadi A, et al. Thermal management of MHD nanofluid within the porous medium enclosed in a wavy shaped cavity with square obstacle in the

presence of radiation heat source, *Int J Heat Mass Transfer*. (2019) **139**:87–94. doi: 10.1016/j.ijheatmasstransfer.2019.05.006

17. Anantha Kumar K, Sandeep N, Sugunamma V, Animasaun IL, Effect of irregular heat source/sink on the radiative thin film flow of MHD hybrid ferrofluid. *J Therm Anal Calorim*. (2020) **139**:2145. doi: 10.1007/s10973-019-08628-4
18. Bhattacharyya A, Seth GS, Kumar R, Chamkha AJ. Simulation of cattaneo-christov heat flux on the flow of single and multi-walled carbon nanotubes between two stretchable coaxial rotating disks. *J Therm Anal Calorim.* (2020) **139**:1655. doi: 10.1007/s10973-019-08644-4
19. Mekheimer SKH, Shaimaa Ramadan F. New Insight into gyrotactic microorganisms for Bio-thermal convection of Prandtl nanofluid past a stretching/shrinking permeable sheet. *SN Appl Sci.* (2020) **2**:450. doi: 10.1007/s42452-020-2105-9
20. Powell RE, Eyring H. Mechanisms for the relaxation theory of viscosity. *Nature.* (1944) **154**:427–28. doi: 10.1038/154427a0
21. Gholinia M, Hosseinzadeh Kh, Mehrzadi H, Ganji DD, Ranjbar AA. Investigation of MHD eyring-Powell fluid flow over a rotating disk under effect of homogeneous-heterogeneous reactions. *Case Stud Thermal Eng.* (2019) **13**:100356. doi: 10.1016/j.csite.2018.11.007
22. Sami UK, Nasir A, Zaheer A. Soret and dufour effects on hydromagnetic flow of eyring powell fluid over an oscillatory stretching surface with heat generation/absorption and chemical reaction. *Thermal Sci.* (2018) **22**:533–43. doi: 10.2298/TSCI150831018U
23. Salawu SO, Ogunseye HA. Entropy generation of a radiative hydromagnetic powell-eyring chemical reaction nanofluid with variable conductivity and electric field loading. *Res Eng.* (2020) **5**:100072. doi: 10.1016/j.rineng.2019.100072
24. Abegunrin OA, Animasaun IL, Sandeep N. Insight into the boundary layer flow of non-newtonian eyring-powell fluid due to catalytic surface reaction on an upper horizontal surface of a paraboloid of revolution. *Alexandria Eng J.* (2018) **57**:2051–60. doi: 10.1016/j.aej.2017.05.018
25. Rahimi J, Ganji DD, Khaki M, Hosseinzadeh Kh. Solution of the boundary layer flow of an eyring-powell non-newtonian fluid over a linear stretching sheet by collocation method. *Alexandria Eng J.* (2017) **56**:621–7. doi: 10.1016/j.aej.2016.11.006
26. Reddy SRR, Bala Anki Reddy P, Bhattacharyya K. Effect of nonlinear thermal radiation on 3D magneto slip flow of eyring-powell nanofluid flow over a slendering sheet with binary chemical reaction and arrhenius activation energy. *Adv Powder Technol.* (2019) **30**:3203–13. doi: 10.1016/j.apt.2019.09.029
27. Hayat T, Nadeem S. Flow of 3D eyring-powell fluid by utilizing cattaneo-christov heat flux model and chemical processes over an exponentially stretching surface. *Res. Phys.* (2018) **8**:397–403. doi: 10.1016/j.rinp.2017.12.038
28. Ghadikolaei SS, Hosseinzadeh Kh, Ganji DD. Analysis of unsteady MHD Eyring-Powell squeezing flow in stretching channel with considering thermal radiation and Joule heating effect using AGM. *Case Stud Thermal Eng.* (2017) **10**:579–94. doi: 10.1016/j.csite.2017.11.004
29. Raghunatha KR, Shivakumara IS. Stability of triple diffusive convection in a viscoelastic fluid-saturated porous layer. *Appl Math Mech Engl Ed.* (2018) **39**:1385–410. doi: 10.1007/s10483-018-2376-8
30. Daba M, Devaraj P. Unsteady double diffusive mixed convection flow over a vertically stretching sheet in the presence of suction/injection. *J Appl Mech Tech Phys.* (2017) **58**:232–43. doi: 10.1134/S0021894417020067
31. Khan ZH, Culham JR, Khan WA, Pop I. Triple convective-diffusion boundary layer along a vertical flat plate in a porous medium saturated by a water-based nanofluid. *Int J Thermal Sci.* (2015) **90**:53e61. doi: 10.1016/j.ijthermalsci.2014.12.002
32. Liao SJ. *Advances in the Homotopy Analysis Method*. Singapore: World Scientific Publishing. (2014) doi: 10.1142/8939
33. Khan SU, Shehzad SA, Abbasi FM, Arshad SH. Thermo diffusion aspects in Jeffrey nanofluid over periodically moving surface with time dependent thermal conductivity. *Thermal Sci*. (2019). doi: 10.2298/TSCI190428312U
34. Mekheimer SKh, Abd elmaboud Y. Simultaneous effects of variable viscosity and thermal conductivity on peristaltic flow in a vertical asymmetric channel. *Can J Phys.* (2014) **92**:1541–55. doi: 10.1139/cjp-2013-0465
35. Abbas Z, Wang Y, Hayat T, Oberlack M. Hydromagnetic flow ina viscoelastic fluid due to the oscillatory stretching surface. *Int J Non-Linear Mech.* (2008) **43**:783–97. doi: 10.1016/j.ijnonlinmec.2008.04.009

Conflict of Interest: The authors declare that the research was conducted in the absence of any commercial or financial relationships that could be construed as a potential conflict of interest.

Copyright © 2020 Khan, Vaidya, Chammam, Musmar, Prasad and Tlili. This is an open-access article distributed under the terms of the Creative Commons Attribution License (CC BY). The use, distribution or reproduction in other forums is permitted, provided the original author(s) and the copyright owner(s) are credited and that the original publication in this journal is cited, in accordance with accepted academic practice. No use, distribution or reproduction is permitted which does not comply with these terms.

frontiers in Physics

ORIGINAL RESEARCH
published: 24 November 2020
doi: 10.3389/fphy.2020.00250

Entropy Optimization of Third-Grade Nanofluid Slip Flow Embedded in a Porous Sheet With Zero Mass Flux and a Non-Fourier Heat Flux Model

K. Loganathan[1], G. Muhiuddin[2]*, A. M. Alanazi[2], Fehaid S. Alshammari[3], Bader M. Alqurashi[4] and S. Rajan[1]*

[1] Department of Mathematics, Erode Arts & Science College, Erode, India, [2] Department of Mathematics, University of Tabuk, Tabuk, Saudi Arabia, [3] Department of Mathematics and Statistics, Imam Mohammad Ibn Saud Islamic University, Riyadh, Saudi Arabia, [4] Department of Mathematics, Faculty of Arts and Science in Almandaq, Albaha University, Albaha, Saudi Arabia

OPEN ACCESS

Edited by:
Ahmed Zeeshan,
International Islamic University,
Islamabad, Pakistan

Reviewed by:
Ali Chamkha,
Prince Mohammad bin Fahd
University, Saudi Arabia
Precious Sibanda,
University of KwaZulu-Natal,
South Africa

***Correspondence:**
G. Muhiuddin
chishtygm@gmail.com
K. Loganathan
loganathankaruppusamy304@gmail.com

Specialty section:
This article was submitted to
Mathematical and Statistical Physics,
a section of the journal
Frontiers in Physics

Received: 21 April 2020
Accepted: 08 June 2020
Published: 24 November 2020

Citation:
Loganathan K, Muhiuddin G, Alanazi AM, Alshammari FS, Alqurashi BM and Rajan S (2020) Entropy Optimization of Third-Grade Nanofluid Slip Flow Embedded in a Porous Sheet With Zero Mass Flux and a Non-Fourier Heat Flux Model. Front. Phys. 8:250. doi: 10.3389/fphy.2020.00250

The prime objective of this article is to explore the entropy analysis of third-order nanofluid fluid slip flow caused by a stretchable sheet implanted in a porous plate along with thermal radiation, convective surface boundary, non-Fourier heat flux applications, and nanoparticle concentration on zero mass flux conditions. The governing physical systems are modified into non-linear ordinary systems with the aid of similarity variables, and the outcomes are solved by a homotopy analysis scheme. The impression of certain governing flow parameters on the nanoparticle concentration, temperature, and velocity is illustrated through graphs, while the alteration of many valuable engineering parameters viz. the Nusselt number and Sherwood number are depicted in graphs. Entropy generation with various parameters is obtained and discussed in detail. The estimation of entropy generation using the Bejan number find robust application in power engineering and aeronautical propulsion to forecast the smartness of entire system.

Keywords: entropy generation, Christov-Cattaneo heat flux, third-grade nanofluid, porous medium, homotopy analytic technique

INTRODUCTION

Nanoliquids are the type of liquids that have small volumetric quantities of nanoscale $(10^{-9} - 10^{-7}\text{m})$ metallic $(Cu, Ti, Hg, Fe, Ag, Au, \text{etc.})$ or non-metallic particles $(TiO_2, SiO_2, CuO, Al_2O_3, \text{etc})$ taken as nano particles. Usually nanoliquids have a colloidal suspension of nanoparticles inside a base liquid for example water, oil, ethylene glycol, etc. Initially, Choi [1] proposed the "nanofluid" term. In general, the effective heat transfer enhancement has the reason of nanoliquids generally restrict up to volume fraction of nanoparticles. Therefore, in the latest technologies and engineering areas, nanoliquids receiving a phenomenal impact. Mushtaq et al. [2] attempted the numerical study of the nanoliquids induced by an exponentially stretchable sheet with rotating flow model. MHD nanoliquid flow toward a porous plate with internal heat generation effects was presented by Reddy and Chamka [3]. Shit et al. [4] studied the convective flow of hydromagnetic nanoliquid with entropy generation mechanism. Recently, Gireesha et al. [5] explained a Hall current effects of two-phase transient nanoliquid flow induced by a stretchable sheet. Reddy et al. [6] performed the combined convection flow of nanoliquid toward a semi-infinite vertical flat sheet with convectively heated boundary and Soret effect. Few more significant studies in this research area are seen in ref's [7–13].

Due to various applications in different technical and industrial areas, the fluid flow problems toward a stretching surface have developed. It finds application in rubber and plastic sheets production, melt-spinning, production of glass-fiber, and metallic plate cooling systems. Sakiadis [14] studied the uniform velocity of a magnetohydrodynamic flow past a solid medium. Magyari et al. [15] examined the first order chemical reaction and heat generation combination on micropolar fluid flow induced by a permeable stretching surface. Gupta [16] analyzed the heat and mass transfer effects of a boundary layer flow induced by a stretchy sheet with suction or blowing impact. Magyari and Keller [17] exposed the fluid flow over exponentially extending sheet with heat and mass transfer impacts. Significances of thermal boundary layer flow for a linearly stretchy sheet with viscous dissipation were examined by Cortell [18]. The cutting-edge research reports on stretching sheet flow are highlighted in these works of literature [19–24].

Fluid flow saturated in the porous surface have numerous applications in various fields like geothermal energy, fuel cell technologies, material processing, etc. Chamkha et al. [25] described the free convective flow past an inclined plate fitted in a porous medium of variable porosity with solar radiation. Khan and Aziz [26] studied the natural convective flow with double diffusion caused by a vertical porous sheet. Oyelakin et al. [27] analyzed the slip flow of unsteady radiative Casson nanofluid toward a stretchy surface. Gorla and Chamkha [28] studied the nanofluid flow toward a non-isothermal vertical plat entrenched in a porous sheet. The same research group extended their work for different models for various applications [29–32].

Heat transport problems in the flow of liquids have been examined by several researchers for the last decade. In 1822, Fourier [33] constructed the heat conduction law. This states that "the heat transfer in a medium with inertial rate." A parabolic-type equation was used to state the heat conduction equation. The problem rising at this time is that there exists no such object or material that satisfies Fourier's law, as argued by Cattaneo [34] when using thermal relaxation time to customize Fourier's law. Later, Christov [35] developed and joined the upper convected Maxwell fluid. This developed model is called a Christov-Cattaneo heat flux model. Loganathan et al. [36] studied the thermal relaxation time effects on Oldroyd-B liquid with second-order slip and cross-diffusion impacts. The Christov-Cattaneo heat flux model for a third-grade liquid with chemical reaction effects was examined by Imtiaz et al. [37].

In the last decade, several scientists have researched entropy generation in the flow of fluids and heat transfer over a stretching surface. In various engineering and industrial divisions, the performance of heating and cooling are of massive importance in different electronic and energy issues. Aiboud and Saouli [38] examined the MHD viscoelastic fluid flow with the application of entropy analysis using Kummer's function. Makinde [39] presented the thermal radiation and Newtonian heating impacts of variable viscosity fluid caused by a semi-infinite plate using shooting quadrature and obtained the entropy generation number. Loganathan et al. [40, 41] verified the entropy analysis for the third grade and Williamson nanoliquid flow caused by a stretchable sheet with various effects. They employed HAM to solve the non-linear governing systems.

Based on our research in previously published works, entropy generation of third-grade nanofluid flow caused by a stretching sheet with a modified Fourier law has not been discussed with a high standard of scientific attention. As far as we noticed in literature, the studies taken for entropy generation are limited with some parameters viz the Brinkmann number, Reynolds number, Temperature difference parameter, and Hartmann number. We have extended our investigations to include thermal relaxation time, the Biot number, thermal radiation, slip parameter, porous parameter, etc. The effective collection and analysis of these results will open new gateways for diverse engineering application in various streams.

PROBLEM DEVELOPMENT

We were interested in analyzing the entropy and Bejan number of third-grade nanofluid saturated in a porous medium with Christov-Cattaneo heat flux. In **Figure 1**, the stretching parameter is taken along x direction where T_W and C_W are represented the wall temperature and concentration, respectively. T_∞ and C_∞ are used to index the ambient temperature and concentration, respectively. A convective heating temperature T_f is stimulated at the bottom of the sheet surface. The Buongiorno nanofluid [42] is used for the present case.

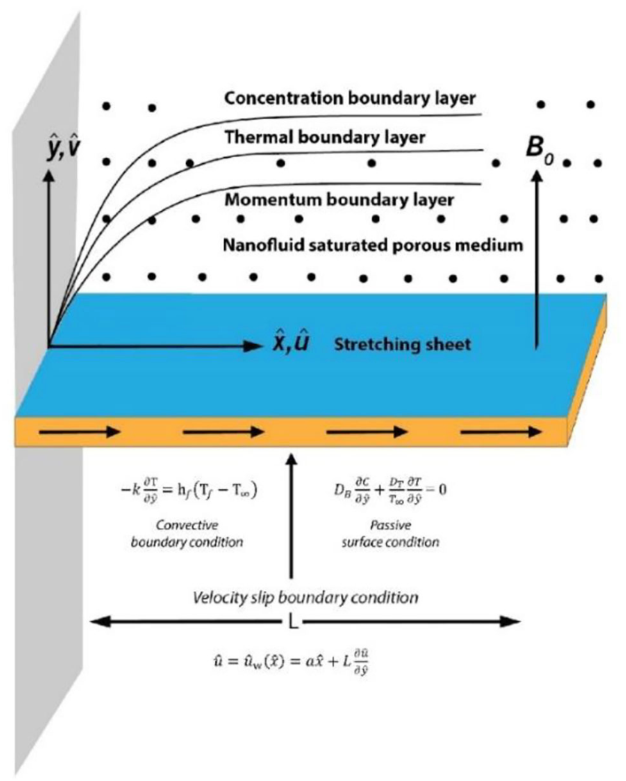

FIGURE 1 | Flow diagram.

Based on his consideration, the slip mechanisms, namely, the Brownian diffusion, inertia, Magnus effect, diffusiophoresis, thermophoresis, gravity, and fluid drainage, were analyzed. He recommended that the thermophoresis and Brownian diffusion are essential slip mechanism in low dimensional materials.

The following is an incompressible fluid model containing body forces with the equation of continuity and motion:

$$div\, v = 0 \tag{1}$$

$$\rho \frac{dv}{dt} = divT + \rho b + J + B \tag{2}$$

Here, ρ is the fluid density, which is taken as a constant, v is the velocity field, b indicates the body forces, J denotes the electric current, and T states the third-grade incompressible fluids Cauchy stress tensor [43]

$$T = -pI + \mu E_1 + A_1^* E_2 + A_2^* E_1^2 + \beta_1 E_3 + \beta_2 \left(E_1, E_2 + E_2 E_1\right) + \beta_3 \left(trE_1^2\right) E_1 \tag{3}$$

where $\mu, (E_1, E_2, E_3)$ and A_1^*, β_i indicate the viscosity coefficient, kinematics tensors, and material modulis as in

$$E_1 = L + (L)^T \tag{4}$$

$$E_n = \frac{d}{dt} E_{n-1} + E_{n-1} L + (L)^T E_{n-1}, \quad n = 2, 3, \text{and} \tag{5}$$

$$L = \nabla v. \tag{6}$$

$\frac{d}{dt}$ is expressed as the material time derivative

$$\frac{d()}{dt} = \frac{\partial ()}{\partial t} + v. \nabla (). \tag{7}$$

The relationship between Clausius-Duhem inequality and thermodynamically compatible fluid is stated by Fosdick and Rajagopal [44]:

$$\mu \geq 0,\ A_1^* \geq 0,\ \beta_1 = \beta_2 = 0,\ \beta_3 \geq 0 \tag{8}$$

$$\left|A_1^* + A_2^*\right| \leq 2\sqrt{6\mu\beta_3} \tag{9}$$

$$T = -pI + \mu E_1 + A_1^* E_2 + A_2^* E_1^2 + \beta_3 \left(trE_1^2\right) E_1 \tag{10}$$

Boussinesq and normal boundary layer approximations were considered by Pakdemirli [45]. We made the following assumptions:

1. The nanoparticles are small and of equal size to the pores.
2. The zero-mass flux of the nanoparticles is included.
3. Christov-Cattaneo heat flux is considering instead of normal heat flux.
4. The magnetic field in the fluid flow is ignored due to a lower magnetic Reynolds number.

$$\frac{\partial u}{\partial x} + \frac{\partial v}{\partial y} = 0 \tag{11}$$

$$u\frac{\partial u}{\partial x} + v\frac{\partial u}{\partial y} = v\frac{\partial^2 u}{\partial y^2} + \frac{A_1^*}{\rho}\left(u\frac{\partial^3 u}{\partial y^2 \partial x} + v\frac{\partial^3 u}{\partial y^3} + \frac{\partial u}{\partial x}\frac{\partial^2 u}{\partial y^2} + 3\frac{\partial u}{\partial y}\frac{\partial^2 u}{\partial x \partial y}\right) + 2\frac{A_2^*}{\rho}\frac{\partial u}{\partial y}\frac{\partial^2 u}{\partial x \partial y} + 6\frac{\beta_1^*}{\rho}\left(\frac{\partial u}{\partial y}\right)^2 \frac{\partial^2 u}{\partial y^2} - \frac{\sigma B_0^2}{\rho} u - \frac{v}{k_p} u \tag{12}$$

$$u\frac{\partial T}{\partial x} + v\frac{\partial T}{\partial y} = \frac{k}{\rho c_p}\frac{\partial^2 T}{\partial y^2} - \frac{1}{\rho c_p}\frac{\partial q_r}{\partial y} + \frac{Q_0}{\rho c_p}\left(T - T_\infty\right) + \tau\left[D_B \frac{\partial C}{\partial y}\frac{\partial T}{\partial y} + \frac{D_T}{T_\infty}\left(\frac{\partial T}{\partial y}\right)^2\right] \tag{13}$$

$$u\frac{\partial C}{\partial x} + v\frac{\partial C}{\partial y} = D_B \frac{\partial^2 C}{\partial y^2} + \frac{D_T}{T_\infty}\frac{\partial^2 T}{\partial y^2} \tag{14}$$

$$u = u_w(x) = ax + L\frac{\partial u}{\partial y},\ -k\frac{\partial T}{\partial y} = h_f\left(T_f - T_\infty\right),$$
$$D_B \frac{\partial C}{\partial y} + \frac{D_T}{T_\infty}\frac{\partial T}{\partial y} = 0 \ at\ y = 0$$
$$u \to 0,\ T \to T_\infty,\ c \to c_\infty \ as\ y \to \infty \tag{15}$$

The energy equation with a Cattaneo-Christov heat flux model is stated as

$$u\frac{\partial T}{\partial x} + v\frac{\partial T}{\partial y} + \lambda_T\left(u^2\frac{\partial^2 T}{\partial x^2} + v^2\frac{\partial^2 T}{\partial y^2} + \left(u\frac{\partial u}{\partial x}\frac{\partial T}{\partial x} + v\frac{\partial u}{\partial y}\frac{\partial T}{\partial x}\right. \right. + \left. 2uv\frac{\partial T^2}{\partial x \partial y}\right) + \left(u\frac{\partial v}{\partial x}\frac{\partial T}{\partial y} + v\frac{\partial v}{\partial y}\frac{\partial T}{\partial y}\right) = \frac{k}{\rho c_p}\frac{\partial^2 T}{\partial y^2} - \frac{1}{\rho c_p}\frac{\partial q_r}{\partial y} + \frac{Q_0}{\rho c_p}\left(T - T_\infty\right) + \tau\left[D_B \frac{\partial C}{\partial y}\frac{\partial T}{\partial y} + \frac{D_T}{T_\infty}\left(\frac{\partial T}{\partial y}\right)^2\right]. \tag{16}$$

Consider the transformation given below:

$$\psi = \sqrt{av}xf(\eta),\ u = \frac{\partial \psi}{\partial y},\ v = -\frac{\partial \psi}{\partial x},\ \eta = \sqrt{\frac{a}{v}}y,$$
$$v = -\sqrt{av}f(\eta),\ u = axf'(\eta),\ \theta(\eta) = \frac{T - T_\infty}{T_f - T_\infty},$$
$$\phi(\eta) = \frac{C - C_\infty}{C_\infty}. \tag{17}$$

The non-linear governing equations are:

$$f''' + ff'' - f'^2 + \alpha_1\left(2f'f''' - ff^{iv}\right) + (3\alpha_1 + 2\alpha_2)f''^2 + 6\beta Ref'''f''^2 - (Mf' + Kf') = 0 \tag{18}$$

$$\left(1 + \frac{4}{3}Rd\right)\theta'' + Prf\theta' + PrS\theta - Pr\gamma f^2\theta'' - Pr\gamma ff'\theta' + PrNb\,\theta'\phi' + PrNt\theta'^2 = 0 \tag{19}$$

$$\phi'' + Lef\phi' + \frac{Nt}{Nb}\theta'' = 0 \tag{20}$$

with the end points

$$\begin{aligned} &f(0) = f_w, f'(0) = 1 + \Gamma f''(0), \theta'(0) = -Bi(1-\theta(0)),\\ &Nb\,\phi'(0) + Nt\,\theta'(0) = 1\\ &f'(\infty) = 0,\ \theta(\infty) = 0, \phi(\infty) = 0 \end{aligned} \tag{21}$$

The non-dimensional variables are

$$\alpha_1 = \frac{aA_1^*}{\nu}, \alpha_2 = \frac{aA_2^*}{\nu}, \beta = \frac{a\beta_1^*}{\nu}, Re = \frac{u_w x}{\nu}, Pr = \rho C_p/k,$$
$$M = \sigma B_0^2/\rho a, Rd = \left(4\sigma^* T_\infty^3\right)/\left(kk^*\right), S = \frac{Q_0}{\rho c_p}, \gamma = \lambda_T a,$$
$$Bi = \frac{h_f}{k}\sqrt{\nu/a}, Nb = \frac{\tau D_B}{\nu}(C_\infty),\ Nt = \frac{\tau D_T}{\nu}\left(T_f - T_\infty\right).$$

The application of physical entitles is such that

$$Re^{\frac{1}{2}} C_f = f''(0) + \alpha_1 f'(0) f'''(0) + \beta Re[f''(0)]^3 \tag{22}$$
$$Re^{-\frac{1}{2}} Nu_x = -(1 + \frac{4}{3}Rd)\theta'(0). \tag{23}$$

The local mass transfer rate becomes identically zero due to the zero mass flux state [46]

$$Re^{-\frac{1}{2}} Sh = \frac{Nt}{Nb}\theta'(0). \tag{24}$$

ENTROPY OPTIMIZATION

The entropy minimization optimization for fluid friction, heat, and the irreversibility of mass transfer are given below:

$$\begin{aligned} S'''_{gen} = &\frac{K_1}{T_\infty^2}\left[\left(\frac{\partial T}{\partial x}\right)^2 + \left(\frac{\partial T}{\partial y}\right)^2 + \frac{16\sigma^* T_\infty^3}{3kk^*}\left(\frac{\partial T}{\partial y}\right)^2\right]\\ &+ \frac{\mu}{T_\infty}\left[2\left(\frac{\partial u}{\partial x}\right)^2 + \left(\frac{\partial v}{\partial y}\right)^2\right] + \left[\frac{\partial u}{\partial y} + \frac{\partial v}{\partial x}\right]^2\\ &+ \frac{RD}{C_\infty}\left[\left(\frac{\partial C}{\partial x}\right)^2 + \left(\frac{\partial C}{\partial y}\right)^2\right] + \frac{RD}{T_\infty}\left[\left(\frac{\partial T}{\partial x}\right)\left(\frac{\partial C}{\partial x}\right)\right.\\ &\left.+\left(\frac{\partial T}{\partial y}\right)\left(\frac{\partial C}{\partial y}\right)\right] + \frac{\sigma B_0^2}{T_\infty}u^2 + \frac{\nu}{k_p}u^2. \end{aligned} \tag{25}$$

Using Equation (25) modified with the help of Equation (17),

$$\begin{aligned} S'''_{gen} = &\frac{K_1}{T_\infty^2}\left[\left(\frac{\partial T}{\partial y}\right)^2 + \frac{16\sigma^* T_\infty^3}{3kk^*}\left(\frac{\partial T}{\partial y}\right)^2\right] + \frac{\mu}{T_\infty}\left(\frac{\partial u}{\partial y}\right)^2\\ &+ \frac{RD}{C_\infty}\left(\frac{\partial C}{\partial y}\right)^2 + \frac{RD}{T_\infty}\left(\frac{\partial T}{\partial y}\right)\left(\frac{\partial C}{\partial y}\right) + \frac{\sigma B_0^2}{T_\infty}u^2 + \frac{\nu}{k_p}u^2. \end{aligned} \tag{26}$$

Dimensionless system of entropy generation is defined as:

$$\begin{aligned} E_G = &Re\left(1 + \frac{4}{3}Rd\right)\theta'^2 + Re\frac{Br}{\Omega}f''^2 + Re\left(\frac{\zeta}{\Omega}\right)^2\lambda\phi'^2\\ &+ Re\frac{\zeta}{\Omega}\lambda\phi'\theta' + \frac{Br}{\Omega}(M+K)f'^2. \end{aligned} \tag{27}$$

The Bejan number states

$$\text{Be} = \frac{\text{Entropy genration due to irrevesablity of heat and mass transfer}}{\text{Total entropy generated}}$$

$$\text{Be} = \frac{\left(\text{Re}\left(1 + \frac{4}{3}\text{Rd}\right)\theta'^2 + +Re\left(\frac{\zeta}{\Omega}\right)^2\lambda\phi'^2 + Re\frac{\zeta}{\Omega}\lambda\phi'\theta'\right)}{Re\left(1+\frac{4}{3}Rd\right)\theta'^2 + Re\frac{Br}{\Omega}f''^2 + Re\left(\frac{\zeta}{\Omega}\right)^2\lambda\phi'^2 + Re\frac{\zeta}{\Omega}\lambda\phi'\theta' + \frac{Br}{\Omega}(M+K)f'^2}. \tag{28}$$

HOMOTOPY SOLUTIONS

There are several techniques available to solve non-linear problems. The homotopy analysis method (HAM) is initially constructed by Liao [47]. Moreover, he altered a non-zero auxiliary parameter [48]. This parameter shows the way to calculate the convergence rate. It also offers great independence with which to make the initial guesses of the solutions.

The initial guesses for satisfying the boundary conditions

$$f_0 = f_w + \left(\frac{1}{1+\Gamma}\right)1 - e^{-\eta}$$
$$\theta_0 = \frac{Bi * e^{-\eta}}{1+Bi}$$
$$\phi_0 = -\left(\frac{Nt}{Nb}\right) * \frac{Bi * e^{-\eta}}{1+Bi}.$$

L_f, L_θ, and L_ϕ are the linear operators

$$L_f = f''' - f'$$
$$L_\theta = \theta'' - \theta$$
$$L_\phi = \phi'' - \phi$$

while obeying the resulting properties

$$L_f\left[E_1 + E_2 e^{\eta} + E_3 e^{-\eta}\right] = 0$$
$$L_\theta\left[E_4 e^{\eta} + E_5 e^{-\eta}\right] = 0$$
$$L_\phi\left[E_6 e^{\eta} + E_7 e^{-\eta}\right]$$

The zero$^{\text{th}}$ order deformation is

$$(1-p)\,L_f\left[f(\eta;p) - f(\eta)\right] = p\,h_f \mathcal{N}_f\left[f(\eta;p)\right]$$
$$(1-p)L_\theta\left[\theta(\eta;p) - \theta_0(\eta)\right] = p\,h_\theta \mathcal{N}_\theta\left[\theta(\eta;p), f(\eta;p), \phi(\eta;p)\right]$$
$$(1-p)L_\phi\left[\phi(\eta;p) - \phi_0(\eta)\right] = p\,h_\phi \mathcal{N}_\phi\left[\phi(\eta;p), \theta(\eta;p), f(\eta;p)\right]$$

where $p \epsilon\ [0,1]$

h_f, h_θ, and h_ϕ are the non-zero auxiliary constants, and $\mathcal{N}_f$, $\mathcal{N}_\theta$, and $\mathcal{N}_\phi$ are the non-linear operators given by

$$\mathcal{N}_f\left[f(\eta;p),\theta(\eta;p)\right] = \frac{\partial^3 f(\eta;p)}{\partial\eta^3} - \left(\frac{\partial f(\eta;p)}{\partial\eta}\right)^2 + f(\eta;p)\frac{\partial^2 f(\eta;p)}{\partial\eta^2} + \alpha_1\left(2\frac{\partial f(\eta;p)}{\partial\eta}\frac{\partial^3 f(\eta;p)}{\partial\eta^3} - f(\eta;p)\frac{\partial^4 f(\eta;p)}{\partial\eta^4}\right) + (3\alpha_1+2\alpha_2)\left(\frac{\partial f(\eta;p)}{\partial\eta}\right)^2 + 6\beta Re\frac{\partial^3 f(\eta;p)}{\partial\eta^3}\left(\frac{\partial f(\eta;p)}{\partial\eta}\right)^2 - (M+K)\frac{\partial f(\eta;p)}{\partial\eta}$$

$$\mathcal{N}_\theta\left[f(\eta;p),\theta(\eta;p),\phi(\eta;p)\right] = \left(1+\frac{4}{3}Rd\right)\frac{\partial^2\theta(\eta;p)}{\partial\eta^2} + Prf(\eta;p)\frac{\partial\theta(\eta;p)}{\partial\eta} - Pr\gamma\left[\left[f(\eta;p)\right]\right]^2\frac{\partial^2\theta(\eta;p)}{\partial\eta^2} - Pr\gamma f(\eta;p)\frac{\partial f(\eta;p)}{\partial\eta}\frac{\partial\theta(\eta;p)}{\partial\eta} + PrS\theta(\eta;p) + PrNb\frac{\partial\theta(\eta;p)}{\partial\eta}\frac{\partial\phi(\eta;p)}{\partial\eta} + PrNt\left[\frac{\partial\theta(\eta;p)}{\partial\eta}\right]^2$$

$$\mathcal{N}_\phi\left[f(\eta;p),\theta(\eta;p),\phi(\eta;p)\right] = \frac{\partial^2\phi(\eta;p)}{\partial\eta^2} + Le f(\eta;p)\frac{\partial\phi(\eta;p)}{\partial\eta} + \frac{Nt}{Nb}\frac{\partial^2\theta(\eta;p)}{\partial\eta^2}$$

$$f(0;p) = f_w, f'(0;p) = 1+\Gamma f''(0:p), f'(\infty;p) = 0$$
$$\theta'(0;p) = -Bi\left(1-\theta(0;p)\right), \theta(\infty;p) = 0$$
$$\phi'(0;p) = -\frac{Nt}{Nb}\theta'(0;p), \phi'(\infty;p) = 0$$

The m^{th} order deformation equations are

$$L_f\left[f_m(\eta) - \chi_m f_{m-1}(\eta)\right] = h_f R_{f,m}(\eta)$$
$$L_\theta\left[\theta_m(\eta) - \chi_m\theta_{m-1}(\eta)\right] = h_\theta R_{\theta,m}(\eta)$$
$$L_\phi\left[\phi_m(\eta) - \chi_m\phi_{m-1}(\eta)\right] = h_\phi R_{\phi,m}(\eta)$$

where

$$\chi_m = \begin{cases}0, & m\le 1\\ 1, & m>1\end{cases},$$

$$R_{f,m}(\eta) = f'''_{m-1} + \sum_{k=0}^{m-1}\Big[f_{m-1-k}f''_k - f'_{m-1-k}f_k' + \alpha_1\left(2f'_{m-1-k}f'''_k - f_{m-1-k}f^{iv}_k\right) + (3\alpha_1+2\alpha_2)f''_{m-1-k}f''_k + 6\beta Ref'''_{m-1-l}\sum_{j=0}^{l}f''_{l-j}f''_j - (M+K)\alpha f_{m-1-k}'\Big]$$

$$R_{\theta,m}(\eta) = \left(1+\frac{4}{3}Rd\right)\theta''_{m-1} + Pr\sum\nolimits_{k=0}^{m-1}\left[\theta'_{m-1-k}f_k\right] - Pr\gamma\left[\left(f_{m-l-1}\sum\nolimits_{j=0}^{l}f_{1-j}'\theta_j' + f_{m-l-1}\theta''_l\right)\right] + PrNb\sum\nolimits_{k=0}^{m-1}\theta_{m-1-k}'\phi_k + PrNt\sum\nolimits_{k=0}^{m-1}\theta_{m-1-k}'\theta_k' + PrS\theta_{m-1}$$

$$R_{\phi,m}(\eta) = \phi''_{m-1} + Le\sum\nolimits_{k=0}^{m-1}\phi_{m-1-k}'f_k + \frac{Nt}{Nb}\sum\nolimits_{k=0}^{m-1}\theta_{m-1-k}'\theta_k'$$

$$f_m(0) = 0, f_m'(0) - \Gamma f_m''(0) = 0, \ \theta_m'(0) - Bi\theta_m(0) = 0,$$
$$\phi_m'(0) + \frac{Nt}{Nb}\theta_m'(0) = 0$$
$$f_m'(\eta)\to 0, \theta_m'(\eta)\to 0, \phi_m(\eta)\to 0 as\ \eta\to\infty.$$

with boundary conditions

$$f_m'(0) = f_m(0) = f_m'(\infty) = \theta_m(0) = \theta_m(\infty) = \phi_m(0) = \phi_m(\infty) = 0.$$

The appropriate solutions $\left[f^*_m, \theta^*_m, \phi^*_m\right]$ are

$$f_m(\eta) = f^*_m(\eta) + E_1 + E_2e^{\eta} + E_3e^{-\eta},$$
$$\eta_m(\eta) = \eta^*_m(\eta) + E_4e^{\eta} + E_5e^{-\eta},$$
$$\eta_m(\eta) = \eta^*_m(\eta) + E_6e^{\eta} + E_7e^{-\eta}.$$

CONVERGENCE ANALYSIS

The auxiliary parameters h_f, h_θ, and h_ϕ act as a vital part of convergence series solutions. The h-charts of $f''(0)$, $\theta'(0)$, and $\phi'(0)$ for Re, γ, and Nb are shown in **Figure 2**. From these curves, the straight line is referred as the h-curve. The convergent approximation is selected from this straight line of the curves. We note that h-curve of $f''(0)$, $\theta'(0)$, and $\phi'(0)$ shrinks as we enhance the range of Re,γ, and Nb, which shows the larger order approximation will be needed if the larger value of Re,γ, and Nb is employed. Approximations values of HAM with CPU time is denoted in **Table 1**.

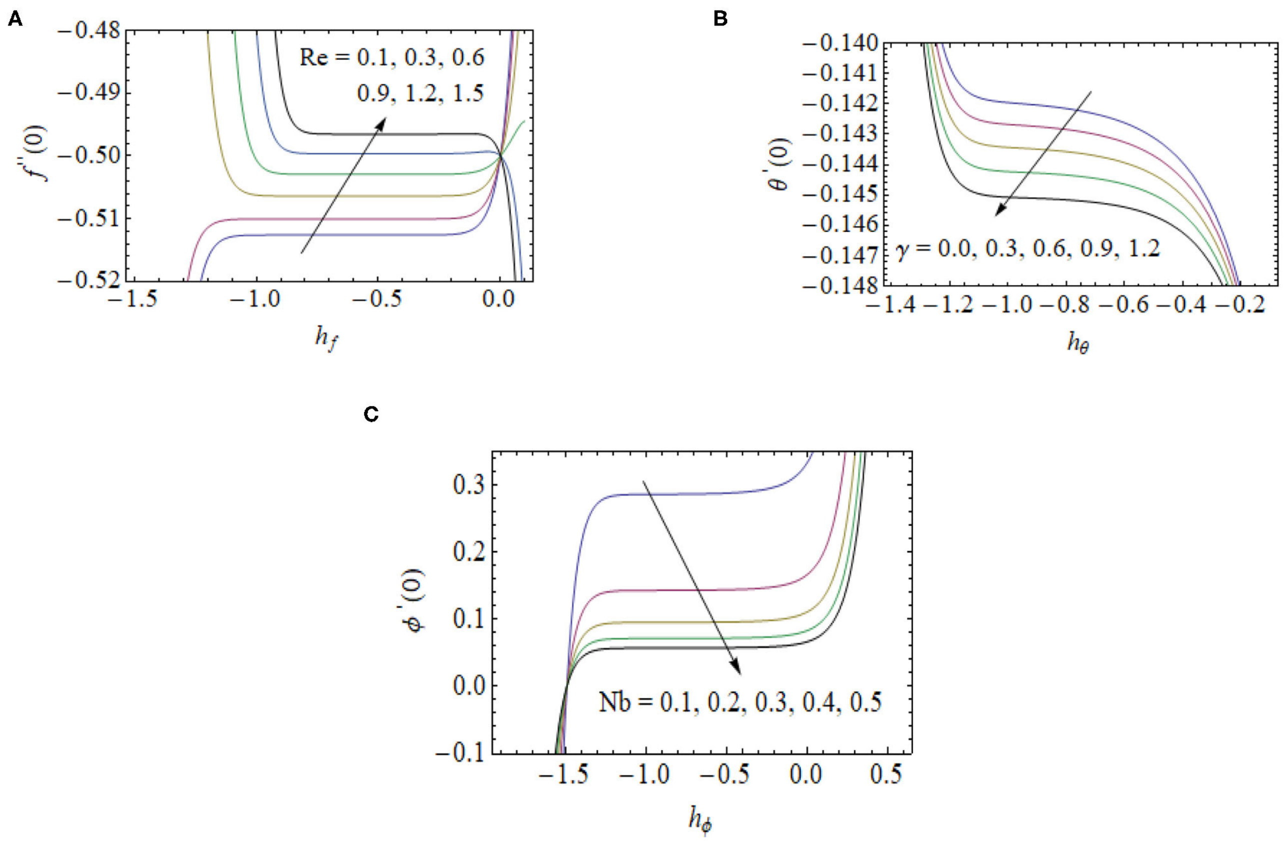

FIGURE 2 | (A–C) $h-$ curves for h_f, h_θ, h_ϕ.

TABLE 1 | Order of approximations of HAM.

Order	$-f''(0)$	$-\theta'(0)$	$\phi'(0)$	CPU time (s)
1	0.5006	0.1603	0.0801	0.422
5	0.5018	0.1474	0.7550	3.688
10	0.5018	0.1454	0.7273	21.781
15	0.5018	0.1441	0.7205	83.750
20	0.5018	0.1435	0.0717	290.735
25	0.5018	0.1432	0.0716	985.219
30	0.5018	0.1432	0.0716	2166.670

COMPUTATIONAL RESULTS AND DISCUSSION

The numerical calculations of velocity, concentration, temperature, entropy generation, and the Bejan number are discussed in this section. The homotopy technique is used for solving the non-linear governing Equations (18)–(20) with boundary conditions (21). The graphical results of entropy, Bejan number, temperature, Nusselt number, nanoparticle concentration, Sherwood number, and velocity profiles are computed via different flow parameters included in this study with the fixed values of $\alpha_1 = \alpha_2 = \beta = Bi = f_w = N_t = 0.2$, $Re = Pr = Le = \Gamma = 1.0$, $M = \gamma = 0.5, Rd = 0.3$, $Hg = -0.1$, $N_b = 0.4$, $Br = 5.0$, and $\lambda = \Omega = \zeta = 1.0$.

Impact on Velocity

It is observed from **Figure 3A** that the velocity is reduced to increase the values of the velocity slip parameter due to the ratio of stretching velocity and the viscosity of the fluid. The effect of the slip parameter in velocity has had more impact in the absence of a porous medium. **Figure 3B** indicates that the velocity diminishes when the magnetic field (M) raises. Improved Lorentz force is observed because of the increasing the values of M that opposes the fluid motion. Thus, we conclude that the velocity profile diminishes.

Impact on Temperature

The impact of the radiation parameter Rd on the temperature profile is examined in **Figure 4A**. The temperature in the radiation parameter is high. Comparing the radiation effects with Christov-Cattaneo and normal heat flux, we observed that the radiation effect is quite low for Christov-Cattaneo heat flux. **Figure 4B** displays the influence of the Biot number on the temperature profile. From this figure, we observed that temperature is a rising function of Bi close to the sheet. Since Bi affects more temperature near the surface. Heat transfer

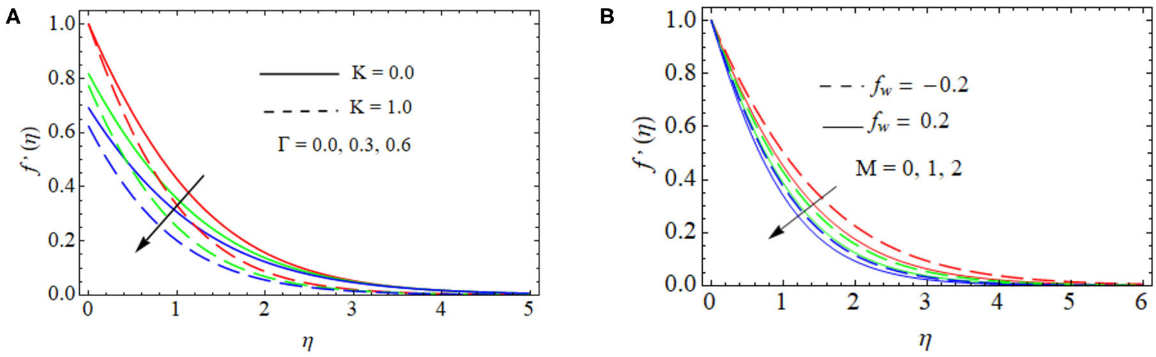

FIGURE 3 | (A,B) Impact of Γ and M on velocity profile $f'(\eta)$.

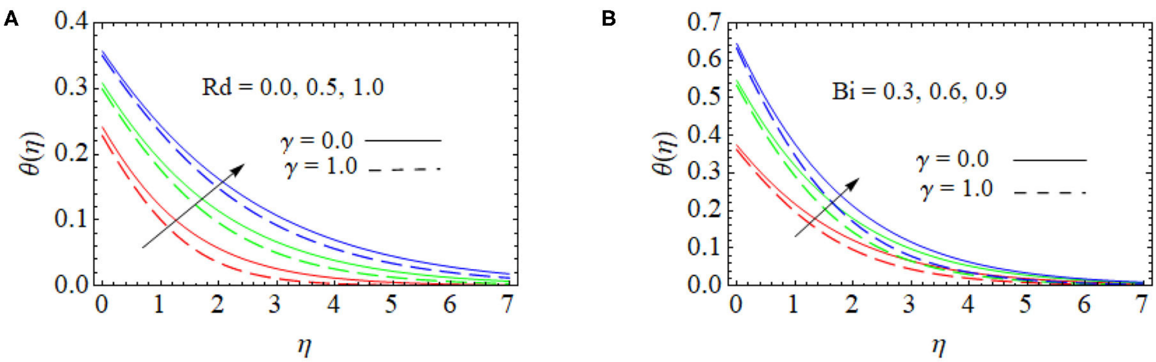

FIGURE 4 | (A,B) Impact of Rd and Bi on temperature profile $\theta(\eta)$.

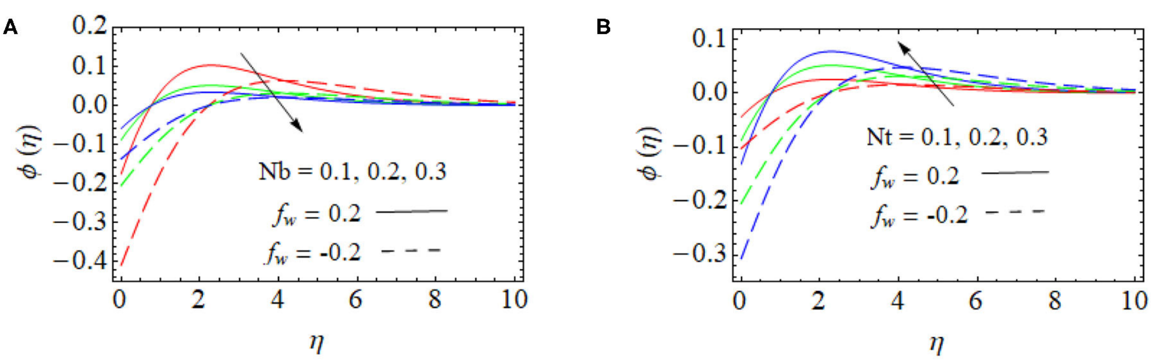

FIGURE 5 | (A,B) Impact of Nb and Nt on concentration profile $\phi(\eta)$.

resistance is higher within the body compared to the surface of the sheet for rising values Bi.

Impact on Nanoparticle Volume Concentration

In **Figure 5A**, the effect of concentration profile with growing values of the Brownian motion parameter Nb is depicted. In suction cases, higher values of Nb increase the concentration profile close to that of the surface of the sheet, and, suddenly, the concentration begins to fall, stabilizing far away from the surface of the sheet. This is due to the appearance of passive surface conditions for the concentration profile. Moreover, the injection at the sheet shows the concentration is rising near the sheet, and it diminishes far away from the surface of the sheet. The influence of the thermophoresis parameter Nt in the concentration profile $\phi(\eta)$. is highlighted in **Figure 5B**. When

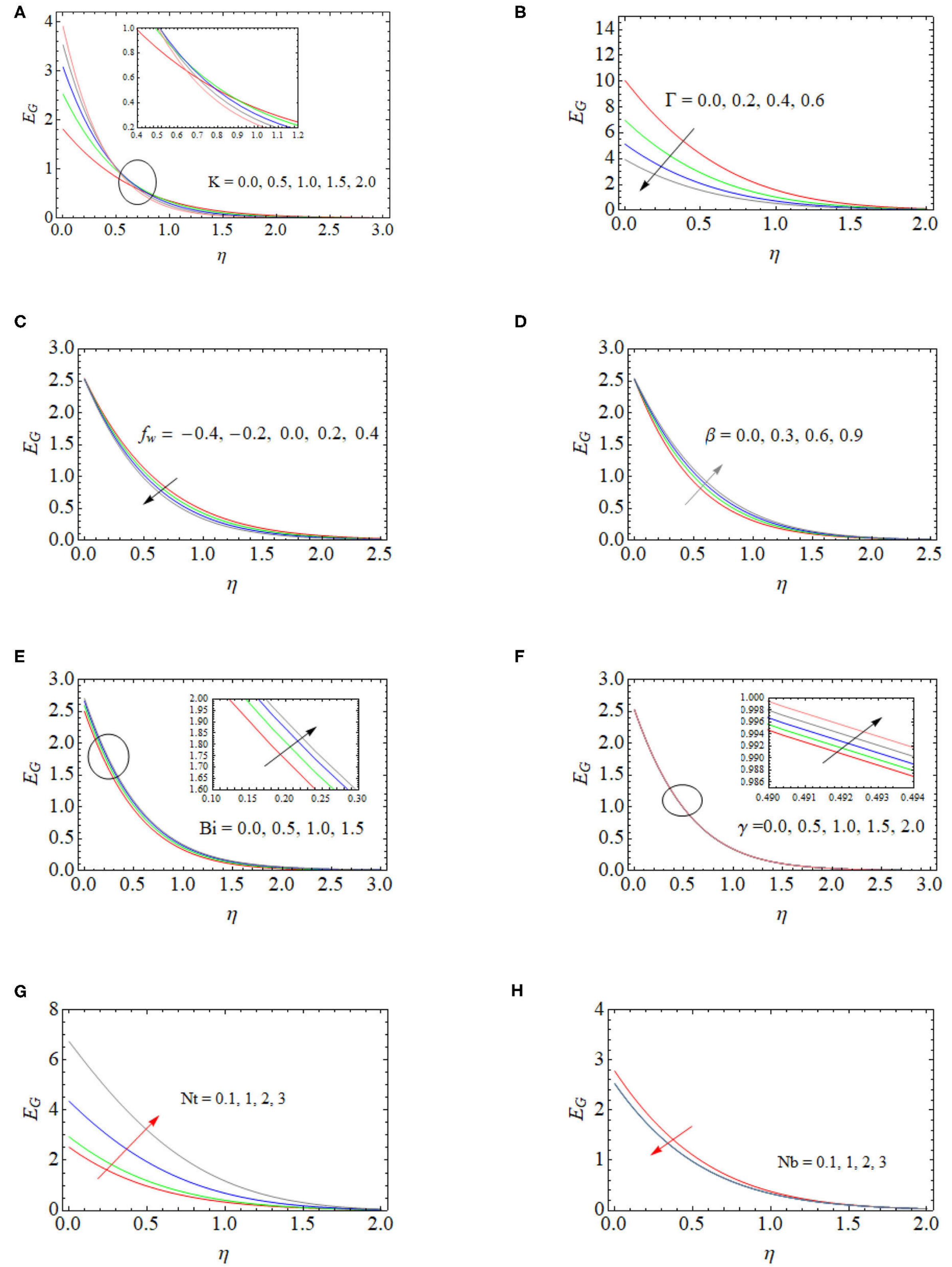

FIGURE 6 | (A–H) Impacts of K, Γ, f_w, β, Bi, γ, Nt, and Nb on entropy generation E_G.

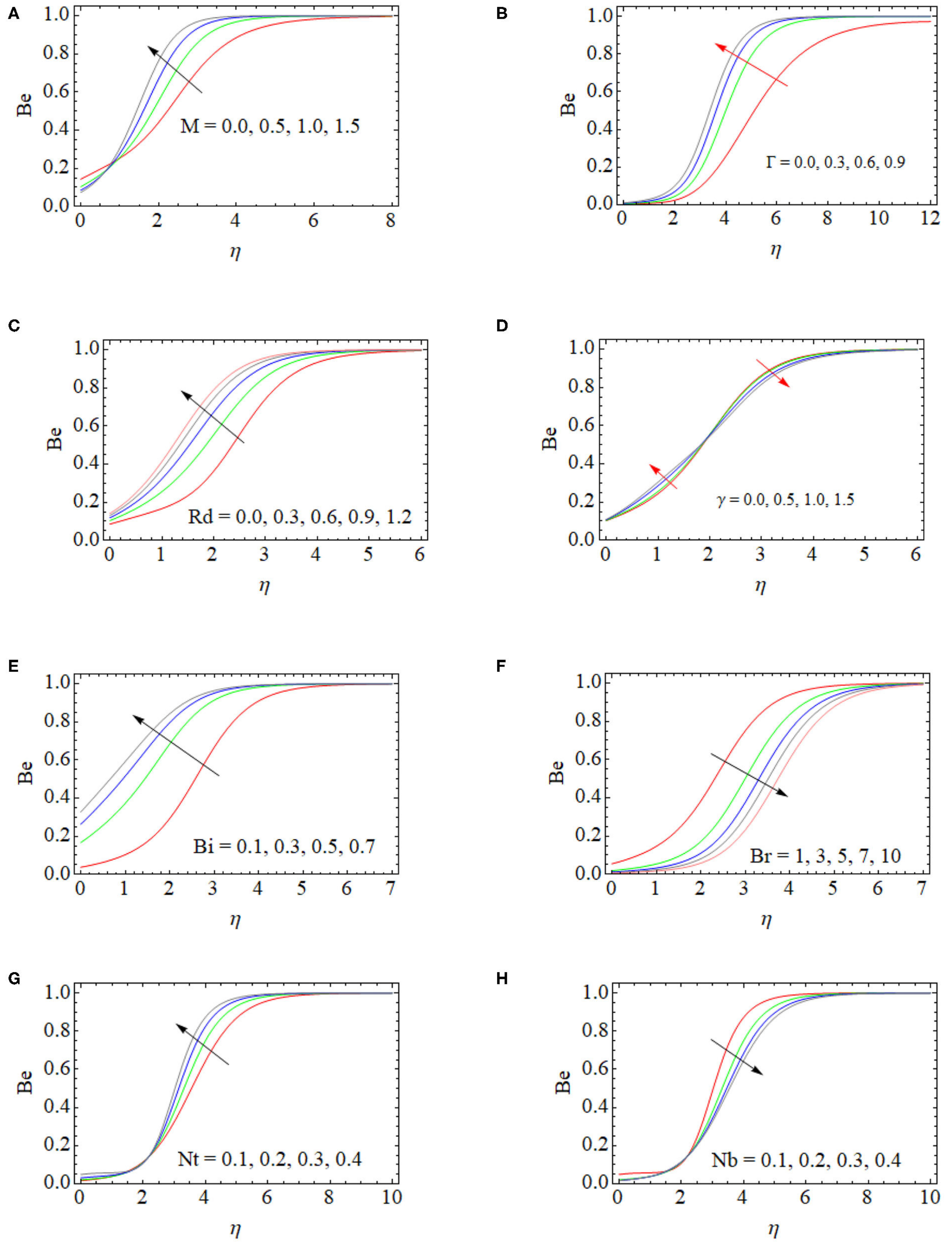

FIGURE 7 | (A–H) Impact of *M*, Γ, *Rd*, γ, *Bi*, *Br*, *Nt*, and *Nb* on the Bejan number *B*.

there is suction in the sheet, with a rise in Nt, the concentration of the liquid decreases near to thsheet at certain stage starts to fall and stabilize away from the endpoints of the surface of the sheet. When there is an injection at the sheet, higher values of Nt decreases the concentration profile near the sheet, and it increases far away from the surface of the sheet.

Impact on Entropy Generation

The Effects of distinct fluid parameters on the entropy generation profile are highlighted in **Figures 6A–G**. **Figure 6A** depicts the influence of porous parameter in entropy profile. Initially, the entropy rate increases for the porous parameter at a certain stage ($\eta = 0.6$) before it becomes to fall. The responses of the slip parameter on entropy generation were succinctly depicted in **Figure 6B**. From this figure, it was obviously noted that entropy generation was inversely proportional to slip parameter. This causes a decrease in large values of slip parameter and temperature gradients in the boundary layer when retaining the fluid friction as we proceed. This occurrence induces a suppression in entropy generation since heat transfer was committed. **Figures 6C–E** displayed the impact of the suction\ injection parameter (f_w.), material parameter (β) and Biot number (Bi) on the entropy profile (E_G). Our examination obtained that higher range of f_w, reduces the entropy generation profile, and the entropy generation rate is enhanced for higher β and Bi.

The effect of thermal relaxation time (γ) on the entropy genation profile is sketched in **Figure 6F**. It is obvious that thermal relaxation time is small for temperature and heat transfer rates. In addition, domination of the irreversibility in heat transfer affected the heat flux. Thus, we have seen a small increase in the entropy of the system. Performance of *Nt* and *Nb* on entropy generation profile (E_G) is shown in **Figures 6G,H**, which shows that entropy is increased with an increase of *Nt*, whereas E_G is inversely proportional to *Nb*. The Brownian motion induces the nanoparticles temperature, but it reduces the temperature gradient on wall. As a result, entropy generation parameter reduces where *Nt* is directly proportional to temperature gradient and creates ambient atmosphere for higher values of E_G.

Impact on the Bejan Number

The Bejan number (*Be*) is a dimensionless quantity that specifies the ratio of entropy generation between heat transfer and the total entropy generation where Bejan numbers take values from 0 to 1. If *Be* is nearly equal to 1, the entropy generation will become more due to heat transfer. It is clear from **Figure 7A** that, with an escalation in the applied magnetic field, there is an augmentation in the Bejan number. The consequence of heat transfer entropy develops as we move up from the surface. The entropy effect has full domination because of the heat transfer while it is also outlying from the region. This is the reason behind how the augmenting value of *M* brings a stronger frictional effect, which leads to an increase in the liquid temperature. There is also a consequent development in the Be, as shown in **Figure 7A**. From **Figure 7B**, it is observed that the *Be* is increased for the increase in the slip parameter (Γ). Physically, larger values of (Γ) enhance the temperature gradient inside the regime, which induces the Bejan number and irreversibility of heat transfer.

Figure 7C states that, with the rise of the radiation constant Rd, the Bejan number is boosted. This is due to the total entropy generation dominated by thermal irreversibility. **Figure 7D** shows the effect of the thermal relaxation time (γ) on the *Be*. At first, the *Be* is augmented for higher values of γ at a sudden point ($\eta = 2.2$). Consequently, the Bejan number profile reduces for the values of γ. **Figure 7E** shows that the Bi displays a trend of raising the Be. The demonstration of such an increasing trend of the Bejan number explains how the entropy production near the surface is large due to the liquid friction—at least relative to that of the heat transfer irreversibility. The variation of the Brinkmann number Br is sketched in **Figure 7F**. This figure shows that the Bejan number is reduced, as we have to enhance the Br. **Figures 7G,H** shows the influence of thermophoresis (*Nt)* and Brownian motion (*Nb*) parameters on the Bejan number. From these plots, we note that *Nt*and *Nb* have inverse effects on the Bejan number profile.

Impact on Physical Entities

Figures 8–11 illustrate the effects of different physical parameters on the local Nusselt number and local Sherwood number. The influence of f_w and γ on Nu_x is shown in **Figure 8**: heat transfer decays for higher values of f_w and γ. The same phenomena can be observed for larger values *Hg* and γ on the Nusselt number profile, as presented in **Figure 9**. The combined effects of *Nb* and *M* as well as *Nt* and *M* are shown in **Figures 10**, **11**, respectively. From these figures, we conclude that thermophoresis (*Nt*) and Brownian motion (*Nb*) parameters have produce the converse trend in the mass transfer rate.

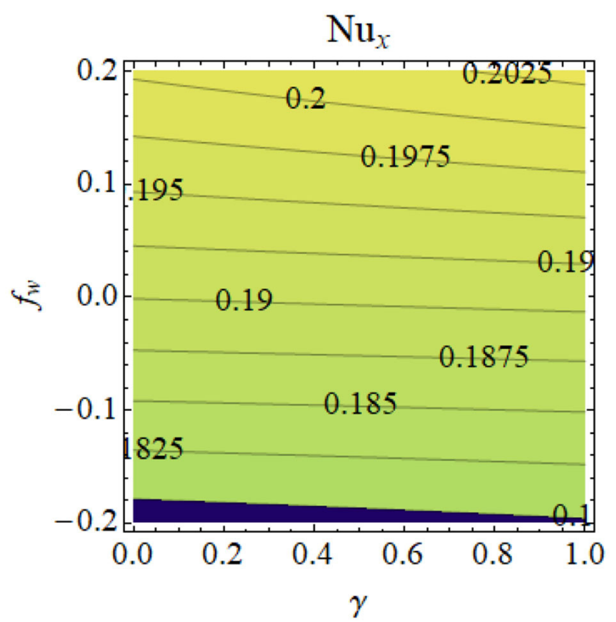

FIGURE 8 | Effects of γ and f_w on Nu_x.

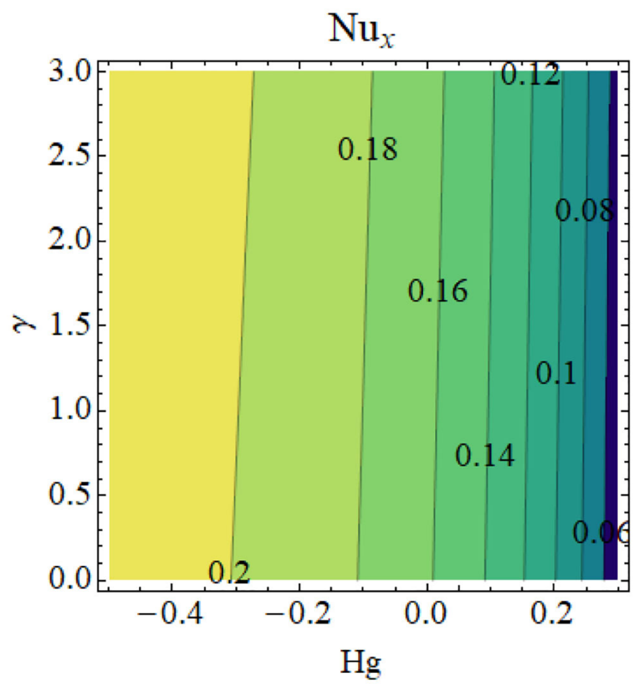

FIGURE 9 | Effects of *Hg* and γ on Nu_x.

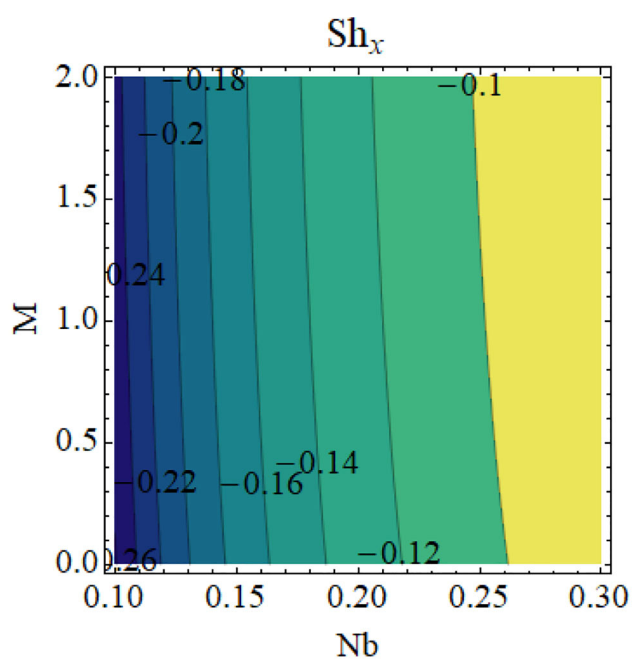

FIGURE 10 | Effects of *Nb* and *M* on Sh_x.

NUMERICAL CODE VALIDATION

In this segment, we examine the code validation of early published works of literature. **Table 2** validates the results of

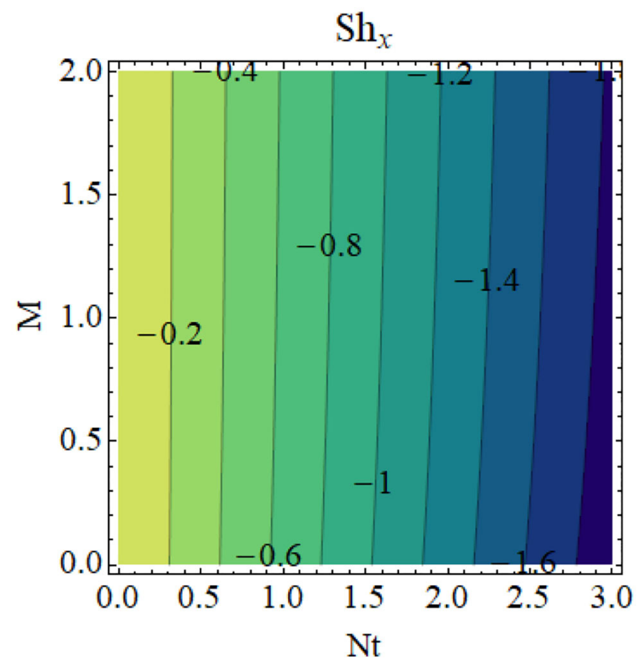

FIGURE 11 | Effects of *Nt* and *M* on Sh_x.

TABLE 2 | Validation of $-f''(0)$ and $-\theta'(0)$ for the limiting case $M = 0,\ K = 0,\ Nb = 0,\ Nt = 0,\ Rd = 0,\ S = 0$, and $Bi \to \infty$.

Order	$-f''(0)$		$-\theta'(0)$	
	Imtiaz et al. [37]	Present	Imtiaz et al. [37]	Present
1	0.81450	0.8145	0.72778	0.727778
5	0.81211	0.812208	0.58070	0.580701
8	0.81235	0.812345	0.57779	0.577789
14	0.81235	0.812353	0.57871	0.578711
17	0.81235	0.812353	0.57878	0.578778
25	0.81235	0.812353	0.57878	0.57877
30	0.81235	0.812353	0.57878	0.57877
35	0.81235	0.812353	0.57878	0.57877

$-f''(0)$ and $-\theta'(0)$ for the limiting case $M = 0$, $K = 0$, $Nb = 0$, $Nt = 0$, $Rd = 0$, $S = 0$, and $Bi \to \infty$ with Imtiaz et al. [37]. Moreover, the skin friction rate is also validated by the same literature [37] when $M = K = 0$ (see **Table 3**). **Table 4** exhibits the matching results of reduced Nusselt number with the references [20, 49–51]. From the above validation, results show that the current simulation is considered an efficient one.

KEY RESULTS

The present research work examines the entropy generation influence on third-grade nanoliquid flow caused by a stretching sheet in the appearance of Magnetic field, radiation, and convective heating effects. Christov-Cattaneo heat flux replaces

TABLE 3 | Comparison of $Re^{0.5}C_f$ for different values when $M = K = 0$.

α_1	α_2	β	*Re*	Imtiaz et al. [37]	Present
0.0	0.1	0.1	0.1	0.04605	0.04605
0.1				1.06680	1.06680
0.2				1.17470	1.17470
0.1	0.0	0.1	0.1	1.12010	1.12010
	0.1			1.06680	1.06680
	0.2			1.01830	1.01830
	0.1	0.0		1.06290	1.06290
0.1		0.1		1.06680	1.06680
		0.2		1.07030	1.07030
		0.1	0.0	1.06290	1.06290
			0.1	1.06680	1.06680
			0.2	1.07060	1.07060

TABLE 4 | Matching results of reduced Nusselt number with the restricting case $Rd = Ec = M = Nt = Nb = \gamma = S = K = \Gamma = f_w = 0$, and $Bi \to \infty$.

Pr	Wang [49]	Gorla and Sidawi [50]	Khan and Pop [20]	Makinde and Aziz [51]	Present
0.20	0.1691	0.1691	0.1691	0.1691	0.1691
0.70	0.4539	0.5349	0.4539	0.4539	0.4539
2.00	0.9114	0.9114	0.9113	0.9114	0.9114
7.00	1.8954	1.8905	1.8954	1.8954	1.8954

ordinary heat flux. HAM is employed to validate the non-linear governing equations. Results of velocity, temperature, nanoparticle volume concentration, the system of entropy, the Bejan number, mass, and heat transfer rates are presented graphically. We obtained the following main upshots:

1. A falling tendency of the velocity profile is detectable while we keep increasing the values of the velocity slip and magnetic field parameter.
2. An augmentation in the range of radiation parameter and Biot number causes an increasing trend.
3. The concentration of the nanoparticle volume fraction is found to be a diminishing function of the thermophoretic parameter. On the other hand, a contrary impact is identified for the Brownian motion parameter.
4. The irreversibility of the system rises as we keep enhancing the values of the Biot number, thermal relaxation time, material parameter, and the Brinkmann number, but an inverse occurrence takes place as we increase the slip parameter and suction/injection parameter.
5. The Bejan number increases with greater values of the slip parameter, Biot number, thermophoresis parameter, magnetic parameter, and radiation parameter, whereas it reduces for larger values of the Brinkmann number and Brownian motion parameter.

DATA AVAILABILITY STATEMENT

The raw data supporting the conclusions of this article will be made available by the authors, without undue reservation.

AUTHOR CONTRIBUTIONS

All authors listed have made a substantial, direct and intellectual contribution to the work, and approved it for publication.

FUNDING

This research was supported by the Research Group Project (RGP), University of Tabuk, Tabuk 71491, Saudi Arabia, under Grant No. RGP-0207-14440.

REFERENCES

1. Choi SUS, Eastman JA. *Enhancing Thermal Conductivity of Fluids With Nanoparticles*, Report No. ANL/MSD/CP 84938, Argonne National Laboratory, Lemont, IL, United States (1995). Available online at: https://ecotert.com/pdf/196525_From_unt-edu.pdf
2. Mushtaq A, Mustafa M, Hayat T, Alsaedi A. Numerical study for rotating flow of nanofluids caused by an exponentially stretching sheet. *Adv Powder Technol.* (2016) 27:2223–31. doi: 10.1016/j.apt.2016.08.007
3. Reddy PS, Chamkha AJ. Soret and dufour effects on MHD convective flow of Al_2O_3-water and TiO_2-water nanofluids past a stretching sheet in porous media with heat generation/absorption. *Adv Powder Technol.* (2016) 27:1207–18. doi: 10.1016/j.apt.2016.04.005
4. Shit GC, Haldar R, Mandal S. Entropy generation on MHD flow and convective heat transfer in a porous medium of exponentially stretching surface saturated by nanofluids. *Adv Powder Technol.* (2017) 28:1519–30. doi: 10.1016/j.apt.2017.03.023
5. Gireesha BJ, Mahanthesh B, Thammanna GT, Sampathkumar P. Hall effects on dusty nanofluid two-phase transient flow past a stretching sheet using KVL model. *J Mol Liq.* (2018) 256:139–47. doi: 10.1016/j.molliq.2018.01.186
6. RamReddy Ch, Murthy PVSN, Chamkha AJ, Rashad AM. Soret effect on mixed convection flow in a nanofluid under convective boundary condition. *Int J Heat Mass Transfer.* (2013) 64:384–92. doi: 10.1016/j.ijheatmasstransfer.2013.04.032
7. Ghalambaz M, Behseresht A, Behseresht J, Chamkha AJ. Effects of nanoparticles diameter and concentration on natural convection of the Al_2O_3-water nanofluids considering variable thermal conductivity around a vertical cone in porous media. *Adv Powder Technol.* (2015) 26:224–35. doi: 10.1016/j.apt.2014.10.001
8. Joshi PS, Mahapatra PS, Pattamatta A. Effect of particle shape and slip mechanism on buoyancy induced convective heat transport with nanofluids. *Phys Fluids.* (2017) 29:122001. doi: 10.1063/1.4996824
9. Chamkha AJ, Abbasbandy S, Rashad AM, Vajravelu K. Radiation effects on mixed convection about a cone embedded in a porous medium filled with a nanofluid. *Meccanica.* (2013) 48:275–85. doi: 10.1007/s11012-012-9599-1
10. Reddy PS, Sreedevi P, Chamkha AJ. MHD boundary layer flow, heat and mass transfer analysis over a rotating disk through porous medium saturated by Cu-water and Ag-water nanofluid with chemical reaction. *Powder Technol.* (2017) 307:46–55. doi: 10.1016/j.powtec.2016.11.017
11. Anitha S, Loganathan K, Pichumani M. Approaches for modelling of industrial energy systems: correlation of heat transfer characteristics between magnetohydrodynamics hybrid nanofluids and performance analysis of industrial length-scale heat exchanger. *J Therm Anal Calorim.* doi: 10.1007/s10973-020-10072-8

12. Liu Z, Li D, Song Y, Pan X, Li D, Xuan X. Surface-conduction enhanced dielectrophoretic-like particle migration in electric-field driven fluid flow through a straight rectangular microchannel. *Phys Fluids.* (2017) 29:102001. doi: 10.1063/1.4996191
13. Zargartalebi H, Ghalambaz M, Noghrehabadi A, Chamkha AJ. Natural convection of a nanofluid in an enclosure with an inclined local thermal non-equilibrium porous fin considering buongiorno's model. *Numer Heat Transf A.* (2016) 70:432–45. doi: 10.1080/10407782.2016.1173483
14. Sakiadis BC. Boundary-layer behavior on continuous solid surfaces: I. Boundary layer equations for two-dimensional and axisymmetric flow. *AIChE J.* (1961) 7:26–28. doi: 10.1002/aic.690070108
15. Magyari E, ChamkhaA J. Combined effect of heat generation or absorption and first-order chemical reaction on micropolar fluid flows over a uniformly stretched permeable surface: the full analytical solution. *Int J Therm Sci.* (2010) 49:1821–8. doi: 10.1016/j.ijthermalsci.2010.04.007
16. Gupta PS, Gupta AS. Heat and mass transfer on a stretching sheet with suction or blowing. *Can J Chem Eng.* (1977) 55:744–46. doi: 10.1002/cjce.5450550619
17. Magyari E, Keller B. Heat mass transfer in the boundary layers on an exponentially stretching continuous surface. *J Phys D Appl Phys B.* (1999) 32:577. doi: 10.1088/0022-3727/32/5/012
18. Cortell R. Viscous flow and heat transfer over a nonlinearly stretching sheet. *Appl Math Comput.* (2007) 184:864–73. doi: 10.1016/j.amc.2006.06.077
19. Vajravelu K. Viscous flow over a nonlinearly stretching sheet. *Appl Math Comput.* (2001) 124:281–88. doi: 10.1016/S0096-3003(00)00062-X
20. Khan WA, Pop I. Boundary-layer flow of a nanofluid past a stretching sheet. *Int J Heat Mass Transfer*. (2010) 53:2477–83. doi: 10.1016/j.ijheatmasstransfer.2010.01.032
21. Rana P, Bhargava R. Flow and heat transfer of a nanofluid over a nonlinearly stretching sheet: a numerical study. *Commun Nonlinear Sci Numer Simul.* (2012) 17:212–26. doi: 10.1016/j.cnsns.2011.05.009
22. Khedr MEM, Chamkha AJ, Bayomi M. MHD flow of a micropolar fluid past a stretched permeable surface with heat generation or absorption. *Nonlinear Anal Model.* (2009) 14:27–40. doi: 10.15388/NA.2009.14.1.14528
23. Ghalambaz M, Izadpanahi E, Noghrehabadi A, Chamkha AJ. Study of the boundary layer heat transfer of nanofluids over a stretching sheet: passive control of nanoparticles at the surface. *Can J Phys.* (2014) 93:725–33. doi: 10.1139/cjp-2014-0370
24. Al-Mudhaf A, Chamkha AJ. Similarity solutions for MHD thermosolutal marangoni convection over a flat surface in the presence of heat generation or absorption effects. *Heat Mass Transfer.* (2005) 42:112–21. doi: 10.1007/s00231-004-0611-8
25. Chamkha AJ, Issa C, Khanafer K. Natural convection from an inclined plate embedded in a variable porosity porous medium due to solar radiation. *Int J Therm Sci.* (2002) 41:73–81. doi: 10.1016/S1290-0729(01)01305-9
26. Khan WA, Aziz A. Double-diffusive natural convective boundary layer flow in a porous medium saturated with a nanofluid over a vertical plate: prescribed surface heat, solute and nanoparticle fluxes. *Int J Therm Sci.* (2011) 50:2154–60. doi: 10.1016/j.ijthermalsci.2011.05.022
27. Oyelakin IS, Mondal S, Sibanda P. Unsteady Casson nanofluid flow over a stretching sheet with thermal radiation, convective and slip boundary conditions. *Alexandria Eng J.* (2016) 55:1025–35. doi: 10.1016/j.aej.2016.03.003
28. Gorla RSR, Chamkha AJ. Natural convective boundary layer flow over a nonisothermal vertical plat embedded in a porous medium saturated with a nanofluid. *Nanosc Microsc Therm.* (2011) 15:81–94. doi: 10.1080/15567265.2010.549931
29. Chamkha AJ, Mohamed RA, Ahmed SE. Unsteady MHD natural convection from a heated vertical porous plate in a micropolar fluid with joule heating, chemical reaction and radiation effects. *Meccanica.* (2011) 46:399–411. doi: 10.1007/s11012-010-9321-0
30. Chamkha AJ. Hydromagnetic natural convection from an isothermal inclined surface adjacent to a thermally stratified porous medium. *Int J Eng Sci.* (1997) 35:975–86. doi: 10.1016/S0020-7225(96)00122-X
31. Chamkha AJ. Solar radiation assisted natural convection in uniform porous medium supported by a vertical flat plate. *ASME J Heat Transfer.* (1997) 119:35–43. doi: 10.1115/1.2824104
32. Chamkha AJ, Al-Mudhaf AF, Pop I. Effect of heat generation or absorption on thermophoretic free convection boundary layer from a vertical flat plate embedded in a porous medium. *Int Commun Heat Mass.* (2006) 33:1096–102. doi: 10.1016/j.icheatmasstransfer.2006.04.009
33. Fourier J. *Theorie analytique de la chaleur, par M. Fourier*. Paris: Chez Firmin Didot, père et fils (1822).
34. Cattaneo C. Sulla conduzione del calore. In: Pignedoli A, editor. *Some Aspects of Diffusion Theory*. Berlin; Heidelberg: Springer (2011). doi: 10.1007/978-3-642-11051-1_5
35. Christov CI. On frame indifferent formulation of the Maxwell-Cattaneo model of finite-speed heat conduction. *Mech Res Commun.* (2009) 36:481–86. doi: 10.1016/j.mechrescom.2008.11.003
36. Loganathan K, Sivasankaran S, Bhuvaneshwari M, Rajan S. Second-order slip, cross-diffusion and chemical reaction effects on magneto-convection of oldroyd-B liquid using Cattaneo–Christov heat flux with convective heating. *J Therm Anal Calorim.* (2019) 136:401–9. doi: 10.1007/s10973-018-7912-5
37. Imtiaz M, Alsaedi A, Shaq A, Hayat T. Impact of chemical reaction on third grade fluid flow with Cattaneo–Christov heat flux. *J Mol Liq.* (2017) 229:501–7. doi: 10.1016/j.molliq.2016.12.103
38. Aiboud S, Saouli S. Entropy analysis for viscoelastic magnetohydrodynamic flow over a stretching surface. *Int J Nonlinear Mech*. (2010) 45:482–89. doi: 10.1016/j.ijnonlinmec.2010.01.007
39. Makinde OD. Second law analysis for variable viscosity hydromagnetic boundary layer flow with thermal radiation and Newtonian heating. *Entropy.* (2011) 13:1446–64. doi: 10.3390/e13081446
40. Loganathan K, Mohana K, Mohanraj M, Sakthivel P, Rajan S. Impact of third-grade nanofluid flow across a convective surface in the presence of inclined Lorentz force: an approach to entropy optimization. *J Therm Anal Calorim*. (2020). doi: 10.1007/s10973-020-09751-3
41. Loganathan K, Rajan S. An entropy approach of Williamson nanofluid flow with Joule heating and zero nanoparticle mass flux. *J Therm Anal Calorim.* (2020) 141:2599–612. doi: 10.1007/s10973-020-09414-3
42. Buongiorno J. Convective transport in nanofluids. *J Heat Transfer.* (2005) 128:240–50. doi: 10.1115/1.2150834
43. Rivlin RS, Thomas AG. Large elastic deformations of isotropic materials. In: Barenblatt GI, Joseph DD, editors. *Collected Papers of RS Rivlin*. New York, NY: Springer (1997). doi: 10.1007/978-1-4612-2416-7_13
44. Fosdick R, Rajagopal K. Thermodynamics and stability of fluids of third grade. In: *Proceedings of the Royal Society of London A: Mathematical, Physical and Engineering Sciences*. London: The Royal Society (1980).
45. Pakdemirli M. The boundary layer equations of third-grade fluids. *Int J Nonlinear Mech.* (1992) 27:785–93. doi: 10.1016/0020-7462(92)90034-5
46. Halim NA, Rizwan Ul Haq, Noor NFM. Active and passive controls of nanoparticles in Maxwell stagnation point flow over a slipped stretched surface. *Meccanica.* (2017) 52:1527–39. doi: 10.1007/s11012-016-0517-9
47. Liao SJ. *The proposed homotopy analysis technique for the solution of nonlinear problems* (Ph.D. thesis), Shanghai Jiao Tong University, Shanghai, China (1992).
48. Liao SJ. An explicit, totally analytic approximation of Blasius viscous flow problems. *Int J Nonlinear Mech.* (1999) 34:759–78. doi: 10.1016/S0020-7462(98)00056-0
49. Wang CY. Free convection on a vertical stretching surface. *ZAMM Z Angew Math Mech.* (1989) 69:418–20. doi: 10.1002/zamm.19890691115
50. Gorla RR, Sidawi I. Free convection on a vertical stretching surface with suction and blowing. *Appl Sci Res.* (1994) 52:247–57. doi: 10.1007/BF00853952
51. Makinde OD, Aziz A. Boundary layer flow of a nanofluid past a stretching sheet with a convective boundary condition. *Int J Therm Sci.* (2011) 50:1326–32. doi: 10.1016/j.ijthermalsci.2011.02.019

Conflict of Interest: The authors declare that the research was conducted in the absence of any commercial or financial relationships that could be construed as a potential conflict of interest.

Copyright © 2020 Loganathan, Muhiuddin, Alanazi, Alshammari, Alqurashi and Rajan. This is an open-access article distributed under the terms of the Creative Commons Attribution License (CC BY). The use, distribution or reproduction in other forums is permitted, provided the original author(s) and the copyright owner(s) are credited and that the original publication in this journal is cited, in accordance with accepted academic practice. No use, distribution or reproduction is permitted which does not comply with these terms.

LIST OF SYMBOLS

a	Stretching rate (s^{-1})
Bi	Biot number
Be	Bejan number
Br	Brinkman number
B_0	Constant magnetic field $(kgs^{=2}\ A^{-1})$
C	Concentration (kgm^{-3})
C_p	Specific heat $(J\ kg^{-1}\ K^{-1})$
C_∞	Ambient concentration (kgm^{-3})
C_w	Fluid wall concentration (kgm^{-3})
Cf_x	Skin friction coefficient
D_B	Brownian diffusion coefficient $(m^2\ s^{-1})$
D_T	Thermophoretic diffusion coefficient $(m^2\ s^{-1})$
E_G	Entropy generation parameter
$f\ (\eta)$	Velocity similarity function
f_w	Suction/injection parameter
h_f	Convective heat transfer coefficient $(W\ m^{-1}K^{-1})$
$\alpha_1,\ \alpha_2,\ \beta$	Fluid parameters
k	Thermal conductivity $(W\ m^{-1}K^{-1})$ K Porous parameter
$\mathcal{L}$	Auxiliary linear operator
Le	Lewis number
M	Magnetic parameter
$\mathcal{N}$	Non-linear operator
Nb	Brownian motion parameter
Nt	Thermophoresis parameter
Nu_x	Nusselt number
Pr	Prandtl number
Q_0	Dimensional heat generation/absorption coefficient
q	Heat flux $(W\ m^{-2})$
Rd	Radiation parameter
Re	Reynolds number
Sh_x	Sherwood number
S	Heat generation parameter
S'''_{gen}	Local volumetric entropy generation rate $(Wm^{-3}K^{-1})$
S'''_0	Characteristic entropy generation rate $(Wm^{-3}K^{-1})$
T	Temperature (K)
T_∞	Ambient temperature (K)
T_f	Convective surface temperature (K)
u_w	Velocity of the sheet $(m\ s^{-1})$
u,v	Velocity components in (x, y) directions $(m\ s^{-1})$
$v_w > 0$	Suction velocity
$v_w < 0$	Injection velocity
x,y	Cartesian coordinates (m)
GREEKS	
χ_m	Auxiliary parameter
$\phi\ (\eta)$	Concentration similarity function
Γ	Slip parameter
γ	Dimensionless thermal relaxation time
η	Similarity parameter
λ_T	Thermal relaxation time
λ	Dimensionless constant
ν	Kinematic viscosity $(m^2\ s^{-1})$
Ω	Dimensionless temperature difference
$\theta\ (\eta)$	Temperature similarity function
τ	Ratio of the effective heat capacity
ρ	Density (kgm^{-1})
σ	Electrical conductivity $(S\ m)$
ψ	Stream function $(m\ s^{-1})$
ζ	Dimensionless concentration difference

(Continued)

Advantages of publishing in Frontiers

OPEN ACCESS
Articles are free to read for greatest visibility and readership

FAST PUBLICATION
Around 90 days from submission to decision

HIGH QUALITY PEER-REVIEW
Rigorous, collaborative, and constructive peer-review

TRANSPARENT PEER-REVIEW
Editors and reviewers acknowledged by name on published articles

Frontiers
Avenue du Tribunal-Fédéral 34
1005 Lausanne | Switzerland

Visit us: www.frontiersin.org
Contact us: frontiersin.org/about/contact

REPRODUCIBILITY OF RESEARCH
Support open data and methods to enhance research reproducibility

DIGITAL PUBLISHING
Articles designed for optimal readership across devices

FOLLOW US
@frontiersin

IMPACT METRICS
Advanced article metrics track visibility across digital media

EXTENSIVE PROMOTION
Marketing and promotion of impactful research

LOOP RESEARCH NETWORK
Our network increases your article's readership